Ground Control in Mining

Tenth Conference

June 10 - 12, 1991

Sponsored by:
U.S. Bureau of Mines

U.S. Mine Safety & Health Administration

West Virginia University

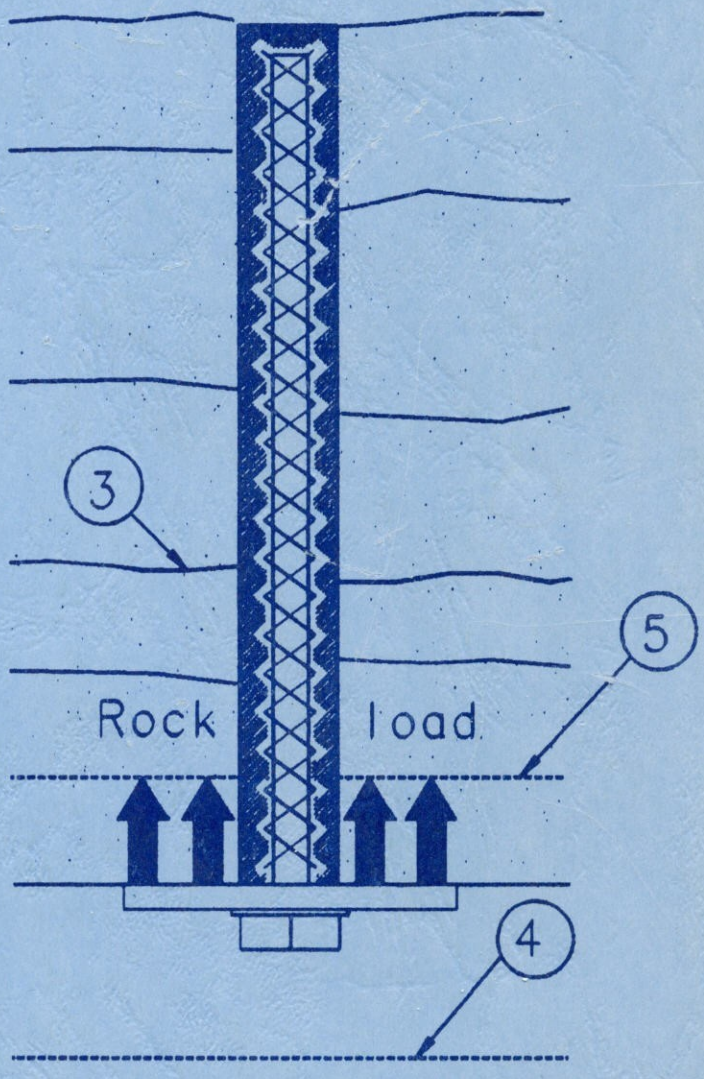

10th International Conference on Ground Control in Mining

PROCEEDINGS

Edited
by
Syd S. Peng

Department of Mining Engineering
College of Mineral and Energy Resources
West Virginia University
Morgantown, WV 26506-6070

Organizing Committee

R. C. Briggs
U. S. Bureau of Mines

F. Carr
Jim Walter Resources, Inc.

I. W. Farmer
University of Arizona

R. Gray
GAI Consultants

M. Karmis
Virginia Polytechnical Institute and State University

A. W. Khair
West Virginia University

S. S. Peng, Chairman
West Virginia University

B. R. Pothini
Island Creek Coal Company

K. K. Wu
Mine Safety and Health Administration

10th INTERNATIONAL CONFERENCE ON GROUND CONTROL IN MINING

TABLE OF CONTENTS

1. Practical Aspects of Longwall Pillar Design, *C. Mark, U. S. Bureau of Mines, Pittsburgh Research Center* . . . . . (1)

2. Assessment of Underground Structural Design, *E. D. Krupa, BethEnergy Mines, Inc., and A. W. Khair, West Virginia University* . . . . . (14)

3. Load and Convergence Measurements in Longwall Faces and Design Guidelines for Face-Support Systems, *R. Ozel, C. Basar, and E. Unal, Middle East Technical University, Turkey* . . . . . (26)

4. A Model for Shield Strata Interaction and Its Implication for Active Shield Setting Requirements, *T. Barczak and D. C. Oyler, U. S. Bureau of Mines, Pittsburgh Research Center* . . (35)

5. Stability of Interpanel-Pillar and Deformation of Gateroad Due to Longwall Mining, *K. Matsui, M. Ichinose, and K. Uchino, Kyushu University, Japan* . . . . . (43)

6. Use of Polymer Grids for Longwall Shield Recovery, *B. E. Travis and R. P. Anderson, Tensar Earth Technologies, Inc.* . . . . . (52)

7. Methods of Controlling Thick and Strong Roof in Longwall Mining, *D. R. Zhu and M. G. Qian, China University of Mining and Technology, China* . . . . . (59)

8. Tensioned Point Anchor Resin System vs. Non-Tensioned Fully Grouted Rebar--Two Case Studies, *J. C. Stankus, Jemmar Corporation* . . . . . (65)

9. Thrust Bolting: A New Innovation in Coal Mine Roof Support, *S. C. Tadolini and D. R. Dolinar, U. S. Bureau of Mines, Denver Research Center* . . . . . (76)

10. An Alternative to a Manual Torque Check on Roof Bolts, *J. A. Cybulski and W. J. Gray, MSHA, Bruceton Safety Center* . . . . . (85)

11. Shear Bond Stresses Along Cable Bolts, *H. S. Mitri and H. Rajaie, McGill University, Canada* . . (90)

12. An Underground Trial of Cable Slings for Remedial Support of Longwall Gateroads, *W. D. Gallant CANMET (Cape Breton), Canada, P. Choquet, Supportek Int'l., and J. MacLachlan and S. Forgeron, Cape Breton Development Corp., Canada* . . . . . (96)

13. Mobile Roof Support for Retreat Mining, *H. G. Wilson, J. H. Fletcher & Co.* . . . . . (103)

14. Application of Time--Domain Reflectometry to Ground Control in Potash Mining, *K. M. O'Connor, U. S. Bureau of Mines, Twin Cities Research Center and T. Zimmerly, Western Ag-Minerals* . . . . (115)

15. An Examination of Energy Calculations Applied to Coal Bump Prediction, *K. A. Heasley, U. S. Bureau of Mines, Pittsburgh Research Center* . . . . . (122)

16. Delineation of Abandoned Workings with an In-Seam Seismic Method, *I. Geldmacher and J. Slade, BHP Engineering (Americas), Inc.* . . . . . (130)

17. Remote Detection of Abandoned Mine Workings Using Radio Imaging Method Techniques, *J. G. Schotsch and T. Sutton, Stolar, Inc.* . . . . . (144)

18. Effects on Surface Topography on the Stability of Coal Mine Openings, *G. M. Molinda, K. A. Heasley, D. C. Oyler, and J. R. Jones, U. S. Bureau of Mines, Pittsburgh Research Center* . . . (151)

19. Site Characterization for Ultra-Close Multi-Seam Mining, *Y. Zhou, C. Haycocks, M. Karmis, and S. G. Haycocks, VPI & SU* . . . . . (161)

20. Mining Under-River in Fuxin Coal Mines, *Y. H. Liang, C. H. Yao, and B. W. Zhou, Fuxin Coal Mine Administration, China* . . . . . (167)

21. Use of DataBase in Ground Control to Identify Weightings and Water Inflows, *G. C. Xiao, R. A. Irvin, and I. W. Farmer, Ian Farmer Associates, United Kingdom* . . . . . (177)

22. Integrating Ground Control and Mine Site Data Through a Geographic Information System, *D. C. Peters and M. A. Smith, U. S. Bureau of Mines, Denver Research Center* . . . . . (184)

23. Determination of the Rock Strength from Portable Rock Tester, *K. F. Unrug and Y. J. Zhang, University of Kentucky* . . . . . (194)

24. Mine Wide Physical Property Trend Identification Using Portable On-Site Test Devices, *T. L. Vandergrift and D. P. Conover, U. S. Bureau of Mines, Denver Research Center* . . . . . (202)

25. Subsidence Prediction in Illinois Coal Basin, *E. Doney, Kerr-McGee Coal Corp. and S. S. Peng and Y. Luo, West Virginia University* . . . . . (212)

26. Determination of the Stopline Subsidence Profile of Phalen 2 West Panel from Within a Near Horizontal Borehole Over the Panel Stopline, *W. D. Gallant, D. J. Forrester, and D. A. Payne, CANMET (Cape Breton), Canada* . . . . . (220)

27. Evaluation of Subsidence Parameters for Inclined Seams in UK Coalfields, *X. L. Yao, D. J. Reddish, and B. N. Whittaker, University of Nottingham, United Kingdom* . . . . . (225)

28. Measurement of Structural Deformation and Tilt During Subsidence, *R. Awasthi, The University of Tennessee, L. R. Powell, U. S. Bureau of Mines, Twin Cities Research Center and E. C. Drumm, The University of Tennessee* . . . . . (233)

29. Drag Pick - Influence of Tool Geometry and Angle of Attack on the Stress Evolution and Cutting Efficiency, *N. I. Aziz, The University of Wollongong, H. Guo, Pasminco Mining, Australia, and G. Rossi, R. Rossi, and P. Trois, University of Caligliari, Italy* . . . . . (243)

30. Roof Sounding Device -- A Loose Rock Detector, *R. C. Repsher, U. S. Bureau of Mines, Denver Research Center* . . . . . (257)

31. Advanced Surveying Method for Measuring Roof Convergence, *M. Z. Rashad and H. A. El-Sageer, Assiut University, Egypt* . . . . . (263)

32. Geomechanical Substantiation of Extraction of Undermined Ore Deposit, *M. V. Kurlenya, S. N. Popov, and I. L. Boltenhagen, Institution of Mining, Novosibirski, USSR* . . . . . (268)

33. Relationship Between Floor Rock Stress and Floor Failure, *X. S. Tan and S. S. Peng, West Virginia University* . . . . . (272)

34. The Influence of Geomining Parameters Over Stress Distribution in and Around Depillaring Faces, *R. Singh, D. Prasad, M. A. Rafiqui, and T. N. Singh, Central Mining Research Station, Bihar, INDIA* . . . . . (281)

35. Finite Element Modeling of Subsidence Induced by Underground Coal Mining: The Influence of Material Nonlinearity and Shearing Along Existing Planes of Weakness, *D. W. H. Su, Consolidation Coal Co* . . . . . (287)

36. The Structural Response of a Steel Lattice Transmission Tower to Mining-Related Ground Movements, *R. W. Bruhn, GAI Consultants, Inc, G. W. Luxbacher and J. R. Ferrell, Island Creek Coal Co., and T. A. Gray, GAI Consultants, Inc.* . . . . . (301)

Author's Index . . . . . (307)

10th INTERNATIONAL CONFERENCE ON GROUND CONTROL IN MINING

PRACTICAL ASPECTS OF LONGWALL PILLAR DESIGN

Christopher Mark, *Mining Engineer*

Pittsburgh Research Center
U. S. Bureau of Mines
Pittsburgh, Pennsylvania

***ABSTRACT

The past decade has provided a wealth of practical experience with longwall pillar design. Design formulas developed specifically for longwalls have proven their value in numerous applications. Analytic methods, including numerical models, have also made important contributions. These advances have been based on basic research into abutment loads, coal pillar mechanics, and the interaction between pillar performance and entry stability.

The goal of this paper is to review the state of the art in longwall pillar design from the standpoint of the practitioner. Actual case histories are presented to illustrate the current capabilities and limitations of pillar design methods. The paper also discusses the advances that can be expected in the future.

INTRODUCTION

Pillar design has long been a central issue for mining research. In the United States, pillar design formulas were first developed for anthracite mining in the first decades of this century (Zern, 1928). Pillar design again became the focus of attention during the mining research "renaissance" of the 1970's and early 1980's. Familiar pillar design formulas were updated in the light of new research (Hustrulid, 1976; Bieniawski, 1984), and powerful analytic and numerical approaches began to be brought to bear.

The rapid growth of longwall mining during the past decade brought a new urgency to the subject of pillar design. Longwall pillars perform the essential function of protecting the gate entries which provide the only access to the face. Blockages in the gates disrupt ventilation patterns and close off emergency travelways, posing serious safety hazards. In addition, the impact of any downtime is magnified on a longwall because such a high proportion of the total mine productive capacity is concentrated at the longwall face.

Developing pillar design methods for longwalls required some new thinking. The goal of entry protection differs from the traditional function of pillar design, which is to prevent "squeezes" caused by widespread pillar failure. The long and narrow geometry of typical gate entry layouts makes a classic "squeeze" highly unlikely. Second, the abutment loads applied to longwall pillars are significantly greater and more complex than those assumed by traditional pillar design methods. Effective longwall pillar design requires some knowledge of abutment loads during all phases of longwall mining, from development all the way into the tailgate.

Considerable progress has been achieved in all these areas. Back-analysis of design performance has established the link between pillar design and gate entry stability, and extensive field measurements have provided insight into the magnitude of abutment loads. As a result tested formulas are now available to assist mine planners in sizing longwall pillars. Analytic and numerical methods have also taken great strides. These advances in design methodology have been accompanied by an awareness of the limitations that still remain to be overcome.

THE POWER OF LONGWALL PILLAR DESIGN

Ten years ago, "trial and error" was the only "method" available for sizing longwall pillars. As many mines first introduced longwalls, they first tried pillar dimensions that had been successful in their previous room-and-pillar developments. All too often the results were unfortunate (Artler, 1985; Gauna, 1988; Brass, 1981; Dangerfield, 1981). Then pillar sizes would be increased over the course of several panels until satisfactory conditions were achieved. Other longwalls experienced difficulties only on some panels, and were often at a loss to explain them.

Still others settled early on a successful design, and then continued to use it without regard to whether the pillars might be wastefully oversized.

Pillar design methods have been able to bring some order into the design process. They reduce a multitude of variables, including the depth of cover, pillar widths, seam height, entry width, panel dimensions, and so forth, into a single, meaningful design parameter--a "stability factor". The stability factor, defined as the ratio between the estimated load-bearing capacity of the longwall pillar system and the estimated design loading, can be used in at least four different applications:

- Preliminary design. Few things can cause more distress to a new longwall operator than to have an otherwise highly successful longwall slowed by serious ground control problems on its first or (more often) second panel. Pillar design formulas can give realistic, conservative estimates of pillar sizes for use in feasibility studies or initial longwall panel design. Two recent, successful examples of preliminary design with pillar formulas were reported at Kerr-McGee's Galatia Mine in Illinois (Doney, 1990) and at Wolf Creek Collieries in Kentucky (Cole et al, 1990).

- Adaptation. No two longwall panels are alike, and as conditions change pillar design formulas help mine planners anticipate rather than react to potential problems. Once a specific stability factor has been shown to be adequate for a given mine, then different designs employing the same stability factor can be employed elsewhere on the property with some confidence. In other words, pillar design formulas can be "calibrated" with site-specific experience.

The depth of cover is the single most important parameter affecting gate entry performance, and in many parts of the coalfields it may change radically from one panel to the next. For example, a Kentucky longwall extracted its first three panels under 1000 feet of cover with excellent conditions. The pillar design employed a 28 and a 100 ft pillar, yielding a stability factor of 1.0. When the same design was used at 1800 ft, the stability factor was reduced to 0.5, and ground conditions were so poor that supplemental support had to be tripled just to maintain a travelway. Pillar design formulas indicated that the width of the large pillar should have been increased to 150 ft to maintain the original stability factor under the greater depth of cover (Barton and Mark, 1989). At a nearby Virginia longwall, pillar widths were increased from 90 ft to 120 ft as the cover has increased from 850 to 1300 ft, and no significant degradation of ground conditions occurred.

Man-made conditions may change as well as natural ones. A common change is a switch from a four- to a three-entry system, or vice-versa. Other mines have kept the same number of entries, but gone from equal to unequal entry centers. Pillar design formulas can show how these changes can be made without beginning all over again "at the bottom of the learning curve".

- Optimization. Longwall pillars that are too large constitute a needlessly wasted resource. An evaluation of survey data collected from 70 longwalls in the early 1980's indicated that the stability factor for tailgate loading was greater than 1.5 approximately 50% of the time (Mark, 1990). In some cases it was as high as 4.0! The same data also indicated that little improvement in gate entry performance is achieved once the stability factor exceeds 1.5. Design methods can be used to safely reduce oversized pillars, thereby improving development drivage rates and adding to the life of the mine.

- Failure Analysis. Several factors may be responsible for the failure of a gate entry, and it is not always obvious what to do about it. Pillar design formulas can quickly indicate whether increasing pillar size could be the solution. In the case of the Kentucky longwall described earlier, the increased depth of cover was clearly identified as the problem, and increasing the pillar size could be expected to help. Many similar cases can be cited, from the rolling hills of southwestern Pennsylvania to the dipping coalbeds of Wyoming.

Increasing the size of the pillars will not always solve the problem, however. A relatively large stability factor can be a clear signal that some other solution is required. For example, hazardous roof conditions developed along the length of one tailgate in Alabama despite a stability factor of 1.4. In this case the problem was apparently low-quality roof support. Once "select" hardwood cribs were substituted for second quality "mixed hardwood", the improvement was sudden and dramatic. In another instance, steel beams had to be used in the tailgate of a Pennsylvania longwall because of roof conditions. The panel was a first panel, however, and its stability factor of 1.7 was much higher than had been safely employed on previous

panels. Severe horizontal stress, due to the presence of an overlying stream valley, was identified as the source of the problem.

These are the strengths of longwall pillar design formulas. They have their limitations too. Chief among these are the difficulties with evaluating abutment loading and pillar strength on a site specific basis. Perhaps more importantly, current longwall pillar design methods do not yet explicitly address all aspects of gate entry design. These issues will be discussed below, after the methods are presented.

LONGWALL PILLAR DESIGN METHODS

Two basic philosophies are available to guide longwall pillar design. The conventional design approach uses large pillars that are sized to carry all the abutment loads to which they will be subjected. The yielding design philosophy, on the other hand, uses only very small pillars which transfer load. At present the vast majority of U.S. longwalls use some form of conventional pillar design, while only a handful of longwalls (all in Utah) employ yielding pillar designs. Because of its wider application conventional pillar design has been the focus of most research.

Longwall pillar design methods may also be classified according to the form that they take. Design formulas consist of relatively simple equations whose output is a stability factor or a required pillar width. Although they represent highly simplified models of the actual problem, they are extremely useful in practical design. Numerical models are far more complex. When properly designed and calibrated, they can be effectively used on panel design, and they can provide valuable insight into ground control problems not strictly related to pillar stability. Far greater efforts are required to use them, however, so they are often less attractive than the "user-friendly" design formulas.

Longwall Pillar Design Formulas

Four longwall pillar design formulas were recently described in a Bureau of Mines Information Circular (Mark, 1990). These are:

- Analysis of Longwall Pillar Stability (ALPS): ALPS was originally developed at the Pennsylvania State University by Mark and Bieniawski (1986), and was later refined at the Bureau of Mines. ALPS is now based on field measurements conducted at 16 longwall panels, and it has been verified by back-analysis of more than 100 case histories.

- Carr and Wilson's Method: A. H. Wilson first developed a method for sizing rib and barrier pillars in British mines during the early 1970's. In 1982, Carr and Wilson modified the original theory to apply to the multientry longwall developments used in the U.S. Carr and Wilson's method has been used extensively by Jim Walters Resources at their Alabama longwalls.

- Choi and McCain's Method: Choi and McCain's method, presented in 1980, was the first design formula developed specifically for the United States. The method was based on field studies, numerical modeling, and observations from Consolidation Coal Co.'s working longwalls in the Pittsburgh seam.

- Hsuing and Peng's Method: Hsuing and Peng's method is unique in that it incorporates some properties of the roof and floor into the pillar design. It was developed from three-dimensional finite element modeling performed at West Virginia University, and is described in the second edition of the book "Coal Mine Ground Control" (Peng, 1986a).

All four of these methods are for conventional pillar design. They each consist of the same three basic elements:

- Estimation of the load applied to the pillar system.
- Estimation of the load-bearing capacity of the pillar system.
- A design criterion, usually a recommended "stability factor."

The methods differ in how they approach each element.

In the first three methods (all but Hsuing and Peng's), the side abutment load is estimated using an approach first developed by King and Whittaker (1971), as shown in figure 1. The only difference between the methods is their choice of the abutment angle ß. ALPS uses ß=21, while the other methods use slightly lower values. For "super critical" panels (figure 1a), the Carr and Wilson's estimate of the side abutment load is 22% lower than ALPS, and Choi and McCain's is 15% lower than ALPS. The differences are even less for "subcritical panels" (figure 1b). Both ALPS and Carr and Wilson's method can also be used to evaluate the distribution of the side abutment load (figure 2).

The critical design loading experienced at a face end (the headgate or tailgate corner) is actually a three-dimensional front abutment, not a two-dimensional side abutment. In ALPS, field measurements were used to develop formulas that estimate the front abutments as a percent of the side abutment. Hsuing and Peng determined the tailgate loading directly from their models.

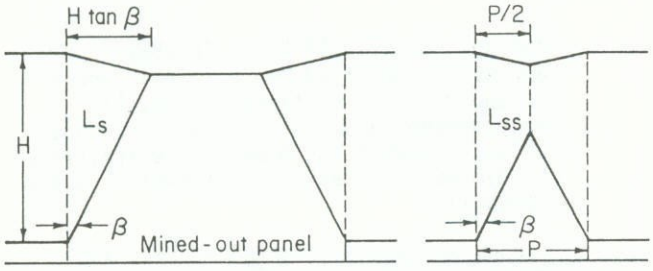

Figure 1. Conceptualization of the side abutment load used in longwall pillar design formulas.

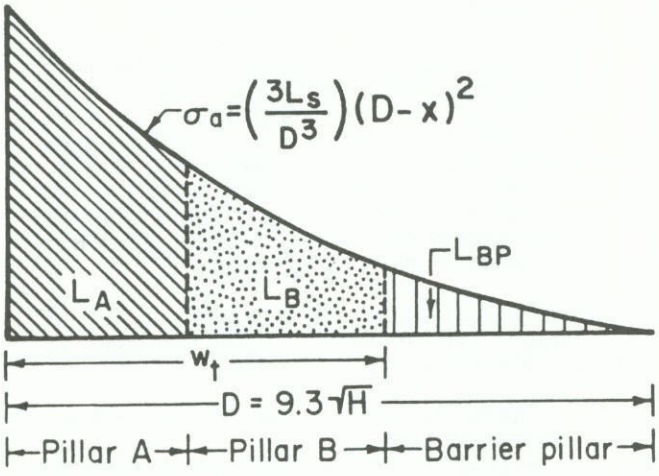

Figure 2. Distribution of the side abutment load.

Two fundamentally different approaches are used for estimating pillar strength and load bearing capacity. The analytic approach, which is derived from the principles of mechanics and which places great emphasis on the triaxial strength of the coal, is used by Carr and Wilson and by Hsuing and Peng. ALPS and Choi and McCain's method employ empirical pillar strength formulas, which were derived primarily from uniaxial testing of coal specimens.

For design criteria, both ALPS and Choi and McCain's methods calculate the stability factor as the load-bearing capacity of the longwall pillar system divided by the total design load. The most recent formulation of Carr and Wilson's method also uses the stability factor approach (Carr and Martin, 1986). These methods can also be used to predict a recommended pillar width once an appropriate stability factor has been set. In the original Carr and Wilson method, the design criterion is the load applied to the pillar closest to the tailgate. Hsuing and Peng's method is the least flexible with regard to design criteria, and only recommends a pillar size.

Some of the methods also have limitations on entry layouts and pillar geometries. Hsuing and Peng's method was developed for an eight-ft seam and a three-entry system employing equal-sized pillars. Choi and McCain's method is also for a three-entry system, but one with a 32-ft "yield" pillar and a large abutment pillar.

The characteristics of the four longwall pillar design formulas are summarized in Table 1.

The predictions of the four formulas are compared in figure 3. The "base case" analyzed in figure 3 is a 6-ft coal seam under 1000 ft of cover, with a 675-ft wide longwall panel. Two three-entry configurations are analyzed, one in which the pillars are equal-sized, and the other in which a 32-ft "yield" pillar is paired with an abutment pillar. The other input parameters and the design criteria used with each formula are described in Mark (1990).

Figure 3 shows that all of the design formulas follow the same general trends. They agree that the depth of cover has a great effect on the required pillar size. In the example, as the cover is increased from 500 to 2000 ft, the formulas indicate that the pillar widths should be increased by factors ranging from 2.5 to 6.0. Most of the formulas also indicate that seam height has a great effect on the required pillar width. Such factors as the panel width, the crosscut spacing, and the entry width are also important, but to a lesser extent.

The Bureau of Mines has developed a large data base of case histories to evaluate the effectiveness of longwall pillar design formulas. In the past year alone, 25 new cases have been added, including nine from western longwalls. The new cases were obtained from Utah, Colorado, Wyoming, Pennsylvania, West Virginia, Alabama, Maryland, and Virginia.

Table 1. Comparison of the Longwall Pillar Design Methods

Characteristic	ALPS	Carr and Wilson	Choi and McCain	Hsuing and Peng
Evaluation of tailgate pillar loading	x			x
Analytical pillar strength method		x		x
Empirical pillar strength method	x		x	
Variable entry configuration	x	x		
Variable coal height	x	x	x	
Roof and floor characteristics				x

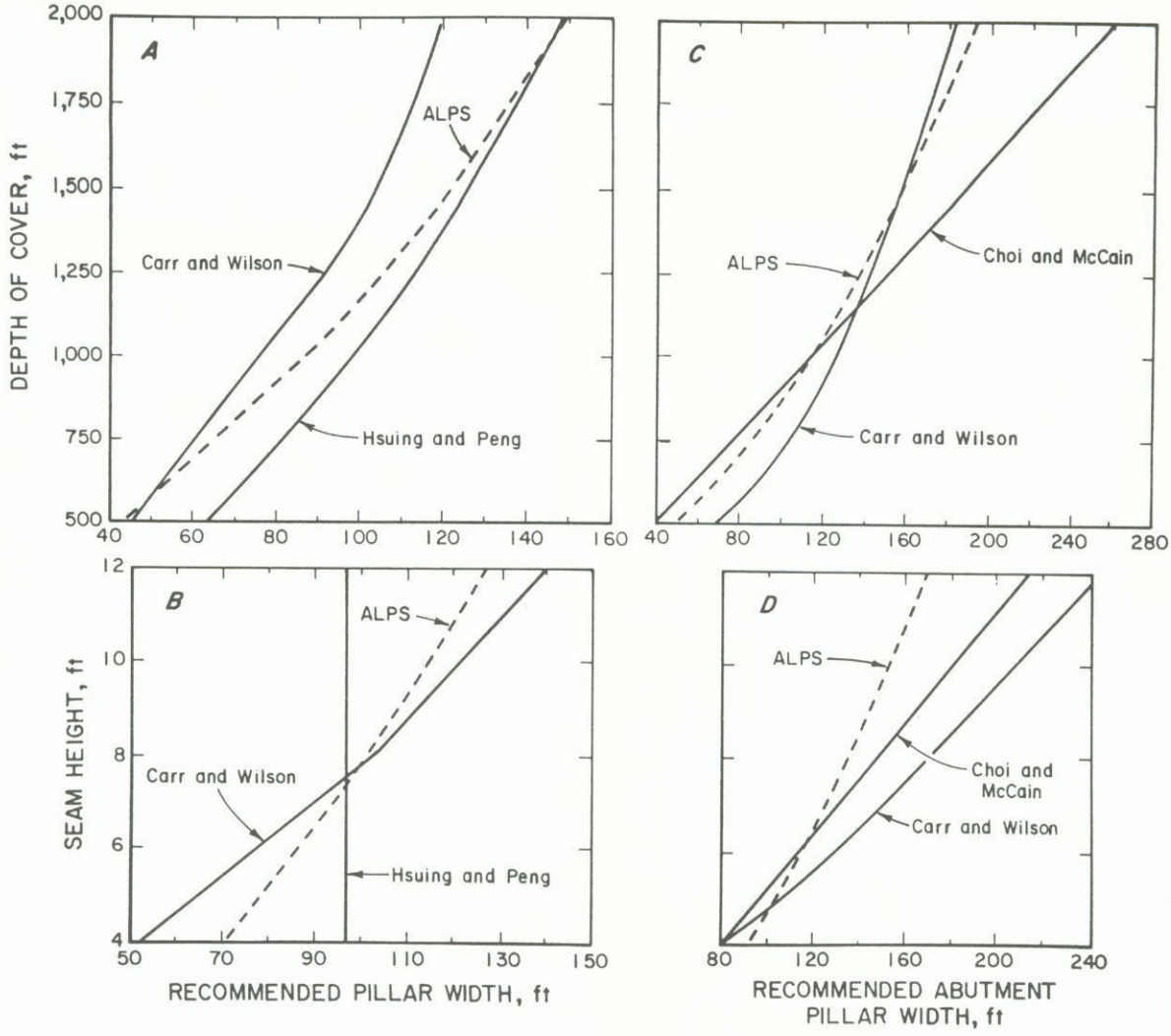

Figure 3. Comparison of the longwall pillar design formulas. A: Three-entry system, equal-sized pillars, 6-ft seam thickness; B: Three-entry system, equal-sized pillars, 1,000 ft of cover; C: Three-entry system, abutment-yield design, 6-ft seam thickness; D: Three-entry system, abutment-yield design, 1,000 ft of cover.

These case histories have been separated into categories of "successful" and "unsuccessful" designs. The unsuccessful designs were those in which intolerable entry conditions occurred, including roof deterioration and falls, severe pillar sloughing and floor heave, and in several cases even pillar bumps. In all cases the problems could be attributed to excessive abutment stresses. The successful designs were those which have been used for many years and in which only minimal ground control problems were reported.

Figure 4 shows the ALPS stability factors calculated for the 80 cases in the data base. Only five unsuccessful designs had a stability factor greater than 1.0, and none exceeded 1.20. On the other hand, nine successful designs had stability factors of less than 1.0. Based on these observations, stability factors of 1.0-1.3 are currently recommended for sizing pillars for tailgate protection with ALPS. The other three longwall pillar design formulas are also capable of segregating the successful cases from the unsuccessful (Mark, 1990).

There is some variability in the required stability factor from mine to mine, as shown in figure 4. For example, longwalls in Virginia and Colorado have successfully employed pillar designs with stability factors of approximately 0.6. At the same time, the stability factor has exceeded 1.0 for unsuccessful designs in Virginia, Wyoming, Pennsylvania, and West Virginia. Identifying the source of this variability, and developing improved design formulas that reduce it, is the central task of current longwall ground control research.

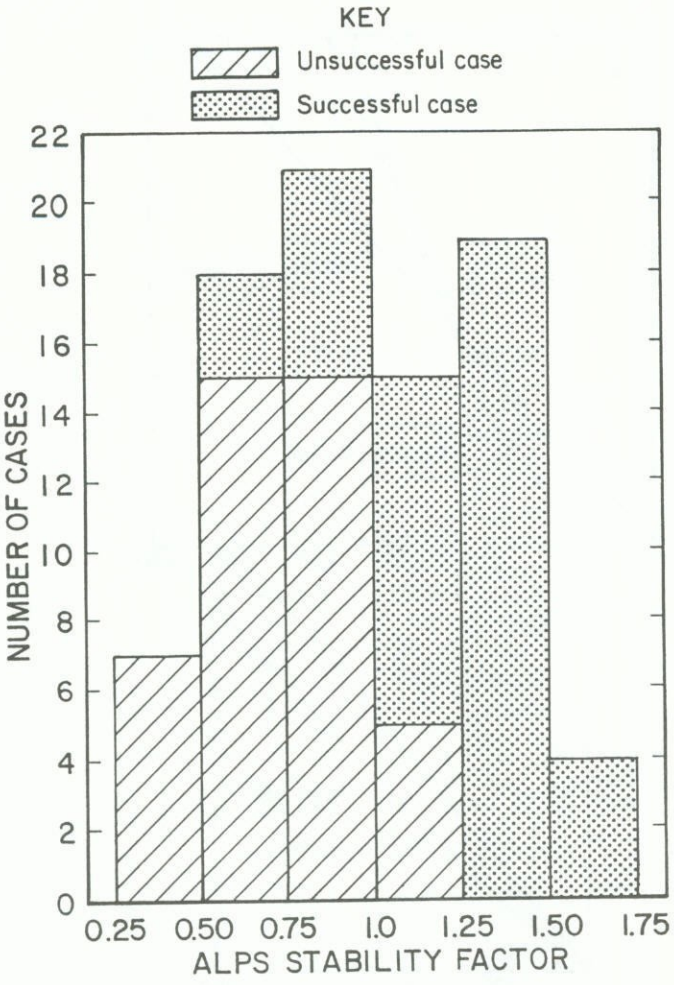

Figure 4. ALPS stability factors calculated for 80 longwall case histories.

Numerical Models for Longwall Pillar Design

Numerical models constitute the other class of longwall pillar design methods. Peng (1986b) lists the three most important advantages of numerical models over empirical formulas as:

- They consider the stiffness of the individual rock layers in the overburden, providing more accurate estimates of pillar loads;

- They consider the effects of roof and floor strata on the strength of the pillars, and;

- They allow more sophisticated failure criteria to be incorporated.

Nevertheless, the use of numerical models in coal mine ground control remains more of an art than a science. Their utility depends largely on the structural analysis background of the practitioner, the limiting assumptions of the specific numerical technique, and the "engineering judgement" applied in setting up the model. Numerical modeling techniques are seldom used for determining absolute stress magnitudes, but rather to establish general trends and relationships between design variables. They have also been very valuable for exploring theoretical concepts of coal pillar mechanics.

Two classes of numerical models have been used extensively for analysis of longwall pillars. These are the finite element and the boundary element methods. The key difference between the two methods is shown conceptually in figure 5 (Kripakov, 1987). The finite element method requires the region of interest to be divided into a network of elements (figure 5a). In the modeling procedure all of the elements in the network interact, and the stresses and displacements are determined throughout the structure. The most recent finite element codes can also include many different types of inelastic, "non-linear" behavior such as cracking, sliding, or creep. The key disadvantage of the finite element method is that it can be very demanding of computer time. Researchers at West Virginia University have made extensive use of finite element models to evaluate longwall pillar performance (Hsuing and Peng, 1985; Hsuing and Peng, 1987; Su and Peng, 1987). Recently, Park and Gall (1989) used a supercomputer for a longwall model that consisted of 7434 mesh elements and featured progressive failure simulation using the Hoek-Brown criterion.

The boundary element method, shown in figure 5b, requires only that the boundaries of the mine openings be divided into elements (discretized). Loadings may then be applied to the boundaries, while the model treats the intact rock as an elastic continuum. The result is that much less computer time is needed to solve the problem. A variation of the boundary element method is the displacement discontinuity method. In a displacement discontinuity model, the seam is represented as a two dimensional thin slit whose properties can be varied from point to point. The surrounding rock mass is still represented as an elastic continuum, but additional seams, bedding planes, or faults can also be represented. The capabilities of displacement discontinuity models have recently been improved with the addition of non-linear coal and gob elements (Zipf and Heasley, 1990). Displacement discontinuity models have been particularly useful for analyzing the complex load distributions occurring with multiple-seam mining (Kripakov et al., 1986; Malecki et al., 1986).

LIMITATIONS OF THE STATE-OF-THE-ART

It is a relatively easy task to generate an impressive list of limitations to our current longwall pillar design methods. At first

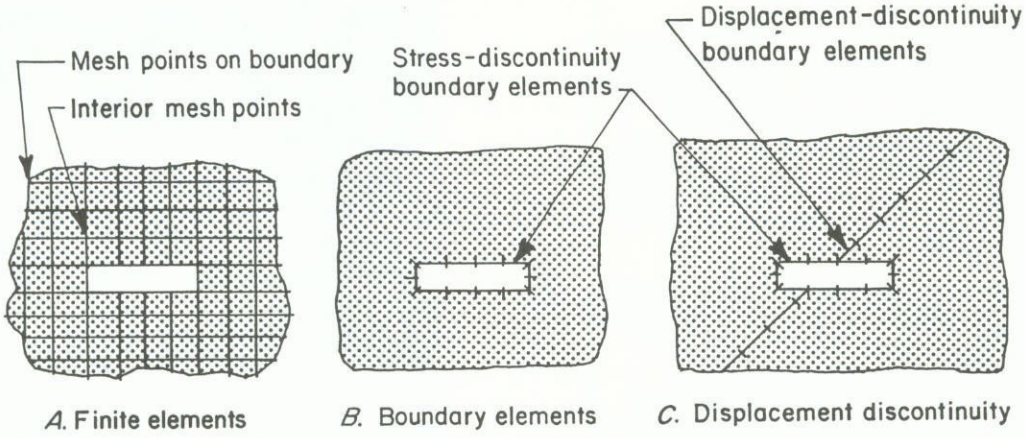

Figure 5. Conceptualization of finite element, boundary element, and displacement discontinuity models.

glance it might seem that, taken together, these flaws must invalidate the entire concept. Yet if our current formulas did not already address many of the most important aspects in the design problem they could not have the success rate demonstrated by figure 4. The goal is to "fine tune" the formulas to reduce the variability evident in figure 4. From a research standpoint, it is essential to focus on those issues which promise to make the greatest practical improvements, rather than those of a more purely scientific interest.

Abutment Load Estimation

The formation of abutment loads is an extremely complex process. Whittaker and King's concept (figure 1) is based on geometry alone, ignoring geology. Subsidence research suggests that the geology-specific behavior of the overburden can have a large effect on surface movements (Karmis et al., 1983), and abutment loads are surely an underground expression of the same phenomena. For example, figure 6 shows stratigraphic columns from two neighboring Virginia longwalls. At the first mine the overburden consists largely of a few massive sandstone units, and we might intuitively expect less-complete caving, more bridging across the gob, and a larger effective "abutment angle". At the second mine, where the overburden contains few massive units, caving might be more complete, resulting in more gob loading and a smaller "abutment angle."

The actual range of abutment angles that have been measured in the field is approximately 10 to 25 degrees (Mark, 1990). The influence of the assumed abutment angle is greatest for "supercritical" panels. For very "subcritical" panels, where the depth of cover is more than twice the panel width, variations in ß have little effect. An important assumption is that the pillars need only carry the load to the midpoint of the panel, an assumption which may not be valid if the previous pillars have failed.

How significant might this variability be in practice? Current Bureau studies are shedding light on the effects of "extremes" of geology and panel geometry on abutment load estimation. Measurements of pillar stresses and the loads in the gob are being made at a site representative of deep-cover conditions with very strong overburden. Preliminary analysis indicates that even here the assumptions used in ALPS yield reasonably accurate estimates of the abutment load. Recent analytical studies have also addressed the influence of overburden behavior on abutment loading (Salamon, 1991).

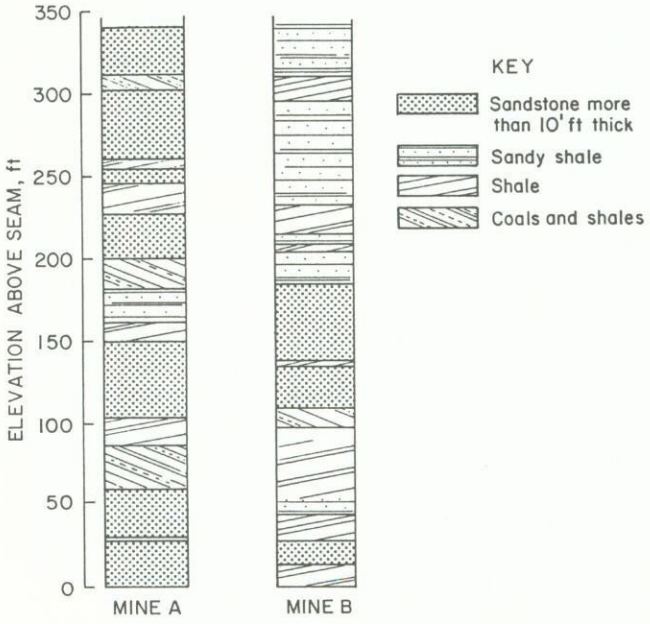

Figure 6. Stratigraphic columns from neighboring Virginia longwalls.
A: 60% of the overburden is massive sandstone.
B: 25% of the overburden is massive sandstone.

Numerical models also have difficulties with abutment load estimation. Finite element models should do the best job, because they can simulate multiple layers and progressive failure of the overburden. But both finite element and displacement discontinuity models are hindered by the need for accurate, field scale, rock properties for the overburden and caved material (gob).

Determining the load carried by the waste, which is in turn determined by the dimensions and stiffness of the gob, is a key concern. Little data on gob characteristics is available. As a result, different modelers have used values for the modulus of the gob that range from 20,000 to 160,000 psi (Maleki, 1990; Kripakov et al., 1988; Hsuing and Peng, 1985). Other researchers have found that changing the gob modulus can change the predicted peak pillar stress by a factor of three (Hackett and Park, 1987). To help resolve this issue, the Bureau is currently testing simulated caved material in the lab (figure 7). Preliminary results indicate that the secant (average) modulus is less than 5000 psi for low-strength gob material subjected to a maximum load of 2000 psi. It also appears that the modulus is an approximately linear function of the applied stress over this load range.

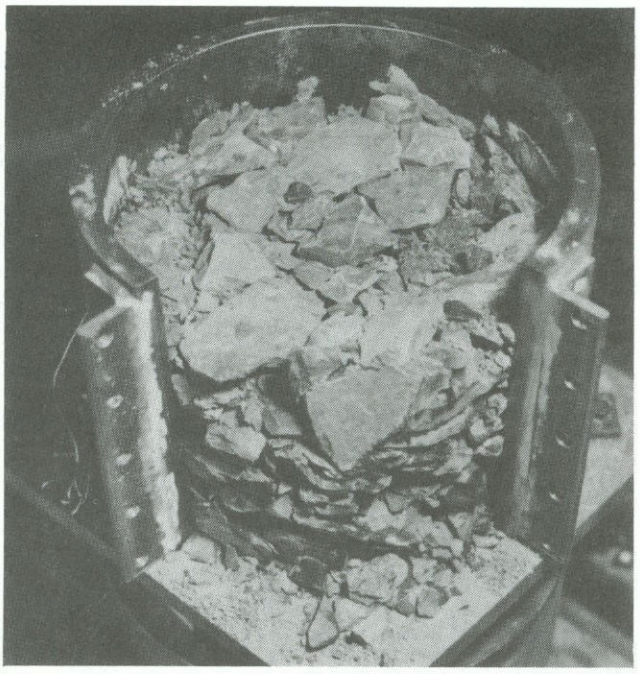

Figure 7. Simulated longwall gob in fourteen-inch diameter compression chamber.

Coal Pillar Mechanics

Current methods for estimating the load bearing capacity of coal pillars are also imperfect. Determination of field-scale material properties remains a problem. Failure mechanics, and constitutive relations in general, raise even more fundamental concerns. Research has barely begun to address the effect of time on pillar strength. In practice it appears that the effects of many of these theoretical shortcomings can be overcome, however.

Modern empirical pillar strength formulas (such as the Bieniawski formula that is used in ALPS) require only a single material property, the "in situ coal strength". The in situ coal strength is defined as the uniaxial compressive strength of coal cube measuring at least three feet on each side. Because such large-scale testing would be prohibitively expensive, the traditional method for determining the in situ coal strength has been to apply a "size-effect scaling factor" to the strength of small coal specimens tested in the lab (Bieniawski, 1984). In the author's opinion, two serious drawbacks largely invalidate the laboratory test approach. First, it is very difficult to determine a meaningful specimen-size coal strength. Laboratory tests on coal are notoriously unreliable because of sampling bias, integrity loss during specimen preparation, and platen effects during testing. For example, a Kentucky operator recently had three different consultants carry out compressive strength tests on coal specimens as part of a longwall feasibility study. The average values reported back were 2700, 5000, and 8500 psi--a range approximately as great as that reported for all U.S. coal seams put together (Singh, 1981).

Better sampling and testing procedures can improve consistency, but leave the second problem of the size effect. There is now considerable evidence that the size-effect scaling factor is not a constant but varies considerably from seam to seam. As figure 8 shows, two-inch specimens from the Pittsburgh seam are approximately twice as strong as similar specimens from the Pocahontas No. 3.

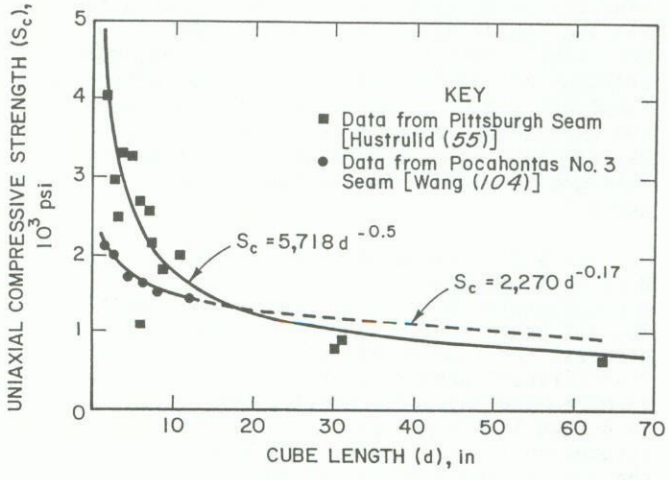

Figure 8. The effect of specimen size observed on the compressive strength of two coal seams.

The disparity is rapidly reduced as the specimen size is increased, because of the different size effects in the two seams.

Fortunately, experience has shown that site-specific coal strength data is seldom necessary for longwall pillar design. For several years this author has consistently assumed the in situ coal strength used in ALPS is 900 psi. There has been no indication that the variability in required stability factor (figure 4) can be explained by variations in coal strength. It may be that while the laboratory strength varies considerably from seam to seam, the in situ strength is more consistent, as suggested by figure 8. Barton and Bandis (1982) observed a similar scale effect on the strength of rock joints.

It is also possible that the uniaxial compressive strength is less important when considering the strength of the "squat" (large width-to-height ratio) pillars typical of longwalls. It is widely accepted that the strength of squat pillars is largely derived from the confinement that is generated within them. Analytic and numerical models therefore focus on the triaxial strength of coal. Although it has been subject to less study, it would seem that the triaxial strength would be subject to the same reliability and scaling problems as the uniaxial strength. More fundamentally, the behavior of coal under very high confining pressures, like those occurring in the core of a "squat" pillar (a pillar with a large width-to-height ratio), is not well understood.

Figure 9 illustrates how current theories predict the strength of coal pillars. It compares five empirical formulas, three analytic formulas, and two numerical model studies using a pillar with a width-to-height ratio of five as the baseline. The figure shows that while the most of the theories predict similar strengths for slender pillars, they diverge widely in their predictions of the strength of very wide pillars.

The theories compared in figure 9 can be divided into three categories. The first group, which includes the numerical models of Hsuing-Peng and Kripakov, Wilson's formula, and Salamon's "squat" formula, indicate that the pillar strength increase exponentially as the pillar width is increased. These theories all assume that confinement grows rapidly within squat pillars, allowing the core stress to build indefinitely. A second group of theories, comprised of the Salamon-Munro and Holland-Gaddy empirical formulas and Barron's analytic formula, indicate the core stress, and the pillar strength, tend towards some maximum, limiting value. A final group of empirical formulas, those of Bieniawski, Sheory, and Obert-Duvall, take a middle road, implying a linear increase in pillar strength.

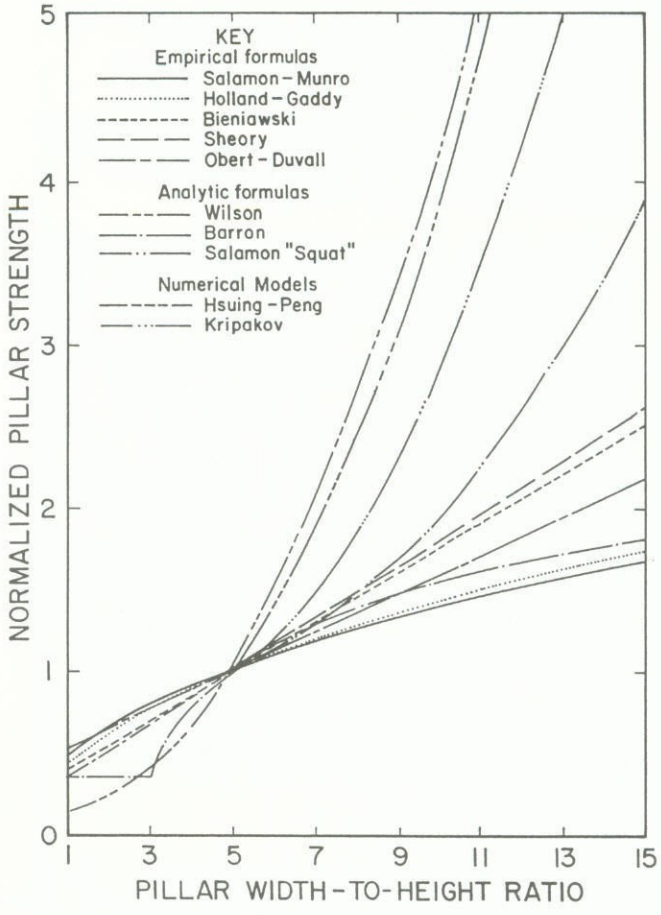

Figure 9. Trends in coal pillar strength predicted by different theories. Exponential increases with increasing pillar width are predicted by Wilson's formula (Wilson, 1983), finite element models (Hsuing and Peng, 1985; Kripakov, 1981), and Salamon's squat pillar formula (Salamon and Wagner, 1985). Linear increases are predicted by three empirical formulas, Bieniawski's (Bieniawski, 1984), Obert-Duvall's (Bieniawski, 1984), and Sheory's (Sheory et. al., 1986). Asymptotic increases are predicted by Barron's theory (Barron, 1984), the Holland-Gaddy formula (Bieniawski, 1984), and the Salamon-Munro formula (Bieniawski, 1984).

Several recent developments may prove useful in resolving these issues. New theoretical concepts proposed by Barron (1984) have raised the issue of the brittle-ductile transition and its applicability to coal pillars. Mark et al. (1988) developed techniques for integrating empirical and analytical coal strength formulas, and for indirectly determining in situ triaxial strength parameters from field tests. Numerical modeling and field observations reported by Iannacchione (1990) indicate that the strength of many pillars may be determined by the low-strength frictional contact between

the pillar and the roof or floor, rather than any characteristic of the coal itself. Finally, measurements have recently been conducted in the cores of large, highly stressed longwall pillars (Campoli and Barton, 1990) and these could provide the information needed to develop and verify constitutive relations for highly-stressed coal.

One final aspect of pillar mechanics that has immediate practical implications for pillar design is the effect of time. It is well known that the strength of rock decreases the longer the load is applied. In longwalls, the maximum design loading at the tailgate is applied for a relatively short time. As stated earlier, the design criterion for this application is ALPS stability factor in the 1.0-1.3 range. It should be expected that long-term applications, such as bleeders or mains, should have other criteria. At one gassy Pittsburgh seam longwall four separate bleeder systems had been blocked by roof falls. Analysis indicated that the problems occurred when the stability factor dipped below 1.5. It appears that such long-term applications may require the stability factors originally suggested by Bieniawski, or 1.5-2.0. The effect of time also becomes more important when designing for "super" longwall panels, because of the longer period of time that the gates will be in use.

Gate Entry Stability

Abutment loads and pillar mechanics relate directly to longwall pillar stability. But for longwalls the bottom line is protecting the gate entries. There is an undeniable empirical correlation between gate entry stability and pillar design, as established by the case histories represented in figure 4. But there is no reason to believe that pillar size is the only factor determining gate entry performance. This author's experience is that two other factors must be considered in a successful gate entry design. These are roof rock quality and artificial support/entry width.

The following example illustrates the relationship between these three elements. Geotechnical surveys were conducted underground at three longwalls operated by a major coal company. The data was summarized as follows:

Mine X
Depth of cover: 650 ft
Pillar design: Three entries on 55 and 70 ft centers
Roof rock: Strong, massive siltstone and sandstone
Primary tailgate roof support: 6-ft resin bolts on 5-ft centers
Secondary tailgate roof support: Three rows of wood cribs

Mine Y
Depth of cover: 1000 ft
Pillar design: Three entries on 90 and 60 ft centers
Roof rock: 4-ft of laminated shale overlain by siltstone
Primary tailgate roof support: 5-ft point-anchor resin bolts on 5-ft centers
Secondary tailgate roof support: Two rows of wood cribs

Mine Z
Depth of cover: 900 ft
Pillar design: Two entries on 100 ft centers
Roof rock: Weak, slickensided mudstones and laminated shales
Primary tailgate roof support: 6-ft point-anchor resin bolts and trusses
Secondary tailgate roof support: One row of yielding steel posts

From this information the ALPS stability factors were calculated, and ratings were applied to the roof quality and tailgate roof support as follows:

Parameter	Mine X	Mine Y	Mine Z
ALPS SF	0.6	0.5	1.0
Roof Quality	A	B	E
Tailgate Support	B	C	C

Where: "A" = Much greater than average
"B" = Greater than average
"C" = Average
"D" = Less than average
"E" = Much less than average

Based on pillar design alone, Mine X and Mine Y both seemed like candidates for tailgate failure. When all factors were considered, however, Mine Z was actually at greater risk than Mine X. Serious tailgate roof control problems later did occur at both Mines Y and Z, while Mine X was untroubled.

This author believes that it is these factors, roof quality and artificial support, that explain the lion's share of the variability in figure 4. Current research efforts are therefore focussed on developing procedures for including them directly in the design process. The first step is to establish quantitative relationships between the three variables. Geotechnical surveys have now been conducted at nearly 50 longwalls, and the data that has been collected is being evaluated using multivariate statistical techniques. The goal is to develop guidelines for selecting the appropriate ALPS stability factor and the artificial support based on site-specific geologic evaluation.

At present, these factors can be indirectly incorporated into the design process by the technique of "calibration" that was described earlier. The site-specific stability factors

determined through back-calculation largely reflect the influence of roof quality and support. So long as neither of these factors changes significantly, the stability factors can be used as the design criteria for future panels.

Yielding Pillar Design

Although 95% of U.S. longwalls employ some form of conventional pillar design, interest in yield pillar design remains strong. The reason is that conventional pillar designs can have some important disadvantages in deep-cover, multiple seam, and/or bump prone conditions. These conditions are rare today, but they will be increasingly prevalent in the future.

The greatest disadvantage of conventional pillar designs in deep cover is that the required pillar size can become extremely large. In the Warrior basin, where the cover approaches 2200 ft, pillars measuring 220 by 300 ft are required just to maintain a stability factor of 1.0. Such large pillars are quite expensive, due to the value of the coal that they contain and the additional time that is necessary to develop them. Yield pillars under similar depths might be one-tenth as wide. Conventional pillars have further disadvantages in multiple-seam environments because they can cause destructive stress concentrations in overlying and underlying seams. Yield pillars are incapable of storing stress, offering significant advantages under these extreme conditions.

The development of design guidelines for yielding pillar systems still presents considerable challenges. Yielding pillar systems require the development of a destressed zone within a pressure arch. Therefore the load transfer mechanics of the roof above the pillars are of immediate concern. These will be largely determined by the geology of the roof. The post-failure load-deformation relations for the pillars themselves are also essential. The importance of the time of pillar yielding, whether during development or during longwall mining, also needs to be determined. It will also be necessary to determine whether certain roof types are more compatible with yielding pillar designs than others, and what the requirements are for artificial support. The span of the yielding pillar system, which is largely determined by the number of entries, will be the critical design parameter.

CONCLUSIONS

The longwall method is currently the safest and most productive for mining coal underground. For a longwall face to reach its full potential, stable gate entries must be maintained. Effective pillar design is often the single most important step a longwall operator can take to protect the gate entries. During the last ten years powerful new pillar design methods have been developed specifically for longwalls, and these methods have removed much of the uncertainty which used to surround gate entry performance.

Current research continues to advance the art and science of longwall pillar design. The next big step for empirical formulas will be to quantify the effects of roof quality and artificial support. The goal is to develop a design methodology for longwall gate entries, of which pillar design will be a critical part.

Fundamental research into abutment load formation and pillar mechanics will help improve the reliability of numerical models. Key factors that are currently being investigated include gob characteristics, the effects of geology, depth, and panel geometry on abutment loading, the strength of squat coal pillars, and the influence of time on pillar strength. Finally, research into the mechanics of yield pillar systems will prepare for the difficult deep-cover, multiple seam, and bump-prone conditions that will become increasingly common in tomorrow's mines.

REFERENCES

1. Artler, R. L. Pillar Design--Continuous Miner Butt Section and Longwall Development Section. Paper in Proceedings 4th Conference on Ground Control in Mining. WV Univ., Morgantown, WV, 1985, pp. 160-165.

2. Barron, K. An Analytical Approach to the Design of Coal Pillars. CIM Bull., v. 77, No. 868, Aug., 1984, pp. 37-44.

3. Barton, N. and Bandis, S. Effects of Block Size on the Shear Behavior of Jointed Rock. Paper in Issues in Rock Mechanics, Proceedings of the Twenty-Third Symposium. UC-Berkeley, Berkeley, CA, 1982, pp. 739-760.

4. Barton, T. M., and C. Mark. Field Evaluation of Three Longwall Pillar Systems in a Kentucky Coal Mine. BuMines RI 9283, 1989, 13 pp.

5. Bieniawski, Z. T. Rock Mechanics Design in Mining and Tunneling. A. A. Balkema, 1984, 272 pp.

6. Brass, J. F. The Evolution of a Longwall System to Suit the Deep Mines in Alabama. Paper in Longwall-Shortwall Mining, State of the Art. Soc. Min. Eng. AIME, 1981, pp. 179-182.

7. Campoli, A. A., T. M. Barton, F. C. Van Dyke, and M. Gauna. Mitigating Destructive Longwall Bumps Through Conventional Gate Entry Design. BuMines RI 9325, 1990, 38 pp.

8. Carr, F., and E. Martin. Development of Pillar Design Alternatives for the Control of

Abutment Stresses During Retreat Longwall Mining in Deep Coal Mines. Paper in Coal Mining Technology, Economics, and Policy 1986, Session Papers from the AMC Coal Convention. Am. Min. Congr., 1986, 14 pp.

9. Carr, F., and A. H. Wilson. A New Approach to the Design of Multi-Entry Developments for Retreat Longwall Mining. Paper in the Proceedings of the 2nd Conference on Ground Control in Mining. WV Univ., Morgantown, WV., 1982, pp. 1-21.

10. Choi, D. S., and D. L. McCain. Design of Longwall Systems. Trans. of the Soc. Min. Eng. AIME, v. 268, 1980, pp. 1761-1764.

11. Cole, J. D., M. Zik, P. M. Lin, P. Tsang, and S. S. Peng. Design of Three-entry System for Super Longwall Panels. Paper in Proceedings of the 9th International Conference on Ground Control in Mining. WV Univ., Morgantown, WV., 1990, pp. 107-116.

12. Dangerfield, B. Longwall Experience in the Pittsburgh Seam. Supplement to the Proceedings of the 1st Conference on Ground Control in Mining. WV Univ., Morgantown, WV., 1981, 6 pp.

13. Doney, E. D. Birth of a Longwall--Initial Planning to Post-Subsidence Mitigation--A Case Study. Paper in Proceedings of the 9th International Conference on Ground Control in Mining. WV Univ., Morgantown, WV., 1990, pp. 298-302.

14. Gauna, M., B. R. Pothini, and H. E. Hamilton. Practical Rock Mechanics for Safety and Productivity Improvement. Paper in 7th International Conference on Ground Control Proceedings. WV Univ., Morgantown, WV, 1988, pp. 126-136.

15. Hackett, T. and H. Park. Ground Control Analysis of Multi-Slice Mining for Thick Western Coal Seams. Soc. Min Eng. AIME preprint 87-39, 1987, 8 pp.

16. Hsuing S. M. and S. S. Peng. Control of Floor Heave with Proper Mine Design-Three Case Studies. Min. Sci. and Tech., v. 4, 1987, pp. 257-272.

17. Hsuing, S. M., and S. S. Peng. Chain Pillar Design for U.S. Longwall Panels. Min. Sci. and Technol., v. 2, pp. 279-305.

18. Hustrulid, W. A. A Review of Coal Pillar Strength Formulas. Rock Mech, v. 8, No. 2, 1976, pp. 115-145.

19. Iannacchione, A. T. The Effects of Roof and Floor Interface Slip on Coal Pillar Behavior. Paper in Rock Mechanics contributions and Challenges: Proceedings of the 31st U.S. Symposium. A. A. Balkema, 1990, pp. 153-160.

20. Karmis, M., T. Triplett, C. Haycocks, and G. Goodman. Mining Subsidence and Its Prediction in the Appalachian Coalfield. Paper in Proceedings of the 24th U.S. Symposium on Rock Mechanics, 1983, pp. 665-675.

21. King, H. J., and B. N. Whittaker. A Review of Current Knowledge on Roadway Behavior. Paper in the Proceedings of the Symposium on Roadway Strata Control. Inst. of Min. nd Metall., 1971, pp. 73-87.

22. Kripakov, N. P. Numerical Modeling in Mine Structure Design. Paper in Underground Mining Methods and Technology, Elsevier Science Publishers, Amsterdam, 1987, pp. 441-455.

23. Kripakov, N. P., L. A. Beckett, D. A. Donato, and J. S. Durr. Computer-Assisted Mine Design Procedures for Longwall Mining. BuMines RI 9172, 1988, 38 pp.

24. Kripakov, N.P., L. A. Beckett, and D. D. Donato. Loading on Underground Mine Structures Influenced by Multiple Seam Interaction. Chap. in International Symposium on the Application of Rock Mass Characterization Techniques in Mine Design (New Orleans, March, 1986). Soc. Min. Eng. AIME, 1986, pp. 225-236.

25. Kripakov, N. P. Analysis of Pillar Stability on Steeply Pitching Seam Using the Finite Element Method. BuMines RI 8579, 1981,

26. Malecki, H. N., J. F. T. Agapito, M. Wansgard, and J. Cort. Gateroad Design Layout for Two Seam Longwall Mining. Int. J. of Min. and Geol. Eng., No. 4, 1986, pp. 111-127.

27. Maleki, H. N. Development of Modeling Procedures for Coal Mine Stability Evaluation. Paper in Rock Mechanics Contributions and Challenges: Proceedings of the 31st U.S. Symposium. A. A. Balkema, 1990, pp. 85-92.

28. Mark, C. Pillar Design Methods for Longwall Mining. BuMines IC 9247, 1990, 53 pp.

29. Mark, C., J. M. Listak, and Z. T. Bieniawski. Yielding Coal Pillars--Field Measurements and Analysis of Design Methods. Paper in Key Questions in Rock Mechanics: Proceedings of the 29th U.S. Symposium on Rock Mechanics (Minneapolis, MN, June, 1988). A. A. Balkema, 1988, pp. 261-270.

30. Mark, C., and Z. T. Bieniawski. An Empirical Method for the Design of Chain Pillars in Longwall Mining. Paper in Rock Mechanics: Key to Energy Production, Proceedings of the 27th US Symposium on Rock Mechanics (Tuscaloosa, AL, July, 1986). Soc. Min. Eng. AIME, 1986, pp 415-422.

31. Park, D. W., and V. Gall. Supercomputer Assisted Three-Dimensional Finite Element Analysis of a Longwall Panel. Paper in Rock Mechanics as a Guide for Efficient Utilization

of Natural Resources: Proceedings of the 30th U.S. Symposium. A. A. Balkema, 1989, 133-140.

32. Peng, S. S. Case Studies Illustrate the Need for a New Concept of Coal Pillar Design. Mining Engineering, v. 38, No. 11, 1986, pp. 1033-1035.

33. Peng, S. S. Coal Mine Ground Control (2nd Edition). Wiley, 1986, pp. 243-245.

Salamon, M. D. G. Deformation of Stratified Rock Masses: A Laminated Model. J. S. Af. Inst. Min. Met., v. 91, No. 1, January, 1991, pp. 9-26.

34. Salamon, M. D. G., and H. Wagner. Practical Experiences in the Design of Coal Pillars. Paper in the Proceedings of the 21st International Conference of Safety in Mines Research Institutes, Balkema, 1985, pp. 3-10.

35. Sheory, P. R., M. N. Das, S. K.Bordia, and B. Singh. Pillar Strength Approaches Based on a New Failure Criterion for Coal Seams. Int. J. Min. Geol. Eng., No. 4, 1986, pp. 273-290.

36. Singh, M. M. Strength of Rock. Chapter 5 in Physical Properties of Rocks and Minerals. McGraw-Hill, 1981, pp. 83-119.

37. Su, W. H. and Peng, S. S. Cutter Roof and Its Causes. Min. Sci. and Tech., v 4, 1987, pp. 113-132.

38. Wilson, A. H. An Hypothesis Concerning Pillar Stability. Min. Eng. (London), v. 131, No. 141, June, 1972, pp. 409-417.

39. Wilson, A. H. The Stability of Underground Workings in the Soft Rocks of the Coal Measures. Int. J. Min. Eng., v. 1, 1983, pp. 91-187.

40. Zern, E. N. (ed). Coal Miners' Pocketbook (Twelfth Edition). Mcgraw-Hill, New York, 1928, pp. 641-645.

41. Zipf, R. K., and K. A. Heasley. Decreasing Coal Bump Risk Through Optimal Cut Sequencing with a Non-Linear Boundary Element Program. Paper in Rock Mechanics contributions and Challenges: Proceedings of the 31st U.S. Symposium. A. A. Balkema, 1990, pp. 947-954.

10th INTERNATIONAL CONFERENCE ON GROUND CONTROL IN MINING

ASSESSMENT OF UNDERGROUND STRUCTURAL DESIGN

Eugene D. Krupa, *Special Engineer*
BethEnergy Mines, Inc.

and

A. Wahab Khair, *Professor*
Department of Mining Engineering
West Virginia University

ABSTRACT

Mine 33 of Beth Energy has serious and complex roof cutter problems causing delay of the advance rate of both the entry development and longwall face retreat. The cost of maintaining these entries is very high due to the requirement of very heavy artificial supports. It was suspected that this problem was caused by multiple factors including high in–situ horizontal stresses and weak roof in the problem areas. In order to alleviate the problem, proper design of panel entry and roof reinforcement were considered.

This paper presents the results of extensive measurements in experimental panel entries of Mine 33 in order to assess the performance of the designed structure and roof support system during the entry development and longwall retreat. An experimental panel entry has been designed and implemented. The designed parameters were varied seeking for the most ideal parameters which provide stable roadways. Changing these parameters accompanied instrumentation of roof, floor, and pillars. Typical instrumentation, including stress meters, convergence measurement stations, and borehole borescope were utilized. Extensive monitoring of the behavior of the designed structure and support system led to the development of a complete stress–deformation history of the roadway and an ideal roof reinforcement, support system, which reduced the cost of entry development by less than a third of the previous method.

BACKGROUND

Beth Energy No. 33 mine is located in Ebensburg, Cambria County, Pennsylvania. Cambria County is located within the Allegheny mountain section of the Appalachian Plateau Province. The geologic structures in the local area include folds, faults, joints, and cleats in the coal. These geologic structures seem to have a genetic relationship with the Allegheny Front (1). The mine's geologic structures have been influenced mainly by Ebensburg Anticline and Wilmore Syncline (2). Current longwall panels lay along the western limb of the Wilmore Syncline oriented south 30° west. Surface topographic relief in the area is less than 500 feet. Overburden thickness varies from 600 feet to 800 feet.

The coal seam in the Beth Energy No. 33 mine is part of the Lower Kittanning formation. The B–seam thickness varies from 48 to 60 inches and consists of two parts. The lower part is 44–48 inches of soft coal and the remainder is bony coal. The coal seam slightly dips from 0 to 6 degrees to the east–south direction. Panel entries are driven 200 feet wide, consisting of three 18–20 feet wide entries and two pillars of 60 x 80 feet block. The mine has a history of cutter roof problems in the entries where the development was ahead of the other entries. This cutter roof problem has delayed the advance rate of both entry development and retreat longwall face considerably and the cost of maintaining these entries was very high due to the requirement of very heavy artificial supports. It was suspected that cutter roof in Mine No. 33 was caused by multifactors including high in–situ horizontal stresses and relatively weak roof in the problem areas. The approach to remedy the problem was two–fold, 1) reducing the effect of in–situ stresses on the roof strata through design of proper panel entry design and implementing yield pillar concept and 2) reinforcement of roof strata considering effective roof reinforcement, support system, and its implementation procedure. Assessment of the effectiveness of the design of the panel entry, roof reinforcement and implementation procedure for the roof reinforcement is the major objective to be presented in this paper.

Methodology

As indicated earlier, to remedy the problem, both reduction of horizontal stresses and reinforcement of roof strata were considered. The combined efforts were expected to stabilize roof strata in the entries. The efforts consisted of

proper design of panel entry and roof reinforcement system. Design of underground structure requires knowledge of stresses (in–situ and mining induced stresses) mine geology, physical and mechanical properties of rock/coal surrounding the opening and geometry and layout of the structure. Assessment of the design parameters involves instrumentation of the structure and measures stresses and strains developed in the structure during the course of action. Hence the performance of the structure can be evaluated and the measured stresses and strains history can be compared with the expected values. To achieve the objectives the following line of action was taken:

Analysis of Mine Geology

Data from core logs of the boreholes associated with current longwall panels revealed that the majority of the strata in the overburden consist of shale and sandstone. The remainder of the strata is underclay, claystone and limestone. The lithologic composition of the area indicated that the immediate roof generally consists of gray shale and dark shale, some siltstone, and thin tabular sandstone as shown in Figure 1. The stratigraphic sections of the overburden–coal–floor indicated that coal seams show some degree of variation in thickness along N–S direction with intermittent appearance of bony coal at the top of the seam. However this variation decreases along E–W direction with less appearance of the bony coal. A thin rider coal is also present from 10 to 20 feet above the Lower Kittanning coal seam. The isopach map of the floor shows that the floor is composed of shale, fire clay, and sandstone as shown in Figure 2.

Standard laboratory tests on lower parts of the seam, soft coal, indicated that the coal has a compressive strength of 633 psi. A series of triaxial compressive tests were conducted on the coal and results exhibited significant effect of confinement on shear strength of coal having an angle of internal friction of 37°. The triaxial stress constant for coal is found to be 3.65. Laboratory tests on the immediate roof rock indicated that it is highly laminated shale, with weak binding, and has a compressive strength of approximately 29030 psi.

Determination of Apparent In–situ Stresses

An overcoring technique was employed to determine in–situ stresses utilizing U.S. Bureau of Mines deformation gauge and recommended procedure (Hooker et al., 1969; Bickel and Donato, 1988). A number of inclined holes were drilled into the coal seam from an underground entry (see Figure 3). Due to discing of the roof strata along the bedding plane, and crushing of the side wall of the hole in coal seam during overcoring, only three holes to a maximum depth of 15 feet were overcored and hole deformations were measured. Overcoring proceeded to a distance of at least 9 inches beyond the planes of measurement. The relationship between the location of measured diametral deformation of the borehole and depth of the overcoring is given in Figure 4. Measured deformations were used in calculation of the in–situ stresses, utilizing values of Young's modulus, E, obtained from testing the overcored sample in biaxial stress chamber.

The values of Young's Modulus, E, presented in Table 1 corresponding to three–diametral deformation (E_1, E_2, E_3, 60° apart in the same borehole) in the coal seam. Two sets of data were obtained from the three holes. The first set is measured in three holes at a depth of 7–10 feet while the second set was obtained at hole depths varying from 11–15 feet. Using Poisson's ratio, determined in uniaxial compression test, and values of E given in Table 1, the stresses were calculated and given in Table 2. The measured stress components in the second set are lower than the first set because the measured stresses in the second set are at deeper positions in the holes, hence less affected by the entry.

Measured in–situ stresses, both vertical and horizontal, corresponding to the depth of overburden are very high. Part of the increase in values of in–situ stress is probably due to the effect of the entry and its proximity to the planes of measurement. Therefore, measured in–situ stresses are not the true representatives of the in–situ stresses in the area and it should be considered as the apparent in–situ stresses, combination of in–situ and induced by entry development, and these magnitudes were considered in analysis of roof stability.

Assessment of the Problem

Fractures, near parallel to the entry face direction were observed in the roof strata, extending through the coal seam. These fractures were there before development of the entry, indicating that this area had experienced tectonic disturbances and evidence of residual stress is there.

Two types of roof problems were observed in the mine which lead to the caving of the mine roof in the entries. These are heavy roof and cutter roof conditions. Both of these problems are initiated by high horizontal stresses and weak/laminated roof strata at the problem area. Heavy roof develops under the action of horizontal stress and the laminated roof with insufficient reinforcement is pushed down and sags. This results in caving of the roof due to the bending stress in the roof strata. Cutter roof was only observed at the rise side of the No. 1 entry which is located at the far rise side. Cutter roof at the mine was suspected to be due to the combined action of vertical and horizontal stress, resulting in vertical and lateral displacements of roof, at the cutter area, respectively.

Design of Panel Entry System

The results of the research at the mine and in the laboratory indicated that apparent in–situ stresses are very high in the mine, and that roof strata are mostly weak. The

direction of average maximum horizontal stress, S_2, is almost parallel (approximately 20°) to the panel entry face, initiating cutter roof along the direction of the panel entry development (see Figure 3). Average minimum horizontal stress, S_3, is approximately 30% less than the maximum and acts almost perpendicularly (approximately 82°) to the direction of the panel entry face. Therefore, reorientation of the panel entry system could slightly improve the cutter roof problem. However, in this stage of the mine plan, panel entry reorientation would not have been feasible. Furthermore with the existence of high vertical stress and pre–existing fracture pattern in the roof, reorientation of the panel entry may not have been effective for improvement of cutter roof.

A panel entry system was designed and implemented. In this design the intention was to reduce magnitude of stresses around the developing entries by way of stress relaxation, utilizing the yield pillar concept (Wilson, 1977). Proper yield pillar sizes based on Wilson's hypothesis and associated equations, utilizing laboratory determined coal properties, were determined. Since the properties of roof and floor strata varied from place to place and with the possibility of presence of fractures, two conditions have been considered in determining the minimum and maximum size of the yield pillar to provide stable entry: a) when roof and floor are strong in comparison to the coal seam, the width of the yield zone was found to be 5.5 feet for totally yield pillars (yield pillar without solid core), thus the smallest dimension for the totally yielded pillars was determined to be 11 feet. For partially yield pillars (yield pillar with solid core) a 20 foot core was required to give a total dimension of 31 feet; and b) when the roof and floor rocks are as soft as the coal seam, the width of the yield zone was found to be 8.5 feet and the smallest dimension of the totally yield pillar was found to be 17 feet. For partially yield pillars an additional core width of 25 feet was required, hence the proper size of the partially yield pillar was 42 feet. In other words the size of the yield pillars were varied from a minimum of 11 feet to a maximum of 42 feet depending on the local geology and the type of yield pillar to be employed. However, in order to cope with the abutment pressure of the longwall the optimum width of the yield pillars was selected to be 31–42 feet depending on the strength of roof and floor rock. An experimental panel entry system as shown in Fig. 5 was designed and implemented. The road ways at a number of blocks were instrumented with stress meters, convergence stations, and borescope boreholes in order to study the behavior of the entries (i.e. roof, yield pillar, rigid pillar, solid coal, and floor) during both entry development and longwall retreat. Past experience in this mine indicated that following caving of one entry, the adjacent entries become stable. In lieu of this development, entry number 4 was kept advanced of other entries. The main reason for keeping No. 4 entry advance was to subject this entry to the highest induced stress concentration rather than No. 1, and if No. 4 failed, No. 1 entry will be stabilized. Due to the large size of the rigid pillar, interaction between the entries was limited only between pairs adjacent to yield pillars (i.e. between 4 & 3 and between 2 & 1 only). The size of the rigid pillar was reduced as shown in Figure 5. Despite reduction of the size of the rigid pillar, development of cutter roof in No. 4 entry did not alleviate cutter roof development in No. 1 entry. Furthermore development of a four entry system delayed the development schedule and so a three entry system proceeded further as shown in Figure 5. Reduction of both yield and rigid pillars and change in sequence of entry advance didn't alleviate the cutter roof problem in No. 1 entry. While changing geometry of the panel entry, the behavior of the roadways was monitored for assessment of pillar and roof stability.

The behavior of pillars during advancement of entries and retreat of longwall face were analyzed through measurements of stress changes within the pillars and deformation characteristics of the pillar. Two or three stress meters were installed in each pillar (both yield and rigid pillars) at depth of 5 and 10 feet or 3, 6, and 9 feet inside the pillar in order to monitor developments and advance of yield zone with the pillars. Floating bolts were anchored inside the pillar corresponding to the location of the stress meter in order to measure deformation/strain in vertical plane of the pillar as shown in Figure 6. Deformation measuring stations (floating bolts) were installed in yield and rigid pillar across each other in order to measure convergence between pillars and lateral movements. Stress changes and deformation, 10 feet, within the pillar during the entry development is shown in Figures 7 and 8. Yielding of the pillar was obvious as it appeared as spalling and sloughage of the pillar (see Figure 9). Figures 10 and 11 show stress and deformation changes within the pillars during longwall retreat. Due to the abutment pressure of the retreat longwall, small pillars were yielded totally (see Figure 10, curves 1 and 2) while the yield zones in rigid pillars have extended to 5 feet thickness as shown in Figure 12 and Figure 10 (curve 3).

To study the direction of cutter development a number of the boreholes were drilled into the roof at the cutter zone and the area before cutter developed. Observation of these holes with the aid of a borescope revealed development and existence of horizontal cracks and strata separation due to the push down of the roof by the lateral stress. A multistage extensometer was designed and installed in a number of blocks to monitor roof strata separation (see Figure 13). Extensometer rods were anchored at 1, 3, 6, and 9 foot intervals in the roof strata and the vertical convergence between these stations and floor as well as roof strata separation were monitored. A total of approximately 17 inches of convergence were measured which included 8 inches of roof strata separation within 9 feet of roof strata as shown in Figures 14 and 15. Figure 14 shows roof strata movement during entry development, while Figure 15 exhibits deformation of center entry during the retreat of longwall face. Furthermore, near

vertical fracture within the plane of cutter roof were present and hole closure near perpendicular to the direction of the cutter roof plane occurred indicating the role of horizontal stress on the development of the cutter roof. Borescoping of the borehole at the center line of the roof indicated lateral movements of the roof strata towards the cutter line, maximum at the roof line and decreased upward, in a step manner, at each step strata separation occurred. Considering the entry development stage, two types of cutters developed in the entries. The first type of cutter was the one which develops at the panel entry face (see Fig. 16) concurrent with entry development. The second type of cutter was developed in the entry in delay time after individual entries were partially advanced a few feet (see Fig. 17). In both cases roof often lost its integrity resulting in caving of the roof. Often these strata breakdowns took place prior to the application of roof bolting resulting in a rough and non–uniform roof line (see Fig. 18). Roof strata exhibited highly laminated with a poor bonding condition. Hence relaxation of the roof strata, through implementation of yield pillar, resulted in adverse effect, causing relative lateral movement of strata along the poorly bonded bedding planes.

Design of Roof Reinforcement System

Since the panel entry design system could not alleviate the cutter roof problem, the emphasis shifted in roof reinforcement and support system. A typical roof reinforcement support system, in the entries with cutter roof problem, is shown in Figure 19 and includes T–5 channel with four rebars, steel beam with yieldable legs and two sets of straps and two super bolts. Despite heavy and costly support system, periodic caving occurred. The design approach was to understand the process of roof cutter development and to determine required and appropriate roof reinforcement in order to preserve the integrity of the fractured roof strata nd to prevent roof caving.

During cutter roof development and further deterioration of the roof strata, motions of roof strata were observed and monitored through borescoping and measurements made from roof extensometers. In order to measure the caved material weight and the vertical load due to the push down of the roof strata, resulting from the action of high horizontal stress, a number of steel beam supports were instrumented with 3.5 in. diameter circular pressure cells having a maximum gauge pressure of 5000 psi. The 20 ton pressure cells were positioned between the steel beam and end plates of the yieldable legs. Within a short period of time pressure exceeded the limit of the cells and caused their rupture. It was realized that load on the beam was more than the dead weight of the broken roof.

To cope with excessive downward pressure of the roof strata, it was designed to reinforce the roof so it could become partially self supporting and transferring some of the vertical load to the strata above the caving horizon and on to the ribs. A primary roof reinforcement system was designed (see Figure 20) and implemented. With the aid of borescope and observation of the failed long bolts (see Figure 21) it was observed that most of the roof strata separation occurred between 6–9 feet into the roof. It was also realized that a complete stop in roof strata movement is not economically feasible. Therefore the length of all primary bolts including angle bolts were reduced to 6 feet, allowing the roof strata to move down in order to release excessive horizontal stresses. Since movement of the strata resulted in dense fracture of the roof (see Figure 21), a truss bolt system supplemented the primary roof reinforcement system as shown in Figure 22. These truss bolts were installed in delay time with respect to the primary roof reinforcement system. The reason for this delay of application of truss bolts was to allow roof strata to move down thus releasing excessive pressure. Then truss bolts were applied to keep fractured roof together and transfer the load, due to the cantilevering effect of the roof strata, on to the ribs. Time of application of the truss bolts was critical. A series of experiments were carried out in the laboratory to find the ultimate strength of truss bolts system for a proper spacing of trusses, and also to develop techniques for determining load on the installed truss bolts. Torque–tension calibration characteristics of the truss bolts were determined (see Figure 23). The laboratory technique was used in the mine to determine load transfer on the installed truss during entry development. The results indicated that roof pressure started to develop in truss bolts approximately 30 feet behind the face and 50 feet behind the face pressure on the truss bolts reached to their full load, hence it was recommended to keep installation of the truss bolts 50 feet behind the primary roof reinforcement. Further modifications in both roof reinforcement and supplemental support systems were made considering geometry and application procedures in order to reduce the cost of the roof support. Time and space will not allow further discussion.

Specially designed roof reinforcement and supplemental support systems stabilized the roof despite the development of the cutter roof. No caving of the roof under the designed system has occurred and furthermore it facilitated the advance of the longwall face very well. Figure 24 shows roof conditions under the action of the designed roof support system in the gob area behind the longwall face.

CONCLUSIONS

Results of the study indicated that in–situ stresses, in particular horizontal stresses, are very high in the problem area of the mine and roof strata are weak, highly laminated with poor bonding conditions. Design and implementation of a panel entry system, using the yield pillar concept, was found to be ineffective, in fact the relaxation of the roof strata due to

the behavior of the yield pillar further deteriorated the laminated strata. On the other hand, roof reinforcement and supplemental systems were found to be the solution to the problem. Proper pattern and application procedures, considering the advancement of the entries, were the major reason for the successful and economical application.

ACKNOWLEDGEMENT

This project was co–sponsored by Beth Energy Mines, Inc. and West Virginia University's Energy and Water Research Center and the College of Mineral and Energy Resources. The writers acknowledge the assistance of Danqing Xu, Research Assistant in the Mining Engineering Department of West Virginia University in preparation of this paper.

REFERENCES

1. Iannachione, A. T. and Puglio, 1979, "Geology of the Lower Kittanning Coalbed and Related Mining and Methane Emission Problems in Cambria County, PA, USBM RI 8354, 31 pp.

2. Watson, B., 1979, "Longwall Produces Record Tonnage," Coal Age, V. 76, No. 3, pp. 64–75.

3. Hooker, V. E., Bickel, D. L., and Johnson, C. F., 1969, "Near Surface Horizontal Stresses Including the Effect of Rock Aniostropy," USBM RI 7224, 29 pp.

4. Bickel, D. L. and Donato, D. A., 1988, "In–situ Horizontal Stress Determinations in the Yampa Coalfield, Northwestern, Colorado," USBM RI 9149, 43 pp.

5. Wilson, A. H., 1977, "The Effect of Yield Zones on the Control of Ground," Proceedings of the 6th International Strata Control Conference, Braniff, Canada, Paper No. I–3, pp. 1–25.

Table 1. Values of Young's Modulus Obtained from Biaxial Tests

Hole No.	Drilling Depth (ft)	Level of stress (psi)	Young's Modulus (x 10^5 psi) E_1	E_2	E_3
A	15	445-550	5.26	6.87	9.35
B	15	530-620	7.3	5.2	9.4
C	14	810-935	9.71	9.72	8.50

Table 2. Calculated Stresses from Deformation Measurements

No. of data		1	2	Average Value
Average ground stress components (psi)	σ_x	-5448	-4028	-4738
	σ_y	-6792	-5695	-6378
	σ_z	-7495	-7116	-7306
	τ_{xy}	-815	-1743	-1279
	τ_{xz}	-281	-403	-342
	τ_{zx}	-394	-614	-504
Principal stress (psi)	S1	-7600	-7398	-7499
	S2	-7304	-5612	-6458
	S3	-4831	-4099	-4465

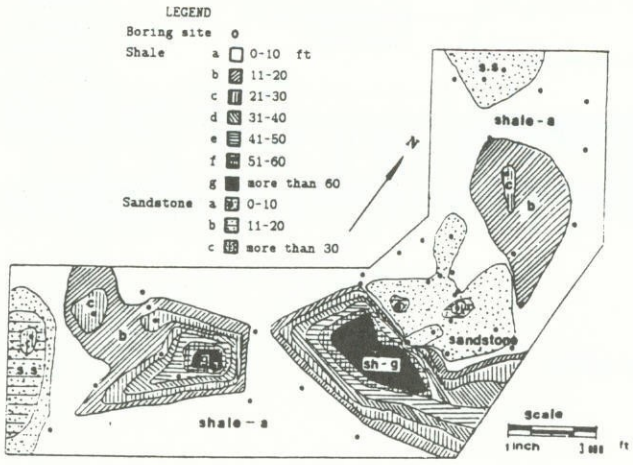

Fig. 1 Lithology of roof strata.

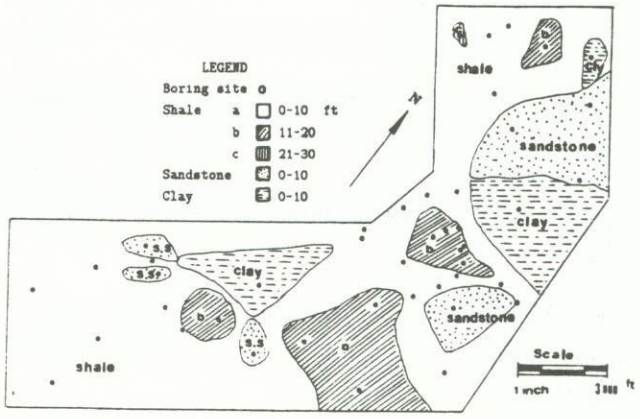

Fig. 2 Lithology of floor strata.

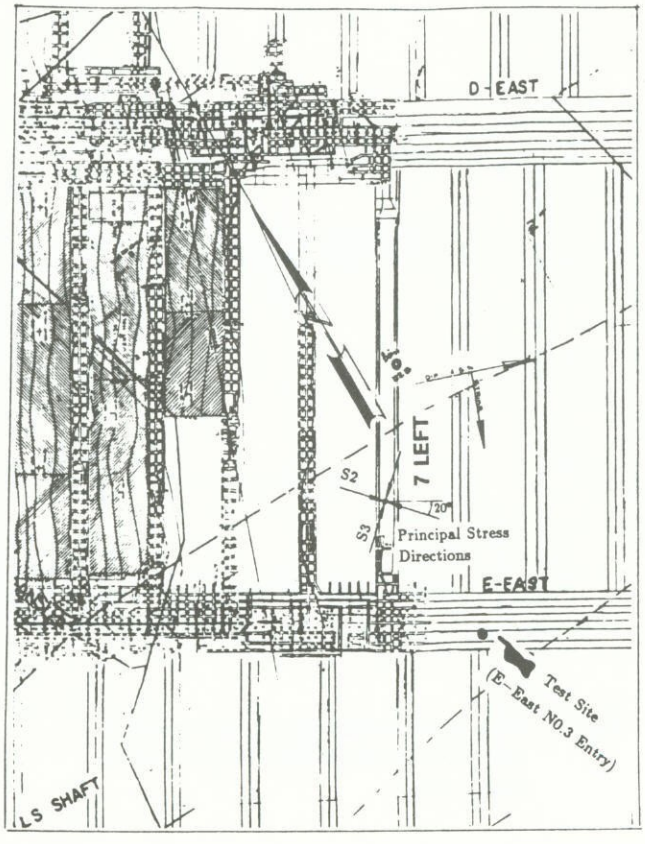

Fig. 3 Longwall panel layout.

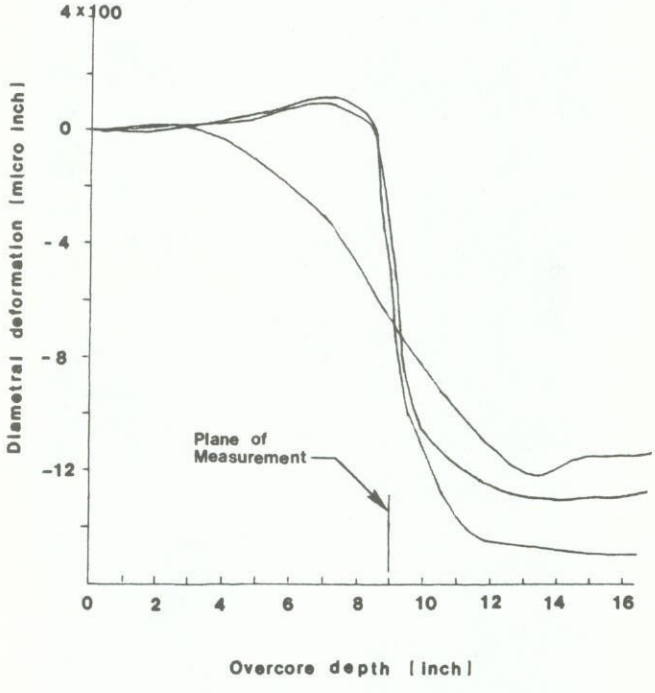

Fig. 4 Relationship between measured deformation of borehole diameter and depth of overcore.

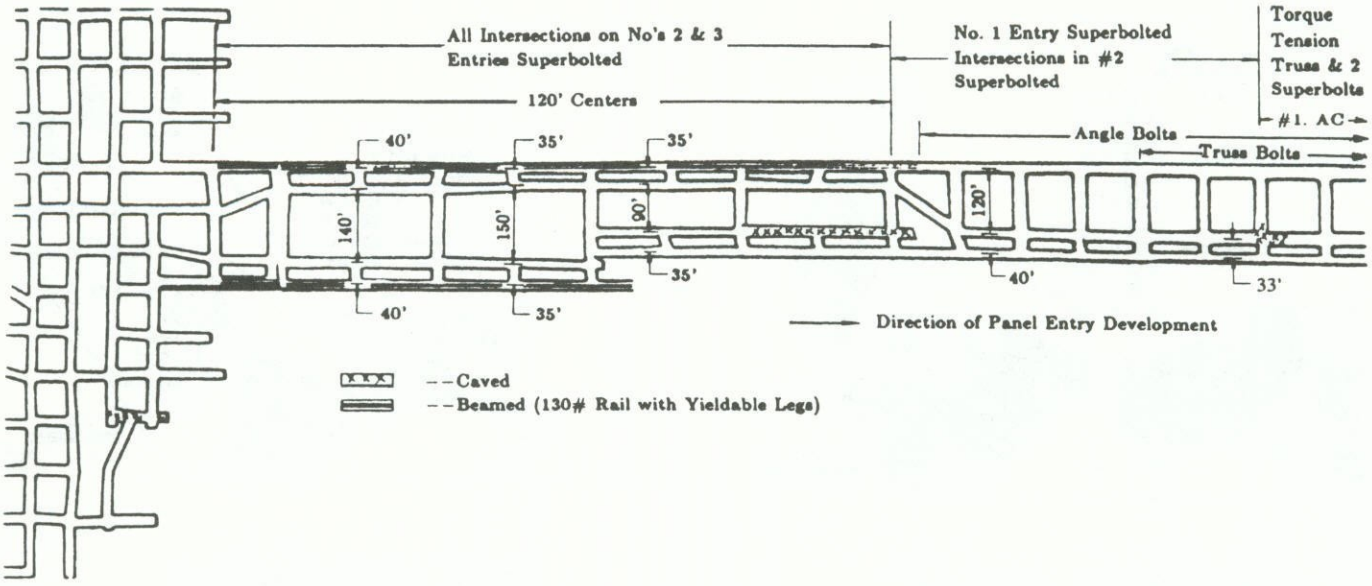

Fig. 5 Experimental panel entry system.

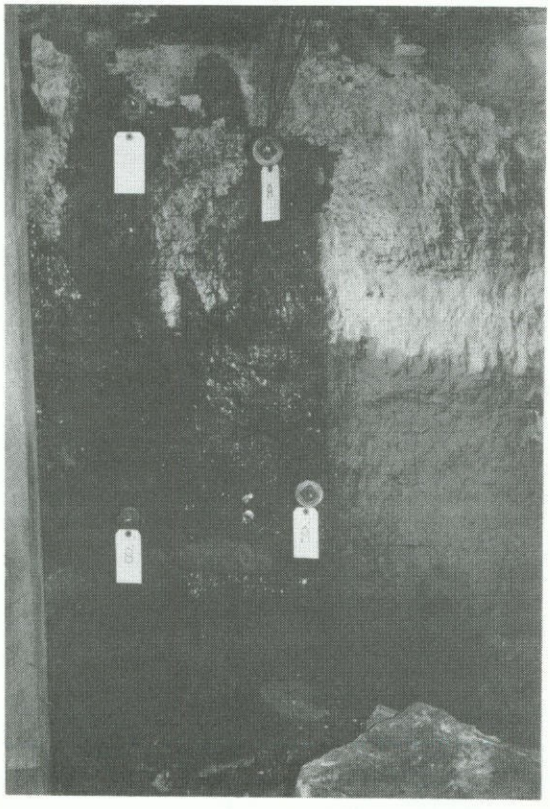

Fig. 6 In pillar deformation and stress changes measuring stations.

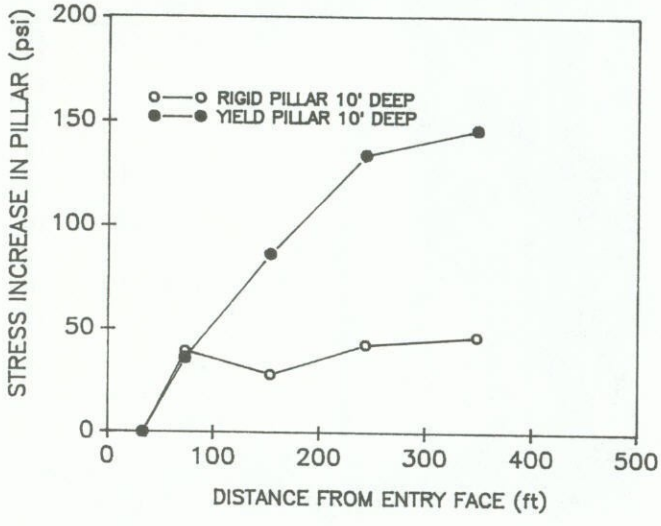

Fig. 7 Measured changes of vertical stress at 10 feet deep inside the pillars during entry development.

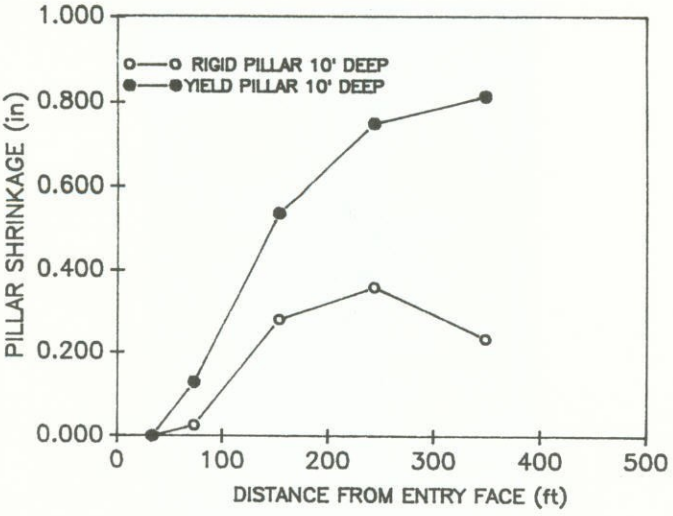

Fig. 8 Measured changes of vertical deformation of the pillar, shrinkage in 28" of rigid pillar and 40" of yield pillar, during entry development.

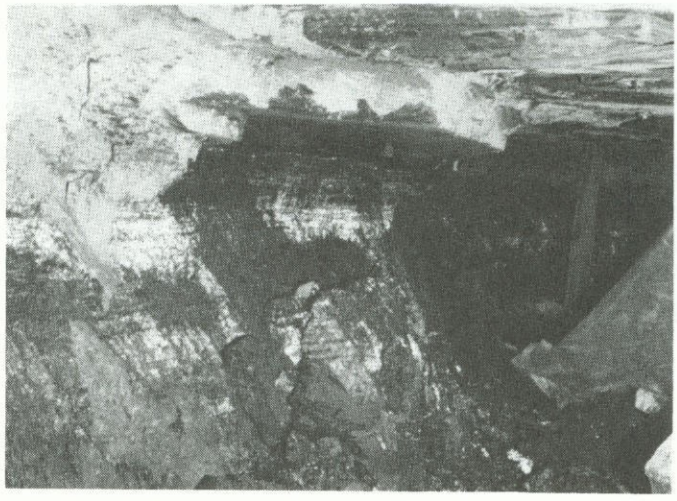

Fig. 9 Spalling and sloughate in yield pillar as a sign of development of yield zone in the pillar.

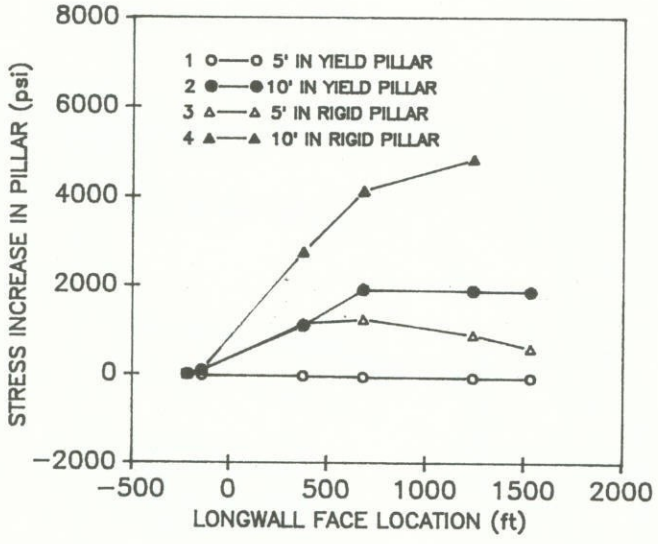

Fig. 10 Measured changes of vertical stress at 5 feet and 10 feet deep inside the pillars during retreat of longwall face.

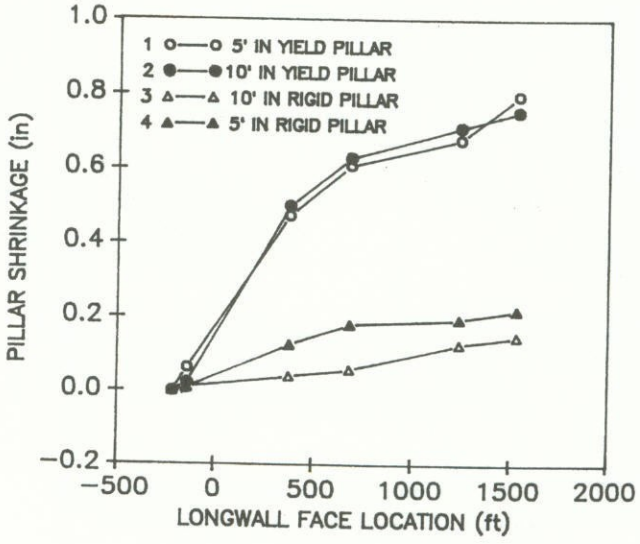

Fig. 11 Measured changes of vertical deformation of the pillar, shrinkage approximately 33" of thickness during retreat of longwall face.

Fig. 12 Appearance of the rigid pillar (left of the figure) and yield pillar (right of the figure) during retreat longwall face at the right side of the yield pillar.

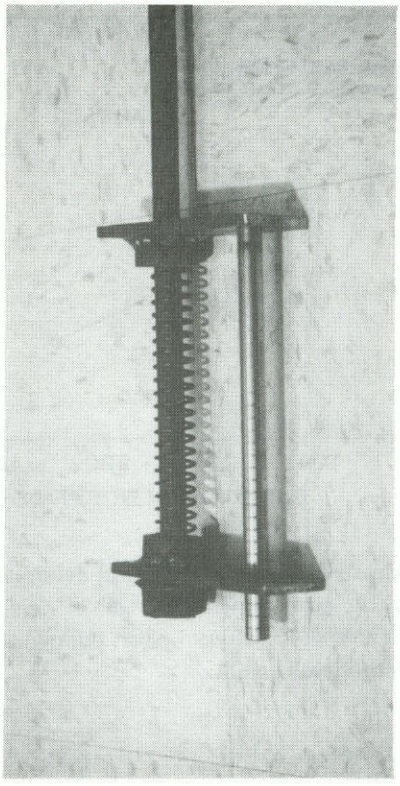

Fig. 13 Typical extensometer anchored at specific depth above the roof line.

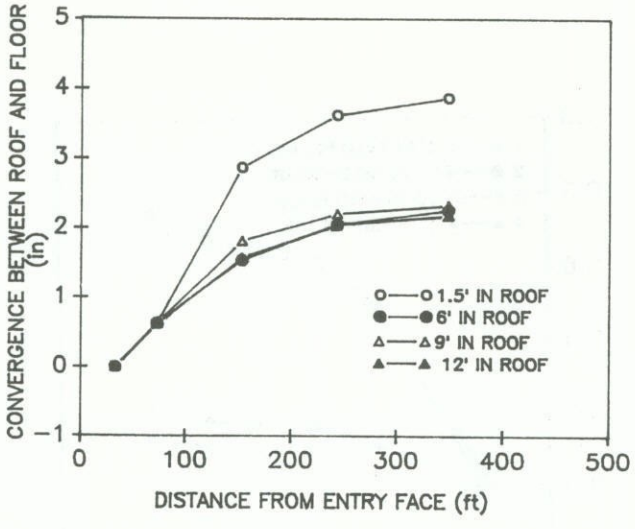

Fig. 14 Measured convergence between roof strata (four horizons) and floor during entry development.

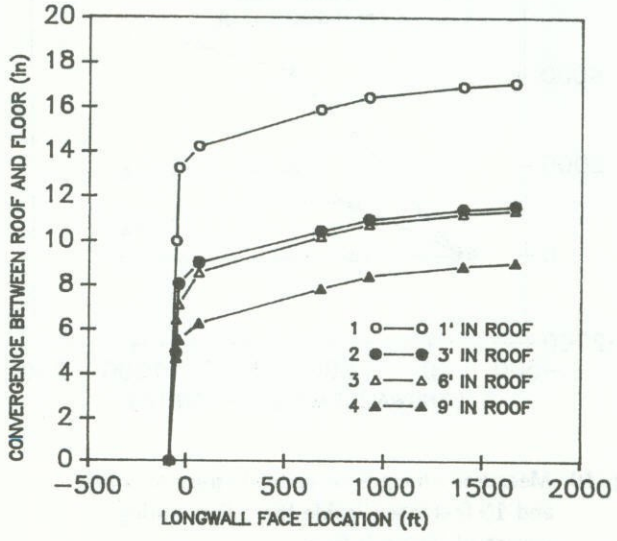

Fig. 15 Measured convergence between roof strata (four horizons) and floor during retreat of longwall face.

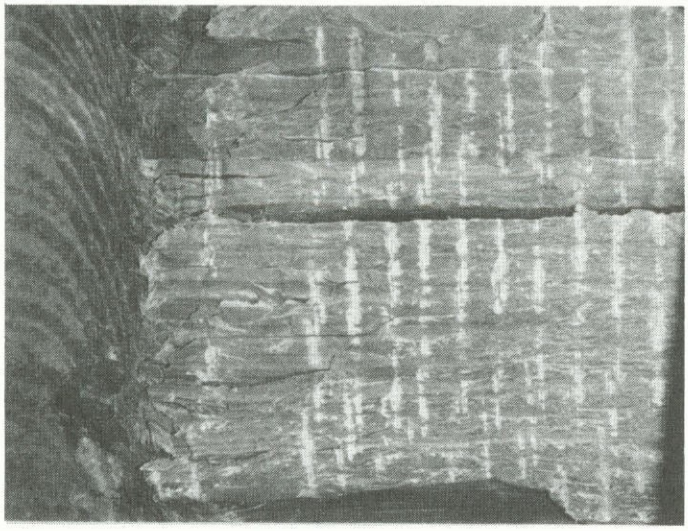

Fig. 16 Cutter roof develops at the face concurrent to the entry development.

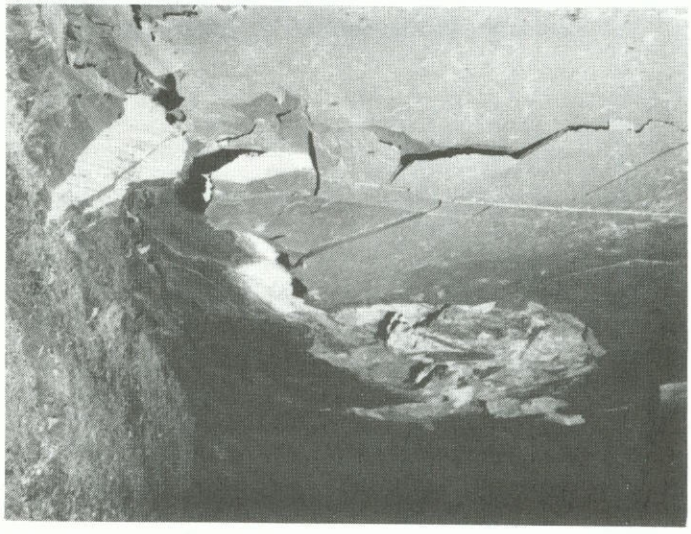

Fig. 17 Cutter roof develops a short distance behind the face and follows advance the entry.

Fig. 18 Rough and irregular roof line develops prior to roof bolting.

Fig. 19 Typical roof reinforcement and supplemental support used in the entries experiencing cutter roof.

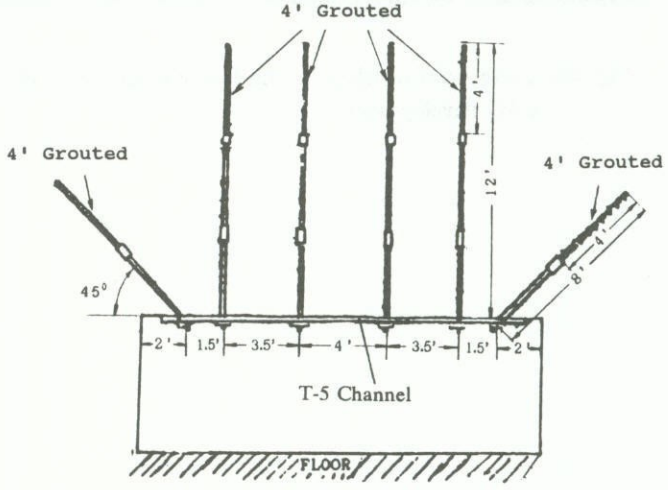

Fig. 20 Primary roof bolting system utilized in experimental panel entry system (entry #1).

Fig. 21 Failed roof bolt at the cutter zone.

Fig. 22 Truss bolt system supplemented with primary roof bolting system.

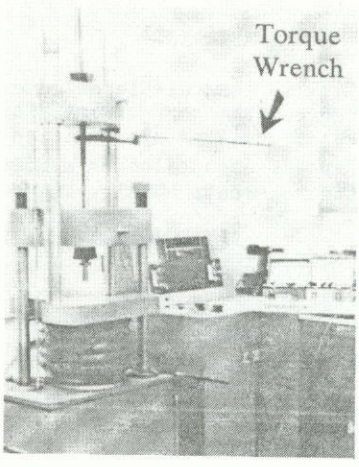

Fig. 23 Torque–tension calibration of truss bolt in the laboratory.

Fig. 24 Performance of primary roof bolting and supplemental roof support system (truss bolt) at the gob.

10th INTERNATIONAL CONFERENCE ON GROUND CONTROL IN MINING

LOAD AND CONVERGENCE MEASUREMENTS IN LONGWALL FACES AND DESIGN GUIDELINES FOR FACE–SUPPORT SYSTEMS

Reha Ozel, *Research Assistant*
Cenk Basar, *Graduate Student*
Erdal Unal, *Associate Professor*

Mining Engineering Department
Middle East Technical University
06531 Ankara
TURKEY

ABSTRACT

The stability in longwall faces depends on the interaction between the roof strata, face supports and floor strata. The load distribution on the other hand, depends upon relative stiffness of the three supporting elements namely, the coal face, support and gob. Therefore, in defining support requirements, it is particularly important to analyze the strata loading, the face convergence and the controlling mechanism provided by supports. The controling mechanism however, depends on the type and characteristics of supports used in longwall faces.

The design guidelines presented in this paper have been developed based on a number of strata control oriented projects carried out in Turkey, load and convergence measurements carried out in 10 longwall faces, in Zonguldak Coal Region, and procedures given in literature.

Evaluation of load and convergence measurements, and analyses of face supports were carried out by means of a computer program, called LONGWALL-METU, developed by the authors. The output of the design analyses include the following: (1) estimation of support capacity for roof supports namely; individual hydraulic props, chock-type power supports and various types of shield supports, and (2) analysis of loading conditions and response of shield support components in terms of stability and structural integrity.

INTRODUCTION

Design of longwalls, in essence, requires determination of (1) the most proper layout and dimensions of longwall panels and gateroads, (2) selection of a suitable excavation method for these opening, and (3) assessment of support requirements in longwall faces and gateroads.

In developing guidelines for longwall faces, on the other hand, considerations should be given to support systems in terms of (1) selection and design, (2) performance acceptance testing, (3) operational considerations, and (4) in-situ performance monitoring. The details associated with these considerations have been given in literature (1). Support selection and design process include determination of the support type, support capacity, and analysis of structural stability of supports and component constructions.

A suitable power support is one of the key factors for successfull longwall operations. Methods currently available for selecting proper support type have been reviewed in literature (2).

Support and strata interaction has been explained by different approaches. Peng and Chaing describes the bulking factor formulation to estimate a "detached roof block" that most be maintained in equilubrium by the support resistance (3). Smart and Redfern suggests an equivalent system stiffness concept and assumes that power supports share load with the coal face and the gob. The total roof and floor loading then will be equal to system stiffness and roof to floor convergence (4). The "equivalent stiffness" concept implies a constant roof load where face convergence is based on the stiffness of ground supporting elements (5). Barczak suggests that support capacity determinations should be based upon face convergence and stiffness of various ground supporting elements (6). The USBM is currently developing a methodology, for predicting support capacity, considering both support stiffness and face convergence (1). In this concept, the total load on supports is defined as the sum of setting load and convergence load.

In this study, a relationship has been developed between convergence and support capacity based on underground measurements. Face support analyses were carried out by means of a computer model. The details associated with load and convergence measurements, support capacity estimation, and face-support analysis will be discussed in the following sections.

LOAD AND CONVERGENCE MEASUREMENTS AND ANALYSES

The load and convergence measurements were carried out in ten longwall faces, in Zonguldak Coal Region, where timber support systems (post and cribs) or hydraulic props were used.

The loads on timber supports were measured by means of load cells located at the bottom of the timber props as well as at four lower corners of the wooden cribs. In longwall faces where hydraulic props were utilized, a special manometer-type load cell was used to measure the loads on props.

During investigations, in addition to support-loads, roof-to-face convergences were also measured by means of telescopic-type mechanical convergence recorders, specifically designed to fit various working heights.

In general, load and convergence measurements were carried out at least at two different locations in a longwall face. In each station, a number of neighboring supports were instrumented. The measurements were initiated with the replacement of the face supports at the face side, and continued until they were removed from the gob side. The load cells and the convergence stations were replaced with the new ones as damaged or lost. The measurements continued for two cycles.

Analysis of support loads were made considering the average values of the maximum loads measured on various support units, the area supported by these units, the inclination of the seam, the friction between roof blocks and the total convergence per unit length of face advance. After this step, the Mean Load Densities (MLD) were calculated based on the average values of the maximum loads measured on supports and the area supported by these units.

The evaluation of in-situ measurements were carried out by means of a computer program as will be explained in a section entitled as " COMPUTER BASED FACE-SUPPORT ANALYSES".

ESTIMATION OF SUPPORT CAPACITY

After determining the MLD values for each longwall face, the support capacity (P_s) associated with each longwall face was estimated by two different approaches, using Equation 1.

$$P_s = MLD \times SF \times \left(\frac{\sin\alpha}{\tan\theta} + \cos\alpha\right) \qquad (1)$$

where, (SF) is the safety factor
(α) is the inclination of the seam
(θ) is the friction angle between blocks

In the first approach, support capacities (P_s) were expressed in terms of the extraction height (H_e), and the relationship between the required support capacity and the seam inclination was presented in a graphical form as shown in Figure 1. These results were also compared with the ones calculated based on the methods suggested by Wilson (7) and Jacobi (8) as shown in Figure 1.

In the second approach, mean load densities were also determined based on measured support loads and then support capacities were calculated by using Equation 1. The relationship between P_s values (ton/m^2) and corresponding total face convergences (mm/m) were presented in a graphical form as shown in Figure 2.

The plot shown in Figure 2 can be utilized in determining support capacity. However, stiffness characteristics of supports should be made available by support manifacturers to operators when purchasing power supports. Assuming that the support stiffness is available, then required support-capacity can be found as a function of setting load.

COMPUTER BASED FACE-SUPPORT ANALYSES

In order to develop design guidelines for various types of face support systems and to evaluate a number of critical design parameters, a computer program was also developed. Support analyses were made based on in-situ measurements as well as on other methods suggested in literature. A simplified flowchart of the computer program is shown in Figure 3.

Evaluation of In-Situ Measurements

The analysis of load convergence data obtained from underground measurements can be realized by utilizing the first part of the main program. A simplified flowchart of the program associated with the analysis of in-situ measurements is given in Figure 4. The input parameters for this part of the computer program are the following:

- seam inclination
- friction angle between roof blocks
- face convergence
- safety factor
- number of measurement at each position of supports
- number of position (supported rows)
- area supported at each position
- total load at each position

The output parameters include the following:

- support capacity (P_s) vs. Convergence relationship in both the text and graphical mode.
- statistical analysis associated with support capacity (P_s) and convergence (regression analyses, best fit etc.) in both the text and graphical mode.
- maximum allowable convergence and minimum support capacity based on the trend of the best-fitted regression curve.

Analyses of Support Types

In this study, three main types of support namely, individual hydraulic props, chocks and shields were taken into consideration.

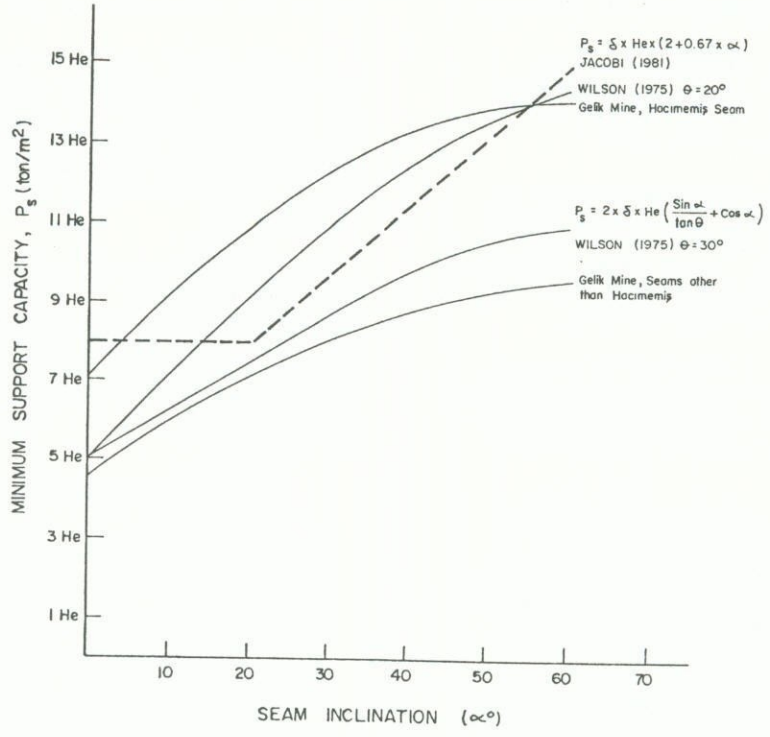

Figure 1. Estimation of minimum load bearing capacity as a function of seam inclination and working height.

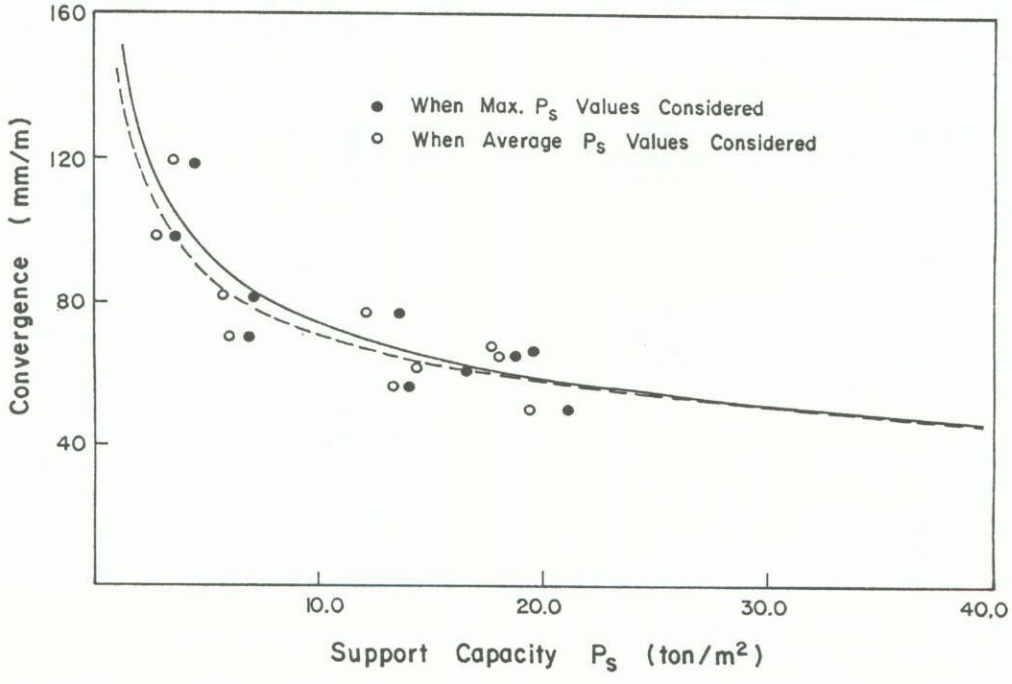

Figure 2. The relationship between support capacities and corresponding total face convergences.

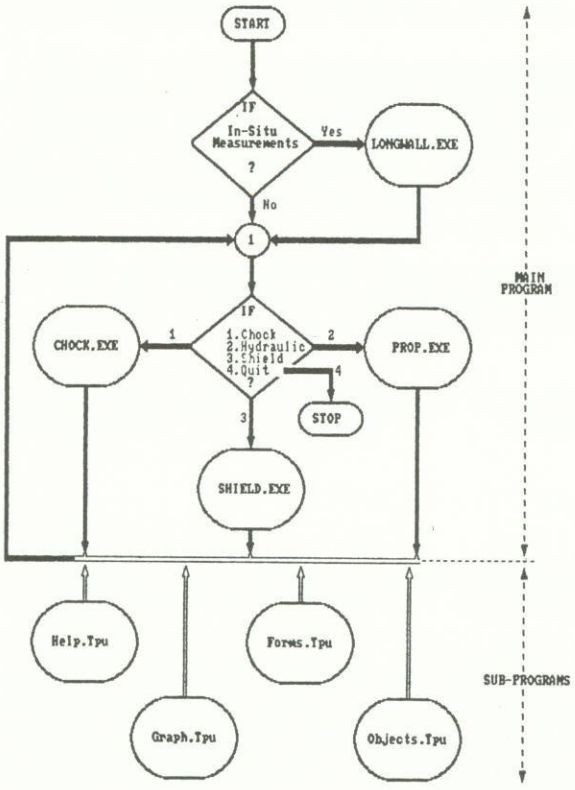

Figure 3. The flowchart of the main computer program.

Hydraulic Props Individual hydraulic props are the earliest type of hydraulic supports. Prop setting load and spacing between props along the face are the two important output parameters in design.

Hydraulic prop setting load (SL) can be determined as a function of nominal capacity of the props, hydraulic efficiency factor and hydraulic safety factor as shown in Equation 2.

$$SL = \frac{\text{Nominal}}{\text{Capacity}} \times \left(\frac{\text{Hydraulic}}{\text{Efficiency}} / \frac{\text{Hydraulic}}{\text{Safety factor}}\right) \quad (2)$$

In order to calculate maximum allowable spacings (S) between props the relationship presented in Equation 3 can be utilized:

$$S = \left(\frac{SL \times n}{P_S \times L}\right) \quad (3)$$

where, S is the spacing between props, n is the number of props in a row, P_S is the support capacity, L is the face to gob distance.

A simplified flowchart of the program associated with hydraulic prop design is presented in Figure 5.

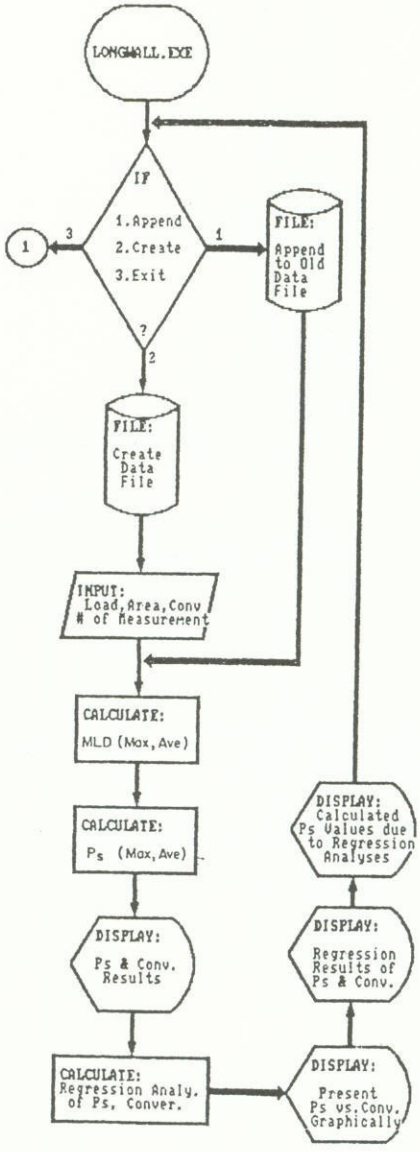

Figure 4. The flowchart associated with the analysis of in-situ measurements.

The input parameters for the computer program are the following: measured MLD per working height, safety factor, nominal capacity of the prop, hydraulic efficiency, hydraulic safety factor, face to gob distance, and friction angle between rock blocks.

Computer outputs associated with hydraulic prop design are the following:

- required support capacities (for various seam inclinations (α) and working heights (H_e)) in both the text and graphical mode.
- nomograms for prop spacings (S) for different number of props in the graphical mode as shown in Figure 6.

Depending on user's interest relationship between (P_S) and (α) suggested by Wilson (7) and

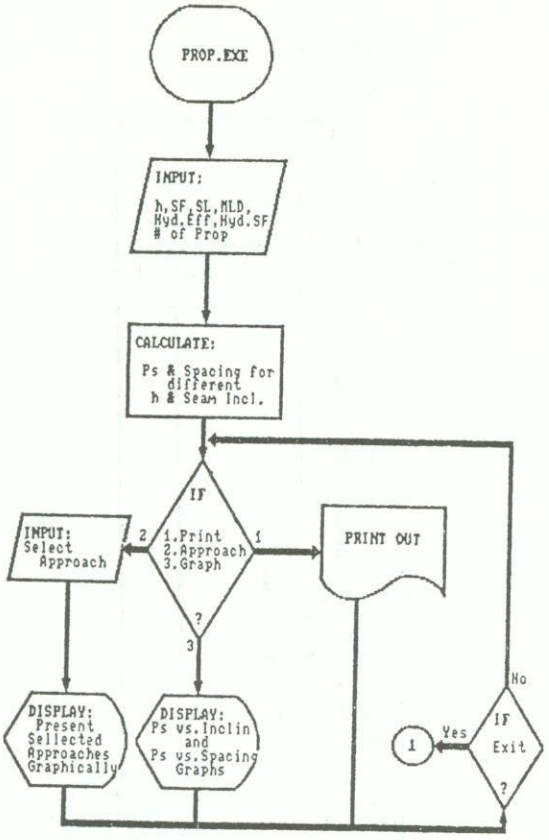

Figure 5. Flowchart associated with hydraulic props.

Jacobi (8) can also be obtained and compared with the ones obtained from current analyses.

Chock-Type Power Supports A chock is made of hydraulic jacks connected by a common roof canopy and floor base. The important input parameters that should be considered in design of chock-type support are the following: the face-to-gob distance, unit weight of the rock, caving height and canopy size (block base area).

Required support capacity depends on roof loading or the weight of the block above the support as shown in Equation 4.

$$\left(\begin{matrix}\text{Weight of the}\\ \text{block}\end{matrix}\right)=\left(\begin{matrix}\text{Volume of the}\\ \text{block}\end{matrix}\right)\times\left(\begin{matrix}\text{Unit weight}\\ \text{of the block}\end{matrix}\right) \quad (4)$$

where,

$$\left(\begin{matrix}\text{Volume of the}\\ \text{block}\end{matrix}\right)=(\text{Base area})\times(\text{Caving height}) \quad (5)$$

Theoretical determination of the block-weight is not an easy task since it requires a number of assumptions in predicting caving height. The same parameter, however, can be determined based on in-situ measurements. As described in an earlier section of this paper, if the loads on face supports were measured and the area supported by these units were determined, the associated mean load density (MLD) can be calculated. Knowing the

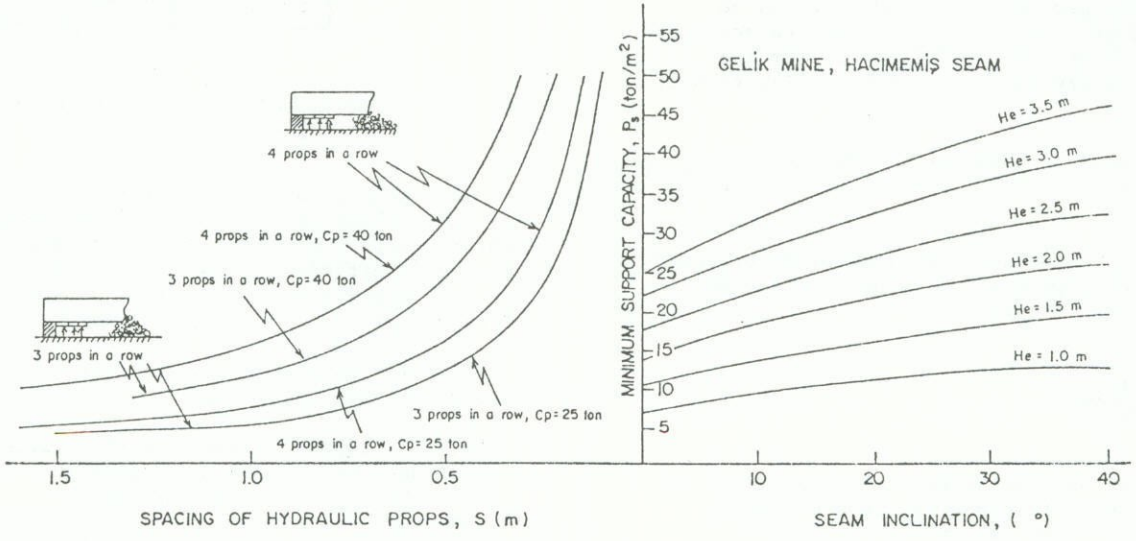

Figure 6. A typical design nomogram for hydraulic props to be used in longwall faces that will be located in Hacımemiş seam.

MLD and the unit weight of the roof, the caving-height can be calculated by using Equation 6.

$$\text{Caving Height} = \text{MLD}/(\text{Unit weight of the roof block}) \quad (6)$$

Considering the input parameters that will be mentioned in the next paragraph, the caving height of the roof-strata and the forces on front and back legs can be determined, as output parameters, for the cases presented in Figure 7.

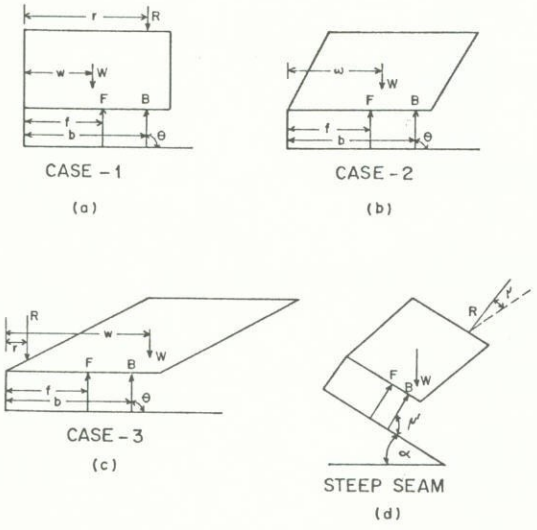

Figure 7. Concept of roof block and forces involved for different cases.

A simplified flowchart associated with chock type of support is presented in Figure 8.

The input parameters for the computer program are the following: spacing of chock supports, face to gob distance, face to front leg distance, face to back leg distance, seam inclination, and angle of the legs.

If the height of the roof block (caving height) is not known it can be determined considering the given parameters such as, seam height, bulking factor, residual bulking factor, and the thickness of interlayer strata (if exist).

The following computer outputs, associated with chock type of support, can be obtained:

- height of the roof block above the support,
- forces on front and back legs.

Multiple seams (upto five) can be considered in this computer program.

Shield-Type Power Supports A shield support consists of an inclined plate whose lower end is hinged to a horizontal base plate sitting on the

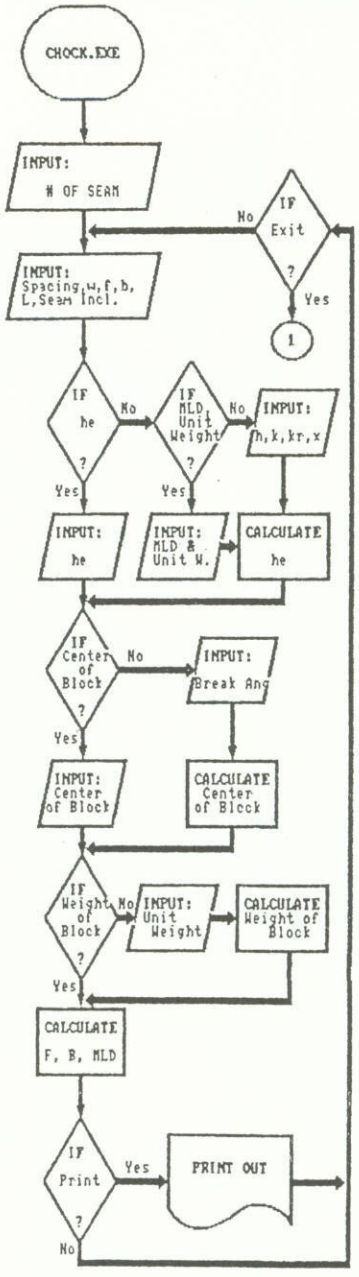

Figure 8. Flowchart associated with chock-type supports.

floor while the upper end is hinged to a horizontal roof canopy in contact with the roof.

Because of the relatively complicated geometry and kinematics of the shields, a proper calculation of load transmission from the props to the roof shield should be required (9). On the other hand, shield type of support includes a wide class of supports due to their structural differences.

Magnitude and position of the resultant forces on the canopy are the critical factors considered during support design. In order to calculate resultant force acting on the canopy, moment should

be taken around points G and S as shown in Figure 9.

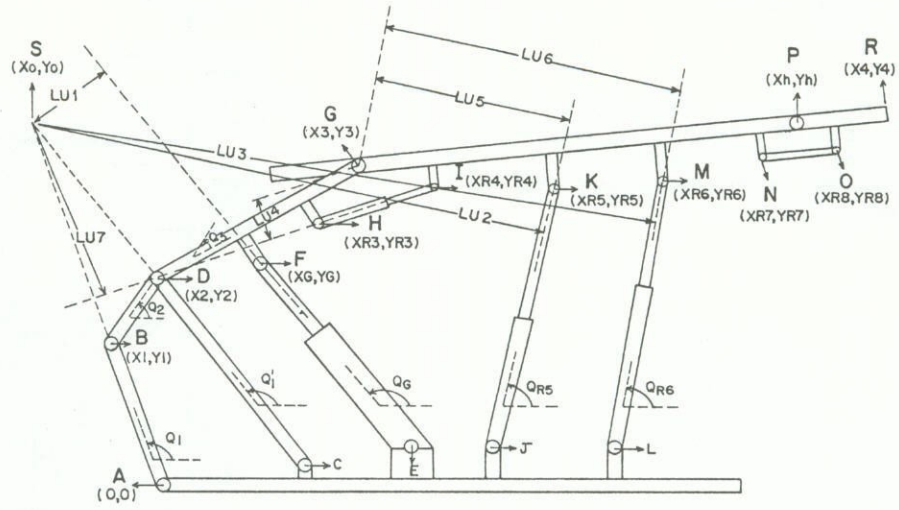

Figure 9. Representation of shield-type power support showing the coordinates of various components.

Consequently, coordinates of the junctions and the distance between the legs and the points S and G can be calculated. Depending on support geometry all joint coordinates and the distances from point S and G to legs can be determined.

The resultant force A and its point of application (point a) were determined using the equations given below:

$$N \times n = T \times (L-d) \quad (7)$$

$$A1 \times b = S1 \times e1 \quad (8)$$

$$A1 = \frac{S1 \times e1}{b} \quad (9)$$

$$A2 \times a2 = S2 \times s2 \quad (10)$$

$$A2 = \frac{S2 \times s2}{a2} \quad (11)$$

$$A2 \times (a2 + b) = S2 \times e2 \quad (12)$$

From Eq(11) and Eq(12)

$$a2 = \frac{s2 \times b}{e2 - s2} \quad (13)$$

$$A3 \times a3 = S3 \times s3 \quad (14)$$

$$A3 = \frac{S3 \times s3}{a3} \quad (15)$$

$$A3 \times (a3 + b) = S3 \times e3 \quad (16)$$

From Eq(15) and Eq(16)

$$a3 = \frac{S3 \times b}{e3 - s3} \quad (17)$$

$$A \times a = S2 \times s2 + S3 \times s3 + N \times n \quad (18)$$

$$A \times (a+b) = S1 \times e1 + S2 \times e2 + S3 \times e3 \quad (19)$$

From Eq(18) and Eq(19)

$$A \times b = S1xe1 + S2xe2 + S3xe3 - S2xs2 - S3xs3 - Nxn \quad (20)$$

From Eq(18) take a as

$$a = (S2 \times s2 + S3 \times s3 + N \times n)/A \quad (21)$$

where, S values indicate setting load of various legs, $A_{1,2,3}$ are support force resultant for

various legs, A is the resultant force, T is the tip load, N is the force in the capsule, n is the distance between the joint and capsule, L is the length of the canopy from joint to tip end, d is the distance between hinge joint and gob end, b is the distance between the pole and hinge joint, a is the distance between resultant force and hinge joint, a1,2,3 are the distances between force resultant of various legs and hinge joint, e1,2,3 are distances of pole (instantaneous center) to the associated legs, $S_{2,3}$ are distances of hinge joint to the associated legs (See also Figure 10).

The methods to determine (A) and (a) for various shield support types (caliper, lemniscated fourleg shield and chock shield) has been given in U.S. (10) and German literature (11).

In this study a generalized formulation was developed which includes all shield support types considering only Figure 11. For example, for lemniscated type the parameters S2, S3, H3, V3, R5, H4, V4, R6, L8, L9, L10 should be taken as zero. And in the case of chock shields S1, R9, H2, V2, L9 should be taken as zero.

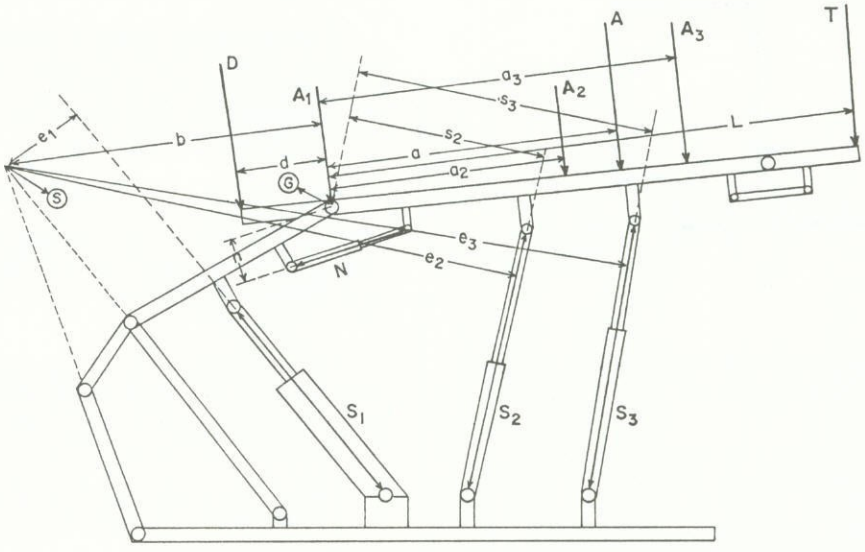

Figure 10. Representation of a shield-type power support with all the forces acting on it.

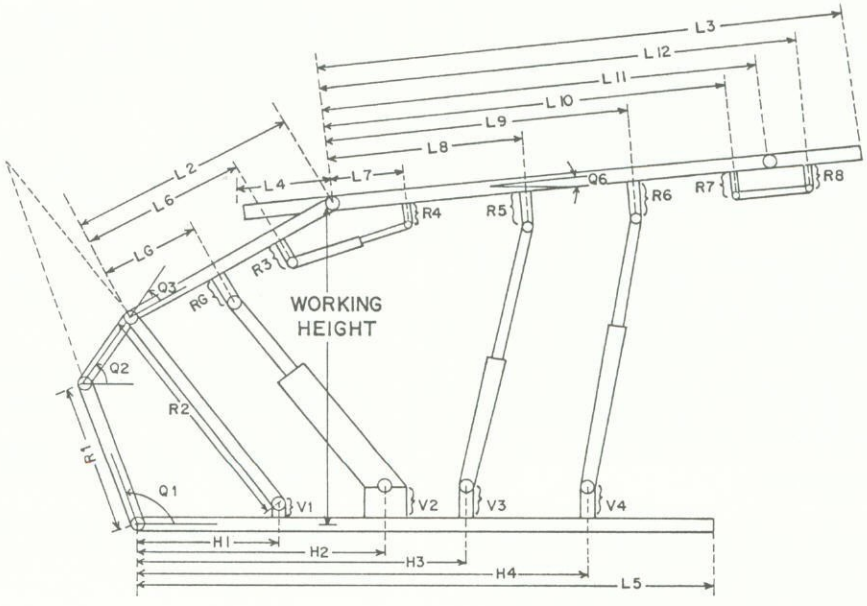

Figure 11. Representation of a shield-type power support with the required input parameters utilized in component construction analysis.

The flowchart associated with shield type of support is given in Figure 12.

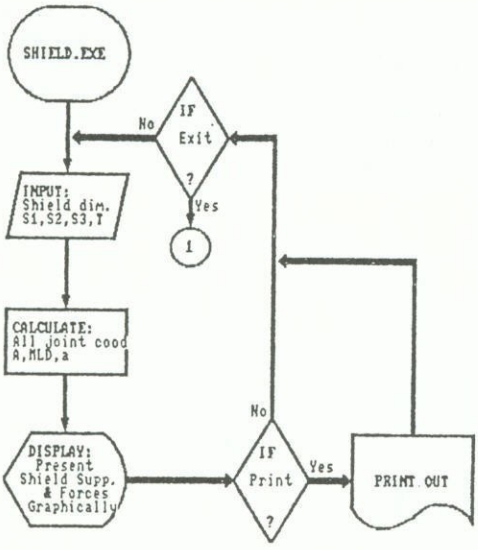

Figure 12. A simplified flowchart for selection and design of shield-type of supports.

The input parameters for the computer program are the following; dimensions of all shield pieces, working height, either inclination of rear lemniscate bar and rear caving shield and angle of rear caving shield from front caving shield, setting loads of legs, tip load, spacing of shield supports (i.e width of canopy).

The output parameters of the computer program for shield type support are as follows: a scaled graphical presentation of the shield support, all calculated coordinate values of the joints, a graphical presentation of resultant force A on the canopy, the mean load density, all calculated distances, angles and forces associated with the shield support. The outputs mentioned above can be seen on a screen, can be obtained as a hard copy from a printer or from a plotter.

If the MLD value is available from measurements then it can be compared with the calculated MLD and accordingly the setting loads on legs can be readjusted. In addition, in order to provide optimum working conditions for the shield supports, the location of the application point of the resultant force (A) can be adjusted by changing a number of input parameters considered.

CONCLUSIONS

In this study a relationship has been developed between face-to-floor convergence and support capacity based on underground measurements. The support analyses for various support types were carried out by means of a computer program called LONGWALL-METU.

The load and convergence measurements were taken in longwall faces where timber supports (posts and cribs) and hydraulic props were used. This was a unique opportunity in determining total load on supports having different stiffnesses. The same type of measurements will continue in a number of longwall faces, at Middle Anatolia Lignite Mines, where shield type of power supports are being utilized.

Considering the graphical relationship between support capacity and convergence and following the design procedures described in this paper the required support capacity of supports and their structural stability can be determined.

In determining support capacity as a function of setting load, however, stiffness characteristics of power supports should be made available by support manufacturers to operators for analysis when purchasing these supports.

REFERENCES

1. Barczak, T.M., D.E., Schwemmer, and C.L. Tasillo, Practical Considerations in Longwall Face and Gate Road Support Selection and Utilization, USBM IC 9217, 1989, 22 p.

2. Hsiung, S.M, Y.M. Jiang, and S.S. Peng, Method of Selecting Suitable Types of Shield Supports at Longwall Faces, Proc. Int. Conf. on Ground Control in Mining, WV. Univ., 1988, pp.51-61.

3. Peng, S.S., and H.S., Chaing, Longwall Mining, John Wiley and Sons, New York, 1984, 708 p.

4. Smart, B.G., and A. Redfern, The Evaluation of Powered Support Specifications From Geological and Mining Practice Information, Rock Mech. Symp., 1987, pp. 367-377.

5. Peng, S.S. and S.M. Hsiung, Method of Determining the Rational Load Capacity of Shield Supports at Longwall Faces, Mining Engineer, Oct. 1987, Vol.147, pp. 161-167.

6. Barczak, T.M., Practical Considerations in Longwall Support Selection, Proc. of 9th Int. Conf. on Ground Control in Mining WV. Univ., 1990, pp. 128-134.

7. Wilson, A.H., Support Load Requirements on Longwall Faces, The Mining Engineer, June 1975, pp. 479-491.

8. Jacobi, O., Praxis der Gebirsbeherschung, 2nd edition, Verlag Glückanf, Essen, 1981, pp. 222-229.

9. Peng, S.S., Coal Mine Ground Control, John Wiley and Sons New York, 1978, pp. 208-278.

10. Curth, E.A., and J.M., Listak, Longwall Roof Support Technology in the Eighties, USBM IC 9066, 1986, pp. 3-12.

11. Çetinkaya, H., Mechanization in OAL-Mines, Seminar Notes, presented at Middle East Technical University, 1988.

A MODEL OF SHIELD–STRATA INTERACTION AND ITS IMPLICATIONS FOR ACTIVE SHIELD SETTING REQUIREMENTS

Thomas M. Barczak, *Research Physicist*
David C. Oyler, *Mechanical Engineer*

Pittsburgh Research Center
U. S. Bureau of Mines
Pittsburgh, Pennsylvania

ABSTRACT

This paper evaluates factors which influence longwall support and strata interaction. The longwall system is composed of an immediate and main roof structure and three supporting foundations: 1) longwall panel, 2) powered roof supports, and 3) gob waste. The main roof forms a structure that is generally supported by all three foundations, while the immediate roof acts as a beam that cantilevers from the coal face to the powered support. In most cases, shield loading involves a complex interaction of both main roof and immediate roof behavior and is a combination of loads produced from subsidence of the main roof and displacements of the immediate roof caused by deformations of the cantilevered roof beam. Since the shield stiffness remains constant for all leg pressures and main roof convergence is irresistible in terms of shield capacity, the shield must be able to control the behavior of the immediate roof or floor structure for shield loading to be sensitive to setting pressures. If the goal is to minimize total shield loading, any active setting force must be offset by reduced passive shield loading to justify the active setting loads. Field data suggest that the typical reductions in passive loading do not justify the required increases in setting pressure in some applications.

INTRODUCTION

The tremendous potential of longwall mining can be realized only if adequate ground control is maintained. Hence, powered roof support specifications are critical to longwall mining. Two primary considerations in shield selection and employment are: 1) its capacity, which is measured in terms of the yield pressure of the hydraulic leg components; and 2) the setting pressure, which is used to actively set the shield against the roof at the beginning of the shield cycle. Several theories of longwall support and strata interaction have been developed, but a wide range of support capacities continue to be used for similar mining conditions (1). Furthermore, setting pressures are arbitrarily selected without consideration of geological conditions. This suggests that support and strata interaction is not well understood.

Since total shield loading is largely developed from the initial setting force, optimum utilization of the available shield capacity requires the selection of an optimum setting force which minimizes total shield loading while maintaining the stability of the immediate face area. Higher than needed shield resistance unnecessarily stresses the support structure and surrounding strata, which may reduce shield life and degrade roof stability. Hence, the potential benefits of optimum shield selection and utilization are improved safety and productivity from better ground control and reduced maintenance expenditures for the shield supports.

Historically, longwall support and strata interaction have been modeled as a detached roof block that must be maintained in equilibrium by the powered support resistance as illustrated in figure 1 (*2*). The premise of this concept is force-controlled roof behavior where face convergence is controlled by the shield resistance. This suggests a strong correlation of shield load development to setting pressures. The detached block concept ignores main roof convergence, which is irresistible in terms of the shield capacity.

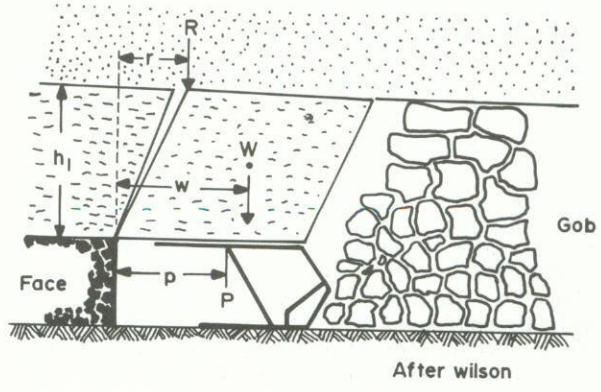

Figure 1. Detached roof model.

More recently, longwall support and strata interaction models have considered the equivalent stiffness of the total ground supporting system (longwall panel, shields, and the gob) as illustrated in figure 2 (*3-4*). This concept promotes a displacement-controlled roof behavior and adequately describes face convergence and subsequent shield loading in response to main roof activity, but tends to ignore the local behavior of the immediate roof, which may be dependent upon shield resistance.

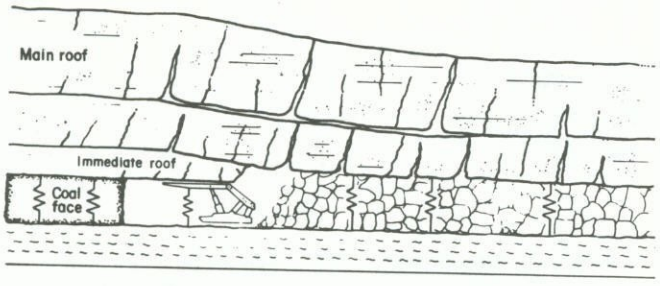

Figure 2. Equivalent system stiffness model.

The purpose of this paper is to incorporate the salient features of these and other concepts to develop a model of longwall support and strata interaction that better describes observed in situ shield response. The model considers shield load development from both the main roof and immediate roof structure. The main roof structure is that portion of the overlying rock mass that maintains sufficient structural integrity to maintain stability such that it does not produce localized loading in the immediate face area. Its weight is widely distributed among the overall ground supporting foundation, being carried by the in situ coal within the panel and the gob waste some distance from the immediate face. As the coal is extracted, the rock mass is known to subside (converge). Hence, while its weight is not directly felt by the powered supports, its downward displacement through subsidence is a source of roof-to-floor face convergence and shield loading. The immediate roof is modeled as a beam of variable bending stiffness that cantilevers from the yield zone within the coal face to or beyond the powered support. Shield loading is described as a combination of loads produced from: 1) convergence of the main roof in proportion to the stiffness of the ground supporting system, and 2) displacements of the immediate roof controlled by the weight and bending stiffness of the cantilevered roof beam and by the resistance developed by the shields.

IN SITU SHIELD LOADING OBSERVATIONS

The data presented in this paper is from an eastern Kentucky longwall that employs 780-ton two-leg longwall shields. The mine operates in the Harlan coalbed with an 8 to 12 ft seam height. The geology is characterized as a laminated gray shale immediate roof overlain by a relatively thick sandstone main roof structure. The sandstone structure is typically within 10 ft of the coal seam.

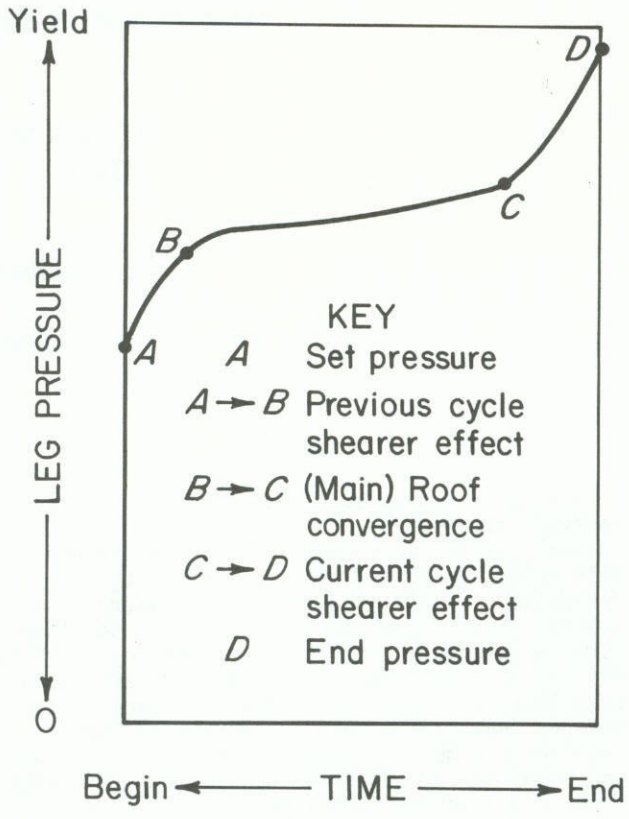

Figure 3. Shield leg pressure loading profile.

Loading Profiles

A typical profile of shield leg pressure development during a mining cycle is shown in figure 3. The shield is initially loaded by actively setting it against the roof by external pressurization of the hydraulic leg cylinders. Once set against the roof, hydraulic fluid is trapped in the leg cylinder and the shield becomes a passive support. Subsequent loads are developed in response to vertical and horizontal displacements of the canopy relative to the base in proportion to the stiffness of the support structure. Hence, total shield loading, as indicated in equation 1, is the sum of the initial load created from actively setting the shield plus the subsequent passive load developed in response to roof convergence.

$$\text{Total shield load } (F_T) = \text{Active setting load } (F_A) + \text{Passive load } (F_P) \quad (1)$$

where $F_P = (K_S \cdot D)$

K_S - shield stiffness

D - shield displacement

Shield loading rates vary during the mining cycle in response to mining activities that affect roof behavior. Maximum loading rates are generated in response to the shearer extraction of face coal in the immediate vicinity of the shield. The shearer effect is seen towards the end of the shield cycle (period C to D in figure 3) by higher rates of roof convergence several tens of feet in front of the approaching shearer and is present after the shearer passes the shield. Typically the shield is lowered before the shearer effect ends, hence the shearer effect is also seen after the support is advanced and reset against the roof at the beginning of the next cycle.

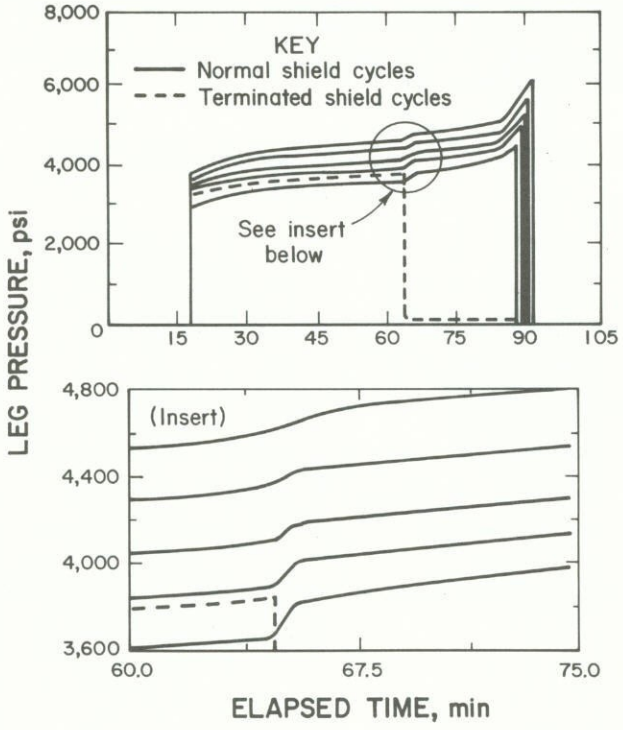

Figure 4. Effect of adjacent shield advancement on shield loading.

Also included at the beginning and end of the cycle are the effects of the advancement of adjacent shields. The change in shield loading produced from the adjacent shield advance is typically an order of magnitude below that of the shearer effect, as illustrated in figure 4 where one shield among the 6 monitored was lowered near the middle of the mining cycle and not reset for the remainder of the cycle.

During the middle portion of the cycle when the shearer is some distance past the shield (estimated at 125-150 feet for the Kentucky longwall), the shearer effect at the beginning of the cycle disappears and a substantially reduced loading rate is observed (period B to C in figure 3). This loading rate is fairly constant which indicates a constant rate of convergence. This is also the lowest loading rate observed during the shield cycle.

Data Correlations

Figure 5 depicts the correlation of passive shield loading, defined as the difference between the leg pressure when the shield was set against the roof (setting pressure) and the final leg pressure when the shield was lowered, as a function of setting pressure for 138 mining cycles representing one full week of mining. To avoid localized effects of individual shield performance in situations where a shield(s) may not be fully participating in providing roof control, an average change in shield loading on 11 consecutive shields was computed. Each data point on the graph represents one mining cycle averaged over these 11 shields.

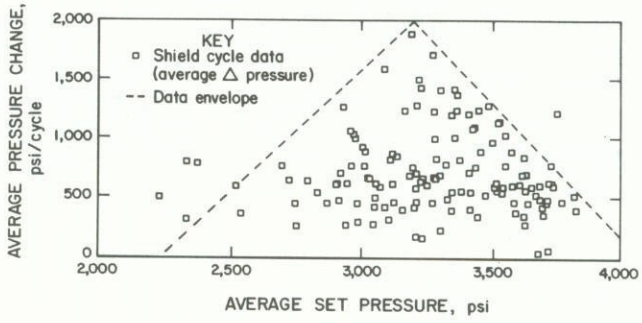

Figure 5. Correlation of passive shield loading to setting pressure.

A weak correlation of passive shield loading in response to different setting pressures was observed. This might be attributed to changes in strata geology or inconsistencies in the duration of the mining cycle. However, the envelope of the data (maximum change in loading corresponding to a given set pressure) suggests some setting pressure dependency. It appears that passive shield loading increased with increasing setting pressures up to approximately 3200 psi, and then decreased with increasing setting pressures for setting pressures above 3200 psi. Since passive shield load development is produced in response to displacement, the observed behavior requires increasing displacements for increased setting pressures up to 3200 psi and reducing displacements for increased setting pressures beyond 3200 psi.

SUPPORT-STRATA INTERACTION MECHANICS

The model proposed in this paper is illustrated in figure 6. The main roof structure is supported by the coal panel, the powered supports, and the gob waste; and the immediate roof is considered as a beam that cantilevers from the coal face to the powered supports. Shield loading in relation to strata mechanics is largely dependent upon whether the immediate roof remains coupled to the main roof. At one extreme, the immediate roof forms a free block that must be maintained in equilibrium solely by the powered support resistance (see figure 1). At the other extreme, there is no well defined immediate roof or the immediate roof

remains coupled to the main roof and shield loading is governed by the behavior of the main roof (see figure 2). In most cases shield loading involves a complex interaction of both main roof and immediate roof behavior and is a combination of loads produced from convergence of the main roof and displacements of the immediate roof caused by deformations of the cantilevered roof beam.

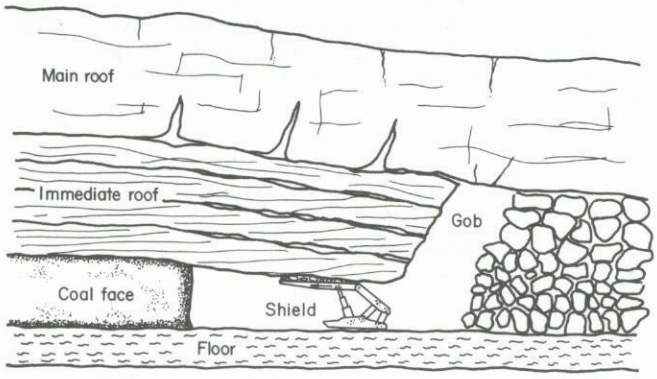

Figure 6. Proposed model of shield strata interaction.

Coupled Main Roof and Immediate Roof Behavior

When the immediate roof remains coupled to the main roof, support and strata behavior is best described by analysis of the equivalent stiffness of the ground supporting system. The underlying principle of a model based on stiffness is that the forces developed in the supporting elements are a function of the applied displacements to the supports and the stiffness of the supports as expressed in equation 2. In the context of underground coal mining, forces are imposed on the supporting system in response to the displacement of the overlying rock mass as the coal seam is extracted. Displacement equates to roof-to-floor convergence.

$$F_{SYSTEM} = [\ K_{SYSTEM}\ ] \cdot D_{SYSTEM} \qquad (2)$$

where $K_{SYSTEM} = K_{COAL} + K_{POWERED\ SUPPORT} + K_{GOB}$
F_{SYSTEM} = roof and floor loading
D_{SYSTEM} = roof to floor convergence

The face coal, powered supports, and gob form a system of parallel supports as illustrated in figure 2, with an equivalent stiffness equal to the sum of these elements. Assuming a constant roof and floor load, it is seen that face convergence is a function of the stiffness of the total ground supporting system. Roof convergence and associated load development in the support elements will be a minimum when the system stiffness of the supporting elements is a maximum. Load distribution among the individual support elements is determined by their relative stiffnesses. Since the shield stiffness is constant for all leg pressures (5), load development in the shield should not be dependent upon shield setting pressures. Hence, total shield loading will be minimized when setting loads are minimized. This suggests that passive shield application where the shield is set in contact with the roof without applying any active force provides optimum employment to minimize shield loading.

A more detailed examination, as shown in figure 7, indicates that the shield acts in series with the immediate roof and floor strata, producing an equivalent stiffness as described in equation 3. The presence of an immediate roof or floor structure, which is also acted upon by the main roof loading (convergence), will cause a reduction in the equivalent stiffness for the powered support system (roof, shield, and floor series). This will result in less shield loading (per unit displacement of main roof convergence) despite the shield stiffness remaining constant.

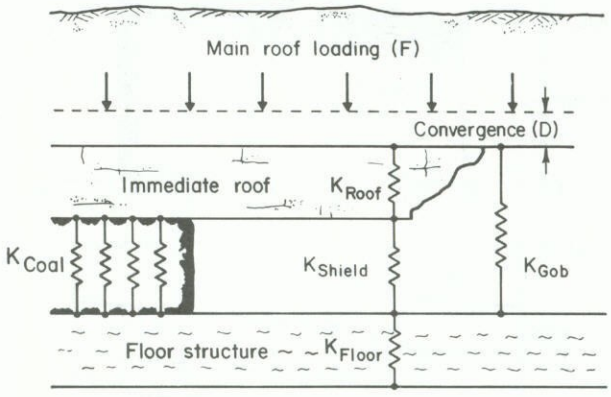

$$K_{POWERED\ SUPPORT\ SYSTEM} = \frac{1}{\frac{1}{K_{ROOF}} + \frac{1}{K_{SHIELD}} + \frac{1}{K_{FLOOR}}} \qquad (3)$$

Figure 7. Model showing shield acting in series with immediate roof and floor strata.

If it is assumed that the stiffness of the roof or floor strata is force dependent; then it can be postulated that the equivalent stiffness of the powered roof support system can be modified by changes in shield forces. For example, if there is a layer of debris on the shield canopy, the stiffness of this debris may increase with compaction from increases in shield force. This increase in stiffness of the roof will produce higher shield loading since more of the roof convergence will be seen by the shield.

Referencing equation 2, any increase in the equivalent stiffness of the powered support system will result in reduced face convergence for a constant roof load. This suggests that higher setting pressures may result in reduced face convergence and passive shield load development. However, it is necessary to consider the relative

stiffness of the powered support system with that of the coal and gob structure to evaluate the effects of increased stiffness of the powered support system. The stiffness of the shield is known to be approximately 1000 kips/in (5), which represents the maximum stiffness attainable for the powered support system (roof, shield, and floor series). A representative modulus of elasticity for coal is 250,000 psi. Computing the stiffness of the coal structure using the relationship K = A * E / L where A = area, E = modulus of elasticity, L = length; the coal structure stiffness is computed as 25,000 kips/in per unit shield width for a six foot seam (L = 6 ft) assuming a very modest 10 ft of coal supporting distance into the face (A = shield width * 10 ft). Since the coal structure stiffness is at least an order of magnitude greater than the powered support system, the powered support stiffness represents only a very small portion of the overall ground supporting system stiffness and therefore has very little effect in terms of controlling main roof convergence.

Therefore, it is concluded that increasing the axial stiffness of the immediate roof or floor by increased shield setting pressures will not significantly reduce face convergence and associated passive shield load development. It is more likely that the increased stiffness of the immediate roof or floor will transmit more of the roof convergence to the shield causing higher shield loading. Hence, passive shield application is recommended under these conditions to minimize shield loading.

Using the equivalent stiffness concept, changes in shield loading due to shearer extraction of the coal and adjacent shield advance are explained in terms of changes in stiffness of the ground supporting system. Coal in the face area is modeled as several parallel elements as indicated in equation 4. Removing elements of coal then reduces the stiffness of the coal structure. The modulus of the coal in the immediate face area may also be reduced due to a loss of confinement from the face extraction, which will further reduce the stiffness of the coal structure in the immediate face area. The reduced coal structure stiffness causes an increase in roof convergence in the immediate face area which produces load development in the shield in proportion to its stiffness.

$$K_{COAL} = K_{C1} + K_{C2} + \ldots\ldots\ldots + {}_{4N} \quad (4)$$

where $K_{C1, C2, \ldots. CN}$ = elements of coal

Similar analyses may be applied to other face functions, such as adjacent shield advance, which is also known to cause an increase in shield loading rate. Shields along the face act as a system of parallel supports providing an equivalent system stiffness equal to the sum of the individual shields as indicated in equation 5. When adjacent shields are lowered, the system stiffness is reduced and additional loading is seen on neighboring shields from the increase in convergence. Since the stiffness of the shields is substantially less than that of the coal, increased loading from shield advance is considerably less than that produced by the shearer extraction, which reduces the more dominant coal structure stiffness.

$$K_{SHIELDS} = K_{S1} + K_{S2} + \ldots\ldots\ldots + K_{SN} \quad (5)$$

where $K_{S1, S2, \ldots. SN}$ = stiffness of individual shields

Detached Immediate Roof Behavior

When the immediate roof becomes decoupled from the main roof, immediate roof displacements exceed main roof convergence and shield load development will be determined by the displacements of the immediate roof. As shown in figure 8, the roof beam will deflect from loading produced by its weight in proportion to the bending stiffness of the beam.

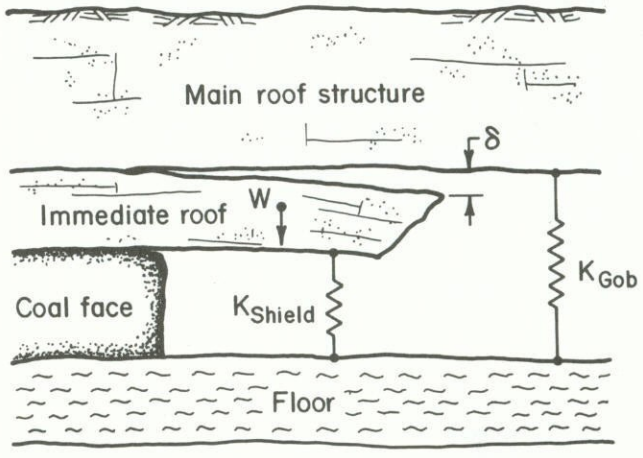

Where

W = Weight of roof beam

δ = Beam deflection

Figure 8. Cantilevered immediate roof beam.

This deflection will then cause a shield displacement and associated load development proportional to the shield stiffness. Since the shield stiffness remains constant for all leg pressures and if it is assumed that the deformation characteristics of the immediate roof do not change, passive shield loading will not be dependent upon the shield setting pressures and active setting is not required. Equilibrium of the strata will be provided by passive shield resistance generated from displacement of the immediate roof.

However, if increasing the setting pressure increases the structural moment of inertia of the immediate roof beam, its bending stiffness will increase as indicated in equation 6, and the

corresponding shield loading from the beam deflection would be reduced. If the immediate strata consists of several bedded layers, then it can be postulated that the frictional forces between layers will increase with increased shield resistance, i.e. setting force, producing a composite beam with increased moment of inertia and beam stiffness.

$$\text{BENDING STIFFNESS} = (12 * E * I) / L^3 \qquad (6)$$

where E = modulus of elasticity
I = moment of inertia
L = beam length

As illustrated in figure 3, shield loading rates are observed to increase from extraction of face coal. The previous section described this increase in shield loading from reduction in coal structure stiffness and associated increase in main roof convergence. The increased shield loading can also be explained in terms of immediate roof behavior. Assuming the immediate roof acts as a cantilevered or simply supported beam, the bending stiffness is highly dependent upon the beam length as indicated in equation 6. Hence, as the beam length increases from removal of the face coal, its stiffness is reduced causing larger deflections that produce additional shield loading. Cutting a 2-ft web could increase the deflection of a 15-ft roof cantilever by an additional 65 pct.

$$\textit{BEAM DEFLECTION}\ (\delta) = \frac{wL^4}{8EI} \qquad (7)$$

where w = distributed load,
L = length,
E = modulus,
and I = moment of inertia.

In the worst case, beam deflections under decoupled immediate roof conditions may be sufficiently large to provide failure of roof strata at the coal face such that the immediate roof forms a free block that is solely supported by the shield. Another possibility is that bed separation of the immediate roof at the main roof boundary causes failure of upper members of the immediate roof that transfers additional loading (weight) onto the cantilevered immediate roof structure directly above the shield. An active setting pressure may improve these conditions provided the structural stiffness of the immediate roof beam is increased by the additional shield resistance.

INTERPRETATION OF MEASURED SHIELD LOADING

Changes in shield loading produced during the mining cycle in response to face extraction (see figure 3) are due to the combination of the reduction in the axial stiffness of the coal structure and lengthening of the immediate roof beam. From the data available at the Kentucky mine site, it cannot be positively determined which is the more dominant factor. Examining the mathematics of the proposed mechanisms, the axial stiffness of the coal structure changes in direct proportion to the area (A) of the coal structure, K = (A * E) / L, while the bending stiffness of the immediate roof beam is a function of the cubic of the beam length (L), K = (12 * E * I) / L^3. This indicates that the roof beam bending stiffness is more sensitive to changes in beam length than the axial coal structure stiffness is sensitive to changes in area. However, it does not conclusively indicate which is the more dominant factor since they are different mechanisms.

A similar analysis can be applied to evaluate shield advancement. The fact that a change in load is seen from lowering of a single shield (see figure 4) suggests that this behavior is due to local activity of the immediate roof, since the lowering of one shield would not significantly change the overall face stiffness (see equation 5).

Figure 9 indicates that shield load development during the middle portion of the cycle when the shearer is not in the vicinity of the shield (period B to C in figure 3) is insensitive to leg setting pressures. This implies that this loading is developed from main roof convergence and that the immediate roof or floor structure stiffness remains constant during this period.

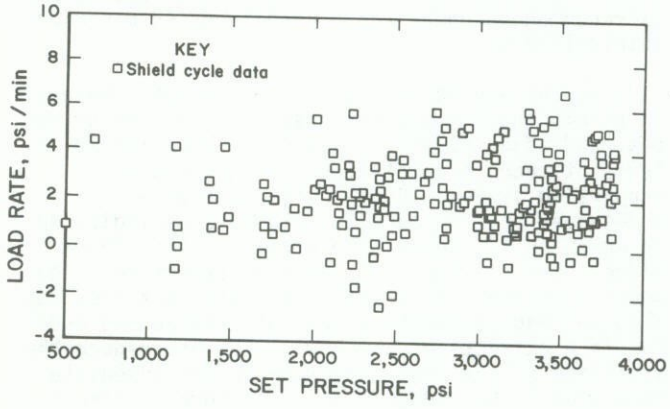

Figure 9. Shield loading from main roof movement and the effect of setting pressure.

Setting Pressure Evaluation

Since the shield stiffness remains constant for all leg pressures and main roof convergence is irresistible in terms of shield capacity, the shield must be able to change the stiffness of the immediate roof or floor for passive shield load development to be sensitive to setting pressures. Increases in axial and bending strata stiffness produce opposite effects relative to passive shield load development. Hence, consideration must be given to the more dominant factor to determine optimum setting forces.

At the mine site from which the data was presented in figure 5, it appears that the axial stiffness effects (increase in material stiffness due to compaction) dominate at low setting pressures (below 3200 psi) while the bending stiffness effects (increase in bending stiffness of the immediate roof beam from interaction among strata layers forming a composite beam) dominate at the high setting pressures (above 3200 psi).

Another explanation for the decrease in shield load development at the higher setting pressures is that the effective axial stiffness of the strata is reduced through crushing of the immediate roof or floor leading to a reduction in modulus for the immediate roof or floor strata. In general, it is not likely that the shield will induce sufficient force to fracture roof or floor material, except at contact asperities which may produce some localized failure and reduced stiffness.

If the factor to be optimized is shield loading, optimum setting pressures can be determined by examining total shield loading as a function of setting pressure. For the data presented in figure 5, this relationship is illustrated in figure 10. The graph shows that minimum total shield loading was developed at the minimum set pressure, which indicates that the benefits derived from reduced passive load development at the higher setting pressures is offset by the higher active setting loads (see equation 1). This suggests that for these conditions, passive shield application would produce the least overall shield loading.

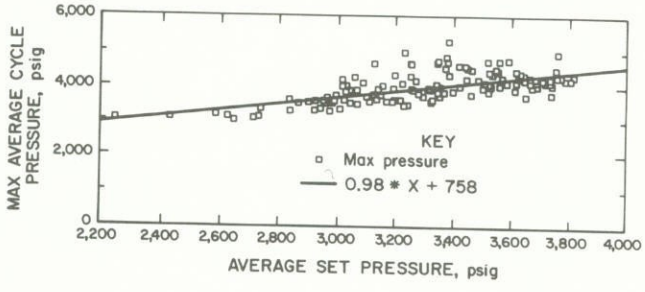

Figure 10. Total shield loading as a function of setting pressure.

SUMMARY REMARKS AND CONCLUSIONS

Strata mechanics associated with longwall mining is a complex interaction of the main roof structure, the immediate roof and floor structure, and the ground supporting elements which are the coal panel, the powered roof supports, and the gob waste. Historical concepts of longwall support and strata interaction do not fit well with measured in situ shield loading. Other concepts need to be explored and the model proposed in this paper is one such concept. Such models may lead to better definitions of support capacity and setting loads for various geological conditions. Optimum employment of shield capacity may increase shield life and improve ground control by minimizing unnecessary shield and strata loading.

Four points are made from the proposed model that are critical to shield capacity and active setting force considerations.

1. The primary function of the powered supports is to control the immediate roof which cannot maintain stability without additional support. The shield has inadequate capacity to significantly affect the behavior (convergence) of the main roof. Main roof behavior is primarily controlled by the stiffness of the coal structure in the face area and the stiffness of the gob waste in the region beyond the face.

2. Total shield loading will be the sum of the initial load generated from active shield setting plus the load generated in response to strata convergence, which is described as the product of the convergence and the shield stiffness. Currently, setting loads represent the majority of overall shield loading since the current philosophy is to set shields at 50 to 60 pct of the yield capacity. Any effort to minimize shield loading must consider both sources of loading.

3. A critical point in understanding shield load development is that the shield stiffness remains constant for all leg pressures. This means that the shield's ability to resist convergence is the same regardless of the setting pressure or overall shield resisting force. Therefore, for displacement-induced roof behavior where force equilibrium of the strata is not attained or controlled by the shields, shield load development is independent of setting pressures.

4. It is postulated that increased shield resistance (setting force) can influence strata behavior in two ways: (1) by increasing the axial stiffness of the immediate roof or floor through compaction of broken debris, or (2) by increasing the bending stiffness of the immediate roof beam by increasing the moment of inertia through frictional forces developed between individual strata layers. Shield loading will increase in response to the debris compaction and decrease in response to increased bending stiffness of the immediate strata.

In consideration of these four critical points, it is concluded that shield response and optimum employment depends on whether main roof or immediate roof behavior dominates. Passive application where the shield is set in contact with the roof without applying any force is recommended for main roof behavior where the convergence is irresistible in terms of shield capacity. Minimizing the setting force will preserve more of

the available shield capacity to accommodate the main roof convergence in these conditions. Immediate roof and floor strata are postulated to exhibit force dependency characteristics relative to their axial and bending stiffness. The ability to minimize total shield loading through active setting forces depends upon the capability of the shield to sufficiently increase the bending stiffness of the immediate strata to offset increased loading from increases in axial stiffness of the immediate strata and to offset the additional load caused by the higher setting loads. Data analyzed from one mine site in eastern Kentucky suggest reduced setting pressures would minimize total shield loading despite apparent reductions in passive shield load development at high setting pressures. Hence, there appears to be evidence for reduced setting pressures in some applications.

The justification for passive support application or reduced setting pressures as proposed in this paper is based upon the criteria to minimize overall shield loading. It is recognized that the reduced setting pressure may produce increased immediate strata convergence, and a decision must be made based upon site specific geological conditions if this increased convergence may cause roof stability problems. However, it should be recognized that the stiffness of state-of-the-art shield supports permits about 1-in of displacement when used totally as a passive support and it is this magnitude of convergence that should be considered in these evaluations.

REFERENCES

1. Barczak T. M. "Selecting the Right Shield Support." Engineering and Mining Journal, May, 1990.

2. Peng S. S. and Chaing H. S. "Longwall Mining." Wiley, New York, 1984, p 218.

3. Peng S. S., Hsiung S. M., and Jiang, J. M. "Method of Determining Rational Load Capacity for Shield Supports at Longwall Faces." Mining Engineer, October 1987, vol 147 No 313, pp 161-167.

4. Smart B. G. and Redfern A. "The Evaluation of Powered Support Specifications From Geological and Mining Practice Information." Rock Mechanics: Key to Energy Production, pp 367-377.

5. Barczak T. M. and Schwemmer D. E. "Stiffness Characteristics of Shield Supports." BuMines RI 9154, 1988, 14 pp.

STABILITY OF INTERPANEL–PILLAR AND DEFORMATION OF GATEROAD DUE TO LONGWALL MINING

K. Matsui, *Associate Professor*
M. Ichinose, *Research Associate*
K. Uchino, *Professor*

Department of Mining
Kyushu University
Fukuoka, 812, JAPAN

ABSTRACT

Retreat longwall method with re–use of gateroad has been traditionally employed in Japan, mainly because of the advantage of higher recovery. But the Miike Colliery has newly introduced the interpanel–pillar system to maximize the production efficiency.

The Department of Mining, Kyushu University, in cooperation with the Miike Colliery and the Coal Mining Research Center (CMRC), has conducted research into the optimum design of interpanel–pillar, because this system may be adopted in other coal mines as well.

Field measurements of the deformation of the gateroads and of stress distribution in the pillar show that the designed layout of the panel and pillar and the supporting system are proper from the viewpoints of gateroad maintenance and spontaneous combustion in the pillar.

INTRODUCTION

Over the past decade the coal production in Japan has almost reduced by half from 17.8 Mt in fiscal 1979 to 9.6 Mt in fiscal 1989. The reason for this drastic reduction was primarily due to the widening price gap between domestically produced and imported coal. In this difficult economic environment, the coal mines have been making extensive efforts to rationalize the mining operation. Introduction of a new longwall mining system at the Miike Colliery is one of the projects to augment coal face productivity to the maximum. Retreat longwall method with re–use of gateroad has been traditionally employed, mainly because of the advantage of higher recovery. But from the viewpoint of production efficiency this method is not suitable, requiring intensive work for side packing and roadway maintenance. Therefore, the interpanel–pillar system, or two–entry gateroad system using larger powered coal winning equipments was adopted to enhance the productivity of longwall mining. In this system, optimum design of interpanel–pillar is of critical importance for achieving safety, economy and efficiency of longwall mining. The optimum pillar must be designed so that it is able to maintain the gateroads until the passage of the second–panel longwall face and to collapse soon thereafter. Improper pillars left in place are not only a waste of precious resources, but also create some problems such as severe roadway closure and spontaneous combustion.

Various pillar design techniques have been developed over several decades for ground control, but very few for spontaneous combustion problems. The coal seam at the Miike Colliery are prone to spontaneous combustion and great efforts have been made for early detection of combustion. However, there is still a possibility that spontaneous heating develops so fast to the uncontrollable stage of combustion that both coal itself and expensive face equipment are left unsalvaged for a long time or permanently. Therefore, it is essential to know in advance whether or not there are potential conditions which may trigger the spontaneous heating of coal. Accordingly the extend of the development of failure zone in the interpanel–pillars has significant importance for assessing the possibility of spontaneous combustion.

The purpose of this study is to assess the stability of the interpanel–pillar under the influence of longwall mining by means of continuous pillar load measurements using hydraulic borehole pressure cell, roadway closure measurements, on–site observations and gas injection technique.

SITE INVESTIGATION

Site description

Site investigation was carried out at the Miike Colliery on Kyushu island as shown in Fig. 1. The colliery is the largest and oldest undersea coal mine in Japan, producing 5.4 Mt in fiscal 1978, 4.5 Mt in 1985 and 2.5 Mt in 1989.

The formations in the Miike coal fields are of Pre–Tertiary, Tertiary and Quaternary ages. The Pre–Tertiary formations consist of granite and crystalline schists which are overlain unconformably by the Tertiary formations. The latter have a thickness of 700 m and comprise beds of sandstone intercalated with shale, conglomerates and coal seams. These seams are exposed in the northeastern districts of Ohmuta City. The Quaternary formations, which have a maximum thickness of 400 m overlie the Tertiary formations under the Ariake Sea.

Within the Tertiary formations there are a total of nine coal seams, of which three are workable. These are known respectively as the Second Upper Seam, Upper Seam, and Main Seam, in descending order. The principal dip of the seams is between 2° and 5° to the southwest – they go deeper as they go further off–shore. Most of the faults in the area are of the normal type, with a tendency to strike eastwest. There is about 50 m thickness of strata between the Main and Upper seams, and 140 m between the Upper and Second Upper seams. A schematic section through the Miike Colliery is shown in Fig. 2.

Fig. 3 shows the study site located in the Second Upper seam in the West–80 area. There are no panels in the other two seams below the investigated area. In this area, the Second Upper seam is at a depth of about 430 m below sea level and the seam thickness varies between 4.0 m and 4.3 m. The seam is overlain and underlain by sandstone, but is locally underlain by shale. Mechanical properties of these rocks and coal deteriorate greatly in the presence of water and shale exhibits a slaking phenomenon when it comes in contact with water. Table 1 lists the mechanical properties obtained from the laboratory and the field tests. Coal samples were taken from the upper, the middle and the lower portion of the pillar at the study site.

The study site was selected in the tail–gate of the East 4th panel. This gateroad was developed during 1988–89 utilizing 25–m–wide diamond–shaped pillars, and was affected by the extraction of both (East 3rd and East 4th) panels. Both faces were 150 m wide. The retreat distance of the East 3rd and the East 4th panels were approximately 680 m and 840 m, respectively. These faces are called the Miike High Power Plant (MHP) face, a new longwall mining system, employing the larger powered, more efficient and mechanized mining equipment (Furukawa, 1989). The extracted height was about 2.8 m, leaving floor coal 1.5 m thick unworked. The rate of face advance was approximately 10 m/day in both cases.

The gateroads were driven by a roadheader of the MRH S–65 from Mitsui Miike Machinery Co., Ltd., and supported by a three–piece set of a trapezoidal shape with a 4.2 m steel beam and two 3.0 m wooden props at 1.0 m centers as shown in Fig. 4. The supports were tied and lagged with wood. In the tailgate strata bolting was employed. Resin–grouted steel bolts and wooden dowels were not installed immediately after the excavation by the MRH S–65, but at about 50 m ahead of the active longwall face. Under poor strata conditions, supplemental wooden props along pillar were also erected ahead of the active face.

Instrumentation

Eight boreholes with 80 mm in diameter were drilled horizontally in the pillar and the tailgate rib of the next (East 4th) panel at the study site, as shown in Fig. 3. Three holes P1 to P3 were used to measure vertical load in the pillar by means of 11 borehole pressure cells developed by the CMRC. These pressure cells were arrayed to determine a profile of vertical load distribution across the instrumented pillar. Cell pressures were transmitted continuously through a phone line to a computer at a surface station and were also available at the site by reading a Bourdon pressure gauge.

Five boreholes G1 to G5 were used to measure permeabilities of the coal seam by means of nitrogen gas injection technique (Barron, 1978), as shown in Fig. 5. Before the installation of the fixed type packer, gas injection testing using movable type packer was conducted in holes G2, G3, G4, and G5. A distribution of fractures along borehole was also observed using a borehole–scope in holes G4 and G5.

Supplemental information was obtained from the measurements of vertical and side closure at the ten stations (D_2 and D_{10}), as shown in Fig. 3. Roadway closure was determined by the variation of height between the marks at the roof and the floor, H, and of width between the marks on the heads of wooden dowels at the sides, W, as shown in Fig. 4.

Monitoring of these variables was conducted during the extraction of both adjacent (East 3rd and 4th) panels.

Results and discussion

Fig. 6 shows the distribution of fractures along the length of boreholes without the influence of longwall mining operation. Observation was not carried out along the entire wall surface of the borehole, but along one scanline through a small field of vision. Therefore, the reliability of the results is not considered very high, and a great deal of flaws formed during drilling are also included in the obtained results. However, several large open cracks and wall collapses were clearly observed within 1.5 m from the mouth of each hole. This implies that failure zone was created around the roadway during and after development. This was also confirmed by means of nitrogen gas injection technique using movable type packers.

The history of pillar loading during the extraction of the East 3rd panel is presented in Figs. 7–9. In the following

discussion, a negative (−) value indicated the distance ahead of the face position to a particular instrument, and a positive (+) one indicates the distance behind the face position to the instrument location. The pressure cell placed at a depth of about 16 m in borehole P2 failed during the setting of the initial pressure and did not respond to ground loads. As the East 3rd face approaches the site, the onset of the forward abutment loading becomes apparent at −40 m in the cell nearest to the active (East 3rd) panel, and the side abutment loading increases the cell pressure. Consequently, failure occurs around the cell and the pressure drops rapidly. Pressure data of the cell at 18 m show the fluctuation similar to a stick–slip behavior as observed in triaxial compression testing, and appear to indicate progressive failure occurring in the pillar. The intermediate cells indicate steady increases in vertical pressure as the face approaches and passes, but no failure occurs in the center of the pillar, forming a pillar core. This seems to be attributed to the existence of high horizontal stress in the pillar center, although not monitored in this study. The cells at 2 m and 4 m, which are farther from the mining panel, do not respond well to both forward and side abutment loadings because of fracturing after the development.

Fig. 10 shows the profiles of vertical load distribution across the instrumented pillar corresponding to several face positions, which clearly exhibits the high magnitude asymmetric loading across the pillar. As the face approaches the study site, the greatest loading takes place within 3 m of the pillar edge near the active panel. After the passage of the face, the greatest loading transfers to the center of the pillar, indicating that coal fracture yielding occurs within about 7 m of the face–side pillar edge and a pillar core is formed in the center of the pillar.

Fig. 11 presents the changes in permeability in the pillar during extraction of the East 3rd panel. Installation of the fixed packer into the borehole G5 failed owing to the hole collapse near the mouth, and the changes in permeability in the tailgate rib of the next (East 4th) panel due to the active (East 3rd) panel were not able to obtain. As mentioned above about pressure data, the changes in permeability of pillar coal also show the influence of longwall mining. The permeability in the coal near the tailgate (G1) shows a higher value than those at the pillar center, representing the fracture formation in the proximity of tailgate during and after development. As the face pulls even with the site, the permeability decreases remarkably because of the installation of fully resin–grouted dowels into the pillar rib, as shown in Fig. 4. However, as the face advances beyond the site, the value becomes greater, indicating the occurrence of fracturing by the side abutment loading. The permeability from G2 also increases after the passage of the face. On the other hand, the permeability in the pillar core shows a low value even after the extraction of the East 3rd panel, indicating that no fracture yielding occurs in the core.

Figs. 12 and 13 show the history of pillar loading with the advance of the next (East 4th) face. Full history of loading until the passage of the face was not able to obtain due to the breakdown of monitoring system for some cells and some operational problems. But some data were taken by reading a Bourdon pressure gage at the site. As the face approaches the study site, the forward abutment loading increases all the cell pressure gradually. The intermediate pressure cell at 12 m shows a rapid drop at −100 m. This indicates that coal yielding is occurring around the cell. However, the pressure begins to increase again with the advance of the face.

Fig. 14 presents the profiles of vertical load distribution across the pillar at several face positions of the next (East 4th) panel. As the next panel face approaches, the maximum pressure of the cell in the pillar center decreases, indicating that coal yielding occurs in the pillar core. Afterwards the pressures of cells nearer the 4th panel begin to increase. However, as the face approaches within 30 m of the study site, the cell pressures decrease and reach the residual strength level of the pillar. This indicates that the fractured yield zone is created across the entire pillar.

Fig. 15 and 16 are observed patterns of the roadway closures in the tailgate of the East 4th panel during the extraction of the East 3rd and 4th panels. The gateroad begins to deform at 20–40 m ahead of the face–line. After the passage of the face, the closures increase rapidly, and tend to reach the constant levels within 200 m behind the face–line. The vertical and side closures exhibit a similar trend, but the former is less than the latter, because the roof rock is relatively strong and almost intact. With the approach of the next (East 4th) face, the gateroad begins to deform rapidly at 40–50 m ahead of the face–line and reaches the peak value at the face–line. Although the study site was located under relatively good strata conditions, pillar and rib spallings were observed and some installed dowels were failed when the face approaches within 30 m. This behavior is anticipated from the results of pressure monitoring in the pillar. However, thanks to the strata bolting, the supports were kept stable without failure and severe distortion. In order to improve the situation further, longer dowels should be installed into both sides. Under poor strata conditions, however, severe spalling of pillar and rib and floor heaving occurred and the wooden props along the pillar were almost broken even after the passage of the first (East 3rd) face. However, it should be noted that under severe strata conditions, roof bolting contributes to the stability of roof without excessive bending and distortion of the roof beam of the support.

Finally the designed width of the pillar was compared with those obtained from various reported methods for pillar design (Peng, 1986). The necessary width of the pillar under the conditions of this study site is estimated to be between 22 m and 45 m. The employed pillar width of 25 m is within the

calculated range and actually the pillar neither created serious gateroad maintenance problem nor showed signs of spontaneous combustion. It can be safely said that the design pillar is appropriate to protect the gateroad under the good strata conditions. However, in order to establish a more general method for pillar design, support system, the post–failure behaviors of roof, floor rocks and coal seam and operational conditions concerning the neighboring coal faces should be taken into consideration.

CONCLUSIONS

Field measurements and observation for assessment of stability of interpanel–pillar of longwall mining for roadway maintenance and spontaneous combustion were performed. Results show that the stability of the pillar is sufficient to maintain the gateroad and prevent air leakage through the pillar under good strata condition, although under poor strata conditions, severe deformation was observed. In order to establish the optimum pillar design method, more experience and field data must be obtained.

ACKNOWLEDGEMENTS

The authors would like to thank Manager Mr. Uesugi, Deputy Managers Messr. Furukawa and Tsuji of the Miike Colliery and Mr. Hatakeyama of the CMRC for their assistance in this research project.

Any opinions stated in this paper are those of the authors themselves and not necessarily those of the colliery and the CMRC.

REFERENCES

Barron, K., 1978, "An Air Injection Technique for Investigating the Integrity of Pillars and Ribs in Coal Mines," International Journal of Rock Mechanic & Mining Sciences & Geomechanics Abstracts, Vol. 15, pp. 69–76.

Furukawa, H., 1988, "Development of High Productivity Plant (called MHP)," Journal of the Mining and Materials Processing Institute of Japan, Vol. 105, No. 11, pp. 808–811, (in Japanese).

Peng, S. S., 1986, "Coal Mine Ground Control," 2nd edition, Wiley, New York, pp. 237–264.

Matsui, K., M. Ichinose, and H. Shimada, 1989, "Estimation of the Mechanical Properties of Weak Rocks by Rod Penetration Test," Journal of the Japan Society of Engineering Geology, Vol. 30, No. 4, pp. 28–34, (in Japanese).

Table 1. Mechanical properties of coal, roof, and floor rocks.

		Sc (kgf/cm^2)	E_{50}, x 10^3 (kgf/cm^2)	St (kgf/cm^2)
Roof				
Sandstone	(dry)	743	82	54
	(wet)	310	36	19
Coal				
Upper	(dry)	129	19	14
	(wet)	115	18	15
Middle	(dry)	302	25	19
	(wet)	255	24	16
Lower	(dry)	301	24	27
	(wet)	288	22	28
Floor				
Sandstone	(wet)	400[1)]	40[2)]	40[3)]
Shale	(dry)	298[4)]	31[4)]	30[3)]
	(wet)	127[4)]	18[4)]	13[3)]

Sc – Uniaxial compressive strength, E_{50} – Tangent Young's modulus at 50% of peak stress, St – Brazilian tensile strength 1): Schmidt hammer test, 2): E_{50} = 100Sc, 3): St = 0.1Sc, 4): Rod penetration test, Sc = 0.11Srp, E_{50} = 2.3Erp (Matsui et al., 1989).

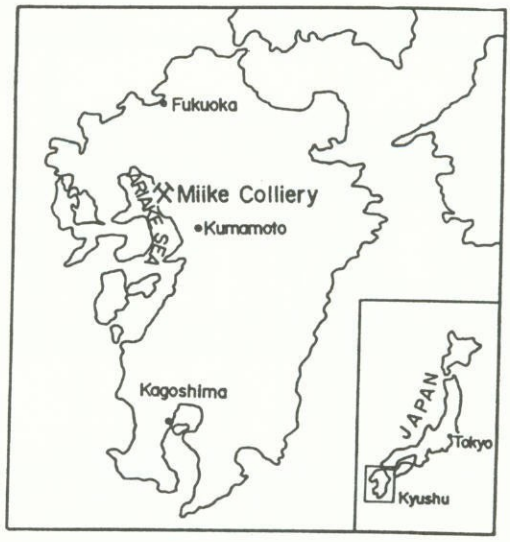

Fig.1 Location map of the Miike Colliery.

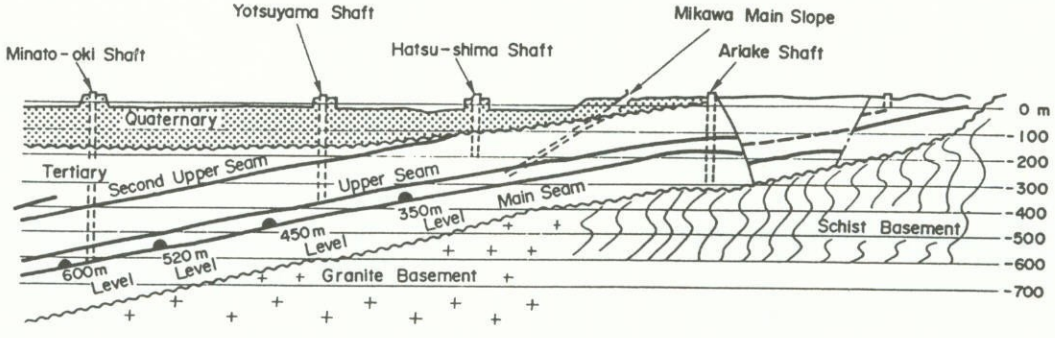

Fig.2 Schematic cross-section of the Miike Colliery, showing simplified geology.

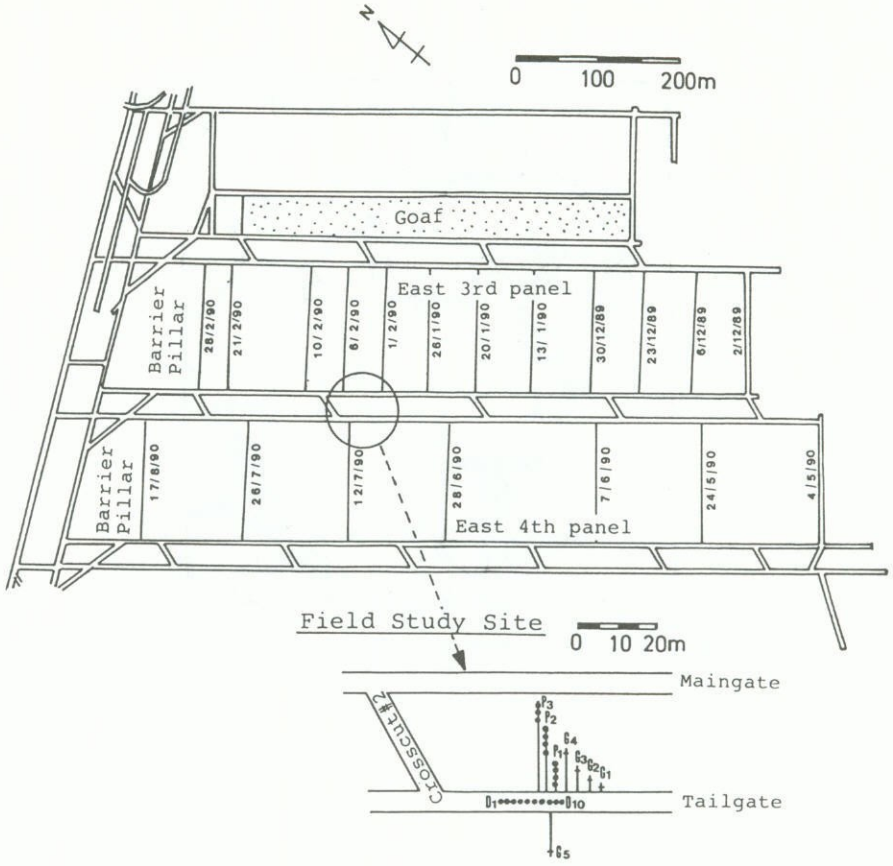

Fig.3 Location of field study site.

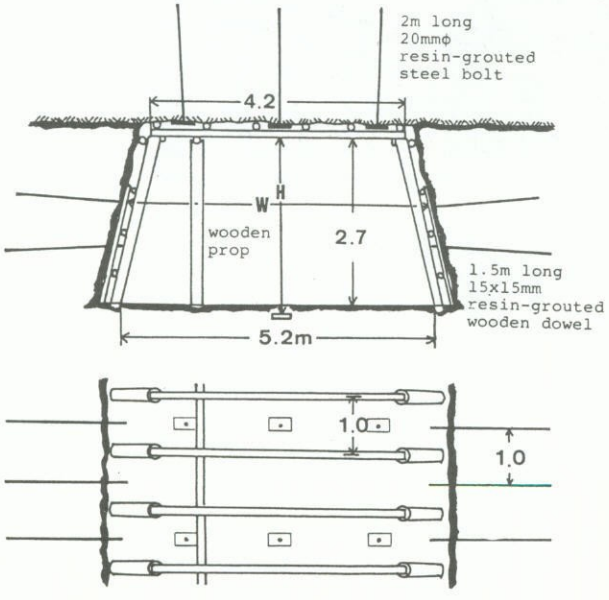

Fig.4 Support system in tailgate.

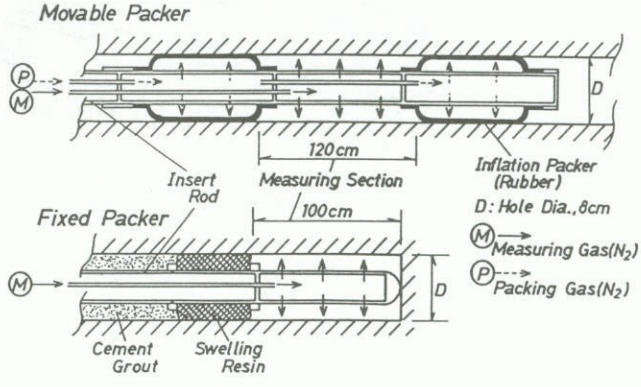

Fig.5 Apparatus of gas injection technique.

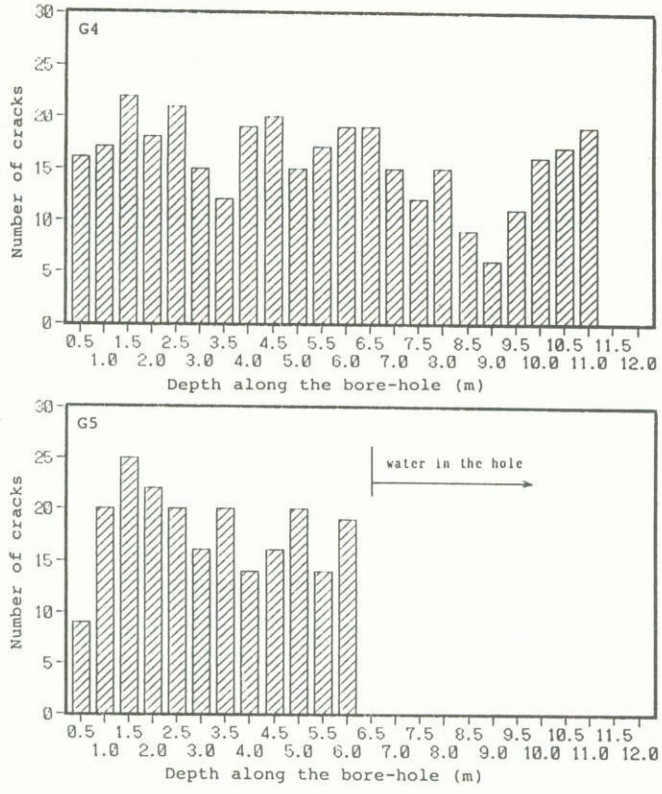

Fig.6 Distribution of fractures in the coal seam.

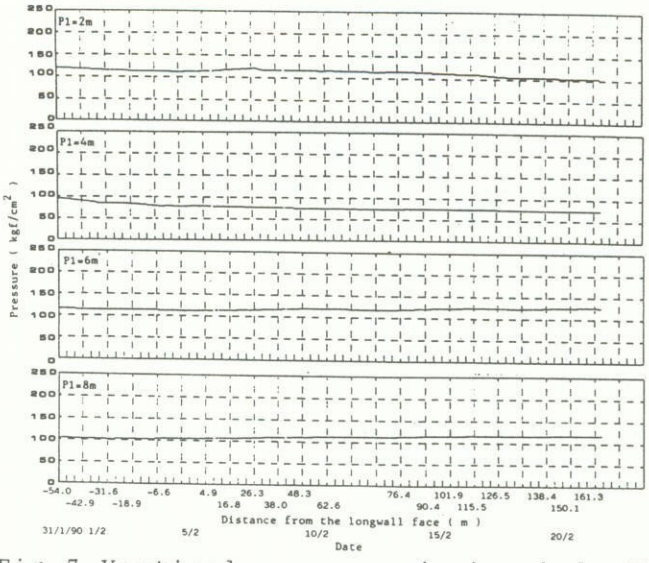

Fig.7 Vertical pressure in borehole P1 during the extraction of the East 3rd panel.

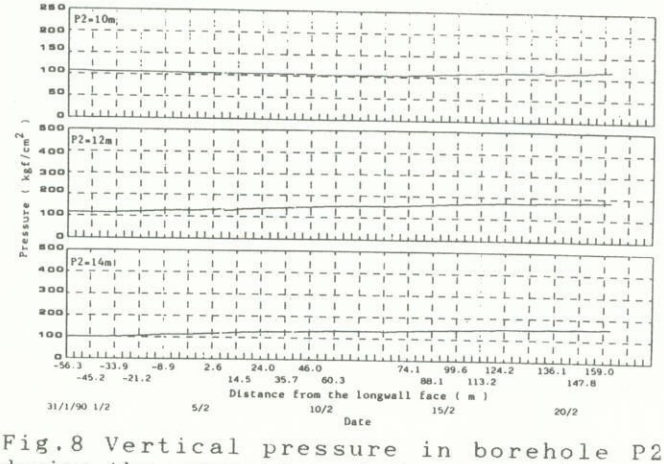

Fig.8 Vertical pressure in borehole P2 during the extraction of the East 3rd panel.

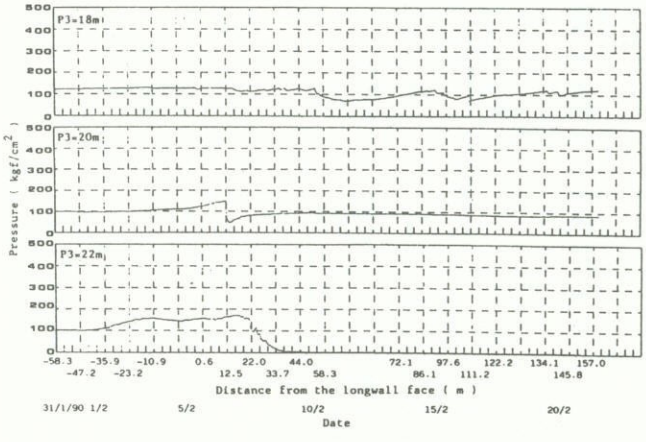

Fig.9 Vertical pressure in borehole P3 during the extraction of the East 3rd panel.

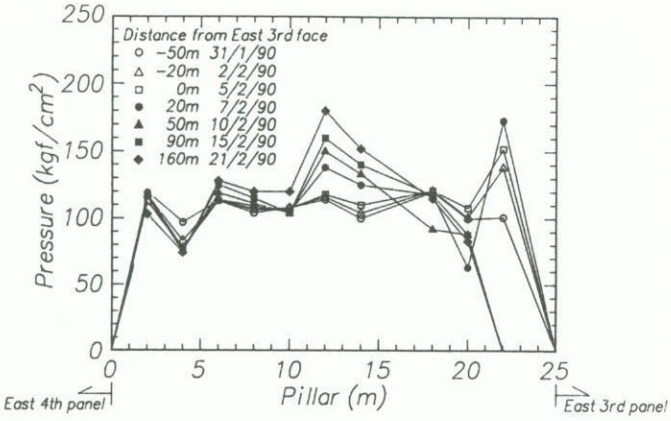

Fig.10 Vertical pressure profile across the instrumented pillar.

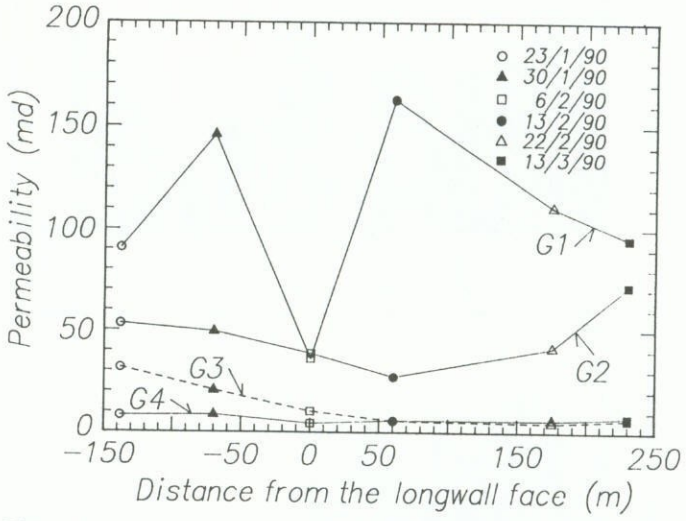

Fig.11 Changes in permeability during the extraction of the East 3rd panel.

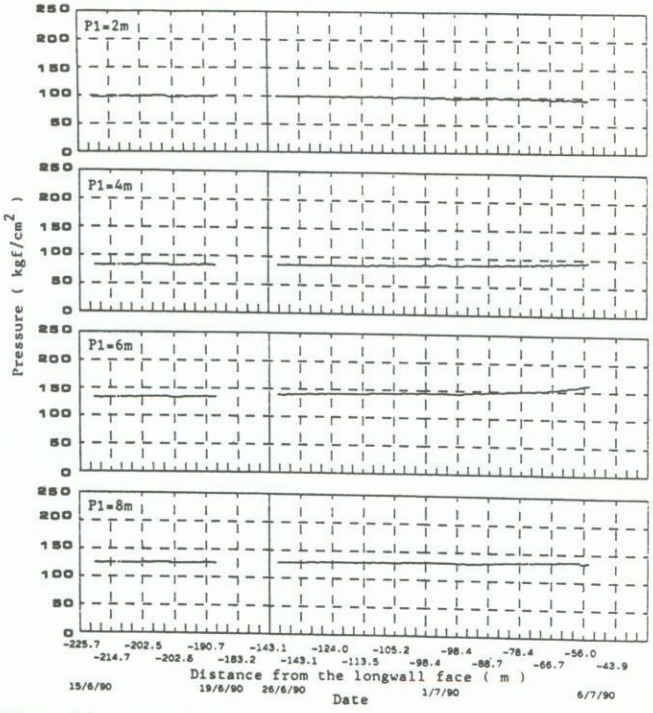

Fig.12 Vertical pressure in borehole P1 during the extraction of the East 4th panel.

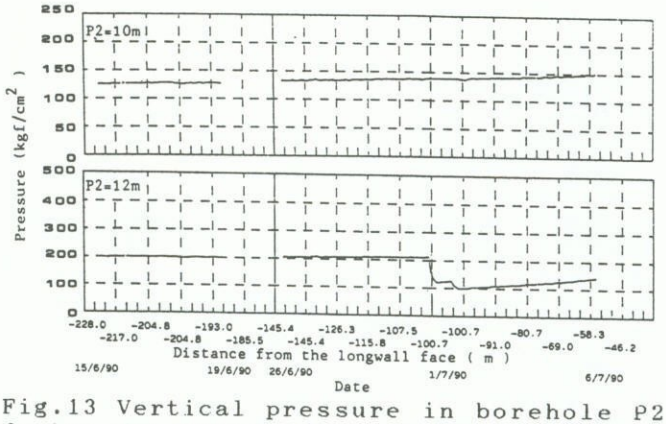

Fig.13 Vertical pressure in borehole P2 during the extraction of the East 4th panel.

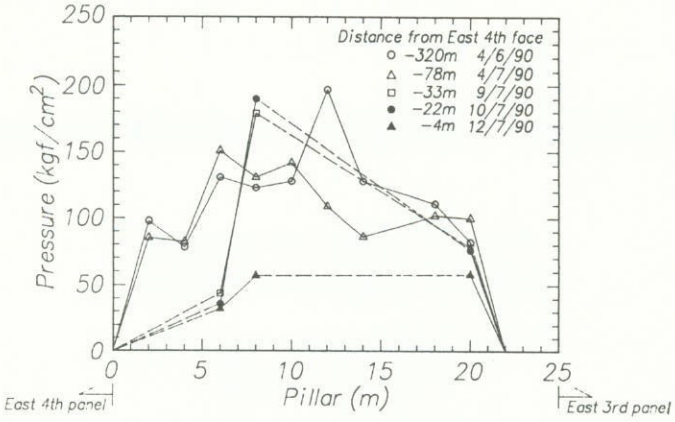

Fig.14 Vertical pressure profile across the instrumented pillar.

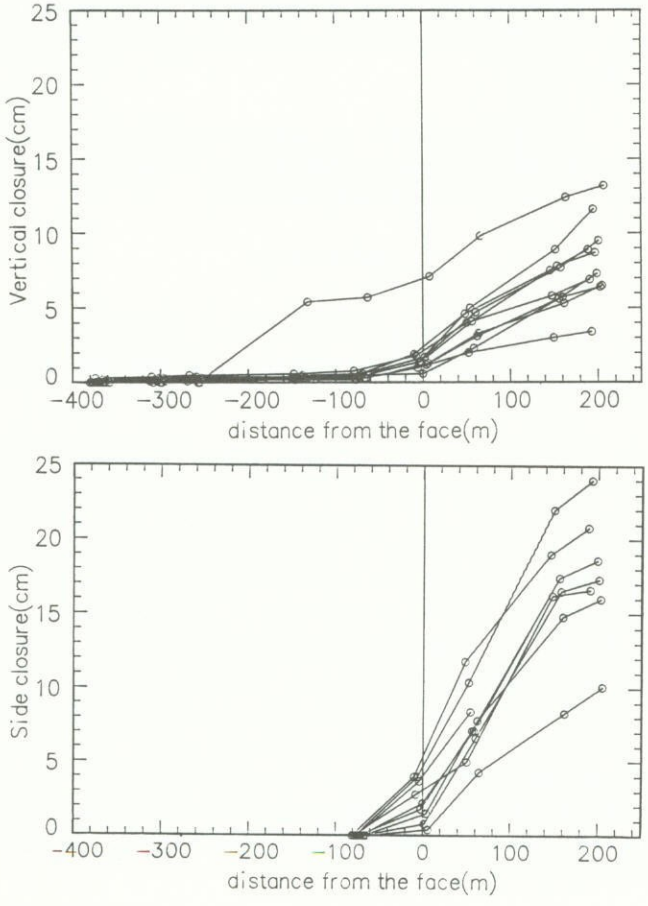

Fig.15 Roadway closures in the tailgate during the extraction of the East 3rd panel.

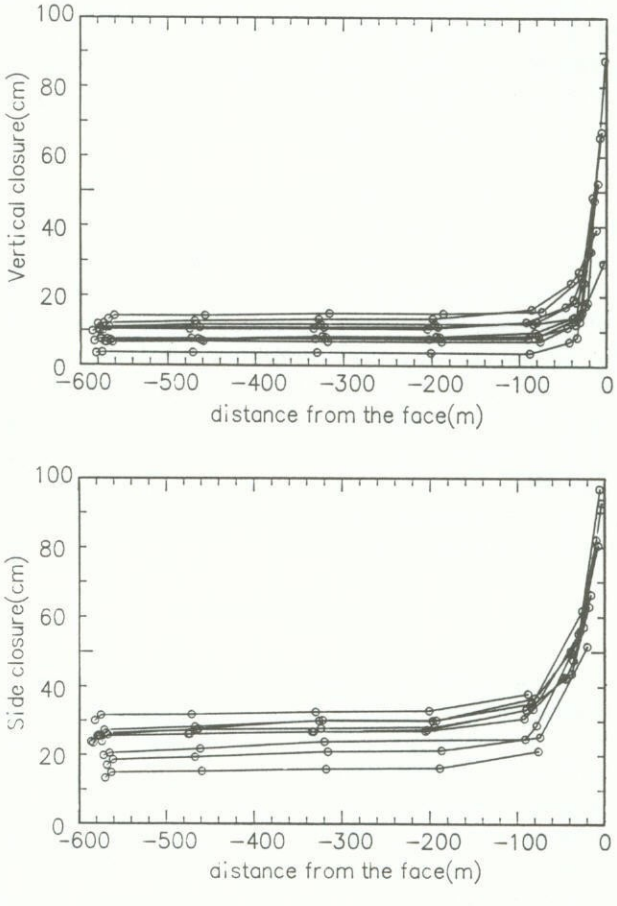

Fig.16 Roadway closures in the tailgate during the extraction of the East 4th panel.

USE OF POLYMER GRIDS FOR LONGWALL SHIELD RECOVERY

Brian E. Travis, *Mining Engineer*
Ronald P. Anderson, *Civil Engineer*

Tensar Earth Technologies, Inc.
Morrow, Georgia

ABSTRACT

The recent development of polymer grids for the underground coal mining industry has created new alternatives for supplemental ground control practices. The grids utilize strong, lightweight polymers – usually special grades of polypropylene. High tensile strengths and resulting load support characteristics are achieved by molecular orientation of these polymers in the manufacturing process.

One of the most important applications of polymer grids as supplemental ground control is in longwall shield recovery. When shields are moved from one face to another, the determining factor in the success of the recovery is the ground control provided by roof support structures along the old face. Whereas primary support is usually provided by roof bolts and cables which run the full width of the panel, supplemental support is often provided by metallic meshes of welded wire or chain–link fence. Lightweight, high–strength polymer grids replace these heavy, cumbersome metallic meshes, giving the operation increased productivity by decreasing installation time and reducing injury downtime.

INTRODUCTION

Underground coal mines which employ longwall mining technology are the most productive and usually most profitable mines in operation. A key factor in longwall productivity/profitability is quick, safe longwall moves since prolonged downtime between lowering of shields on the old face to raising them on the new can translate into thousands of tons of lost production, and therefore hundreds of thousands of lost revenue. For this reason, once a longwall move has begun, it often takes precedence over every other underground mining operation, except safety.

Fortunately, speed and safety go hand–in–hand in a longwall move. The use of lightweight, high–strength polymer grids as supplemental roof control helps provide a safe working space for personnel and equipment during recovery (extraction) of the shields. Moreover, the grids help keep the recovery area clean and uncluttered of gob debris thereby leaving a smooth, level bottom, which facilitates transport of shields along the face. The grid's chief benefits are their ease, speed, and safety of application.

This paper describes the polymer grid(s) currently being used for longwall shield recovery, and the procedure by which several mines have successfully used them.

DESCRIPTION

There are currently two types of biaxially oriented polypropylene grid structures used in underground coal mining operations.

BX3316 is a self–extinguishing polymer grid, incorporating a halogen type flame retardant additive, with antimonytrioxide as a synergist component. The flame retardant compound used is certified by the manufacturers tc meet a V–O criteria under the U.L.–94 flammability test. A blend of stabilizers is incorporated into the compound, to provide high temperature stability during processing, along with protection against oxidation and ultra–violet (U.V.) light degradation. As for the base polypropylene base carrier, it provides for high physical properties, proper melt flow characteristics, and the ease of dispersion of the flame retardant additives. The polymer is also inherently resistant to most biological and chemical attack when utilized in even the most alkaline or acidic environments.

BX3320 is comparable in structure and physical properties to the BX 3316, except that it is not a self–extinguishing product. The base resin is a polypropylene copolymer, pigmented white for high visibility. Like the BX3316, the non–flame retardant BX3320 offers high tensile

strength, high flexural rigidity, a lightweight structure, along with good impact resistance.

MANUFACTURING PROCESS

The production of polymer grids for underground mining applications is accomplished in a three stage manufacturing process:

Sheet Extrusion

A multi–component blending system allows for precise control of the raw material additives mix. This on–line blender feeds directly to the extruder, which compresses and melts the plastic pellets, and then pumps the molten extrudate. A gear pump and a melt mixer are included in the extrusion system, to provide for a very accurate, consistent flow of a homogeneous melt. At the end of the extruder is a sheet die, which evenly distributes the molt flow across the desired sheet width.

The sheetline portion of the process accepts the molten sheet, cools it slowly and uniformly, controls the sheet thickness, and provides for a smooth surface finish. The sheet thickness tolerance are very tight in the sheet process, with a +/– 1.0% specification in both the machine and transverse direction. The sheet thickness is monitored at all times with an on–line thickness profiler. The finished sheet is then wound onto large reel carts for transfer to the next process.

Sheet Punching

The second stage of the polymer grid production process involves punching the solid sheet with a pattern of holes, prior to its orientation. Specially designed punch tools and heavy duty presses are required. Several hole geometries and punch arrangements are possible, depending upon the finished product properties of the grid, in order to meet the requirements of the ground control application.

Once punched the sheet is again wound onto reel carts, for transfer to the orientation process.

Orientation

The polymer raw materials used in the manufacturer of the grids are selected for their excellent physical properties. However, the very high strength properties of the finished grid are not fully realized until the base polymer's long chain molecules are stretched (Oriented) for the mining grid, this is accomplished in a two stage process.

Initially, the punched sheet is heated to a critical point in the softening range of the polypropylene polymer. Once heated, the sheet is stretched in the machine direction, through a series of heated rollers. During this uniaxial stretching, polymer is drawn from the junctions into the rigs as the orientation effect passes through the junction zones. This guarantees continuity in molecular orientation in the resultant structure.

In the second stage, the uniaxially oriented grid enters a heated tenter frame (stenter) where the material is stretched in the transverse direction, at right angles to the initial stretch. This biaxial stretch process imparts a high degree of orientation and stretch throughout all regions of the grid.

Exiting the stretching process, the material is quenched (stabilized), and then slip and wound to meet customer roll dimension requirements.

PREPARING POLYMER GRID SCREENING (SURFACE)

Typically the BX 3320 is used for longwall shield recovery (screening). It is available in 13 ft. x 200 ft. roll dimensions. These rolls are joined together on the surface to eliminate most of the time consuming fastening (dinging) underground on the longwall face.

The rolls are laid out side by side with a two (2) ft. overlap at the seams. The seams are then joined by means of a wire or plastic tie. It is recommended to use a four (4) inch spacing on the fasteners down the length of the seams. (Figure 2). The number of mats required depends on the width of the longwall face.

The mats are then rolled up and ready for transport underground. Typically they are folded and placed on supply cars and stored in the head or tailgate.

LONGWALL SCREENING – PRIOR TO RECOVERY

Bolts are installed, at an angle, where the roof and rib meet. This usually requires ten (10) to twelve (12) roof bolts with plates and turnbuckles. These are spaced thirty (30) inches apart or the width of cut of the shearer. Approximately four (4) inches of bolt should be left exposed and installed between 2 + 16 and 1 + 86 and 2 + 00 and 2 + 27. (See Figures 3 and 4).

The first roll is then attached, by chain, to the shearer and pulled onto the face. When the shearer has advanced two hundred (200) feet the second roll is attached to the tail of the first roll and the shearer is advanced another two hundred (200) feet. This is done until the rolls are laying end to end the entire length of the face.

A spool of 9/16 inch or 3/4 inch wire rope is placed on a spool stand in the next crosscut. (Figure 5). Then the wire rope is attached onto the shearer and pulled to the tailgate allowing it to run on the toes of the shields. Then the wire

rope is unhooked from the shearer and a loop is made in both ends using three (3) crosby clamps. (Figure 6). These loops are then hooked onto the first roof bolt in the head and tail gates and tensioned with a come–a–long.

The leading edge of the polymer grid is then fastened to the rope (dinged). The seams between the 200 foot rolls are also fastened. (Figure 7). Once the rope and seams are dinged, the rope is placed under the canopy tips. The shields can then be lowered and advanced and the remainder of the roll is hung under the canopy tip. (Figure 8). A full face pass is made and the procedure is repeated until the stopping point is reached. The shields are now encompassed with the polymer grid and the wire ropes on thirty (30) inch centers running the length of the face.

The remaining gap between the canopy tips and the face is then bolted and planked and longwall equipment recovery can begin. (Figure 9).

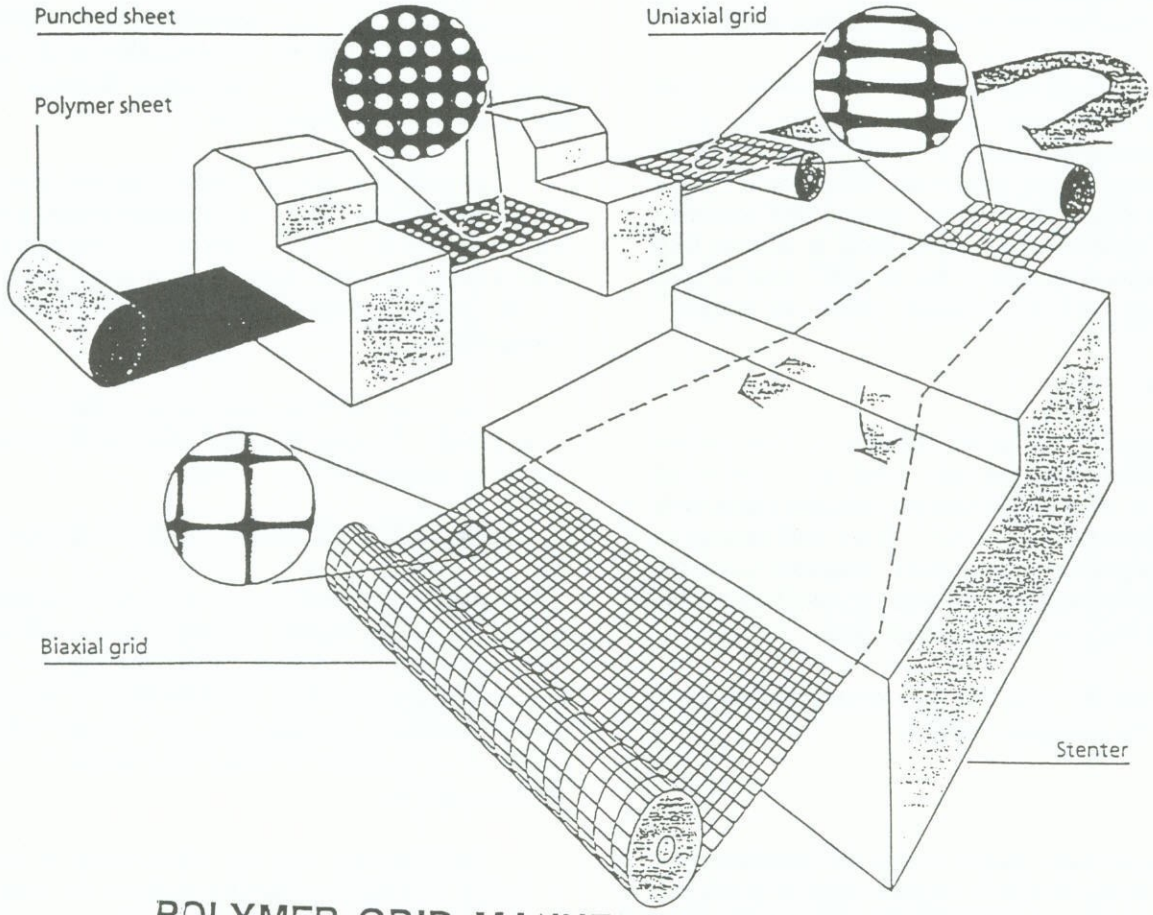

POLYMER GRID MANUFACTURING PROCESS

FIGURE 1

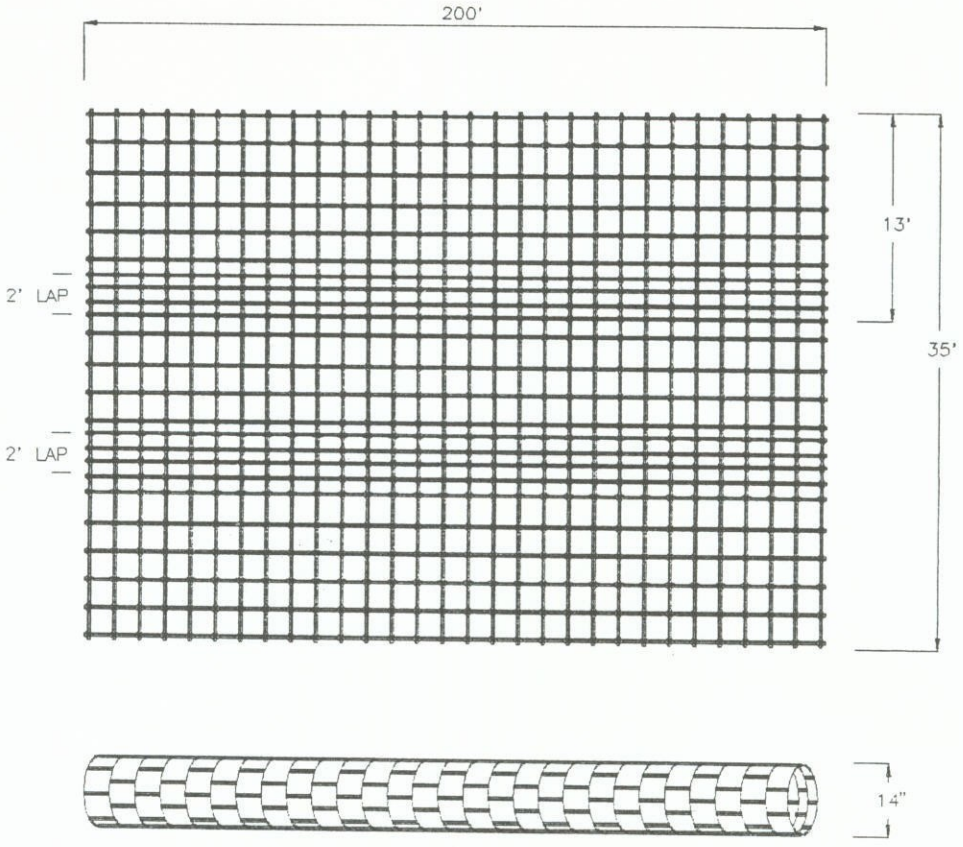

PREPARATION OF POLYMER GRID SCREENING

TENSAR BIAXIAL GEOGRID

FIGURE 2

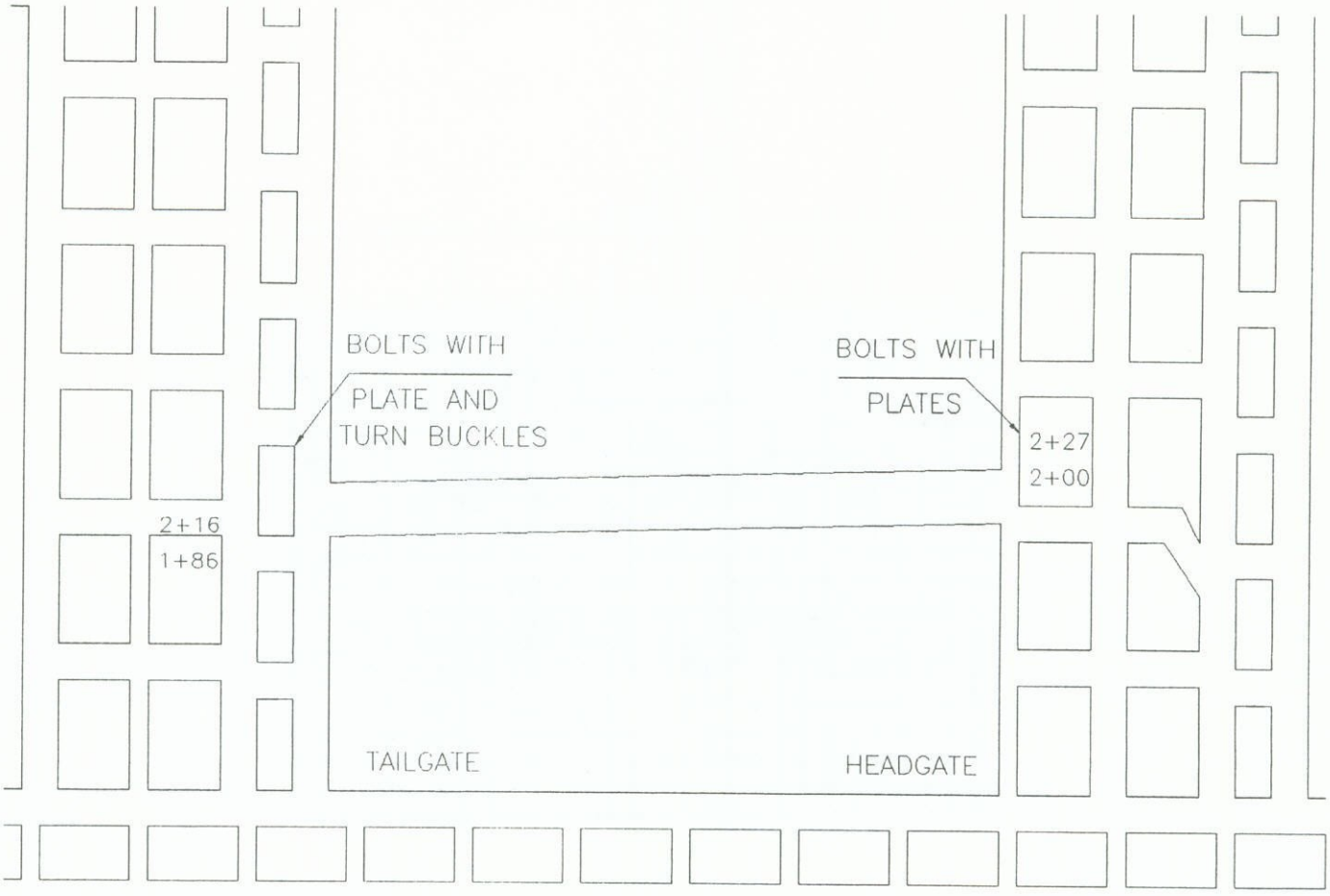

FIGURE 3

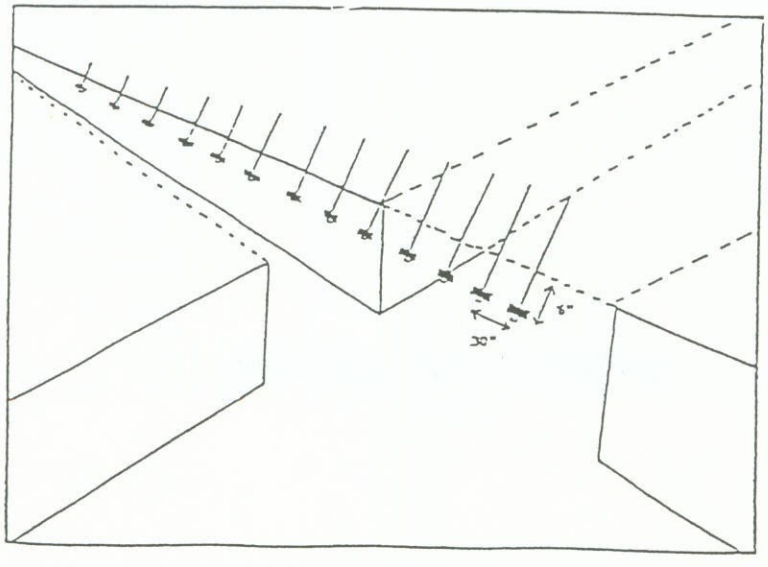

FIGURE 4

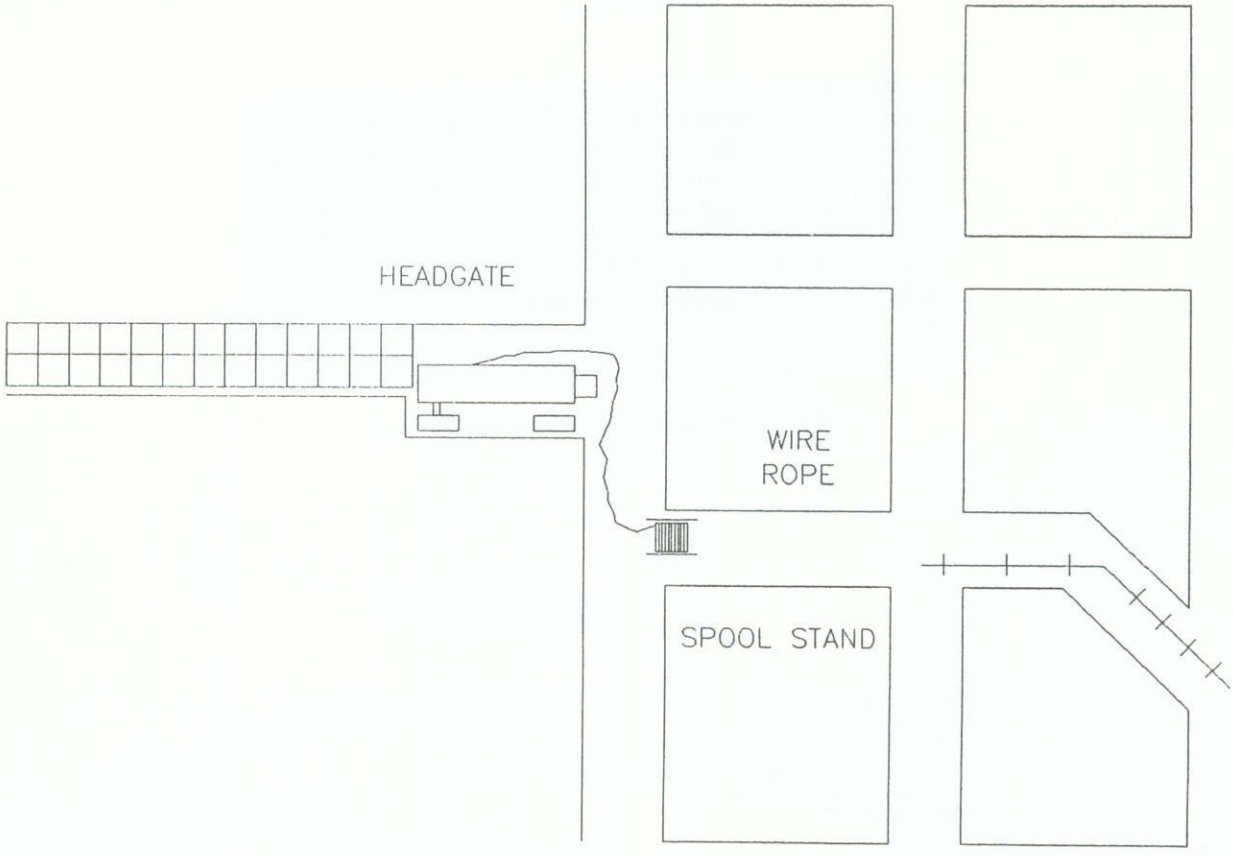

FIGURE 5

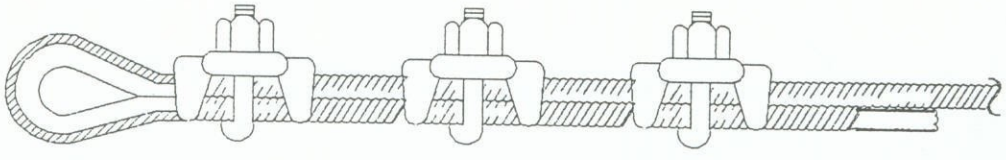

FIGURE 6

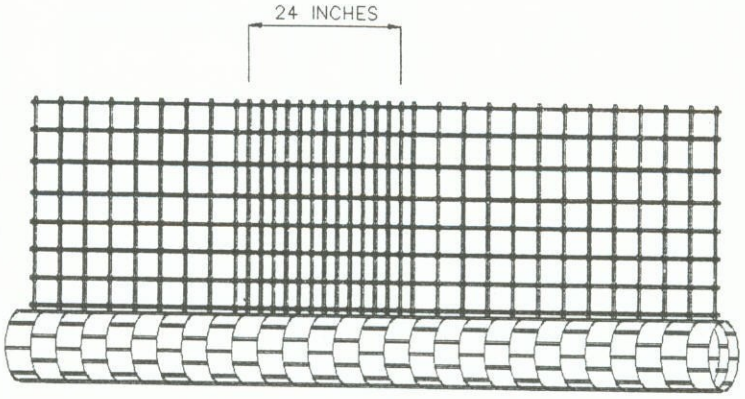

TENSAR BIAXIAL GEOGRID

FIGURE 7

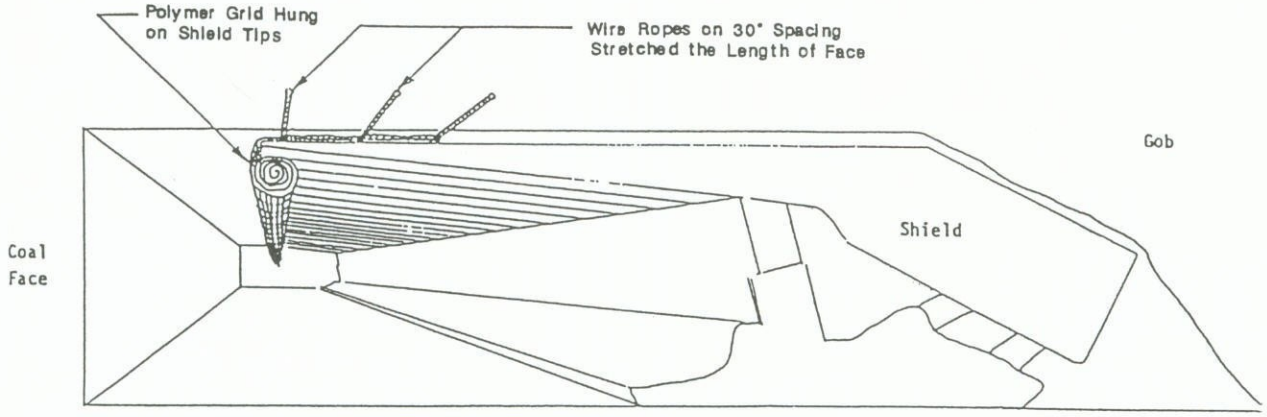

FIGURE 8

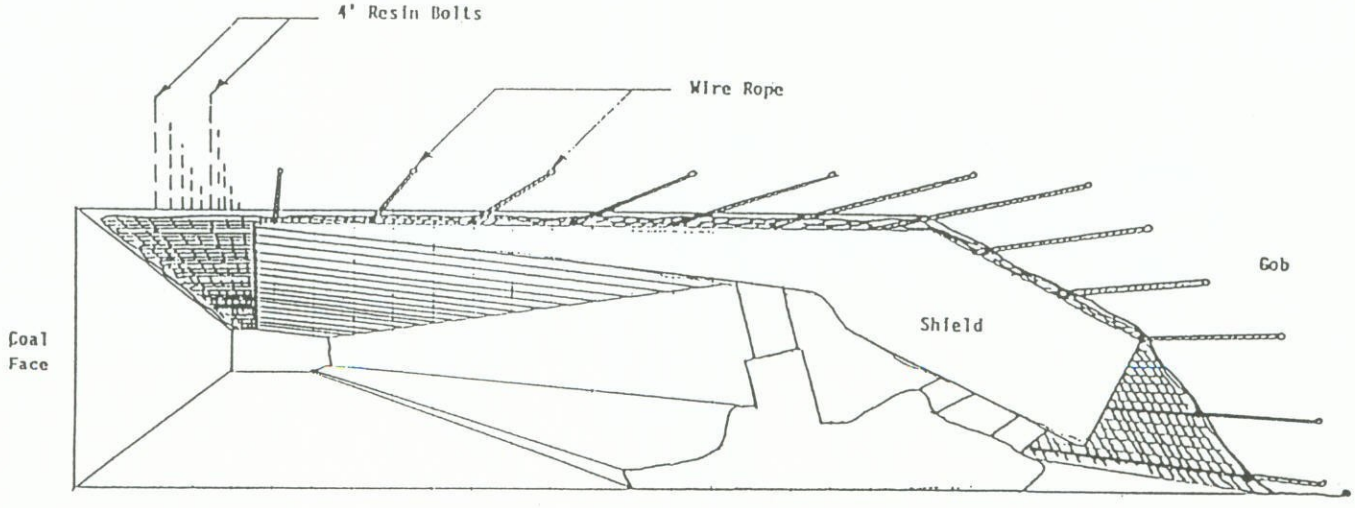

FIGURE 9

10th INTERNATIONAL CONFERENCE ON GROUND CONTROL IN MINING

METHODS OF CONTROLLING THICK AND STRONG ROOF IN LONGWALL MINING

Deren Zhu, *Associate Professor*
Minggao Qian, *Chairman and Professor*
China University of Mining & Technology
Xuzhou

and

Mea Wan, *Engineer*
Zaozhun Colliery
Shandong
CHINA

ABSTRACT

The principle of roof control in longwall mining is to control main roof fractures so as to reduce roof weighting, plus reasonable and effective design of supports to reduce the convergence and premature caving of the immediate roof. This paper introduces a comprehensive test for better roof control based on the geological conditions of coal seam No. 16 in Zaozhuan Colliery, China.

INTRODUCTION

A better roof control is the key to ensure a safe and productive longwall mining. Based on the analysis of the behavior of the overlying strata in longwall mining, there are two methods of roof control:

1. Employing optimum panel layout and extraction technology to reduce the effect of main roof fractures and movement on a working face.
2. Designing a rational and effective support that conforms with the main roof movement and control collapse of the immediate roof.

Longwall panel should be designed to offer correct measures for roof control based on the geological conditions of the roof, coal, and floor.

In Chinese coal mines, the geological conditions of many coal seams are very complex. Some seams are overlain by thick and strong sandstone, others have the roof consisting of weak and fractured shale, and still others have soft floor such as soft mudstone. Therefore it is very important to select extraction and support technologies based on seam occurrence and roof and floor conditions.

Zaozhuan Colliery, China extracted coal seam No. 16. Its roof is thick and strong sandstone and the floor is soft mudstone. Therefore it is difficult to achieve a good roof control. In order to gain a better roof control, the colliery has performed a comprehensive study in longwall panel No. 6216 with success.

GEOLOGICAL CONDITIONS OF COAL SEAM NO. 16

Fig. 1 is a stratigraphic column for seam No. 16. It was 0.6–0.8 m thick including a dirt band of 0.1–0.2 m thick. The immediate roof was limestone of 6–8 m thick, and the immediate floor was mudstone 0.25–0.3 m thick, below which it is sandstone 2.5 m thick.

Table 1 shows the mechanical properties of the roof and floor. It can be seen that limestone roof is a strong stratum with uniaxial compressive strength 58.7 MPa (8629 psi), but the immediate floor with uniaxial compressive strength 10.1 MPa (1485 psi) is a soft one causing the floor control problems.

CHARACTERISTICS OF ROOF FRACTURE AND MOVEMENT

According to observations of longwall panels in seam No. 16 there were four characteristics of roof fractures and movement:

1. Roof weighting was severe

Almost all longwall panels in seam No. 16 had severe roof weighting, especially the first weighting. Based on underground measurements, the first weighting interval was 30–40 m and during the weighting period, support pressure was twice as large as that in non–weighting period. The severe roof weighting often caused roof fall accidents. For example in panel No. 6217, a severe roof fall occurred during the first weighting with 20 m wide roof collapsed. It stopped coal mining activities for many days.

2. More roof convergence and cavity

In longwall panels of seam No. 16, roof convergence was more than 250–300 mm (10–12 in.) which was about 35% of the mining height. The larger convergence caused the immediate roof to break and cave even during nonweighting period. A special feature was that the caving height was usually less than 2 m.

3. Friction props dig deep into the floor

Friction props were used for face support before the test was performed in longwall panel No. 6216. The props usually sunk all the way through the mudstone floor of 0.25–0.3 thick. This contributed to large roof convergence and more roof cavities.

4. Lower support resistance

Based on underground measurements the resistance of the friction props used in longwall panels of seam No. 16 was lower, averaging 50–70 KN (5.6 – 7.84 tons) due to the soft mudstone floor. The maximum resistance, P, of the prop was determined by

$P =$ (uniaxial compressive strength of the mudstone floor) (prop's bearing area)

$=$ (10.1 MPa) (0.0072 m^2)

$=$ 72.7 KN (8.2 tons)

The computed result was consistent with in–situ measurements mentioned above.

Based on the characteristics of roof fractures and movement mentioned above, it was concluded that the limestone stratum could be divided into two layers; a 5–6 m thick upper layer and a 1–2 m thick lower layer (Fig. 2). Fracturing of the upper layer caused roof weighting while fracturing of the lower layer caused roof cavities during non–weighting period.

According to the operational statistics for panel No. 6105 the interval of the first roof fall caused by fracturing of the upper layer and that of the first weighting caused by fracturing of the upper layer were 14.5–20.5 m and 30.7–34.0 m, respectively, which were consistent with the underground measurements of 12–13 m and 29–30 m, respectively (1).

Therefore the objectives of roof control in seam No. 16 were to weaken the roof weighting, especially the first weighting caused by the upper layer, and to reduce the roof falls during nonweighting period caused by the lower layer.

METHODS OF ROOF WEIGHTING CONTROL

Analysis of the fracture process of the main roof considered as a Kirchoff plate supported by Winkler elastic foundation indicated that there are three methods for controlling roof weighting caused by a thick and strong main roof:

1. To reduce the strength of the main roof so as to decrease the roof weighing interval by injecting high–pressure water into the main roof. It can be seen from Fig. 3 that as the roof weighting interval decreases the length of the fractured main roof blocks reduces. Therefore its rotation before it reaches a new self–equilibrium condition becomes slower and its effect on a working face should be weaker.

2. To decrease the elastic modulus of the coal seam or immediate roof so as to increase the distance between the faceline and the fracture of the main roof occurring in front of the faceline. It can be seen from Fig. 4 that increasing the distance between the faceline and fracture line can also decrease the effect of main roof block rotation on the working face.

3. To change the direction or shape of the longwall faceline so as to control and reduce the effect of main roof fractures. This can be illustrated by Figure 5, which shows the distribution of main roof fractures under different boundary conditions, based on the analysis of main roof fracture process using the computer simulation code, FEAEBP (3).

Comparison of Fig. 5a and 5b shows that the main roof fractures in Fig. 5b develop slower and the area affected by the fracture process is smaller than those in Fig. 5a. Therefore the case shown in Fig. 5b should have a weaker roof weighting than that shown in Fig. 5a.

Comparison of Figs. 5a and 5c indicates that a large portion (areas A and B) in Fig. 5c is protected by the triangular cantilever structure of the main roof (1). Therefore the roof weighting is weaker in Fig. 5c than in Fig. 5a.

CONTROL OF ROOF WEIGHTING BY THE UPPER LAYER

In panel No. 6216 the 3rd method mentioned previously was easily applied to its use of friction props. Figure 6 shows the plane view of panel No. 6216 which was divided into two faces of 110 m wide each being divided by a middle entry.

The total panel width was 230 m. The direction of the set up room for face No. 1 was at an oblique angle to the tail and middle entries. As the face advanced, the angle was changed slowly and then became a straight one. During the first fracture of the upper layer its unsupported gob cantilevered to from a stair– shape (Fig. 6a). The direction of the setup room of face No. 2 was perpendicular to the middle and head entries. As the face advanced its direction remained unchanged. Therefore when the first fracture of the upper layer occurred, its unsupported gob cantilevered to form a rectangular shape (Fig. 6b).

Fracture development and distribution in the upper layer with stair–shape and rectangle–shape resemble those shown in Fig. 5b and 5a, respectively. Therefore the first weighting in Face No. 1 will be weaker than in Face No. 2.

Underground observations in panel No. 6216 concerning the first roof weighting showed that when Face No. 1 had advanced for a distance of 22 m from the setup entry the lower layer of the roof strata collapsed 1.5–2.0 m high (Fig. 7). When the interval was 27 m, the first roof weighting began at position A near the tailentry and then the weighting moved slowly from A to B and C. Finally when the interval reached 37 m the weighting moved to D near the middle entry. The whole roof weighting period lasted for 10 days, but the area and pressure of the roof weighting reduced day by day.

On the other hand, the roof weighting process in Face No. 2 was different from that in Face No. 1. When Face No. 2 had advanced for 22 m from the setup entry the lower layer collapsed. When the interval was 25–27 m the first weighting occurred at the center of the face and then the weighting moved toward both the middle and head entries. The roof weighting period lasted for about 5 days, but the area and pressure of the roof weighting was stronger day by day, and also stronger than that in Face No. 1.

Therefore change in the direction of a longwall faceline can indeed reduce the roof weighting pressure and area.

CONTROL OF ROOF CAVING BY THE LOWER LAYER

The resistance and stability of friction props used in seam No. 16 were considerably lower because they usually sunk deep into the mudstone floor resulting in large roof convergence and caving.

In order to improve the conditions in some longwall panels, both coal and mudstone were totally extracted and the props setup on sandstone main floor. This way prop resistance increase from 50–70 KN (5.60–7.84 tons) to 150–200 KN (16.8–22.4 tons) per prop. Roof convergency decreased from 250–300 mm (10–12 in.) to 100–150 mm (4–6 in.) and roof caving reduced significantly. But this method resulted in more production work and decreased the quality of coal produced.

In panel No. 6216, another method of controlling the lower layer was employed (Fig. 9). In this method the last row (nearest the gob) of friction props was replaced by the breaker props which have the following advantages:

1. It has a larger bearing area at the bottom which reduces its penetration into the floor and increases its resistance and stability. When the prop reaches its designed capacity of 800 KN (89.6 tons), it produces a pressure density on the floor of only 2.7 MPa (397 psi) which is less than the uniaxial compressive strength of the floor.

2. Its higher setting and final resistances reduce roof convergence and prevent the lower layer from detaching from the upper layer of the limestone roof resulting in less fractures and caving during nonweighting period.

Figure 10 shows the average load of the breaker props measured in the panel. It indicates that the average setting load of the props was 389 KN (43.6 tons) i.e. 83% of the designed setting load. During nonweighting period the average final load was 533 KN (59.7 tons), i.e. 67% of the designed final load. During roof weighting period, the average load was 779 KN (87.2 tons), i.e. 97% of the designed final load.

Due to higher prop resistance, roof convergence measured in this panel reduced to 100–150 mm (4–6 in.) and there was no roof caving reported and insured safe production of the panel. The results demonstrated that the method for controlling the lower layer of limestone roof was successful.

A better roof control in longwall panel No. 6216 also demonstrated that soft floor greatly affects roof convergence and roof caving in longwall mining and floor control is just as important as roof control in some panels.

CONCLUSIONS

1. According to the fracture characteristics of the limestone roof in seam No. 16 of Zaozhuan Colliery, China, the roof strata can be divided into two layers: the upper and lower layers. Fracturing of the upper layer caused the roof weighting while breakage of the lower layer caused the roof caving during nonweighting period.

2. Underground observation of longwall panels in seam No. 16 indicated that props sunk deep into the floor resulting in low prop resistance, large roof convergence and more roof caving.

3. A series of tests were performed in panel No. 6216 to improve roof control including change in the direction of the faceline to reduce the area and pressure of the roof weighting, and application of the breaker props to reduce the amount of floor penetration. As a result prop resistance and stability increased, and roof convergence and caving decreased.

4. The test in longwall panel No. 6216 demonstrated that rational extraction and support technologies must be selected based on seam occurrence and roof and floor conditions. It was also noted that sometimes floor control is more important for gaining a better roof control.

REFERENCES

1. Zhu, D., 1986, Structure of the Roof at the End of Longwall Face and Its Support, Ground Movement and Control Related to Coal Mining, The AusIMM Illawarra Branch Symposium, pp. 226–231.

2. Zhu, D., Qian, M., and Peng, S. S., 1989, A Study of Displacement Field of Main Roof in Longwall Mining and Its Application, Proceedings of the 30th U.S. Symposium, West Virginia University, pp. 149–156.

3. Zhu, D. and Qian, M., 1988, A Computer Simulation of Breakage of the Main Roof in Longwall Mining, Proceedings of the 7th International Conference on Ground Control in Mining, Morgantown, WV, pp. 205–211.

4. Qian, M. and Zau, G., 1988, Deformation and Roof Pressure of the Overlaying Strata, Proceedings 26th U.S. Symposium of Rock Mechanics.

5. Qian, M., Zhu, D., and Wang, Z., 1986, The Fracture Types of Main Roof and Their Effects on Roof Pressure in Coal Face, Journ. CIMT, No. 2, pp. 9–17.

6. Niu, X. and Gu, T., 1983, Controlling Hard Roof by Mean of Injecting Water, Journ. CCS, No. 4, pp. 1–10.

Table 1. Properties of Roof and Floor

Strata	Density g/cm^3	Tensile Strength MPa	Compressive Strength MPa	Interval Angle Degree
Roof	2.69	58.7	2.82	25.35
Dirt Bed	2.16	61.2	2.15	37.20
Floor	2.32	10.1	0.69	37.52

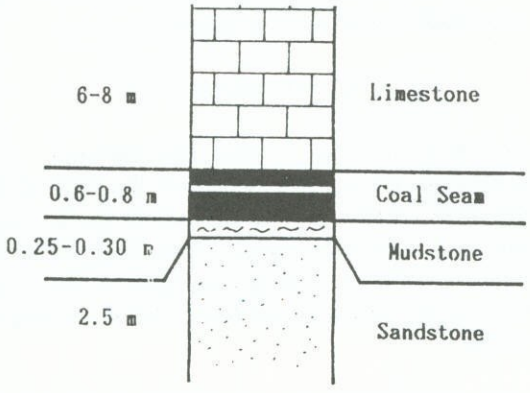

Fig. 1 Stratigraphic Column of Seam No.16

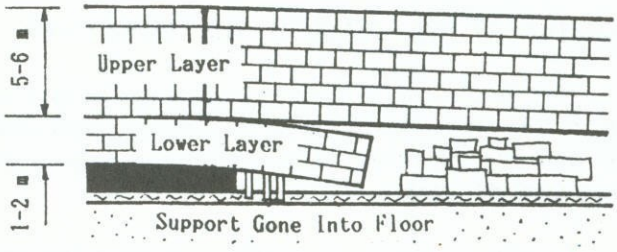

Fig.2 Upper and Lower Layers of Roof Strata

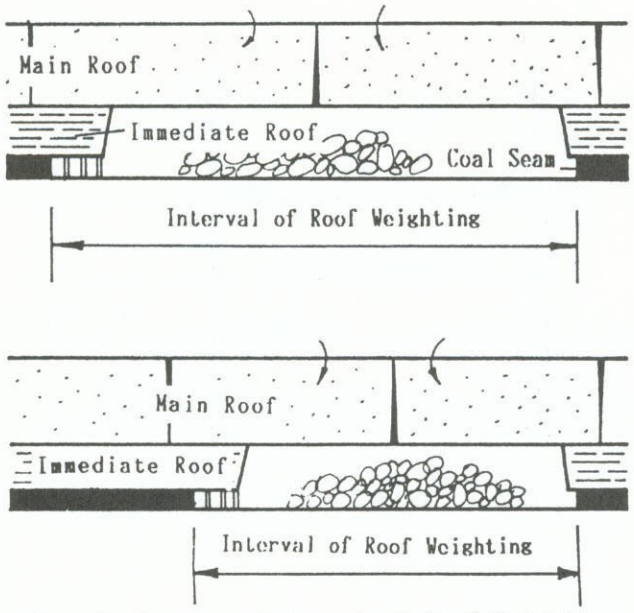

Fig. 3 Decrease Interval of Roof Weighting

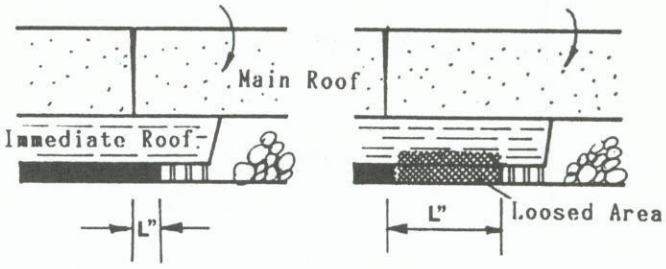

Fig. 4 Increase of Distance between Face and Fracture Lines

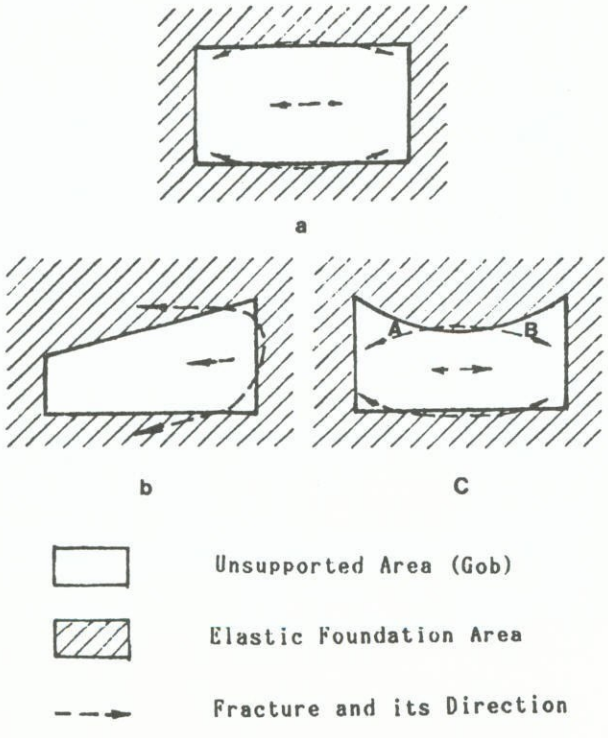

Fig. 5 Distributions of Main Roof Fracture

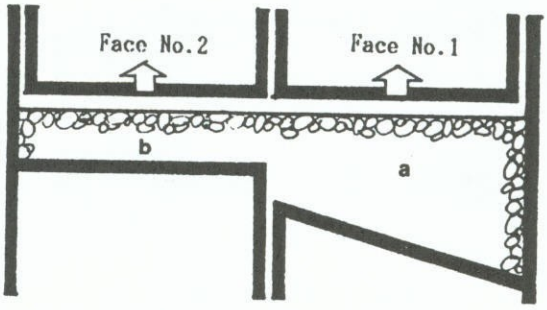

Fig. 6 Plane View of Panel No.6216

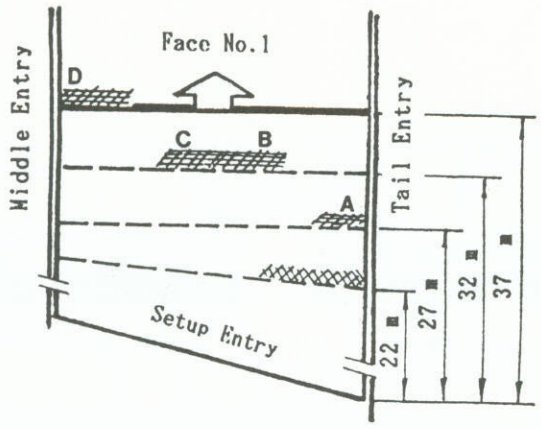

Fig. 7 Roof Weighting of Face No.1

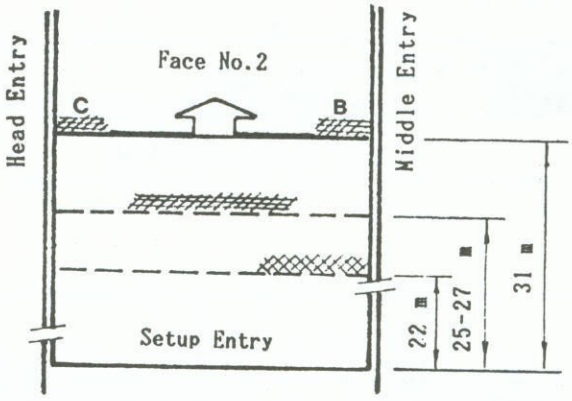

Fig. 8 Roof Weighting of Face No.2

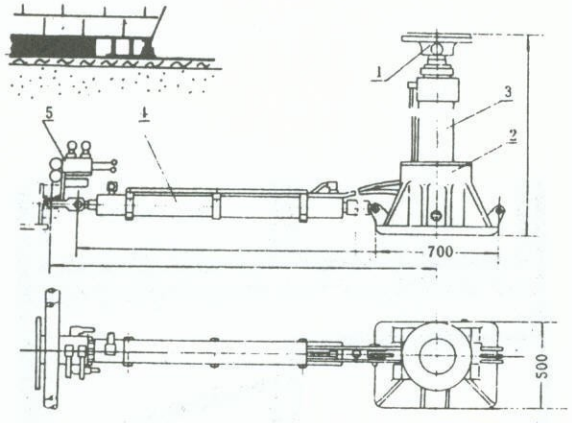

Fig.9 Breaker Prop

1 — Prop Cap, 3 — Prop, 4 — Jack,

5 — Control Valve 2 — Base

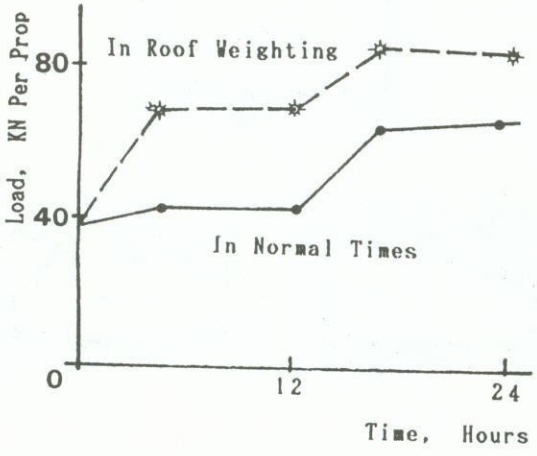

Fig. 10 Average Load of Break Props

TENSIONED POINT ANCHOR RESIN SYSTEM VERSUS NON–TENSIONED FULLY GROUTED REBAR – TWO CASE STUDIES

John C. Stankus, *Mining Engineer*

Jennmar Corporation
Pittsburgh, Pennsylvania

ABSTRACT

Jennmar Corporation, in an effort to improve mine roof control, has conducted extensive study and research comparing tensioned point anchor resin systems versus the use of non-tensioned fully grouted rebar. Preliminary indications are showing that in thinly laminated, weak strata, tensioned point anchor resin systems are providing more effective roof control than the non-tensioned fully grouted rebar.

In this paper two case studies are presented in which tensioned point anchor resin systems were utilized to stabilize and control the mine roof in two different mines. Both mines are alike in many ways, but yet very different in other aspects. However, the mines do share one main common factor, and that being the non-effectiveness of the non-tensioned fully grouted rebar in controlling the thinly lamininated strata in each respective mine.

INTRODUCTION

Before proceeding with the individual case studies, some discussion pertaining to the correct identification and description of the various roof control systems is necessary. Even in the field today, there is still much confusion over the proper terminology that applies to the different systems.

Figure 1 shows the traditional headed rebar that is fully grouted and non-tensioned. Diameters include #5(5/8"), #6(3/4"), #7(7/8), #8(1"), and #9(1-1/8") rebar. Strength values are specified by grades as per ASTM specification A615-89. Grade ratings include grade 40 and 60. Installation procedure includes drilling an appropriate length borehole, inserting the resin cartridge and bolt with plate into the hole, mixing the resin, and holding the bolt in hole until the resin hardens. No torque is applied and there is no installed load. A hardened steel washer is not normally used with a non-tensioned fully grouted rebar system.

JENNMAR HEADED REBAR

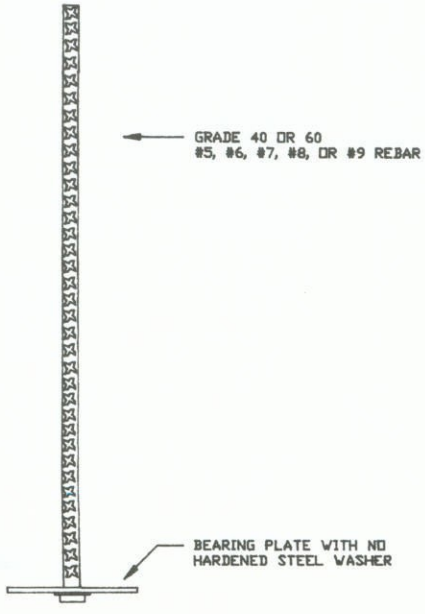

FIGURE 1 - HEADED REBAR

In Figure 1A is shown a torque/tension roof bolt. This type of roof bolt is an elementary form of a point anchor resin system. As in the headed rebar, diameters include #5(5/8"), #6(3/4"), #7(7/8"), #8(1"), and #9(1-1/8"). Stronger systems can be made from the grade 75, .677(3/4"), .804(7/8"), or .914(1") J-Bar.

The J-Bar has a special design on the bar deformations that aid in the mixing of the resin. The difference between the headed rebar and the torque/tension system is that instead of a forged head on the bottom end, the torque/tension system has a threaded end that protrudes out the bottom of the mine roof borehole. The threaded end comes equipped with hardened steel washer, optional anti-friction washer, and a flange nut with shear pin or similar delay mechanism. This system must be utilized with resin and the purpose of the shear pin in the flange nut is to permit mixing. Once the resin is mixed and hardens, the flange nut is rotated, the shear pin shears, and a torque is applied.

An installed load is achieved with the torque/tension system, but the amount of initial installed load and what portion of that load contributes to the beaming effect is a function of several factors. If the system is fully grouted with one type of resin, bolt tension is only achieved in the extreme bottom portion of the bolt, and very little installed load is applied to the beaming effect. If two types of resin are utilized, i.e. a fast set resin in the top part of the borehole and a slow setting resin in the bottom, tension is only achieved in the lower portion of the bolt encapsulated in the slow set resin. Also, primarily due to high frictional torque losses inherent to the system, even with the use of an anti-friction washer, high installed loads are difficult to achieve. Individual bolter operator characteristics during the mixing and holding procedure also produce inconsistent installed loads. By definition, because this system is dependent upon a full column resin anchor, it does not qualify as a true "point anchor".

JENNMAR TORQUE/TENSION SYSTEM

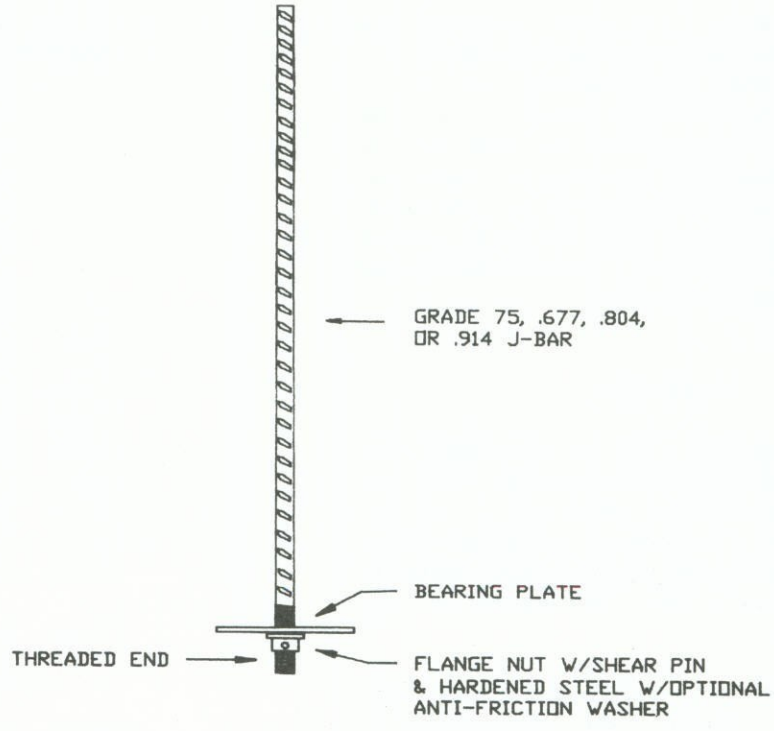

FIGURE 1A - TORQUE/TENSION BOLT

Figure 2 shows a Combination roof bolt system. The Combination bolt comes equipped with a rebar or J-Bar top section that provides for a full column resin anchor. The bottom portion of this system is comprised of a headed smooth bar with round hardened steel and plastic anti-friction washer. The J-Bar and smooth bar comes in grades 55, 60, and 75. This material is manufactured to ASTM specification F432-89, which provides for a much better quality rod as opposed to the rebar specification A615-89. The bottom portion of this bolt is connected to the top section by a special coupler that is equipped with a shear device that permits the resin to be mixed and a torque and installed load to be applied once the resin has hardened. The installation procedure is similar to the non-tensioned, fully grouted rebar in that mixing of the resin and holding of the system is required. However, once the resin hardens, a torque is then applied. This type of system can and has been referred to as a point anchor resin system(Karabin and Hoch, 1979). However, in the true definition, because of the full column anchor, it really is not a "point anchor". Tension or installed load is achieved only in the lower portion of this system and not in the entire length from end to end.

JENNMAR COMBINATION BOLT SYSTEM

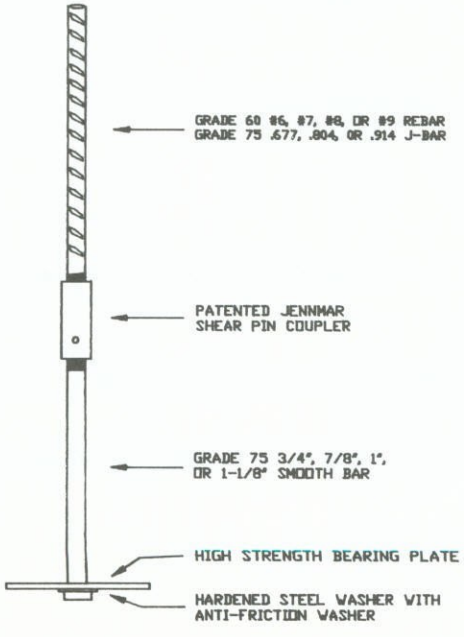

FIGURE 2 - COMBINATION BOLT

JENNMAR INSTA'L COMPRESS'ION

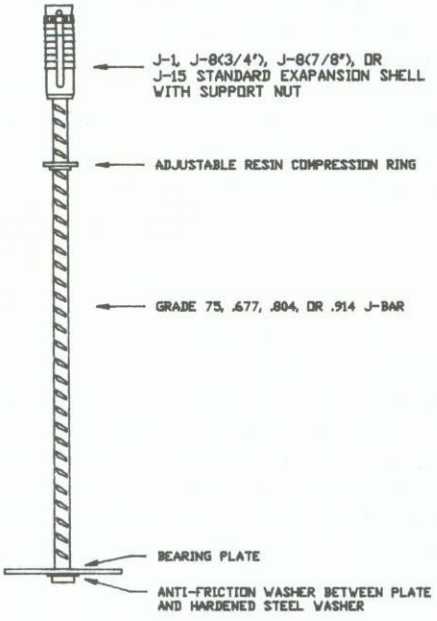

FIGURE 3 - POINT ANCHOR RESIN SYSTEM

A true point anchor resin system is shown in Figure 3. Shown in this figure is one type of InSta'l Compress'ion roof bolt which comes equipped with an expansion shell, resin compression ring, round hardened steel and plastic anti-friction washer. This system is designed to be used with resin. In this system a true "point anchor" is achieved. The expansion shell provides the initial anchorage at the extreme end or "point" of the system and the resin, once hardened, secures and continues the anchorage and installed load. The installation of this type system is much faster because there is no holding time and minimal mixing time. Once the hole is drilled, the resin cartridge is inserted into the borehole with the complete InSta'l system following. The bolt is inserted completely into the borehole, rotated, and torqued. During the rotation cycle, initial expansion shell anchorage is delayed by a shear pin mechanism on the standard, four prong malleable shell and a bail strap delay on the bail type expansion shell. This momentary delay provides an additional mixing action on the resin.

CASE STUDIES

Underground investigation was conducted at two different mine sites. One mine is located in southern West Virginia and the other mine is located in eastern Kentucky. For each case study a general geologic description is provided along with what effective roof control system was utilized for each mine.

MINE NO. 1

The study mine is located in eastern Kentucky in Leslie County. The mine is a large deep mine with average overburden depth of 1200 ft. Mining is being conducted in the Hazard #4 seam by continuous and longwall mining methods. The Hazard No. 4 seam is found in the Middle and Lower Pennsylvanian Breathitt Formation. The Breathitt Formation consists mostly of siltstones, sandstones, and shales. The seam dips slightly towards the northeast and average seam thickness is approximately 78 inches. In Figure 4 is shown a generalized stratigraphy of the roof and floor rock.

Roof control problems began to occur in the development of a submains section for future longwall sections. A five entry submains was being driven by continuous mining methods with the primary roof control system being comprised of grade 60, fully grouted #5(5/8") and #6(3/4") rebar. Large falls began to occur outby the active working face. Figure 5 is a map of the section showing the location and size of some of the roof falls. The size and extent of the roof falls necessitated the cessation of mining and temporary abandonment of the section.

At this point in time Jennmar Corporation commenced an extensive study of the roof conditions in this section. Numerous test boreholes drilled to a depth of 20 feet into the mine roof strata were subjected to stratascope study. Test boreholes were examined near fall areas, at the face, and outby the roof fall area. In all boreholes examined, the lithology was fairly consistent with the general stratigraphy as shown in Figure 4. Also very consistent was the size and fineness of the laminated shales and sandy shale. In boreholes near the fall areas a definite pattern of strata fracture/bed

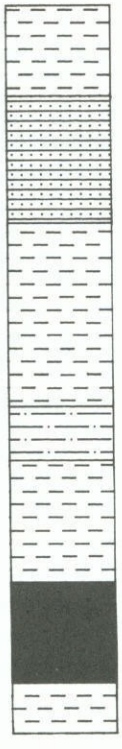

4.2′ SHALE, MED. GREY, LAMINATED

6.1′ SANDSTONE, MED. GREY, LAMINATED

8.3′ SHALE, MED. GREY, LAMINATED

2.5′ SANDY SHALE, DK. GREY, LAMINATED

6.2′ SHALE, MED. GREY, LAMINATED

5.9′ HAZARD NO. 4 SEAM

2.5′ SHALE, BLACK

FIGURE 4 - STRATIGRAPHY MINE #1

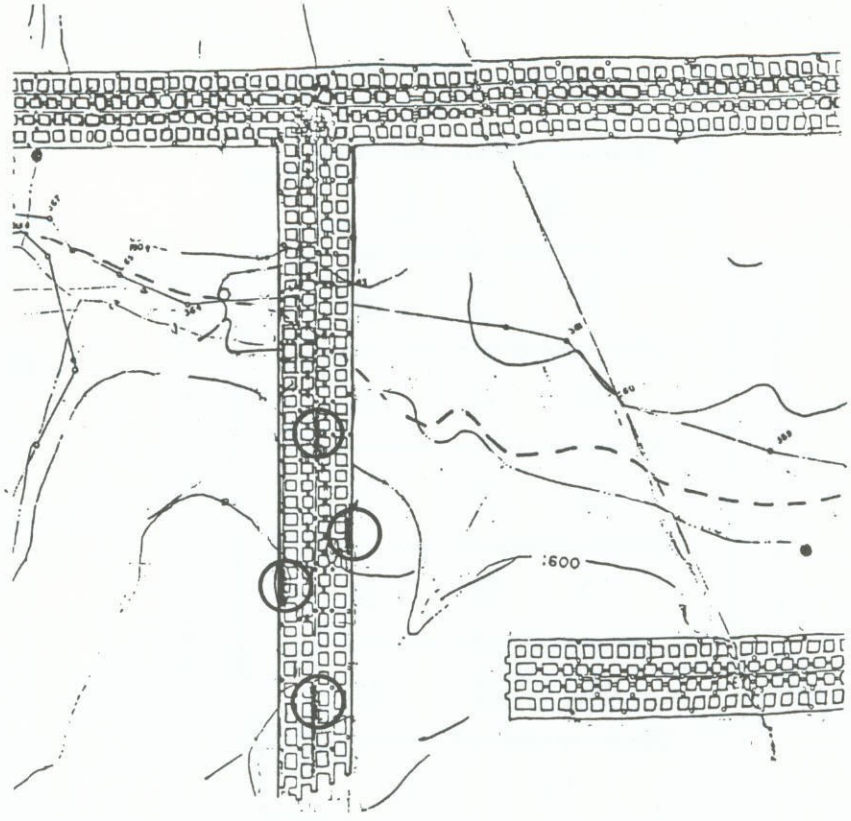

FIGURE 5 - MINE #1, ROOF FALLS
(CIRCLES INDICATE FALL AREAS)

separation could be detected. In these boreholes, highly fractured and separated strata was observed immediately at or slightly above the roof bolt anchorage horizon. This type of activity is normally associated with an inadequate beaming effect. The immediate course of action was to rehabilitate the area that had already been mined with a supplemental support plan and then formulate a primary roof control plan for the submains and future gate entries.

Utilizing the Jennmar Roof Control Cadd system, a supplemental support plan was designed utilizing a 7/8 inch diameter truss system and tensioned 1 inch diameter Combination roof bolts. Figure 6 shows a vertical and lateral view of the computer generated supplemental plan that was used to rehabilitate this area.

Once the area was rehabilitated, the design of a new primary roof control plan was commenced. Due to the highly laminated nature of the strata and height to which the laminations carried into the roof, it was decided that it would be impractical to try and fully grout a rebar for the length that might be necessary. Instead, a tensioned point anchor resin system with a high installed load was chosen. Due to the amount of overburden and the anticipated abutment pressures from the planned longwall, a grade 75, 7/8 inch diameter system was chosen. Figure 7 shows the plan utilized for the headgate entry. This computer generated plan is designed around the grade 75, .804 J-Bar, InSta'l Compression system comprised of J-8 expansion shell, resin compression ring, and anti-friction washer. The high strength steel roof channel was chosen to provide an increased bearing surface and control sloughing of the immediate roof. Wood planks and headers were not used because testing has shown that a loss in bolt tension and installed load can occur with wood over a period of time due to wood deterioration, shrinkage, etc. Pull tests were conducted on both the 7/8 and 1 inch systems to determine anchorage capacity and resin amount. Figure 8 shows some actual pull test data demonstrating strength of both systems. Two equivalent feet of resin was found to be the minimal amount for the 7/8 inch system in this strata.

This system was adopted for all submain and gate entry development. The roof control has been stabilized and to date, since adopting this point anchor resin system, no roof falls have occurred.

SUPPLEMENTAL ROOF CONTROL PLAN

CASE STUDY MINE #1

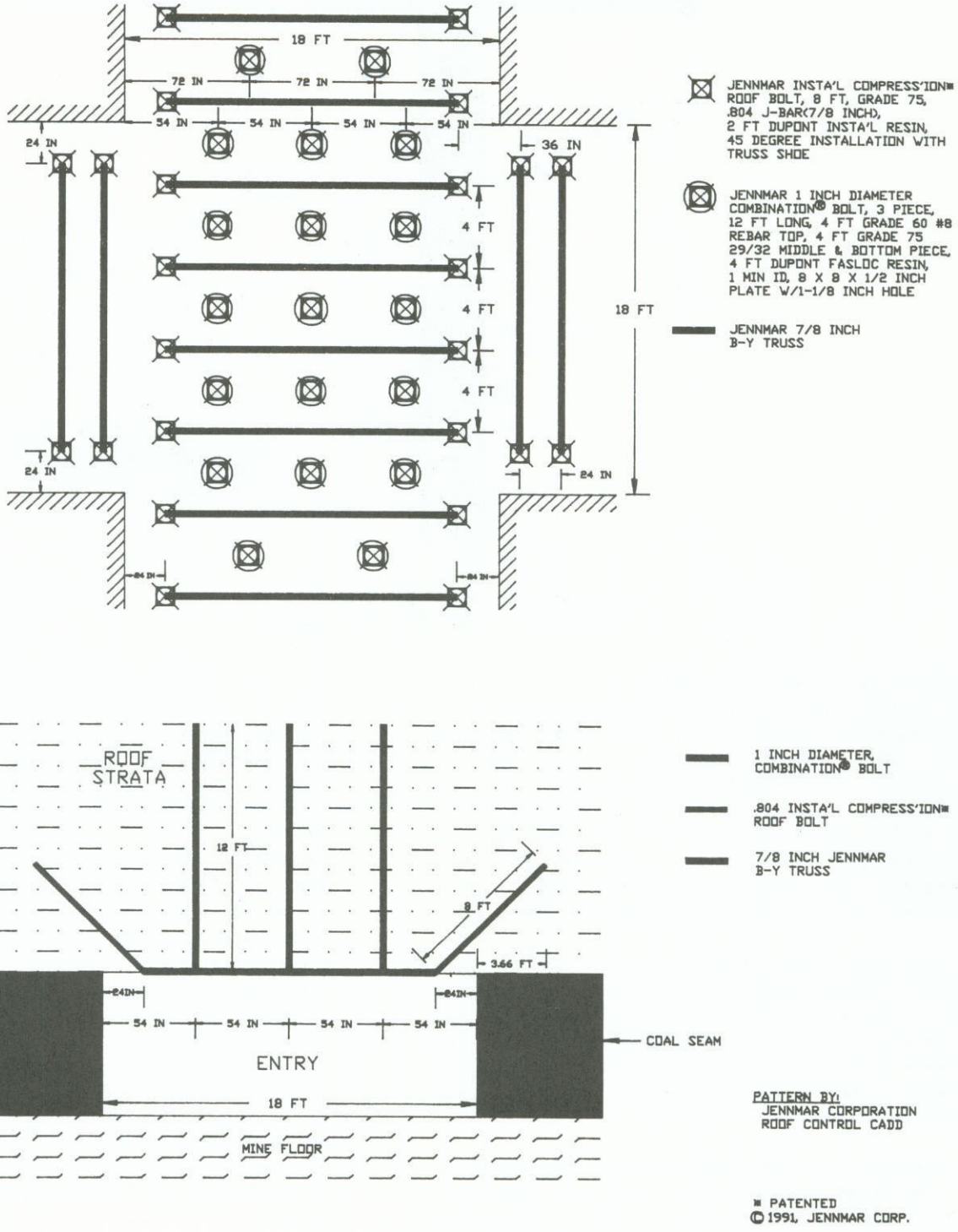

FIGURE 6 - VERTICAL & LATERAL VIEWS, SUPPLEMENTAL ROOF CONTROL PLAN

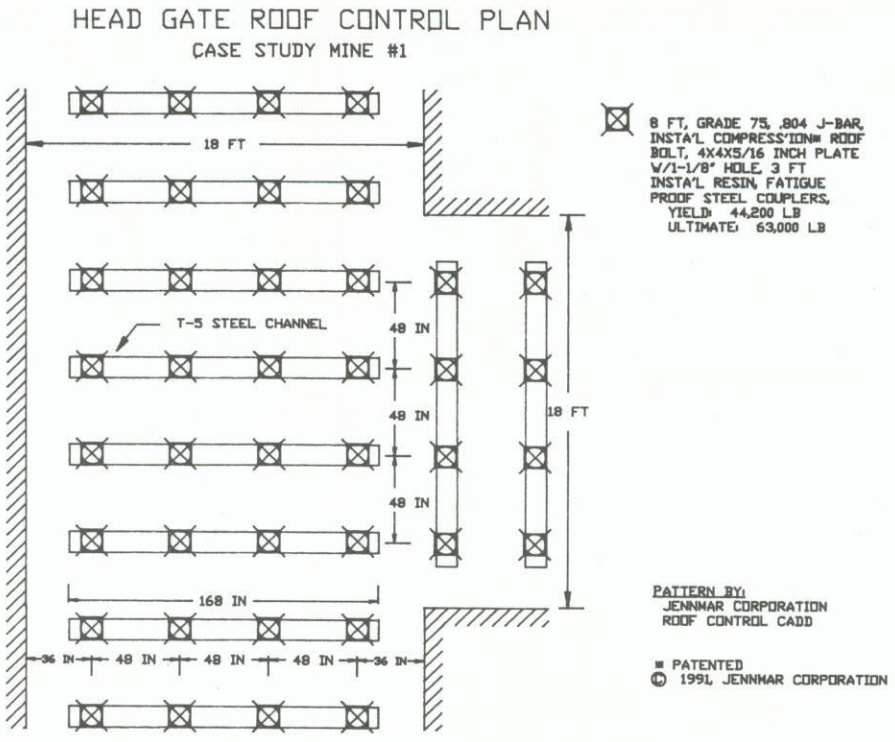

FIGURE 7 - PRIMARY ROOF CONTROL PLAN

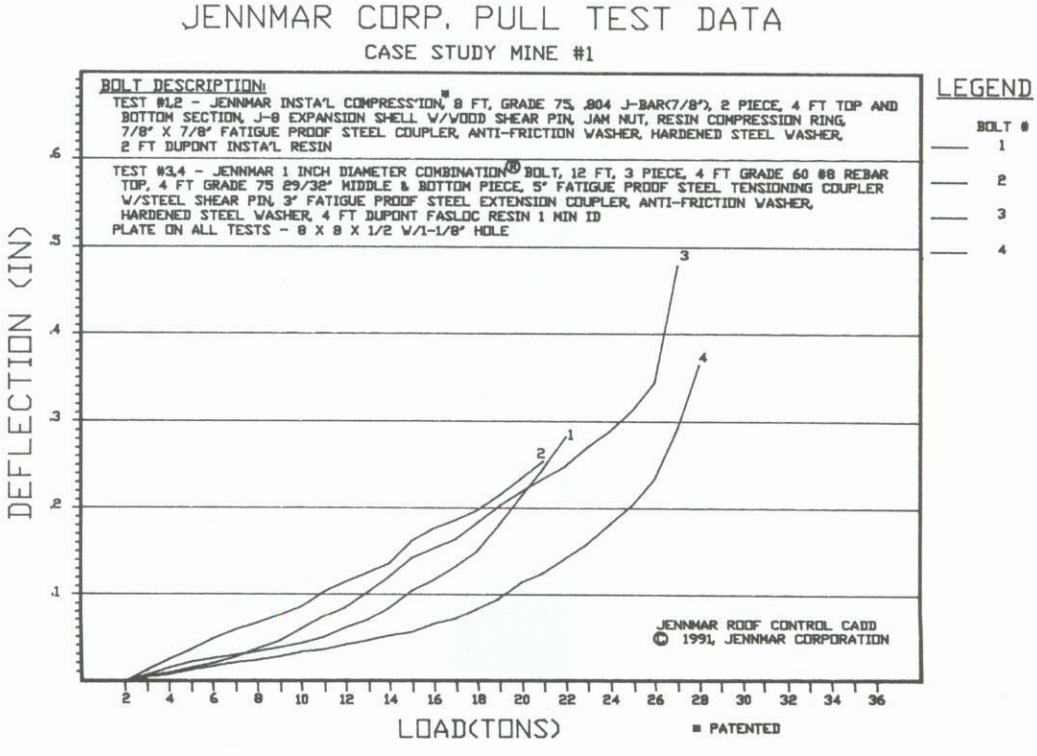

FIGURE 8 - PULL TEST DATA

MINE NO. 2

The study mine is located in southern West Virginia in Logan County. The mine is a small drift mine under relatively shallow overburden with an average depth of 300 feet. The seam being mined is the Welch seam with an average thickness of approximately 40 inches. Room and pillar mining is being conducted by the continuous mining method. The immediate roof is comprised mainly of laminated grey shales and sandy shales with some sandstone. Figure 9 shows a generalized stratigraphy for this mine.

The mine, which has not been in operation for a very long period of time, initially utilized non-tensioned, fully grouted, #5(5/8") and #6(3/4") rebar for primary support. Also, for a more cost effective installation per hole, it is critical that a 1 inch diameter borehole be drilled for the roof bolt system.

Numerous roof falls began to occur in two different sections of the mine. The falls were large and failure occurred very suddenly with little or no warning. Figure 10 shows the sections where the roof falls occurred. Jennmar Corporation commenced an underground study of the roof conditions. Roof falls were examined and stratascope studies were conducted in test boreholes. Figure 11 shows actual photographs of one of the roof falls. Clearly evident in the roof cavity is the finely laminated nature of the strata. The stratascope examinations revealed finely laminated shales and sandy shales. Stratascope examination of older areas revealed some laminated strata, but clearly the laminations were not as fine. The strata near the mine entrance also appeared to contain a much higher percentage of massive sandstone. It was evident that a change in strata composition correlated with the location where roof failures began to occur.

5′ SHALE, MED. GREY, LAMINATED

6.1′ SANDSTONE, LT. GREY

7.5′ SANDY SHALE, MEDIUM GREY, LAMINATED

11.5′ SHALE, MED. GREY, LAMINATED

3.4′ WELCH SEAM

2.5′ SHALE, DARK GREY

FIGURE 9 - STRATIGRAPHY MINE #2

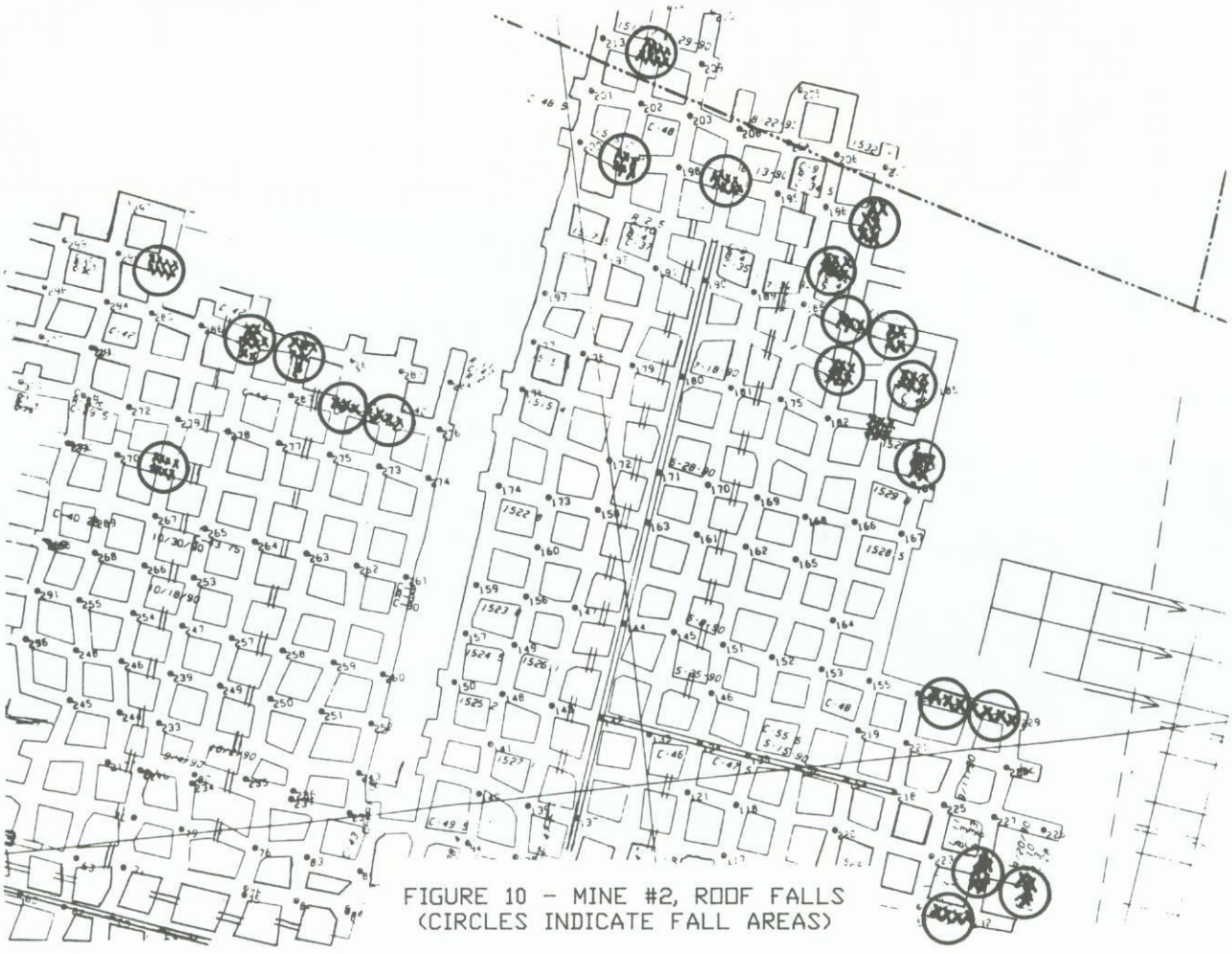

FIGURE 10 - MINE #2, ROOF FALLS
(CIRCLES INDICATE FALL AREAS)

Mine officials agreed that a tensioned system with resin would provide a more effective beaming effect. However, it was also determined, that if a 1-3/8 inch diameter borehole had to be drilled to accommodate the point anchor system, the added costs of the larger borehole would not be economically feasible. A tensioned point system was needed, but it would have to work in a 1 inch diameter borehole.

To accommodate this requirement of a tensioned point anchor resin system for the 1 inch borehole, Jennmar Corporation has developed the InSt'al "B" system. This system is basically a 5/8 inch diameter system in either grade 60 or 75 rebar or smooth rod. In low seam conditions, either of these rods can be bent for easy hole insertion and no notching of the bar is required. The InSta'l "B" is comprised of the J-1 standard type expansion shell with shear pin, support nut, and anti-friction washer. If strata conditions permit, this system can be used with a minimum of 6 inches of resin.

In this study mine, based upon such factors as entry width, overburden depth, rock density, etc., it was determined that a minimal bolt length of 48 inches with an installed load of at least 16,000 lbs would be necessary to produce the desired beaming effect. For this reason a grade 75, #5 rebar, with J-1 expansion shell, and anti-friction washer was chosen as the primary bolt system. Pull tests were conducted with various amounts of resin, and it was determined that a minimum of 1 equivalent ft. of resin was required to achieve bar yield strength in this particular strata. No change to bolt spacing was made and the InSta'l "B" was installed on full pattern.

Since the switch to the tensioned point anchor resin system was made, mining has progressed safely and no roof falls have occurred to date. Figure 12 shows photographs of an area bolted with the InSta'l "B" system. In the photographs it can be seen that the roof is under control with no indications of any roof failure.

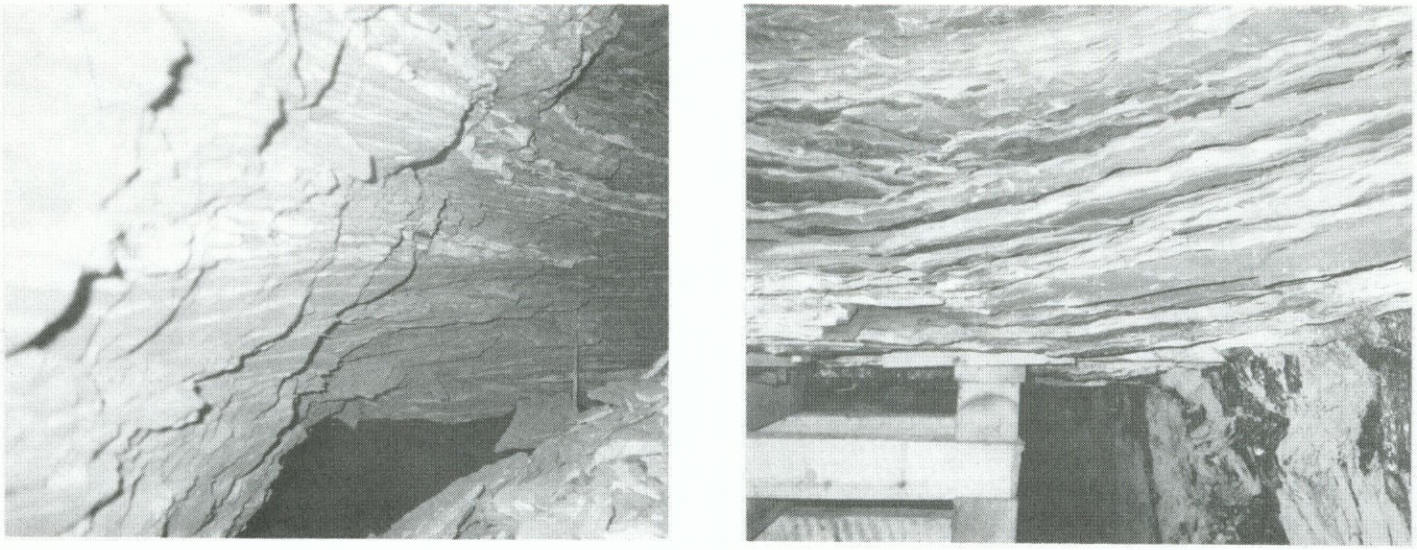

FIGURE 11 - MINE #2, ROOF FALL
SHOWING LAMINATED STRATA

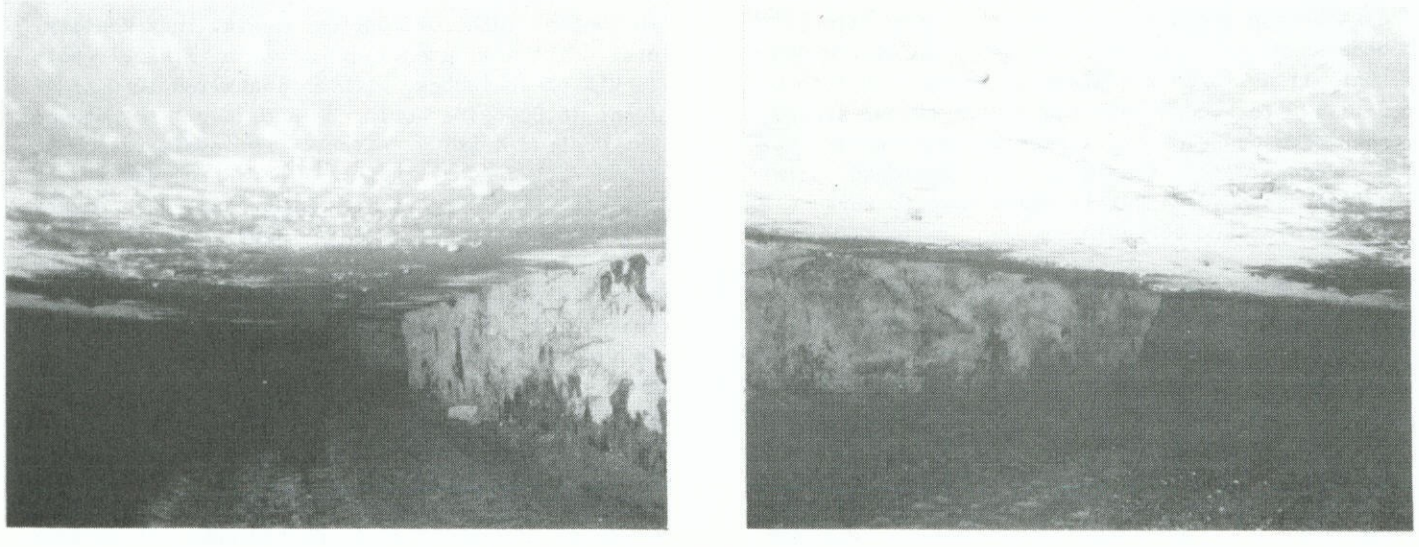

FIGURE 12 - MINE #2, SECTION BOLTED WITH
INSTA'L 'B' POINT ANCHOR RESIN SYSTEM
FOR ONE INCH BOREHOLE

SUMMARY

As stated in the introduction, these case studies are of two mines that are alike in many ways, but also very different. Mine No. 1 is a very large and deep longwall mine. Justification can be made for the capital expenditure for the larger and stronger 7/8 inch diameter InSta'l point anchor system. In Mine No. 1 the roof pressure as a function of depth and the anticipated abutment pressure will require a much larger and stronger system than that required in Mine No. 2. In this case study, the small drift mine presents a different type of situation. The mine entries must remain open, but the effect of a roof fall is not as pronounced as it would be in the longwall mine, whose longwall face is stopped or delayed by roof problems in the gate entries. Mine No. 2 has less overburden pressure to contend with and there is no need for a system as large as required in Mine No. 1.

However, both mines do share the same general type of finely, laminated strata comprised of mostly weak shales and sandy shales. In both case studies, the switch from a non-tensioned fully grouted rebar to a tensioned point anchor resin system improved the roof control in both mines.

The key in both applications is that with the tensioned system, an installed load is applied to the roof strata as soon as possible after mining. By fine tuning the system through adjustment of the anti-friction washer, the torque/tension ratio can be "matched" to the particular strata. Some factors that must be considered in determining what torque/tension ratio should be utilized are:

1. Overburden depth.
2. Strata composition.
3. Fineness and number of laminations.
4. Number of changes in the type of rock comprised in the laminations.
5. Rock physical properties - compressive strength, Young's modulus, Poisson's ratio, density, moisture content, etc.
6. Mining plan and planned life of entry.

By "matching" the torque/tension ratio to the strata, the "Optimum Beaming Effect"(OBE) can be achieved. What this means, is that given a particular type of strata, by proper bolt spacing and installed load per bolt, the summation of the resultant upward compressive force can in effect produce a beaming effect that could support any amount of strata, at any depth. For the roof to begin to fail, the vertical downward pressure would have to exceed the summation of the upward forces created by the installed load for each roof bolt.

InSta'l, Insta'l "B", Insta'l Compress'ion, Compress'ion, Combination Bolt, J-Bar, J-1, J-8(3/4"), J-8(7/8"), J-15, and Roof Control Cadd are proprietary, patented and/or registered trademarks/products of Jennmar Corporation.

REFERENCES

1. Karabin, G.J. & Hoch, M.T., 1979, An Operational Analysis of Point Resin-Anchored Bolting Systems, U.S. Department of Interior, MSHA, IR 1100, 14 pp.

10th INTERNATIONAL CONFERENCE ON GROUND CONTROL IN MINING

THRUST BOLTING: A NEW INNOVATION IN COAL MINE ROOF SUPPORT

Stephen C. Tadolini, *Mining Engineer*
Dennis R. Dolinar, *Mining Engineer*

Denver Research Center
U. S. Bureau of Mines
Denver, Colorado

ABSTRACT

A new innovation in coal mine roof support has been developed by the Bureau of Mines at the Denver Research Center. The technique, called "Thrust Bolting,"[1] converts a traditional passive roof support system, a full or partial column rebar bolt, into an active support system by following a specific installation process. The thrust bolting system provides two advantages from a ground control standpoint. First, because the system is active, no roof movement is necessary to put the bolt into tension. This eliminates the possibility of strata separations in sedimentary roofs, minimizing progressive-type roof failures. Secondly, the tension placed on the system is independent of mechanical devices or torques. This eliminates the highly variable frictional losses that occur between the bearing plate and the bolt head and in the threaded portions of traditional active support systems. These two improvements create a safer working environment for mining personnel. An additional advantage of this improved support system is the reduced cost of installation and maintenance. The initial support cost is reduced by a minimum of 30 percent per bolt when compared to similar conventional support systems. The labor intensive and potentially hazardous torque-tension test, required for most tensionable active support systems, is not required for thrust bolts. The potential for improved support performance and cost reduction of thrust bolting has generated a considerable amount of interest from both industry and MSHA. This paper will describe, in detail, the theory and application of thrust bolting and present the results of two underground coal mine case studies.

[1]The term "Thrust Bolting" is presently being copyrighted. United States and foreign patents have been applied for by the Bureau of Mines.

INTRODUCTION

Millions of roof bolts are installed each year to provide structural support in underground U.S. metal, nonmetal, and coal mines. Approximately 45 pct of the bolts used are expansion anchor, 45 pct are resin-assisted combination or full-column resin-grouted bolts, and 10 pct are friction anchored. These bolting systems can be described in terms of being an active or a passive system depending on the principal methods used by the support system to develop the support. Active systems will put the roof into compression by tensioning the support system, allowing the immediate roof and surrounding strata to become self-supporting. The expansion anchored bolts are the main active type of support used. A major advantage of this system is that the roof or structure is placed into compression to resist downward movements by tensioning the support. Primary disadvantages include the relatively weak anchorage, loss of support when system tension dissipates, torque-tension requirements, and non-uniform tensioning (1-3). Passive systems, such as full or partial-column resin-grouted bolts, have superior anchorage and, in the case of full-column resin-grouted bolts, superior stiffness and shear resistance (4). However, passive systems provide support through resistance to rock movement, which could be a disadvantage if an active force is important in maintaining the stability of the mine structure. Combination and point resin-anchored bolts combine the best qualities of the active and passive systems because an active force is applied with a grout or grout-assisted anchor. However, combination bolts are mechanically more complex, most have difficult installation procedures, and support costs are higher than either the expansion anchored or the resin-grouted bolts. The Bureau of Mines developed an active support system called "Thrust Bolting" that does not require the complex mechanical components and installation procedures of the combination systems. Thrust bolting converts a traditionally passive grouted

bolt system into an active support system by following a specific installation procedure. The technique uses the same headed rebar hardware as a resin-grouted bolt. However, the support system, installed with the thrust bolting technique, becomes an active system with the same superior anchorages and stiffnesses associated with the resin-grouted rebar. Essentially, an additional stability component of an active force can be added to a full or partial-column resin-grouted system for little or no additional cost. Furthermore, the support hardware costs for thrust bolting are substantially less than combination or frictional support systems.

DESCRIPTION OF THE METHOD

The application of thrust bolts is a simple bolting technique when the proper equipment modifications have been made and the installation procedure is followed. The support hardware is identical to that used for a passive, headed rebar, resin-grout system. The bolt is a traditional headed rebar of any diameter with a forged head, the roof bearing plate is usually 6 by 6 in, and the anchor a resin-grouted system. For the first portion of the installation, the procedure is the same as for a passive resin-grouted full or partial column system. A borehole is drilled to a depth that is at least 1 in deeper than the length of the rebar. The borehole diameter should be approximately 0.125 to 0.250 in larger than the bolt diameter. The resin cartridge, with a 15 second set time, is placed in the borehole, and the bolt is pushed up through the resin cartridge and spun the required time, usually recommended by the manufacture, to ensure adequate mixing and bonding (figure 1). From this point the installation procedure differs from that of the passive system. The full force of the bolter hydraulic system is incorporated into creating the final "thrust" onto the bolt via the head. On figure 1, Item 1 indicates the head of the bolt where the thrust is applied through the axis of the bolt. When the thrust is applied to the bolt head, the bolt is forced upward along with the immediate roof. Item 2 shows the position of the immediate roof after bolt installation but prior to the thrust being applied.

Figure 2 shows a cross-section of the bolting system after the resin has cured and the applied thrust is removed from the bolt head. The rebar is now in varying degrees of tension from the head to the top of the bolt. This tension occurs along the entire bolt length, but dissipates as it is transferred through the rock mass through the rock/resin interface (5). When the bolt is thrust into the borehole, any cracks, separations, or partings are closed, and the rock is deformed elastically by the applied forces (item 3). When the load is removed, these cracks, microfractures, and partings try to reopen, and the rock attempts to rebound. The movement is met by the resistance of the support system. Item 4 shows the position of the roof prior to the thrust being applied and item 5 the position of the roof as the thrust is applied. The difference between the final and the initial roof horizon when thrust is applied, is the roof movement that

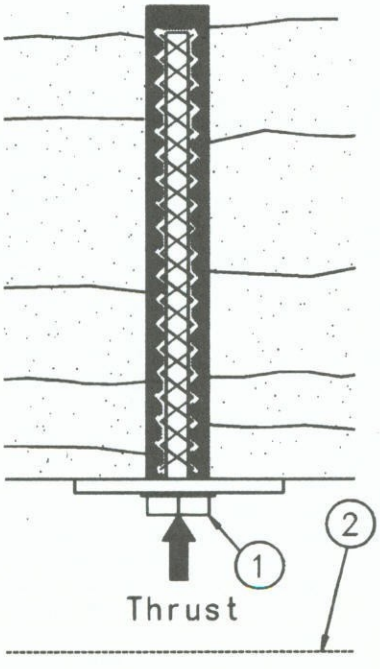

Figure 1 - The resin has been mixed and the upward bolt "thrust" is being applied.

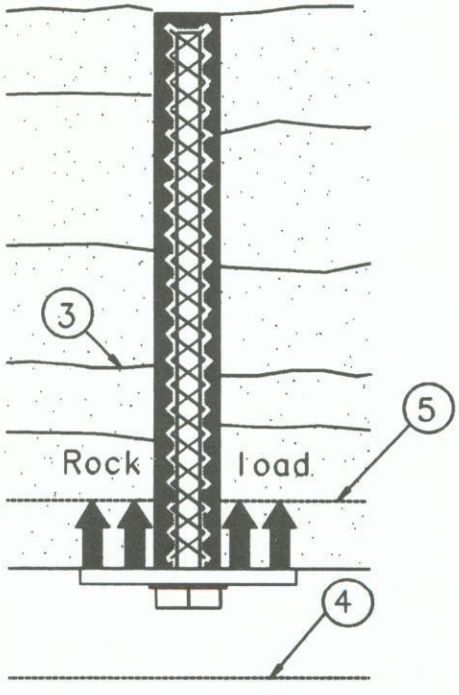

Figure 2 - The insertion load is removed, an active force is applied to the bearing plate, and bolt tension is developed.

develops the bolt tension. This bolt tension produces a compressional force on the roof (figure 2). The amount of roof movement and the loads on the bolt, bearing plate, and roof will depend on the applied thrust and the stiffness of roof and support system.

THRUST BOLTING THEORY

Bolt Load Equation

The amount of final load on the support system can be varied by the amount of thrust applied to the head of the bolt during installation or by varying the column length of the resin-grout. The applied thrust, coupled with the known stiffness of the roof and the stiffness of the support, can determine the amount of force on the bolt and subsequently on the roof. The equation is in the form:

$$F_b = \frac{K_b \times F_t}{K_r + K_b}$$

where: F_b = force on the bolt and roof, lb,

K_b = stiffness of the support, lb/in,

F_t = applied thrust, lb, and

K_r = stiffness of the roof, lb/in.

Stiffness values for both the support and the roof are calculated by applying the equation:

$$K = \frac{P}{\delta}$$

where: K = stiffness, lb/in

P = load, lb, and

δ = displacement, in.

For the force-stiffness equations, the roof stiffness is determined by the amount of roof deformation developed when a force is applied to a square area equal to the size of a traditional bearing plate (6 by 6 in).

Bolt Stiffness

Resin-grouted bolt stiffness has been determined in the laboratory using traditional pull test equipment and ultrasonic measurement systems (5). The calculated stiffness results, obtained experimentally on a 4-ft full-column resin-grouted bolt, are shown in figure 3. The fully grouted stiffness values level off at approximately 1,520,000 lb/in. This is the resin-grouted stiffness value to use in the equation. In the event that a partial column resin-grouted bolt is desired, the stiffness constant of the bolt must be calculated using a traditional spring constant formula.

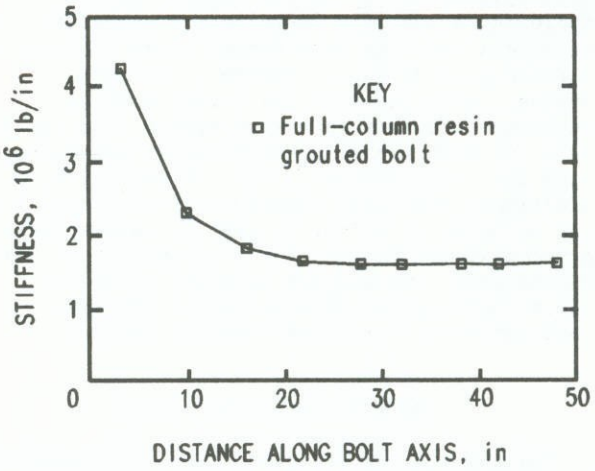

Figure 3 - The stiffness values for a full-column resin-grouted bolt.

Roof Stiffness

The required roof stiffness is based on the amount of force applied to the bolt and bearing plate coupled with the resulting roof deflection. This is essentially a foundation problem where the bearing plate is the footing and the roof is the semi-infinite medium (6). This stiffness could be calculated from laboratory-determined elastic properties based on the testing of small volume specimens. However, these laboratory-determined properties do not include the effects of roof separation or the inherent reduction of physical properties when larger volumes of material are involved. Therefore, it was concluded that the value should be determined, experimentally, in an underground mine. To complete the experiments, bearing capacity equipment was modified to examine the actual roof deflections when loads were applied to a 6 by 6 in piece of steel. This dimension was representative of the traditional bearing plates used in conjunction with most support systems. The deflections were measured by attaching a closure meter between the ram and a measurement bracket. These deflections are converted to stiffness values by dividing the load by the amount of displacement. Roof stiffness measurements were then obtained from an underground coal mine in western Colorado. The results indicate that the tested roof had an average stiffness value ranging from 130,000 to 171,000 lb/in. The average value of stiffness for this particular roof, which consisted of shale and sandy shale, was 150,000 lb/in. It was determined that an average stiffness value of 150,000 lb/in would be appropriate for calculations and calibrations in this particular mine site. If stiffness values for the specific mine are not available, the value of 150,000 lb/in is typical and can be used for preliminary calculations (7).

Thrust Bolting Nomograph

A nomograph, figure 4, has been constructed to permit the quick determination of the required bolt thrust for a fully grouted bolt (minimum length of 4 ft). On the y-axis, determine the final amount of desired or required amount of bolt load (F_b); go to the right until the stiffness of the immediate roof line is intersected. The value for the required bolt thrust is obtained by going straight down to the x-axis. For example, if a final bolt load of 5,000 lb is required and the roof stiffness is 150,000 lb/in as shown on the figure, line (a) would be extended directly across from the 5,000 lb reading located on the y-axis until the line intersected the approximate location of the roof stiffness (K_r) of 150,000 lb/in. The line would then be drawn straight down to the x-axis, line (b), where the required bolt thrust (F_t) is determined to be approximately 5,500 lb. The nomograph can be used similarly in exactly the opposite direction if it is desired to determine the final bolt load (F_b) by applying a known thrust (F_t). Values for typical bolting forces have been calculated for a fully grouted bolt and are shown in table 1.

Table 1. Typical bolting force values for a fully-grouted bolt.

Applied Thrust	Bolt Load
5,000 lb	4,551 lb
6,000 lb	5,461 lb
7,000 lb	6,371 lb
8,000 lb	7,281 lb
9,000 lb	8,192 lb
10,000 lb	9,102 lb

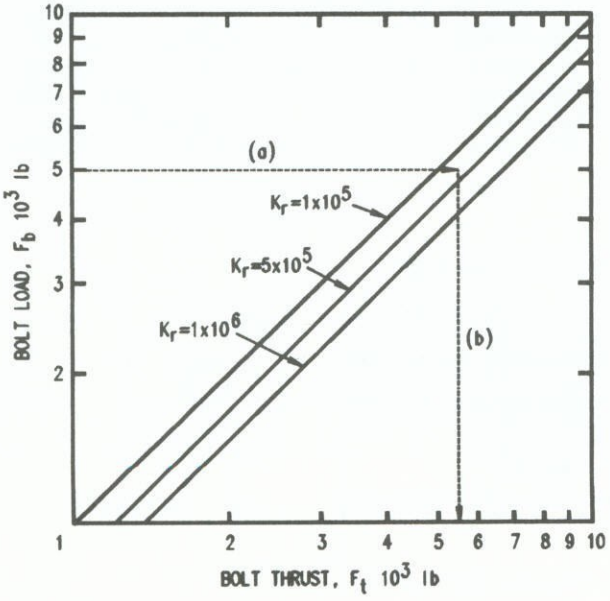

Figure 4 - Thrust bolting nomograph for a full-column resin-grouted bolt.

By using the thrust bolting technique, the amount of final load developed on an underground support system can be controlled by the amount of force applied on the head of the bolt during installation. The stiffness of the support system can be varied by reducing or increasing the bonding or column length of the resin grout.

EQUIPMENT MODIFICATIONS

Minor equipment changes and calibration adjustments are required to install and verify the thrust bolt installation. This includes an additional valve on the bolter, a high-strength bolt installation stinger, and a calibration cell.

Roof Bolter

The installation of thrust bolts requires pressures that are usually not required for normal bolt installation procedures. The normal upward thrust provided for passive resin-grouted bolts is usually between 2,000 to 3,000 lb. These low pressures are usually required in the upward force on the drill head to minimize the bending of steel during drilling. To accommodate the low pressures desired for drilling and still provide the high pressures required for thrust bolting, a diversion valve is installed at the hydraulic feed package that supplies the pressure to the bolting head. By leaving this valve in the off position, only drilling pressures are made available to the feed cylinder. When the valve is turned to the on position, the entire hydraulic pressure developed by the bolter is available to the feed cylinder for the installation of thrust bolts. The diversion valve is in line with a feed package where the amount of pressure can be controlled and calibrated for specific applications. The diversion valve and feed package are shown in figure 5. The bolting machines used in this investigation were made by the J. H. Fletcher & Company,[2] but other bolting machines could be similarly modified. The diversion valve and the mounting brackets for each side cost approximately $175.00 and requires about 3 hours/bolter head to install on the existing machine.

Bolt Stinger

To accommodate the large forces applied to the head of the bolt during installation, modifications were required to the bolt stinger. The stinger was designed to accommodate both the drilling of the bolt hole and the installation of thrust bolts without having to be removed between functions. This assisted the bolter operators, because the required wall thickness and loading plate on the stinger increased the weight of the tool. This requirement led to the unique design in which the stinger is used for drilling as well

[2]Reference to specific products does not imply endorsement by the Bureau of Mines.

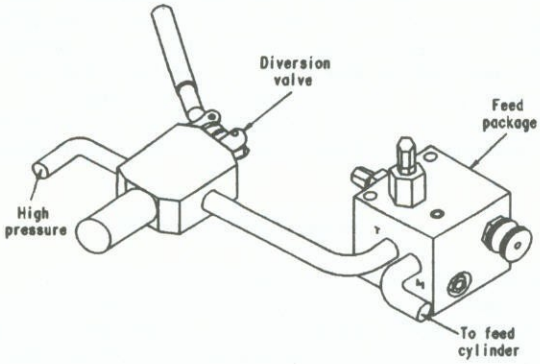

Figure 5 - The required feed and diversion package modifications required to perform thrust bolting.

as roof bolt installation. This helped reduce total bolt installation time and essentially eliminated the problem of bent stingers. The thrust bolting stinger is shown in figure 6.

Calibration

To ensure that the proper amount of force was being applied during the thrust bolt installation, a calibration device was designed and constructed (figure 7). It consists of a donut pressure cell bladder encased between two round steel platens. The calibration cell is placed between the bolt stinger and the bolting machine head. Loads are recorded while the full thrust of the machine is applied. The cell was designed so the loads could be easily read and adjusted from a remote position on the bolter. The bolter can be calibrated at the beginning of the shift and routinely on each bolting cycle. Once the feed cylinder pressures were established, experience showed that the bolter loads changed by approximately 3 pct during the entire shift. This was probably due to hydraulic temperature and minor hydraulic pressure changes.

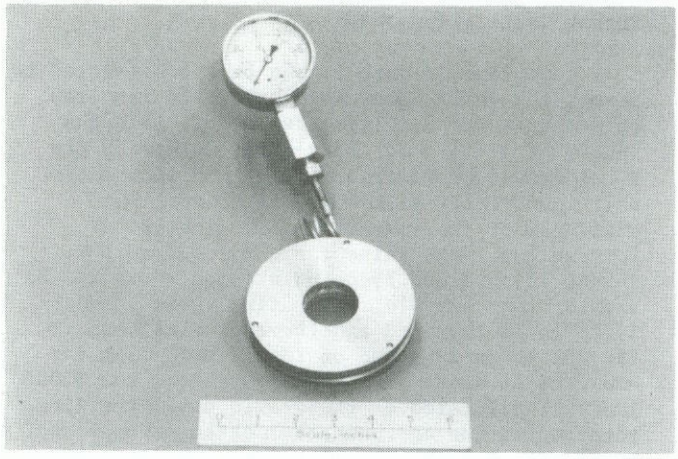

Figure 7 - Thrust Bolting calibration load cell.

CASE STUDIES

Two test areas were established in underground coal mines using the thrust bolting support system. The bolts were installed as the primary support system in a room-and-pillar operation and in a longwall operation with a three-entry gateroad configuration.

Test Site #1

The first test site was established in a western room-and-pillar operation. The massive test site contained approximately 20,000 ft^2 of roof openings and was supported by about 1,250 thrust bolts. The investigation used 8-ft long, 3/4-in diam, grade 60, headed rebar bolts. The bolts were placed into a 1-in-diam borehole with a 4-ft equivalent length of resin. The developed panel contained nine sets of entries with a development pillar dimension of 60 ft by 120 ft on centers, leaving a final opening width of approximately 20 ft. The immediate roof in the area consisted of approximately 1-ft-thick coal member and 7 to 8 ft of a shale, sandy shale material. The pillars were recovered during the retreat mining cycle, leaving only the closest

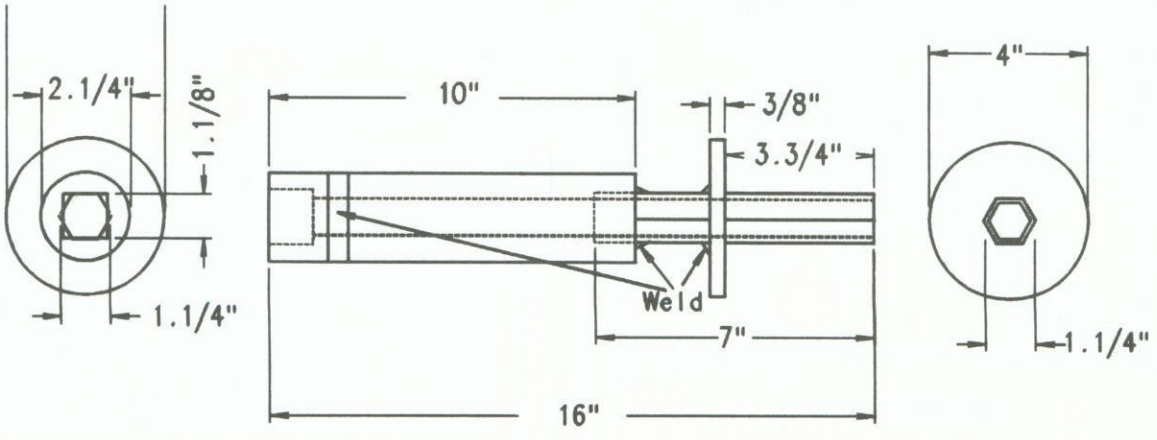

Figure 6 - The thrust bolting stinger.

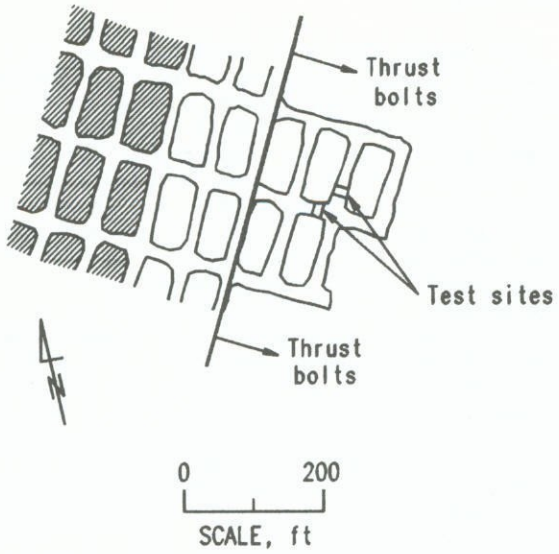

Figure 8 - Test site configuration in a room-and-pillar mine.

two entries adjacent to the test area for a long-term bleeder system. Two separate test areas were instrumented in the massive test area to examine various installation loads and monitor the immediate roof. The test site is shown in figure 8.

The bolts in the test areas were instrumented with Goodyear pressure pads. This was an effective and inexpensive instrument to monitor the initial and subsequent loads applied to the bearing plate, which is an indication of load being developed along the ungrouted and grouted length of the bolt axis (8). Differential sag stations were installed at the center of the test areas to monitor roof movements or separations in the supported strata. The stations were established at 1, 3, 5, and 8 ft above the collar of the hole.

The test area was installed and monitored six times during a 64-day period. The bolt installation loads, with varying degrees of thrust, were within ±5 pct of the calculated or predicted loads. The loading trends and patterns from the Goodyear pressure pads in test area No.

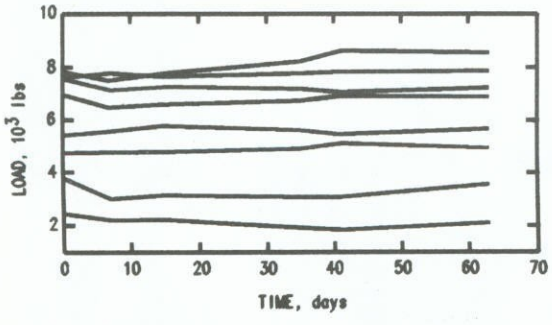

Figure 9 - Pressure pad loads, test site No. 1, test area No. 1.

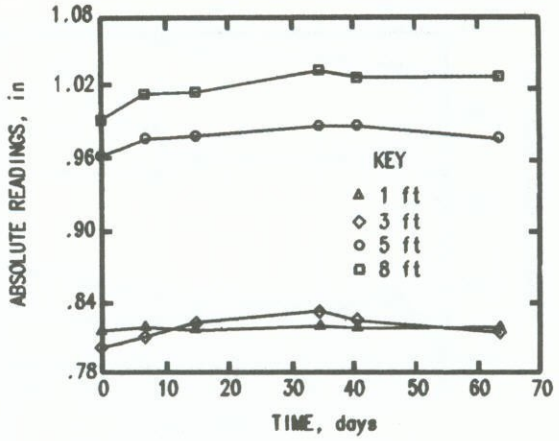

Figure 10 - Absolute differential sag-station measurements, test site No. 1, test area No. 1.

1 and the readings from the differential sag stations, are shown in figures 9 and 10, respectively.

As clearly shown, the loads fluctuated slightly over the duration of the test period This was confirmed by the small amount of roof movement measured by the differential sag stations. The sag stations located immediately above the coal, at 1 ft, showed that the interface between the coal and the shale remained intact throughout the term the test period was monitored.

The loading trends and patterns from the

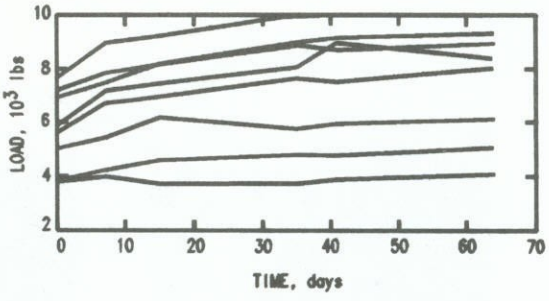

Figure 11 - Pressure pad loads, test site No. 1, test area No. 2.

Goodyear pressure pads in test area No. 2 and the absolute readings from the differential sag stations are shown in figures 11 and 12, respectively. The bolt loads determined by the Goodyear pressure pads in this area exhibited a gradual increase in load throughout the period of the test site evaluation. This same pattern was also evident in the differential sag station data. The sag station readings indicated minor roof movements (0.05 in maximum) at the 5-ft anchor. A visual inspection of the immediate roof with a fibre-optic borescope indicated that no visible separations had occurred. However, the pillars in the area were being subjected to large abutment loads being transferred from the retreat pillar section. This led to high degrees

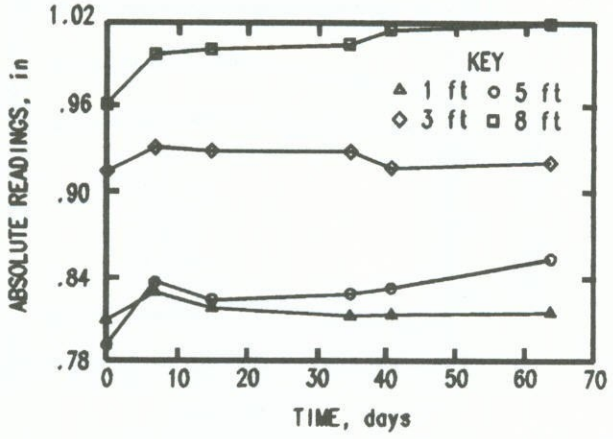

Figure 12 - Absolute differential sag-station measurements, test site No. 1, test area No. 2.

of rib sloughage and pillar spalling and created effective roof spans in excess of 23 ft. The support system continued to perform satisfactorily throughout the duration of the test despite the high loading conditions. The pillar behavior and rib sloughage in test area No. 2 is shown in figure 13. The Department of Labor Mine Safety and Health Administration (MSHA) examined the test site during installation and during routine inspections. They concluded that the thrust bolting system was adequate and could be included in the roof control plan for normal operational use.

Test Site #2

The second test site was established in a western longwall operation. The mine develops three-entry gateroad systems with a yield-stiff pillar configuration. The final pillar dimensions in the test area of the yield pillars were 45 ft by 70 ft, and the stiff pillar dimensions were 75 ft by 75 ft. This area of the mine had approximately 1,050 ft of overburden. The immediate roof consisted of 1 to 2 ft of a black shale that is very susceptible to weathering. The next 6 ft consisted of a competent shale interbedded with a sandy shale. The roof support being used was a 5-ft resin-assisted expansion anchor bolt. The effective column length of the resin was 2 ft. The mine operator had determined, through trial-and-error testing, that support systems installed in tension helped prevent the failure of the black shale and reduced minor rib cutters during panel development and extraction.

The test site was designed and installed on the normal bolting cycle in approximately 8,400 ft^2 of mine roof, supported solely with 5-ft-long, 3/4-in, grade 60 thrust bolts. The test site, shown in figure 14, concentrated on monitoring the behavior of the entries, rooms, and intersections. The installation loads and subsequent loading trends and patterns were monitored with 55 Goodyear pressure pads. The roof movements and deflections were monitored by using magnetic anchors installed at 6 levels to a depth of 12 ft. The depths of the anchors varied slightly, but were approximately at 2, 4, 5, 6,

Figure 13 - Rib sloughage and general ground conditions.

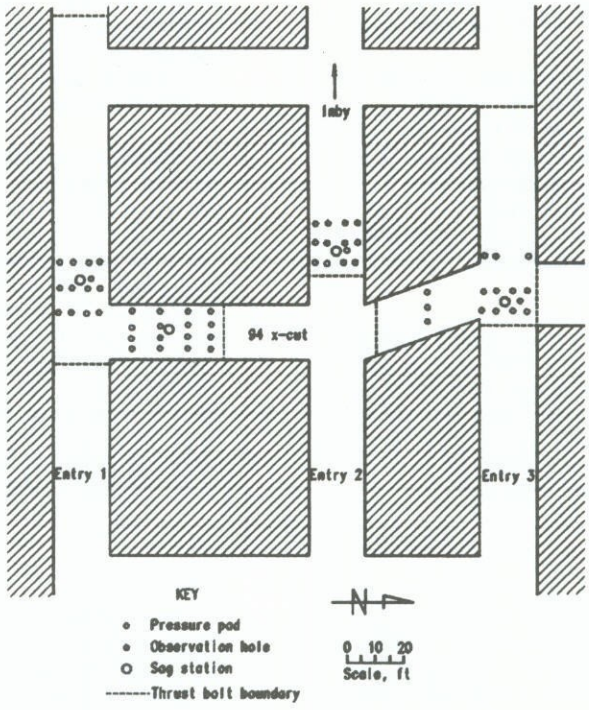

Figure 14 - Test site configuration in longwall gateroad entries.

7, and 12 ft. The anchor at the top of the hole was used as the datum. Any separations or movements occurring at any of the stations installed below this point could help locate strata separations and provide necessary input to support performance.

The bolts, installed with a full-column of 15-second resin, were spun with a 10-second spin and thrust upward with a 10-second application of 8,000 lb force. The measured stiffness of the roof in this area was approximately 150,000 lb/in. The final bolt tension with these parameters should have resulted in 7,281 of force, or 16,549 psi on the 3/4-in bolt tendon. The average installation load measured immediately after installation was 6,093 lb. This was approximately 19.5 pct lower than the predicted force. This loss of initial bolt load was attributed to the introduction of the Goodyear pressure pad between the bearing plate and the immediate mine roof. The pressure pads have relatively low stiffness values which affect the final (K_b) support stiffness in the thrust bolting equation. At the time of this paper, the test site has been in place 3 months, and the instrumentation has been read and evaluated three times. The loads on the bolts have fluctuated only an average of 197 lb, and the largest roof displacement has been 0.04 in. More importantly, the immediate roof and intersections have remained stable with no signs of excessive loading or roof deterioration. No evidence of the minor cutters, previously experienced with full-column resin-grouted bolts, have been visible to date. The test area will be monitored until the extraction of the longwall panel to assist in the evaluation of long-term stability. The mine operator and miners, with the permission of MSHA, have elected to use the thrust bolting technique during the entire development of the next gateroad system.

COST COMPARISONS

While the developed loads, system performance, and safety are the first priority in any underground mining operation, cost considerations are an important parameter. The bolting and support cost for any operation can make it more or less profitable depending on initial support cost and the subsequent cost for cleanups, re-support, and injuries. The headed rebar bolt is the most economic system available from bolt manufactures. For this discussion a cost evaluation will be based on a 5-ft fully grouted thrust bolt. The initial cost is approximately $1.90 for a 3/4-in, 5-ft, grade 60 headed rebar bolt. The resin cost is approximately 21 cents per equivalent foot, or $1.05 per bolt. Because any installed bolt requires a similar diameter hole and a bearing plate, this cost is not considered. The total cost per thrust bolt is $2.95.

The bolt being used at the mine with test site No. 1 was a resin-grouted threaded system. In this system the bolt is installed with a partial column of grout. After the grout cures, the bolt is tensioned from the bottom with a threaded nut. A 5-ft, 3/4-in diam bolt of this type was quoted at a cost of $4.45. The cost for the required

3-ft equivalent column of resin is 63 cents. This results in a bolting cost of $5.08 per bolt.

The bolt cost at the mine with test site No. 2 considers a resin-assisted expansion anchor bolting system. This system incorporates a traditional expansion anchor bolting system into a 2-ft equivalent length of resin grout to increase anchorage capacity. The cost is $3.89 for a 5/8-in, 5-ft bolt and for a 2-ft equivalent length of resin, 42 cents. This results in a material cost of $4.31 per bolt.

In large underground coal mining operations it is not unusual to install 100,000 roof bolts per year. The total cost of these described bolting systems are shown in table 2. The results show that support cost can be reduced by 72 and 46 pct when thrust bolts are substituted for the tensionable rebar and resin-assisted bolting systems, respectively.

Table 2. Bolting cost comparisons.*

Bolt type	Bolt/resin cost	Total Cost 100,000 bolts
Thrust bolts	$2.95	$295,000
Tension rebar	$5.08	$508,000
Resin assisted	$4.31	$431,000

*Material cost only.

CONCLUSIONS

The thrust bolting technique develops an active support system utilizing installation procedures with a full or partially grouted headed rebar bolt. No mechanical bolt devices are used to generate the active force. The system requires only minor modifications to the roof bolting machine and the construction of a high-strength bolt installation stinger. The primary factors that affect the bolt load are the applied thrust, the bolt system stiffness, and the roof stiffness. An equation has been developed that shows the relationship between these factors. Based on this equation, a thrust bolting nomograph has been developed that can be used to determine the amount of bolt thrust required to obtain desired final bolt loads for various roof stiffnesses. However, the nomograph shows that for a wide range of roof stiffness only a small change in the bolt load will occur for an applied bolt thrust.

Both underground case studies showed that thrust bolting can be an effective method of roof support in underground coal mines. The support system performed extremely well under adverse ground conditions, evidenced by the small amounts of immediate roof movements and the elimination of small roof cutters. An additional advantage of the thrust bolting system is the reduced bolting material cost. As shown, cost were reduced by a minimum of 46 pct and a maximum of 72 pct when comparing initial bolt cost with the systems currently used underground at the two mines where tests were conducted.

Further advantages of the thrust bolting system, obvious to mining operators, are that no torque-tension measurements are required, no or very little bolting materials become unusable because mechanical components become damaged or corroded, and simple bolt installation is completed in 20 seconds. Bureau of Mines personnel are continuing to examine the effectiveness of support systems under a wide range of geological conditions. The ultimate goal of these investigations is to provide engineered support designs that will provide safe, economically feasible, working areas under diverse and hazardous underground mining conditions.

ACKNOWLEDGMENTS

The authors would like to thank Ronald Stucki, Vice President and General Manager, Cyprus Coal Colorado Operations and Jim Miller, Senior Mine Engineer, Utah Fuels, Inc. for their continued support and enthusiasm during this investigation.

REFERENCES

1. Karabin, G. J., and W. J. Debevec. Comparative Evaluation of Conventional and Resin Bolting Systems. MSHA IR 1033, 1976, 22 pp.

2. Tadolini, S. C. Anchorage Capacities in Thick Coal Roofs. BuMines IC 9058, 1986, 12 pp.

3. Tadolini, S. C. The Effects of Torque-Tension Relationships on Roof Bolt Systems. Proceedings 92nd Canadian Institute of Mining and Metallurgy General Meeting, May 6-10, Ottawa, Canada, 1990, 10 pp.

4. Karabin, G.J. and M.T. Hoch. Contemporary Roof Support Systems Provide a Diversified Approach to Modern Ground Control. Paper in Proceedings, Annual Institute on Coal Mine Health and Safety Meeting. VPI., 1980, pp. 249-268.

5. Tadolini, S. C. and R. C. Dyni. Transfer Mechanics of Full-Column Resin-Grouted Roof Bolts. BuMines RI 9336, 1991, 14 pp.

6. Coates, D. F. Rock Mechanics Principles. Canadian Department of Energy, Mines, and Resources. Mine Branch Monograph 874, revised 1970.

7. Barry A. J. and O. B. Nair. In Situ Tests of Bearing Capacity of Roof and Floor in Selected Bituminous Coal Mines. BuMines RI 7406, 1970, 20 pp.

8. Tadolini, S. C. and B. F. Ulrich. Evaluation of Bearing Plates Installed on Full-Column Resin-Grouted Bolts. BuMines RI 9044, 1986, 12 pp.

AN ALTERNATIVE TO A MANUAL TORQUE CHECK ON ROOF BOLTS

Joseph A. Cybulski, *Supv. Mining Engineer*
William J. Gray, *Mining Engineer*

Mine Safety and Health Administration
Bruceton Safety Technology Center
Pittsburgh, Pennsylvania

ABSTRACT

In response to the mining of reserves with increasingly adverse ground conditions and the roof support recommendations of current rock mechanics theories, roof support systems have continued to improve. A few of these newer bolting systems, while giving improved performance, require a new method to check bolt installation. Previously, a torque wrench had been the sole means to check the installed torque of a roof bolt. However, due to the characteristics of some of the newer bolting systems which can prevent a reliable manual torque check and a recent change in the federal roof control regulations, an alternative method to a manual torque check is gaining acceptance. This alternative method involves monitoring the hydraulic pressure of the roof bolting machine torque circuit and provides a safe, reliable and quick way to check bolt installation in those instances when an accurate manual torque check cannot be made.

INTRODUCTION

The need for an alternative to a manual torque check is clearly illustrated when the characteristics of mechanically-anchored, resin-assisted bolts are examined. These systems, which have risen in popularity during the last few years, combine the use of a mechanical anchor along with polyester resin to enhance the anchorage capacity and bleed-off characteristics of tensioned bolt installations. However, when fast-setting resin is used with a mechanical anchor, making a meaningful torque check can be difficult. Once the resin begins to gel, the entire bolting system may become locked. A spring-back condition may exist where the anchor and bolt are held fast by the resin. In this case, torque higher than the actual installed torque can be applied to the bolt head but since the top end of the bolt is locked in by the resin, the bolt may twist in torsion and then spring back when the torque wrench is released. A second type of misleading reading may result where the bolt is not held tight but the resin provides sufficient resistance to alter the assumed torque-tension ratio. In both of these cases, a manual check with a torque wrench will not correspond to the installed bolt tension. As a result, an alternate method to check some mechanically-anchored, resin-assisted bolts is essential.

The federal standards for roof, face and rib support which went into effect March 28, 1988, address this area. 30 CFR Part 75, Section 75.204(f)(4) states "In each roof bolting cycle, the actual torque or tension of the first tensioned roof bolt installed with each drill head shall be measured immediately after it is installed. Thereafter, for each drill head used, at least one roof bolt out of every four installed shall be measured for actual torque or tension." This revised standard is performance-oriented and does not require the use of a torque wrench, as in the past, but only requires that the tension or torque be measured. This allows for the introduction of new technology in the area of torque or tension measurements. One new means of measuring installed bolt torque is to monitor the hydraulic pressure in the roof bolting machine rotation (torque) circuit. In theory, the torque output of a roof bolting machine is proportional to the pressure in the rotation circuit. To check the feasibility of using a pressure gage to monitor installed bolt torque, underground investigations were conducted at various mines. The following summarizes one such investigation conducted at a southwestern Pennsylvania coal mine.

IN-MINE TESTS

The first step of the investigation was to have the company install pressure gages on the various bolting machines in use. Since the mine used continuous mining machines with integral bolters, pressure gages were also installed on these machines. In all, four types of machines were evaluated: continuous miner, two types of single-boom center bolters, and a single-boom bolter used during longwall recovery operations. To accurately measure the torque and thrust during the testing, a torque-thrust-rotation sensor (fig. 1) was used. The sensor mounts directly on the drill head during bolt installation and measures the actual torque output, thrust and RPM which is digitally displayed on the read-out box. The test procedure was to install bolts with compression pads at various pressure settings while recording the peak pressure (from machine-mounted gage), torque, thrust and installed bolt tension. The bolt was then checked with a torque wrench. The bolts being installed were mechanically-anchored, resin-assisted. To ensure a reliable manual torque check, the bolts were installed without resin to eliminate the possible problems previously discussed.

This test procedure was used to evaluate the four different machine types. The data obtained from one of these tests is listed in Table I. The

second column lists the peak pressure, the third and the fourth columns list the torque and thrust obtained from the sensor, the fifth column presents the bolt load taken from a compression pad and, finally, the last column is the torque reading obtained when using a torque wrench. When analyzing the data, it becomes obvious that an increasing pressure results in an increased torque output and increased bolt load (tension). When a linear regression analysis is performed using pressure and torque output values, a correlation coefficient, r, of 0.98 is obtained. The correlation coefficient indicates the quality of fit achieved by the linear regression. Values of r close to 1.00 indicate a better fit than values close to zero. Therefore, the equation developed through linear regression, $T = -7.75 + P\ (.15)$ where P is pressure and T is output torque, fairly accurately describes the linear relationship between pressure and torque for this particular bolting machine. Similar results were obtained from analyses of the data generated from tests on the other three machine types. Once an equation is developed for a particular machine, a chart like the one shown in Table II can be generated which can be used to help establish an installed pressure range to correspond to the approved installed torque range.

One factor which must be considered when setting an installed pressure range is the effect of thrust applied to the roof bolt during installation. A pressure gage will only indicate the available torque at the drill head and not necessarily the installed torque of a roof bolt. Some of the available torque will be lost in overcoming the effect of thrust on the roof bolt during installation. The ideal solution would be to eliminate the thrust completely but since that is not feasible, the next best situation is to have a consistent thrust application for every installation. When the thrust is consistent, additional torque can be applied to compensate for the torque loss due to thrust. The amount of additional torque needed to overcome thrust will vary since it depends on the amount of thrust applied and the frictional characteristics or tension-torque ratio of the particular roof bolt system. Using the torque-pressure chart that was generated, the following example will show how to approximate the additional torque needed to compensate for thrust when using a pressure gage to monitor installed torque. First, assume that the following conditions exist:

1. An installed torque range of 200 to 250 ft-lbs is required.

2. The thrust applied during installation will be 1,000 lbs.

3. The tension to torque ratio is 50 lbs tension for every ft-lb of torque.

The first step is to calculate the torque loss due to thrust during bolt installation. The torque loss equals the thrust divided by the tension-torque ratio, in our example 1,000 lbs ÷ 50 lbs/ft-lbs = 20 ft-lbs. Therefore, the output torque range needed for the correct installed torque range would increase by 20 ft-lbs to 220 - 270 ft-lbs. Using the chart to obtain the pressures corresponding to this torque range results in a pressure range of 1,500 - 1,850 psi. The pressure range has been rounded off to the nearest 50 psi. This approach can be used to establish an installed pressure range on any roof bolting machine equipped with a pressure gage. The results obtained from such an analysis should be verified underground, since the application of thrust during bolt tightening may alter the assumed tension-torque ratio.

Once an installed pressure range is established for a particular roof bolting machine, the pressure gage can be marked accordingly using reflective tape or some other means. An alternative to marking a standard off-the-shelf gage is to use one of the several customized torque/pressure gages currently on the market. One type is a standard gage fitted with an additional rotating window calibrated in ft-lbs. Another type has a fixed face plate calibrated in both psi and ft-lbs. Caution should be exercised if these customized gages are used. As stated earlier, each model of roof bolter may have its own unique pressure/torque ratio. Therefore, a customized gage should only be used on the roof bolter model and hydraulic system for which it was developed. No gage with a fixed preset pressure/torque ratio can be used universally. The use of a custom gage on the wrong machine could result in a torque output drastically different from the torque indicated by the gage. Figure 2 shows the pressure-torque ratios obtained from four bolting machines used at one mine. If all the machines in figure 2 were fitted with the same customized gage and set up with a hydraulic pressure of 1800 psi in the torque circuit, the actual torque output from the various machines would range from about 150 ft-lbs to over 400 ft-lbs. However, the customized gages would all be indicating the same torque output for each machine. This clearly indicates the importance of using the correct custom gage for a particular machine. Also evident from this example is that one installed torque range would be replaced by four distinct pressure ranges (one for each machine) which deliver the desired torque output. In this regard, the use of the pressure gage method can add complexity to the roof control program of a given mine. The ideal situation is to have a mine with all its roof bolting machines hydraulically identical. In this instance, all the machines would have the same installed pressure range.

In addition to the thrust, several other factors can affect the pressure gage method. The first of these, temperature, does not affect the actual pressure-torque ratio but the amount of pressure available. A machine that is cold can develop a higher pressure, up to 200 psi, than when the same machine is at operating temperature due to the higher viscosity of cold hydraulic fluid. Since it only takes a few minutes for a machine to reach its operating temperature, this should not pose a serious problem. The remaining two factors, component wear and RPM, can affect the pressure/torque ratio. As the hydraulic system components wear, the system becomes less efficient requiring higher pressures for the same torque output. The effect of wear on the system components can be noticed in as little as two weeks under some conditions. To monitor the effect of wear, a periodic check of the pressure-torque ratio should be made. This periodic check can be made in one of three ways. First, a bolt can be installed dry and checked with a torque wrench. Second, a compression pad or load cell can be used to determine the actual installed bolt tension at a given pressure. Finally, some type of in-line torque meter, installed on the drill head, can be used to check the output torque at a given pressure.

Another factor which can affect output torque is the rotational speed (RPM) of the drill head motor during bolt installation. The torque output at a given pressure is dependent on the RPM. Increasing rotational speed, up to the rated RPM, results in an increasing torque output. Above the rated RPM the torque output remains constant. Because of this inherent characteristic of the drill head motor, erratic RPM during bolt installations can alter the torque output. A higher RPM also produces more momentum in the drill head, which can result in increased torque

output when compared to a lower RPM.

GUIDELINES

The effects due to RPM, thrust, and component wear are not unique to the pressure gage method but are present every time a roof bolt is installed. A reliable manual torque check immediately assesses the effects of these factors since the actual installed bolt torque is measured directly. Using a pressure gage, on the other hand, is an indirect method of checking the installed bolt torque and requires additional precautions to monitor and control the effects of RPM, thrust, and component wear.

When a pressure gage is used, the following steps should be taken to ensure that the correct installed bolt torque is achieved:

1. A periodic check of the torque-pressure ratio to assess the effects of hydraulic system wear.

2. A consistent roof bolt installation procedure regarding thrust and RPM.

CONCLUSION

In addition to its use with the mechanically-anchored, resin-assisted bolts, the pressure gage method can also be used where high installed torque or the mining height make it difficult to obtain an accurate manual torque check. The pressure gage method is currently being used in about 50 mines and appears to be a viable alternative in those instances when a reliable manual torque check cannot be made. As an added safety bonus, this pressure gage check can provide the operator with a reliable, easy way to check every bolt installed.

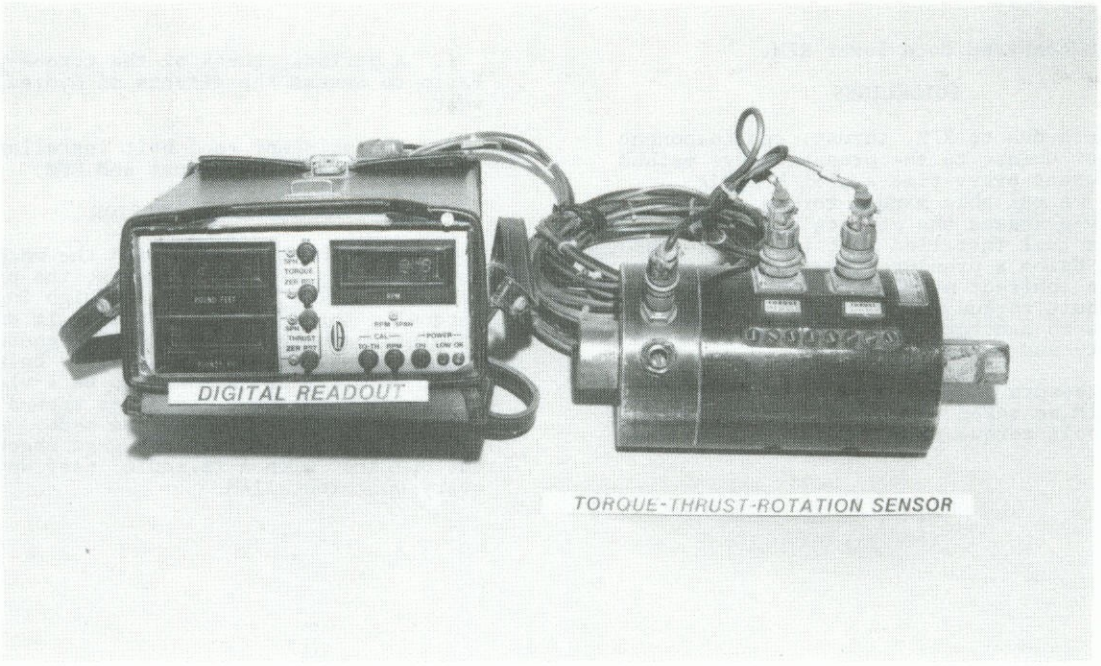

FIGURE 1. INSTRUMENTATION

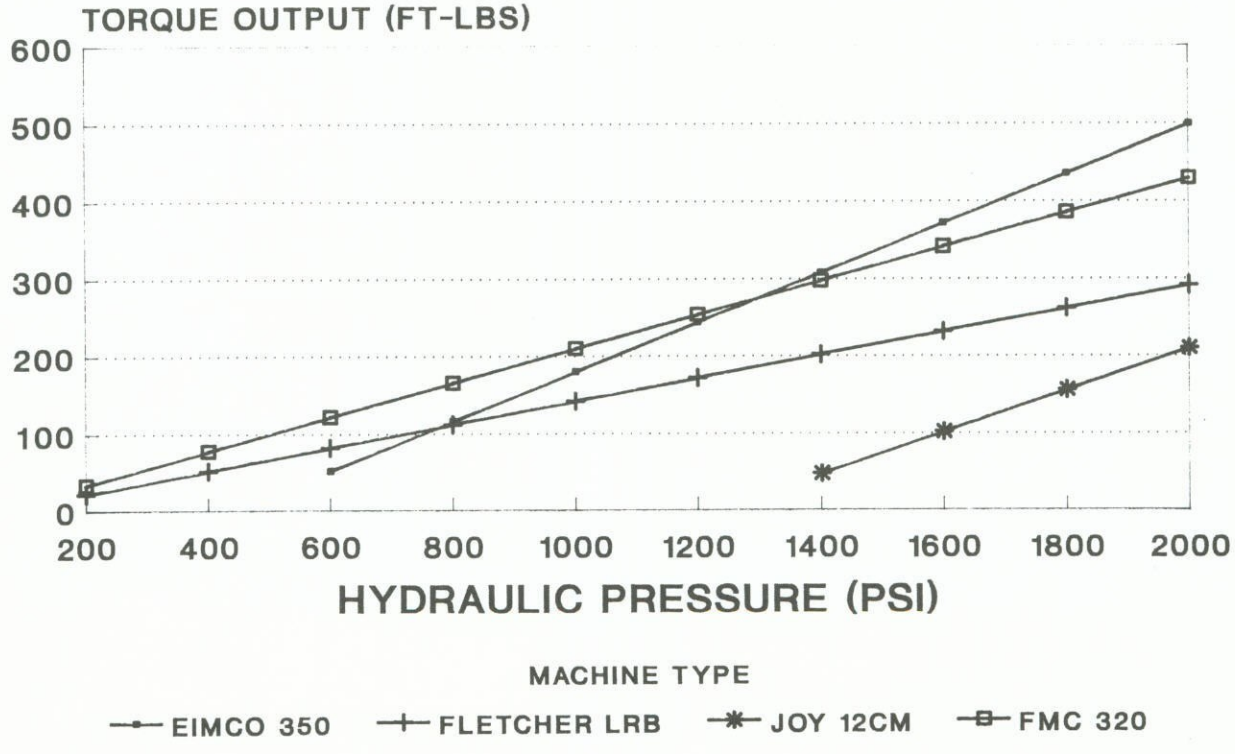

FIGURE 2. PRESSURE-TORQUE RATIOS OF VARIOUS BOLTING MACHINES

TABLE I. In-Mine Data

Bolt No.	Gage (PSI)	Sensor Torque (Ft-Lbs)	Sensor Thrust (Lbs)	Bolt Tension (Lbs)	Torque Wrench (Ft-Lbs)
1	1000	133	<1000	5900	115
2	1000	138	1300	7600	175
3	1000	150	1200	7400	160
4	1200	168	1000	8200	210
5	1225	158	1000	6400	155
6	1225	176	<1000	8200	250
7	1325	183	<1000	10000	220
8	1325	193	<1000	8800	255
9	1470	195	<1000	9500	235
10	1470	204	<1000	8800	200
11	1575	229	<1000	11300	300
12	1810	260	<1000	11200	>300

TABLE II. Pressure-Torque Relationship

TORQUE (FT-LBS)	PRESSURE (PSI)	
150	1052	
160	1118	
170	1185	
180	1252	
190	1318	
200	1385	
210	1452	
220	1518	
230	1585	Installed
240	1652	Pressure
250	1718	Range
260	1785	
270	1852	
280	1918	
290	1985	
300	2052	

$T = -7.75 + P(.15)$
$R = .98$

10th INTERNATIONAL CONFERENCE ON GROUND CONTROL IN MINING

SHEAR BOND STRESSES ALONG CABLE BOLTS

Hani S. Mitri, *Assistant Professor*
Hossein Rajaie, *Postdoctoral Fellow*

Department of Mining and Metallurgical Engineering
McGill University
Montreal, Quebec, CANADA

ABSTRACT

The behaviour of grouted cable bolts used for rock reinforcement as a means of ground control in hard rock mining is investigated. The study utilizes an analytical model which is based on the variational principle to calculate the shear bond stress distribution along the embedded length of cable bolt. In this paper, a comprehensive parametric study which covers both geometric and mechanical design parameters involved is presented. Special emphasis is placed on studying the characteristics of the grout model represented by Winkler springs. This involved varying the maximum shear strength of the grout, its residual strength and the slip occurring between the cable and the borehole wall.

INTRODUCTION

The use of fully grouted, untensioned steel cable bolts as ground supports has become increasingly popular in hard rock mine operations over the past 15 years or so. This is mainly due to their superior structural performance of transmitting high shear stresses from the rock to the surface area of the cable when slip takes place between the cable and the surrounding matrix. However, the efficiency of this type of support system depends on the adequate selection of such design parameters as the spacing between cables, the size and length of cable and the strength properties of the grout. It is for this reason that many studies, both theoretical and experimental, have been undertaken on the subject particularly with respect to rock bolts with the objective of identifying their structural characteristics as practical tool for ground support. An analytical model has been previously developed by the authors using Winkler-type springs to simulate the grout between the cable and the wall of the borehole drilled into the host rock. In this model, the total potential energy of a system consisting of a cable segment, the grout and the host rock in its proximity is minimized using Euler-Lagrange equation. The bond-slip characteristic model of the springs is assumed to be trilinear to account for strain softening and residual shear resistance.

In the following sections, a brief review of literature is first presented. The analytical model adopted is only briefly described. This is followed by a detailed presentation of the variation-of-parameter study.

HISTORICAL REVIEW

The pioneering experimental work by Hawkes and Evans [1] demonstrated the presence of a linear relationship between the axial stress and corresponding surface shear stress of the bolt before debonding at the end face occurs. Based on this result, they derived an expression to describe the distribution of shear stress along the length of the anchor. Philips [2] simplified Hawkes and Evans' equation and concluded that the distribution of shear stress in hard rock is an exponential function while in soft rock it takes a linear form. Gato [3] performed a series of tests on reinforcing bars in concrete and showed that the bearing pressure that develops at the lug interface can be resolved into two components; a component parallel to the rod axis which acts as a bond stress and a radial component which tends to split the surrounding matrix. Several other studies confirmed the exponential distribution of shear stress along the length of anchor when there is no slip between the anchor and the matrix [4,5,6]. Several numerical modelling attempts were made to obtain the shear stress distribution along the anchor. These were done using axisymmetric finite element models which incorporated either two materials, i.e. steel and rock with linear elastic behaviour [7] or three materials i.e steel, rock and grout, with elastic plastic behaviour [6,8,9,10]. The design of rock bolt and cable bolt support systems has traditionally been carried out by empirical design rules developed either from field practice and local experience or from rockmass classification studies. Also, laboratory-based empirical formulae have been derived and presented in the literature. For example, Cassidy [11] reported a simple equation for calculating the cable bolt spacing as a function of the basic design parameters like the rockmass density, the strength of the cable and its orientation. Ballivy [12] proposed a design procedure to determine the

embedded length of passive anchors in the rockmass. His work was based on the equation first developed by Hawkes and Evans [1]. The Golder Method was proposed by Mathews et al.[13] in which selected geotechnical factors have been combined as a stability number, N, and plotted against a shape factor, F, to assess empirically the stability of the surface boundary of an open stope. A high stability number and a low shape factor should reflect stable exposures while the opposite should reflect instability. More recently, Mitri and Rajaie [14] presented the formulation of a special "cable support" finite element for the design of cable bolt support by numerical modelling. The "cable element" formulation is based on the assumption that the grouting material can be idealized by a continuous, Winkler-type spring running parallel to the cable and connecting the cable surface to the borehole wall. Thus, the inherent shear-slip behaviour between the cable and the host rock can be accounted for.

According to Littlejohn and Bruce [15], there are generally four possible modes of failure of a cable bolt support system. As illustrated in Figure 1, these can be classified as: (1) failure within the rockmass, (2) failure of the cable bolt, (3) failure of the rock-grout interface and (4) failure of the cable-grout interface. Only a few failures of cable bolting due to breaking of steel strands have been reported. Most reported failures have been due to large blocks slipping off the cables; the strands tend to be left with a curled and twisted shape and totally stripped off the grout.

ANALYTICAL MODEL

One of the principal problems in cable bolting is the transfer of load from the rockmass to the cable elements through the shear bond interface. Therefore, the behaviour of the bonding element between the two materials is one of the most important parameters in cable bolting design.

An analytical model based on the variational principle has been previously developed by the authors to calculate the shear bond stress distribution along the cable bolt [16]. The model assumes that the cable bolt is installed in an intact, homogeneous rock-mass and that the grout material between the cable and the borehole wall in the rock can be idealized by a set of continuous, Winkler-type springs parallel to the cable axis as shown in Figure 2. The shear-slip behaviour of such springs is assumed trilinear, i.e. linear elastic to the peak point, followed by a softening response to the point of constant residual strength; see Figure 3. A linear elastic behaviour is assumed for both the rock and the cable materials. Based on the work reported by Tepfer [17], the relation between the shear bond stress and the normal (radial) stress acting on the cable surface was taken to be linear.

The analytical approach is based on the minimization of the total potential energy of the cable-spring-rockmass system using calculus of variation. Euler-Lagrange equation is derived from the functional form, and is then solved for the shear bond stress.

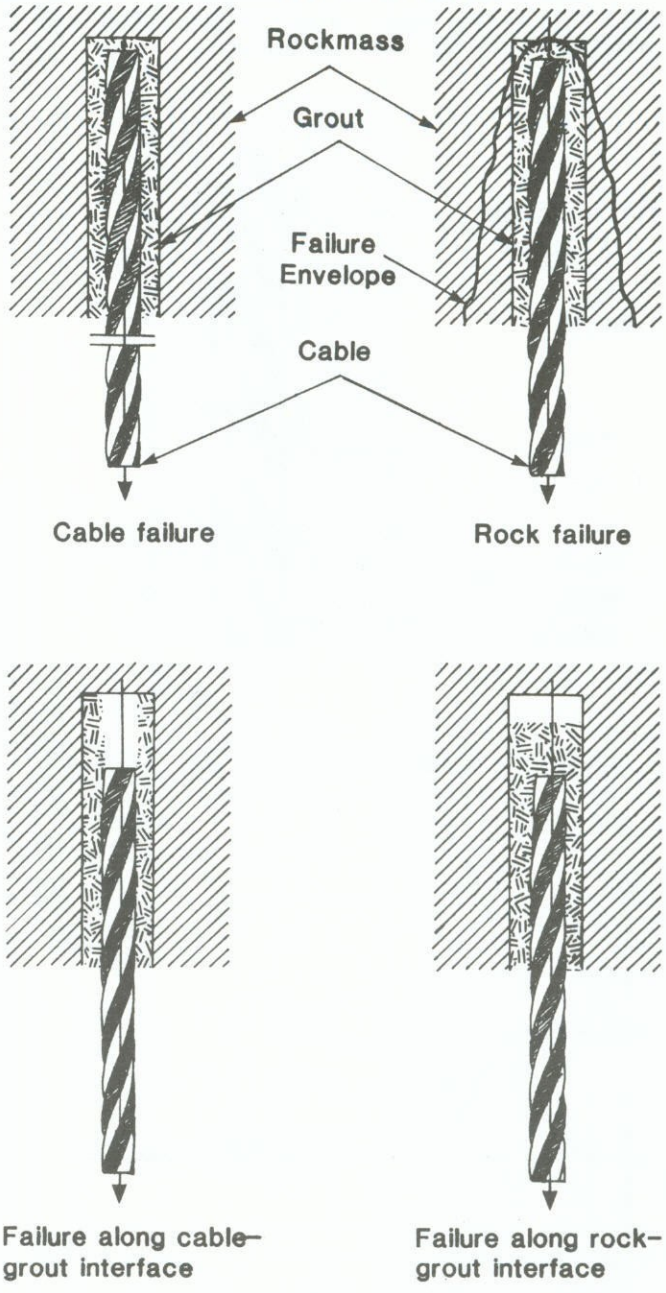

Figure 1: Possible failure modes of cable bolts

The solution of the resulting differential equation leads to three possible situations depending on the maximum slip occurring along the cable. These situations correspond to the elastic, softening and residual shear stress ranges defined by the grout model (Figure 3). Since the value of the maximum slip is not known a priori for a given end load, P, some form of iteration is necessary. A computer program has been written to facilitate the calculation of shear stress distribution for any of the three possible cases. In all cases, however, the shear bond stress at any point along the cable bolt surface is given by:

$$\tau = -\frac{1}{\Sigma_c} \cdot \frac{dq}{dz} \qquad (1)$$

where q is the axial force in the cable (in z-direction Σ_c is the cable perimeter.

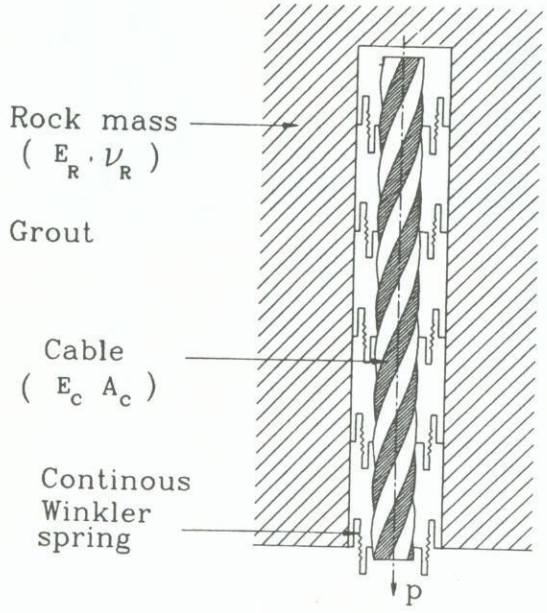

Figure 2: Simulation of grout and interfaces

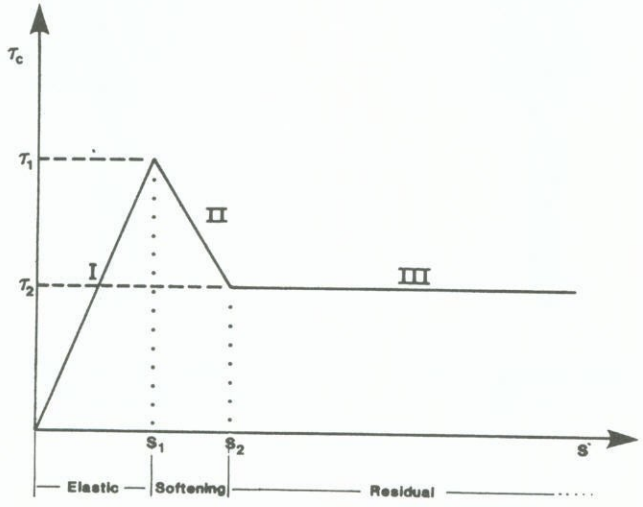

Figure 3: Winkler spring model

PARAMETRIC STUDY

Although there are many different types of cables available for use as cable bolt supports, the 7-wire cable has been found to be the most commonly used by the mining industry. Sometimes, two of such cables are inserted in a single drill hole to achieve a greater support strength. In this study, a single 7-wire cable has been adopted. Unless otherwise specified, the following data has been employed:

wire diameter	=	5.05 mm
cable diameter	=	15.2 mm
cable perimeter	=	63.34 mm
cross section area	=	138.7 mm^2
modulus of elasticity	=	194 GPa
Poisson's ratio	=	0.3

In the following, a variation-of-parameter study is presented to demonstrate the effect of changes in the cable anchorage length, its perimeter, its cross-sectional area and the slip occurring at the unloaded end. To better understand the response of the analytical model, only one parameter is varied at a time while keeping all others constant. Figure 4 presents the shear bond stress distribution along the cable when the anchorage length is varied from 100 mm to 1100 mm. As can be seen from the figure, the shear bond stress is virtually uniform for short lengths up to 200 mm. When the length is 1100 mm, the shear bond stress distribution exhibits both the linear elastic range and softening (post-peak) range of the Winkler model. The stress towards the loaded end is in the softening range. Varying the perimeter of the cable's cross-section appears to have a substantial effect on its load carrying capacity; see Figure 5. For example, when the perimeter is varied from 36 mm to 76 mm, the strength of the cable rises from 180 kN to 338 kN, when the anchorage length is 1500 mm.

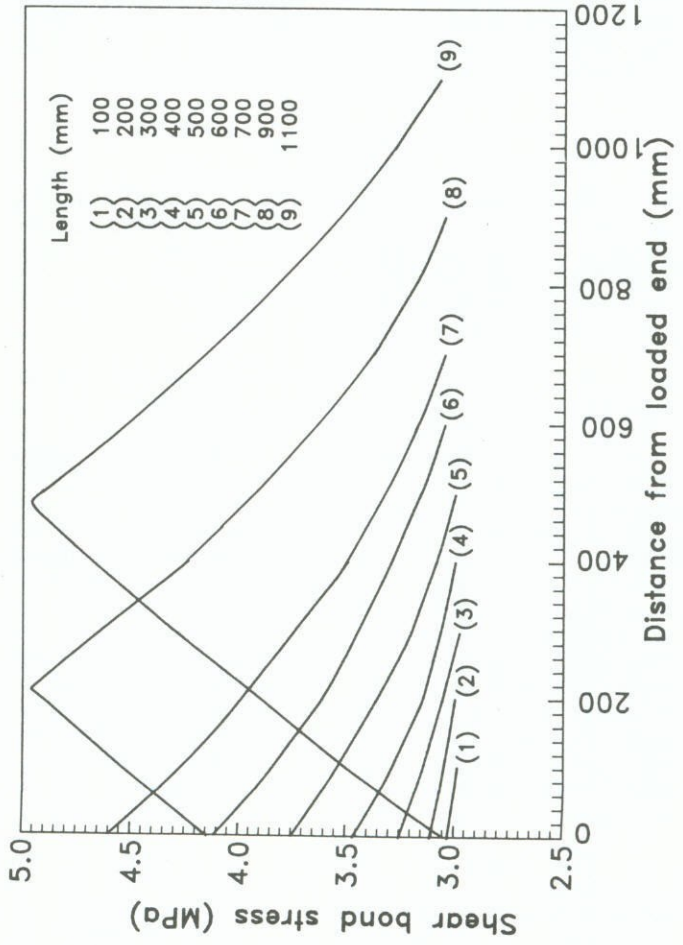

Figure 4: Effect of variation of anchorage length

Using the same length of 1500 mm, the influence of cross- sectional area of the cable is investigated. The results are shown in Figure 6. They indicate little change in the load carrying capacity when the area is changed by as much as 100% (compare curves (1) and (4) on Figure 6).

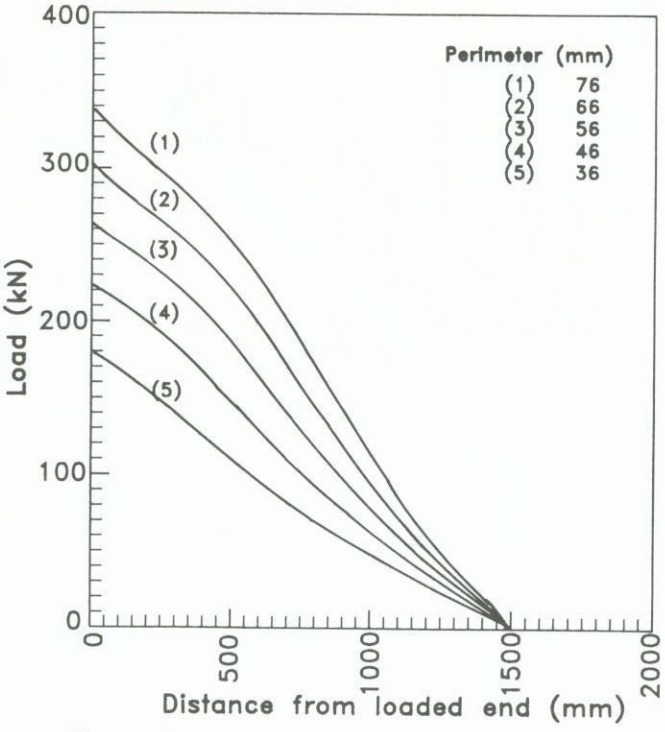

Figure 5: Effect of change of perimeter

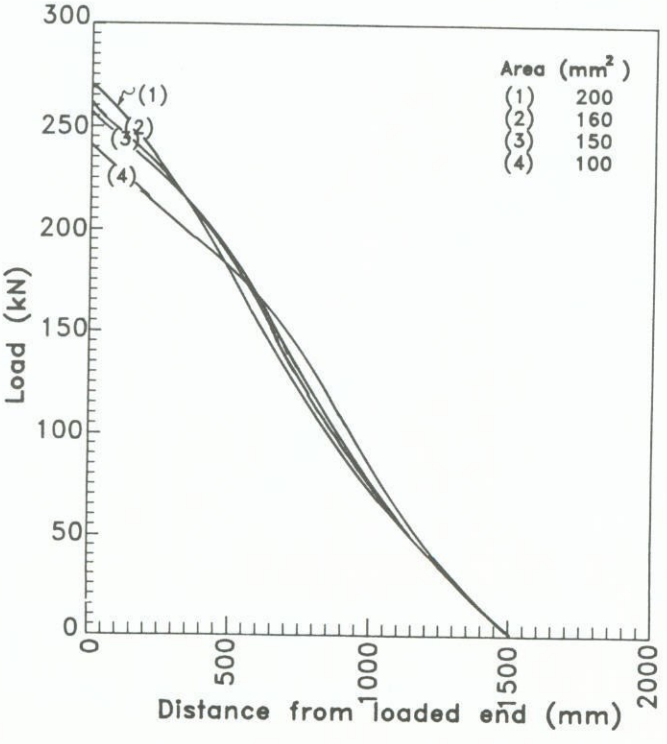

Figure 6: Effect of change of cross-sectional area

In the previous runs, a value for the slip at the unloaded end of cable was assumed and kept constant to reflect the presence of a small shear stress component at the end. When this is increased, as is the case in Figure 6, the load carrying capacity of the cable is improved significantly. This is evident from consideration of curves (1) to (5) on Figure 6. Also, when large slips are involved, e.g. curve (5), it implies that a large portion of the cable will be under the residual shear strength and the post-peak or softening stress; see curve (5) on Figure 7. On the contrary, small slips (e.g. curves (1) and (2)) imply a shear stress distribution below the peak shear strength of the grout model.

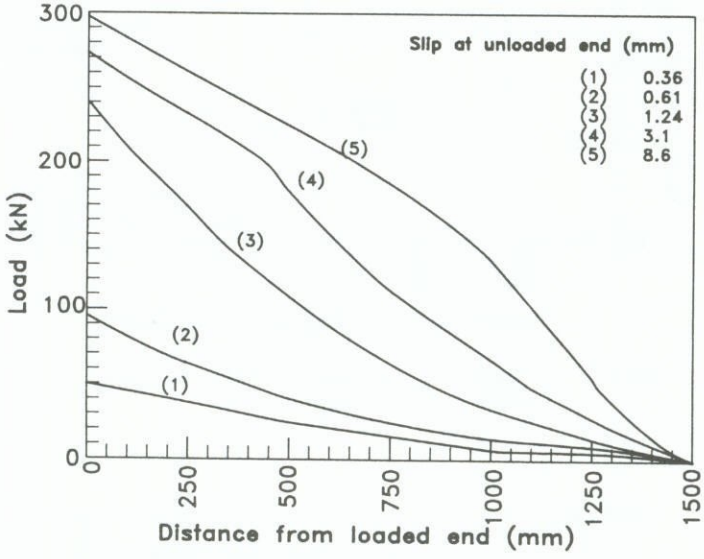

Figure 7: Axial load distribution for different end slips

WINKLER MODEL

As mentioned earlier, the Winkler spring model representing the grout is characterized by the trilinear curve shown in Figure 3. The model is defined by three basic parameters. These are: the peak bond stress, the residual strength and the slip at which the peak shear stress occurs. The effects of variation of the three parameters as shown in Figures 9, 10, and 11 respectively. In all, the anchorage length is kept constant at 1500 mm. Also, the perimeter, the cross-sectional area and the slip occurring at the end previously investigated are held constant. It is seen from Figure 9 that the model is perhaps most sensitive to the variation in residual strength. Higher residual strength has direct benefits on the strength characteristics of the cable bolt. The sensitivity of the model to the peak bond stress places second. A reduction of 20% in peak bond stress results in about 10% reduction in strength (Figure 9). The variation of slip at peak bond stress appears to have very little effect on the load carrying characteristics of the cable, see Figure 11.

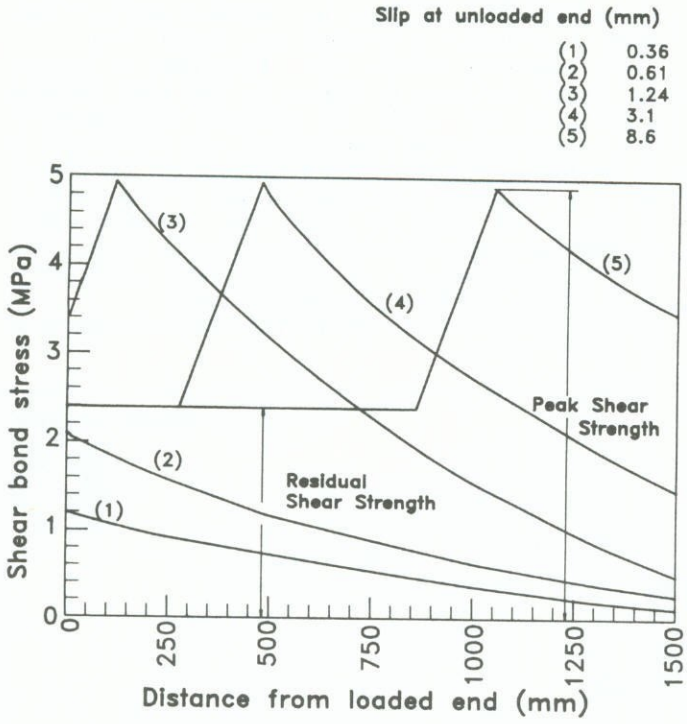

Figure 8: Shear bond stress distribution for different end slips

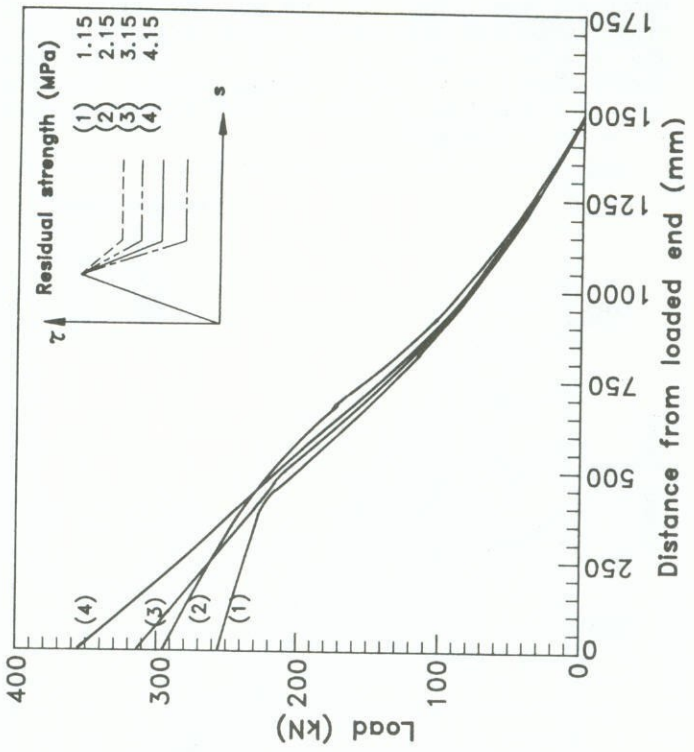

Figure 10: Variation of residual shear strength of Winkler model of Winkler model

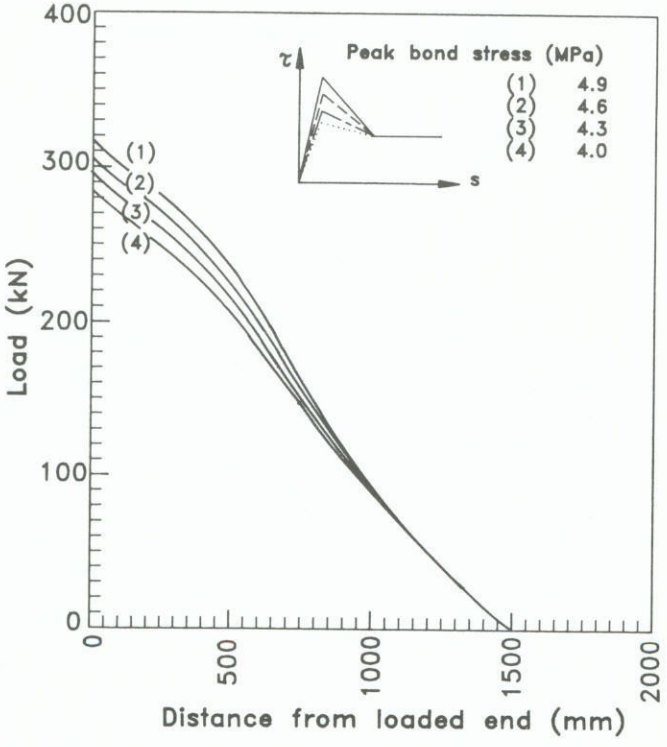

Figure 9: Variation of peak bond stress of Winkler model

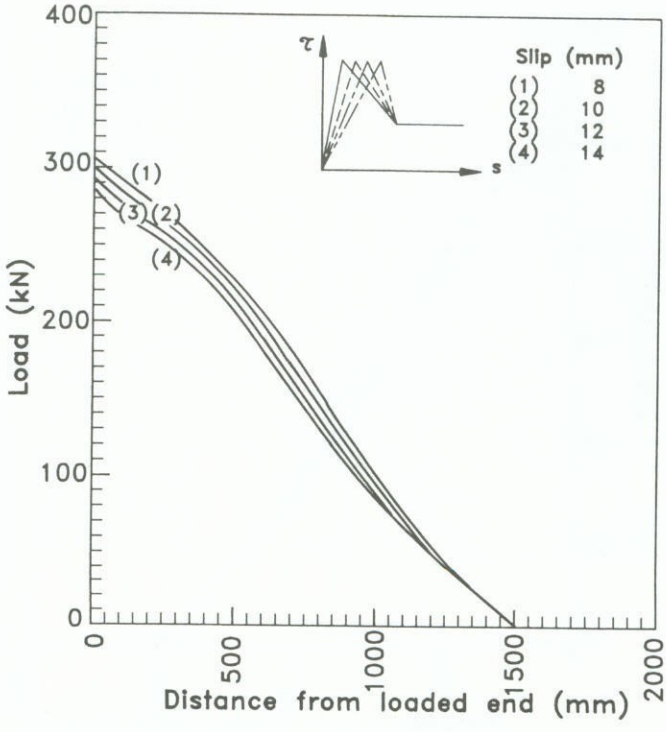

Figure 11: Variation of slip at peak bond stress of Winkler model

CONCLUSIONS

An analytical model based on the variational method has been previously developed to help estimate the distribution of shear bond stress and axial load along the embedded length of fully grouted, untensioned cable bolts. The model takes into account of the shear slip behaviour of the cable with respect to the borehole wall and the mechanical properties of both the cable and the rock mass. The load carrying capacity of the cable can be derived for a particular amount of slip at the loaded face of cable bolt. The prediction of the load carrying capacity by the analytical model has been compared with experimental results. In general, the approach shows good correlation with the laboratory test results.

A sensitivity analysis has been carried out to demonstrate the relative effects of the input parameters on the model. In particular, the perimeter of the cable appears to have a significant effect on its ultimate capacity. The peak shear strength of the Winkler spring characteristic model also influences the load transmitted to the bolt by shearing action. The distribution of the shear bond stress depends on the amount of slip taking place at the unloaded end of the cable; it takes an exponential form when such slip is small enough to be in the linear elastic range of the Winkler spring.

ACKNOWLEDGEMENT

This work has been funded through a research grant from the Natural Science and Engineering Research Council of Canada (NSERC). The authors are grateful to NSERC for their support.

REFERENCES

1. Hawkes, J.M. and Evans, R.H., "Bond stresses in reinforced concrete columns and beams", The Journal of the Institution of Structural Engineers, Vol. XXIX, No. X, pp. 323-327, December (1951).
2. Philips, S.H.E., "Factors affecting the design of anchorages in rock", Cementation Research Ltd., Report No. R48-70, December (1970).
3. Gato, Y., "Cracks formed in concrete around deformed tension bars," ACI Journal, Vol. 68, No. 4, pp. 244-251, April (1971).
4. Farmer, I.W., "Stress distribution along a resin grouted rock anchor", International Journal of Rock Mechanics and Mining Sciences, Vol. 12, pp. 347-351 (1975).
5. Dunham, R.K., "Anchorage tests on strain gauged resin bonded bolts", Tunnel and Tunnelling, pp. 73-76, September (1976).
6. Ballivy, G. and Lahoud, A., "Integral method for the design of grouted rock anchors", International Symposium Rock Mechanics, pp. 761-768, Montreal, September (1987).
7. Coates, D.F. and Yu, Y.S., "Three dimensional stress distribution around a cylindrical hole and anchor", Proceedings of the 2nd International Conference on Rock Mechanics, Belgrade, pp. 175-182, (1970).
8. Hollingshed, G.W., "Stress distribution in rock anchors", Canadian Geotechnical Journal, Vol. 8, No. 4, pp. 588-592, November (1971).
9. Yap, L.P. and Rodger, "A study of the behaviour of vertical rock anchors using the finite element method", International Journal of Rock Mechanics and Mining Sciences, Vol. 22, No. 2, pp. 47-61, (1984).
10. Ballivy, G. and Aticin, P.C., "Le role du scellement dans les ancrages actifs injectes dans le rocker", Canadian Geotechnical Journal, Vol. 26, No. 4, (1986).
11. Cassidy, K., "The implementation of a cable bolting program at the Con Mine", C.I.M. Special Volume 22, Can. Inst. Min. Met., pp. 67-71 (1980).
12. Ballivy, G. and Dupuis, M., "Laboratory and field evaluation of the bonding strength of grouted rock anchors", Underground Rock Engineering, pp. 97-102 (1980).
13. Mathews, K.E., Hoek, E. Wylie, D.C. and Stewart, S.B.V., "Prediction of stable excavation spans for mining at depth below 1000 m in hard rock", CANMET report no. 802-1571 (1981).
14. Mitri, H.S. and Rajaie, H., "Stress analysis of rock mass with cable support - a finite element approach", CANMET Specialty Conference on Stresses in Underground Structures, Ottawa, Ontario, pp. 110-119, October 2-3, (1990).
15. Littlejohn, G.S. and Bruce, D.A., "Rock anchors-design and quality control", 16th U.S. Rock Mechanics Symposium, ASCE, pp. 77-88 (1977).
16. Rajaie, H. and Mitri, H.S., "Shear stress distribution along grouted cable bolt supports - a variational approach. Submitted for publication to Computers and Geotechnics (1990).
17. Tepfer, R., "Cracking of concrete cover along anchored deformed reinforcing bars", Magazine of Concrete Research, Vol. 31, No. 106, pp. 3-11, March (1979).

AN UNDERGROUND TRIAL OF CABLE SLINGS FOR REMEDIAL SUPPORT OF LONGWALL GATEROADS

William D. Gallant, *Senior Technologist*
Pierre Choquet, *President*
Jim MacLachlan, *Technical Assistant*
Steve Forgeron, *Chief Geologist*

Cape Breton Coal Research Laboratory, CANMET,
Sydney, Nova Scotia, CANADA
Supportek International, Sydney, Nova Scotia, CANADA
Cape Breton Development Corporation, Quebec City, Quebec, CANADA

ABSTRACT

This paper describes a joint cooperative project between the CANMET Cape Breton Coal Research Laboratory and the Cape Breton Development Corporation to conduct a trial of split set cable slings for remedial support in longwall gateroads. Slings were installed in two test sections of the 2 West panel, Phalen Mine which exhibited deformation and the potential for excessive deterioration when subjected to the front abutment of the wallface.

Roadway support behaviour was monitored at the trial sites, including lengths of roadway with the standard support of steel sets without remedial support. Observations were made on convergence, loading of the steel supports, loading of the slings, and wallface performance.

Comparisons are made of the results obtained from the areas with remedial support to that without, which demonstrates that the slings provided effective remedial support limiting further deterioration of the roof. Improved face end conditions have contributed to increases in safety and productivity of the longwall panel.

INTRODUCTION

The key to highly productive longwall mining is to maximize face utilization. Many factors can cause impediments to production. Ideally these factors can be identified and measures taken to alleviate them.

Phalen Colliery discovered one such impediment to production was excessive deformation of the gate ends which adversely affected the rate of advance. Upon investigation, it was discovered that the areas of deformation were closely associated with a specific geology. It was also discovered that this condition would prevail on further panels. To address the problem which existed in a significant length of pre-driven roadway, a remedial support was identified. Split set cable slings were seen as a potential remedy to this existing problem. The following describes a trial conducted to assess their performance for this purpose.

BACKGROUND

Geology

The Sydney Coalfield is part of a large carboniferous basin beneath the Atlantic Ocean between the province of Newfoundland and Cape Breton Island, Figure 1. Land based reserves account for only 4% of the total. It is Pennsylvanian in age and contains eleven major seams, although extensive workings have only occurred in the Harbour and Phalen Seams. The predominant rank is high volatile 'A' bituminous.

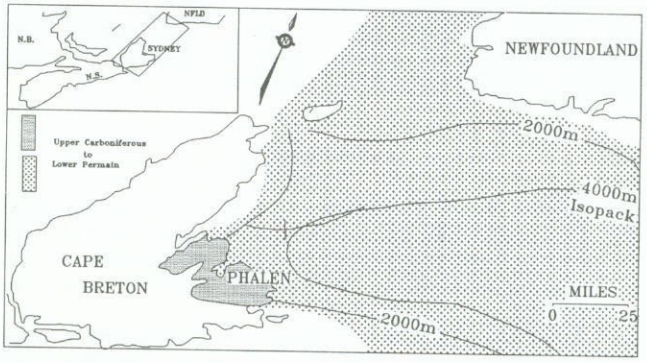

Figure 1 - Plan of Sydney Coalfield (after King and MacLean 1976).

Generally, the seams outcrop on shore and dip northward under the sea at 4° to 10° with local variations from 2° to 40°. Major faulting has occurred only on the margins of the basin, but the remainder is relatively undisturbed by tectonic activity. Extensive sandstone channels exist which occasionally have eroded the seams.

Phalen Colliery, located in New Waterford, is the newest of Cape Breton Development Corporation's three active mines and is utilizing panel and pillar, single entry retreating longwalls, Figure 2. The seam being mined is the Phalen. The workings are overlain by the Lingan Mine Harbour Seam workings with an interburden of 130 m (1). Cover increases as mining advances northward at a slope of 10° approximately.

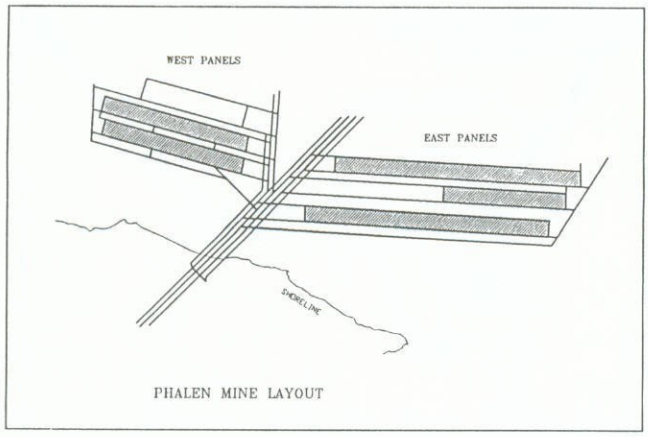

Figure 2 - Plan of Phalen workings (schematic).

Structurally the mine is divided into two distinct zones with the line of demarcation running along the colliery deeps. To the east, the seam thickness is relatively consistent varying from 2.0 to 2.9 m. The immediate roof is composed of splint, shale and mudstone. In localized areas, river channels have cut deeply into this argillaceous sediment cover. In such areas sandstone can be found close to or on top of the seam. Generally, the geological conditions of the east side are consistent and have supported productive mining.

By contrast the western zone is characterized by a westward thickening stone split. Seam thickness is erratic ranging from 1.4 to 2.1 m. Roof and floor geology is also erratic with rapid vertical and horizontal changes in faces attributed to depostion by an unstable fluvial environment. The complex geological environment of the west side creates greater potential for instabilities.

1 West Panel Experience

Phalen 1 West panel began production in May 1987. It was 150 m wide by 1400 m long single entry retreat panel. The gateroads were 4.9 m wide supported by RSJ section steel supports. Shortly after startup instability problems were encountered on the gate ends. Deformation of the steel supports developed ahead of face, which caused problems in advancing the face equipment when closure became severe. Several sections of gateroad presented similar conditions and caused similar problems at the face.

Reconnaissance of 1 West and 2 West identified several discontinuous zones exhibiting deformation. These areas were identified by roof beam deflection, overbreak and by cracking of the roof at the corners. Remedial support in the form of timber posts were placed and at the face hydraulic props were utilized. Although some improvement was realized, production was still hampered by the deformation of the steel supports. An investigation was initiated to identify the causes of instabilities and develop procedures to alleviate them. Examinations were conducted into: the quality of support installation, interaction of the overlying workings and local lithology. No strong correlation was established with the instabilities. Exploratory core drilling was conducted to identify the overlying roof of the west side.

Results of the drilling program are summarized in cross-section and plan view in Figure 3. From east to west, a sandstone channel is thickening; to the extreme west it is on top of the coal. In the central area, it is pinching out and is underlain by a heterogeneous mixture of shale, thin coal beds, mudstone and siltstone. The eastern section is characterised by the Rider Seam in the immediate roof. Trending northward, these conditions will exist on future west side panels.

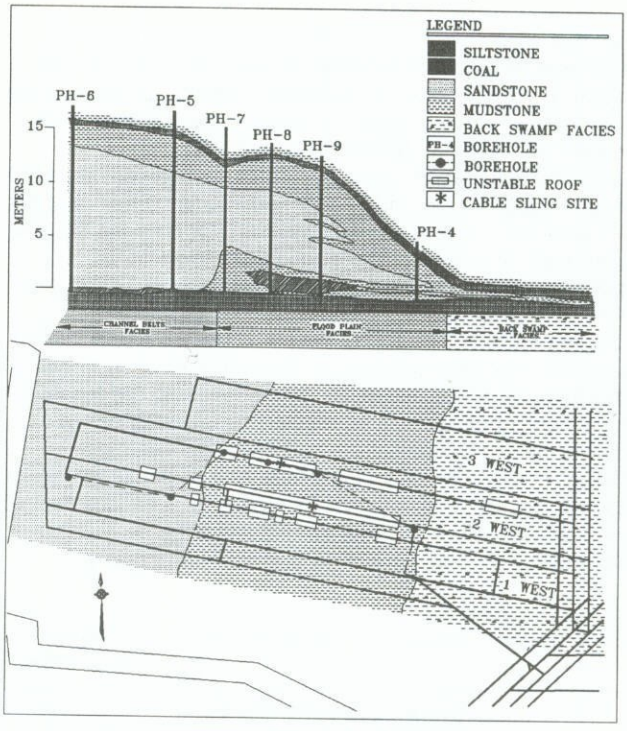

Figure 3 - Geological plan and section of Phalen west side including identified areas of instability.

Overlaying the mapped areas of deformation with the geology plans clearly illustrated a strong correlation. The less competent roof in the central area was susceptible to delamination causing increased loading of the steel supports, when aggravated by the front abutment loading increased causing severe deformation and inhibiting production.

Initial Experiment with Remedial Support

During the working of 1 West, several experiments were conducted with remedial support for the areas of instabilities. One experiment consisted of the installation of four split set cable slings (2). Colliery staff observed the behavior of slings and were very encouraged by their performance in controlling further deformation. Because these preliminary results were encouraging, a larger scale trial was developed to assess their suitability for remedial support of the colliery gateroads.

TRIAL

Objective

The objective of the trial was to evaluate the performance of split set cable slings and assess their suitability as remedial support for the instabilities described. Traditionally, remedial support consisted of wooden props, wooden chocks or hydraulic props. These supports provided some resistive force to the roof but they restricted free space and often were removed to provide clearance. Slings were seen as having the

potential to provide an active force to the roof without restricting free space.

Concept

The trial concept was to perform a systematic measured comparison of gateroad behavior of areas with the remedial slings to areas with only the standard support. Location of the trial site would be in a length of roadway identified as being unstable with uniform conditions throughout.

Upon implementation, other factors came into consideration, standard support type and spatial restrictions. Steel supports of 29 kg/m on 1 m centers were standard for both the top and bottom level of 2 West. The support profiles differed, trapezoidal on the top level or rectangular on the bottom level. It was decided to locate a trial site in both levels.

Locating the trial site on the bottom level was free of spatial restrictions, the site was choosen based purely upon mapping of the unstable areas, Figure 3. Site location on the top level was influenced by the spatial restrictions imposed by the conveyor belt. Fortunately, an area was identified with sufficient room to the low side of the belt to permit installation of the slings. This site was also located in an area identified as being unstable. Each site was divided into three sections of 20 m length. The sites are described in Table 1 below:

Section	Length	Support #	Support Type	Potential Deformation
		Site #1, 2 West Bottom Level		
1	20 m	630-650	Rectangular	Slight
2	20 m	651-671	Rectangular + Slings	Moderate
3	20 m	672-692	Rectangular	Moderate
		Site #2, 2 West Top Level		
1	22 m	781-803	Trapezoidal	Moderate/ Severe
2	20 m	804-824	Trapezoidal + Slings	Moderate
3	19 m	825-844	Trapezoidal	Severe

Table 1 - Trial site descriptions.

Design

Split set cable slings are proprietary equipment commercially available. Those used in the trial consisted of 0.013 m (1/2") diameter high strength (185 kN) cable, type SS39 split sets 1.5 m (5'), cable grips and cement cartridges, Figure 4. The cable is run across the roof, anchored in inclined holes drilled over each rib side. Gypsum based cement cartridges are placed at the end of the hole to provide permanent anchorage for the cable. Cable grips provide a reaction surface for the end of split set. Impact energy from a jackleg drill is used to drive the split set, cable grip and cable up into the hole. As the second end of the cable is installed, tension is developed in the cable as the split set is driven in. The split sets provide immediate anchorage, stronger more permanent anchorage is provided by the cement after it is set.

Remedial support for the trial consisted of 20 slings in the center section (Section 2) of each site.

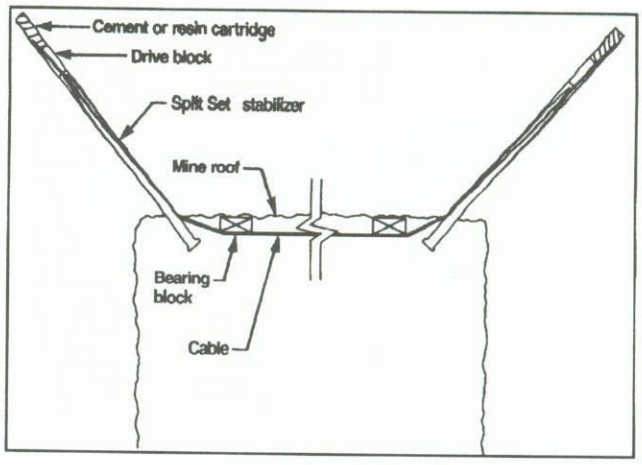

Figure 4 - Schematic representation of split set cable sling [after Ingersol-Rand (CAN) 1989].

Implementation

Installation was performed by a two-man crew with assistance from CBCRL staff. Equipment consisted of a jackleg drill and tapered steel. The only piece of equipment not readily available at the mine was the driver tool for the split sets.

Many impediments to installation existed in the roadway: conveyor belt, monorail, struts, corrugated sheets, etc. Time required for installation varied depending on site conditions. Observations made indicate the average installation time was 53 minutes. The shortest time was 23 minutes, based upon a composite of individual tasks (drill, cement placement, measure and cut cable, insertion). The times quoted, however, refer to the times required to install one sling but excludes any time occupied with such tasks as cutting corrugated sheets and moving struts.

Monitoring

Monitoring of the trial consisted of observations of support behavior, roadway deformation and wall performance, i.e. records of wall retreat rate, tonnage and delays associated with the movement of the top end. Geotechnical instrumentation was used to record cable tension (3), the loading imposed on the steel supports and vertical closure of the gates, Figures 5 and 6.

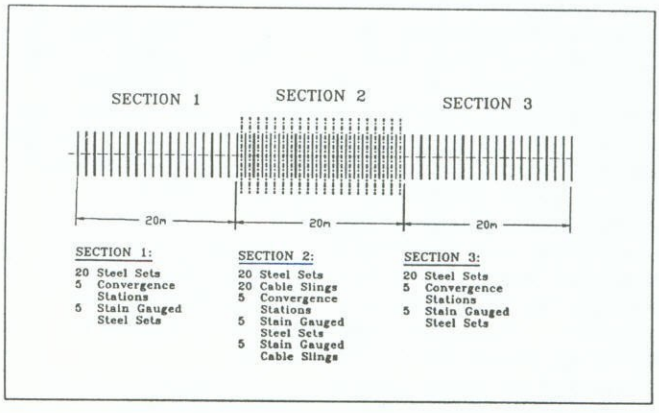

Figure 5 - Representative plan view of trial sites showing sling locations and monitoring stations.

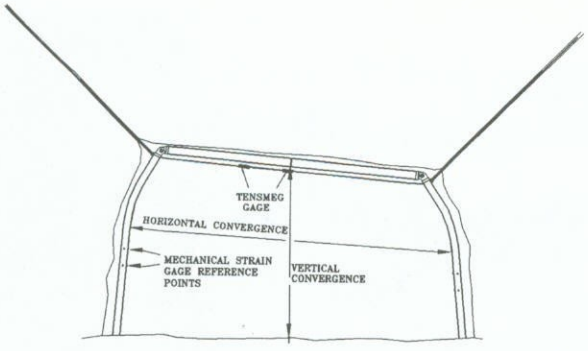

Figure 6 - Representative cross-section through trial site showing slings and instrumentation.

The use of extensometers in the roof was planned but due to the broken ground, drilling was impossible. Photographs were taken regularly to provide a visual record of conditions. Table 2 describes the instrumentation used.

Parameter	Instrumentation	No. of Units/Site
Cable Tension	Tensmeg Gauge	5
Steel Support Loading	Mechanical Strain Gauge	15
Closure Vertical	Convergence Station	15

Table 2 - Geotechnical instrumentation of sling trial.

A contract was let to Supportek International to supply and demonstrate installation of the tensmeg gauges. Readings were taken at intervals beginning monthly and finishing up on a slice-by-slice basis as the face retreated through the sites. Information was referenced to date, time and distance from the wallface. Access was of course not available behind the face where caving destroyed the installation.

Analysis was conducted by CBCRL/CBDC and Supportek. Data has been handled with spreadsheet and graphing packages to produce the following curves:

1) vertical closure vs distance to face
2) cable tension vs distance to face
3) support loading vs distance to face
4) face retreat rate across each section of each site
5) delays across each section of each site

Photographic records have been compiled referencing position of the face at time photograph was taken.

RESULTS

Convergence

Roof to floor convergence patterns observed in sections with and without slings are similar. Onset of convergence is first noticed 50 to 100 m ahead of the wallface reaching a maximum of 100 to 200 mm. Measurement of convergence was restricted by the stageloader in Site #2. Level supports destroyed the measuring stations in both sites. It was at the level supports where the greatest loss of height occurred but not measured by the stations.

Side to side convergence was monitored in Site #1 only, the belt and trailing equipment in Site #2 restricted this measurement. Patterns are similar for sections with and without slings. In all cases a slight convergence developed not exceeding 50 mm.

Loading of Steel Sets

Loading of the steel sets was described in terms of maximum stress, bending moment and axial load. Observations begin at a time well after installation of the set and represent only a change in loading condition rather than an absolute measure. Data collection has been hampered by instrument malfunctions and data quality suffered from operator sensitivity of the mechanical strain gauge.

Patterns of loading are very scattered and incomplete. Axial load changes for example, ranged from +100 to -100 kN (-compressive), although no clear patterns are seen in any section with or without slings. This is most likely caused by the various states of loading existing prior to monitoring. Maximum stress and bending moments produce similar scattered trends.

Cable Sling Tension

Loading of the cable slings is clearly defined by the readings of the tensmeg gauges, Figures 7a and 7b. In both sites, the slings were tensioned to 23 to 38 kN upon installation. Relaxation of approximately 5 to 10 kN is observed after installation, which may be instrument drift. All cable loads were stable until influence by the wallface except one located in Site #2 on the top level. It shows a significant drop. This may indicate total unloading at this time, but may have been damaged when some of the other cabling was severed and subsequently repaired during the period when the unloading is observed.

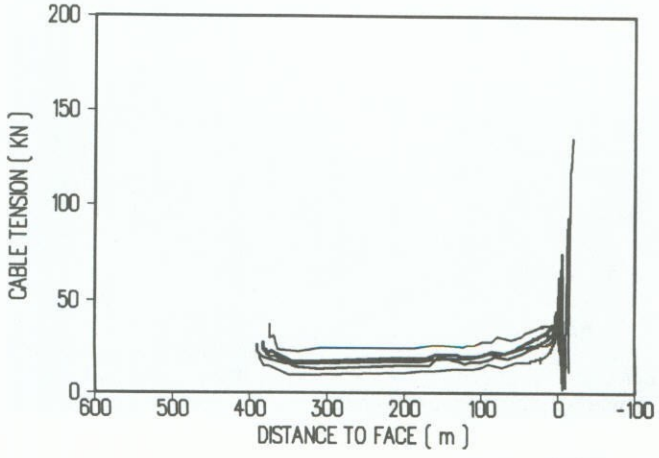

Figure 7a - 2 West bottom level (Site #1) cable tension vs distance to face.

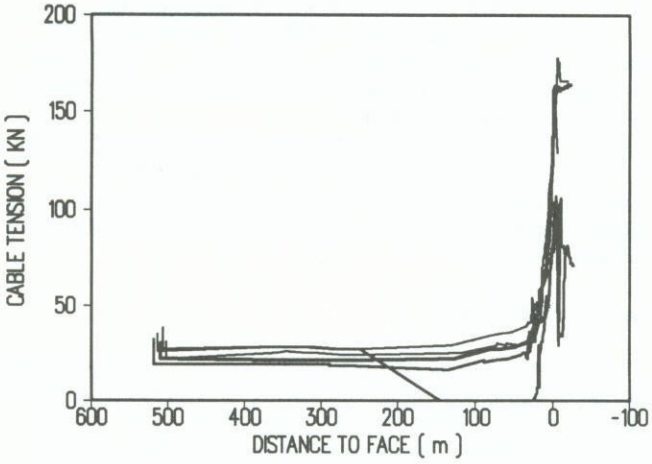

Figure 7b - 2 West top level (Site #2) cable tension vs distance to face.

Loading begins as a gentle, irregular increasing trend at 160 m and 80 to 100 m ahead of the face for Site #1 and #2 respectively. Rates of loading in both sites begin to increase dramatically at 20 m ahead of the face. Loading peaks at the gob edge reaching a maximum of 40 to 180 kN in Site #1 and 100 to 180 kN in Site #2. Load quickly dropped off past this point. Cable strength is estimated at 185 kN.

Photographic Record

Photographs clearly illustrate the conditions experienced at the gate ends. In Section 3 of Site #1 on the bottom level [Figure 8(a)], view from the face towards the gate, the roof is seen to be severly deformed. A vertical shear has developed in the high corner of the road and roof strata is seen laying on top of the level support. Section 2 of the same site supported with slings exhibited a markedly different behavior, Figure 8(b). The roof is contained by the slings, the shear was not permitted to propogate. Useable space beneath the level supports is increased.

(a) without slings

(b) with slings

Figure 8 - 2 West bottom level (Site #1) gate end conditions as viewed from wallface.

Similar behavior was observed in Site #2 on the top level, Figure 9(a) and (b). Roof strata is again lying over the level supports after shearing developed on the low side corner [Figure 9(a)] in Section 3. Slings in Section 2 contained the roof material [Figure 9(b)] and prevented development of the vertical shear.

(a) without slings

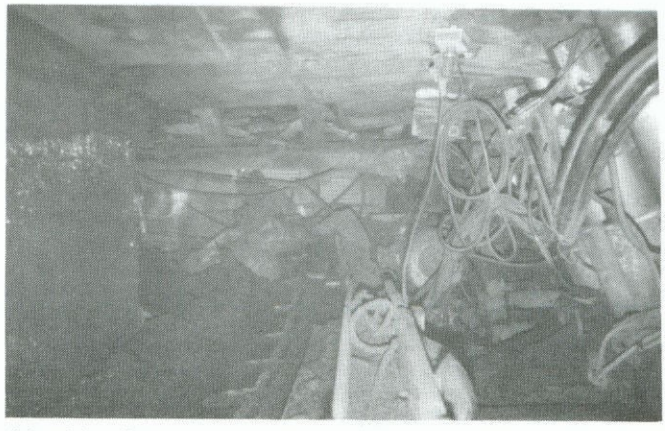

(b) with slings

Figure 9 - 2 West top level (Site #2) gate end conditions as viewed from wall.

Wall Performance

Wall performance was recorded by average retreat (m/shifts) and average face end delays (hrs/shift). This information is presented in Figure 10. The wall performance as expected was most adversely affected by the conditions on the top level which contained the angle discharge and stageloader units.

Face end delays in both sites were greater for the sections without slings, up to seven times as much on the top level, where free space was more crucial for face operation. Production was not seriously affected by the conditions on the bottom level, although it was very tight, the face was able to advance reasonably well.

Advance rates for Site #2 on the top level reflect the conditions experienced on the top end. Production has decreased by approximately 15 to 30% by face end delays in the sections without slings.

The level of safety was increased by the slings as can be seen in Figures 8b and 9b: by containing the hazards of the broken roof, by increasing valuable space and by reducing exposure to open roof.

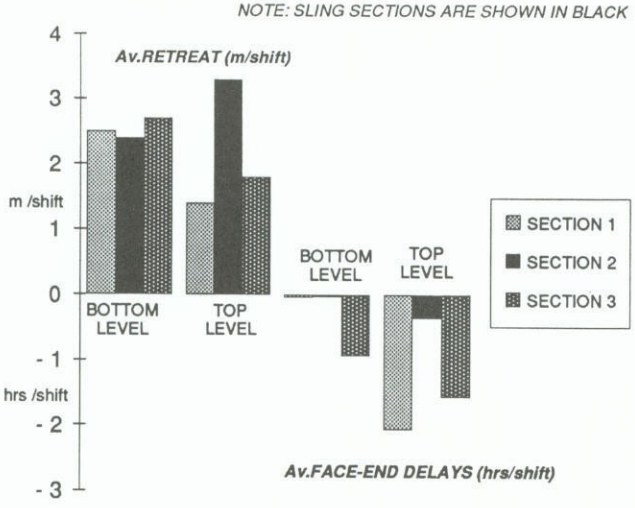

Figure 10 - Trial Sites #1 and #2 average delays and advance per shift.

DISCUSSION

Cable slings have significantly contributed to the support of Phalen 2 West gateroad. Benefits were realized in safety and productivity.

Parameters observed such as convergence and loading of the steel sets do not clearly identify these benefits because measurements were not possible in the area of the level supports where most deformation and closure developed. Use of the mechanical strain gauge to observe loading of the steel sets was inappropriate. It was not sufficiently robust to withstand the underground environment and exhibited operator sensitivity. Loading states of the steel supports varied and were unknown when the points for the mechanical strain gauge were applied. Therefore, it is difficult to draw conclusions with any certainty from this data.

Measurement of cable loading has shown that the slings have provided an active resistive force to the roof and accepted increasing load as the face approached. The front abutment caused this increased loading. First noticeable at 160 m ahead of the face with significant effects occurring within 20 m.

The failure mechanism of the standard steel supports was a progressive delamination of the immediate roof, Figure 11(a) and (b). Broken material rested on the roof beams and moved down hill in some instances permitting additional free space for the unravelling to continue. Front abutment stress changes aggravated this condition causing further instability and additional deformation.

Slings installed in existing areas of instability provided an active resistive force to the roof, Figure 11(c). Delamination and unravelling were controlled resulting in less deformation and increased stability. Front abutment stress changes causes less deformation to the reinforced rock mass and subsequently provided improved conditions conducive to improved safety and productivity.

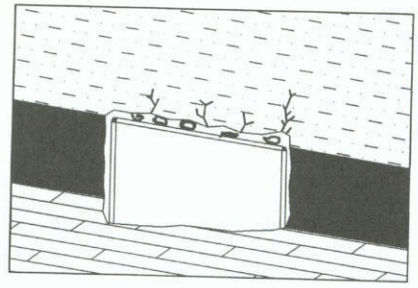

(a) existing instability

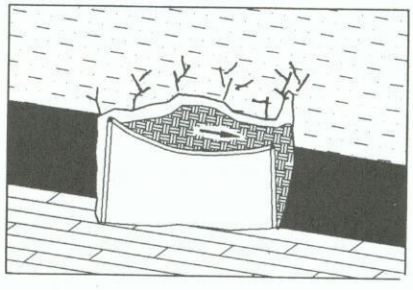

(b) advanced deterioration

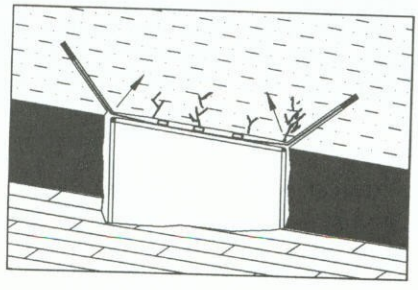

(c) containment of slings

Figure 11 - Failure mechanism and reinforcement provided by sling.

CONCLUSIONS

The trial was successful in demonstrating the use of an alternative form of remedial support in Phalen 2 West panel. Cable slings applied an active resistive force to the deteriorated roof limiting further deformation to the gateroads. Their application has provided benefits in safety and productivity. The main conclusions reached are:

1. Split set cable slings have provided effective remedial support for the gateroads of Phalen 2 West.
2. Productivity and safety have been enhanced by the use of slings.
3. Tensmeg gauges provided an accurate means of monitoring cable tension.
4. Convergence measurements and monitoring of steel set loading did not clearly demonstrate the benefits realized by the slings.

RECOMMENDATIONS

Many lessons were learned during the installation and monitoring of this trial. Refinements were made as the skill level of the crew was developing. To optimize the design of remedial support with cable slings, the following recommendations are made:

1. Further study be conducted to optimize design of cable sling to site specific conditions, i.e. anchorage capacity, spacing, hole inclination, etc.
2. Monitoring be conducted beginning with initial installation of standard support at time of roadway drivage to provide a complete picture of support behavior.
3. Measurement of steel set loading be conducted with a more reliable and accurate technique than presented.

REFERENCES

1. Forrester, D.J., Gallant, W.D. and Forgeron, S. "Cable slings as remedial gateroad support on Phalen 2 West"; CANMET Division Report CRL 90-22(OP); November 1990.
2. Forgeron, S. and MacDougall, P. "Review of the use of cable slings at Phalen"; Cape Breton Development Corporation Interal Report; July 1987.
3. Supportek International "Report on an instrumentation program on split set cable slings used as remedial support in longwall gateroads at Phalen Mine 2 West panel"; DSS Contract Report 23440-9-9017/01-SQ; October 1990.

10th INTERNATIONAL CONFERENCE ON GROUND CONTROL IN MINING

MOBILE ROOF SUPPORT FOR RETREAT MINING

H. Gene Wilson, *Manager*

J. H. Fletcher & Co.
Huntington, West Virginia

ABSTRACT

Mobile Roof Supports (MRS) look similar to a longwall shield on crawler tracks. The MRS units offer a safe, productive method of extracting the 40% to 60% product left normally unrecovered in room and pillar mining.

The units feature radio control, self–contained power units, crawler track drive, and a 600 ton yield.

Cribbing and setting posts in retreat mining has been a necessary burden to production. The MRS reduces this burden. Long blocks of coal can be developed to further reduce move and tram time, thus increasing production.

The MRS units have successful safety records. The workers are removed from the immediate fall area, and we feel back injuries have been reduced by the workers not setting posts. While MRS units have been damaged in falls, the other capital equipment has been unharmed.

The MRS product line has undergone normal product improvement and evolution. Product evolution is seen in our development of machines for particular mine requirements. Through the continuing development of the MRS, Fletcher presents the coal industry with a safe, productive method of retreat mining with potential to develop new mining methods.

INTRODUCTION TO MOBILE ROOF SUPPORTS

Mobile Roof Supports (MRS) look similar to longwall shields, except on crawler tracks. Figure 1 names the basic machine components and illustrates the canopy motion. The fore and aft tilt is controlled by the operator's valving to the roof support cylinders. The side to side tilt is a function of the roof profile. The canopy is a rigid fabrication guided through its stroke by the lemniscate. The lemniscate/caving shield control the canopy within a 1–1/2" total variance from true straight line motion. The roof cylinders are a typical longwall shield design. Each cylinder is load tested to verify the 150 ton yield rating. Each cylinder is fitted with rapid relief valves and rock burst valves. The crawlers use a 16" wide forged pad driven by dual sprockets. A variable displacement hydraulic motor powers the gearing to produce 80 feet per minute tram speed. A grease cylinder and shims are used to adjust the track. Each unit is fitted with a plow or dozer blade to assist maneuverability in caving situations. The system is radio controlled through XP solenoid valves with manual overrides. An MRS system is generally made of four (4) units. The four units are deployed in sets of two (Figure 2). They are then "walked" through their respective mine plan by lowering the canopy on one unit, advancing that unit approximately 10' and resetting the canopy. The procedure is then repeated by the other unit. Both machines are kept in a close pattern.

CURRENT MOBILE ROOF SUPPORTS

J. H. Fletcher & Co. has shipped three MRS systems; one (1) in eastern Kentucky to Martin County Coal, two (2) in West Virginia, one to Omar Mining and one to Elk Run Coal. The dimensional parameters for each location are somewhat different. The first units shipped (11/88) were to MCC. The basic collapsed height is 63" with a 134" extended height. The second units shipped (2/90) were to Omar Mining. These units are basically the same as MCC's except were fitted with a canopy extension to increase their reach to 13'. The third units shipped (5/90) were to Elk Run. The basic collapsed height is 45" with a 96" extended height.

WHY USE MOBILE ROOF SUPPORT

The obvious question is why use mobile roof supports. They are a capital equipment investment. They do require maintenance. They do require training and definitely have a learning curve associated with them. They also are the safest way going to recover the 40% to 60% coal normally left unrecovered in room and pillar mining.

In today's world with insurance rates and health benefits being what they are, the MRS offers additional safety in what may be the most dangerous mine environment. Consider this quote from COAL Magazine, in a July '89 article entitled, "More back–saving, load raising devices you can build cheaply," "68% of mine maintenance injuries involved handling of timbers, posts, caps, and cribbing materials..." The nature of an MRS system reduces material handling, reducing back injuries. The most obvious safety advantage –– the worker is removed from the immediate fall area. The safety aspects of the MRS don't stop with the worker. The system also protects the other capital equipment.

To date, the MRS program boasts a perfect safety record to the worker. The MRS units have been covered in falls and have required repair work, but the other equipment has been virtually unharmed. Several instances where individual MRS units were covered by falls occurred due to the operators taking short cuts while moving the units. Instead of being walked, or two units moved short distances alternately, one was moved all the way out to the outby end of the block, leaving the other unit to be brought out without protection.

Another answer to why use mobile roof supports is productivity. As mentioned earlier, 40% to 60% of the coal is untouched in room and pillar mining. As shown by the mine plan on 50' center (30' x 30' blocks), there is 36% untouched coal (Figure 2). As the block size grows, so does the percentage of untouched material. Let's consider splitting one of these blocks. To split a block, a large number of posts must be set. This number is determined from roof plans varying from mine to mine. Shown is a simple illustration using 40 posts (Figure 3). After supplying, cutting, and setting these posts, the split yields approximately 35% block recovery. In comparison, we have a system using eight posts (Figures 4 thru 7). The cut sequence has evolved from one mine experience and yields 90% block recovery. In this case recovery jumps from 35% to 90% while setting 32 less posts. The increased recovery increases production, however, a greater increase in production is realized by reducing the time required to set the posts.

How to further increase production? Not so long ago the first "super sections" appeared. The primary reason for a super section is to increase production by keeping place change time down and cutting time up at its maximum. Long blocks of coal can be developed to maximize cutting time. Shown in Figure 8 is a 100' x 30' block. The cut sequence could be similar to that shown. The MRS units would be deployed as shown. The continuous miner would then take the first cut at approximately 45°. The miner would reposition to approximately 60° and take the second cut. For each of the remaining cuts, the MRS units would walk towards the miner, keeping a tight pattern. The longer block represents a potentially more productive mining method.

TAILORED ENGINEERING

J. H. Fletcher & Co. tailors each MRS system to each particular application. One of the ways this is done is by offering three radio options. The system can be controlled by one, two or four transmitters (Figure 9, 10, and 11).

Tailored design allows the maximum vertical canopy force by limiting the tilt of the four (4) roof cylinders. "Only the vertical component of the leg force should be used to determine the capacity of the support." The vertical canopy force vs. canopy height is plotted for a proposed new design (Figure 12).

The proposal demonstrates how J. H. Fletcher & Co. designs a machine to a customer's requirements. This particular design allows for future mining height changes. With cylinder modifications and a control link change the unit will reach an additional 21–1/2" (Figure 13).

SUMMARY

The MRS product line has undergone normal product improvement and evolution. Product evolution is seen in our development of machines for particular mine requirements. Through the continuing development of the MRS, Fletcher presents the coal industry with a safe, productive method of retreat mining with potential to develop new mining methods.

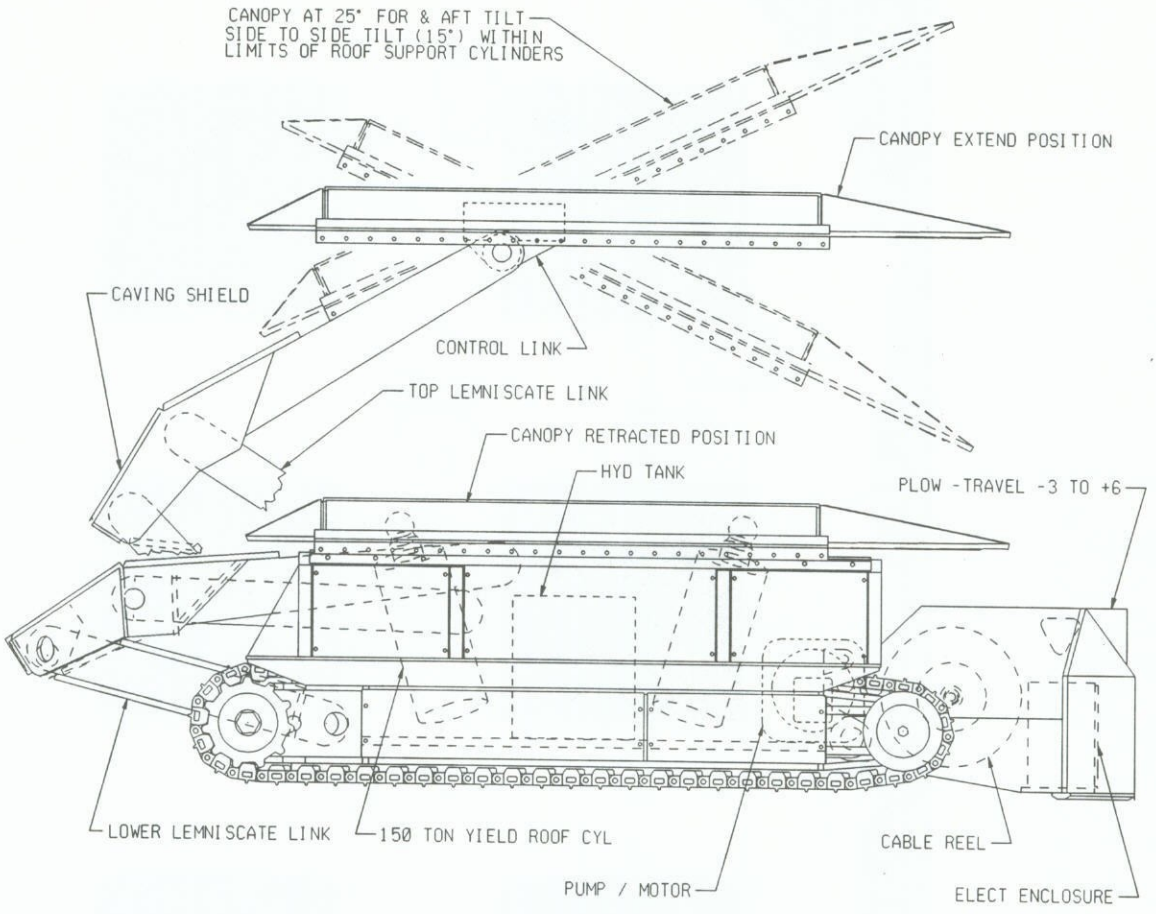

Fig. 1 MRS Components.

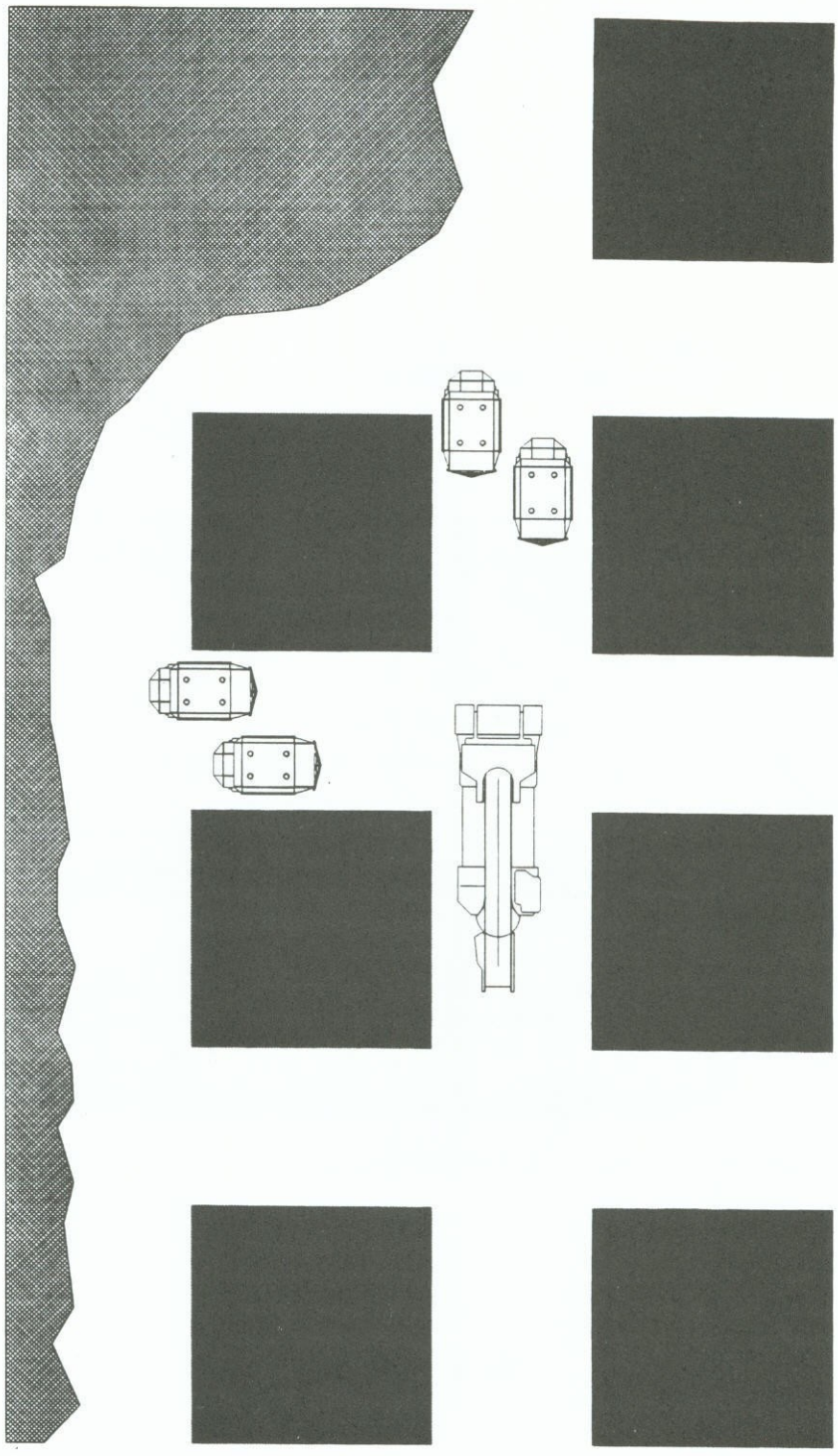

Fig. 2 MRS Deployment.

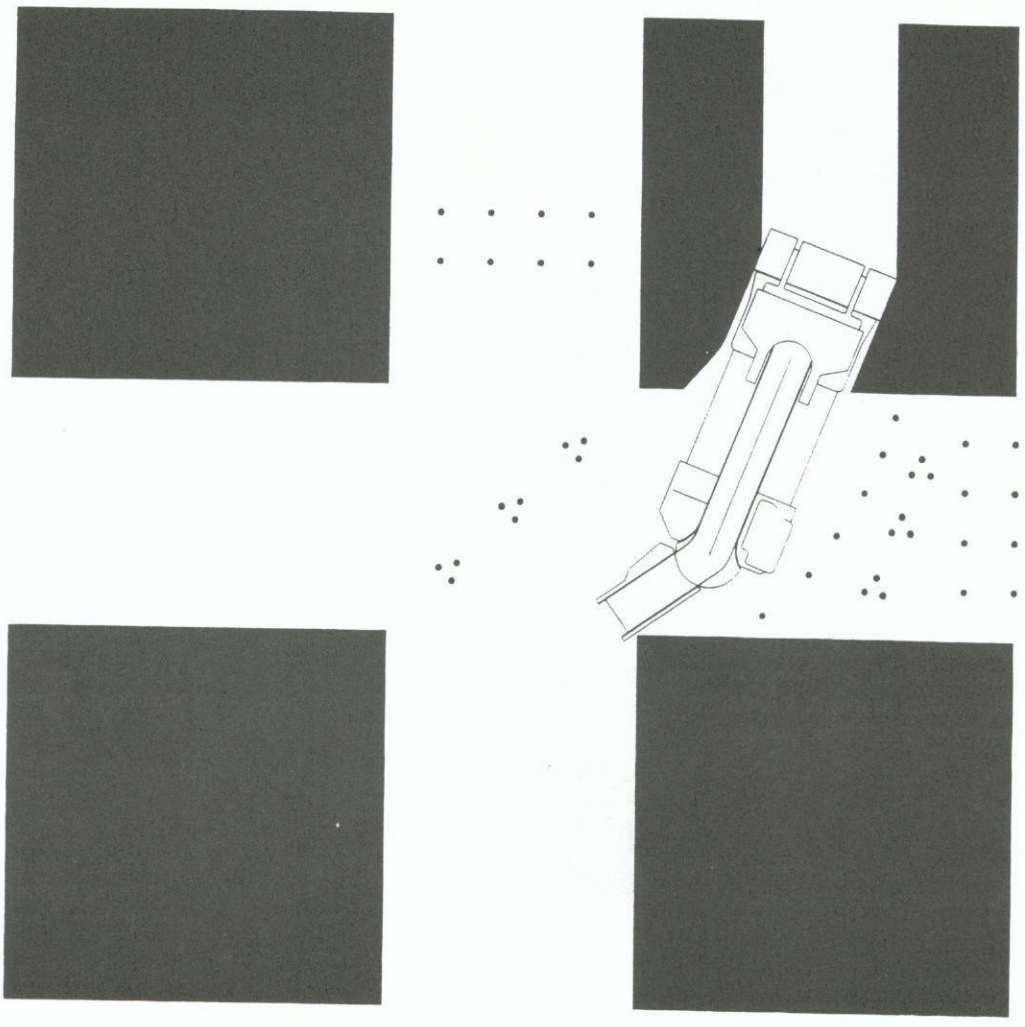

Fig. 3 Split 30' x 30 ' block. Set minimum 40 post.

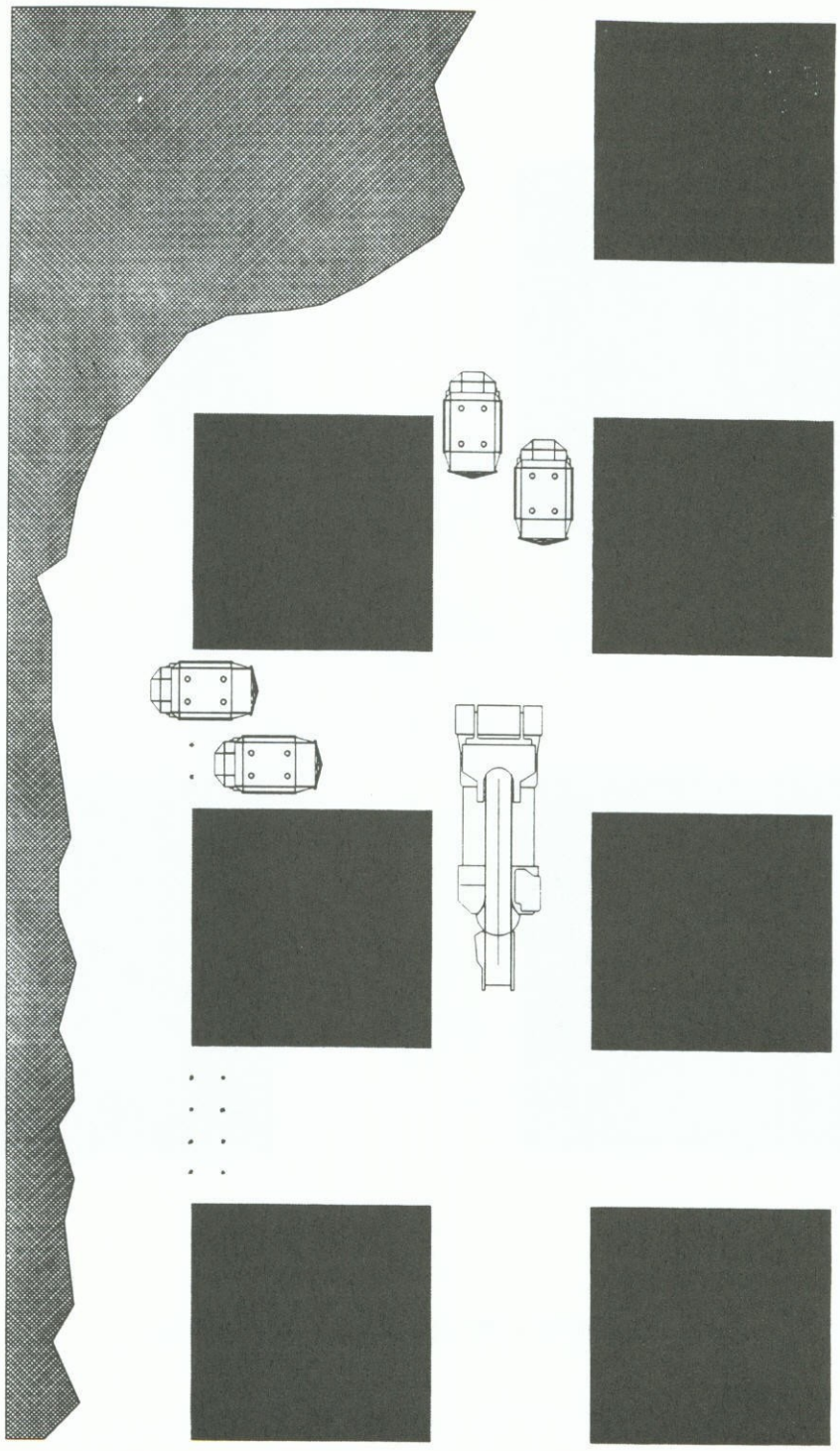

Fig. 4 Pulling 30' x 30' block using 8 posts 6 of 8 are knocked down when MRS is set.

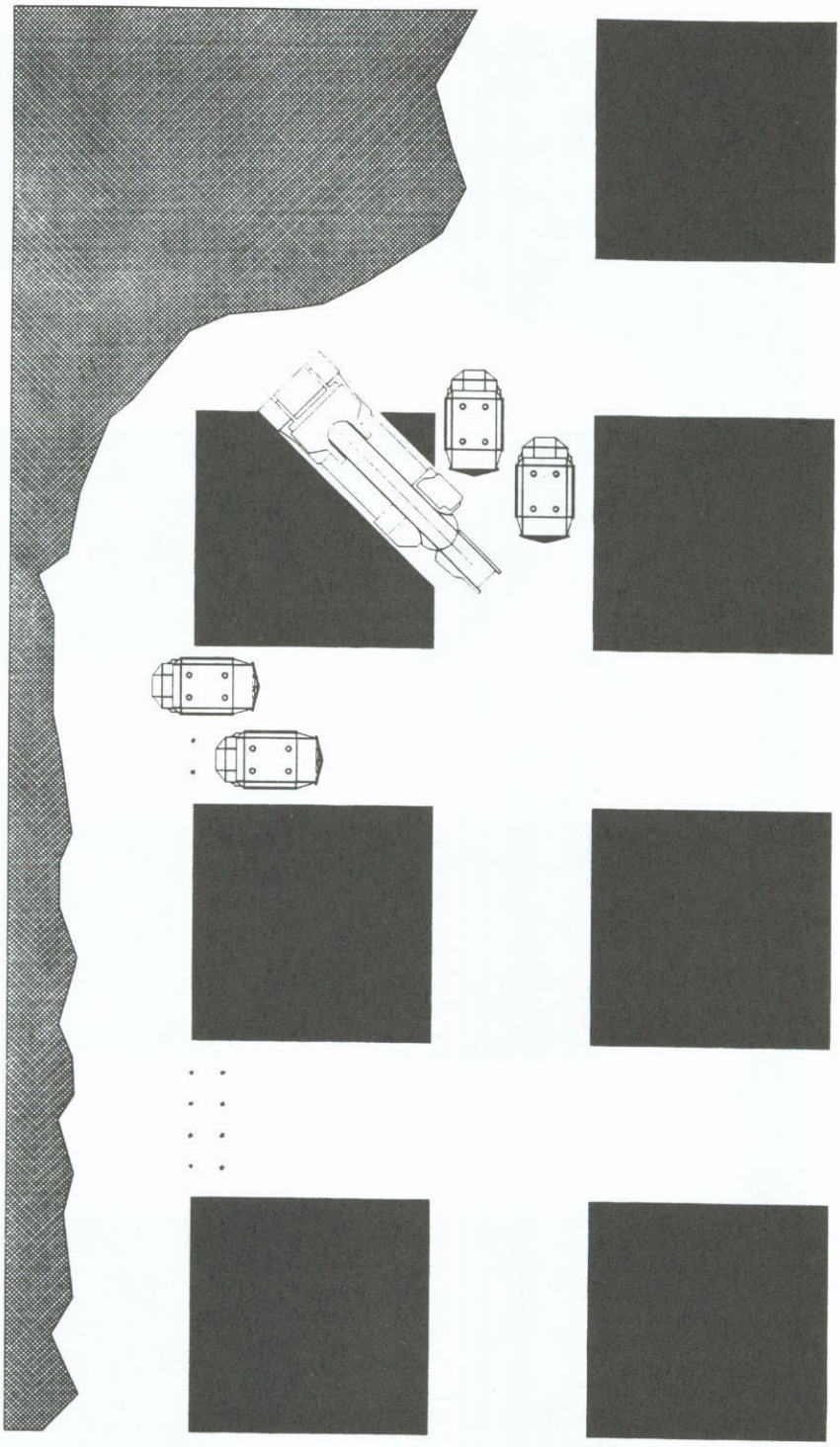

Fig. 5 First lift – miner will pull out and the MRS units will be "walked" towards it.

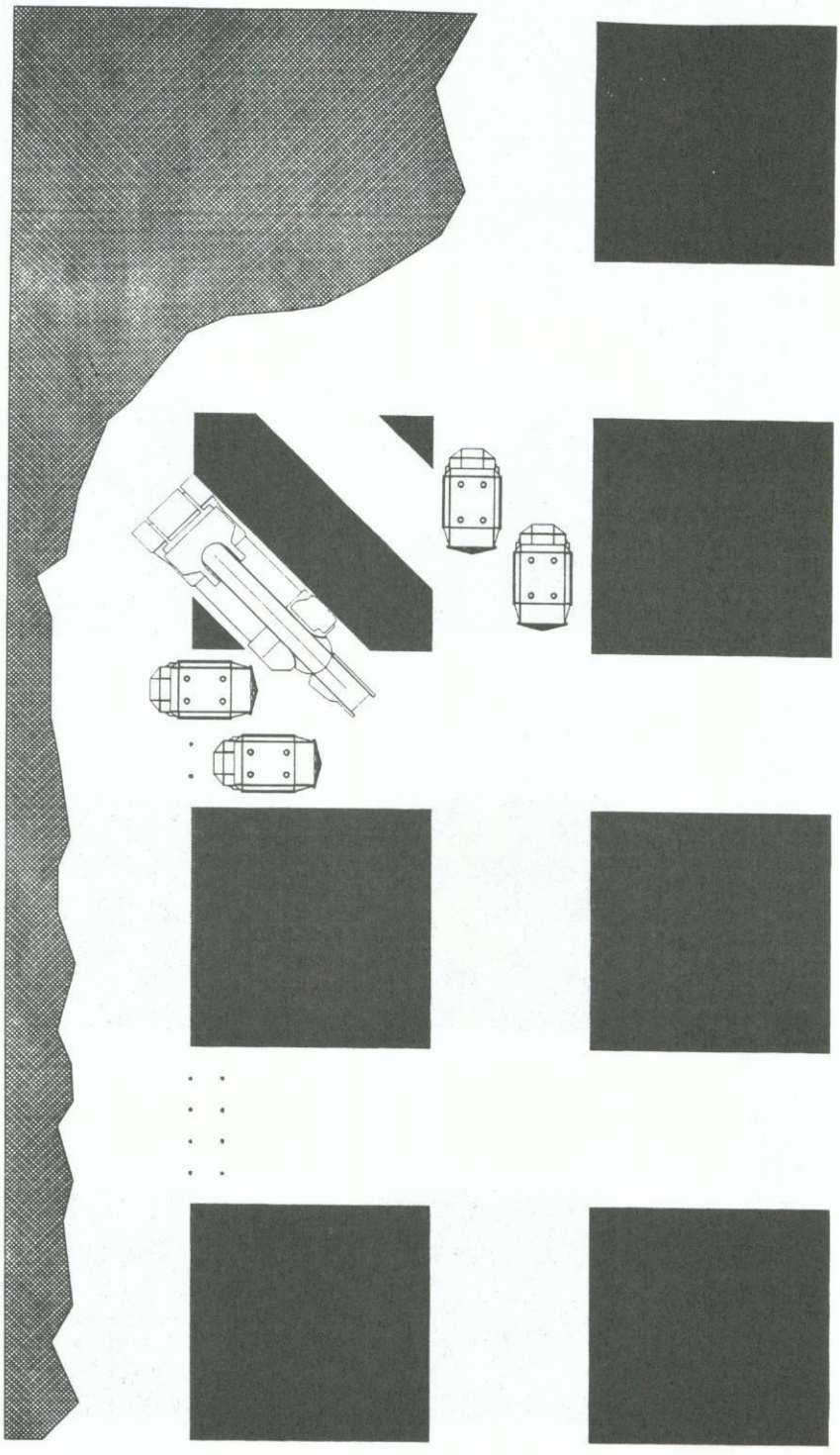

Fig. 6 Second lift – miner will pull out and the MRS units will be "walked" towards it.

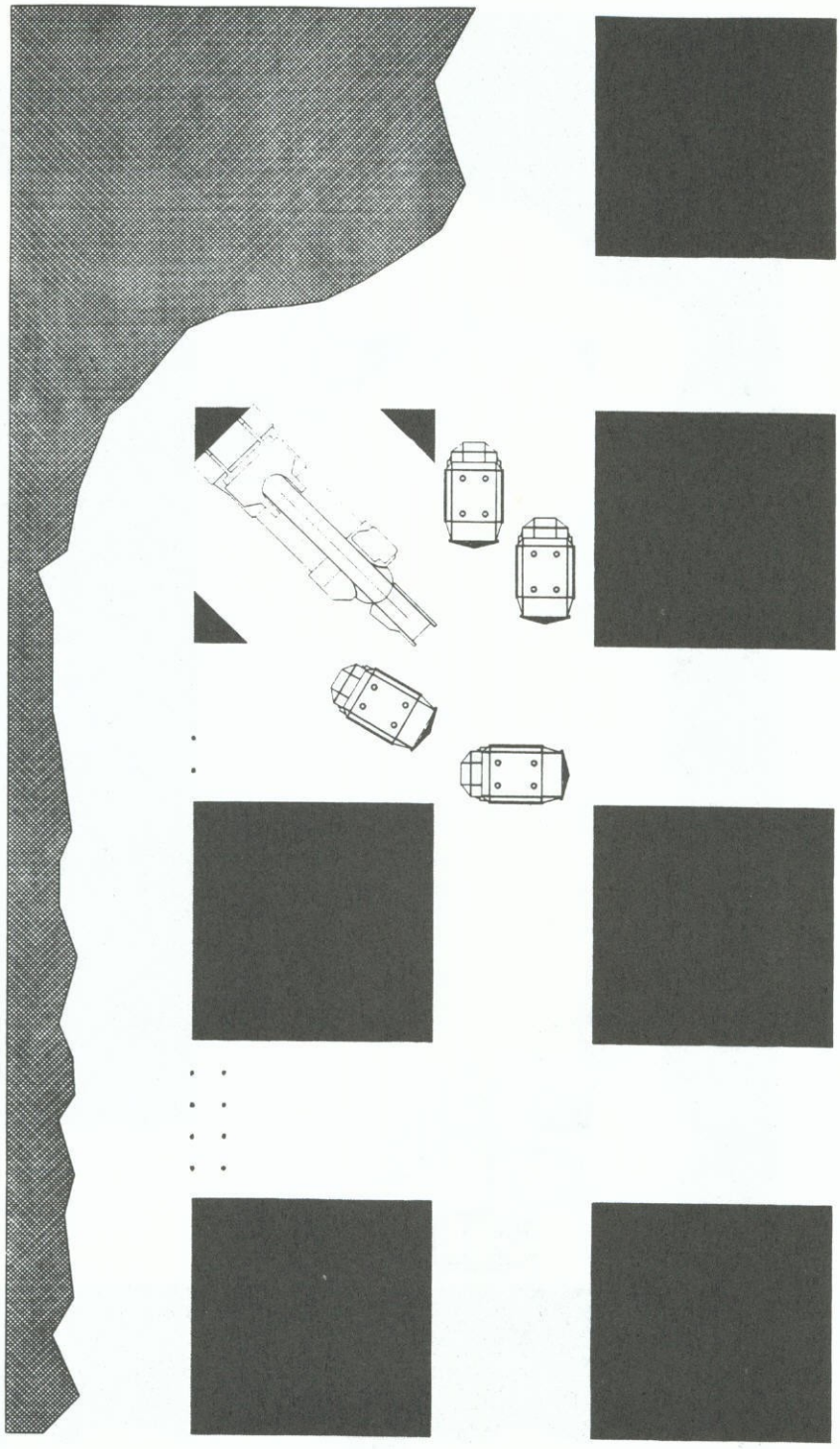

Fig. 7 Final lift – MRS units have been moved to form a 14'–16' roadway, miner will pull out and start on next block.

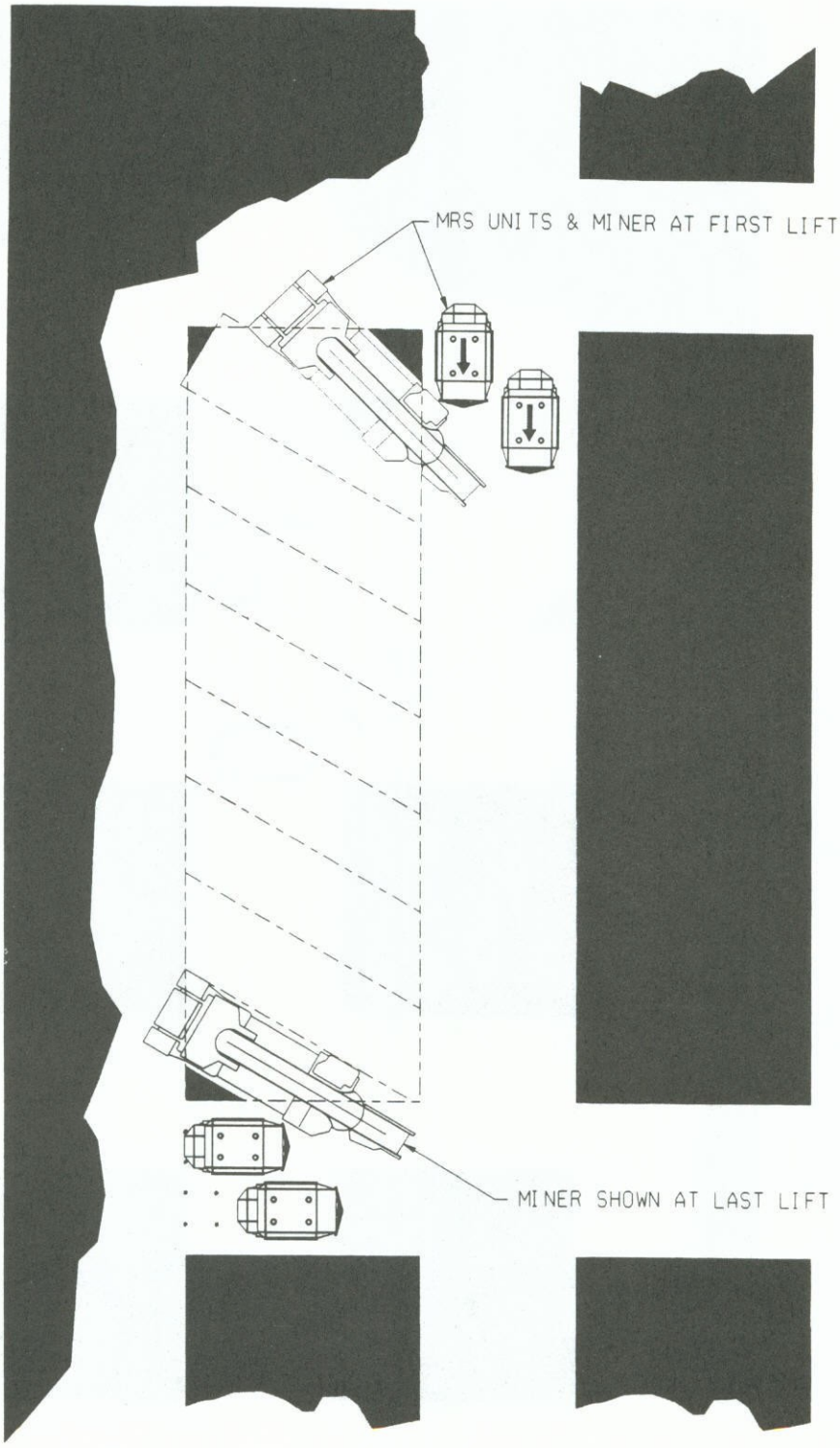

Fig. 8 100' x 30' block.

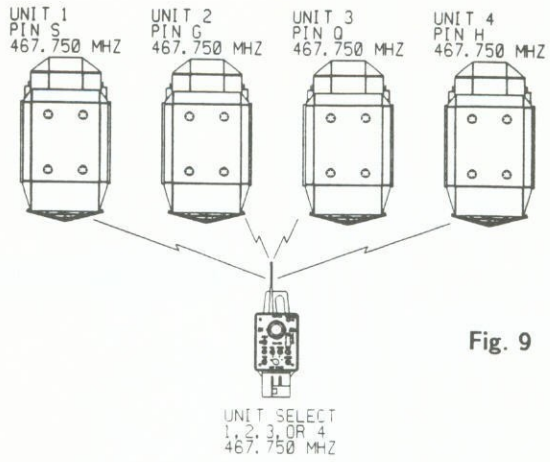

Fig. 9 4 MRS units. 1 Transmitter.

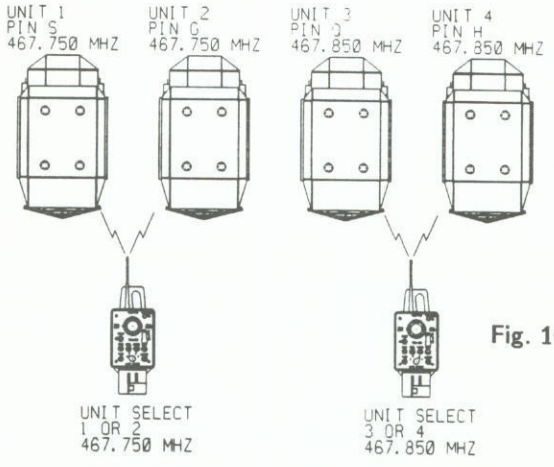

Fig. 10 4 MRS units. 2 Transmitter.

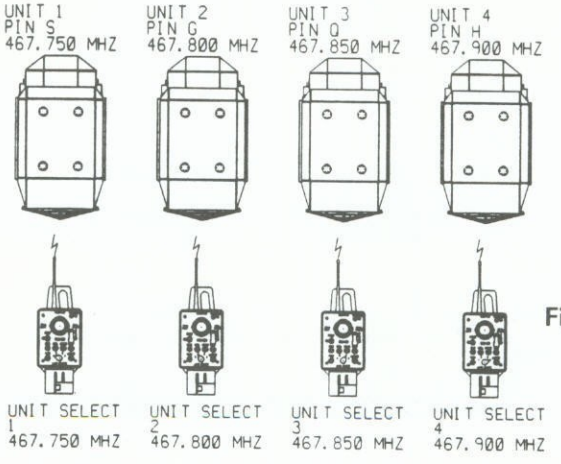

Fig. 11 4 MRS units. 4 Transmitter.

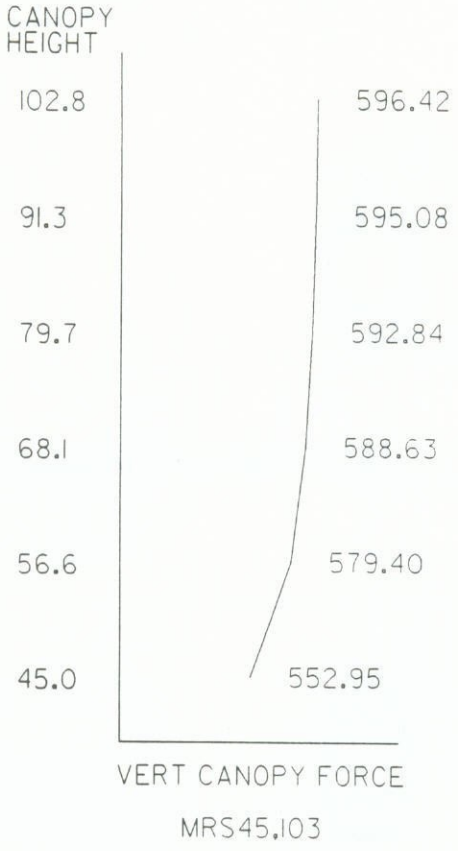

Fig. 12 Vertical canopy force vs. canopy reach.

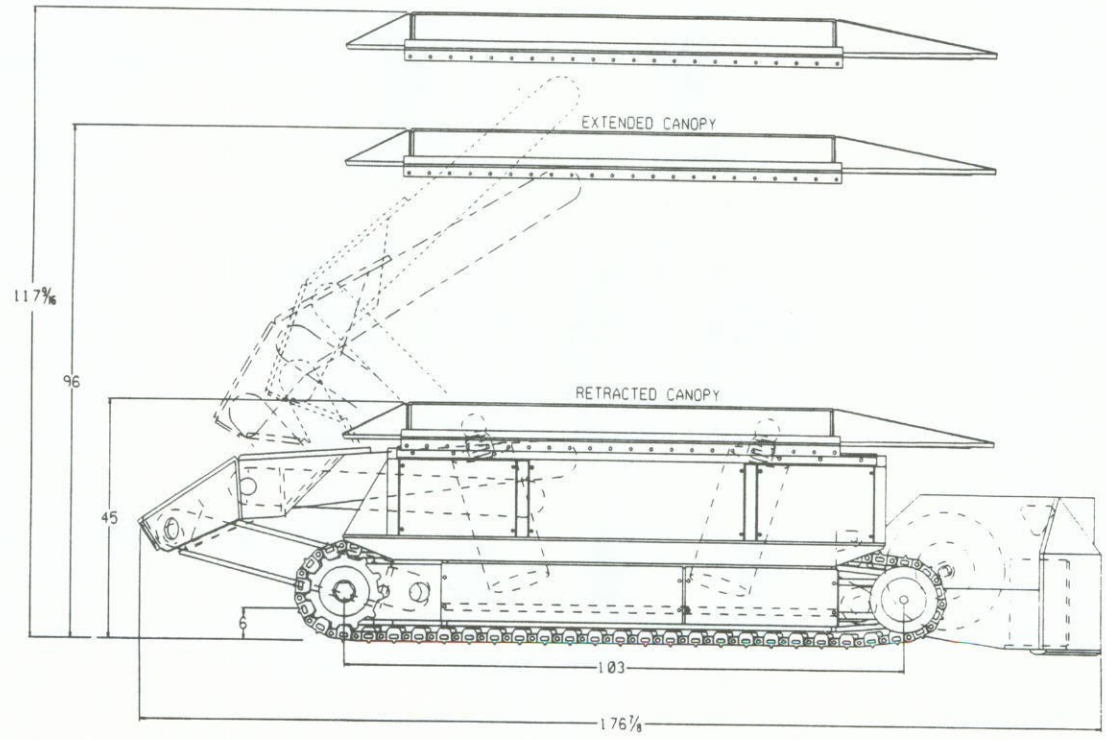

Fig. 13 Canopy shown at optional height, control link & cyl change required additional reach built into existing lemniscate/caving shield.

10th INTERNATIONAL CONFERENCE ON GROUND CONTROL IN MINING

APPLICATION OF TIME DOMAIN REFLECTOMETRY TO GROUND CONTROL

Kevin M. O'Connor, *Civil Engineer*
Twin Cities Research Center
U. S. Bureau of Mines
Minneapolis, Minnesota

and

Ty Zimmerly, *Mining Engineer*
Western Ag-Minerals
Carlsbad, New Mexico

ABSTRACT

An example application is presented in which Time Domain Reflectometry (TDR) was utilized to monitor roof strata movements during pillar extraction in a potash mine. The study was initiated when Western Ag-Minerals decided to implement secondary mining of pillars in order to extend the life of their Nash Draw Mine. A prototype operation was conducted in one mine panel to assess mining equipment and procedures, and to determine if ground control problems would develop. An instrumentation array was installed by personnel from New Mexico Tech and Western Ag to monitor strata movements, changes in pillar stress and surface subsidence, and these data are being analyzed by the Bureau of Mines. This paper is limited to a discussion of roof-floor convergence and roof strata movement to illustrate the application of TDR to ground control. Plots are presented which demonstrate the capability of distinguishing location, magnitude and mode of rock movement using TDR to interrogate coaxial cables grouted into holes drilled in the roof.

INTRODUCTION

TDR Operating Principle

Time Domain Reflectometry (TDR) is an electrical pulse testing technique originally developed to locate breaks in power transmission cables. Recently, this technique has been adapted to monitor caving of rock induced by underground mining. Coaxial cables are grouted into a rock mass (Figure 1) and progressive rock movement deforms the cable. Ultrafast rise time voltage pulses are sent down along the cable from a TDR cable tester. Cable defects such as crimps, short circuits or breaks cause reflected pulses which are detected by the tester. Pulse reflections from all changes in geometry along the cable are superimposed on the input pulse to form a reflected TDR signature. Consequently, the signature consists of many individual reflections associated with localized deformations along the cable. The characteristics of a TDR signature are determined not only by the magnitude of cable deformation but also by the type of cable defect (crimp, shear, break, etc.).

Assuming a constant pulse propagation velocity, the distance to the cable defect is proportional to the elapsed time between initiation of the voltage step pulse and the arrival of the returned voltage. The cable tester converts this time to distance so it is possible to determine the location of a cable defect as well as the type and magnitude of cable defect by inspection of the recorded TDR signature.

Installation

Features of an installation for performing TDR measurements are shown schematically in Figure 1. Prior to installation an appropriate connector (e.g., UHF) is attached to the top-of-the-hole end and the cable is connected to a TDR cable tester via a special 50-ohm connector cable. The cable is crimped at appropriate intervals (e.g., 1.2 m (4 ft) was used in this study) to optimize resolution and a reading is made to ascertain that all crimps will be recorded. The crimps must be deep enough to ensure a strong reflection but not so deep as to cause a short circuit in the cable. After being adequately crimped, the cable is lowered down hole and bonded to the surrounding rock with an expansive cement grout that is tremied into the hole. Recommended installation procedures are presented by Dowding et al. (1986).

Distinguishing Cable Deformation

The capability of distinguishing cable crimps from cable breaks, shears, abrasions, etc. provides a convenient means for improving the accuracy with which cable defects can be located. Without reference crimps along a cable, accuracy is on the order of 2% of the distance from the tester to a cable defect so that a defect at a distance of 30 m (100 ft) can only be located to within 0.6 m (2 ft) of its actual position. If a cable is crimped at selected intervals, however, a set of reference reflections is recorded each time the cable is tested. The locations of cable defects which are created by rock mass movement can then be determined with respect to these references. If reference crimps are made in a cable every 1.2 m (4 ft), the accuracy with which defects can be located becomes

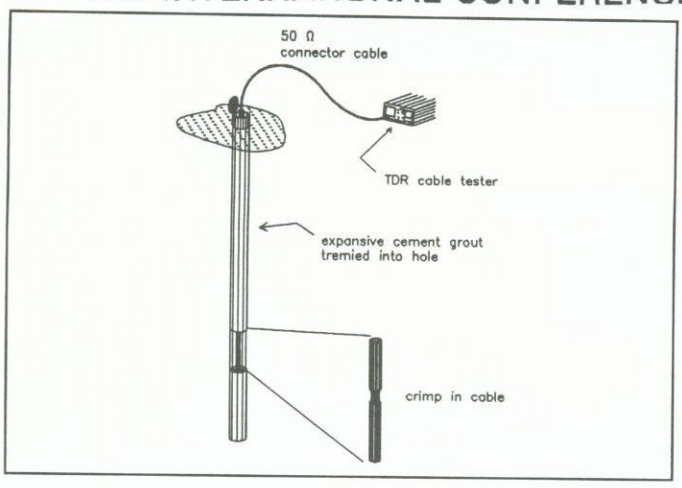

Figure 1. Schematic TDR Installation.

2.4 cm (1 in).

Significant recent developments in the interpretation of TDR signatures are presented in Dowding et al (1989) with respect to quantifying changes in TDR signature magnitude due to cable deformation as well as distinguishing cable shear from cable extension. Laboratory tests (Su, 1987) have shown that shearing of a cable produces a short voltage reflection spike, whose amplitude increases in direct proportion to the amount of deformation as shown in Figure 2b. On the other hand, extension causes only a subtle, trough-like voltage reflection that increases in length as the cable is extended as shown in Figure 2a.

Particularly significant is the difference in reflection signature for tensile failure versus shear failure. As shown in Figure 2, extension necking produces a small negative but extended voltage reflection trough just before the large positive open circuit reflection. On the other hand, shearing produces a distinctive negative voltage reflection spike before the large positive open-circuit reflection.

EXAMPLE APPLICATION OF TDR TO GROUND CONTROL

An example application is presented in which Time Domain Reflectometry (TDR) was utilized to monitor roof strata movements during pillar extraction in a potash mine. The study was initiated when Western Ag-Minerals decided to implement secondary mining of pillars in order to extend the life of their Nash Draw Mine located 12 miles east of Carlsbad, New Mexico (Figure 3). The langbeinite being mined is less plastic than sylvite which is more commonly mined in the Carlsbad Potash Basin, and it was not certain that previous experience with pillar recovery at other mines would be applicable. Therefore, a prototype operation was conducted in one mine panel to assess mining equipment and procedures, and to determine if ground control problems would develop. An instrumentation array was installed to monitor strata movements, changes in pillar stress and surface subsidence.

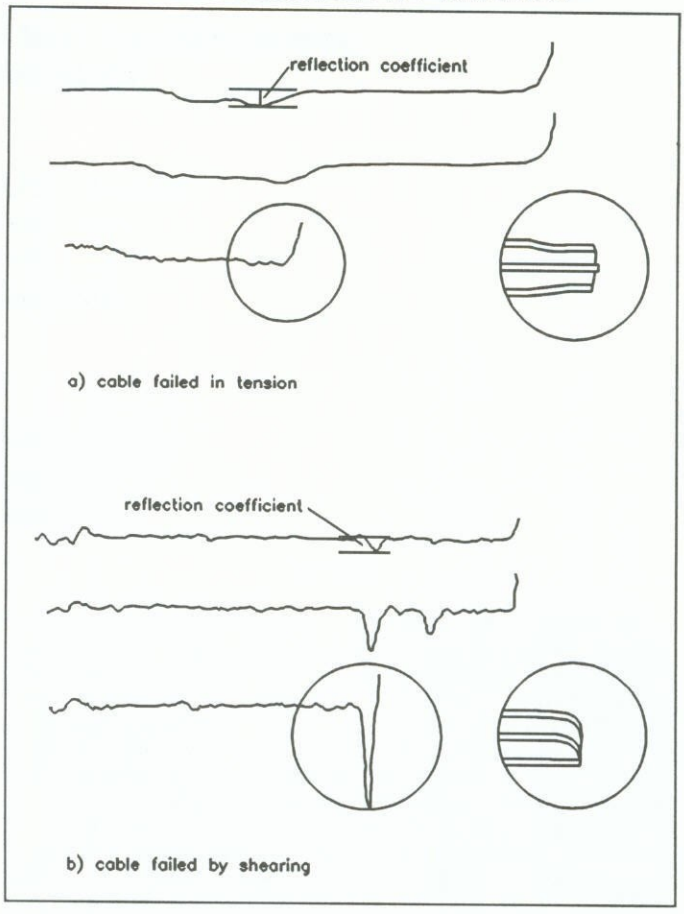

Figure 2. Comparison of Termination Signatures (Su, 1987)

Stratigraphy and Mining Method

The mine is at a depth of 380 m (1250 ft) in the 4th ore zone of the McNutt Potash Member where langbeinite is extracted using conventional room and pillar techniques. The overburden (Beauheim, 1987) consists of approximately 9 m (30 ft) of Quaternary caliche, sand and gravel, 30 m (100 ft) of siltstone and fine-grained sandstone (Dewey Lake Red Beds), 98 m (320 ft) of dolomite, anhydrite, gypsum and siltstone (Rustler Formation), and 244 m (800 ft) of halite with thin beds of anhydrite and polyhalite (Upper Salado Formation). Clay seams are common at the base of these anhydrite and polyhalite beds, and the immediate roof at Nash Draw consists of halite layers separated by clay partings.

The pillar extraction program was conducted from December 5, 1988 to January 31, 1989. The pillars were rectangular 19 m (62 ft) long by 13 m (44 ft) wide with rooms and breakthroughs approximately 2 m (7 ft) high by 8.5 m (28 ft) wide. Forty-six pillars (Figure 4) were split along their long axis with cuts 8.5 m (28 ft) wide and 3 m (10 ft) deep using the undercut and blast technique. This left 2.4 m (8 ft) wide by 19 m (62 ft) long strip remnant pillars and increased the extraction ratio from 58% to about 84%.

Figure 3. Mine Location.

Instrumentation

A mine level instrumentation array was installed to monitor roof-floor convergence, roof strata separation and changes in pillar stress. Convergence was monitored at the 51 locations shown in Figure 4a using a Philadelphia rod to measure the distance between spads driven 2.5 cm (1 in) into the roof and floor. To monitor roof strata separation, coaxial cables were crimped at 1.2 m (4 ft) intervals and grouted into roof bolt holes 6 m (20 ft) deep at 15 of these locations (three are highlighted in Figure 4b). The cables were interrogated using a Tektronix 1502 TDR cable tester with a strip chart recorder for hardcopy of TDR reflection signatures.

CONVERGENCE DATA REDUCTION

It is assumed that roof-floor convergence was primarily due to roof deflection with relatively little floor heave or squeezing of unmined pillars. This assumption is based on observations made by the authors during pillar recovery operations. The motivation for making this assumption is to demonstrate a relationship between convergence measurements and TDR measurements.

Convergence, Slope and Curvature Profiles

Convergence measurements were made at locations spaced 15 to 24 m (50 to 80 ft) apart (Figure 4). If these locations had been more closely spaced (e.g., at 1 m intervals), it would be valid to assume that roof deflection varied linearly between these points. The piecewise linear profile along

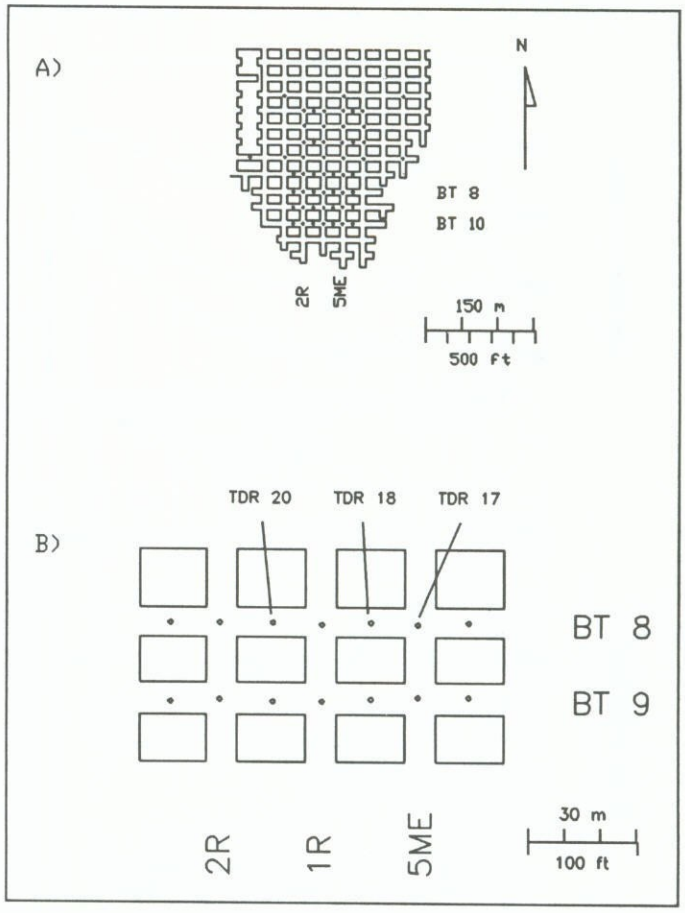

Figure 4. Mine Level Instrumentation Array: A) convergence measurement locations, B) TDR locations along BT8.

each line of points would closely approximate the actual deflected roof profile along each mine entry. Furthermore, the difference in convergence between adjacent points divided by the 1 m spacing would be a good approximation of slope between these points, and the difference in slope between two adjacent measurement intervals divided by the 1 m spacing would be a good approximation of roof curvature. At spacings of 15 to 24 m, however, the assumption of a linear variation in convergence between points is not valid due to the large changes in slope which occurred.

Convergence profiles were estimated by fitting spline functions through data points for each entry (Figures 5a and 6a). A fifth-order polynomial (Herriot and Reinsch, 1983)

$$S(x) = A_i + B_i(x-x_i) + C_i(x-x_i)^2 + D_i(x-x_i)^3 + E_i(x-x_i)^4 + F_i(x-x_i)^5$$

was forced to fit through the measured convergence, S, at monitoring locations, x_i, and the constants A_i, B_i, C_i, D_i, E_i and F_i were computed for each measurement interval so that the first and second

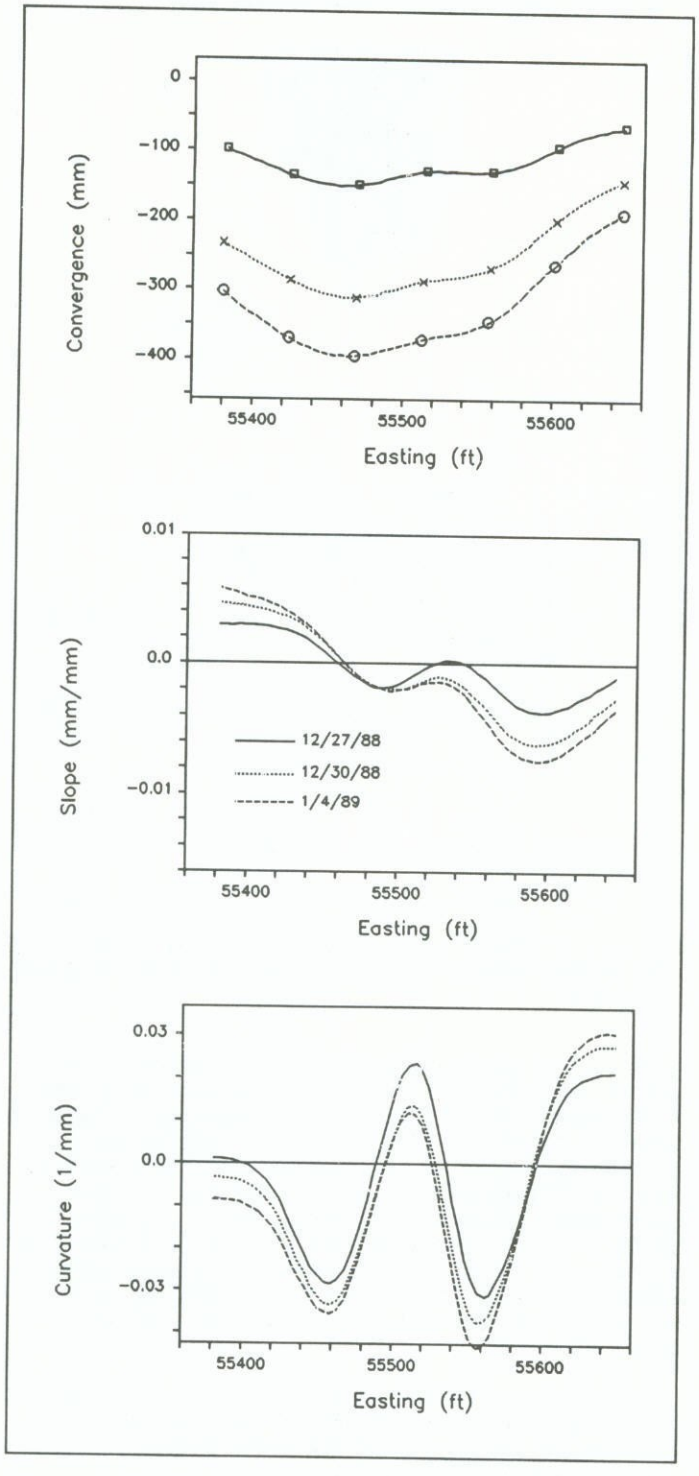

Figure 5. Computed Convergence, Slope, and Curvature Profiles along East-West Entry BT8.

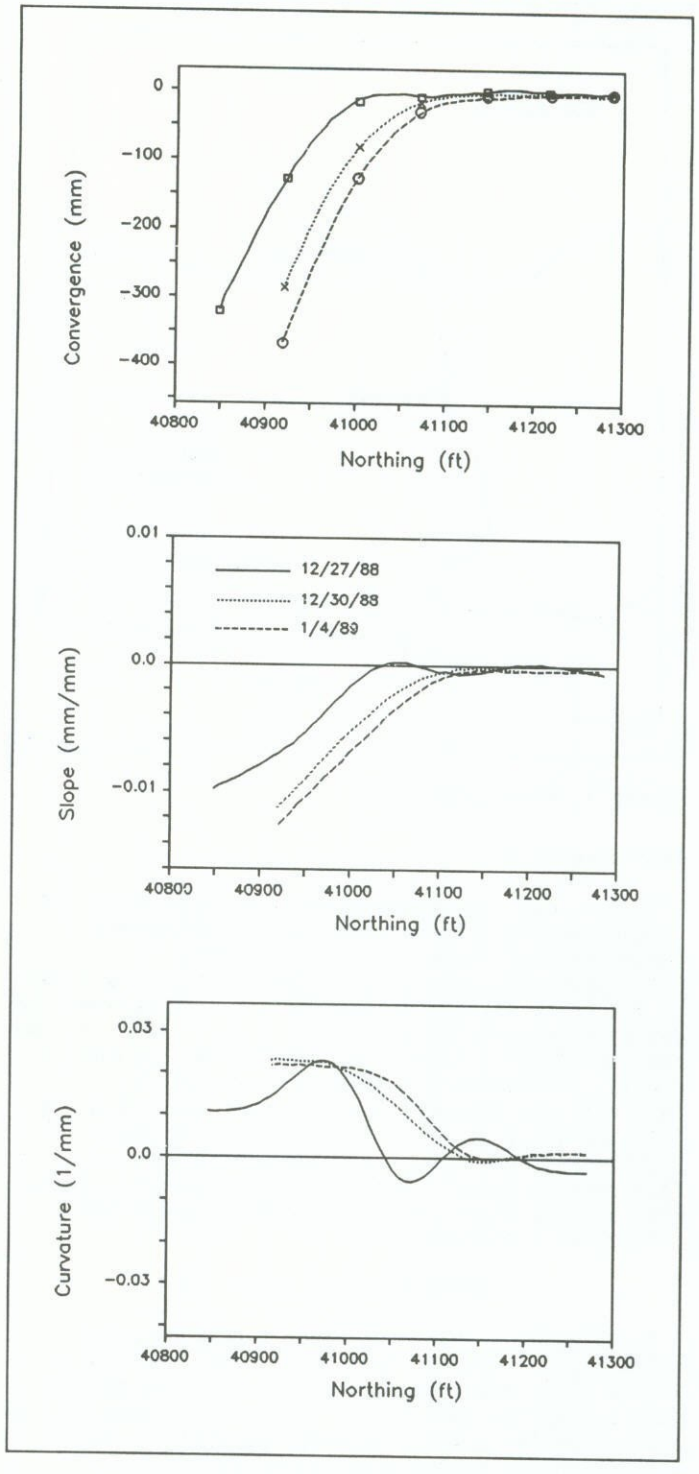

Figure 6. Computed Convergence, Slope, and Curvature Profiles along North-South Entry 1R.

derivatives, S′ and S′′, are continuous between intervals. The first and second derivatives are estimates of the slope and curvature profiles (Figures 5b,c and 6b,c). Where the convergence profile has a positive slope, the values in Figures 5b and 6b are shown as negative to be consistent with subsidence engineering sign convention (NCB, 1975), and positive curvature in Figures 5c and 6c indicates that the convergence (i.e., roof deflection) profile is concave upward.

TDR DATA INTERPRETATION

It is apparent from the contour plot in Figure 7 that the roof deformed into a three-dimensional bowl but it is useful for purposes of this paper to

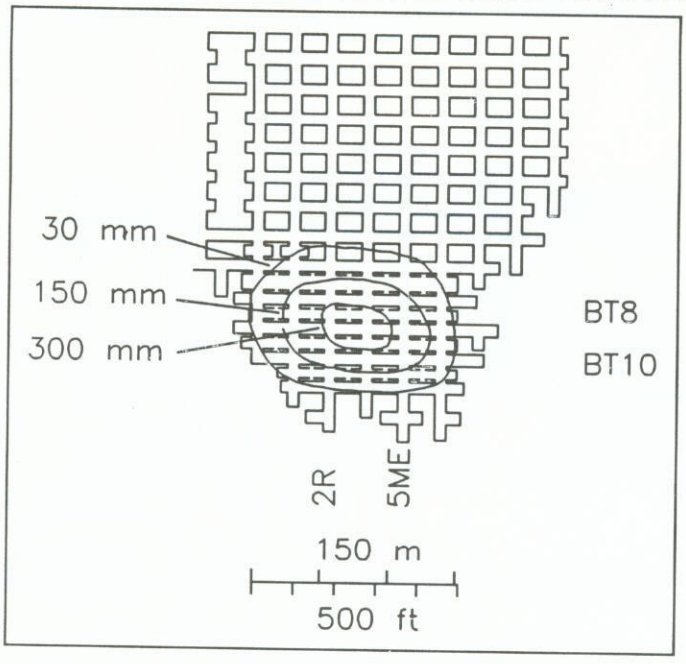

Figure 7. Convergence contours on 12/30/88.

consider this deformation in the context of simple beam bending. This simplifying assumption makes it possible to estimate horizontal displacements within the roof strata for comparison with shear along the clay parting at a depth of 3.6 m (12 ft) as indicated by changes in the TDR signatures (Figure 8).

Beam Deflection Analogy

The convergence profiles (Figures 5a and 6a) were assumed to represent deflected beam profiles. Furthermore, it was assumed that plane sections through a beam taken normal to its axis remained plane as the beam deflected. Under these assumptions, horizontal displacement of a point is linearly proportional to its distance from the neutral axis.

There is a clay parting in the roof at a depth of approximately 3.6 m (12 ft) and shearing of the coaxial cable at this depth is apparent in the TDR signatures (Figure 8). Treating this depth as the deflected beam thickness and assuming a prismatic beam cross section, the neutral axis is located at a depth of 1.8 m (6 ft). For extreme fibers the east-west and north-south components of horizontal displacement are the product of 1.8 m times the slope shown in Figures 5b and 6b respectively.

TDR Shear displacement

The convergence contours shown in Figure 7 indicate that the roof deformed into a bowl centered over north-south entry 1R. This mode of deformation implies that points in the immediate roof experience two horizontal components of displacement in addition to the vertical component. Computed components of horizontal displacement at a depth of 3.6 m (12 ft) are plotted versus time in Figure 9 for the TDR cable locations highlighted in Figure 4. The north-south component is consistently greater than the east-west component reflecting the asymmetrical shape of the convergence bowl.

Changes in TDR signatures were converted to shear displacement using calibrations presented in Dowding et al (1989) and Kim (1989). Shear displacement of the cables at TDR 18 and TDR 20 (Figures 9b and 9c) is consistent with the north-south component of horizontal displacement along entry 1R. Shear displacement of the cable at TDR 17 (Figure 9a) is not consistent with this north-south component since it is closer to entry 5ME (Figure 4). For purposes of brevity, profiles along 5ME were not included in this paper but the convergence contours in Figure 7 illustrate the smaller north-south gradient along entry 5ME compared with entry 1R.

TDR Tensile Displacement

The magnitude of TDR shear displacement attained a peak value and then decreased as the "face" advanced past BT8 on 12/21/88. This decrease in magnitude of the TDR reflection (Figure 8) is actually associated with tensile deformation of the coaxial cable and has been observed during laboratory calibration tests (Su, 1987). This tensile deformation occurred as the immediate roof strata separated from the overlying main roof along the clay parting. Tensile cable failure is evident in the signature for TDR 20 (Figure 8a).

In addition to the reduction of the TDR reflection magnitude and tensile failure at a depth of 3.6 m (12 ft), there are reflections at a depth of 0.6 m (2 ft). These reflections appear in the signatures for TDR 20 and TDR 18 (Figure 8) and coincide with a gap that developed on 12/20/88 as mining of the pillars between BT8 and BT9 (Figure 4) was completed. At entries 3R and 4R this gap was observed to increase from 25 mm (1 in) to 112 mm (4-1/2 in) during the period from 12/20/88 to 12/29/88. Unfortunately, there has not been a reliable laboratory calibration developed for grouted coaxial cables subjected to tension (Dowding et al, 1989) so changes in the TDR signatures cannot be quantitatively correlated with gap formation. Note that there is no indication of tensile deformation in the signatures for TDR 17 which infers that strata separation did not occur east of entry 1R (this was confirmed by other cables).

INTERPRETATION OF ROOF BEHAVIOR

The above interpretation of TDR signature changes infers a scenario in which both the immediate roof and main roof cantilevered as a laminated beam without strata separation. When pillars on both sides of BT8 had been mined on 12/21/88, yielding of the remnant pillars accelerated the convergence rate and strata separation occurred.

SUMMARY

A case history has been presented in which TDR was incorporated into a prototype pillar recovery operation for purposes of monitoring roof strata behavior. Fifteen cables were installed to a depth

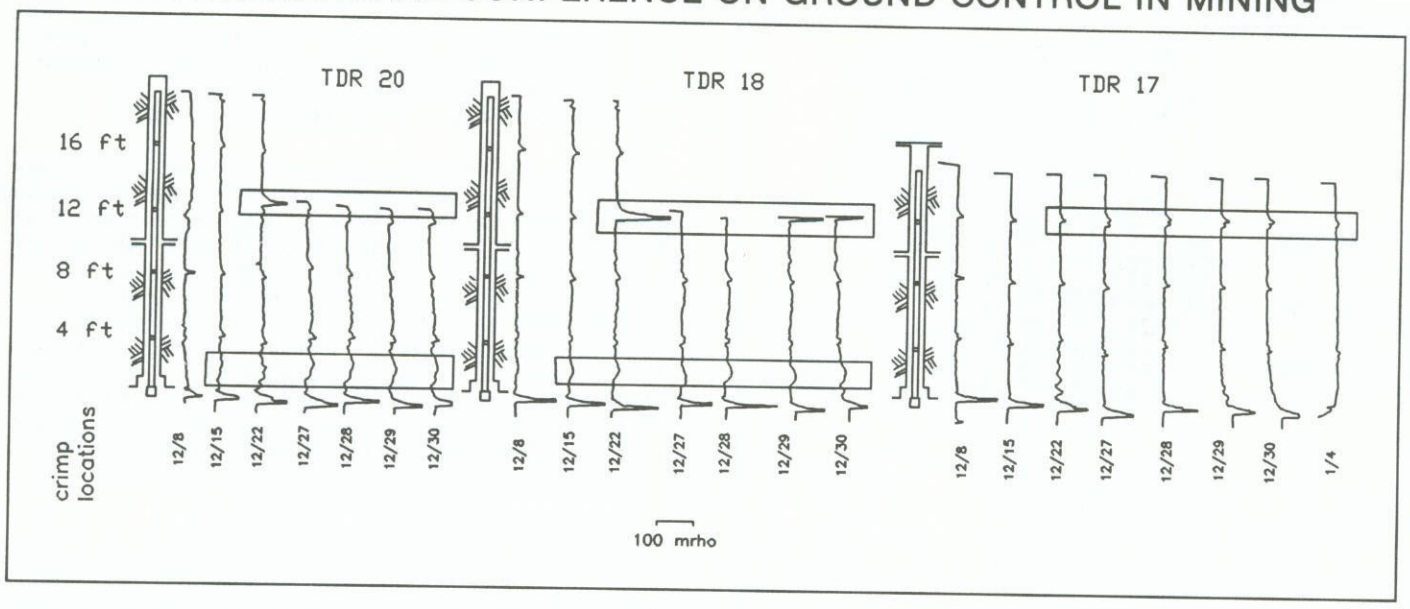

Figure 8. Reflection Signatures for Cables along BT8.

of 20 ft and monitored in conjunction with an array of fifty-one convergence measurement points. A spline function was used to compute convergence and slope profiles along entries and a simple beam analogy was used to compute horizontal displacement for comparison with observed TDR shearing. Changes in magnitude of TDR refections were converted to displacement using previously developed correlations and these were compared with the computed horizontal displacements. It appears that the TDR displacement coincides with one component of horizontal displacement and not the total displacement vector. Essentially the roof deflected as a laminated beam without strata separation until pillars had been mined on either side of the measurement location. At that point yielding of the remnant pillars caused convergence to accelerate and strata separation occurred. This was reflected as a decrease in magnitude of the TDR reflection. Also tensile deformation of the cable occurred as a shallow slab developed in the immediate roof in the central portion of the convergence bowl.

ACKNOWLEDGEMENTS

The authors would like to thank Western-AG Minerals Company for permission to publish the results of this test program. In particular, the encouragement of Mr. Morris Worley, Mine Manager, and Mr. Don Boyd, Mine Superintendent are greatly appreciated. The study was performed while the first author was a faculty member in the Department of Mining, Environmental and Geological Engineering at New Mexico Tech and the support of Dr. George Griswold was critical to the success of this program. In addition the authors would like to acknowledge the contributions of Ms. Kathy Littleton, Ms. Jackie Francke, and Mr. Earl Downs.

REFERENCES

1. Beauheim, R.L. Interpretation of Single-WellHydraulic Tests Conducted At and Near the Waste Isolation Pilot Plant (WIPP) Site, 1983-1987. Sandia Report SAND 87-0039, Sandia National Laboratories, Albuquerque, 1987.

2. Dowding, C.H., M.B. Su, and K.M. O'Connor. Choosing Coaxial Cable for TDR Monitoring. Proceedings, 2nd Workshop on Surface Subsidence Due to Underground Mining, Morgantown, West Virginia, June, 1986, pp. 153-162.

3. Dowding, C.H., M.B. Su, and K.M. O'Connor. Measurement of Rock Mass Deformation with Grouted Coaxial Antenna Cables. Rock Mechanics and Rock Engineering, V. 22, No. 1, 1989, pp. 1-23.

4. Herriot, J.G. and C.H. Reinsch. Translation of Algorithm 507: Procedures for Quintic Natural Spline Interpolation. Algorithm 600, ACM Transactions on Mathematical Software, V. 9, No. 2, June, 1983, pp. 258-259.

5. Kim, M.H. Quantification of Rock Mass Deformation with Grouted Coaxial Cable. M.S. Thesis, Dept of Civil Engineering, Northwestern University, Evanston, Illinois, 1989.

6. National Coal Board. Subsidence Engineers' Handbook. Camgate Litho Limited, London, 1975.

7. Su, M.B. Quantification of Cable Deformation with Time Domain Reflectometry Techniques. Ph.D. dissertation, Northwestern University, Evanston, Illinois, 1987, 111 p.

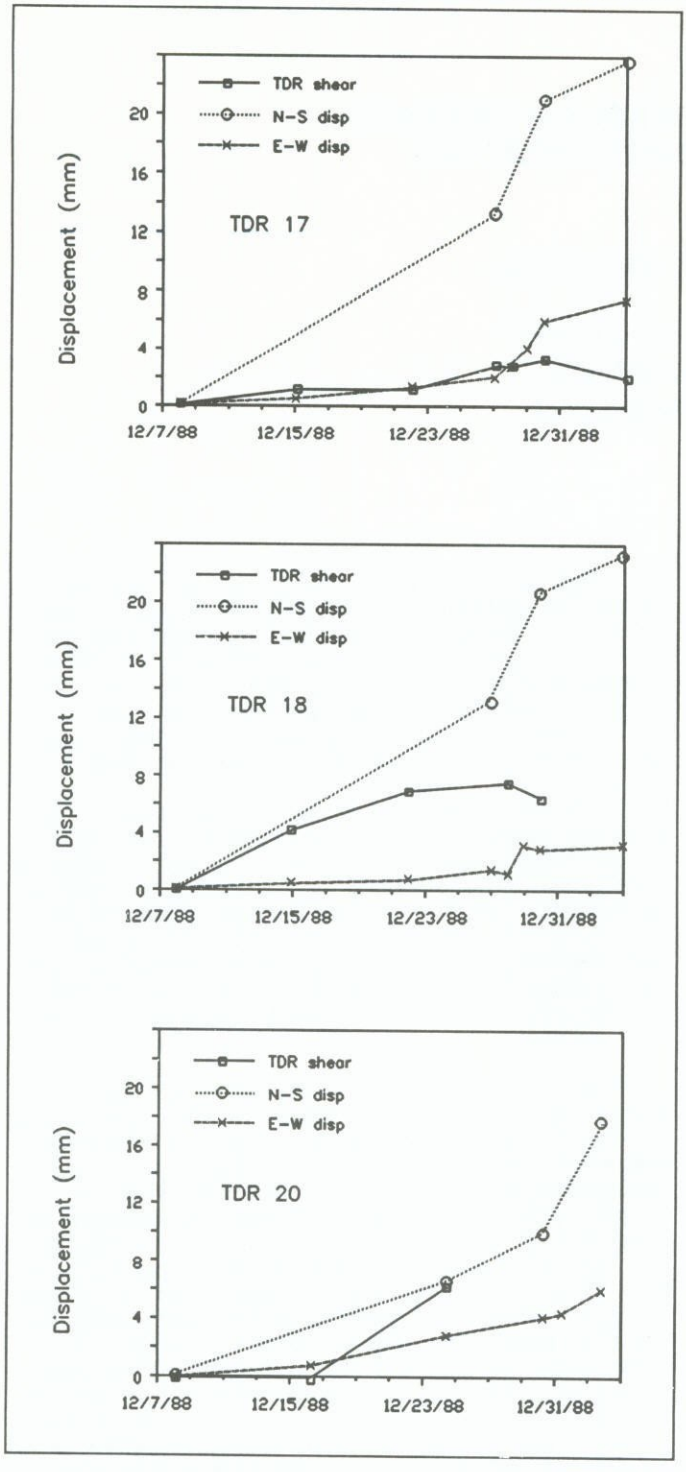

Figure 9. Displacement Time Histories for TDR Locations along BT8.

10th INTERNATIONAL CONFERENCE ON GROUND CONTROL IN MINING

AN EXAMINATION OF ENERGY CALCULATIONS APPLIED TO COAL BUMP PREDICTION

Keith A. Heasley, *Mining Engineer*

Pittsburgh Research Center
U. S. Bureau of Mines
Pittsburgh, Pennsylvania

ABSTRACT

Pillar recovery in deep coal mines with competent roof and floor can concentrate stresses and generate hazardous bumps. Actual calculation of the geologic strain energy released in association with these coal bumps has been rare, although energy release values have been utilized successfully for indicating burst potential in numerous hard-rock mines. This paper advances the current knowledge of energy release calculations as applied to coal bumps through an extensive analysis of an actual bump occurrence. The U.S.B.M, displacement-discontinuity code, MULSIM/NL, is used to produce a numerical model which generates stress, displacements and energy values associated with a pillar retreat section. This model is calibrated with actual field data, and then dissipated energy values from the model are examined as to their suitability for indicating bump potential. Ultimately, it is determined that prudent application of dissipated energy calculations can be used as a tool to investigate the coal bump potential of a mining plan or cut sequence.

INTRODUCTION

On October 18, 1983, two miners were killed by a bump on a continuous miner section in which a barrier pillar was being extracted at the Olga Mine in McDowell County, West Virginia (1). Because of these two coal-bump fatalities and a dozen others in the Appalachian area in the time period between 1959 and 1986, the Bureau of Mines established a major research effort to alleviate the safety hazards associated with coal bumps. As part of this effort, an investigation of the geologic strain energy released in association with coal bumps was initiated.

It was hypothesized that calculated energy values may provide better insight, or even a certain predictive capability, regarding the occurrence of coal bumps. For many years, it has been understood that energy changes occur in the rock mass during mining. Basically, the very act of creating an opening underground causes the gravitational potential and tectonic strain energy of the rock mass to be redistributed. Part of this redistributed energy goes to increasing the elastic strain energy of the nearby rock mass while another part of the redistributed energy is dissipated or released. This released energy can take a passive form such as heat, sound, etc, or it may appear as dynamic energy driving a damaging rock burst or coal bump.

It is not surprising, then, to find that in the past the energy release rate (ERR) has been found to correlate with the incidence or risk of damaging rock bursts. In the 1960's, the concept of ERR as an indicator of burst potential was pioneered in deep hard-rock mines in South Africa (2, 3, 4). More recently, energy release rate computation and application have improved (5, 6), and use of the ERR concept at burst-prone hard-rock mines has become common.

However, the application of energy concepts to bump-prone coal mines has been limited. Crouch and Fairhurst (7) applied a displacement-discontinuity model with an energy release calculation to simulated coal mining sequences and demonstrated a technique for selecting an optimum cut sequence for bump control based on the energy values. Similarly, Zipf and Heasley (8) applied an energy calculation to a set of idealized cut sequences for pillar retreat mining and demonstrated the superiority of the Olga Mine cut sequence for maintaining a uniform energy release and therefore minimizing bump potential. Finally, in a more practical situation, Maleki et al. (9) used energy calculations in conjunction with stress and displacement calculations to analyze and recommend alternative mining plans for an active mine experiencing bump problems.

MULSIM/NL and the Energy Calculations

In this paper, the energy calculations are implemented in the computer code, MULSIM/NL (10). This code uses the displacement-discontinuity variation of the boundary-element method (BEM) to calculate three-dimensional stresses and displacements caused by mining tabular deposits such as coal seams. From these stresses and displacements, MULSIM/NL calculates energy quantities for the seam

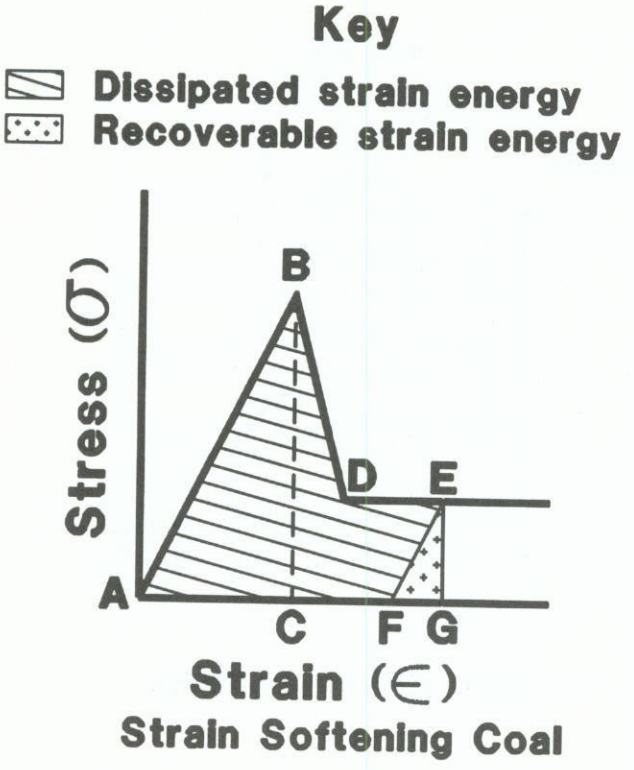

Figure 1. Schematic of strain-energy values.

materials. The energy quantities discussed in this paper are called the "strain-energy" values and consist of; the total strain-energy, the recoverable strain-energy and the dissipated strain-energy. An explanation of these three quantities is best accomplished by reference to figure 1. In this figure a typical strain-softening curve for an idealized coal is shown. As the coal is initially loaded along the elastic portion of the curve (line AB), the work needed to strain the coal is stored as elastic strain energy (area ABC). Since any unloading of the coal is assumed to occur along the same line, all of the input work is totally recoverable. However, as the coal is loaded past the point of peak stress (point B) to the residual stress portion of the curve (line DE), any unloading of the coal is assumed to occur along a line parallel to the initial loading (line EF) and not along the original loading curve (ABDE). Thus, the "recoverable" strain energy for a coal material at point E is equal to area EFG, while the "total" work energy applied to the material is equal to area ABDEG. The difference between the total energy area and the recoverable energy area is the area ABDEF which is known as the "dissipated" energy since it must have been liberated to the environment.

The analysis in this paper will examine the increases in dissipated strain-energy between one mining step and another. Any increase in dissipated strain-energy between steps implies that energy was dissipated to the environment. It is postulated that the larger the increase in dissipated energy between steps the more likely that the energy will be dissipated dynamically as a coal bump. Therefore, the model steps with the highest increases in dissipated energy should correlate with the greatest bump hazard.

Olga Mine

The specific site chosen for the application of energy calculations to coal bump prediction was the 9-Right section at the Olga Mine in McDowell County, West Virginia. This section of the Olga Mine had been heavily instrumented with coal stress cells, coal extensometers, convergence stations, and microsiesmic transducers in the mid 1980's as part of the Bureau of Mines early research effort to alleviate coal bumps. The detailed monitoring and observation of the strata behavior in 9-Right provided invaluable insight into the causes and possible control of coal bumps (11, 12). Also, The wealth of convergence and stress data available from the instrumented 9-Right section provides excellent model calibration information.

The Olga Mine operated in the Pocahontas No. 4 Coalbed which is a friable coal with an average unconfined compressive strength of 2,400 psi (for 2-in. cubes) (11). In the 9-Right study area, the coal averaged 66 in thick and the overburden ranged between 1400 and 1600 ft. The Eckman Sandstone forms the immediate and main roof at Olga and is a very massive, strong and stiff unit (24,200 psi compressive strength; 5,160,000 psi elastic modulus). The floor of the No. 4 Coalbed in the 9-Right area is composed of 0 to 5 ft of siltstone and/or shale underlain by 50 to 75 ft of the Upper Pocahontas Sandstone. This strong sandstone (21,900 psi compressive strength) provides a competent, massive floor which does not heave or break readily.

At the time of the study, mining at Olga was conducted exclusively by room-and-pillar methods using continuous miners, and the majority of the coal extraction was pillar retreat mining which involved removing old barrier pillars that had been left to protect access roadways driven many years previous. The 9-Right section of the mine was initially chosen for the instrument site because it contained large (350 by 160 ft) barrier pillars, pillars A-G in figure 2, which were of the same size and shape as the pillars involved in the 1983 fatalities. The configuration of the study area at the beginning of the detailed investigation is diagramed in figure 2a.

The full-extraction mining method at Olga involved first splitting the 350 by 160 ft "barrier" pillars into 55 by 70 ft "chain" pillars and then pulling the chain pillars in a retreating pillar line. During the time of the study, the large barrier pillars B, D, and F were each split into ten chain pillars (fig. 2b). At the same time, barriers A, C, and E were each split into four chain pillars on the right and a 200 by 160 ft barrier pillar on the left. The barrier pillar splitting in 9-Right was discontinued on April 22, 1986 when a lost-time injury occurred from a chain pillar bump during the splitting of barrier pillar G (fig. 2b). After the bump, a 9 by 9 array of 55 by 70 ft chain pillars had been outlined (fig. 2b).

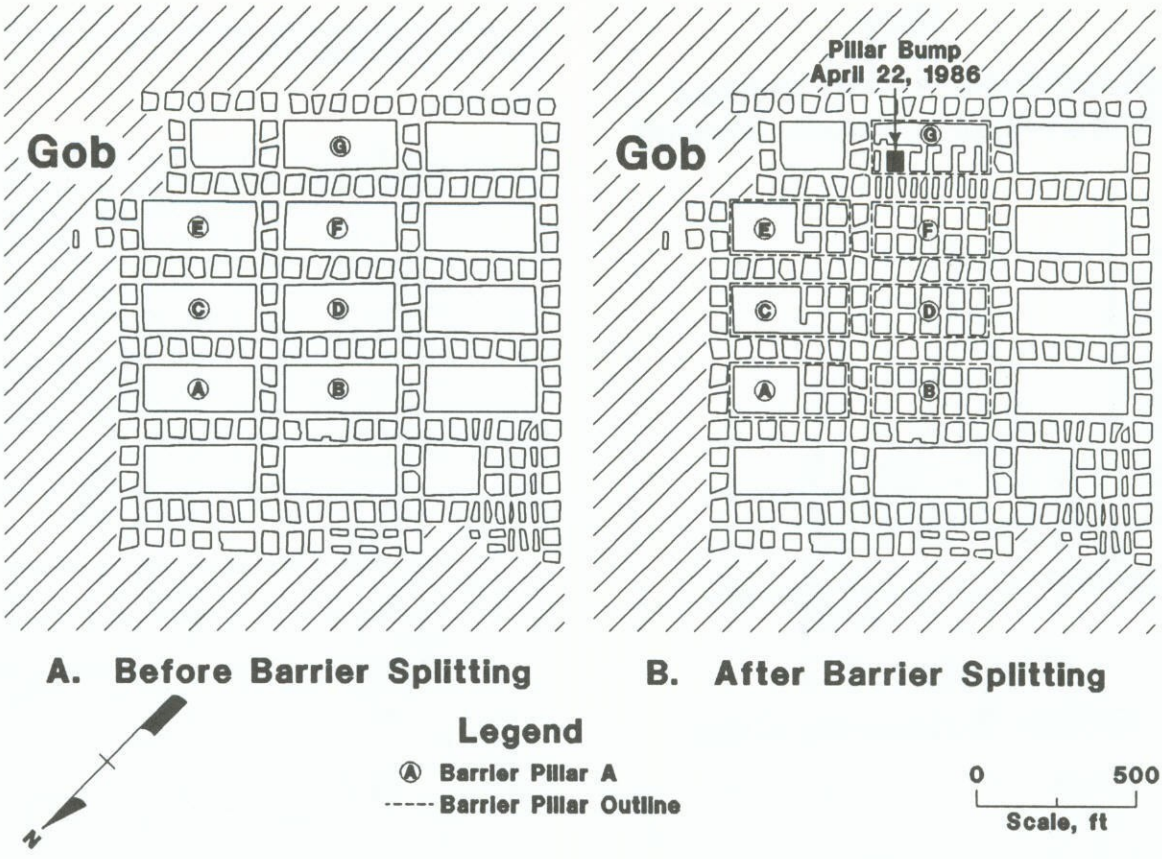

Figure 2. 9-Right at Olga Mine.

These chain pillars were subsequently pulled using the Olga Mine's unique pillar recovery method (11).

MODEL CALIBRATION

The first step towards investigating the utility of the MULSIM/NL energy release calculations for analyzing bump potential was to calibrate the model input parameters using actual field observations. In any structural model the "quality" of the input material properties directly contributes to the validity of the model results. In this particular model, with strain-softening coal and energy release calculations, the accuracy of the results are extremely dependent on the accuracy of the input materials. For this reason, a fair amount of effort went into a multi-faceted approach for determining the optimum values of the input parameters (13).

The input values for the elastic moduli of the coal, the elastic moduli of the surrounding media, and the failure strength of the coal were determined by a systematic process in which the parameters were adjusted until the model results corresponded as closely as possible to actual observed convergence and pillar behavior (11). Examples of the degree of similarity between the final calculated seam closure and pillar failure, and the observed seam closure and pillar failure are shown in figures 3 and 4. From these figures, it appears that the optimized input parameters provide fairly accurate stress and displacement responses in the model. The elastic moduli utilized in these optimized models were 60,000 psi for the coal, 750,000 psi for the surrounding media, and 7,500 for the gob material.

For the complete stress-strain behavior of the coal, additional insight was obtained from an extensive set of triaxial tests published by Barron (14). The trends noted in these tests combined with the peak strength magnitudes as determined by calibration of the model with field observations, result in the optimized stress-strain curves used for the coal elements as shown in figure 5.

MODEL OF LOST-TIME BUMP

The second step in investigating the utility of energy release calculations for analyzing bump potential was to formulate the 9-Right section of Olga into a model which detailed the April 22, 1986, lost-time bump occurrence. A schematic of the MULSIM/NL model is shown in figure 6. The coarse grid in this model is 40 by 40 blocks, each measuring 45 ft on a side. The fine mesh occupies coarse blocks 11 through 30 in the x direction and 16 through 35 in the y direction. These boundaries define a fine mesh grid of 100 by 100 elements, each measuring 9 ft on a side. Using these 9 ft elements the mine plan is modeled with 18 ft wide entries and 54 by 72 ft pillars. The height of the coal seam throughout the model is 66 in and the

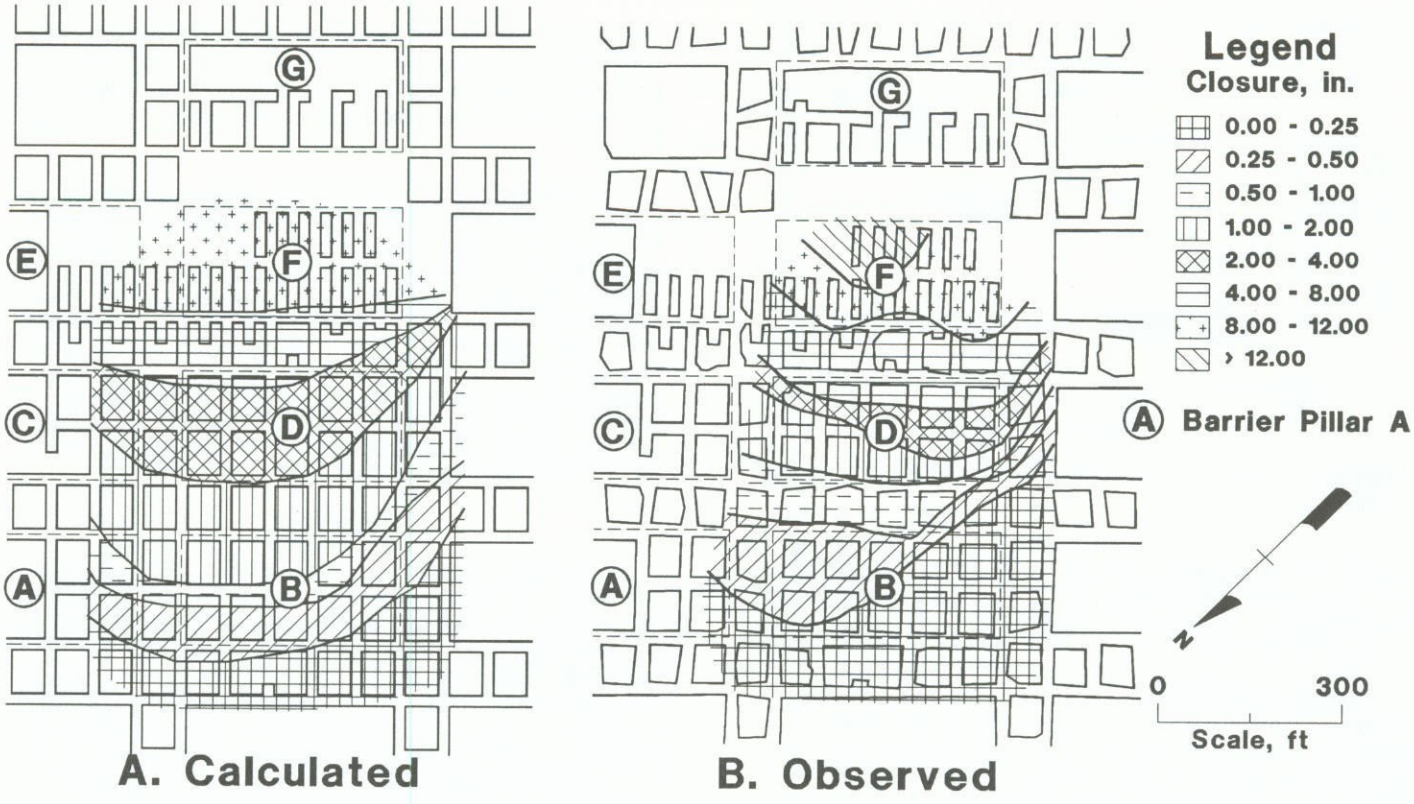

Figure 3. A comparison of the calculated and observed convergence.

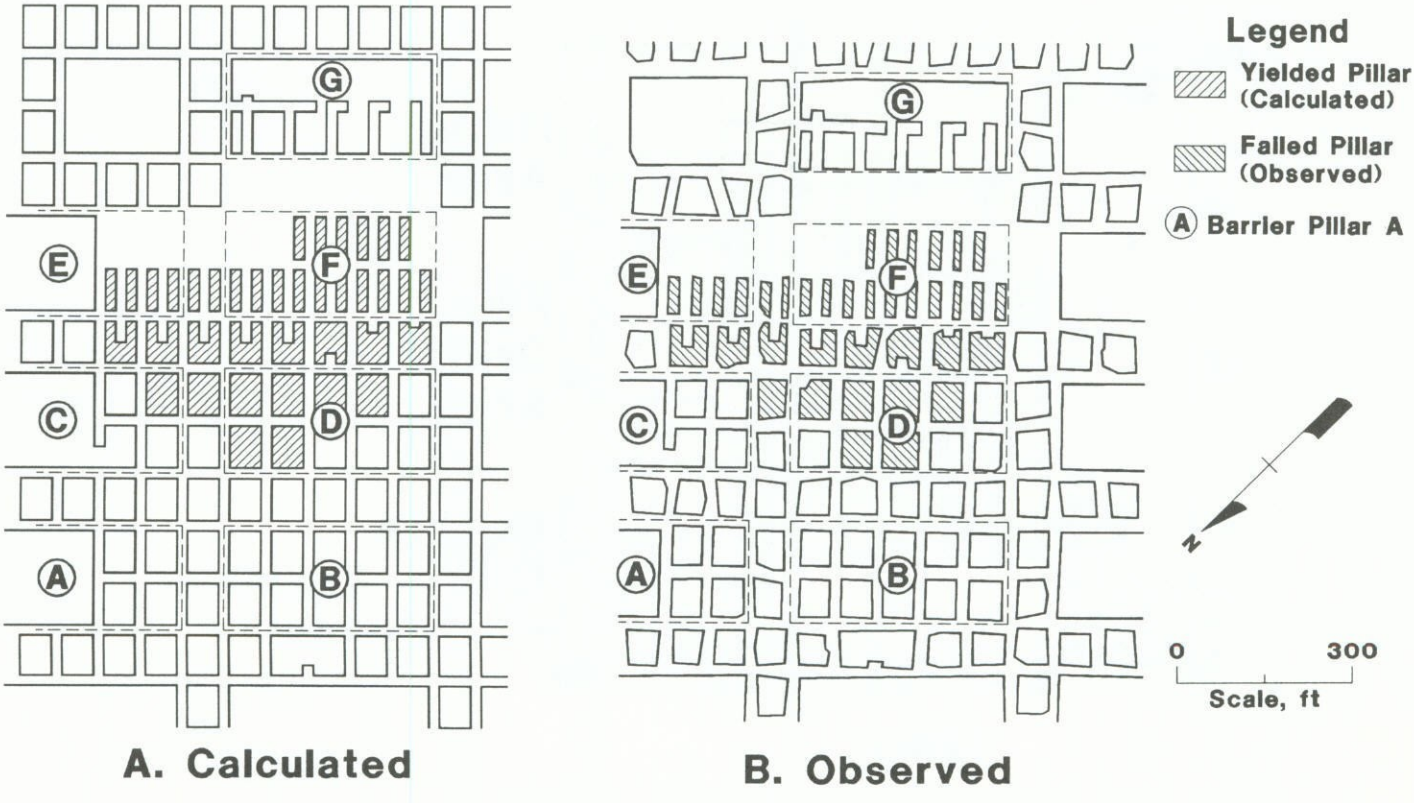

Figure 4. A comparison of calculated and observed pillar failure.

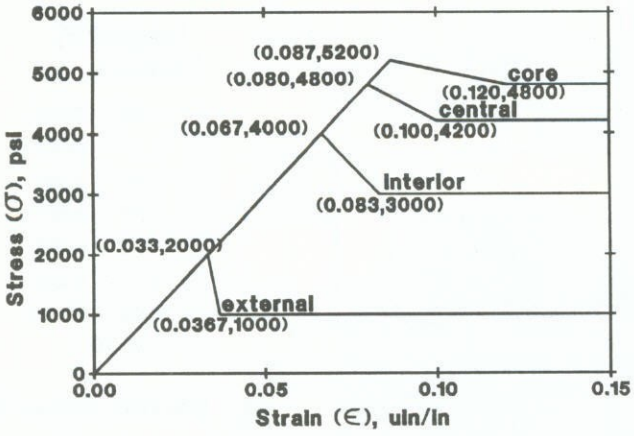

Figure 5. The strain-softening curves for the coal elements.

depth of the seam is set at 1500 ft. The surrounding rock mass is modeled with an elastic modulus of 750,000 psi, a Poisson's Ratio of 0.25, and a density of 158 lbs/ft^3.

The coal seam material properties used in the fine grid of the model correspond to the four stress-strain curves presented earlier in figure 5. In keeping with the philosophy that increased confinement produces a stronger element, the "external" curve was assigned to the exterior of the pillar and then the succeeding curves; "interior", "central" and "core" were assigned in progression towards the center of a pillar. This material property sequence allows the model to simulate both yielded perimeters and high stressed cores on the pillars.

The mining steps used in the energy calculation model of the April 22nd bump are shown in figure 7. The size of these steps range from 2 to 16 extracted elements. However, each of the steps were extracted in one location at approximately the same time; therefore, the energy calculations from this model can generally be associated with one extraction event at a specific location. In order to normalize the values of the energy calculations between different steps, all subsequent energy values are averaged by the number of elements extracted in that particular step.

RESULTS

The graph of the energy results from the numerical model is shown in figure 8 and it contains the changes in dissipated strain-energy plotted against the mining step. When examining figure 8, it should be noted that the absolute value of the dissipated energy is not important for analyzing bump potential since its magnitude can vary greatly depending on model input parameters. Instead, it is the relative magnitude of successive dissipated energy values which can highlight an increase in energy activity and may be indicative of bump potential. In consideration of this point, two peaks

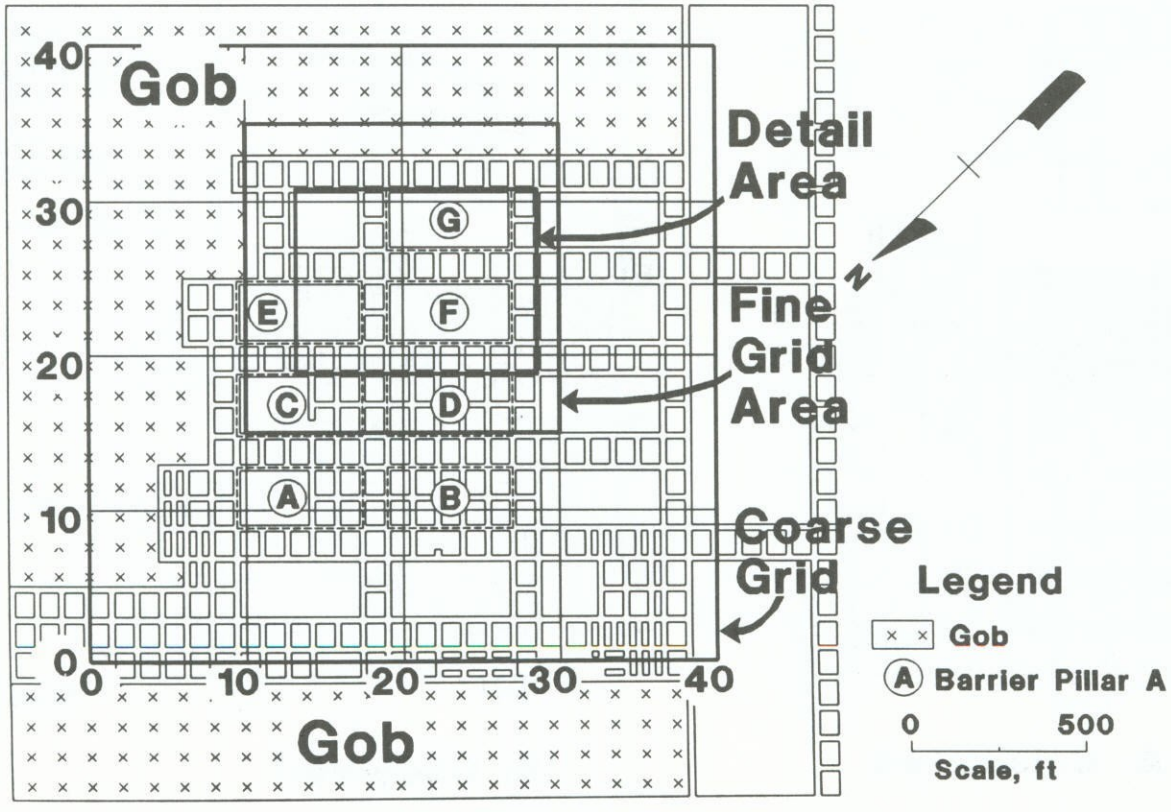

Figure 6. Schematic of the MULSIM/NL grid.

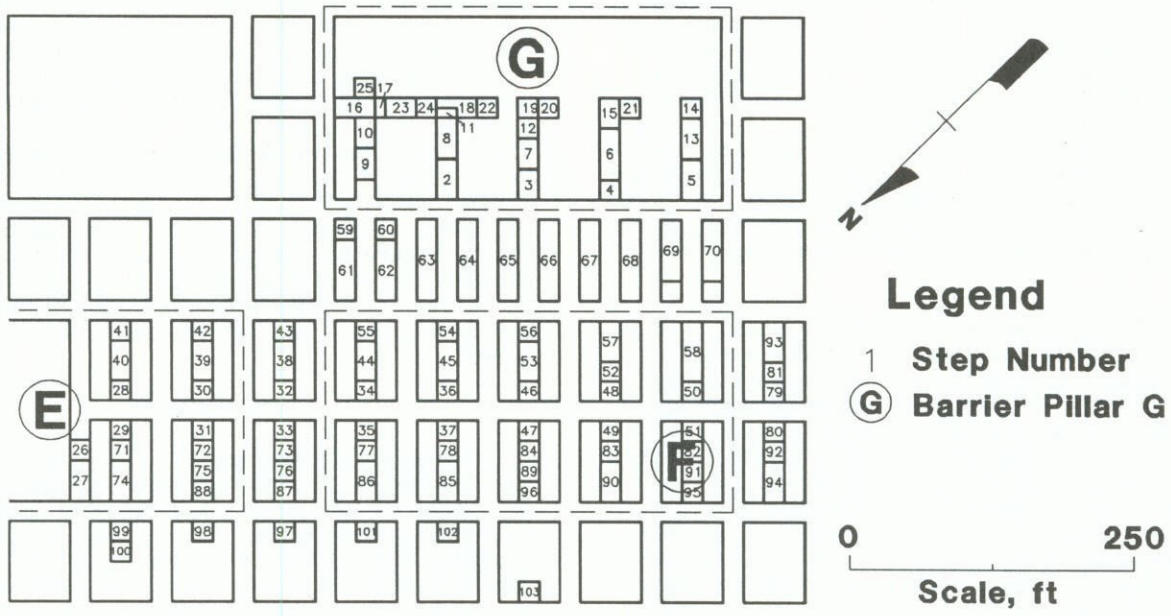

Figure 7. Detail of mining steps used in the model.

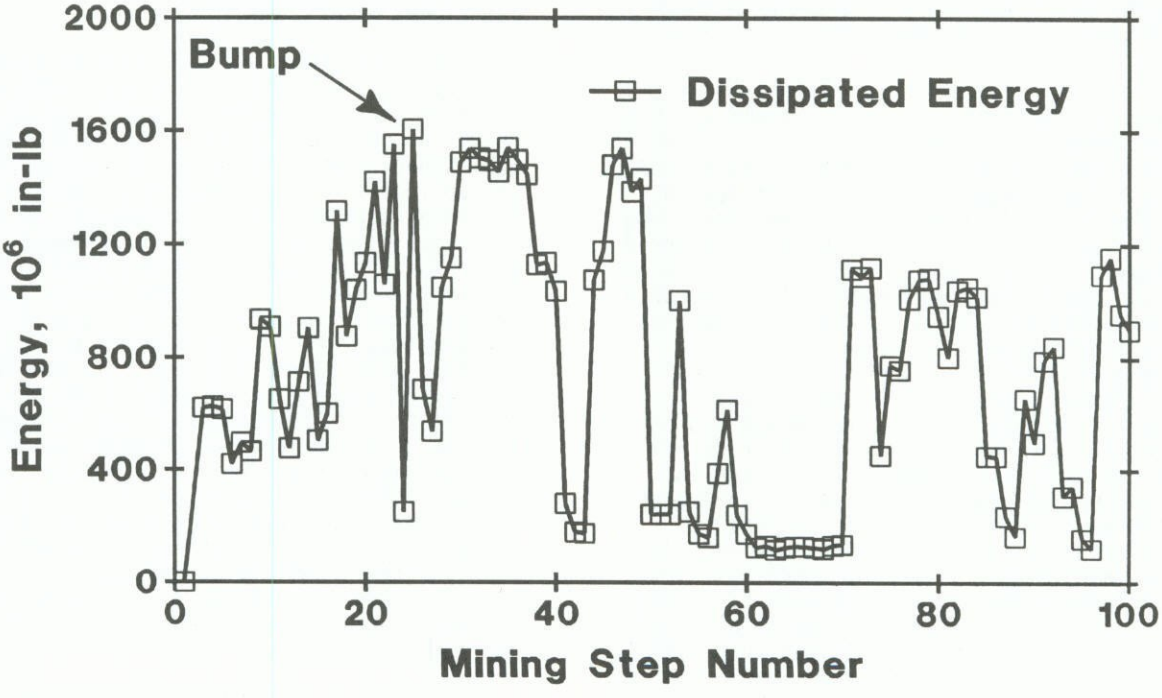

Figure 8. Change in dissipated energy for the cut sequence.

in the dissipated strain-energy in this figure (steps 23 and 25) are somewhat higher than any of the other values. This result is encouraging since both steps 23 and 25 directly preceded and were in the area of the April 22nd bump. Other steps in the model (30-37 and 46-49) also show considerable increases in dissipated strain-energy. A look back at figure 7 shows that the extracted elements in these later steps with large increases in dissipated strain-energy are what the Olga miners call "bump" cuts because this type of initial cut into a pillar has often been associated with bump activity.

It should be noted that all of the steps in figure 8 which show large increases in dissipated strain-energy are "protruding" into high stress areas. This trends seems reasonable considering that increases in dissipated energy come from both the extraction of high stress coal and the yielding and/or material code changes of elements in the surrounding area. Hence the extraction of the elements near a highly stressed area causes considerable element yielding and an associated large redistribution of stress, and also a large number of elements to change material curves. This yielding and material property changes then generates a large increase in dissipated energy. Also, it seems reasonable that any area where numerous elements are close to failure and/or the local mine stiffness is reduced will show even greater increases in dissipated energy when a cut protruding into a high stress area is taken. This scenario of taking a cut in a high stressed area where many of the elements are close to failure seems to be the case with step 25 and the April 22nd lost-time bump.

The question naturally arises as to why an actual bump occurred during step 25, but no noticeably large bumps occurred during the other mining steps which also showed large increases in dissipated energy. The answer to this question requires some additional insight. First, the bump that occurred during step 25 caused a lost-time accident; therefore, it was highly noticeable and well documented. Second, according to the miners, the bump during step 25 was not exceedingly large but was only slightly bigger than many other bumps which occurred throughout the mining of the 9 Right section. However, because these other bumps did not cause injuries, accurate records of their occurrence was not kept; therefore, their timing and location can not be compared to the dissipated energy predicted by the model. Finally, the model does not account for all of the possible inhomogeneities of the mining environment which may, in reality, determine the exact occurrence of a coal bump. For instance, some pillars may be a slightly different (stronger, partings, slickensided, etc.) than others; the pillar may required some anomalous seismic source to trigger the actual dynamic failure; or the mine stiffness may change from one location to another irrespective of the pillar configuration. Any of these situations, and many others, could just as likely explain the exact timing and location of an actual bump and the reason why the dissipated energy calculated by the model does not unequivocally predict the bump occurrence. However, the main point to be made from this entire examination of energy calculations for bump prediction is that the model did show a large amount of dissipated energy in the same place and at approximately the same time as the actual lost-time bump accident and therefore may have been able to forecast the bump hazard. Also, the model consistently indicates large increases in dissipated energy associated with the initial cuts into the pillars ("bump cuts") which have historically had a high incidence of bumps. Thus, the model appears to fairly accurately associate large increases in dissipated energy with potential bump situations; therefore, it should prove very useful for optimizing mining plans and cut sequences for minimum bump hazard.

CONCLUSIONS

The research presented in this paper has demonstrated several innovative modeling techniques and has advanced the current knowledge of energy calculations applied to coal bumps. In the MULSIM/NL program, the use of non-linear materials, in particular strain-softening coal, as a part of a displacement-discontinuity model has greatly increased the accuracy and realism of the modeled stresses and displacements. Also, the ability of the modeled coal to "fail" and dissipate energy has created a entirely new and useful approach for investigating coal bumps. In fact, the strain-softening behavior of the coal and the associated energy changes in the area of the extracted coal appear to be some of the necessary keys to successfully modeling coal pillar bumps.

In the introduction, it was postulated that energy calculations may provide a certain predictive capability as to the location and timing of a coal bump. A considerable degree of this capability has indeed been demonstrated by the investigation presented in this paper. However, from the experienced gained in this investigation, it appears that conclusive bump prediction using energy calculations has some very practical limitations due to the extreme sensitivity of the energy calculations on the value of uncertain input parameters and to the impossibility of modeling all of the actual geologic anomalies. Although, the sensitivity of the calculated energy results to the input properties of the geologic material may very well parallel the true situation underground where small differences in geology or rock properties may ultimately dictate the precise location and timing of coal bumps. Nonetheless, the sensitivity of the energy calculations to uncertain material properties and the inability of the model to account for geologic anomalies appear to be the practical limitations to conclusive prediction of coal bumps using calculated energy values.

However, even without conclusive predictive capabilities, the analysis of the energy values generated by the MULSIM/NL model can provide considerable insight into the possible locations, timing and cut sequences associated with potential coal pillar bumps. And in particular, with the judicious choice of input parameters and the proper analysis of the output energy values, the numerical

model can be successfully used as a tool to investigate the coal bump potential of a mining plan or cut sequence. In fact, energy investigations of active bump-prone mines utilizing the techniques presented in this report can greatly increase operators awareness of potential bump situations and help minimize bump-related accidents.

REFERENCES

1. Blankenship, C. & A. T. Castanon. Multiple Fatal Bump Accident (Outburst). MSHA, 1983, 17 pp.

2. Cook, N. G. W., E. Hoek, J. P. G. Pretorious, W. D. Ortlepp & M. D. G. Salamon. Rock Mechanics Applied to the Study of Rock Bursts. J. S. Afr. Inst. Min. and Metall., v. 66, 1966, p. 436-528.

3. Salamon, M. D. G. Elastic Analysis of Displacement and Stresses Induced by Mining Seam or Reef Deposits (part I). J. S. Afr. Inst. Min. and Metall., v. 64(4), 1963, p. 128-149.

4. Hodgson, K. & N. C. Joughin. The Relationship between Energy Release Rate, Damage, and Seismicity in Deep Mines. proc. of the 8th U.S. symp. on rock mech., 1966, p. 194-203.

5. Salamon, M. D. G. Energy Considerations in Rock Mechanics: Fundamental Results. J. S. Afr. Inst. Min. and Metall., v. 84, 1984, p. 233-246.

6. Gay, N. C., W. D. Ortlepp, J. A. Ryder, O. Steffen & H. Wagner. The Future of Rock Mechanics in South Africa. World Min. Equip., Jan., 1984, p. 36-39.

7. Crouch, S. L. & C. Fairhurst. The Mechanics of Coal Mine Bumps and the Interaction between Coal Pillars, Mine Roof, and Floor. Bu Mines OFR 53-73, 1973, 88 pp.

8. Zipf, R. K. & K. A. Heasley. Decreasing Coal Bump Risk through Optimal Cut Sequencing with a Non-Linear Boundary Element Program. proc. of the 31st U.S. symp. on rock mech., 1990, p. 947-954.

9. Maleki, H., J. Aggson, F. Miller & J. F. T. Agapito. Mine Layout Design for Coal Bump Control. proc. of the 6th internl. conf. on ground control in mining, 1987, p. 32-46.

10. Zipf, R. K. MULSIM/NL Theorectical and Programmers Manual. Bu Mines IC, in press.

11. Campoli, A. A., D. C. Oyler & F. E. Chase. Performance of a Novel Bump Control Pillar Extracting Technique during Room-and-Pillar Retreat Coal Mining. Bu Mines RI 9240, 1990, 40 pp.

12. Condon, J. L. & R. D. Munson. Microseismic Monitoring of Mountain Bumps and Bounces: a Case Study. proc. of the 6th internl. conf. on ground control in mining, 1987, pp. 1-9.

13. Heasley, K. A. An Examination of Energy Calculations Applied to Coal Bump Prediction. Bu Mines RI, in press.

14. Barron, K. An Analytical Approach to the Design of Pillars in Coal. Part 3: Coal Testing and Size Effects. Ottawa: Dept. Supply and Services, 1985, 138 pp.

10th INTERNATIONAL CONFERENCE ON GROUND CONTROL IN MINING

DELINEATION OF ABANDONED WORKINGS WITH AN IN–SEAM SEISMIC METHOD

I. Geldmacher, *Senior Geophysicist*
J. Slade, *Manager-Geosensing*

BHP Engineering (Americas) Inc.
Herndon, Virginia

ABSTRACT

In–Seam Seismic (ISS) methods have been used extensively worldwide for the past 10 years to assist mine planning, especially longwall mining in coal seams. The technique is only starting to gain wide acceptance in North America where it is being applied in a much wider variety of applications than was initially considered. Surveys elsewhere have concentrated on the detection of faults (structures) in coal mines prior to longwall mining. The majority of surveys in North America has been the location of abandoned workings which were not adequately surveyed prior to closure.

Modeling data based upon the lithological logs, geophysical logs and interpreted sections show whether the method will be successful prior to carrying out the survey.

The surveys have been performed to locate abandoned workings from the surface and underground using both seismic reflection and transmission techniques. Data from coal seams in both Illinois and West Virginia will be presented.

A second method where ISS surveys are being applied to detect old workings will be presented. The ISS tomography produces an image of the P–wave and Channel Wave velocities which is representative of the material through which the signal traveled thus identifying the location of the old workings. Data from Texas will serve as an example.

INTRODUCTION

To solve the problem of locating obstructions in a coal seam, the In–Seam Seismic (ISS) technique has gained a distinguished reputation among coal mine operators worldwide for reliability and protecting mine profits. For more than a decade, ISS technology has been an effective production tool for underground coal mines in Australia, Britain, and Germany. U.S. coal mines are now increasingly using ISS to give them an edge in this intensely competitive world environment. This paper will focus on recent ISS applications in the U.S. to locate old mine workings. After a brief description of the technique and the equipment, three case histories are presented. All three examples have been obtained in a day–to–day production mode with no extensive academic efforts. The first case describes in some detail the application of ISS methods in a West Virginia underground coal mine to locate abandoned workings ahead of the current face. The second and third example show ISS utilized from the surface in a borehole–to–borehole mode overlying the targeted old works.

THE ISS TECHNIQUE

In principle the ISS technique involves generating an acoustic or "seismic" signal (for example, by setting off a small explosive charge or "shot") at one point within the coal seam and then measuring the reflected and/or transmitted signals at another point using a "detector" in the coal seam.

Based on this principle two different techniques, ISS reflection and ISS transmission, can both be customized for a particular problem.

The ISS reflection technique is preferred when a large area has to be surveyed and easy underground access is available in some form (see Figure 1). Typically, multiple shot points and detector points are located along the same roadway or any similar access point in the active underground mine facing towards the old workings area. If no underground access is available these points can also be obtained through vertical boreholes. A complete ISS reflection survey will then produce a plan view of the obstructed feature, similar to a mine map. An example is the outline of a system of old workings ahead of the current mine area.

The ISS transmission technique is preferred when the area of interest is more concentrated. The typical arrangement will

involve (at least) two boreholes (or two opposed access points in an underground development) allowing access to the coal seam for one shot and one detector point (see Figure 2). The information obtained then determines whether along the direct line between the two holes any disturbance of the seam can be found or not. An example is the determination of the extent of abandoned workings beyond a given survey line.

THE ISS EQUIPMENT

For working in a mine environment a rugged, portable and safe data acquisition system was developed by BHP Engineering.

The system basically consists of three independent elements which can be located at different places within the mine (see Figure 3). The "heart" of the system is a laptop–like portable computer (the field control unit or FCU). From the FCU the data acquisition process is fully directed and controlled. At the detector location custom designed in–seam geophones record the seismic signal and store it in "intelligent" buffers (the remote seismic digitizer or RSD). The geophones (and the shot points) are physically placed into the coal (i.e. for underground surveys they are implemented in small horizontal boreholes, deep enough to get away from any rib effects; in surface work vertical holes allow access to the coal). The RSDs are simply connected to the geophone output through a single–pair cable through which the survey data are subsequently transferred to the FCU, checked and stored for detailed processing. The third element is a real–time switch incapsulated in a small metal cylinder. This switch is positioned at the shotfiring site to transmit the moment of ignition to the FCU via one single–pair cable. The system has been approved for intrinsic safety in a hazardous environment. Approvals for the United States (from the Mine Safety and Health Administration (MSHA), Approval No. 2G– 3829–0) for Australia as well as for South Africa have been obtained, and applications for the even more stringent rules and regulations of the European Community have been submitted.

Due to the flexible arrangement of the equipment, it's safety features and it's easy–to–use mode of operation the system has proven to work efficiently and unsurpassed in performance on a day–to–day basis throughout the world for almost a decade (see Figure 4).

THE PROBLEM

Abandoned mine workings in a given coal deposit are known to have a significant impact on a mine's operational safety and profitability. However, the problem is site–specific and the best solution to the mining engineer on–site can differ from mine to mine. Some abandoned, but well–mapped mines can easily be approached by leaving a 200' safety zone to the current face and therefore they are no major problem for today's highly mechanized mining processes. An unknown exploration drive from an ancient mine on the other hand can cause significant problems if the active mine operation runs into it and eventually may even justify to shut down an active, profitable mine site. This is to be taken into consideration especially if only little or no knowledge is available regarding the shape, extend or current state of the old workings.

For the ISS technique old workings (or any other obstruction in the coal seam) are basically an area which interrupts the signal propagation in a characteristic way. While in a "clean" coal seam the seismic waves (or channel waves) travel in a clear, predictable mode (which can be observed between any shot/detector point combination) the obstruction modifies this pattern. The pattern itself depends on numerous things such as seam thickness, length of travel path, height and length of obstruction, roof and floor conditions, and others (see Figure 5).

The ISS reflection technique can be customized in a relatively simple way in any underground old workings environment. As mentioned above (see Figure 1) the ISS signal characteristic of a signal travelling between a shot point A and a detector point B depends upon the path A–B itself. In a reflection layout this path is not the direct way from A to B, but includes a reflected portion (i.e. the signal travels from point A to the obstruction and is then bounced off to be recorded at B). Depending on the distance (and other coal characteristics) between the survey set–up and the target (i.e. the old workings) the recorded signal will be different. This difference can be used to determine the boundary of the old mining area (in relation to the current workings). An important consideration is the accuracy of the final "old workings mine map". For a data set with good quality data the accuracy can be better than 10% of the target distance (e.g. the boundary of old workings 800 feet ahead of the current mine area can be located within 80 ft.). The ultimate confirmation to find the accuracy of a survey in unknown territory is a field experiment with a known target feature. Numerical modeling of a given problem also offers numerous possibilities in checking, confirming, and reevaluating ISS reflection data (see Figure 6). For the location of old workings all these (and more) methods can be applied and together will provide a good overall picture. The West Virginia case described below will give an example of the ISS reflection technique.

If no underground access to the coal is available the detection of old workings can economically be achieved by the ISS transmission technique (see Figure 2). Since the abandoned mine is a local clear–cut feature it generally has well–defined (vertical) corners, edges or borders against the virgin coal. Therefore, the ISS signal between any set of transmission–points A and B will "see" whether there is in fact "clean" coal (as between A and B in Figure 2) or some portion of the coal has been replaced by a cavity (as between A and B_2

in Figure 2). However, if only transmission data are available it is extremely difficult to point out the exact location along A–B (i.e. locate the position of the old workings between A and B). BHPE is currently researching the problem with tests of surface 3–D phones. Below, the second case history with data from Illinois will illustrate the ISS transmission technique.

If an ISS transmission survey can be extended to a degree where the source/detector positions "surround" the target (see Figure 7) area a processing technique called "seismic tomography" can reveal a map– like coverage of the old workings. The third case history presented below will show an example of this method in a Texas lignite deposit.

ISS REFLECTION IN WEST VIRGINIA

The case presented here is a summary of the results from an underground In–Seam Seismic (ISS) reflection survey carried out during a 6–hour field stay at Marrowbone Development Company.'s Western Mingo No. 1 Mine in Naugatuck, West Virginia, in January 1991.

The survey was carried out in preparation of a large scale exploration survey to pre–define accuracy and reliability levels. The target area was well mapped and known in detail by the mining company, however no knowledge was passed on to the field personnel in order to obtain an unbiased picture from the ISS alone.

Before discussing details it has to be pointed out that due to the short survey length, the area with a confident coverage is limited; all investigations concentrate within the first 200 m (approx. 600 feet) of the coal; and all data and values are presented in the international mks–system (e.g. distances are given in meters [m]).

A total of 25 5–feet long horizontal boreholes at an average spacing of 30 feet were prepared by the mine to position shots and detectors (see Figure 8).

From the data processing numerous characteristics of the ISS reflection method can be illustrated (see Figure 9–12). Feature 1 is a typical singlepeak echo which can be found in every ISS reflection image. Though persistent, it is interpreted as a so–called "apparent reflection". To rely on any reflection image a continuous image (over at least 3 echos) has to be present. ISS reflection therefore exhibits difficulties if (sharp) bends or corners are part of the target. The number of single echoes which can be regarded as a "true" reflection depends on the given survey lay–out, shot–detector spacing, detector–detector–spacing and other factors. Feature 3 (in Figure 10) is an example of a signal with a good confidence. The reflection signals delineate a reflection target at a distance of approximately 110–115 m. Since the feature appears to be of a relatively small extension (parallel to the direction of the roadway in which the survey took place) it is difficult to mark the exact edges. From the nvestigation the best estimate is that this "advanced development" lies somewhere between hole 16 and hole 8 and has a maximum extension (parallel to the roadway) of 40 m. It has to be stressed that these values are estimates only since the bend in the survey line complicates an exact reading.

With the second feature (4) shown in Figure 10 the most irritating reflection target was identified. Depending on the parameters of the analysis it seems to "jump" back and forth relative to the roadway. It's position in line with feature 3 is misleading since other images position feature 4 further back. Since it is very sensitive to the physical parameters of the processing it can be interpreted as a corner area in the workings where sufficient coverage is (physically) limited. Numerous arrivals in the first 100 m of the area were investigated (see Figure 11). These small features or "apparent reflections" (marked as feature 5) are regarded to be non–relevant for a reflection analysis since their appearance is erratic.

A valuable guiding value for the significance of a reflection signal can be obtained from a so–called "confidence spectrum" (Figure 11). As illustrated in the spectrum at the top of the plot the only signals with a good confidence value are to be found in the (upper) left corner of the striped area (feature 2). This reflection suggests that feature 2 is a slightly bending roadway. The roadway character is illustrated by two distinctive reflections. It is difficult to decide on the width of the roadway since the signal is not travelling in the coal but within the air–filled roadway.

To summarize the ISS investigations all non–relevant signals have been suppressed where possible and the result is shown in Figure 12. Feature 1 is still persistent and the roadway in the (upper) left corner (feature 2) as described above is obvious. The "advanced development" (feature 3) shows with a clear response, feature 4 has been defined as well as possible, and the "apparent reflections" (feature 5) are minimized.

After the data have been presented to Marrowbone Development Company a mine map was made available to evaluate the performance of the ISS method (see Figure 13). The comparison between the mine map and the ISS findings are remarkable. Shape and position of the old workings could well be identified. The accuracy of the method in terms of positioning was found to be in an acceptable 10% range (of the target feature).

ISS TRANSMISSION IN THE ILLINOIS BASIN

A borehole–to–borehole ISS transmission survey was carried out during the fall of 1990 from the surface over the old (abandoned) Bernard Mine located west of Cutler Echoes

Company & Kathleen Mine in Cutler, Illinois. The survey targets old workings in the Herrin No.6 seam under a surface cover of approximately 110 to 120 feet (see Figure 14).

The survey was performed to economically determine the maximum extend of the old works towards the south, relative to the proposed new underground developments of the Kathleen Mine. The survey was performed in multiple phases to minimize costly drilling expenses.

The complete survey consisted of a total of 15 boreholes. Geophones were grouted in at 6 locations. The remainder of the holes served as shot point locations. Average borehole spacing was 750 feet.

From earlier works in the area and numerical modeling of the seismic wave propagation the characteristic response of the ISS signal was well known (see Figure 15). The modeling concluded with the finding that ISS transmission methods are likely to work despite the fact that problems may arise from a fire clay layer in the floor of the seam. Considering the limitations outlined by the modeling results the dispersion analysis had to be performed with particular care, however, a "clean" travel path in coal could generally be well differentiated from a "disturbed" travel path influenced by old workings between a shot point and a detector point (see Figure 16).

The final ISS interpretation indicates a slightly different location of the old workings (see Figure 17). It became evident that the old works penetrated about 800 feet further south than previously expected. The survey results will aid in planning the new mine developments.

ISS TRANSMISSION TOMOGRAPHY IN TEXAS LIGNITE

An ISS survey was planned to locate the abandoned Bear Grass No. 2 Mine in Northwestern Resources lignite deposit near Jewett, Texas. Preliminary information about the old works were sparse and partly contradictory to the findings obtained from drilling (see Figure 18). The gently dipping lignite formation averages a thickness of about 8 to 9 feet with a carbonaceous clay parting of 1 to 1.5 feet thickness under a 90 to 150 feet of cover. Roof and floor are described as a clay formation. The survey was to use ISS reflection techniques in a borehole–to–borehole mode, however, during the preliminary drilling and from the difficulty of the target the mode of operation was modified to allow an ISS tomographic technique to be employed. Field operation was carried out during a total of 4 days late in 1990.

A total of 43 boreholes were utilized in the final survey. Geophones were grouted in at 7 locations.

The extent of the survey area forbids to collect data simultaneously at all 7 geophones (as would have been useful). A maximum of 5 detectors recorded data at the same time.

A tomographic analysis depends primarily on the number of intersecting rays which pass through the subsurface and thereby provide a sufficient number of transmitted seismic signals through the target feature (i.e. the old workings). The complete ray path image (see Figure 19) shows that a sufficient coverage with the given borehole layout can only be expected in the southern portion of the survey area.

For the final tomographic image (see Figure 20) a (simplified) interpretation can be summarized by stating that the high velocity zones correlate with the blocks of lignite which are non–mined, and low velocities correlate with workings. Between the line from shothole 9019 to 9023 and the geophone in hole 9069 there is an intermediate–to–low level zone which correlates well with the zone where most cavities were encountered during drilling. This zone extends to the east to include the mine shaft.

A final interpretation (see Figure 21) shows the re–adjusted position of the old works relative to the survey boreholes.

ACKNOWLEDGEMENT

We would like to thank Cutler Mining Company, Marrowbone Development Company, and Northwestern Resources for the permission to publish the survey results.

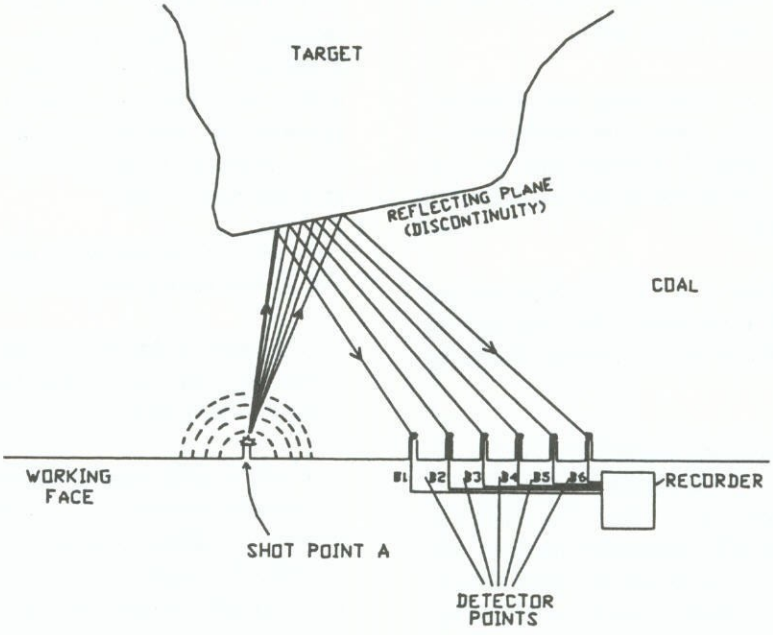

PLAN VIEW OF A COAL SEAM

Fig. 1. Schematic ISS Reflection Layout

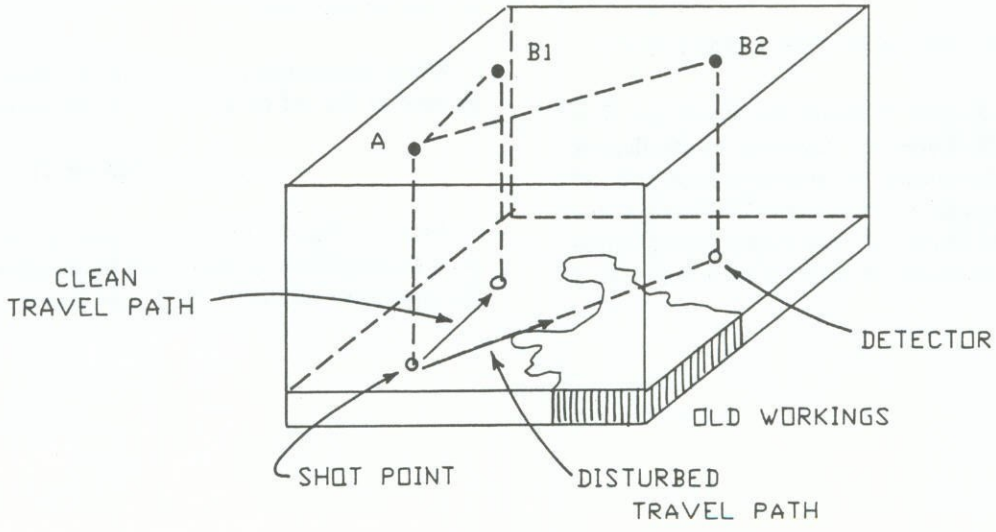

Fig. 2 Schematic ISS Transmission Layout

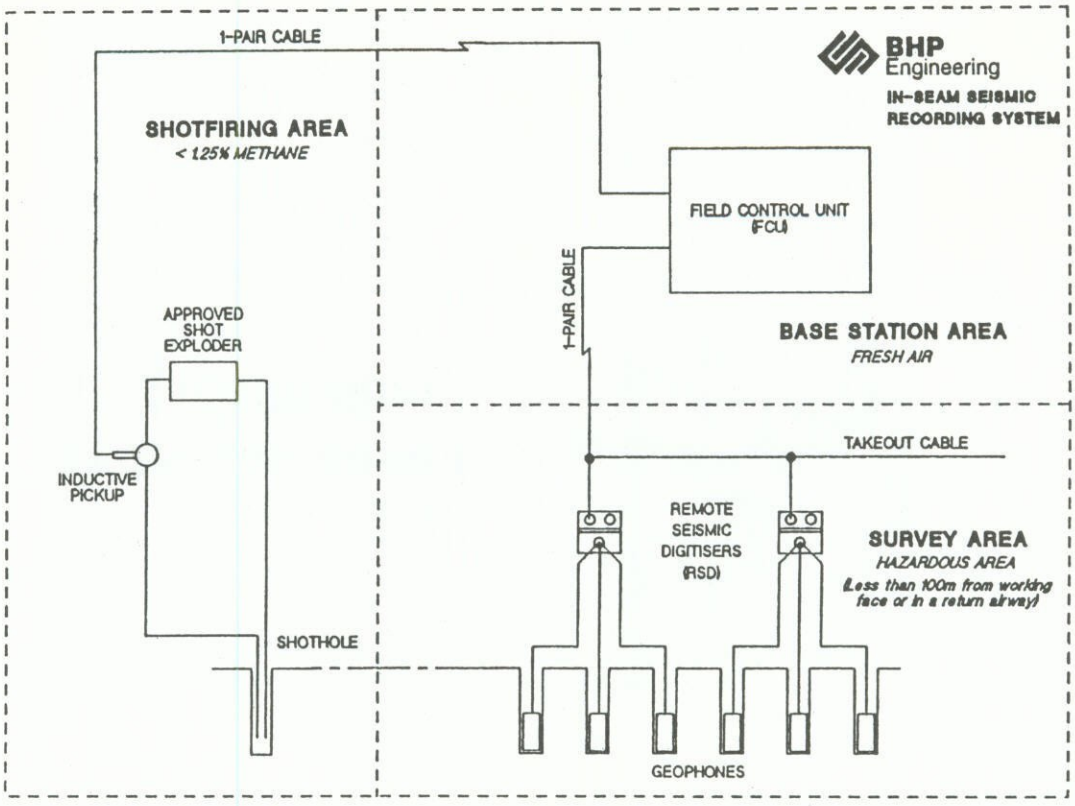

Fig. 3 ISS Equipment Flow Chart

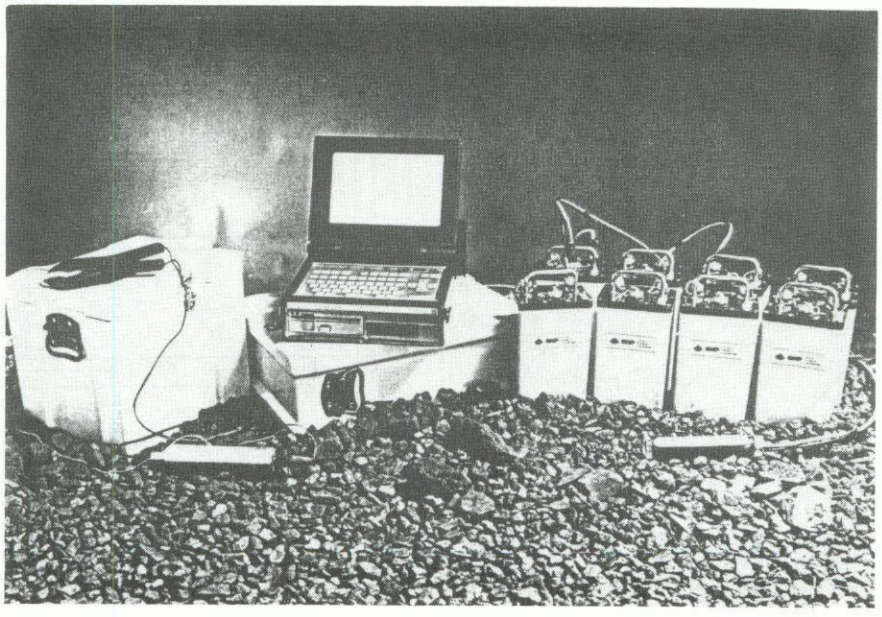

Fig. 4 ISS Equipment

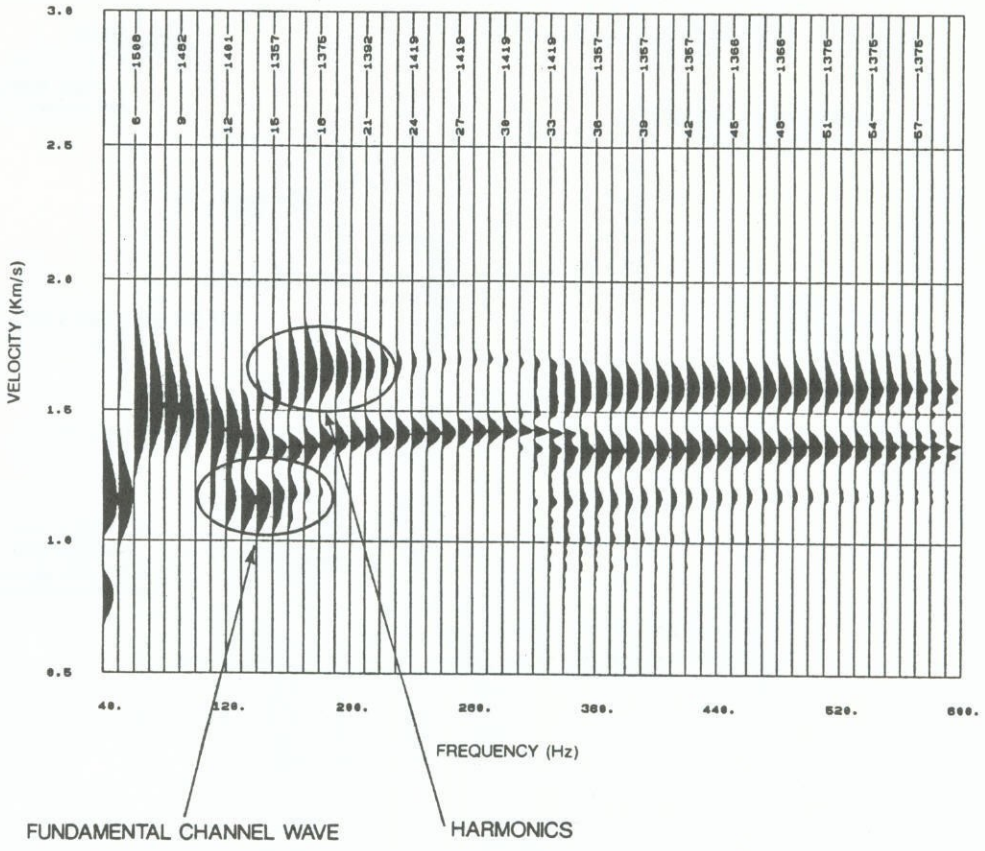

Fig. 5 Signal characteristic (dispersion curve) of seismic signal.

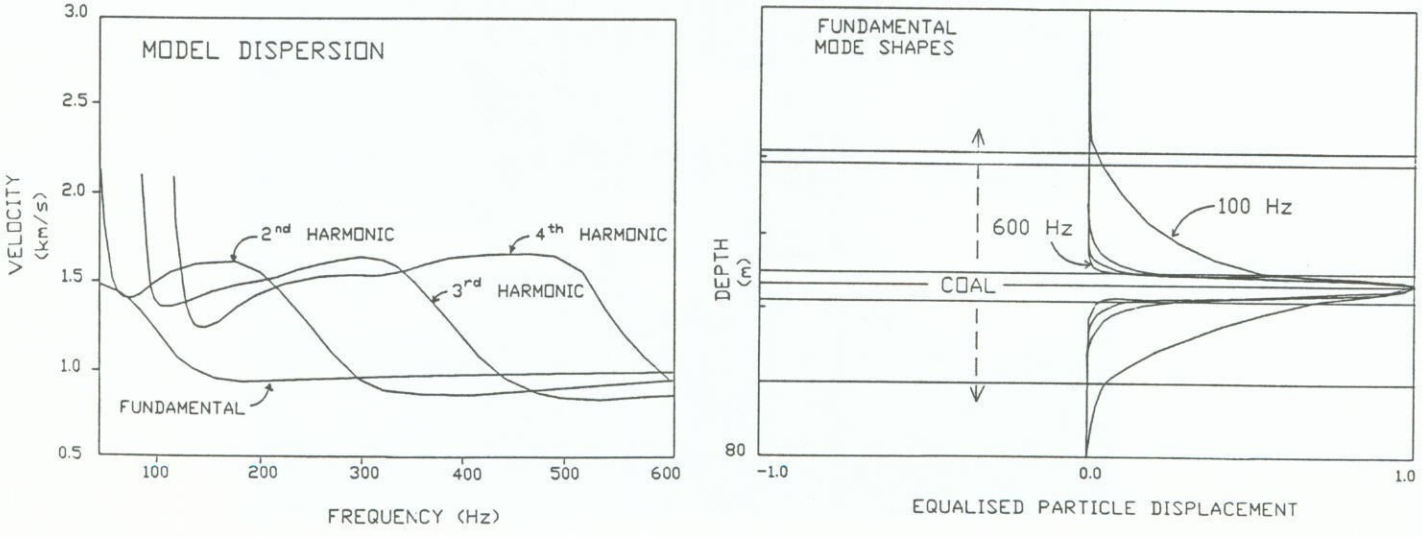

Fig. 6 Numerical modeling of ISS signal characteristic.

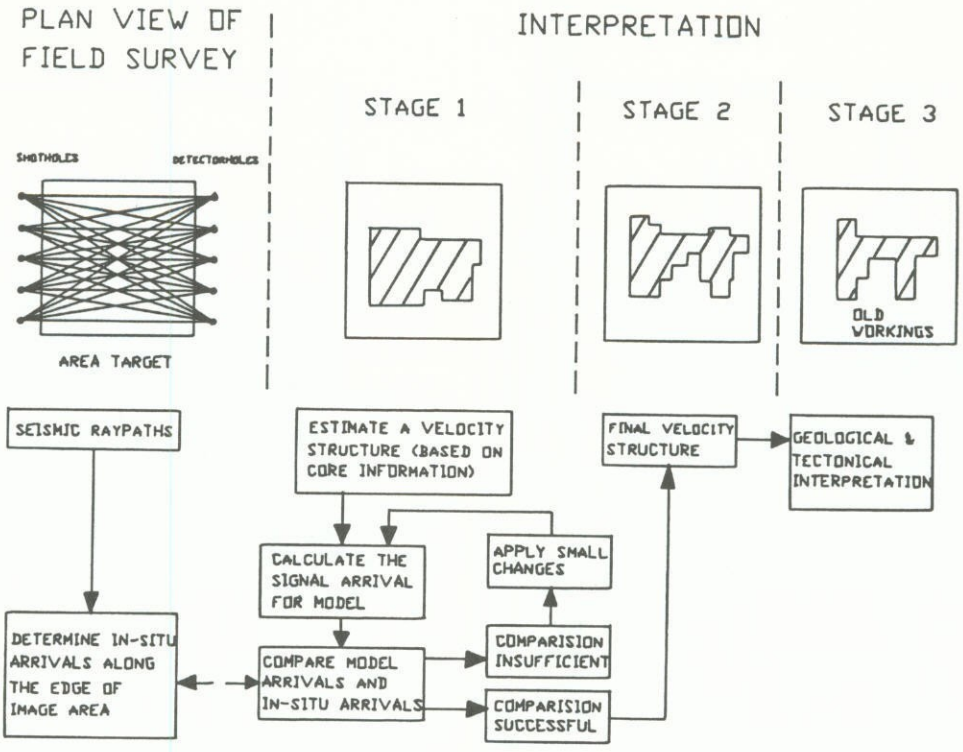

Fig. 7. Tomography flow chart.

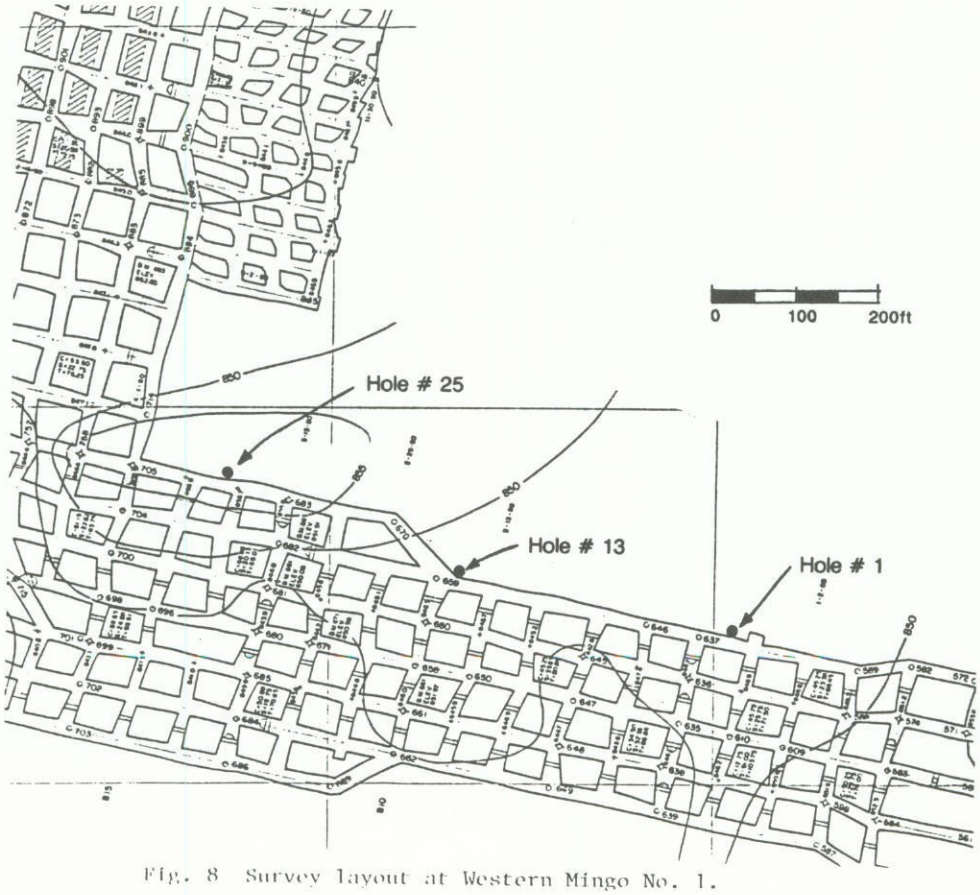

Fig. 8 Survey layout at Western Mingo No. 1.

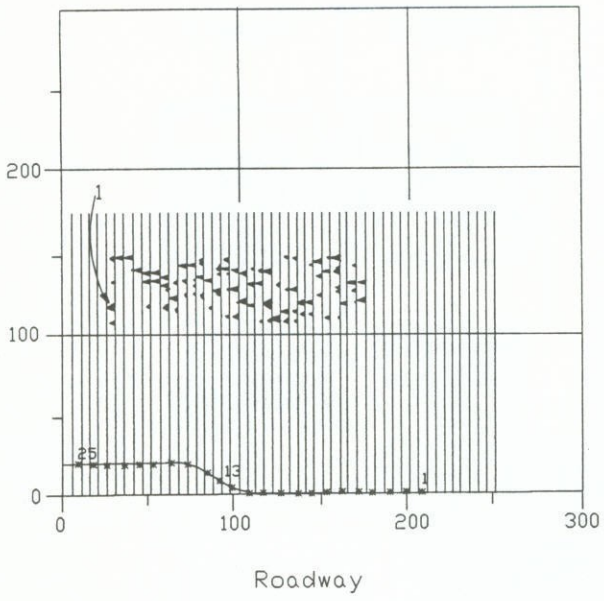

Fig. 9 ISS Reflection Results
(for explanation see text)

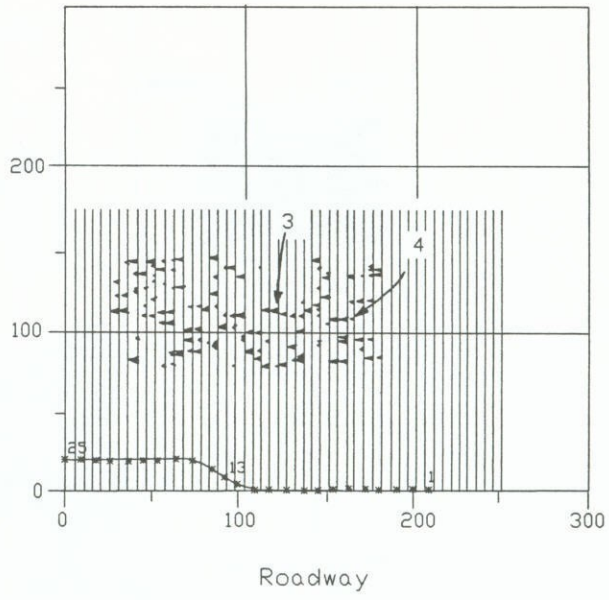

Fig. 10 ISS Reflection Results
(for explanation see text)

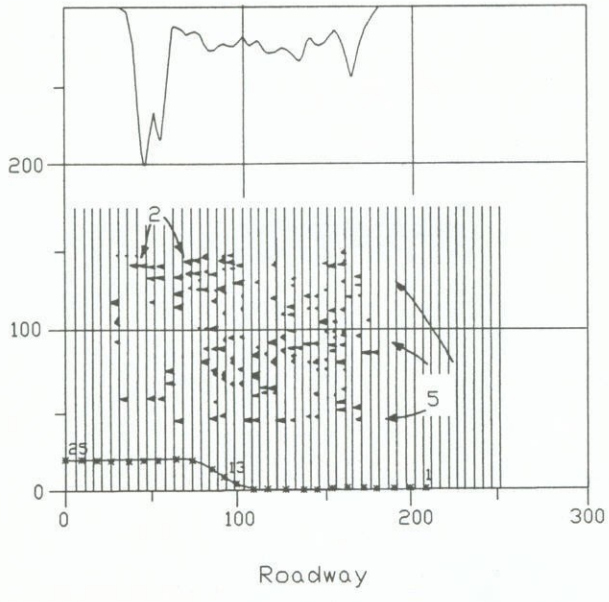

Fig. 11 ISS Reflection Results
(for explanation see text)

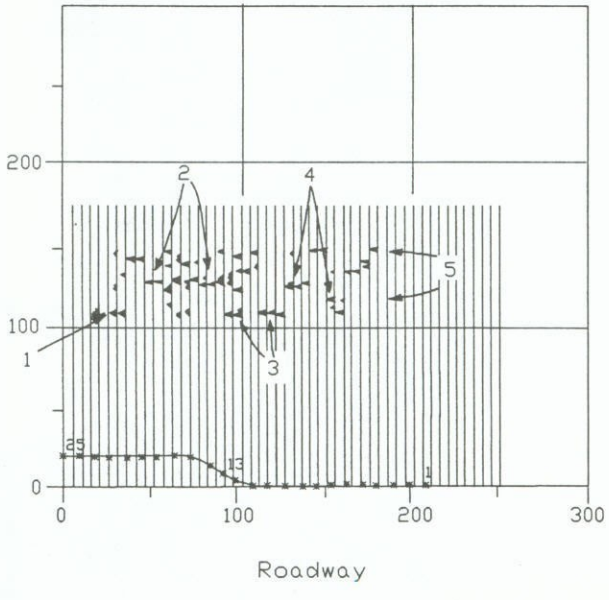

Fig. 12 ISS Reflection Results
(for explanation see text)

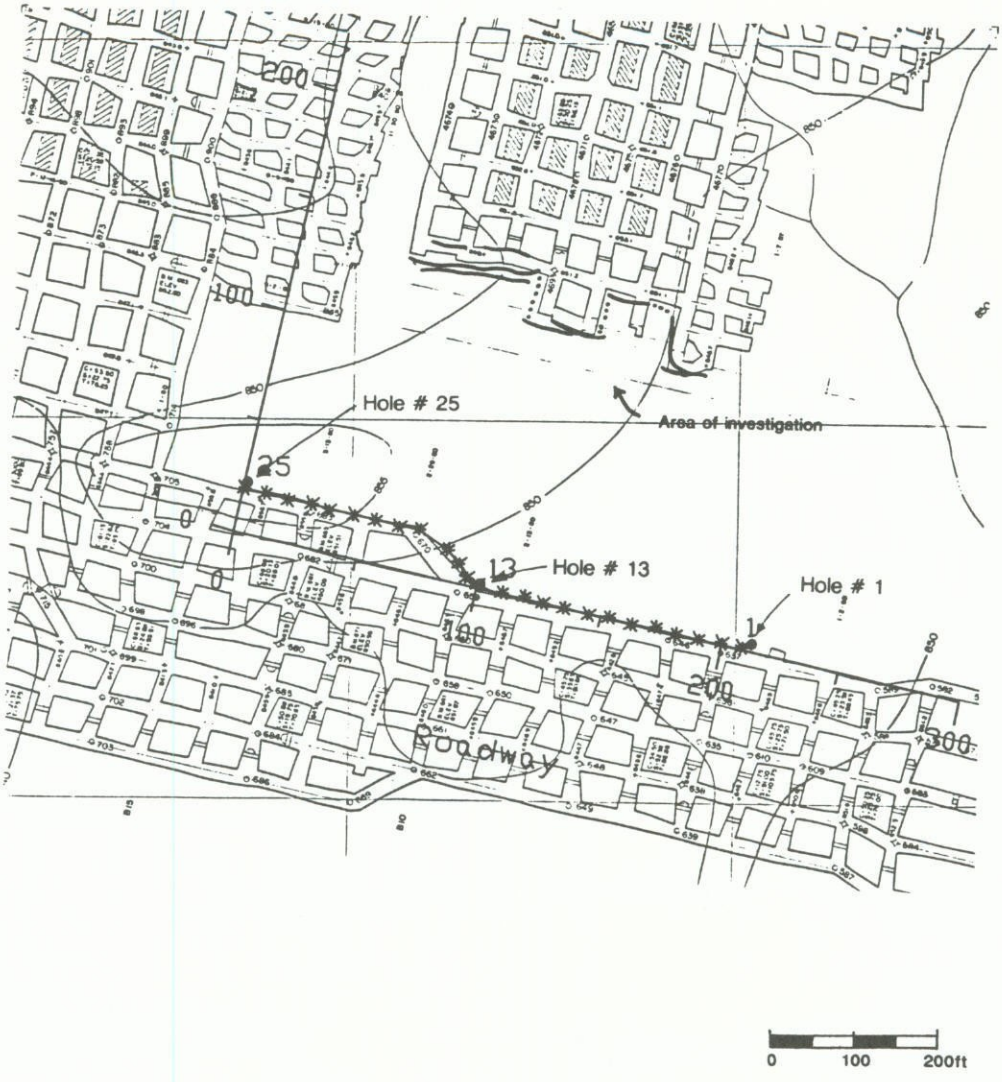

Fig. 13 ISS Reflection Results (for explanation see text).

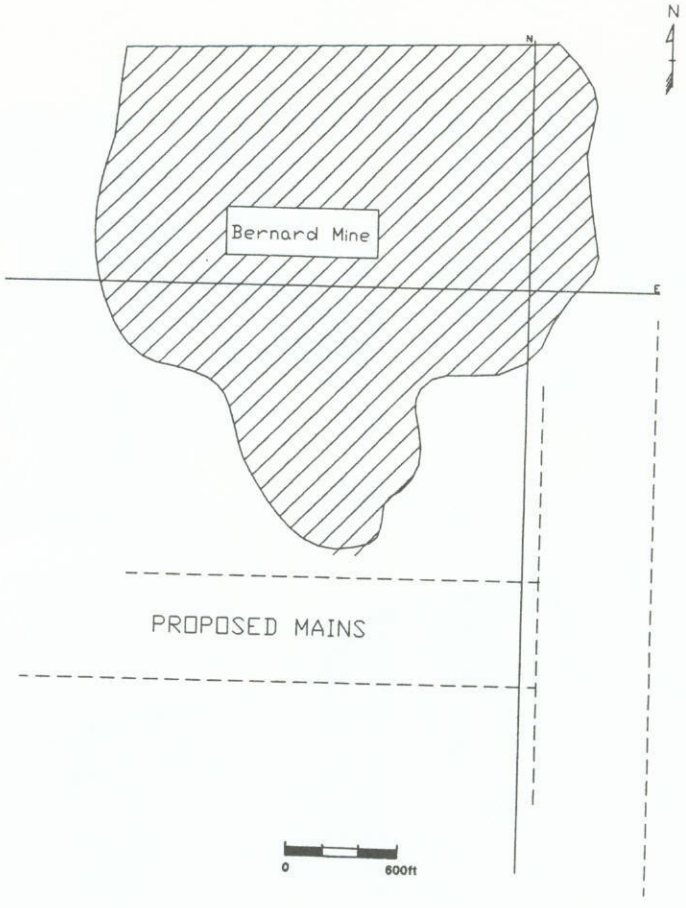

Fig. 14 Target area at Cutler Mining Co.

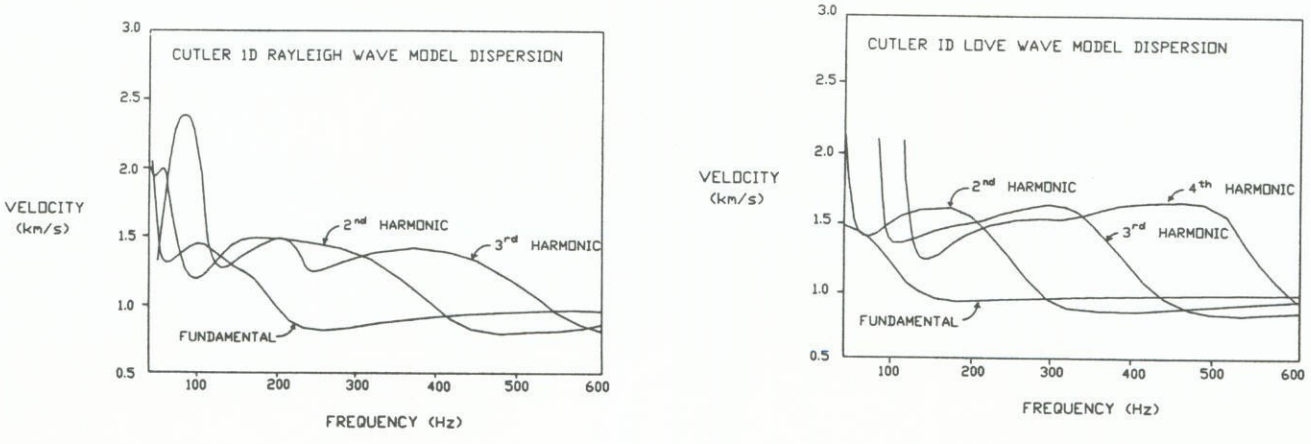

Fig. 15 Modeling results.

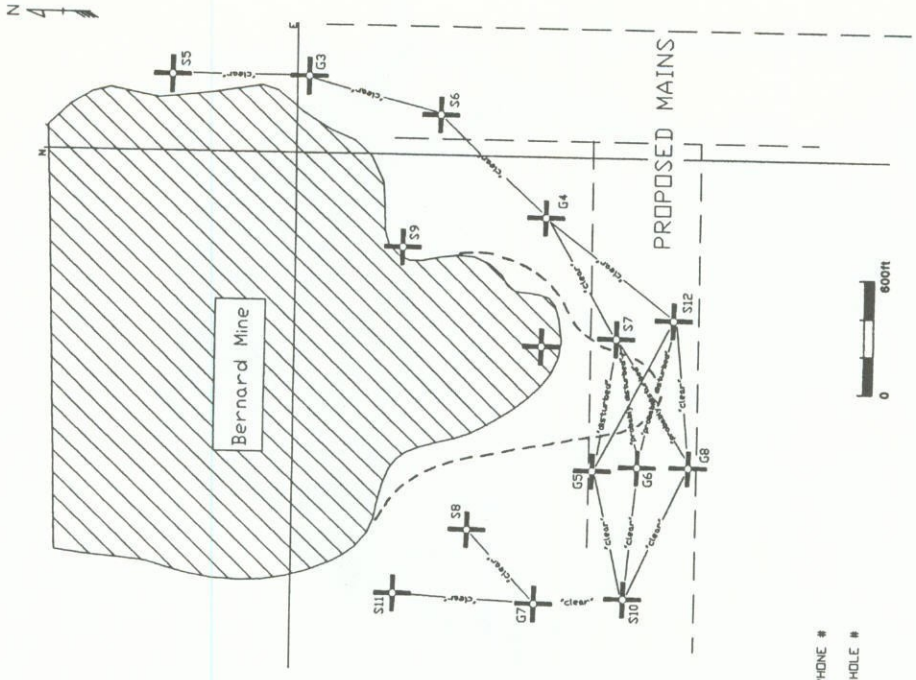

Fig. 17 Final ISS interpretation for Cutler Mining Co.

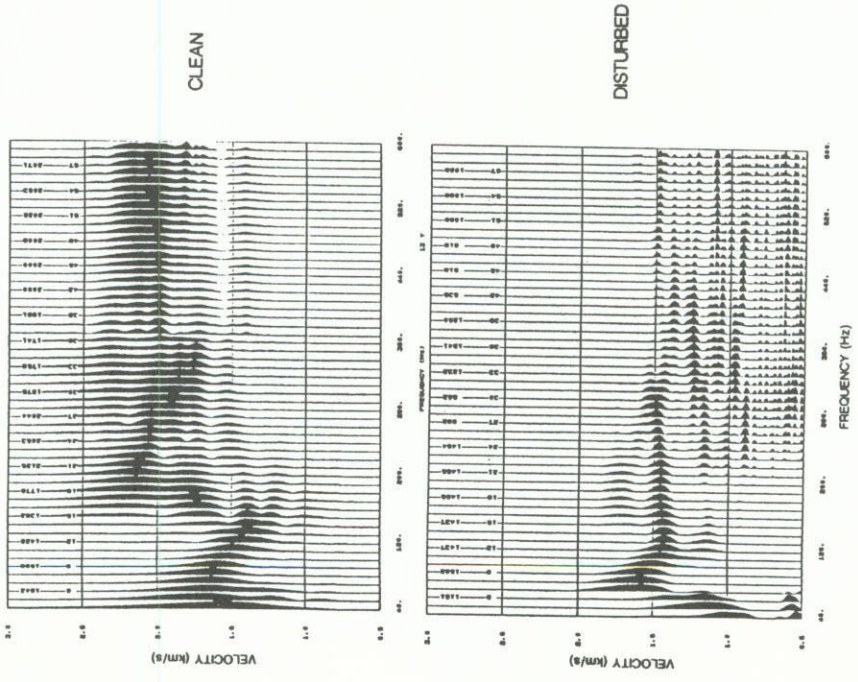

Fig. 16 Dispersion analysis through different seam portions.

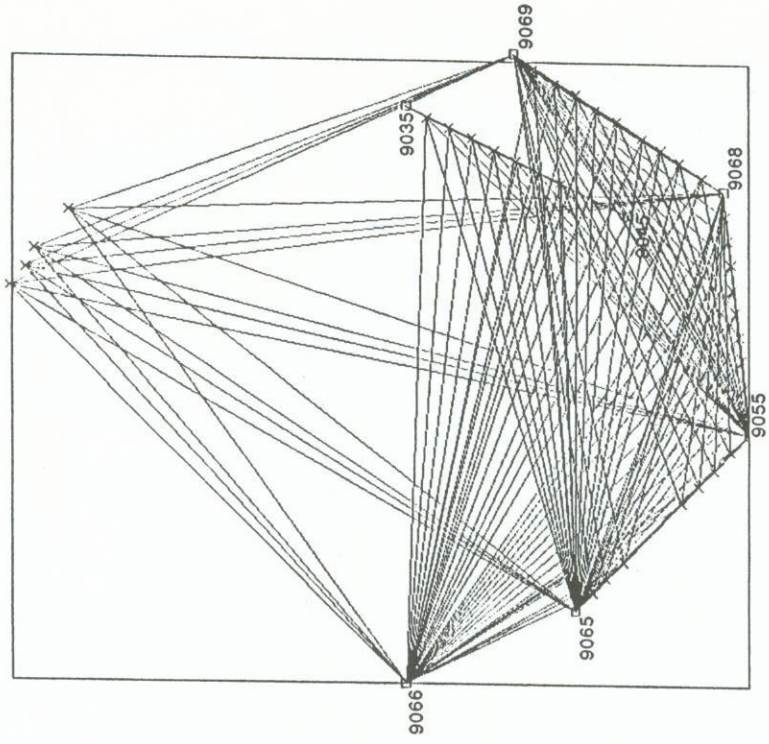

Fig. 19 Ray path coverage in survey area.

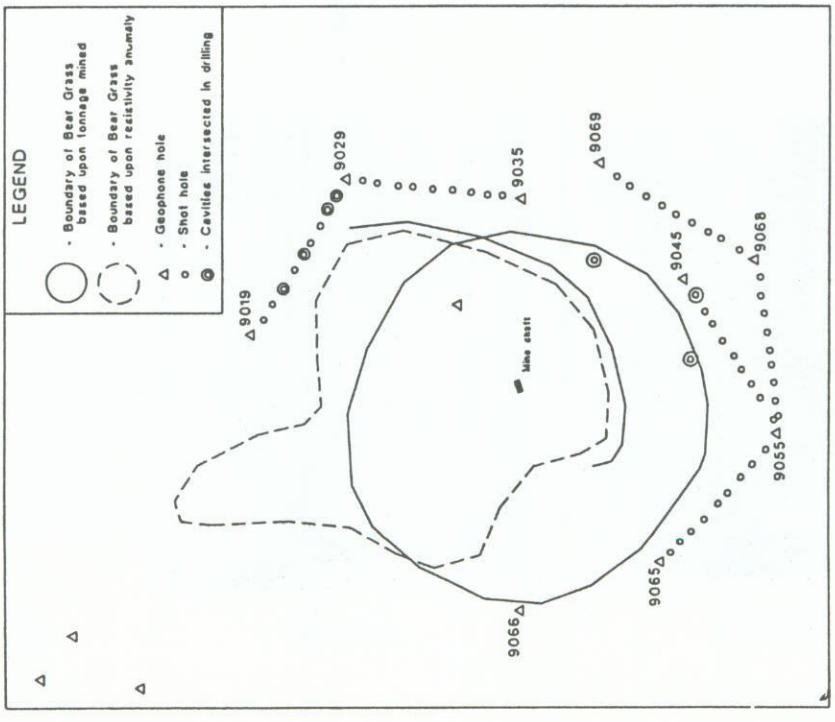

Fig. 18 Northwestern Resources survey area.

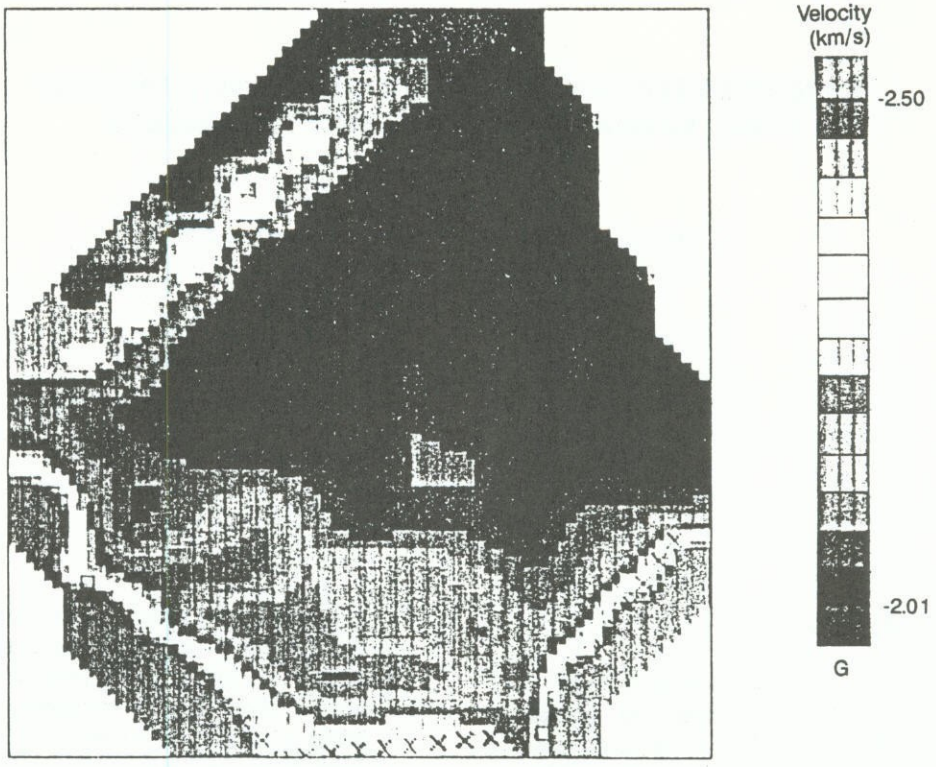

Fig. 20 Tomographic image

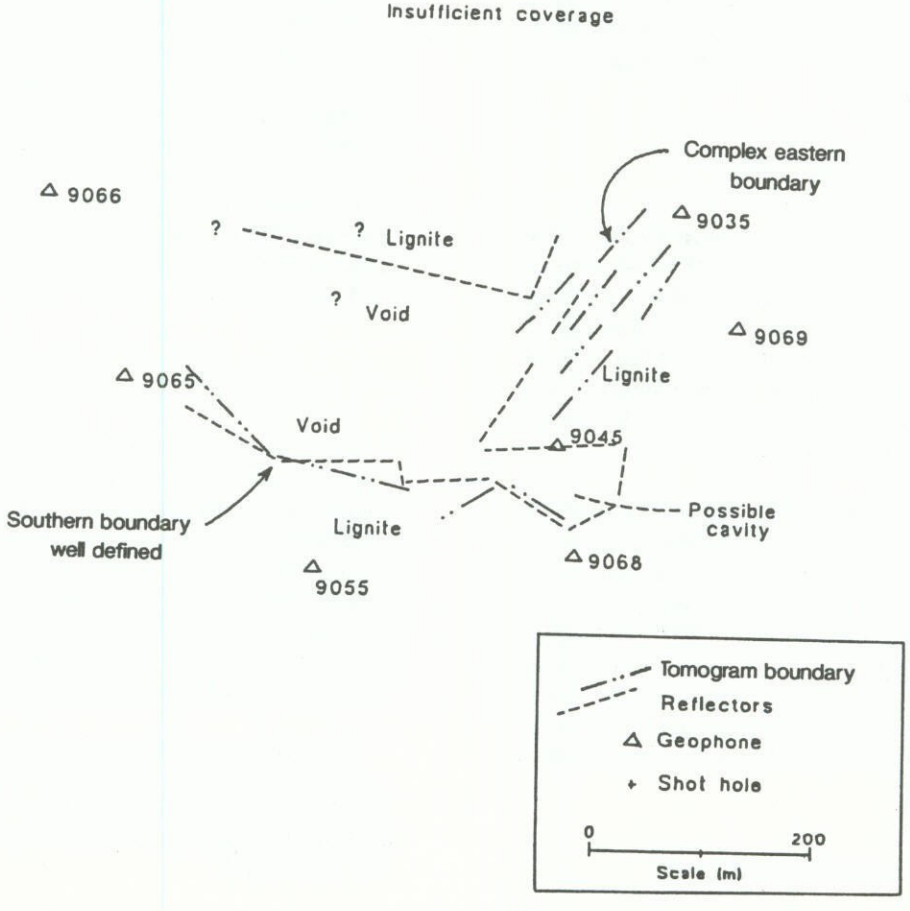

Fig. 21 Final interpretation for Northwestern Resources' survey site.

10th INTERNATIONAL CONFERENCE ON GROUND CONTROL IN MINING

REMOTE DETECTION OF ABANDONED MINE WORKINGS USING RADIO IMAGING METHOD TECHNIQUES

James G. Schotsch, *Director of Operations*
Stolar, Inc.
Westminster, Colorado

and

Tommy Sutton, *Chief Mining Engineer*
Buck Creek Mining, Inc.
Sullivan, Indiana

ABSTRACT

Unmapped abandoned mines are hazards for underground mines, surface mines and surface structures. The Radio Imaging Method (RIM) provides a cross borehole technique to remotely detect abandoned mine works. RIM was used at the Buck Creek Mine, an underground coal mine, to determine the extent of unmapped mine works. The information provided by the RIM survey assisted the mine planners in developing their mine.

INTRODUCTION

Unmapped abandoned mines are hazards for underground mines, surface mines and surface structures. Mining operations risk employee safety, flooding, decreased reserves and loss of revenue. Damage to surface structures can range from cracked foundations to a total loss of the structure. Mine engineers and architects can eliminate the risks when they know where unmapped mine works are located.

Radio Imaging Method (RIM) technology provides remote sensing of subsurface geologic features. Production panels in coal, trona, and potash mines have used in-mine RIM techniques to image a variety of geologic features.[1,2,5,6] Crosshole RIM techniques have provided information for long term mine planning.[4,5] Recently, RIM has been used to detect abandoned mine works at an underground coal mine, several surface coal mines and at a surface construction site.

RADIO IMAGING METHOD

When a mineral seam is surrounded by more conductive layers, a natural waveguide for transmission of radio waves exists in the formation. The RIM survey method is based upon the transmission of radio waves along ray paths in the waveguide. A radiating antenna is used to excite seam wave propagation. Energy is coupled from the radiating antenna to the natural seam waveguide causing electromagnetic (EM) wave signal energy to travel along a straight ray path in the seam to a distant receiving antenna. When the signal energy arrives at the measuring station, an electromotive force (emf) is induced in the receiving antenna. The emf voltage is measured by a calibrated receiver. The measured amplitude and phase are analytically processed to determine the attenuation rate and phase shift along the ray path. Geologic anomalies that intersect the ray path cause measurable changes in the attenuation rate and the phase shift of the propagating EM wave.[7]

CROSSHOLE SURVEY PROCEDURE

In a crosshole RIM survey, a transmitter and a receiver probe are lowered in separate boreholes to the target seam. Radio signal amplitude and phase are measured on ray paths between the boreholes. Measurements are made and recorded at different frequencies and depths. When the measurements of a borehole pair are complete, the transmitter or receiver unit will move to another borehole and the measurements of another borehole pair will begin.

Typically, all of the ray paths within range will be measured during a survey. The operating range will depend on the signal frequency, seam height and the electrical properties of the surrounding rock layers and the bulk coal.[8]

Between each pair of boreholes, a radio signal is launched in one borehole and received (measured) in a companion borehole. Along the ray paths, geologic anomalies cause the EM wave propagation constants to change rapidly.[7] In detecting unmapped mine works, the RIM signal is measurably altered by flooded mine openings and caved mine works.

With respect to the optimum ray path length, consideration must be given to the size of the target anomaly relative to the length of the ray path and the anomaly's effect on the signal measurements. For example, when one ten foot wide abandoned mine entry is the critical target, a ray path 500 feet long may not be appropriate. A ray path distance of 200 feet may be necessary to insure that one entry provides a significant portion of the total signal attenuation.

The RIM probes require at least a 2 inch I.D. PVC casing in a borehole. The probes are 13 feet long and 1.75 inches in diameter. The components of the probe are the antenna, the transmitter or receiver unit, the battery pack and the optic light to analog converter. Each probe is suspended in a borehole by an optic fiber cable.

Both probes are operated from the receiver site. A PC computer commands the probe's power, frequency, battery checks and calibration checks. An oscilloscope provides a visual display of the received, phase coherent signal.

BUCK CREEK APPLICATION

Site Characterization

The Buck Creek Mine is located five miles south of Sullivan, Indiana. The surface topography is flat. The primary land use is farming. The seam being mined is the Indiana No. 5 Coal Seam and its depth is approximately 300 feet. The seam has an average height of five feet and dips to the southwest.

The two compartment slope for the Buck Creek Mine was started in January, 1989 and coal production began in May, 1989. The Buck Creek Mine is operating two sections. Both are adjacent to the Ebbw Vale Mine, a flooded abandoned mine. Currently, one section is mining south of the Ebbw Vale Mine and the second section is mining north of the Ebbw Vale Mine. Each section produces coal with a continuous miner unit and shuttle car face haulage. The mine uses belt haulage and rubber tired vehicles.

The Ebbw Vale Mine map is known to be inaccurate. Buck Creek wants to safely mine the reserves surrounding the abandoned mine without interrupting mining to drill horizontal test holes. Figure 1 is a mine map of the survey area.

The Ebbw Vale Mine was opened in the early 1920's and closed in 1933. This mine typically developed two or three entry mains and two entry sub-mains. Production rooms were developed to the left and right of the sub-mains. The water table in the area is typically 150 feet above the seam, so the Ebbw Vale Mine is assumed to be flooded.

The inaccuracy of the available map of the Ebbw Vale Mine is confirmed by two sources. First, the last date posted on the map is May, 1930. However, the Indiana Department of Mines and Minerals records indicate the mine was closed in 1933 and that 300,000 tons of coal were extracted from the mine after the last posted date.

The second source is the occurrence of unmapped mine voids which have been intercepted by boreholes. At least four exploration boreholes near the perimeter of the Ebbw Vale Mine have drilled into mine works where the map indicates solid coal.

Survey Procedure

The RIM survey project at the Buck Creek Mine was conducted in three phases. The first phase was signal calibration measurements in the mine using in-mine RIM equipment. The second phase was crosshole signal calibration. The third phase was the crosshole survey of the borehole picket line. A follow-up in-mine calibration was conducted in October, 1990 in the development entry near the borehole picket line north of the abandoned mine.

In-Mine Calibration

In March, 1990, in-mine RIM signal calibration measurements were conducted to provide signal source strength and signal attenuation rate information in order to estimate the same parameters for the crosshole system. In-mine RIM equipment are hand carried transmitter and receiver units. Each is attached to a 30 inch loop antenna. Typically, the antenna is mounted to a tripod.

During the calibration survey, the RIM transmitter was stationary and the receiver was moved away from the transmitter station. Measurements were recorded on intervals of 50 feet. The results are shown on Figure 2 and labeled "Original In-Seam Calibration". The source strength (y-intercept) is 164 dB and the attenuation rate (slope) is 14.3 dB/100 feet.

Based on the in-mine measurements, the crosshole RIM parameters were estimated to be a source strength

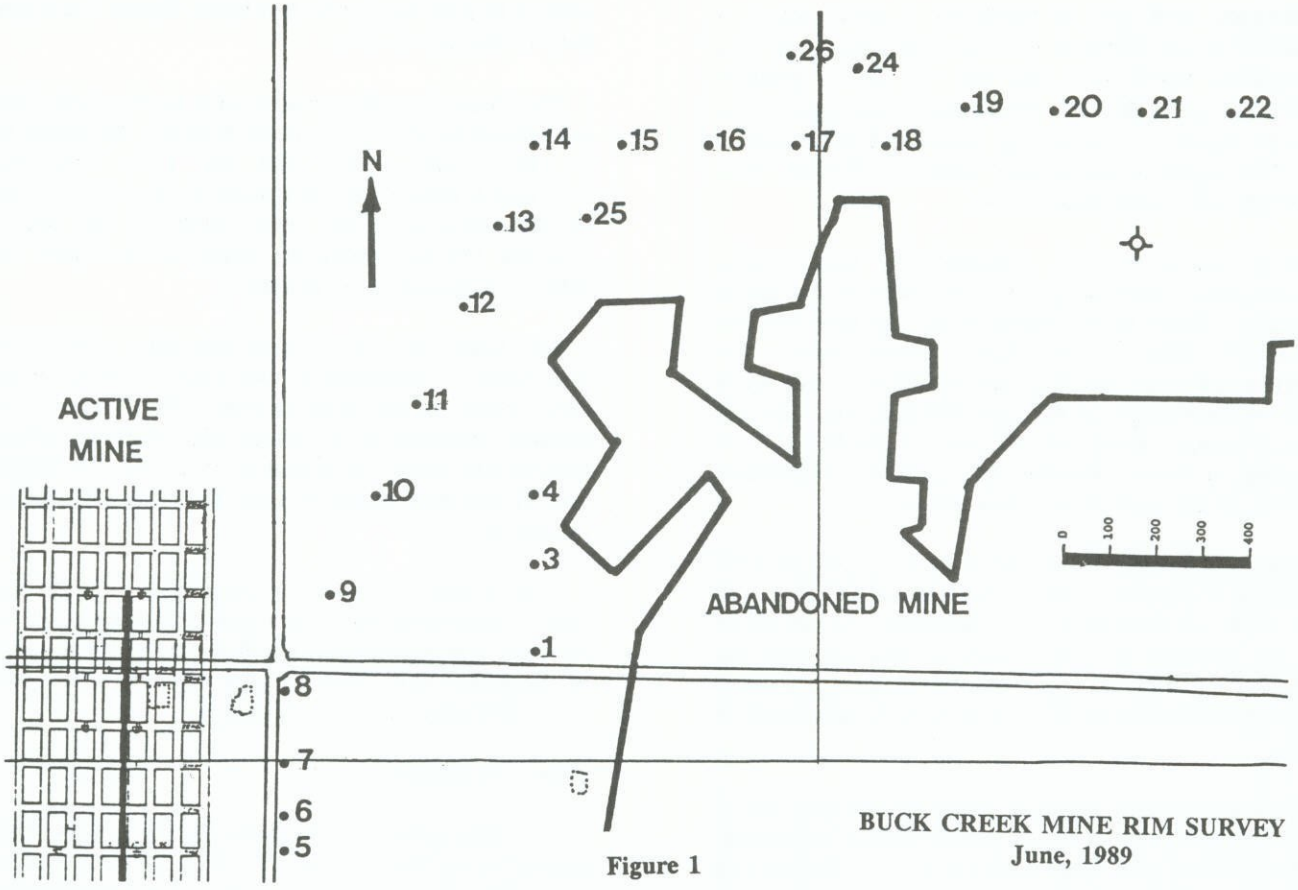

BUCK CREEK MINE RIM SURVEY
June, 1989

Figure 1

of 120 and an attenuation rate of 20 dB/100 ft. A decreased crosshole source strength was expected because of the difference in coupling efficiency between the in-mine and crosshole antennas. An increase in the attenuation rate was expected because the higher moisture, solid coal causes the EM wave energy dissipation to increase per unit of travel distance.

In October, 1990, additional in-mine calibration data was measured in an area much closer to the crosshole survey area than the original in-mine calibration. This calibration was conducted to verify that the coal seam within 300 feet of the Ebbw Vale Mine has a higher attenuation rate than the original in-mine or crosshole calibration measurements indicated. On Figure 2, the data labeled "In-Mine Calibration North of Abandoned Mine" presents the RIM parameters in this area to be a source strength of 169 dB and an attenuation rate of 25.4 dB/100 feet.

The significantly higher attenuation rate of the seam waveguide adjacent to the abandoned mine is believed to be due to water infusion into the seam from the flooded abandoned mine. Water was observed running out of the mine rib closest to the abandoned mine during the October, 1990 calibration.

Crosshole Calibration

In April, 1990, RIM signals were measured between four boreholes in unmined coal and between three boreholes in abandoned mine works. This phase had three objectives. One - to determine the crosshole RIM parameters for the four available frequencies and to select the optimum frequency. Two - to determine the contrast between mined and unmined ray paths. Three - to determine the spacing for the boreholes in the picket line. The locations of the calibration boreholes are labeled 1 through 8 on Figure 1.

The four boreholes in undisturbed coal, BH5 to BH8, were located 700 feet west of the abandoned mine. They were positioned in a straight line at intervals of 80, 120 and 160 feet. The varied spacing provided six distances to measure for a signal amplitude vs. distance calibration graph.

Three hundred (300) kHz was the frequency selected for the survey because it appeared to have the best combination of range and sensitivity. In Figure 2, the data labeled "Original BH/BH Calibration" presents the crosshole RIM system parameters from this calibration survey. The source strength equals 114 dB and the attenuation rate equals 20.3 dB/100 feet.

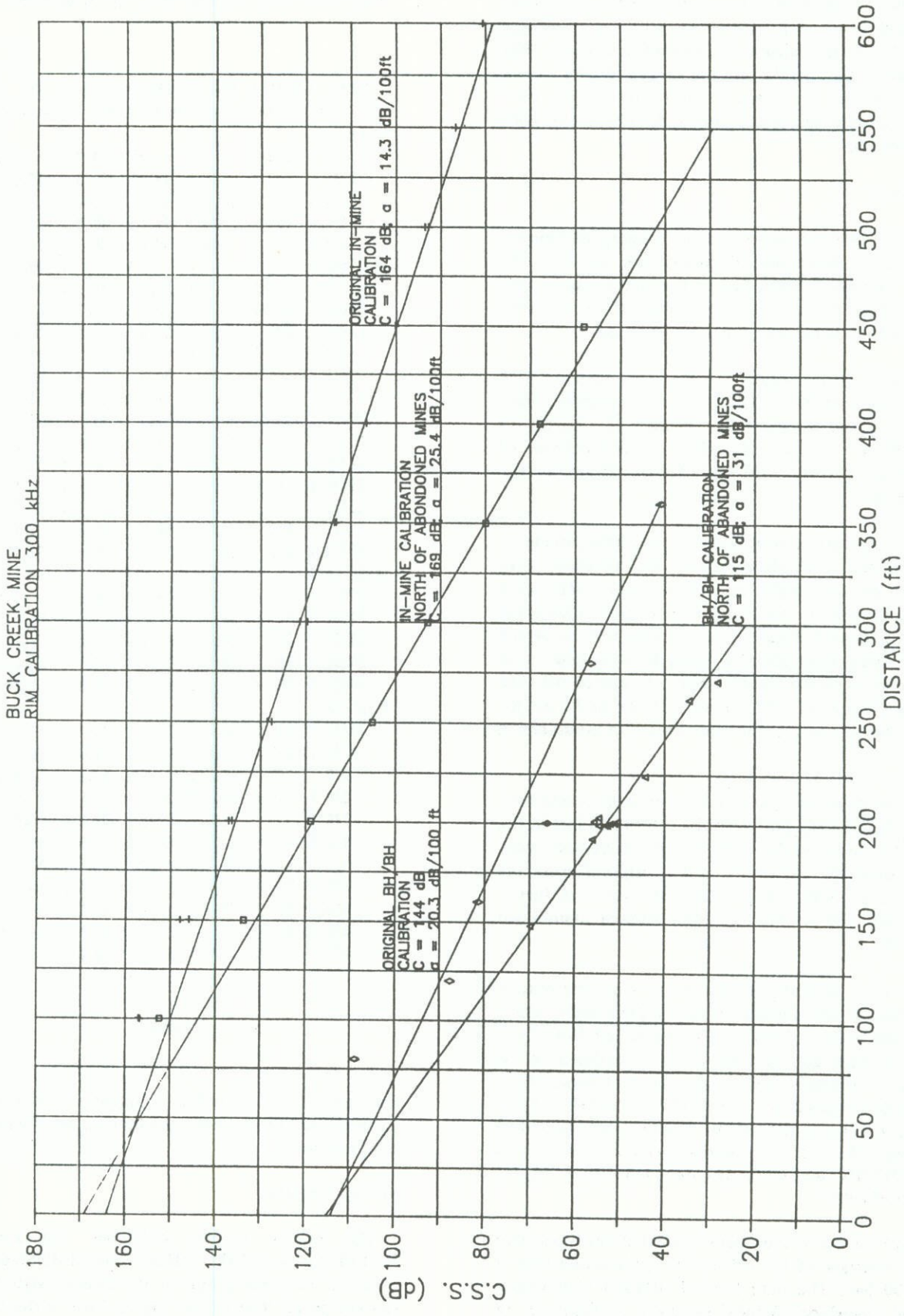
BUCK CREEK MINE
RIM CALIBRATION 300 kHz
ORIGINAL IN-MINE CALIBRATION C = 164 dB; α = 14.3 dB/100ft
IN-MINE CALIBRATION NORTH OF ABONDONED MINES C = 169 dB; α = 25.4 dB/100ft
ORIGINAL BH/BH CALIBRATION C = 144 dB α = 20.3 dB/100 ft
BH/BH CALIBRATION NORTH OF ABANDONED MINES C = 115 dB; α = 31 dB/100ft
C.S.S. (dB)
DISTANCE (ft)
0
20
40
60
80
100
120
140
160
180
0
50
100
150
200
250
300
350
400
450
500
550
600

Figure 2

Three boreholes, BH1, BH3 and BH4, were positioned 100 feet west of the mapped Ebbw Vale Mine in expected solid coal. These boreholes were initially positioned to be the calibration boreholes; however, they intercepted mine voids at the seam depth. As a consequence, the ray paths between these holes were used to compare disturbed and undisturbed ray path measurements.

RIM Survey

In June, 1990, crosshole radio imaging techniques were used to determine if abandoned mine works extended beyond a picket line of boreholes. The survey results indicated that the Ebbw Vale Mine extended further to the north than the map depicted.

This phase of the project was the measurement of 15 ray paths between 15 boreholes. These boreholes were positioned to be a picket line around the northwest corner of the Ebbw Vale Mine. The locations of boreholes numbered 8 through 22 are shown on the map in Figure 1.

As the ray path measurements were being made, it became evident that either all of the ray paths were disturbed or the calibration RIM parameters were incorrect. Based on the original crosshole calibration data, the measured signal strengths were well below the expected signal strength. For example, at a distance of 200 feet, the expected signal amplitude was 52 dB. The actual measurements (MSS) were closer to 30 dB for many of the ray paths. The survey data is tabulated in Table 1.

After the measurements were completed, it was then believed that the ray paths within 200 to 300 feet of the abandoned mine works were being attenuated more strongly than the ray paths in the original crosshole and in-mine calibration areas. It was considered unlikely that all of the ray paths crossed abandoned mine works.

There were several reasons for this determination. First, none of the boreholes intercepted mine voids. Second, the group of ray paths within 300 feet of the abandoned mine had very similar attenuation rates. If the area in question had been mined, it would have been partly production panels. The uniformity of the attenuation rates indicated the area was not disturbed by mining. Third, the ray paths through known mine works, BH1/BH3 and BH3/BH4, had significantly higher attenuation rates.

A graph of the survey data indicated this area had a source strength of 115 dB and an attenuation rate of 31 dB/100 feet. The data labeled "BH/BH Calibration North of Abandoned Mines" is shown in Figure 2. In

06/25/90, JGS
BUCK CREEK MINE, ABN MINE PROJ, PHZ 3, 06/22/90

Tx/Rx	Dist	MSS	CSS	ATTN RATE	115 =C 31 =@ STD	XLOS
Disturbed						
13/15	339	0	0	34.0	10.2	10.2
18/17	200	21	44.0	35.5	53.0	9.0
17/18	200	21.8	44.8	35.1	53.0	8.2
4/3	161	24	46.1	42.8	65.1	19.0
1/3	199	16	39.0	38.2	53.3	14.3
Abn Zone	0				115.0	
16/26	271	3.8	28.1	32.1	31.0	2.9
15/16	201	27.4	50.4	32.1	52.7	2.3
18/19	200	28	51.0	32.0	53.0	2.0
24/17	224	20.7	44.2	31.6	45.6	1.4
19/18	200	29	52.0	31.5	53.0	1.0
17/16	199	29.6	52.6	31.4	53.3	0.7
17/26	199	30.1	53.1	31.1	53.3	0.2
24/19	262	10.2	34.4	30.8	33.8	-0.6
24/18	192	33.2	56.0	30.7	55.5	-0.6
24/26	148	48	69.7	30.6	69.1	-0.6
13/14	199	31.5	54.5	30.4	53.3	-1.2
12/13	203	31.4	54.5	29.8	52.1	-2.4
15/14	201	32.6	55.6	29.5	52.7	-2.9
Transitn						
12/11	245	21	44.9	28.6	39.1	-5.8
22/21	200	38.7	61.7	26.6	53.0	-8.7
20/21	201	38.1	61.1	26.8	52.7	-8.4
20/19	201	34.2	57.2	28.7	52.7	-4.5
20/21	201	38.1	61.1	26.8	52.7	-8.4
Orgnl CAL						
10/11	230	31.3	54.9	26.1	43.7	-11.2
9/10	253	35.6	59.6	21.9	36.6	-23.1
8/9	249	47.3	71.3	17.6	37.8	-33.5
5/6	80	89.7	108.7	7.8	90.2	-18.5
7/6	121	68.5	89.3	21.2	77.5	-11.8
8/7	161	62.3	84.4	19.0	65.1	-19.3
5/7	200	47.2	70.2	22.4	53.0	-17.2
7/5	200	47	70.0	22.5	53.0	-17.0
8/6	281	37.4	61.9	18.9	27.9	-34.0
8/6	281	40.4	64.9	17.8	27.9	-37.0
8/5	361	21.7	47.3	18.8	3.1	-44.2

Table 1

October, 1990, in-mine calibration measurements verified that the survey area had higher normal signal attenuation.

Survey Results

The survey results indicated two ray paths, BH13/BH15 and BH17/BH18, crossed disturbed areas. Figure 3 is a bar graph of the Excess Signal Loss of the ray paths. The Excess Signal Loss is the difference

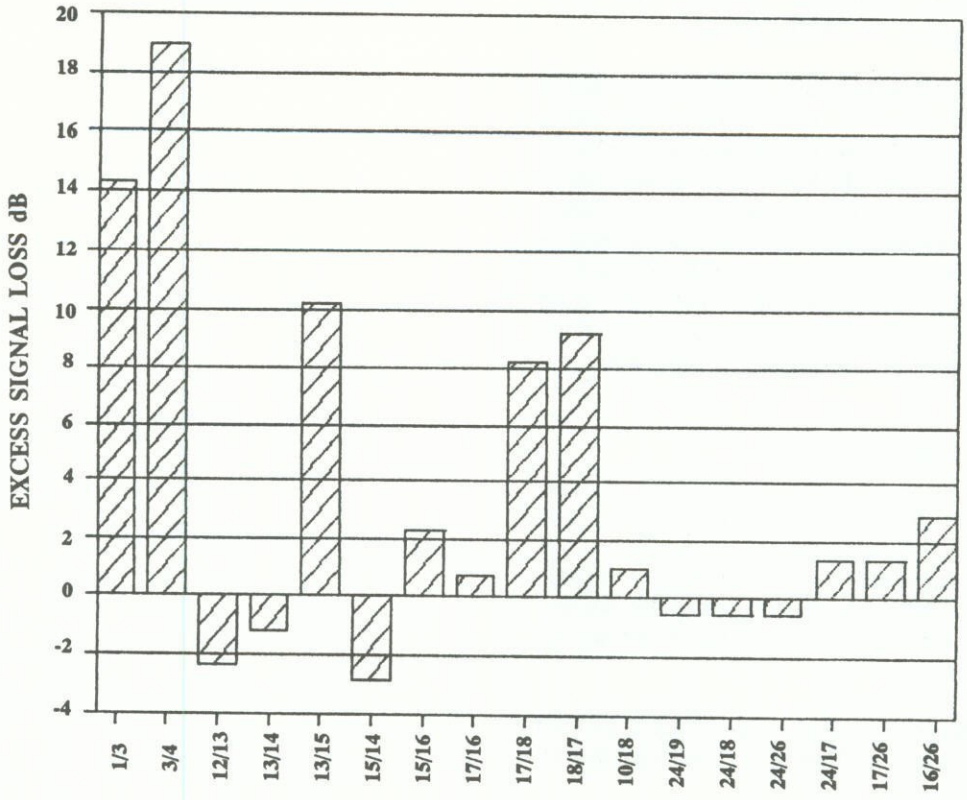

Figure 3

between the corrected amplitude of the received signal (CSS) and the expected signal (STD). Ray paths BH1/BH3, BH3/BH4, BH13/BH15, and BH17/BH18 exhibit a significant excess signal loss. Ray paths BH1/BH3 and BH3/BH4 were known to be disturbed by abandoned mine works. Ray paths BH13/BH15 and BH17/BH18 were interpreted to be disturbed by abandoned mine works.

Ray path BH13/BH15 was more than 300 feet from mapped mine works. To check this area, BH25 was positioned 100 feet southeast of the ray path and it intercepted a mine void. Measurements between BH25 and other boreholes were not possible because the hole collapsed above the seam.

When considering the possibility that ray path BH17/BH18 was disturbed, it was noted that the ray path crosses the projection of a development main of the Ebbw Vale Mine. This would be a likely area for mine works which are advanced beyond the map posting. Two boreholes, BH24 and BH26, were drilled to make additional measurements in the area north of BH17 and BH18. These two new holes provided five additional ray paths in the vicinity of ray path BH17/BH18. The evaluation of the additional ray paths indicated no abandoned mine works were located north of the new boreholes.

Based in part on the RIM Survey, the Buck Creek mine plan for extracting the coal reserves north of the Ebbw Vale Mine is being designed with prudent barriers between the operating mine and the unmapped abandoned mine works. The azimuth for the northeast mains was rotated to the north and the location of the mains bordering the northern edge of the Ebbw Vale Mine was altered.

Survey Comments

There is merit in varying the borehole spacing. It was expected that the major variable in this project would be the existence or non-existence of mine works between any two boreholes. However, the changing electrical characteristics of the coal seam increased the difficulty of interpreting the measurements. Most of the

ray paths in this project were approximately 200 feet and not disturbed by abandoned mine works. By measuring different distances, defining the RIM parameters would be a continuing process.

In addition to spacing, borehole configuration should be considered. Examination of available mine maps could indicate where the most likely advanced mining occurred. These areas should have closer spaced holes. In the case of areas with possible development entries, a diamond configuration with two holes positioned in line with the development projections may be the best setup. This would make possible multiple RIM measurements in high probability areas as well as increasing the chance of intercepting a mine void.

REFERENCES

1. Fry, R., Schotsch, J., Stolarczyk, L. G., "The Radio Imagining Method (RIM) - A Means of Detecting and Imaging Anomalous Geologic Structures in a Coal Seam", 1985, Proceedings of the 4th Annual Conference on Ground Control in Mining, Morgantown, West Virginia, July.

2. Hill, D., "Radio Propagation in a Coal Seam and the Inverse Problem", J. of Research Standards, Vol 89, No. 5.

3. Lloyd, T. W., Semborski, C. A., Stolarczyk, L. G., "RIM: A Method of Predicting Coal Seam Discontinuities", Proceedings 1986 Annual Meeting of the American Institute of Mining Engineers, New Orleans, Louisiana.

4. Miller, C., Doe, S., Stolarczyk, L., "Evaluation of Buried Coal Seams Using Cross-Hole Radio Imaging Method", 1986 8th Annual WVU International Mining Electrotechnology Conference, Morgantown, West Virginia.

5. Miller, C., Schreiber, B., "Advancements in the RIM Technique for Identifying Ground Shifts and Faults on Longwalls", 1990, AMC CONVENTION '90, Cincinnati, Ohio.,

6. Stolarczyk, L. G., Fry, R., "Radio Imaging Method (RIM) for Diagnostic Imaging of Anomalous Geologic Structures in Coal, Trona, Gilsonite and Quartzite Seams", 1989, 118th Annual Joint SME-TMS Exhibit, Las Vegas.

7. Stolarczyk, L., "Radio Imaging in Seam Waveguides", Geotechnical and Environmental Geophysics, Vol. III: Geotechnical, pp. 187-209.

8. Wait, J. R., "Note on the Theory of Transmission of Electromagnetic Waves in a Coal Seam", 1976 Radio Science, Vol. II, No. 4.

10th INTERNATIONAL CONFERENCE ON GROUND CONTROL IN MINING

EFFECTS OF SURFACE TOPOGRAPHY ON THE STABILITY OF COAL MINE OPENINGS

Gregory M. Molinda, *Geologist*
Keith A. Heasley, *Mining Engineer*
David C. Oyler, *Mining Engineer*
J. Richard Jones, *Geologist*

Pittsburgh Research Center
U. S. Bureau of Mines
Pittsburgh, Pennsylvania

ABSTRACT

An investigation was conducted to determine the nature and frequency of coal mine roof failure beneath valleys. A mechanism for this failure, and suggestions for controlling this problem are presented.

Hazardous roof conditions identified in a number of mines were positively correlated with mining activities beneath stream valleys. Mine maps with overlays of unstable roof and locations of stream valleys show that 52% of the instances of all unstable roof in the surveyed mines occurred directly beneath the bottom-most part of the valley. The survey also showed that broad, flat-bottomed valleys were more likely to be sites of hazardous roof than narrow-bottomed valleys. Evidence of valley stress relief was found beneath a number of valleys in the form of bedding-plane faults and low-angle thrust faults. This type of failure, previously believed to be only a shallow phenomenon, was found at mining depths as great as 300 ft. In situ horizontal stress measurements in a mine beneath a valley and the adjacent hillsides confirmed valley stress relief. Underground mapping showed that roof falls in excess of 100 ft in length and up to 25 ft high closely aligned with the valley axis. Numerical analysis of 13 valleys overlying one mine property showed the effect of the valley excavation on horizontal and vertical stress. Thickness of cover, valley shape, and the orientation of the valley relative to the maximum regional horizontal stress all influence the "valley effect" on roof stability.

INTRODUCTION

It has long been observed that coal mine roof appeared to become unstable when mining beneath stream valleys. The extent of the problem is not clear, but what is clear is that mining without regard to topography is risky. The objective of this investigation was to 1) document the stability of coal mine roof beneath changing topography, 2) investigate the principal mechanisms of failure in order to better understand how and when surface topography influences roof stability, 3) investigate the effect of topography on the in situ stress regime, and 4) verify a numerical model which returns the original state of stress in the mine given the depth of cover and valley shape.

EVIDENCE OF VALLEY STRESS RELIEF

It is well known that strata readjustments around surface excavations can result in stress relief failures such as bedding plane slip, thrust faulting; gouge zones, bedding plane separation, and bed folding (1-2). These failures can be seen in excavations for dams and bridge abutments. There is also abundant surface evidence of strata failures due to buckling of valley floor members. Tensional jointing in valleys is easily seen in road cuts, highwalls and underground near outcrop (3). Violent failures of surface strata in stream valleys and quarries also have been documented (4-5). There appears to be no doubt that high horizontal stresses can be sustained at the surface. These stress relief failures usually occur near the surface (15-50 ft deep), but there is also evidence that compressional relief failures can occur much deeper.

It is thought that V-notch valleys concentrate stresses at their apex, and older more mature valleys appear to be in a stress-relieved state. The broad, flat-bottomed valleys may be stress-relieved because of valley rebound due to unloading as well as the transfer of stress laterally due to loading of the valley walls. Figure 1 shows how relatively unconfined valley floor members beneath the broad valley can move when subjected to lateral forces and thereby dissipate those transmitted forces. The figure also shows how strata which is more confined beneath a V-notch valley will not move and will concentrate stresses which are then relieved by cutter roof. Investigation of roof falls beneath

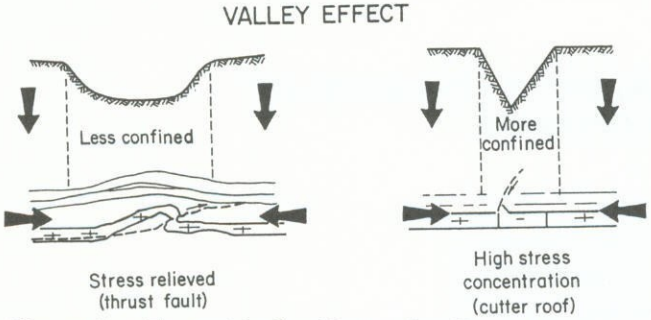

Figure 1. Theoretical effect of valley shape on horizontal stress and roof control at depth.

valleys has indicated that valley stress relief may be the mechanism causing unstable roof to depths of 300 ft.

MINING EXPERIENCES BENEATH STREAM VALLEYS

Data relating to mining experience beneath stream valleys were collected in order to determine if unstable roof could be attributed to surface stream valleys. Operators from seven mines located in Western Pennsylvania and West Virginia were questioned, with mapping conducted at five of the mines to determine the nature of roof quality beneath stream valleys (figure 2). There appears to be a clear relationship between areas of roof instability in the mines and proximity to stream valleys. This relationship is mentioned by numerous operators, but is rarely quantified or mapped. The following case histories describe the influence of valley topography on four of these Appalachian mines.

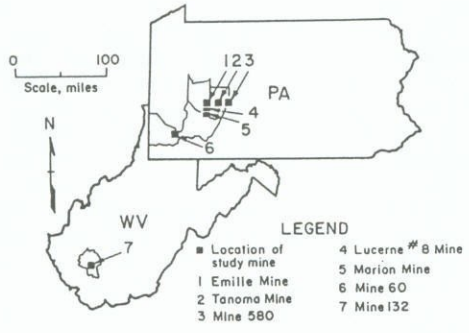

Figure 2. Location of study mines.

Tanoma Mine

Figure 3 shows the Tanoma Mine located in Indiana County, Pa. Local terrain features gently rolling hills with a dendritic drainage pattern and relief averaging 300 ft. The mine outline is shown with local drainage overlayed. Also shown are areas of roof instability as reported by the operators. The mine historically has experienced extremely difficult roof control when trying to advance its western sections beneath Crooked Creek and Rayne Run. Poor roof conditions also exist beneath some of the smaller tributaries overlying other parts of the property. Detailed mapping was conducted in sections Main C and A-15 (figure 3). Crooked Creek valley over Main C is flat-bottomed and more than 1200 ft in width. Maximum relief in the area is about 400 ft with about 200 ft of overburden above the section. Extreme instability in the section necessitated tunnel liners in 50% of the mined section beneath the stream valley. Evidence of valley stress relief is present in section Main C. Pulverized clay beds and low angle slip planes indicate horizontal movement. Bedding plane faults and mud slips occur parallel to the valley and are the result of horizontal compression.

Evidence of similar stress relief is present in the Northwest Extension. Prominent, broad slip planes exit the roof at 45° isolating roof blocks which then drop out. Bedding plane separation due to horizontal cpmpression also occurs.

Mine section A-15 crosses beneath a tributary of Crooked Creek (figure 3). The valley bottom at this point is 400-500 ft across, with approximately 284 ft of overburden. The roof instability in this section appears to be a result of horizontal compression perpendicular to the trend of the valley. Bedding-plane faults with gouge zones parallel the valley and cause the major roof falls (figure 4). Because the roof strata are confined beneath 284 ft of overburden, horizontal compression from valley side loading may cause only slight dislocation of the strata, but enough to severely disrupt the roof.

The relationship of roof failure to mining beneath valleys at Tanoma Mine is apparent, and the main cause is poor rock mass quality due to horizontal stress failures caused by valley stress relief.

Mine 132

Mine 132 is located in Boone County, W.Va. and is working the Powellton Seam (figure 2). Coal thickness ranges from 4.5 to 8.0 ft. Figure 5

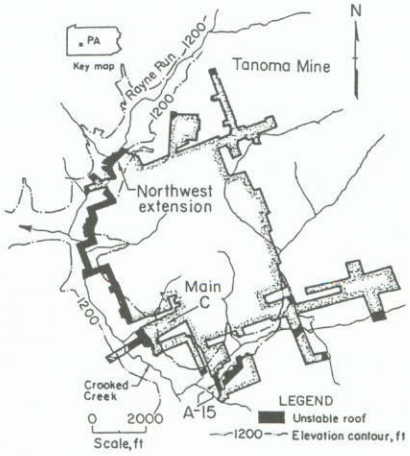

Figure 3. Tanoma mine outline and relationship of unstable roof to surface drainage.

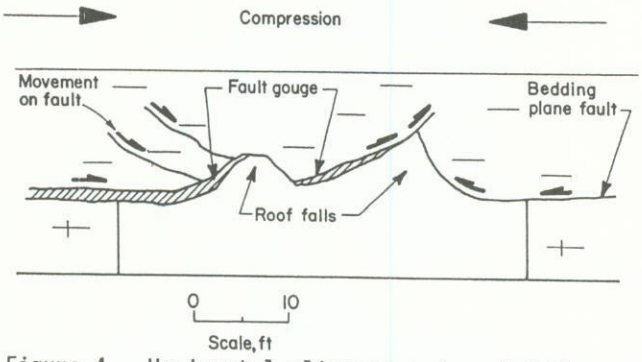

Figure 4. Horizontal slippage and roof failure in Tanoma Mine caused by compression beneath a valley.

presents the mine outline with local drainage overlain. The West Fork of Pond Creek is the major drainage on the property. The valley is flat and averages 600 ft wide. Terrain in the area is severe, with relief of over 1000 ft.

Two sets of mains extend beneath Bandy Green Branch Creek, which drains into the West Fork of Pond Creek. Here the coalbed is under about 160 ft of cover. On the surface, the valley is narrow and V-notched and not more than 100 ft wide, with a steep stream gradient of 37%. The roof is unstable where the mains cross beneath the stream valley. Workings extending beneath other stream valleys on the mine property have relatively stable roof. At Mine 132 instability problems occur only beneath Bandy Green Branch.

Figure 6 is a map of roof conditions beneath Bandy Green Branch. The zone of roof instability coincides with the valley bottom. Roof falls more than 100 ft long and more than 20 ft high are common. Bedding-plane faults are the cause of roof failure. These horizontal failures are similar to those observed at the Tanoma Mine (section A-15 and Main C). Bedding-plane faults also curve into the roof and their linear traces parallel the valley trend. As illustrated in figure 4, horizontal slippage occurs in both directions perpendicular to the fault traces and isolates roof blocks which then fall into the mine openings. Fault gouge is several inches thick between beds and contributes to roof instability. Slippage occurs as a result of horizontal compression from valley stress relief. Compression causes slippage between beds, and when a zone of weakness is reached (i.e., in the valley bottom where there is less confinement from overburden), the fault plane bifurcates into the roof. Figure 6 locates in situ stress measurements which confirm stress relief beneath the valley.

Lucerne #8 Mine

Lucerne #8 Mine is located in Indiana County, Pa. in the Upper Freeport coalbed (figure 2). The coal height is about 50 inches. Terrain is gently rolling and valleys are broad, ranging from 100 ft up to 1200 ft in width. Relief averages between 300 and 400 ft. The depth of the mine ranges from 50 ft to 700 ft.

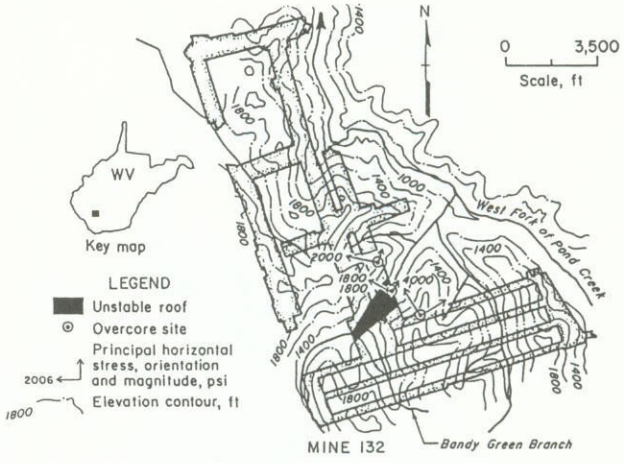

Figure 5. Mine 132 outline and relationship of unstable roof to surface drainage, and results of horizontal stress measurements.

Figure 7 shows the mine outline with surface drainage overlayed. Unstable roof rock conditions coincide with several drainage basins, but not all. Thrust faults and bedding plane faults are responsible for roof instability in several of the related areas. The area known as the Flats has particularly unstable roof.

The structural failures in the Flats area are thrust faults. These thrust faults and associated roof falls are closely aligned with the valley trend. Figure 8 shows three exposures of thrust faults in two entries of the Flats area. Relatively large-scale folding and thrust faulting is a result of compression oriented northwest-southeast, or perpendicular to the valley trend. This deformation may be a result of compression due to valley-wall loading which occurred at some time during the valley

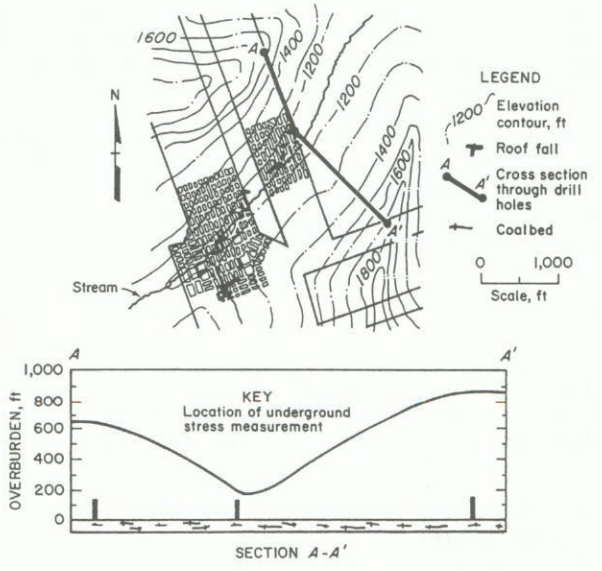

Figure 6. Map of roof failure beneath Bandy Green Branch and location of overcore holes.

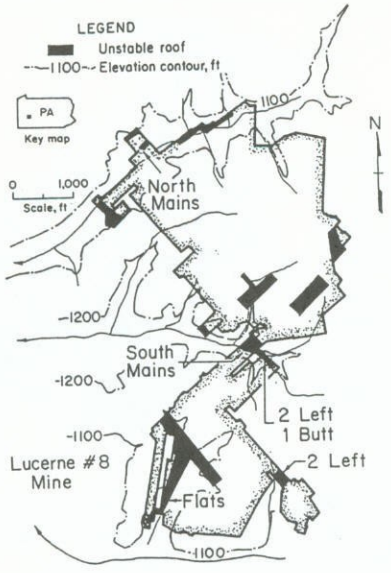

Figure 7. Lucerne #8 mine outline and relationship of unstable roof to surface drainage.

downcutting. Another possibility is that the sequence is reacting to a regional stress on the area and that the valley provided an unconfined zone for stress relief.

Unstable roof in the area of the South Mains is also due to thrust faulting which parallels the stream valley (figure 7). Here the coalbed is offset more than 24 inches. Falls up to 12 ft high, severely disturbed roof rock, and numerous gouge zones characterize the zone, which is 150-200 ft wide. Section 2-left, 1-butt is also disturbed by the same fault zone. These two sections are located directly beneath a stream valley with less than 100 ft of overburden.

The 2-left development to the south crosses beneath a valley at a depth of less than 100 ft. The coalbed is offset more than 18 inches by thrusting, with the axis of the fault again paralleling the stream valley. Here, roof problems were controlled by longer pillars.

Thrust faulting in the North Mains section also contributes to roof instability. This section underlies the Hooper Creek valley. Numerous roof falls have been caused by bedding-plane and thrust fault failures which parallel the valley.

Mine 60

Mine 60, located in Washington Co., Pa., works the Pittsburgh Coalbed (figure 2). Relief averages 300-350 ft over the property. Little Chartiers Creek flows north over the western side of the mine. Overburden averages 500 ft beneath Little Chartiers Creek. Figure 9 shows the mine outline and the areas of unstable roof. There is a close relationship between the valley bottom and unstable roof. Roof failure is often related to active stress and begins as cutter roof. Mine operators report that the most severe problems

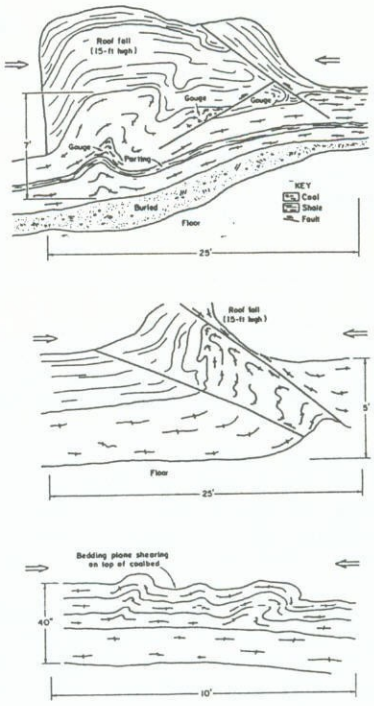

Figure 8. Thrust faulting and bedding disruption in the Flats section of Lucerne #8 due to horizontal compression.

occur in north-south drivage, but they expect difficult mining whenever the mine passes beneath the Little Chartiers Creek valley. In addition, adjacent mines report similar problems beneath this valley. This is an example of unusually high horizontal stress severely affecting roof quality in relatively low relief. There was no evidence of rock mass disturbance prior to mining, indicating that the pre-mining horizontal stress was never great enough to fracture the roof strata or cause bedding plane failure. When coal is mined (ie. confinement removed), stress is released and cutters form. Such stress cannot be generated by static overburden loading and must be related to regional stress.

RELATIONSHIP OF VALLEY GEOMETRY TO THE FREQUENCY OF ROOF FAILURES

Data from the mines previously described as well as several others was collected and analyzed to determine the frequency and nature of occurrences of roof failure beneath stream valleys. In addition, the influence of valley geometry on roof failures was examined. The mines used for this portion of the study are all located in Western Pennsylvania. Operators were questioned and asked to identify the areas of unstable roof on base maps. All areas of unstable roof were included, except those which were related to unconsolidated or inherently weak strata. The large zones of poor quality roof were categorized into discrete regions by fitting to a grid of approximately 1000 ft squares. The surface terrain above each area of unstable roof was characterized by several variables including

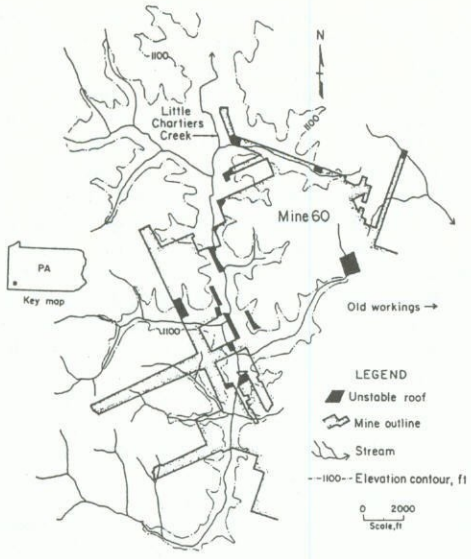

Figure 9. Mine outline and relationship between unstable roof and surface drainage at Mine 60.

thickness of cover, amount of relief of associated valley, width of the associated valley floor, valley shape factor (height of relief/width of valley floor), and proximity of the bad top occurrence to the valley floor (figure 10 A). The distribution and frequency of unstable roof was then determined with respect to these variables.

Thickness of cover at the five mines ranged from 20-715 ft. It was found that unstable roof was normally distributed with respect to thickness of overburden. With the present data, which include 169 examples of unstable roof, there appears to be no clustering of occurences towards thin or thicker cover. This is also true when considering only those examples of unstable roof that occur directly beneath the valley floor (0-20% valley location, figure 10 A). This indicates that amount of overburden alone does not influence roof instability in the test group.

The location of unstable roof relative to the valley floor was the most significant relationship observed, with 52% of unstable roof occurring beneath the portion of the valley with 20% of the maximum relief.

Less than 10% of the unstable roof was found beneath the valley portion with 80-100% of the maximum relief (figure 10 B, 11). Poor rock mass quality beneath the valley floor may result from valley wall loading and lateral stress transfer. These types of failures due to poor rock mass quality have been described above and are common to the Appalachian region.

The relationship between the shape of the valley and all occurrences of unstable roof was also significant. The variable used is the ratio of the height of relief of the associated valley to the width of the valley floor. This ratio also defines the confinement of the valley floor. Sixty-six percent of unstable roof instances

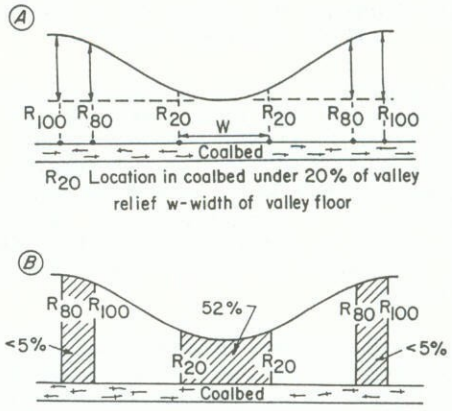

Figure 10. A) Valley cross section showing geometric variables used in parametric study. B) Valley cross section showing location of most instances of unstable roof (52%), and location of least instances of unstable roof (10%).

occurred beneath valleys with confinement factors between 0.2 and 0.6 (figure 11). This indicates that unstable roof is more likely to occur beneath broad valleys than it is under narrow-floored valleys.

In summary, the data suggest that the most likely site of unstable roof relative to topography occurs when mining advances beneath a valley floor which is broad and flat-bottomed and, thus, less confined. The least likely location of unstable roof is beneath the top of the adjacent valley wall.

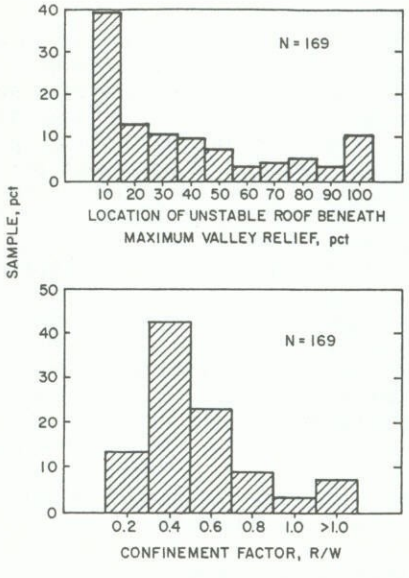

Figure 11. Distribution of unstable roof with respect to location beneath valley and valley shape.

FIELD STUDY OF THE VARIATION OF HORIZONTAL STRESS BENEATH A VALLEY

BethEnergy Mine 132 was selected as the test mine to determine the effect of a valley on in situ horizontal stress. The study site, previously described, is located beneath Bandy Green Branch valley, which is a steep-walled (37% slope gradient), V-shaped valley. Severe roof failures occur in numerous places beneath this valley, and these failures closely follow the valley trend.

Four core holes were drilled into the roof in order to measure the horizontal components of stress (figure 5). Two holes were located beneath the valley floor and one hole was located under each adjacent hillside. These locations were chosen to test the effect of the valley on the horizontal stress field. The Bureau of Mines borehole deformation gauge (BDG) and the overcoring method were used. Figure 12 shows the arrangement of boreholes and stress measurements. A total of 16 stress measurements were successful, with the highest measurement taken at 24.3 ft into the roof in hole 4. Several tests were unsuccessful because of core breakage, which contributed to instrument failure. All four holes were drilled within 5 ft of a coal barrier in order to minimize the effect of the mine opening. The final successful test at hole No. 1 was at 15.7 ft into the roof. Because this height is still within one opening width of the mine roof the measurement may be affected by the mine opening. The other three holes were drilled more than 17 ft into the mine roof and these measurements are thought to represent premining horizontal stress.

The trend of the principal stress in all four test holes at BethEnergy is northwest, ranging between N32W-N87W. Stresses trending northwest at BethEnergy may reflect the regional stress in Boone Co., WVa., or may be a local phenomena related to topography. A northwest orientation is perpendicular to the direction of the stream valley, and explains the horizontal roof failures documented beneath the valley (figure 6). These compressional failures, which are located along the trend of the valley, were caused by stresses which were parallel to bedding and oriented northwest-southeast. The ratio of measured horizontal/calculated vertical stress beneath holes #2 and #4 (beneath the valley) is 10.2 and 10.2, and between holes #1 and #3 are 2.8 and 4.1 respectively (Table 1). This increased ratio beneath the valley reflects its reduced confinement and the increased potential for valley stress relief failures.

Table 1. Relationship between measured stress and calculated stress at Mine 132.

HOLE #	OVERBURDEN (FT)	CALC. VERT. STRESS (PSI)	MEASURED HORIZ. STRESS (PSI)	CALC. HORIZ. STRESS (PSI)	EXCESS HORIZ. STRESS (PSI)	HORIZ. STRESS / VERT. STRESS
1	655	720	2000	238	1762	2.8
2	160	176	1800	81	1719	10.2
3	875	962	4000	317	3683	4.2
4	160	176	1800	81	1719	10.2

The total horizontal stress field is considered to be the sum of the stress due to overburden and gravitational loading, the stresses being transferred horizontally to the valley bottom due to the "valley effect," and the regional stress. The total horizontal stress is considered to be at least as great as the magnitude of the largest measured stress at each hole. If the poisson effect of gravity loading (Table 1, Calculated Horizontal Stress) is subtracted from the largest horizontal stress at each hole, there is excess stress present at each site. Excess stress is calculated to be 1762 psi at hole #1, 1719 psi at hole #2, 1719 at hole #4 and 3683 psi at hole #3 (Table 1). This excess stress is the sum of the stress contributed by the "valley effect" and the regional stress. The horizontal stress contributed by the "valley effect" is calculated to be 297 psi by a numerical model. By removing this stress from the measured value (1800 psi) the remaining "regional" stress beneath the valley is 1503 psi. There is no "valley effect" at hole #3 so the measured stress minus the calculated horizontal stress due to overburden equals the regional stress (3683 psi). The difference between calculated regional stress beneath the adjacent hill (3683 psi) and the calculated regional stress beneath the valley (1503 psi) is 2180 psi. This represents the amount of stress relief beneath the valley due to bedding plane faulting.

It has been noted in some West Virginia mines that entries adjacent to roof falls experience stable roof due to stress relief. In fact, a "caving entry" was successfully used at Kitt Mine to destress outside entries in a longwall development section. Movement along bedding planes as roof strata moved toward the cave is believed to be the mechanism of stress relief. This type of roof failure is exactly the type of movement which has occurred beneath the Bandy Green Branch at Mine 132. Therefore, it is considered that the bedding plane faults which disrupt the roof integrity have partially relieved the excess stress beneath the valley.

Two stress measurements at the bottom of hole #2 indicate that here the stress field is strongly biaxial. With little confinement to the northeast, failure would be likely to occur parallel to the valley trend. Similar conditions exist at the bottom of hole #1 but may not result in poor rock mass quality due to higher confinement (ie. greater overburden).

To summarize, the stress measurements at Mine 132 indicate that stress relief has occurred beneath the valley bottom. It is estimated that over 2000 psi of stress relief has occurred through bedding plane slippage. Additionally, the measured northwest orientation of the principal horizontal stress is consistent with the trend of the bedding plane failures in the mine roof beneath the valley. This means that these failures could well have been caused by a northwest horizontal stress.

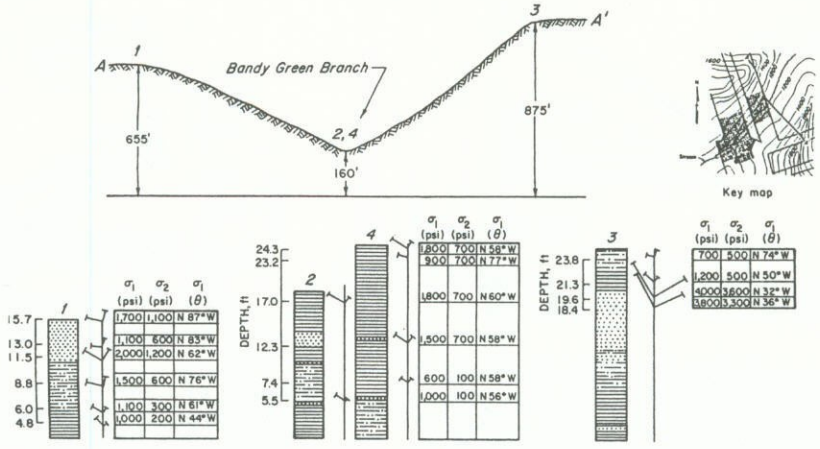

Figure 12. Horizontal stress measurements in the roof strata around Bandy Green Branch valley.

NUMERICAL ANALYSIS OF THE STRESS REGIME AT MINING DEPTH AT MINE 132

A good estimate of the stress field under a given valley can be critical to the optimum mine design in this area. Therefore, in order to better define the effect of the valley topography and the regional stress on the geologic stress field at the mine level, a numerical analysis of 13 valleys overlying the study mine (BethEnergy Mine 132) was performed (figure 13). This analysis primarily consisted of two parts. Initially, a numerical model of the stress in each valley was performed and the changes in the mine stress due to the topography were examined, then the approximate regional stress was vectorially added to the topographic stress and the resultant stress field was again examined. This numerical analysis provided considerable insight into the mine-level stress field below valleys and helped explain some of the geologic features and ground-control problems actually found below these valleys.

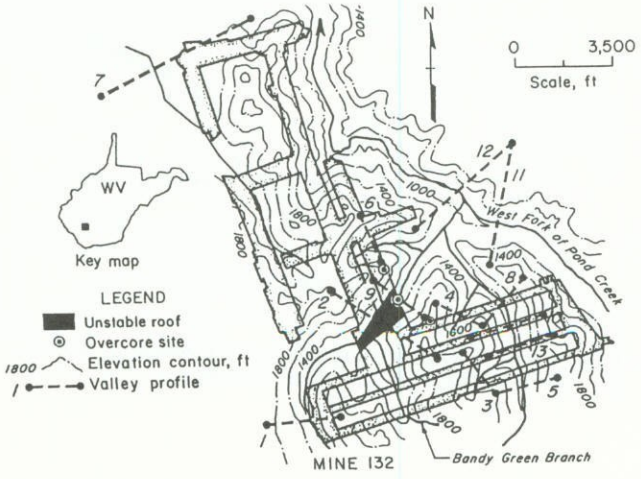

Figure 13. Valley profiles over Mine 132 used in numerical analysis.

The numerical method used in the topographic analysis was the explicit finite-difference technique as implemented in the program FLAC[1]. Figure 14 is a comparison of horizontal stresses at mine level due solely to the weight of overburden and the modeled stresses affected by topography. The increase in stress beneath each valley due to surrounding topography is apparent.

Figure 15 shows the actual cross sections of valleys #9 and #12 with three coal seams simulated at depths of 50, 150, and 300 ft below the valley floor. Figure 16 shows the horizontal (sxx) and vertical (syy) stresses along the three different seams under valley #9 as calculated by the FLAC model. Examination of the horizontal stress curves reveals that they do not decrease as the overburden decreases under the valley, as would be expected. Rather, the horizontal stress is actually concentrated under the valley at the two greater depths. This stress concentration is a result of the two ridges "pushing" toward the valley center. The lack of horizontal stress increase at the 50-ft level is a result of this area being on the border of a horizontal stress-relief zone generated under the valley bottom. The final observation from figure 16 is that at the two shallower depths, 50 and 150 ft, the

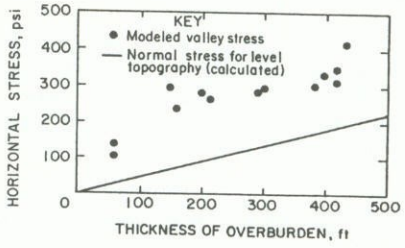

Figure 14. A comparison between the modeled horizontal stress at mine level under the valleys at Mine 132 and the theoretical horizontal stress for a level topography.

[1]This does not imply endorsement of the program by the U.S. Bureau of Mines

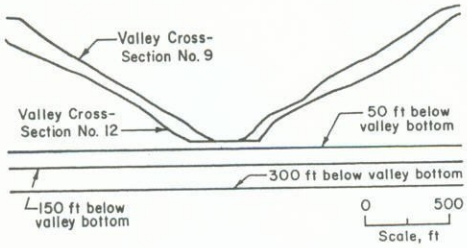

Figure 15. Cross section of valleys #9 and #12 with simulated coalbed horizons at Mine 132.

horizontal stress is greater than the vertical stress calculated beneath valley #9. Through geologic time, this higher horizontal stress would be expected to cause compressional features such as bedding plane slips or small thrust displacements. This model provides a mechanism for the compressional roof failures observed beneath Bandy Green Branch at the 160 ft depth. Horizontal compression exceeded confining pressure from overburden and overcame cohesion along bedding planes. When this horizontal stress concentration exists, shear failure is more likely.

In order to investigate the effect of the valley shape on the stress field, figures 17 and 18 present comparisons of the horizontal and vertical stresses at identical depths under valleys #9 and #12. Horizontal stresses show a decided drop under valley #12 at the 50-ft level (figure 17). This drop in horizontal stress at the center of valley #12 is a result of the wider valley bottom which generates a larger stress relief zone that encompasses the 50-ft level. The stress relief zone under valley #9 did not encompass the 50-ft level.

Examination of the horizontal stresses in figure 18 shows that the effect of the horizontal stress relief zone at 300 ft below the two valleys is negligible and therefore, the curves are practically superimposed. At this depth, the difference in the shape of the two valleys makes no difference in their effect on horizontal stress, although there is still a "valley effect" horizontal stress concentration due to overburden removal.

The regional stress was then vectorially added to the topographic stress in order to get the total geologic stress field at Mine level beneath each valley. The initial results from adding the regional stresses to the topographic stresses are shown in Table 2.

This table also gives the valley orientation (reference to the south), and the offset of the valley from the regional stress, which is the number of degrees the strike of the valley is offset from the orientation of the maximum regional stress. The table also shows the maximum and minimum horizontal stresses and the vertical stress as calculated by FLAC.

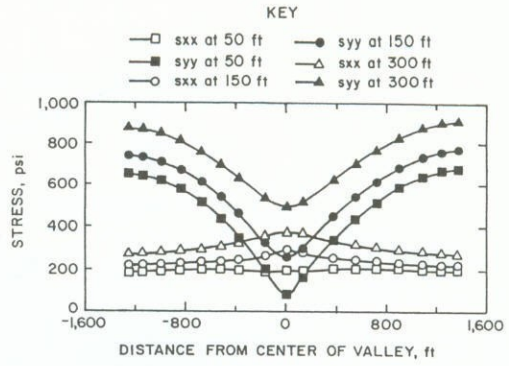

Figure 16. The horizontal (sxx) and vertical (syy) stresses at various horizons below the apex of valley #9 at Mine 132.

Table 2. Comparison of Total Geologic Stress Fields of all Valleys at Mine 132

Valley #	Valley Bearing	Offset from Regional Stress (deg)	Maximum Horizontal Stress (psi)	Minimum Horizontal Stress (psi)	Vertical Stress (psi)
1	S 14 E	56	1,735	812	631
2	S 17 E	53	1,674	752	451
3	S 56 W	54	1,704	790	600
4	S 40 W	70	1,700	766	565
5	S 15 E	55	1,666	742	450
6	S 72 W	38	1,706	817	621
7	S 27 E	43	1,779	881	726
8	S 41 E	29	1,579	719	290
9	S 29 W	81	1,694	672	267
10	S 20 E	50	1,646	725	344
11	S 82 E	12	1,456	604	73
12	S 45 E	25	1,527	576	69
13	S 20 E	50	1,636	720	367

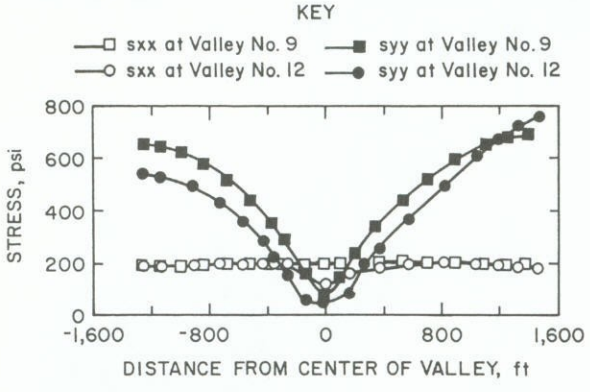

Figure 17. A comparison of stress between valley #9 and 12 at Mine 132 at 50 ft deep.

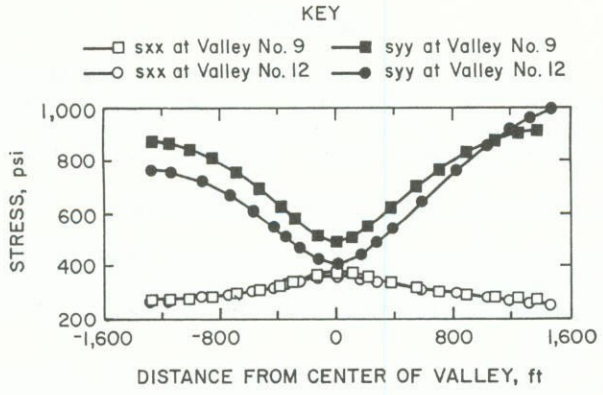

Figure 18. A comparison of stress between valley #9 and #12 at Mine 132 at 300 ft deep.

When the offset angle is 90 degrees, the concentrated horizontal compressive stress at the valley center due to the topography will vectorially add to a maximum with the regional stress. The closer the offset angle is to 90 degrees the higher the maximum horizontal stress will be. Figure 19, which is a three-dimensional plot of maximum horizontal stress plotted against offset angle and depth, aids in the visualization of the interactive effect of both the offset angle and the depth. From this figure, it is apparent that the maximum horizontal stress does indeed increase with both the offset angle and depth as presumed. Therefore, when the regional stress is considered, not only does the shape of the valley influence the stress field, but so does the orientation of the valley with respect to the direction of the principal regional stress.

Because a number of shear-type failures had been observed underground, it seemed reasonable to investigate the maximum shear stress developed in the various valleys. Therefore, a calculation of the maximum shear stress in the three-dimensional stress field and the normal force on the maximum shear plane was performed. The results of the maximum shear stress calculation are presented in Table 3. Clearly, some of the shear stresses in this table are fairly high, especially considering the minimal values of the normal stresses providing the shearing restraint.

To further investigate the relative probability of shear failure in the stress fields under the modeled valleys, a ratio of the maximum shear stress to the normal stress on the shear plane was developed. This ratio is also presented in table. A higher ratio is more likely to produce a shear-type failure in that particular valley. This shear stress to normal stress ratio agglomerates the effects of depth, valley topography, the regional stress and the relative orientation of the valley into one number which quantifies the probability of shear failure in that valley. Examination of table 3 shows that the two valleys where the coal seam is the shallowest, #11 and #12, have the greatest possibility of shear failure. This is a direct result of the high horizontal regional stress and

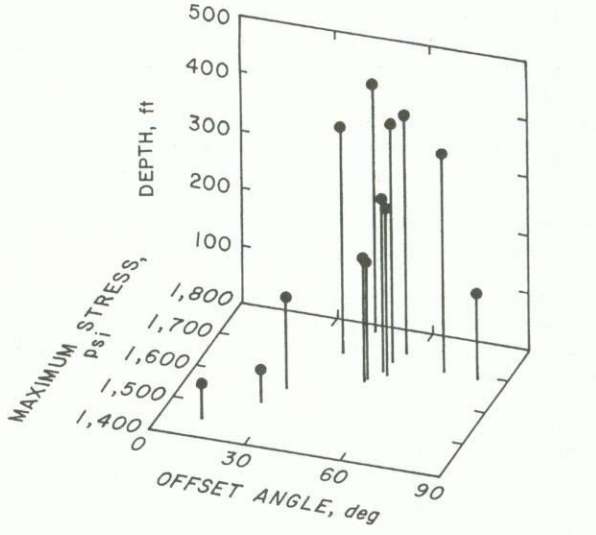

Figure 19. A three dimensional graph showing the increase in maximum horizontal stress with offset angle and depth of valleys above Mine 132.

Table 3. Shear stresses expected in the Powellton Coalbed in Mine 132.

Valley	Depth of Coalbed (ft)	Maximum Shear Stress (psi)	Normal Stress on Shear Plane (psi)	Ratio Shear Stress/ Normal Stress
1	415	552	1,183	0.47
2	300	611	1,060	0.58
3	415	554	1,148	0.48
4	380	567	1,132	0.50
5	290	608	1,058	0.57
6	395	547	1,157	0.47
7	430	529	1,250	0.42
8	160	644	934	0.69
9	150	714	981	0.73
10	200	651	995	0.65
11	60	692	765	0.90
12	60	729	798	0.91
13	214	635	1,000	0.64

the lack of overburden to provide confinement and is not substantially influenced by the valley shape or orientation.

The valleys forming the watershed above Mine 132 are in various stages of evolution, with the West Fork of Pond Creek being the most mature. The state of stress at the coalbed level beneath them depends on the shape of the valley, the depth of cover, and the orientation of the valley with respect to the principal regional stress. The relative risk of compressional failure based on shear stress is given in Table 3. Finally, perhaps the most important factor in whether failure will occur, given the necessary stresses, is the shear strength of the roof sequence.

CONCLUSIONS

A detailed study of the distribution of unstable roof in 7 mines in WVa. and Pa. showed a strong correlation between roof failure and specific locations beneath stream valleys. Unstable roof tended to occur beneath the broader, flat-bottomed valleys more often than beneath the more confined narrow-bottomed valleys (66%). The mechanism of failure varied significantly between mine properties, but numerous instances of valley stress relief were observed, even to depths of 300 ft.

Measurement of horizontal stress, as well as evidence of compressional failures has indicated that stress relief has occurred beneath a valley in southern West Virginia.

Numerical modeling of 13 valleys overlying a mine in West Virginia indicate that the valley excavation tends to concentrate horizontal stresses beneath the valley apex. V-notched valleys retain this concentration due to bottom confinement, but a model of a broad-bottom valley shows that there is a stress relief zone developed down to 50 ft beneath it. Large shear stresses can form in broad valleys because of the reduced confinement, making this type of valley one of the most subject to shear failure. With greater depth, stresses are again concentrated beneath the apex. Additionally, valleys oriented at large angles to the direction of maximum regional stress are at greatest risk to high shear stresses. Valleys that have existing stress relief failures and are still subjected to horizontal compression will experience the most significant compressional roof failure.

The shear strength of the immediate roof sequence plays a role in whether stress will be relieved by strata failure prior to mining or wheter stresses will remain concentrated and be relieved by cutter roof failure during mining.

Thickness of cover, shape of the valley, and the magnitude and orientation of the regional stress to the valley orientation all influence the stress field at the mine level.

REFERENCES

1. Fergusen, H.F., and Hamel, J.V. Valley Stress relief in Flat-lying Sedimentary Rocks. Proceedings of the International Symposium on Weak Rock, Tokyo, Japan, September 21-24, 1981.

2. Fergusen, H.F., Personal Communication, 1989.

3. Sames G., and N.N. Moebs. Hill Seam Geology and Roof Instability Near Outcrop in Eastern Kentucky Drift Mines. BuMines RI 9267, 1989. 32pp.

4. Simmons, G. Stream Anticlines in Central Kentucky. U.S. Geological Survey, Professional paper 550-D, pp. D9-D11, 1966.

5. Personal Communication, Joe Wallach, Canadian Atomic Energy Control Board, Ottawa, Canada, 1990.

10th INTERNATIONAL CONFERENCE ON GROUND CONTROL IN MINING

SITE CHARACTERIZATION FOR ULTRA–CLOSE MULTI–SEAM MINING

Yingxin Zhou, *Research Associate*
Chris Haycocks, *C. T. Holland Professor*
Michael Karmis, *Professor and Head*
S. Gavin Haycocks, *Graduate Research Assistant*

Department of Mining and Minerals Engineering
Virginia Polytechnic Institute and State University
Blacksburg, Virginia

ABSTRACT

Data from these field studies and previous case study data have been combined to define ultra-close seam mining environments and relate them to observed failure conditions. A rating system for ultra-close multi-seam design has been developed and field studies have verified the applicability of the design criteria according to geologic structures, lithology and spatial data. This rating system has been combined with design and depth considerations to create a protocol for quantitatively predicting potential damage in ultra-close seam mining conditions. A brief discussion of the characteristics of ultra-close seam mining and its related failure mechanisms is also presented.

INTRODUCTION

Field observations show that ultra-close workings of less than 25 feet frequently involve unique failure mechanisms of the total innerburden. Such failures can also affect the structural behavior of both upper and lower seam pillar by increasing their effective height. The decision on how close vertically two mines can operate is a complex one but dependent in large part on a combination between the structural integrity of the innerburden and mining factors. The mining factors have a major influence on stability through the selection of opening widths, pillar sizes and pillar location and give the engineer some flexibility to achieve a stable design.

Stability assessment across a mining area involves the following major factors in determining whether or not the innerburden will be stable:

Fixed:
- Innerburden characteristics
- Innerburden thickness
- Depth

Operational Variables:
- Relative pillar sizes and locations
- Opening widths
- Mining sequence and system
- Opening widths
- External loading factors

Results from studies show that pillar load transfer mechanisms in ultra-close seam mining does not differ significantly from that in multi-seam mining with greater innerburden thicknesses[1]. In ultra-close seam mining the innerburden is the predominant structural component determining the stability of the two seams being mined. Failure of the innerburden can then cause pillar instability with damage to both operations. A stable innerburden design is therefore essential taking into account all the complex and interrelated geologic structural and mining conditions.

OPERATIONAL VARIABLES

Operational or design variables offer the potential to improve stability under some conditions. Careful control of the mining process is however a necessary part of this control particularly for relative location of the operations between the two seams.

Relative Pillar Locations

The structural integrity of the innerburden is primarily governed by the relative positions of upper and lower pillars. Primary loading conditions are governed by the position of upper and lower seam pillars or gob edges relative to one another. From this, three basic innerburden loading conditions that contribute to failure have been identified: 1) self loading of the innerburden in columnized design layout; 2) partially offset pillars; and 3) totally offset pillars [1].

Columnized pillars produce a symmetrical stress field

in the innerburden, but at depth can create a high stress gradient which can contribute to shear failure at the lower rib edge. At a relatively short distance from the lower seam, the upper pillar can transfer very high concentrated pressure to the rib edge of the lower pillar. Even at shallow depths shear failure is still the predominant failure mechanism when the ratio of opening width to innerburden thickness is less than five. Tensile failure of the innerburden is also possible, with the innerburden failing under its own weight.

Partially offset pillars are frequently due to surveying errors in mines designed for columnization or when operating under a mine of unknown layouts[2]. The high stresses developed on the offset ribside normally generate shear failure (also known as cutter roof failure) in the innerburden which, during collapse, produces tensile failure above the opposite rib line.

Totally offset pillars are structurally the most undesirable of the relative positions between upper and lower seam openings. This type of loading can be further subdivided into three categories: a) small upper pillar; b) medium-sized upper pillars; and c) large upper pillars. With other conditions being equal, the stability of the innerburden increases from case a) to case c) due to more evenly distributed lower stress concentration and the protective action provided by larger upper pillars.

Pillar Sizes

When designing for ultra-close seam mining, the possibility of innerburden failure must be considered in determining pillar sizes. It is important to note that when the pillar or the innerburden fails, it also increases the probability of failure of the other component. For pillar stability considerations, the required factor of safety should be applied to the combined pillar height if the innerburden is expected to fail.

A failed innerburden increases the effective pillar height to:

$$H = t_1 + t_2 + h$$

where t_1 and t_2 are the mineable coal thickness of seam 1 and seam 2, respectively.

A detailed discussion on pillar stability in ultra-close multi-seam mining is found in Zhou and Haycocks [3].

Opening Widths

Innerburden stability is important in pillar design because failed innerburden results in increased pillar height, which reduces pillar stability by reducing the width-to-height ratio of the pillar. Innerburden failures occur as a result of tensile, shear or shear/tensile failures, and are frequently controlled by geologic structures. The precise failure mechanisms for any situation are controlled by seven primary factors [1].

Based on the analysis of innerburden stability the following criterion can be established for the probability of tensile failure when

$$W > 5H \qquad (1)$$

where W is the opening width; H is the innerburden thickness.

For columnized pillars, the innerburden can be represented by a modified clamped beam loaded by self-weight (Figure 1).

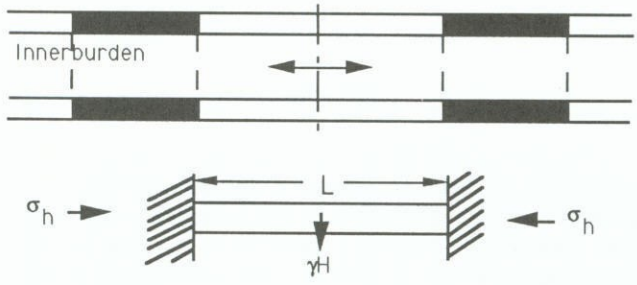

Figure 1. Self loading of innerburden in columnized design

The minimum stable innerburden thickness, given the tensile strength, σ_t, and a safety factor of SF, can be estimated by the following equation:

$$H' = SF\frac{W^2}{2\sigma_t}\frac{\eta[\gamma_2+(\gamma_1-\gamma_2)\eta]}{\eta^3+E_2/E_1(1-\eta)^3} \qquad (2)$$

where H' is the minimum stable innerburden thickness; W is the opening width; η is the percent of rock type 1 making up the the innerburden; γ is the weight density, respectively; E is the Young's modulus, and 1 and 2 denote rock type 1 and 2, respectively.

In Equation (2), the unit weight of the innerburden has been adjusted by broadly dividing the innerburden into two types of strata: soft (e.g. shale, clay, etc.) and hard rock (e.g. sandstone and limestone), as represented by types 1 and 2.

When pillars are offset, the loading conditions become much more complicated. One way of dealing with this situation is conversion of the external load into self-weight of the innerburden and application of the solutions for simple columnization. However pillar offsetting, which creates unevenly distributed load, is not easily incorporated through uniform self-loading. A

second approach which has been developed based on extensive photoelastic modeling of pillar offsetting uses the stress concentration due to pillar offsetting as a multiplier for the stresses (Figure 2)[1,3].

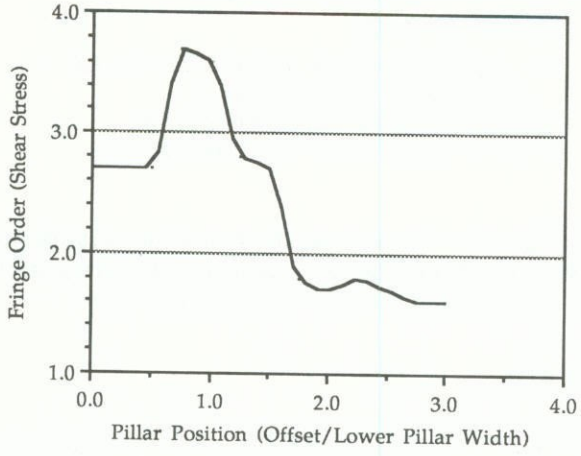

Figure 2. Effects of pillar offsetting on upper pillar stress

External Loading Factors

Depth Increasing depth means increasing stress which becomes a major factor in pillar stability and the development of shearing in the roof. Realistic determination of innerburden strength can be very complex as in situ loading conditions and rock properties are often difficult to ascertain. But depth can result in high stress concentrations at the corners of openings thereby causing shear failures to develop.

Mining Systems and Sequence In ultra-close seam mining, the type of mining system used and the sequence of mining are amongst the most important controllable factors. The best sequence is to mine the top seam first for both longwall and room-and-pillar mining. If the lower seam is mined first using a longwall system, caving of the strata may render the upper seam unminable unless the vertical distance is so great as to place the upper seam in the main roof. Mining using a room-and-pillar system under a seam mined by longwall is often undesirable because of the high stress concentrations under the remnant pillars. Whatever systems and sequence are selected, stress concentrations under and over pillars are going to be a major problem unless simultaneous mining is practiced.

Water and Gas Pressures The effects of ground water is usually evaluated based on the amount of water inflow or joint water pressure and the sensitivity of the rock to moisture. Depending upon the degree and extent of fracturing of the overburden strata, surface water may percolate to the upper seam. increasing the probability of lower seam water problems. The number of open fissures in the coal due to interaction may also increase the possibility of gas outbursts.

Equipment Loading The weight of heavy mining equipment and its repetitive movement may subject the innerburden to some dynamic loading. This condition should be taken into account especially when the innerburden becomes very thin. Figure 3 shows the effect of the weight of a mining machine on innerburden stability. Note the the rapid increase in the effect of equipment loading with decreasing innerburden thickness.

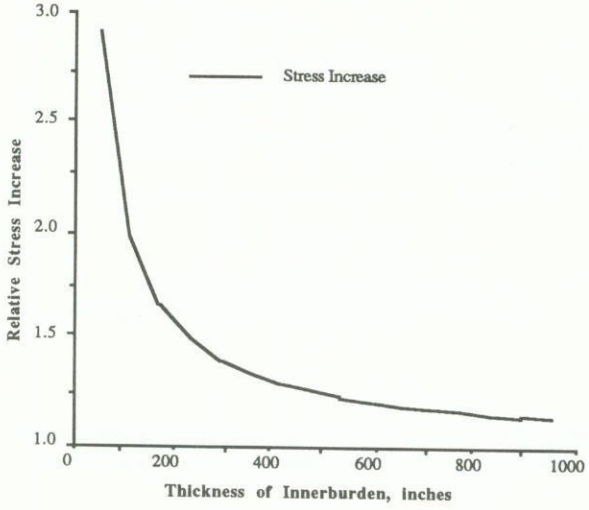

Figure 3. Effect of equipment loading on stress increase in innerburden

INNERBURDEN CHARACTERIZATION

Innerburden characterization involves the following four major categories: lithology, structure, water and time. In practice lithology and structure can be difficult to determine and new mines must characterize the innerburden based on interpolation between boreholes. Existing operations where accessible can investigate the innerburden by drilling and mapping of discontinuities with optimum results.

Lithology

The type of rock present in the innerburden is important in terms of its shear and tensile strengths, reaction to weathering and inherent structural characteristics[4]. Complex geologic features often make it difficult to model the innerburden and indeed, adverse geologic conditions may provide the dominant failure mechanism of the innerburden.

Previous analyses of multi-seam mining have shown

profound effects of percentage hardrock in the innerburden on interaction effects. This has been a simple but effective way to incorporate rock type into analytical studies and hardrock is defined as massive sandstones or limestones. As an example, Figure 4 shows the minimum innerburden thickness requirement for stability as a function of opening width/pillar width and percent of hardrock in the innerburden.

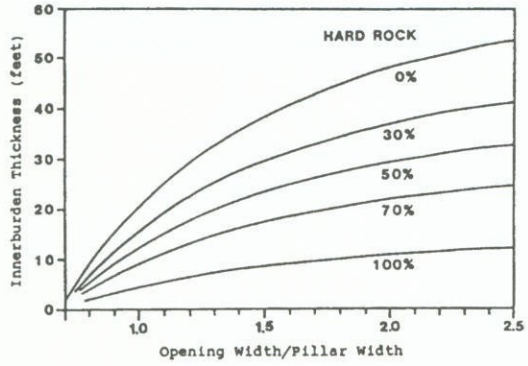

Figure 4. Min. innerburden requirement as a function of opening width/pillar width ratio

Degradation with time due to water and weathering is a major characteristic that must be anticipated in design.

Structure

Innerburden Layering Typical innerburdens can range from massive sandstones to highly laminated shales. Factors, such as sandstone channels, scours, pinch-outs, slickensides, and clay veins are not uncommon in the Appalachian coalfields and these structural anomalies, especially under the influence of seam interaction, constitute a discontinuity in the innerburden, thereby posing a potential hazard.

In practice it has been found that in unjointed roof rocks the number of layers in the innerburden have a significant effect on stress transfer in both case studies and physical modeling[5,6]. In terms of load transfer, innerburden layering affects both the size and shape of the pressure bulb. Generally, an innerburden with more layers will tend to deform more and transfer load to a greater distance.

Joint Sets A highly jointed innerburden will almost invariably fail after coal in the lower seam is extracted. The determining factors for instability are the spacing, length and orientation of the joints in relation to mine layouts in both seams. Rating of geological discontinuities is based on the Rock Mass Rating[7] system with the introduction of a joint influence coefficient.[8] A joint influence coefficient is assigned to each joint set in the innerburden calculated by:

$$JIC = (EFAC)(DFAC) + SFAC$$

where JIC = joint influence coefficient;
EFAC = $1/\cos(\theta)$;
θ = angle between the joint and the normal to the strike of the entry (deg.);
DFAC = weight factor due to the dip;
SFAC = weight factor due to the spacing.

A large JIC value indicates that the joints set is likely to cause problems while a low value means that the joint will have little influence on innerburden stability.

Time Factor

The effects of time are reflected in whether the interaction is purely active, active/passive, or purely passive, as defined by the following:

1) Mining is concurrent in both seams, a purely active condition;

2) Mining in one seam is complete, but the ground is still in the process of settling, an active/passive condition;

3) Mining in one seam is complete, and the ground has settled, reaching a new equilibrium, a purely passive condition.

Case studies have shown that in most situations, a period of two years proves to be adequate, although in some instances it may take five, 10, or 15 years for the strata to settle [9,10].

Characterization by Rating

To overcome the difficulties in quantifying geologic data and to provide initial guidelines, it was necessary to develop a system that could model the innerburden. The final geologic characterization of the innerburden was included in a rating system as shown in Table I.

To allow for maximum flexibility of the rating system, a weighted average factor has been introduced for the final overall rating. Each parameter is rating from very poor to very good. However, each factor will necessary have a different weight according to its importance to the mining situation. The total number of factors evaluated are then weighted to obtain the overall average rating, as given by the equation:

$$r = \frac{\sum_{i=1}^{6} w_i r_i}{\sum_{i=1}^{6} w_i}$$

where W_i = weight assigned to factor i; and r_i = rating coefficient of factor i.

Table I. Proposed rating system for ultra-close multi-seam mining

Factors ⬇ \Rating ➡	1	2	3	4	5
Rock Type of the Innerburden	Massive, clean, smooth gray sandstone or sandy sandstones; some massive hard shale	Massive, clean, smooth gray sandstone or sandy sandstones; some massive hard shale	Interbedded shale and sandstone; crystalized sandstones and conglomerate	Finely interbedded shale and sandstone; massive thinly laminated shale beds	Slumps, deposits, channel scours, fire clays, kettlebottoms, slickensides, pinchouts
M-Index (IBT/LST)	> 6.3	5 - 6.3	4 - 5	3.5 - 4	< 3.5
Geologically Weak Zones	None	Not Likely	Likely	Localized	Large Scale
Time Between Mining	> 5 years	2 - 5 years	1 - 2 years	0.5 - 1 years	< 0.5 years
Ground Water	Completely dry in both seams	Mostly dry in lower seam; dry in upper seam	Moist only in both seams	Moderate pressure upper seam wet	Very wet, rock very sensitive to to water
Innerburden Layering	1 - 5	6 - 8	9 - 11	12 - 19	> 20
Hard Rock in Innerburden (%)	> 70	51- 70	31 - 50	11 - 30	< 10

If, for example, two factors are being evaluated with weighting points of 10 and 20, respectively, and the rating for the two factors are poor and very good, respectively, the overall rating is then:

$$r = \frac{(-1)(10) + (2)(20)}{10 + 20} = 1.0$$

indicating an overall good rating.

This rating system allows the innerburden to be rated in the absence of certain factor, as is often true in mining situations. As in any classification system, the engineer must exercise judgment as to whether the information on certain factors can be ignored and the reliability of the rating if such is the case. The system also provides flexibility for modifications to widely differing geologic conditions, where some factors become more important than others. The final roof ratings are used as a modifiers on a minimum safe thickness.

APPLICATIONS IN DESIGN

Initial design is carried out by following a simplified beam or plate theory. Requirements for innerburden stability is then modified to accommodate the effects of offsetting pillars, great depth, and less than ideal geological conditions.

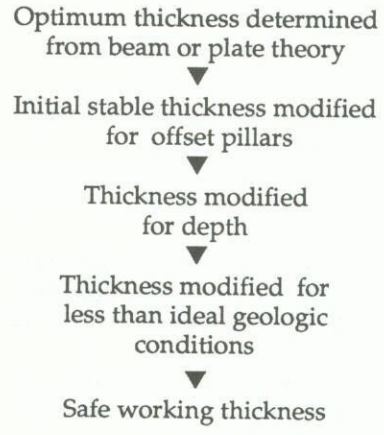

Figure 5. Simplified design protocol.

Application of the site characterization approach is best carried out minewide by contouring the differences between the final modified design thicknesses and the actual thickness of the overburden.

Plots of raw field data offer considerable support to this approach as shown in Figure 6. It should be noted that the upper and lower rating ranges are missing from the graph as these represent extreme conditions. The lower range because pure unbedded sandstone is very

unlikely to be encountered, and the upper range because any mining under such adverse conditions would be extremely difficult.

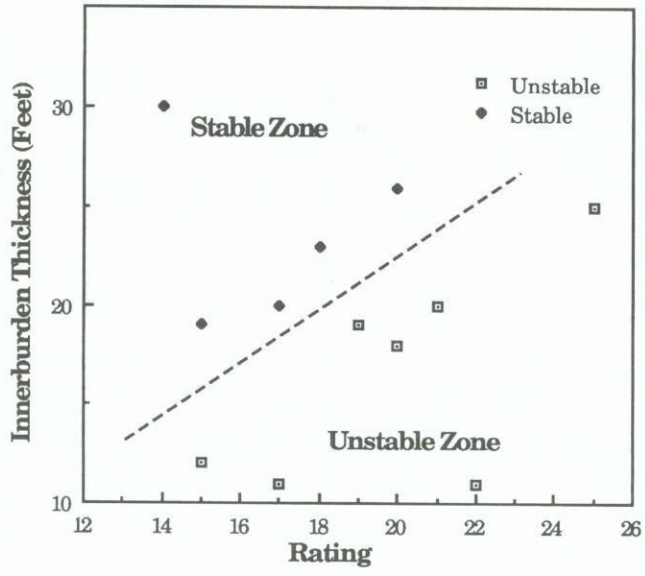

Figure 6. Raw data plot showing distributions of stable and unstable ultraclose mining conditions

CONCLUSIONS

Based on the research conducted to date the following conclusions can be drawn:

1. Geologic and structural integrity of the innerburden is the major factor in determining innerburden stability.

2. Opening width is the most significant operational variable in improving innerburden stability.

3. Careful columnization of pillars is essential for optimum stability.

4. Increasing lower pillar size relative to upper pillar dimensions may significantly increase lower seam roof stability for stacked pillars.

5. Evaluation of how close vertically seams may be safely mined can be achieved if adequate definition of the innerburden geology and structure can be achieved.

REFERENCES

[1]Zhou, Y. & Haycocks, C., 1989. Failure mechanisms in ultra-close seam mining. Proceedings, 30th U.S. Symposium on Rock Mechanics, West Virginia University, Morgantown, pp. 613-620.

[2]Matetic, R. J. & Chekan, G. J., 1988. Comparative study of pillar load transfer associated with multiple-seam mining. U.S. Bureau of Mines, RI 9176, 20 p.

[3]Zhou, Y. & Haycocks, C., 1990. Pillar stability in ultra-close seam mining. Proceedings, 31st U.S. Symposium on Rock Mechanics, W. A. Hustrulid & G. A. Johnson (Eds.), Golden, CO., pp. 137-144.

[4]Moebs, N. & J. L. Ellenberger. Geologic structures in coal mine roof. 1982, U.S. Bureau of Mines, IC 8620, 16 p.

[5]Ehgartner, B. L., 1982. Pillar load transfer mechanisms in multi-seam mining. M.S. Thesis, VPI & SU, Blacksburg, VA.

[6]Wu, W., 1987. An analysis of close seam interaction problems in the Appalachian coal fields. Ph.D. dissertation, VPI & SU, Blacksburg, VA.

[7]Bieniawski, Z. T., 1989. Engineering Rock Mass Classification. New York: John Wiley.

[8]Grenoble, A., Haycocks, C., & Wu, W., 1985. Computerized evaluation of near-seam interaction. Proceedings, 2nd Conference on the Application of Computers to the Coal Industry, Tuscaloosa, AL, pp. 317-322.

[9]Stemple, , D. T., 1956. A study of problems encountered in multiple-seam mining in the eastern United States. M.S. Thesis, VPI & SU, Blacksburg, VA.

[10] Engineers International, 1981. Investigation of problems and benefits of underground multiple seam coal mining. Final Technical Report, Dept. of Energy Contract DE-AC01-70ET14242.

10th INTERNATIONAL CONFERENCE ON GROUND CONTROL IN MINING

MINING UNDER RIVERS IN FUXIN COAL MINES

Liang Yin-Huai, *Engineer-Professor of Coal Mining*
Yao Ci-Shu, *Senior Engineer-Professor of Coal Mining*
Zhou Bing-Wen, *President, Staff & Miners' Tech. University*

Fuxin Coal Mines Administration
Fuxin, Liaoning, CHINA

ABSTRACT

In Fuxin Coal Mines, there are more than 20 million tons of coal buried under seasonal streams. The coal seams are mostly shallow. We have mined more then 50 mining blocks distributed in 5 coal mines. Their natural conditions are different, and the consequences are also more or less different. However, no stream–water–inrush accidents under regular mining conditions are the same. There were 3 exceptions. They were caused by unexpected roof caving which made valleys or alluvia subside as funnel–like cavities and let in inrush of stream flow. The key to our success in mining shallow under–stream coal seams, according to our analysis, is that valleys or alluvia subside gently and basically evenly with contractible tension fissures and that fissures both in valleys or alluvia and in rock seams are blocked up or sealed by cohesive deposits either from alluvia or rock. This paper treats: (1) some typical illustrations of mining shallow coal seams of different occurrences under streams of different sizes, flowing capacities and valley structures, (2) observations of the height of caved and fissured zones and subsidence of valleys or alluvia, (3) observations of underground water flow before, during, and after mining and the fluctuation with respect to stream flow, (4) observations and analyses of blocking up of fissures caused by mining, and (5) feasibility of mining shallow under–river coal seams.

INTRODUCTION

Our under–river coal seams are mostly shallow. The shallowest ones are 12 to 30 m under valleys. The medium depth is 60 to 80 m. Only a small part is buried at a depth over 150 m. On the other hand, the streams flowing over the seams are small and seasonal. In dry seasons, they appear as brooklets and split into 2 or more branches each with a width of 3 to 5 m and a depth of 0.3 to 1 m. Yet, their valleys are usually more than 100 m in width and full of water flow with large capacity in rainy seasons. It is still venturous to mine such coal seams without safety breakthrough though the streams are small. For example, the Chengnan Coal Mine mined a coal seam, 3 m thick, 40° dipping and 30 to 50 m deep, beyond a seasonal stream, by the room and pillar method before our country's liberation. The mining failed because of the fall of some upper–part supports which induced a sudden caving of roof and resulted in inundation of the mine. This shows that mining under streams should keep roof caving under control and avoid funnel–like cavities formed in valleys or alluvia nearby. Other inspirations are that small pits of excavating sand beyond water flow are readily filled by moistened sand surrounding them and that surface fissures caused by mining are readily sealed by surrounding soil during rainfall. We then hold that shallow under–river coal seams may be mined without risks should the surface subsidence be gentle and the hydrolyzed muddy and sandy materials nearby be capable of blocking up fissures that act as conduits for of water inflow. What we should do under favorable conditions are improving mining methods to mitigate ground movement and reduce the height of caved and fissured zones, taking precautions against inundation, and observing ground movement and the fluctuation of water flow both in the valley and underground. Based on these ideas, we have tried to mine them with care and succeeded. We have mine 85% of our workable under–stream reserves. Now, mining shallow under–river coal seams is not a difficult problem in our mining area. The following illustrations are typical and worth introducing to our foreign fraternity.

PRIMARY TRAIL

Our primary trial was made in the old 5th incline of the Pingan Coal Mine from 1958 to 1960. The coal seam there was 2 to 2.6 m thick. It was dipping at an angle of 25° and buried at a depth from 12 to 186 m. The seasonal Xi River flowed over it from its deep part to its shallowest part, about 400 m across. The river averaged 100 m in width. In dry seasons, there were only several water courses flowing in its

valley, each with a width of 1 to 3 m and a depth of more or less than 0.3 m, but the alluvium 3 to 5 thick was rich in water and the weathered sandstone below, 4 to 5 m thick, was also water bearing. Both of them contained more than 20% of mud and silt. Rock strata above the coal seam were composed of shale, sandy shale, and sandstone. All of them are hydrolyzable. Small cubic samples of shale are apparently softened and covered by mud after being soaked in water within a day. Those of sandy shale are so too, but the time of soaking is doubled or tripled. Sandstone is decomposed into grains of sand and silt after a week's soaking.

As the stream is very small, and the fully moistened alluvium is able to flow under certain motive force and the rocks are hydrolyzable and thus capable of blocking up the paths of water inflow, the coal seam there is very favorable for trying our primary under–stream mining. However, for safety reasons, its deep part with a depth from 136 to 186 m was mined first. Besides, the underground pump station was extended, and observations on surface subsidence, fissuring in the valley, behavior of the roof and fluctuation of underground water flow were performed. For making surface subsidence gentle and basically even, the cover–caving longwall mining method was adopted. As the width of the mining block, the 4th block on the west side of the incline, was much larger than that of the stream, the block was divided into 3 sub–blocks with the one under the stream in the middle. The two on both sides were mined before the mining of the middle one, and then the middle one was mined in the dry season for reducing water inflow.

The mining of the 4th block was smooth. The 3 longwall coal faces advanced without hitches. The roof caved normally without unusual consequence related to water inflow. Ground movement was gentle, and typical subsidence basins were formed on the surface. When the under–stream sub–block was mined, the subsided valley was in the middle of the basin. Fissures in the valley were soon blocked up by alluvial sand surrounding them. The maximum depth of subsidence was 1.6 to 1.8 m, about 70% of the extraction height. Underground water flow increased, but the increase did not exceed the forecasted quantity so that the pump station was marginal. On account of the effects, the first mining of the trial was successful. However, as engineers paid their attention to mining and safety only and neglected accumulating technical data, the history of mining was not summarized and reported, nor related data, except the results of subsidence observation, were recorded so that more detailed analysis could be made.

Mining of the 3rd block was all the same, but mining of the 2nd block was somewhat different because the mining depth reduced to 36 to 86 m. In mining the latter's under–river sub–block, the roof of the upper part of the coal face was somewhat damp. Caved rock far from the face was drenched to a certain degree. A tiny water path appeared in the lower gate which clearly increased the underground water flow. Roof control was strengthened. Any carelessness might cause local roof caving in the face. Hence, the mining was performed under strict precautions for avoiding the formation of funnel–like cavities in the valley. Consequently, the mining was also successful.

The most distinguished but venturous achievement of the trial is the mining of the 1st block because the mining depth is 12 to 30 m only. Under normal conditions, a coal seam with such a shallow depth under stream is unworkable, nor there is any precedent. However, for probing the limit of the workable depth limit, the block has been mined. The determination was made on the basis of the following considerations and precautions: (1) the upper reach of the stream had been undermined so that the poor water flow was further reduced. (2) Mining the two side sub–blocks first would drain a part of the water contained in the alluvium and thus reduce the possible water inflow to the under–stream sub–block in the middle. (3) This part of the valley was about 20 m wide in dry seasons. (4) The length of the coal face had been planned to be 45 m already. A short coal face might be mined rapidly. (5) The subsidence of a narrow sub–mining–block might be small. Again, a narrow sub–mining–block might be mined out before the arrival of violent subsidence so that water inflow might be reduced. This would be so especially as the valley was placed on the ending side of the mining. (6) A chain pillar on the lower side of the upper gate would improve the maintenance of the gate, reduce the area of crossing and thus protect the roof of the upper part of the coal face from unexpected caving. Fig. 1 shows the plane and cross section of the mining layout and surface subsidence.

In mining the under–river sub–block, roof control was quite a difficult problem. Before the coal face approached the bottom of the valley, the roof was damp and deteriorated greatly. When the face was immediately under the valley, the roof of its upper part even became drenched and fissured. Water drops fell from moistened fissures gradually. For avoiding unexpected roof caving, mining operations were performed with great care. Coal was shot by standing firing, with a pull of 0.8 m. Firing length was limited to 5 m. Roof bars were articulated as soon as possible. Lagging boards were placed on bars immediately after. The operation of cover caving was performed carefully so as to have the caved roof fallen smoothly and evenly without further deteriorating the roof inside the coal face. In this way, the coal face advanced 1.6 m daily and the sub–block was mined out within 2 months. There was not any serious accidents caused by unexpected roof caving. No funnel–like cavities were formed in the valley. Subsidence fissures in the valley were blocked up by alluvial sand and silt as usual, but the blocking could not check water inflow for lack of muddy components from shale and sandy shale. However, inundation was avoided. The pump station was still able to drain off underground water though water

inflow apparently increased.

Surface subsidence was much different from that of the 2nd block. It was not fully developed. Subsidence basin was not formed. Slopes and curvatures were greater. The final maximum subsidence depth was 1.2 m. The subsidence rate averaged 1.67 mm/day, but it was around 8 mm/day at the end of the mining and rose to its maximum of 38.3 mm/day thereafter.

Based on the above stated effects, we might say that the mining achieved its goal, i.e., to have the very shallow under–river coal seam mined. Yet an accident happened at the crossing of the abandoned coal face and the upper gate more than 10 days later. The accident was caused by the fall of some timber sets which in turn caused a sudden roof caving leading to the formation of a funnel–like cavity beyond the valley, and inrush of water and alluvial material. This was a black mark on the achievement though its influence on the mining was indirect. Hence, the achievement is not worth spreading except the conditions are very favorable. However, taking the trial as a whole, it is successful. It leads to the large–scaled under–river mining in the Qinghemen Coal Mine.

MINING UNDER QING RIVER

The Qing River is much larger than the Xi River but it is still a seasonal river. In dry seasons, its most part is divided into two branches, each around 5 m in width, more or less than 0.5 m in depth and with a flow velocity of ± 0.7 m/sec. In light rain days of rainy seasons, the two branches, each with a width of 20 to 50 m, a depth of 0.8 to 1.0 m and a velocity of 1 to 2 m/sec, almost merge . In heavy rainy days, the parameters of the combined flow are width over 200 m, depth 3 to 5 m and velocity 2 to 3 m/sec. Water in stream flow and underground water supply each other. In dry seasons, water table is higher than the water level of the stream flow, and underground water feeds the flow. In rainy seasons, the latter feeds the former. Parameters obtained from borehole hydrogeological tests are as follows: $Q = 14.423$ 1/m sec, $K = 300$ m/day and $R = 300$ to 400 m in the alluvium, $Q = 0.6$ 1/m sec and $K = 2.014$ m/day in weathered sandstone, and $Q = 0.00463$ 1/m sec and $K = 0.0106$ m/day in various water bearing sandstone strata.

The Qing River runs over the Qinghemen Coal Mine from north to south and covers about 15% of the mine's workable reserves. A small–scaled incline mine is constructed to mine the shallow part at the southwest corner of the mining area for probing the way of under river mining in the large–scaled shaft mine. It is called the 3rd incline. Its layout is shown in Fig. 2. The coal seam there is 0.7 to 1.6 m thick. It is dipping at an angle ranging from 2° to 7° and buried at a depth from 23 to 125 m. Its north side is mined first and divided into 5 blocks with the 2nd block 65 to 75 m in depth under the west branch of the stream and with the 4th block 90 to 125 m in depth under the east branch. We centered our discussion on the mining of the 1st and 2nd blocks.

The alluvium overlying all the blocks is 1 to 2 km in width and 3 to 5 m in depth. It is rich in water which is chiefly originated from rainfall. The main components of the overlying strata are sandy shale (containing layers of shale) and sandstone, but the composition varies apparently. The content of sandy shale is 87% in the north of the blocks but becomes 18.2% in the south. Table 1 shows the physicomechanical properties of the 2 kinds of rock obtained by analyzing a whole–strata sample from the south of the 1st block.

Soaking tests of small blocks of sandy shale shows that most of the samples become soft and expand 2 hours after soaking, become mud–covered 2 hours later, and become fully muddied another 4 hours later. The grit sandstone shows that all of the samples are fully decomposed into sand and silt after 8 hours soaking. The fine–grained sandstone shows that all the samples break into small cubes along the cleavages 8 hours later. These tests indicate that most sandy shale and all the grit sandstone have the function of blocking up the caved fissures. Hence, they are originally pervious but become water–tight should it be compact, water–bearings should it be porous with its outcrop in contact with the alluvium or pervious should it be porous without contacting the alluvium.

According to the No. 1 borehole which is in the north of the 1st block, there are 2 water–bearing sandstone strata overlying the coal seam. They are 8.65 and 2.2 m in thickness and 41.05 to 49.70 and 68.30 to 70.50 m in depth, respectively. The total thickness is about 15% of that of the overlying strata. According to the No. 3 borehole in the south of the block, there are 3 such strata. They are 2.95, 22.55 and 9.25 m in thickness and 8.9 to 11.85, 15.15 to 37.70 and 47.5 to 56.75 m in depth, respectively. Their total thickness is about 69% of that of the overlying strata. There is a common feature of the two that is the lowest water–bearing strata are close to the coal seam. Water contained in these strata is supplied by that contained in the alluvium and slightly varies with the weather.

The 1st block on the north side of the incline was mined first. It was divided into 3 panels with the 1st panel close to the stream. The north mining block of the 1st panel was mined by the cover–caving longwall mining method from the end of 1960. The mining operation went smoothly at first. Roof control was performed without any hitch. Water flow in the 1st panel increased gradually from 15 to 30 m^3/hr in the 1st month and remained at the level around 30 m^3/hr within the later 15 days, but increased rapidly and rose to the peak of 91 m^3/hr in the following 20 days. Simultaneously the immediate roof of the coal face became damp and roof control became difficult. A falling–off fluctuation ranging from the peak to the gorge of 56.8 m^3/hr then appeared in the next 14 days. In

this period of time, the immediate roof was drenched and fissure occurred inside the coal face and water dropped from the fissures gradually but uninterruptedly. Roof control became very difficult. The fluctuation was ended at the downfall point of 74.9 m^3/hr and followed a sudden fall to 48 m^3/hr. Afterwards, the water flow was around 50 m^3/hr till the mining block was mined out and the immediate roof returned to be damp simultaneously. The whole history of the fluctuation of water flow is shown in Fig. 3.

According to the observation and our analysis, the whole history of the fluctuation was caused by caving of the 2 water–bearing sandstone strata. As the lower one was only slightly more than 3 m above the coal seam, it was readily caved with its water content discharged. Yet, it was only 2.2 m thick, its water content was finite. Again, water supply from the alluvium was slow. Stable water flow was thus the result of the balance of the discharge and supply. The next increase of water flow was caused by caving of the main roof which contained the upper water–bearing sandstone stratum. This water–bearing stratum was 8.65 m thick, so its water volume was much larger. This caused the rapid increase and rise to the peak. After the fluctuation, its static water content was exhausted. Water supply from the alluvium maintained the stable flow of around 50 m^3/hr.

For improving roof condition, the room and pillar mining method was tried in the middle mining block of the panel, and the cover–caving and partial packing longwall mining method was tried in the south block. In China, the very thin pillar of the room and pillar mining method is called the breaker pillar for it is left for the immediate roof to cave inside the mined–out room without influencing that of the unmined neighboring rooms. It is capable of controlling the height of roof caving inside the rooms and keeping the caved arches of the rooms separately without joining each other within a certain period. This delays and mitigates main roof caving and thus improves roof condition. Partial packing in longwall coal faces may also mitigate main roof caving but not so effectively.

In the middle mining block, rooms and pillars were 90 m in length and around 30 m and 4 m in width, respectively. The room was mined by a longwall coal face from its inner side outwards. The immediate roof was caved cycle by cycle as the longwall coal face did for avoiding sudden caving of the lower water–bearing stratum which might be followed by water inrush. However, the main roof did not cave for a long time because of the pillar's support. In this way, the immediate roof of a room became damp as late as nearing the end of mining. Consequently, roof condition was much improved and roof control became much easier. It was surprising that water flow decreased gradually instead of increase and became stable at the level around 30 m^3/hr, the same as that before the 2nd time of increase in water flow in mining the north mining block. This indicated that caved fissures acting as water conduits in the north mining block were blocked gradually and that the main roof did not cave (Fig. 4).

In the south block, the mined–out space was packed with strips of packs. Strips were 5 m in width and spaced at an interval of 5 m. However, the main roof settled, fissured and broke step by step and caved at last. Caving was delayed for about a month. Yet, the coal face was under great pressure during the whole history of caving. Discharge of water from the upper water–bearing strata made the immediate roof deteriorate further, so the roof condition was just a little better than that of the longwall coal face without packing. Water inflow conformed to the behavior rules appeared in the north mining block but the capacity was smaller. The maximum flow was 77.4 m^3/hr, and the stable flow was around 30 m^3/hr. The flow returned to its normal value around 15 m^3/hr about 5 months after.

Borehole detection showed that the 3 mining blocks were different in the height of roof caving and the total height of caving and fissuring. The primary values of the caving height were 1.7 m in the north mining block, 1.1 m in the middle one and 3.3 m in the south one. The primary caving was limited to within the immediate roof of sandy shale, but its height was still influenced by the mining method. It was the successive caving that made the lower water–bearing stratum break and fall. However, the difference in the total height of caving and fissuring was much greater. The height was 25.9 m in the north mining block, 30.4 m in the middle one and 41.2 m in the south one. This difference was not only caused by the mining method but also caused by the behavior of rock caving. Fig. 5 shows the record of the detection.

Surface subsidence was also different with different mining methods. According to the observation, the maximum subsidence depth caused by longwall mining was 820 mm (823 mm if partial packing); that caused by room–and–pillar mining was 609 mm. The maximum subsidence rates were 13.4 (13.5) mm/day and 5.86 mm/day, respectively. Surface tension fissures caused by longwall mining were up to 70 mm in width, but those caused by room–and–pillar mining were 10 mm in width only.

According to the difference in roof conditions, water inflow, height of caving and fissuring and surface subsidence stated above, the room–and–pillar mining method was most favorable for mining under–river coal seam under the natural conditions of the incline mine. Yet, the longwall mining method was preferable to the mining of deep under–river coal seams in the shaft mine.

Mining the 2nd block was very important to the under–river mining in the Qinghemen Coal Mine because the west branch of the Qing River ran over there and the coal seam there was the shallowest from the valley all over the mine. It

was expected that mining then would afford experience to the successive mining.

The coal seam there was 63 to 73 m under the stream valley. The percentage of sandy shale was 30 to 70%. Sandstone in and close to the immediate roof became harder. The mining method was the "room–and–pillar", but the room's width was reduced to around 25 m, and the length was also shortened as shown in Fig. 4. For getting a better roof condition and delaying the main roof caving roof control was strengthened. Improved frictional metal props with high setting load were used for supporting the immediate roof. Cribs made of steel rails were used for strengthening supports and inducing caving of hard sandstone in the immediate roof. In this way, the primary roof convergence averaged 5.15 mm; the maximum convergence under the maximum roof load of 8.6 t/prop was 46.8 mm, and the average convergence and roof load were 27.7 mm and 6.0 t/prop, respectively. Roof convergence along the strike rose from 5.15 mm to around 35 mm as the coal face advanced by 14 m. Immediate roof caved after the advance of 15 to 16 m. Afterwards, its caving span was 5 to 6 m. It was dry till the room was mined out.

Water inflow was small. The initial water flow in the block was around 15 m^3/hr. It made the flow increase after the immediate roof of the 1st room caved, rise to the 1st peak of 27 m^3/hr after caving in the 2nd room and rise to the 2nd peak of 36 m^3/hr as the fissured zone extended to the upper water–bearing strata (Fig. 6). According to the observation and the small water inflow, the main roof did not cave before the block was mined out.

Surface subsidence was mitigated by the improved mining too. As shown in Fig 7, the maximum subsidence depth, under the west branch of the stream's flow was 450 mm only not only much smaller than the 823 mm of the longwall mining with packing in the 1st panel of the 1st block but also smaller than the 609 mm of the room–and–pillar mining in the panel. Its minimum, under the stream valley too, was 189 mm the influence of which was very small. The maximum subsidence rate was 3.54 mm/day, also smaller than those of the 1st panel. The maximum lateral movement was +77 mm and −92 mm, whereas that of the longwall mining with packing was +122 mm and −238 mm. Other subsidence deformations were also smaller than those of the longwall mining with packing in the 1st panel. Table 2 shows the comparison. With smaller surface subsidence, a better roof condition and small water inflow, the under–river mining in the 2nd block was successful.

Fig. 6 also shows the rule of water inflow in the whole history of under–river mining in most of the blocks of the incline mine. The rule of the fluctuation of water inflow is that underground water flow increases from the normal to the 1st peak as the lower water–bearing stratum caves thoroughly and rises to the 2nd peak as the upper water–bearing stratum is either caved or fissured. The higher peak shows that the stratum is caved, and the lower peak shows that the stratum is fissured only. The downfall means that the stratum's static water content has exhausted, and the stable flow means that the inflow comes from the alluvium through the it's outcrop. The flow returns to normal as the caved fissures are fully blocked and the space of the caved water–bearing stratum was filled with regenerated rock which blocked the discharge from the stratum.

Water inflow during under–river mining is not originated from the stream flow. This may be proven by the following facts: (1) The fissured zone have not contacted the alluvium. (2) The chemical contents and properties of the underground water are the same as those of the alluvial water but different from those of the stream water according to analyses. (3) Water inflow is out of the influence of rainfall. Table 3 shows some of underground water flow during rainy days. (4) Inundations of subsidence basin by flood water have not made underground water flow increase. There were several times of such inundations appeared in July of 1962, July of 1963 and July and August of 1964. The flooded areas and depths were 6,400 m^2 and 0.2 m, 10,000 m^2 and 0.5 m, 26,500 m^2 and 0.7 m and 28,000 m^2 and 0.8 m, respectively. The corresponding underground water flows are shown in Table 3.

MINING UNDER THE ZHUANJIAOMAO RIVER

24 under–river mining blocks of the Dongliang Coal Mine have been mined out safely. One of them is outstanding because of its very shallow depth, complicated geological condition and special roof control. It is a mining block of the 2nd incline of the mine beyond the Zhuanjiaomiao River with its shallowest part 26 m under the edge of the river and with its deepest part 68 m under the flood area of the river. The coal seam there is 3.3 to 4.6 m in thickness and dipping at an angle from 10° to 20°. It is severely faulted. There are 4 larger faults with their downthrow (upthrow) ranging from 3 to 10 m and more than 6 smaller faults with their downthrow ranging from 0.5 to 2 m (Fig. 8).

The river is also seasonal. In dry seasons, it is divided into 2 branches each with a width of 3 to 5 m and a depth of 0.2 to 0.3 m. In rainy seasons, it is full of water flow with high flowing capacity. It often overflows its banks during heavy rainy days. Its flood area is shown in Fig. 8. According to the historical record, the maximum flowing capacity is 77 m^3/sec. and the highest level of flood is 3.5 m higher than the surface.

The alluvium is 2.1 to 7 m in thickness and rich in water. According to the hydrogeological test, $Q = 4.56$ 1/m sec, $K = 89.44$ m/day and $R = 126$ m. The weathered sandstone is also water–bearing but with much less water content. It is pervious rather than water–bearing. Shale and

sandy shale are the chief components of the overlying strata ranging from 42.6 to 79.6%. Shale is plastic and expansible as wetted by water. It is completely water–tight. Sandy shale becomes muddy after being soaked in water 3 days. It is also water–tight basically. Sandstone is coarse–grained with high content of cementing mud. It is readily hydrolyzed into sand and mud and thus has the function of blocking up caved fissures. this is the only but most favorable condition for such an adverse under–river mining there.

For safety of mining, the mining block was mined by a specially designed room and pillar mining method as shown in Fig. 9. Pillars were left for supporting the immediate roof without caving within a predetermined period. During this period, roof pressure became greater and greater resulting in the pillars being fractured gradually and collapsed at last. This led to gentle roof caving of large area accompanied by mitigated subsidence of all the above rock strata. The area of such caving and subsidence was around 3,000 m^2 each. Large pillars made such caving intermittent, but subsidence along the strike joined together. Surface subsidence of the inner part of the mining block is shown by the I–I' cross section of Fig. 10. The maximum subsidence was 0.5 m only surely because of the effect caused by the special treatment of roof control. The strikewise surface subsidence of the outer part is shown by the I–I' cross section of Fig. 10. There were 3 values of maximum subsidence, 0.95 m, 1.15 m and 1.25 m, each corresponding to a caved sub–block. Any of them was greater than that of the inner part because the outer part was much larger and severely faulted and the extraction height was higher so that subsidence was much larger. They were closely related to the sub–block's caving span, number of pillars in the sub–block, influence of faults and extraction height. However, they would be smaller should the surface subsidence be observed in the upper part, closer to the stream bank. With the aid of the water–tight strata and blocking of the caved fissures, water inflow was small as shown in Fig. 11. Fig. 11 also shows that underground water flow is not related to rainfall.

A roof accident occurred at the intersection of several faults. A funnel–like cavity was thus formed on the surface. Yet, under the actions of the water–tight strata and the function of blocking the caved fissures by alluvial and hydrolyzed sandy and muddy materials, the cavity and induced water flows were rapidly blocked up. Water inflow was 10.3 m^3/hr only. However, the accident was avoidable at the intersection had it not been mined. Hence, the mining was still successful.

CONCLUSION

According to the experience of our coal mines accumulated in the last 30 years, shallow and very shallow coal seams under small rivers, common in many mining areas, can be mined if the following natural conditions are present and demands are satisfied: (1) There are water–tight rock strata with enough thickness and hydrolyzable rock and the hydrolyzed materials block up the caved fissures, (2) Reliable roof control measures are used for reducing the height of the caved and fissured zones so they would not extend to the alluvium nor water–bearing strata of high capacity and mitigating surface subsidence so that it is gentle and the amount small, (3) Roof control must be performed very carefully so as to avoid roof accident, and (4) A well organized lookout, alarm and disaster–relief system is necessary.

REFERENCES

1. Technical Section of the Qinghemen Coal Mine Initial Summary of the Trial of Mining Under the Qing Stream (Interior Report).

2. Technical Section of the Qinghemen Coal Mine Report on the Trial of Under–Stream Mining in the 3rd Incline of the Qinghemen Coal Mine (Int. R.).

3. Technical Section of the Dongliang Coal Mine Practice of Mining Very Shallow Under–Stream Coal Seam in the 2nd Incline of the Dongliang Coal Mine (Int. R.).

4. Technical Section of the Qinghemen Coal Mine Observation Results of Roof Pressure & Convergence of Under–Stream Coal Faces.

5. Department of Geology & Survey of the Fuxin Coal Mines Observation Results of Surface Subsidence of Under–Stream Mining.

Table 1. Physicomechanical Properties of Sandy Shale and Sandstone of the 1st Block

Item	Rock	Compressive Strength, (kg/cm^2)	Density (g/cm^3)	Porosity (%)
1	Sandy shale	57	2.2	6.1
2	Sandstone	47	2.0	13.4
3	Sandstone	102 to 130	2.2	8.6 to 10.4
4	Sandstone	685 to 830	2.5	2.4 to 2.8
5	Sandstone	505	2.4	6.2
6	Sandy shale	103	2.2	12.8

Table 2. Comparison of the Maximum Subsidence & Deformations of the 2 Blocks

Block	Mining Method	Strain (mm/m)	Slope (mm/m)	Curvature ($1/m^2$)
1st	Longwall	+6.7,-6.3	+17.9,-16.7	+1.02,-1.83
2nd	R & P	+2.4,-3.4	+10.4,-8.5	+0.38,-0.42

Table 3. Relationship Between Underground Water Flow (m^3/hr) and Rainfall (mm)

Yr.-Mo.	61-4	62-5	62-7	63-4	63-7	64-4	64-7
Rainfall	1.1	69.8	259.5	11.1	273.2	36.6	259.2
Incline	166.5	114.3	114.9	80.0	89.0	122.4	141.9
1st R&P	66.9	25.6	19.4	24.9	28.1	15.0	8.3

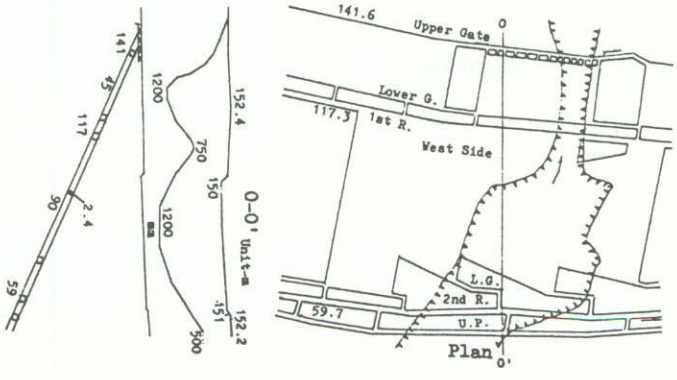

Fig. 1 Layout of mining a very shallow under–river coal seam.

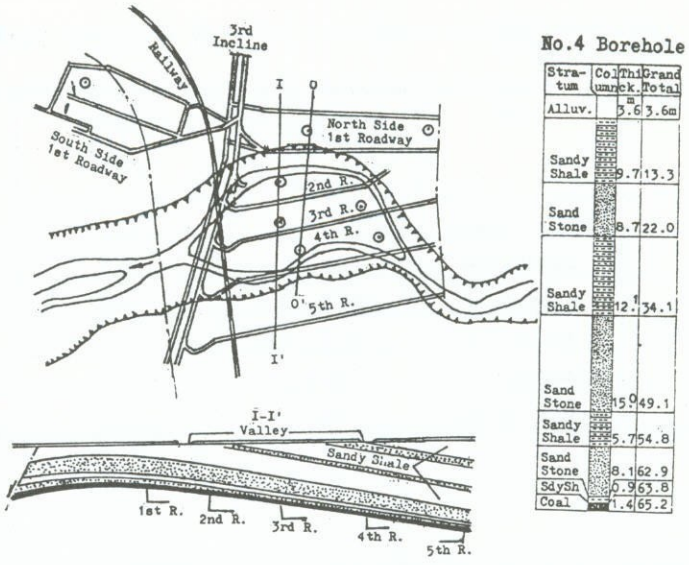

Fig. 2 Layout of the 3th incline of the Qinghemen coal mine.

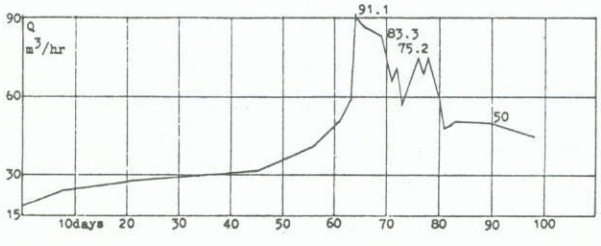

Fig. 3 Fluctuation of underground water flow in mining the north mining block.

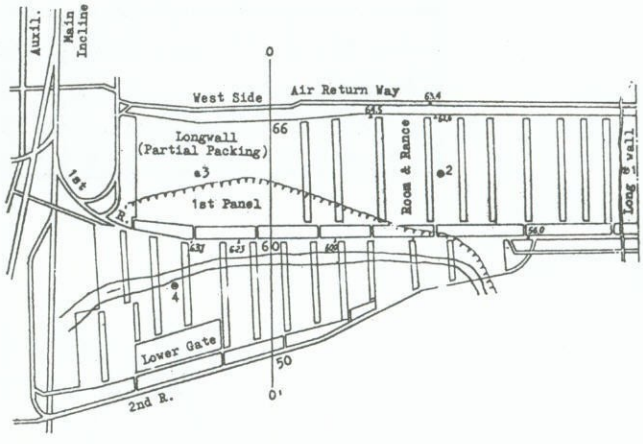

Fig. 4 Layout of the 1st and 2nd block and the room and pillar mining method.

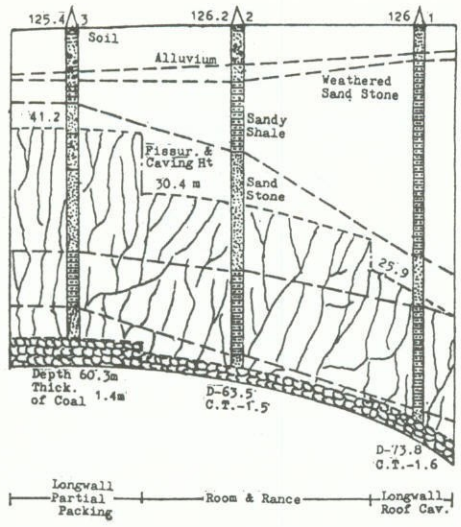

Fig. 5 Borehole detection of caving and fissuring of roof rock.

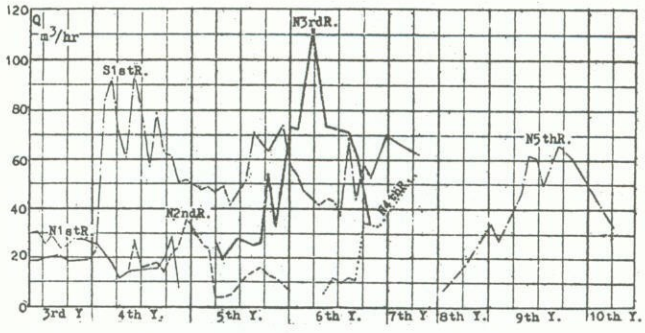

Fig. 6 Underground water flow during under–river mining in the 3rd incline mine.

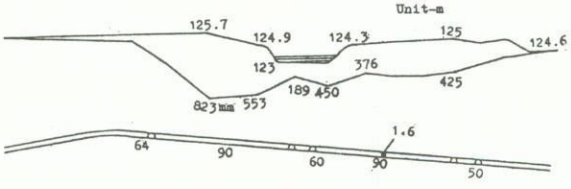

Fig. 7 Surface subsidence caused by under–river mining in the 1st and 2nd blocks.

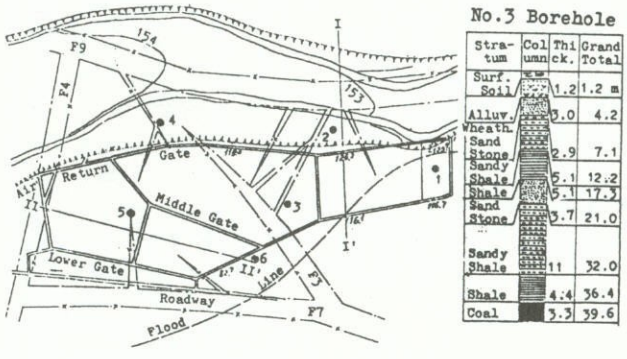

Fig. 8 Layout of the 3rd mining block of the 2nd incline of the Dongliang coal mine.

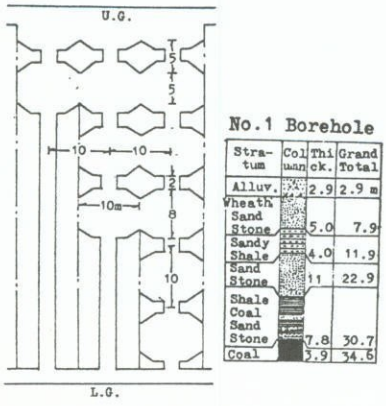

Fig. 9 Layout of the room and pillar mining method.

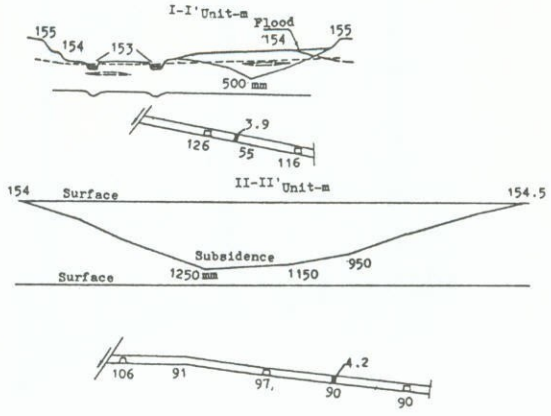

Fig. 10 Surface subsidence of the mining block.

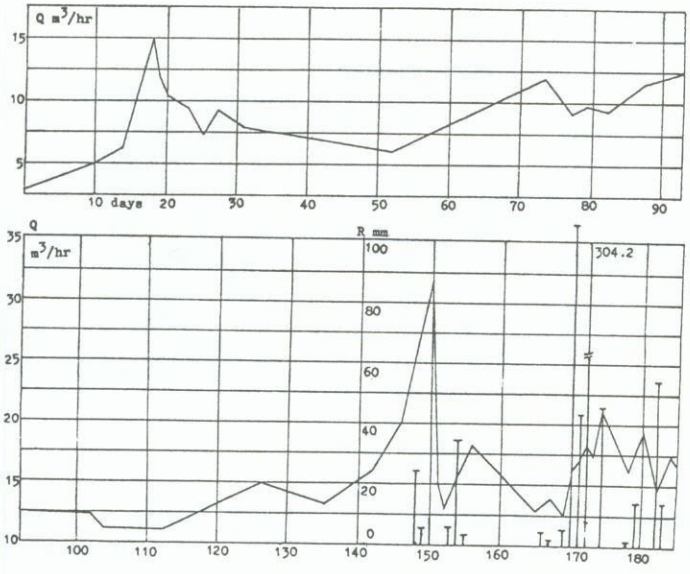

Fig. 11 Underground water flow of the mining block and the related rainfalls.

10th INTERNATIONAL CONFERENCE ON GROUND CONTROL IN MINING

USE OF DATABASE IN GROUND CONTROL TO IDENTIFY WEIGHTINGS AND WATER INFLOWS

G. C. Xiao
R. A. Irvin
I. W. Farmer

Ian Farmer Associates,
11-12 Skinnerburn Road
Newcastle upon Tyne, NE4 7AN
UNITED KINGDOM

ABSTRACT

A database, incorporating historical data from British mines, to study the factors affecting inflows from proximate aquifers into longwall workings, showed that a main casual factor was the immediate roof strata lithology. When this comprised principally stronger sandstone, there was a tendency for periodic inrushes associated with face weighting. This phenomenon is explained by the collection of water in bed separation cavities, where free water connected to a high pressure head aquifer source, may be trapped.

INTRODUCTION

In the past, the principal factor governing water inflow into mine workings was considered to be the depth of cover beneath an aquifer or water source. Garritty, (1981, 1982, 1983) in a study of water inflows into longwall workings beneath the North Sea and the Permian aquifer in the coalfields of North East England, showed that there was a high risk of inflows when:

(a) Cover to the sea bed or the base of Permian was less than 140m or 100m respectively.

(b) Faults with throws greater than 1m connected the workings to the water source.

(c) The competence of the immediate roof strata was relatively high - particularly where the first 20 - 30m contained less than about 35% of mudstones.

(d) Major roof breaks formed, usually associated with a major roof weight.

Garritty's work is certainly the most thorough investigation of water inflows in British Coal Measures rocks, and although he did not seek to explain the inflows in terms of specific mechanisms, these can be inferred from his conclusions and the coal face geometry. Thus inflows occur during strata fracturing following caving at a time when major roof breaks occur in strong rocks often accompanied by weighting. This induces continuous fractures in the cofer which also connect to the water source. This is exacerbated by faulting and ameliorated by the presence of weaker and less permeable rocks which fracture easily and recompact quickly.

It is, unfortunately, not an easily modelled prototype situation, and when similar inrushes occurred during the initial stages of development in the Selby Coalfield (Wilby, 1990), and similar strata were postulated for the new Asfordby Mine (Hindmarsh, 1990), it was decided to develop Garritty's work in a more systematic way.

DATABASE COMPILATION

In complex engineering design, situations such as coal mines, database compilations of case history data combined with graphics programs, can represent a strong alternative to more conventional design approaches. A menu driven software database package storing all necessary information offers easy access, search, edit and report facilities for preparation of various sets of data for analysis, and search for trends and correlations.

A database was compiled, using dBASE4 software (Ashton Tate, 1987), for all known historical mine water inflows into British coal mines. Data on geology, geomechanics, water inflow, mine geometry, and operations were collected from mine plans, borehole logs, reports, and minutes stored in mine records. Opinions of geologists and other experts was incorporated into the database.

The data was analyzed using graphical, statistical, and geostatistical techniques to determine the major factors affecting inflow of water into workings and underground openings in British Coal Measures strata. The data was then used to predict, empirically, water flow into proposed new mine developments.

The database comprised 5 database files containing information from different sources. These were respectively:

MINING, the master database file containing records based on mine workings.

INFLOW, a second master database file containing records of inflow events into mine workings.

BOREHOLE, WATER AND FLDSTEST, three auxiliary database files containing respectively, records of borehole logs, mine water analysis, and field tests.

A list of all the field data subheadings is given in Appendix 1, the INDEX NO is a device for relating the files. Thus a particular INDEX No relates a specific mine working to an inflow

event, and where available, to geology, water sample, and flow data. In this case, British Coal Area and mine codes were used as part of the site identification. Additional codes were used to link similar workings and mines.

Data was obtained from central and mine records in collaboration with experienced geologists and surveyors. In total, data was obtained from 685 longwall faces, 246 borehole logs, and 734 water analyses. These numbers do not necessarily reflect the true extent of mine water problems since the records include both wet workings and an arbitrary number of dry ones for comparison. Some records were large and included a group of similar workings.

Many records have the opinions and explanations of geologists or surveyors on particular inflow problems stored in the memo field COMMENT. These often include key information for understanding inflow.

While compiling the database, additional software was developed to ease compilation and correlation. Graphics programs were also developed in quickBASIC (MICROSOFT, 1987) to graphically represent mine plans and aquifer data.

TRENDS AND CORRELATIONS

When compiled, the database provides a rapid method for examining trends and correlations between identified variables. In this case, a starting point was the work of Garritty.

Three particular areas were examined in detail. These comprised: Horden and Blackhall mines from the North East coalfield which are well documented case histories and a major part of Garritty's (1981) study; Wistow mine, part of the new Selby coalfield and a mine subject to large and unexpected inrushes and weightings; and Asfordby mine, in the developing Vale of Belvoir coalfield, where inrushes were considered possible in view of the proximity of aquifer rocks.

(a) Horden and Blackhall mines

Initially data from two mines beneath the Permian aquifer in the North East of England coalfield, Horden and Blackhall, were examined. These are two of the best documented mine inflow cases in recent years. Further information and location maps are given in Farmer (1985).

Water inflow at Horden mine mainly occurred in the High Main seam. This was worked under the North Sea with less than 100m cover to the base of the Permian aquifer. Boring from the seam encountered a static head of 228m at the base of the Permian.

In the early 1960s, several longwall faces were worked encountering only minor water feeders. However, after 1963, roof water caused delays on two adjacent 210m longwall faces at cover depths below the base of the Permian of 75 and 90m. Subsequent abandonment of a longwall face with flows of 41 1/s led to a decision to develop 65m retreat faces with 50m pillars, but while some of these encountered only minor feeders, others encountered heavy feeders up to 50 1/s. Some of these were associated with faulting; some with coarse saturated Coal Measures sandstones.

At adjacent Blackhall mine, the Low Main seam was worked at about 100m below the base of the Permian aquifer. Inflow events were usually associated with severe face weighting, and after several 200m longwall faces had experienced heavy inflows, narrow faces were worked with substantial pillars. Some of these faces also encountered water problems.

Figure 1 summarizes inflow data at both Horden and Blackhall. Figure 1A is plotted in a West-East direction with distances to National Grid Reference Line X=445000. Plotted are (a) the cover to the base of the Permian aquifer, (b) the lithology of the 30m of roof above the seam expressed as the percentage rocks - principally mudstones and seatearths, (d) the lithology of the 100m of roof strata above the seam expressed as percentage of incompetent rocks, (e) the maximum flow rate of inflow events and (f) the throw of faults close to faces. Figure 1B is plotted in a South-North direction with distances to National Grid Reference Line Y=540000.

The immediate conclusion from the data is that while a low cover thickness to the aquifer is important, it is quite clear that there is a significant correlation between lithology and inflows. Except for those specifically associated with faults, there is a quite significant correlation between inflows and the presence of a high percentage of competent rocks in the immediate roof.

(b) Wistow mine

The water inflows in the A block at Wistow mine in the Yorkshire coalfield are the most notable such events of recent years in Britain. The first two longwall faces at a cover depth below the Permian aquifer base of 77m had respective inflows of 121 and 11 1/s. The inflows followed heavy weightings, and subsequent faces were changed to shortwall faces, with a panel width of 46m. When one of these experienced an inflow of 136 1/s, the length was successfully reduced to 37m, but the block was eventually abandoned as uneconomical. Subsequent workings in C block at a depth of 200m below the base of the Permian were water free.

Figure 2 plots the same data as Figure 1 for Wistow mine in a West-East direction from National Grid Reference Line X=45000. Once again the correlation between a high percentage of competent rocks in the roof and water inflows is quite clear.

(c) Cotgrave and Clifton mines

The ameliorating effect of weaker and more impermeable rocks can be seen by looking at data from Cotgrave mine in the Nottinghamshire coalfield in Figure 3. Situated on the western side of a relatively undisturbed Carboniferous sedimentary basin, and dominated by mudstone sequences within the main coal bearing succession, the South Nottinghamshire coalfield has rarely been affected by water inflows - even when working at very shallow depths beneath the Permo - Trias Bunter Sandstone.

At Cotgrave mine several longwall faces in the Deep Hard seam have been worked 45m below the Bunter Sandstone, including one district which stopped at a 5m fault heading away from the face. After a few months, this became damp and minor water flushes were experienced in methane boreholes. Similar experiences were obtained at nearby Clifton mine. In both cases, mudstones comprised 60-70% of the immediate roof, and of the full sequence to the base of the Permian.

BED SEPARATION

Hoare and Whitworth (1978) and Elliott (1978) amongst others have proposed a relatively simple explanation for water inrushes in the Est Midland Cannock Chase coalfield. Following an inrush at West Cannock No. 5 mine, boreholes were drilled upwards from the seam, and water flows were observed at heights of 18, 38, and 44m in one borehole, and 38 and 69m in a second borehole.

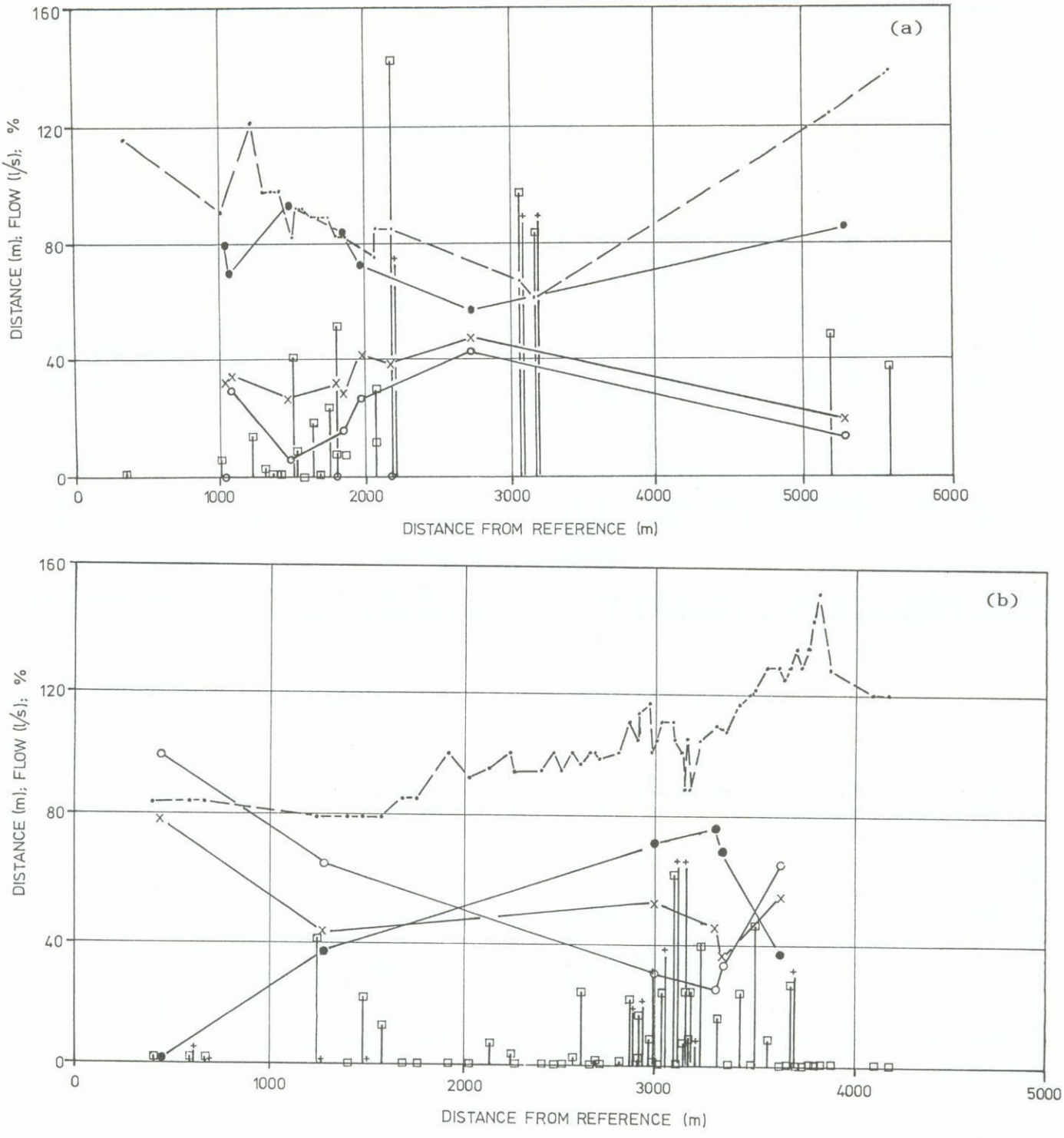

Figure 1 Historical inflow data at (a) Horden and (b) Blackhall mines beneath the Permian aquifer in Durham, referenced to National Grid Reference Lines (a) X=445000 in a West-East direction and (b) Y=540000 in a South-North direction. Plots are:

- Cover to base of Permian aquifer
- ● % sandstone in 30m of roof above seam
- 0 % weak rocks in 30m of roof above seam
- x % weak rocks in 110m of roof above seam
- □ Maximum flow rate of inflow events
- \+ Throw of faults close to face

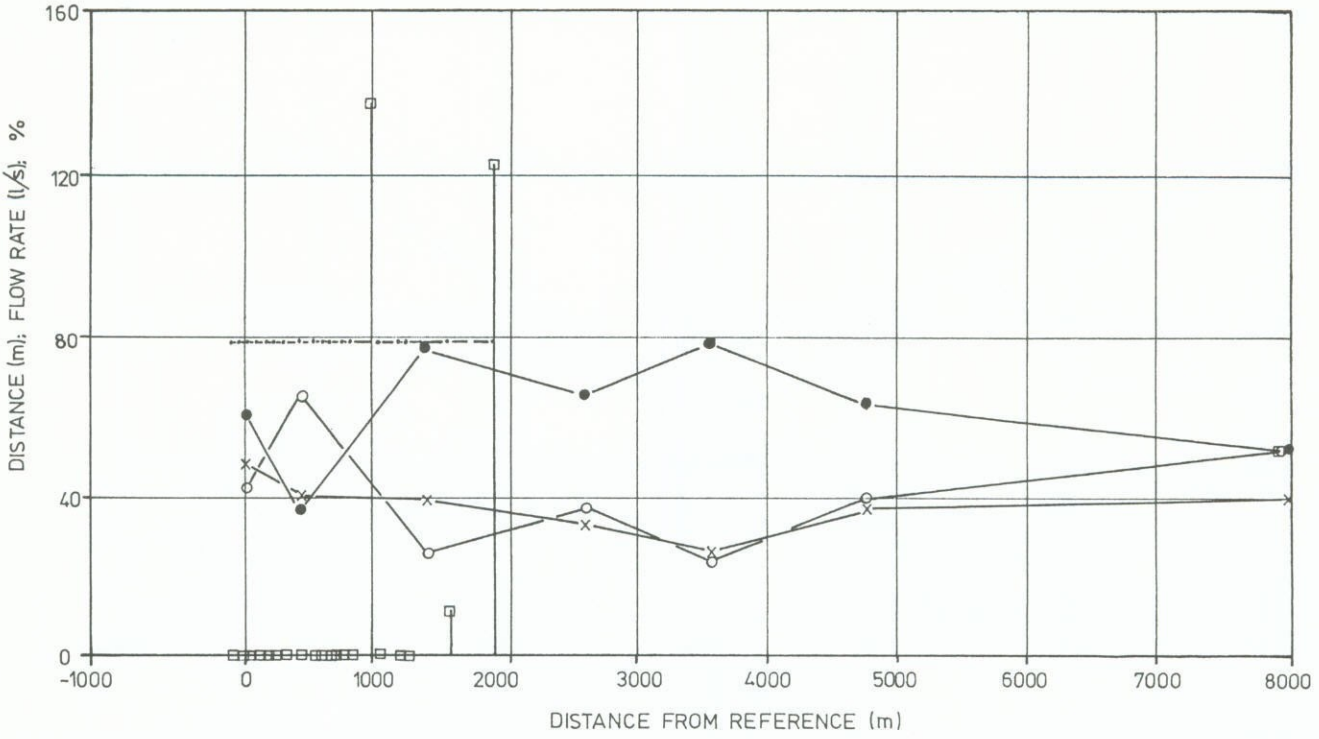

Figure 2 Inflow data at Wistow mine, referenced to National Grid Reference Line X=4555000 in a West-East direction. The plots and symbols are the same as in Figure 1.

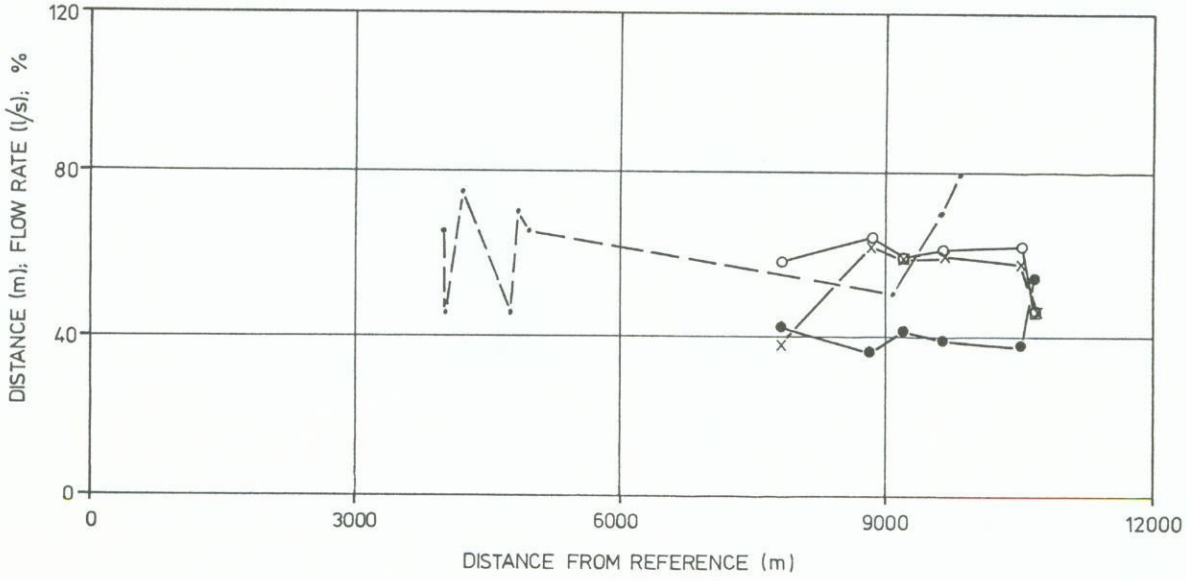

Figure 3 Cover to base of aquifer and lithological data plotted using the symbols in Figure 1 for Clifton and Cotgrave mines, referenced to National Grid Reference Line X=455000 in a West-East direction. Significant inflows were not measured.

In each case, water in quantity was observed only where bed separations had occurred.

The geology of this mine is not typical of those previously discussed. The Coal Measures between the Park seam and the Trias aquifer have a relatively small proportion of sandstones and siltstones, usually muddy and fine grained, and a relatively high proportion of mudstones and seatearths which tend to swell and soften in the presence of water. Oxidation of the pre-Trias surface of the Coal Measures is common, with a reddened zone of low permeability weathered soft red marls for 10-15m below the unconformity. The basal part of the Trias is a variable thickness sandstone called the Littleworth Beds, 0-30m thick, below the Bunter pebbles comprising relatively loose shingles and gravels.

There is also a saturated zone (Pugh, 1980) of coarse Coal Measures sandstones extending for a variable distance up to 100m below the unconformity, depending on the continuity and dip of the Coal Measures, and the availability of permeable cleats and joints in coal seams and sandstones, respectively. Water problems in the Cannock Chase coalfield have been mainly associated with this saturated zone; this was confirmed chemically. In most cases the observed bed separations occurred above the roof of coal seams in the cyclothem below the saturated zone, the water contained by underlying low permeability seatearths. The bed separations opened above the caving zone behind the face, and inrushes occurred when face breaks connected through to these separations above the face, invariably in the immediate 30m above the face. Water in bed separations above this height did not effect the face, and only rarely connected through to the face where faults occurred.

INRUSH AND WEIGHTING MECHANISM

Weightings on longwall faces occur when a thick bed (usually of sandstone) fails to break at the caving line behind the face supports, and hangs in the goaf until the reaction forces at the sides and face exceed the resistance of the bed. The resultant rapid energy release and accompanying face closure, unless designed into the yielding characteristics of the face supports, can cause damage and lost production. The most severe weightings are usually at the beginning of a face, when a double span collapse may be expected, or where water at pressure may be present in the proximate strata. In the latter case there may be the additional hazard of water inrushes.

Under normal circumstances, when a face has been established, and provided it is long enough to simulate two-dimensional conditions normal to the face line, fractures induced by the front abutment stress, will be sufficient to establish a satisfactory caving regime. Abnormal circumstances may be created by narrow faces, thick nether roof beds and, particularly, thick beds associated with water pressure.

Consider for instance a typical Coal Measures sandstone with a laboratory strength of $85MN/M^2$ (12,000 psi) measured on a 25mm (1 inch) specimen. Then for say a 10m (33ft) thick bed, this will reduce in inverse proportion to the square root of the dimension (Farmer, 1984), giving an estimated rock mass strength of about $5MN/m^2$. Although Boundary or Finite Element analysis is more accurate, an estimate of maximum beam stress can be obtained from beam theory:

$$\sigma_x = \frac{qL^2}{2t^2}$$

Where L is the span and q the body weight to γt per unit length and width where γ is the rock unit weight and t the beam thickness.

Thus for the hypothetical beam section, assuming $\gamma = 25KN/m^2$ ($156\ lbs/ft^3$), L will be approximately $60m$ ($200ft$). This assumes, however, a body weight of $0.25MN/m^2$ per m. If the beam is subject to a head of 250m of water through connection to an aquifer, this increases q by an order of magnitude and, in this case, either the span is reduced, or the thickness increased, for the same thickness or span respectively. More importantly, the potential energy released at collapse is also increased by an order of magnitude.

CONCLUSION

There is a correlation between heavy water inflows often associated with strata weights and the proportion of weak, low permeability rocks in the immediate 30m of roof strata above longwall faces, when aquifer rocks occur above the face. Inrushes occur when the percentage of these rocks falls below 30% in the proximate roof. The cover to the aquifer rocks is a less important parameter. When the percentage of weaker rocks is high, inflows do not occur even when aquifer rocks are in close proximity to the face.

Inrushes are associated with a high percentage of strong sandstone rocks in the immediate roof. In this case bed separation with poor caving may allow water reservoirs to form which can be connected to high pressured aquifer sources. This builds up high reaction forces at the abutments with the potential for large strain energy release and water inflow at failure.

ACKNOWLEDGEMENTS

The authors gratefully acknowledge the assistance provided by the geologists and surveyors of British Coal Areas and mines and the geologists of the British Coal HQTD during the completion of the Aquifer Database.

The views expressed are the authors' and not necessarily those of the British Coal Corporation.

REFERENCES

Ashton Tate. dBASE IV, Developer's Edition, 1987

Elliott R.R. Strain Zones and water migration above a working panel. Unpublished Geological Branch Seminar paper, National Coal Board, London, 1978

Farmer I. Coal mine structures. Chapman & Hall, London, 1985

Farmer I. Engineering behaviour of rocks. Chapman & Hall, London, 1984

Garritty P. Effects of mining surface and subsurface water bodies. Ph.D. Thesis, University of Newcastle upon Tyne, 1981

Garritty P. Water percolation into fully caved longwall faces. Strata Mechanics, Ed. I.W. Farmer, Elsevier, Amsterdam, pp25-29, 1982

Garritty P. Water flow into undersea mine workings. Int. Jl. Mining Eng., vol. 1, pp237-251, 1983

Hindmarsh W.E. Asfordby - a new mine for the future. Trans. Instn. Metall. (sect. A:Min. Industry), Vol. 99, A1-A14, 1990

Hoare R.H. & Whitworth K.R. Water occurrences affecting coal faces in the Cannock Chase coal-field, Western Area. Unpublished Geological Branch seminar paper, national Coal Board, London, 1978

MicroSoft. QuickBASIC - Version 3.0 MicroSoft, 1987

Pugh W.L. Water problems at West Cannock, No. 5 colliery. Mining Engineer, Vol. 139, pp669-679, 1980

Wilby G.E. The first five years of a new mine. Mining Engineer, Vol. 150, pp23-28, 1990.

Appendix 1: Data field headings of the Aquifer Database

Field name	Format	Definition
*-Database File: **MINING.DBF**		
INDEX_NO	C 7.0	Index number for relating database files
PANEL_NAME	C 8.0	Panel name
SEAM_CODE	C 3.0	British Coal seam code
SEAM_NAME	C10.0	British Coal seam name
COAL_RANK	C 4.0	Coal rank code
PNLCORNER	C 2.0	Panel corner (BL or TR)
CNR_X	N 6.0	Corner coordinate X
CNR_Y	N 6.0	Corner coordinate Y
AQFR_NAME	C20.0	Aquifer name
COVER	N 3.0	Cover to aquifer (m)
AQFR_THICK	N 3.0	Aquifer thickness (m)
INFLW_CODE	N 1.0	Code of water inflow classification
PANEL_DPTH	N 4.0	Panel depth (m)
START_YEAR	C 4.0	Starting year of working
FINISHYEAR	C 4.0	Finishing year of working
PANEL_WDTH	N 4.0	Panel width (m)
PANEL_LEN	N 4.0	Panel length (m)
EXTR_HIGHT	N 3.1	Extraction height (m)
WORKNG_DIR	N 3.0	Working direction (deg)
WORKNG_DIP	N 3.0	Working dip (deg)
AVR_ADV_RT	N 3.0	Average advance rate (m/week)
STRATA_DIR	N 3.0	Strata dip direction (deg)
STRATA_DIP	N 3.0	Strata dip (deg)
L_PLR_WDTH	N 4.0	Width of left pillar (m)
R_PLR_WDTH	N 4.0	Width of right pillar (m)
B_PLR_WDTH	N 4.0	Width of back pillar (m)
LEFT_PANEL	C 8.0	Name of left panel
RGHT_PANEL	C 8.0	Name of right panel
BACK_PANEL	C 8.0	Name of back panel
UP_PANEL	C 8.0	Name of overworking
DOWN_PANEL	C 8.0	Name of underworking
STRIP_PACK	N 1.0	Strip packing (0-1)
RETREATING	C 2.0	Retreat or Advance (R or A)
CLT_MJ_DIR	N 3.0	Major cleat direction (deg)
JNT_MJ_DIR	N 3.0	Major joint direction (deg)
STRN_AQF	N 4.1	Strain at the base of aquifer (mm/m)
M_MAX_SUB	N 4.2	Maximum subsidence (m)
OLD1_DAT	C 4.0	Date of old working 1
OLD1_HGHT	N 3.1	Extraction height of old working 1 (m)
OLD1_DIST	N 4.0	Distance to old working 1 (m)
OLD2_DAT	C 4.0	Date of old working 2
OLD2_HGHT	N 3.1	Extraction height of old working 2 (m)
OLD2_DIST	N 4.0	Distance to old working 2 (m)
SO4_PPM	N 6.0	Sulphate content of mine water in ppm
CL_PPM	N 6.0	Chloride content of mine water in ppm
M_MEMO	N 2.0	Code of what is inside the MEMO field
COMMENT	M10.0	Comments stored in the MEMO field
*-Database File: **INFLOW.DBF**		
INDEX_NO	C 7.0	Index number for relating database files
PANEL_NAME	C 8.0	Panel name
EVENT_MNTH	C 2.0	Event month
EVENT_YEAR	C 4.0	Event year
FLWRT_FRST	N 4.0	Initial flow rate (l/s)
FLWRT_MAX	N 4.0	Maximum flow rate (l/s)
FLWRT_LNG	N 4.0	Residual flow rate (l/s)
ADVANCE	N 4.0	Face advance at the time of inflow (m)
ADVANCE_RT	N 4.0	Advance rate at the time of inflow (m/week)
I_AQF_DIST	N 4.0	Cover to aquifer at the point of inflow (m)
I_AQF_DPTH	N 4.0	Aquifer depth at the point of inflow (m)
FLT_DIST	N 4.0	Distance to nearby fault (m)
FLT_THRW	N 4.0	Fault throw (m)
FLT_DIR	N 3.0	Fault dip direction (deg)
FLT_HADE	N 3.0	Fault hade (deg)
I_MEMO	N 2.0	Code of what is inside the MEMO field
COMMENT	M10.0	Comments stored in the the MEMO field
LITHO_CODE	N 1.0	Code for lithology data sets
INCPTNT30	N 2.0	% of incompetent rocks within 110m
INCPTNT55	N 2.0	% of incompetent rocks within 75m
INCPTNT75	N 2.0	% of incompetent rocks within 55m
INCPTNT110	N 2.0	% of incompetent rocks within 30m
MIDCPTNT30	N 2.0	% of competent rocks within 30m
CPTNT30	N 2.0	% of mid-competent rocks within 30m
INCPTNT	N 4.0	Thickest incompetent rock (m)
POSTN_INCP	N 5.1	Position of the thickest incompetent rock
*-Database File: **BOREHOLE.DBF**		
INDEX_NO	C 7.0	Index number for relating database files
BH_REF	C11.0	Borehole reference number
BH_NAME	C25.0	Borehole name
X_GRID	N 6.0	National Grid Reference X
Y_GRID	N 6.0	National Grid Reference Y
BH_LEVEL	N 4.0	Borehole starting level (m)
INCLINED	N 4.1	Borehole inclination (deg)
SEAM_CODE	C 3.0	Seam code of the seam under consideration
PANEL_NAME	C 8.0	Name of a representative nearby panels
AQFR1_NAME	C20.0	Name of aquifer 1
AQFR1_CVR	N 4.0	Cover to aquifer 1 (m)
AQFR1_DPTH	N 4.0	Depth of aquifer 1 (m)
AQFR1_THCK	N 4.0	Thickness of aquifer 1 (m)
FLOWRATE1	N 4.0	Rate of water inflow from aquifer 1 (l/s)
PRESSURE1	N 4.0	Water pressure of aquifer 1 (psi)
AQFR2_NAME	C20.0	Name of aquifer 2
AQFR2_CVR	N 4.0	Cover to aquifer 2 (m)
AQFR2_DPTH	N 4.0	Depth of aquifer 2 (m)
AQFR2_THCK	N 4.0	Thickness of aquifer 2 (m)
FLOWRATE2	N 4.0	Rate of water inflow from aquifer 2 (l/s)
PRESSURE2	N 4.0	Water pressure of aquifer 2 (psi)
LITHO_CODE	N 1.0	Code for lithology data sets
INCPTNT110	N 2.0	% of incompetent rocks within 110m
INCPTNT75	N 2.0	% of incompetent rocks within 75m
INCPTNT55	N 2.0	% of incompetent rocks within 55m
INCPTNT30	N 2.0	% of incompetent rocks within 30m
MIDCPTNT30	N 2.0	% of competent rocks within 30m
CPTNT30	N 2.0	% of mid competent rocks within 30m
INCPTNT	N 4.1	Thickest incompetent rock (m)
POSTN_INCP	N 5.1	Position of the thickest incompetent rock
SLAKEINDEX	C 2.0	Slake index of incompetent rock
B_MEMO	N 2.0	Code of what is inside the MEMO field
COMMENT	M10.0	Comments stored in the the MEMO field
*-Database File: **WATER.DBF**		
INDEX_NO	C 7.0	Index number for relating database files
SITE	C20.0	Site of water sampling
SEAM_CODE	C 3.0	British Coal seam code
PANEL_NAME	C 8.0	Panel name
SITE_X	N 6.0	Site coordinate X
SITE_Y	N 6.0	Site coordinate Y
LEVEL_Z	N 5.0	Site ordinance level (m)
SMPL_YEAR	C 2.0	Year of water sampling
SMPL_MONTH	C 2.0	Month of water sampling
SMPL_DATE	C 2.0	Day of water sampling
SO4_PPM	N 6.0	Sulphate content of water sample in ppm
CL_PPM	N 6.0	Chloride content of water sample in ppm
OTHER_NAME	C10.0	Name of another chemical of interest
OTHER	N 6.0	Content of the other chemical in ppm
W_MEMO	N 2.0	Code of what is inside the MEMO field
COMMENT	M10.0	Comments stored in the the MEMO field

*-Database File: FldTEST.DBF

INDEX_NO	C 7.0	Index number for relating database files
SEAM_CODE	C 3.0	British Coal seam code
COAL_RANK	C 4.0	Coal rank code
PANEL_NAME	C 8.0	Name of a representative panel
BH_NAME	C25.0	Name of the tested borehole
TESTSTRATA	C25.0	Name of the tested strata
PERM1_V	N 5.2	Primary vertical permeability (md)
PERM1_H	N 5.2	Primary horizontal permeability (md)
PERM2_V	N 5.1	Secondary vertical permeability (md)
PERM2_H	N 5.1	Secondary horizontal permeability (md)
STRESS1	N 3.0	Major principal stress (kPa)
STRESS2	N 3.0	Intermediate principal stress (kPa)
STRESS3	N 3.0	Minor principal stress (kPa)
STRSS2_DIR	N 3.0	Direction of the major horizontal stress
CLT_MJ_DIR	N 3.0	Major cleat direction (deg)
CLT_MR_DIR	N 3.0	Minor cleat direction (deg)
JNT_MJ_DIR	N 3.0	Major joint direction (deg)
JNT_MR_DIR	N 3.0	Minor joint direction (deg)
C_MEMO	N 2.0	Code of what is inside the MEMO field
COMMENT	M10.0	Comments stored in the the MEMO field

INTEGRATING GROUND CONTROL AND MINE SITE DATA THROUGH A GEOGRAPHIC INFORMATION SYSTEM

Douglas C. Peters, *Mining Engineer*
M. Antoinette Smith, *Computer Programmer/Analyst*

Denver Research Center
U. S. Bureau of Mines
Denver, Colorado

ABSTRACT

Part of the ground control research at the U.S. Bureau of Mines is involved with improving ground control data collection and analysis methods. A geographic information system (GIS) is being used within this research effort to standardize the data collected and provide a common graphical and tabular format and analysis system for researchers to access information on underground coal mines. In addition, GIS's can perform relational analyses on multiple map and tabular data sets which are not possible through map-creation or CAD packages or through data bases alone.

In addition to standardizing ground control analyses, there is an increasing need for rapid analysis of ground control data in connection with increasing production rates at longwall mines. The examination of a large number of interrelated parameters and their impact on short-term mine safety and productivity under the time constraints imposed by rapid production requires computer-aided techniques. A GIS provides the means to quickly, quantitatively, and reproducibly evaluate mine-wide conditions.

This overview of GIS techniques for mine data integration and analysis, using a mine in Colorado as an example site, will cover the input of data into a GIS, including mine-wide monitoring system data and general data such as roof control plans and geology. The methods to geographically reference these data sets and retrieve and combine them also will be covered. Automation of such processes briefly will be reviewed to allow future users to automate their mine data analyses.

INTRODUCTION

Geographic information systems (GIS's) have seen wide use in geography and related disciplines over the past 10 years or so and are rapidly gaining wide acceptance in geological and engineering fields. Mining applications of GIS's still are few, although the map- and data-intensive nature of tracking and managing mining operations provides for numerous potential applications of GIS's to mining.

For many mines, and especially for mines that have an automated monitoring system installed and collecting data, the volume and variety of data on the mine site and on changing mine conditions over time can border on being overwhelming. Manual analysis or compilation of these data into an interpretable form (such as maps) not only is time consuming, but also is prone to error from misposting of locations or data values. A GIS being used by the U.S. Bureau of Mines affords the means to further automate the data collection process and to overlay, integrate, and analyze diverse data sets which all are referenced to the same geographic area.

For example, a typical data set that would be acquired through a mine-wide monitoring system would be pillar and panel loading data taken during mining. These data can be read automatically into a GIS-compatible format and related to other data sets, such as surface subsidence measurements, shield leg pressures, roof characteristics, or time and location of bumps and roof falls in and around a panel. In addition, textual data, such as roof control plans and accident reports, and graphical information, such as shield designs, can be attached to appropriate locations or areas of the mine and subsequently retrieved in relation to particular parameters or searches for those locations (e.g., in response to a critical pressure value being reached in a nearby pressure cell or shield).

There are two general types of GIS's in use today: vector and raster. Vector GIS's store and manipulate data in point, line, and polygon formats. The raster GIS's, on the other hand, store data in a grid cell format. An example of a vector-format map would be a contour map where the lines are continuous features, whereas a raster-format map would look like a satellite image or an ore deposit block model where the map is made up of discrete cells.

There can be overlap between the formats, both in terms of data relationships and data analysis. However, the way the two systems store and manipulate the data are not directly

compatible (i.e., some translation of data is needed to be able to work in both systems). The discussion of methods in this paper will be restricted to the vector type of GIS, specifically the ARC/INFO[1] software package, although the basic concepts for data input and analysis should be applicable to raster systems as well.

---

[1] Use of product names does not imply endorsement by the U.S. Bureau of Mines.

The degree of automation of a GIS and of the mine data analysis is determinable by the user. The mine data simply can be stored in the GIS and be available for interactive retrieval and analysis. At the other extreme, programs can be written within the structure of a GIS to perform set series of data analyses, comparisons, and map generations upon entry of the appropriate monitoring data to the GIS format.

Please see Aronoff (1989) and Star and Estes (1990) for a general discussion of GIS's and their applications. A training manual by Environmental Systems Research Institute (ESRI) (1990) also provides some general information about GIS's and their analysis processes and more specific discussion of how to use ARC/INFO, the GIS created by ESRI. Bylinski (1989) and Warnecke (1990) provide shorter discussions of GIS's with some examples of their applications.

DATA INPUT FOR A GIS

GIS's can accept data in a number of formats from a variety of sources. The most common formats for data entry are transfer of ASCII files, direct keyboard entry, and map digitizing into the GIS's own format. All three methods have been used for data from a mine in Colorado which is a study site for Bureau research projects. Other formats include DXF (data exchange format) from programs such as CAD systems and more software- or hardware-specific formats that a particular GIS may be designed to accept.

Although uses of computers in mine operations are steadily increasing, the majority of mine maps, especially for older mines or smaller operators, are not in digital form. The only way to capture these data for use in GIS's or other programs is to digitize them manually on a digitizing table or semi-automatically through a scanning and vectorizing process. Likewise, any other map-format data not in digital form, such as geologic maps, will have to be digitized or reduced to numerical data that can be keyed into the GIS. Any mine which uses a standard CAD program to maintain its maps can transfer data to a GIS without additional labor expense to digitize the maps.

Tabular data, such as production figures, textual information, or instrument pressure readings, could be keyed in manually through a data base or spreadsheet program or entered directly into the data base subsection of a GIS. A more sophisticated method of mine data collection and entry, primarily for numerical data from in-mine instruments, can be achieved through a mine-wide monitoring system such as that described by Conover et al. (1990) and Hanna et al. (1991). The monitoring system also can perform its own processing and analysis functions prior to or separate from entry of the data into a GIS.

The internal format of the GIS will vary somewhat depending on the type of data base system used in a particular GIS. Most GIS's use a relational data base model for data storage which can interrelate multiple layers (arrays) of data for a given map and multiple maps of the same area. The original format/arrangement of data being transferred into the GIS from other software may not be directly compatible with the record and field structure of the GIS data base,

A) Mine-Monitoring System Output:

```
03/16/90 01:00:00
B6,B7,B8
SAMPLE,SAMPLE,SAMPLE
02:00:00,  4273,   ,  1646,   ,  4038,
03:00:00,  4273,   ,  1646,   ,  4116,
04:00:00,  4273,   ,  1646,   ,  4116,
05:00:00,  4273,   ,  1646,   ,  4116,
06:00:00,  4273,   ,  1646,   ,  4116,
07:00:00,  4273,   ,  1686,   ,  4155,
08:00:00,  4351,   ,  1686,   ,  4155,
09:00:00,  4351,   ,  1686,   ,  4234,
10:00:00,  4351,   ,  1686,   ,  4234,
11:00:00,  4430,   ,  1764,   ,  4312,
12:00:00,  4430,   ,  1764,   ,  4390,
21:00:00,  4665,   ,  1921,   ,  4782,
22:00:00,  4665,   ,  1999,   ,  4782,
23:00:00,  4665,   ,  1999,   ,  4861,
01:00:00,  4939,   ,  2234,   ,  5253,HIHI
```

B) Input to ARC/INFO:

```
B6  19900316 2 4273
B6  19900316 3 4273
B6  19900316 4 4273
B6  19900316 5 4273
B6  19900316 6 4273
B6  19900316 7 4273
B6  19900316 8 4351
B6  19900316 9 4351
B6  1990031610 4351
B6  1990031611 4430
B6  1990031612 4430
B6  1990031621 4665
B6  1990031622 4665
B6  1990031623 4665
B6  19900317 1 4939
```

Figure 1. Example of A) data output from mine-wide monitoring system (first line is the starting date and hour of data in the file; data are in "time, B6 cell pressure, B7 cell pressure, B8 cell pressure" format; "HIHI" refers to a pressure value exceeding the 5,000 psi limit set for such an alarm) and B) part of same data for pressure cell B6 reformatted for use in the ARC/INFO GIS (the date and hour have been rearranged to the form of "YEAR,MONTH,DAY,HOUR" without the commas).

so some reformatting of the data may be necessary (through manual keyboard editing or automatic preprocessing) before it can be transferred to or accessed within the GIS (e.g., see Figure 1).

DATA MANIPULATION IN A GIS

Map Information

Once a map or map-type information has been entered into a GIS, the topology of the "coverage" (as map-format data are called in ARC/INFO) must be created before the map can be used in any analysis process. The term "topology" refers to the interrelationships of features of the map (e.g., what is to the left and right of a boundary line, locations of intersections of lines, etc.).

After this point, the map data can be used in any analysis process or be related to any other data set that geographically overlaps with that map. All data in a GIS are scale-independent, unlike hardcopy maps. The term "scale-independent" refers to the fact that any data stored in a GIS are not tied to a particular scaling factor (e.g., 1 in. = 400 ft) as hardcopy mine maps are, but are referenced only to a standard geographic coordinate system. There are numerous possibilities for coordinate systems, the most common for mine sites being the State Plane system (which covers most recently surveyed data), the Universal Transverse Mercator system (UTM; which most large-scale U.S. Geological Survey topographic maps, including digital elevation models, are based upon), and local mine coordinate systems (which probably are based on the State Plane system, but offset from the State Plane baselines; more common for older mines). All mine data and maps to be compared or otherwise analyzed must be in the same coordinate system, or the data sets will not coincide with respect to their coordinates.

Figure 2 shows an example of a mine map for a mine in Colorado (without annotation) as it is stored in one of the coverages which contains the active and abandoned workings. Figure 3 shows a map composition using Figure 2 and other

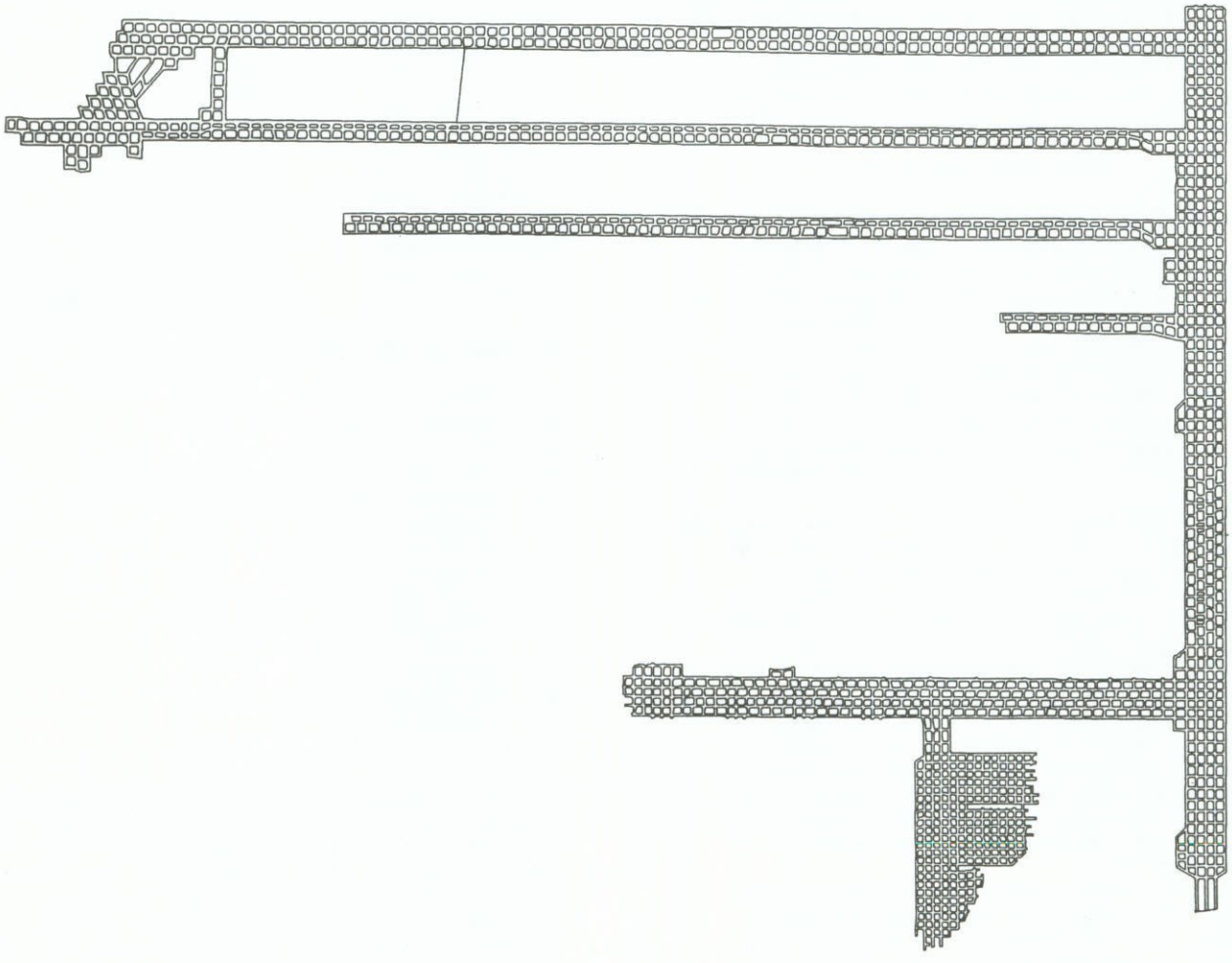

Figure 2. Map of active and abandoned workings of a mine in Colorado, without annotation. Figure depicts the graphical (polygon) information contained in a single coverage, but does not show tabular data related to coverage features.

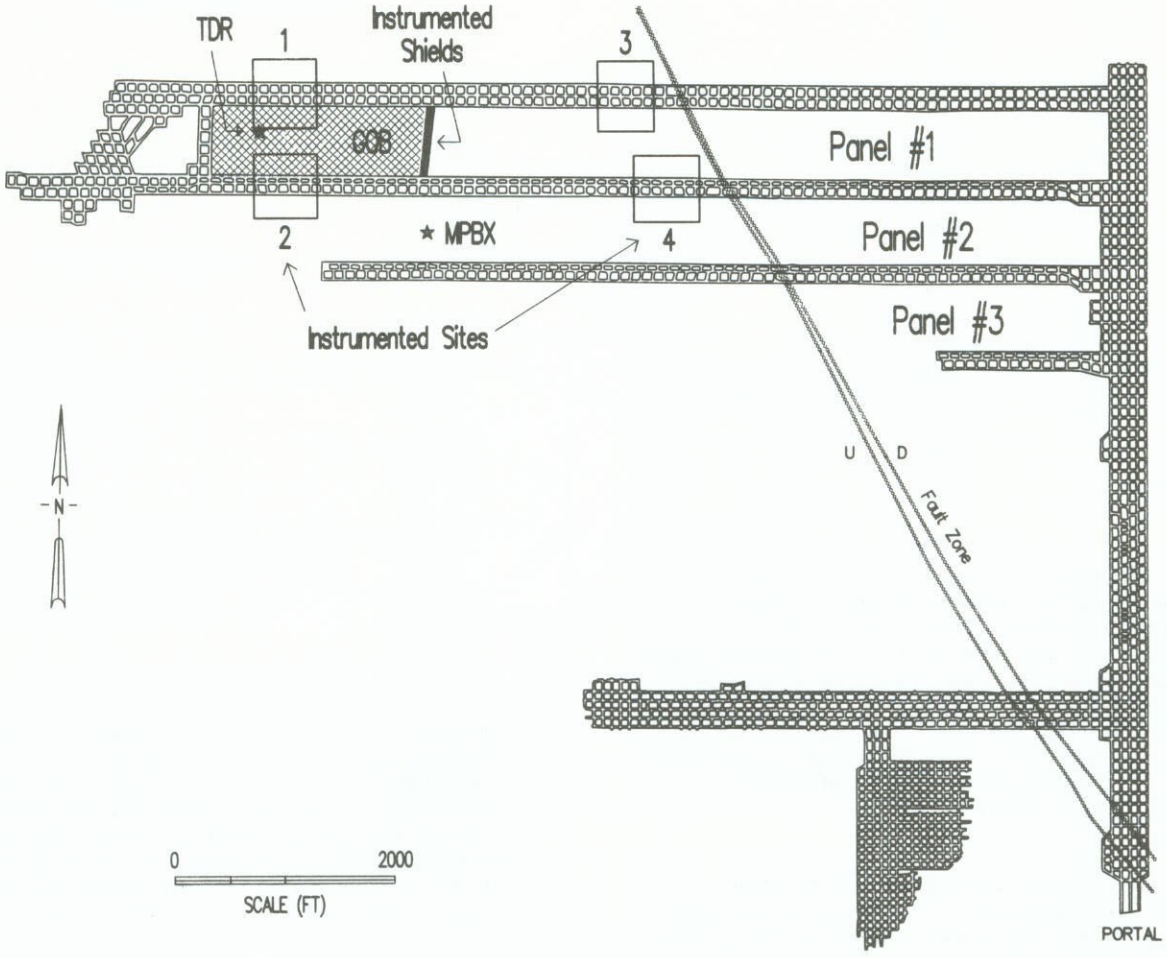

Figure 3. Map composition based on Figure 2 and additional fault and instrument site coverages, including annotation and standard map features (scale bar and north arrow) which clarify to the user what the map is showing.

coverages that contain fault locations and outlines of instrumented sites in the mine, as well as miscellaneous annotation and standard map items. Except for the annotation and standard map items shown for map clarity, the same combination of data can be performed as part of an analysis process. An example analysis would be identifying how close an instrumented site, or individual instrument, is to a fault or how the instrument readings vary with proximity to the fault to define the effect of the fault on roof stability and stress buildup.

Stationary rock mechanics instrument locations (such as borehole pressure cells (BPC's) and extensometers) are considered map-type data because each instrument has a geographic location to which readings are related. Figure 4 shows a close-up of one of the instrument sites in the mine in Colorado with instrument ID's listed. Readings collected by the mine-monitoring system from these stationary instruments are converted to tabular form. Because of the multiple readings from these instruments per day and the months-long life of the instruments, there is a large body of data for each instrument location. The ARC/INFO GIS is unable to directly relate all readings for an instrument to that instrument location in an interactive format due to limitations of the INFO data base. Further considerations involved with tabular data will be discussed in the next section.

Data collected from instruments that move during mining can be related to a unique location in the mine, even though the distance between locations may be only a few feet. For example, the instrumented longwall shields at the mine in Colorado provide time-weighted average (based on the set-stationary-move cycle for each shield) pressure readings as the shields and shearer retreat along the panel.

Both stationary and moving instrument locations are stored as point coverages, and the instrument readings are referenced to these

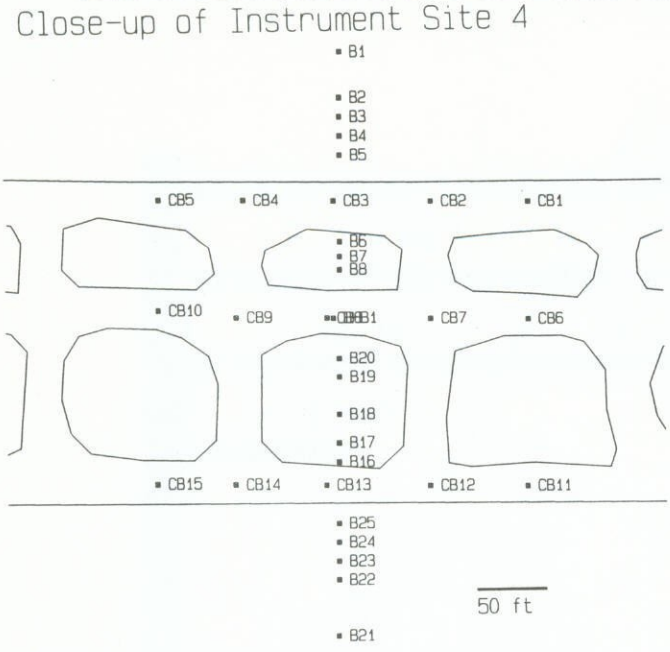

Figure 4. Close-up of an instrument site (site 4 on Figure 3) in the mine in Colorado showing the instrument ID numbers (from tabular data associated with the coverage). The mine workings are derived from the coverage shown in Figure 2. The area shown is about 350 ft by 315 ft. Locations labelled "CB" are instrumented drill holes in the mine roof (extensometers or pressure cells). Other locations are cylindrical or borehole pressure cells.

points. These point coverages can be used wholesale (all instruments) or on an instrument-versus-instrument basis when comparing data sets (e.g., what are the pressure readings in both stationary and moving instruments when they come within a specified distance of one another?). A graphical example of such a comparison of locations is shown in Figure 5.

The list of potential comparison and analysis processes which can be pursued is too long to go into in the space available. The instructions for commands available in ARC/INFO for data manipulation and analysis fill a basic set of nine manuals. However, basically any comparison you can imagine doing with two-dimensional map data, split into multiple layers, can be performed within a GIS. The caveat to this statement is that, the more complex the analysis, the more intricate will be the command sequence and the longer it will take to complete the process. Clearly, any map-based ground control data, such as locations of roof falls, faults, instrument locations and readings, locations and types of supports, etc., can be compared and results derived from those comparisons.

Figure 6 provides a graphical representation of a potential analysis using coverages for shield pressures (in the form of a mesh map), fault locations, mine workings, and instrument locations. Although not shown here so as to prevent visual clutter, pressure data from the instrument locations could be included in the

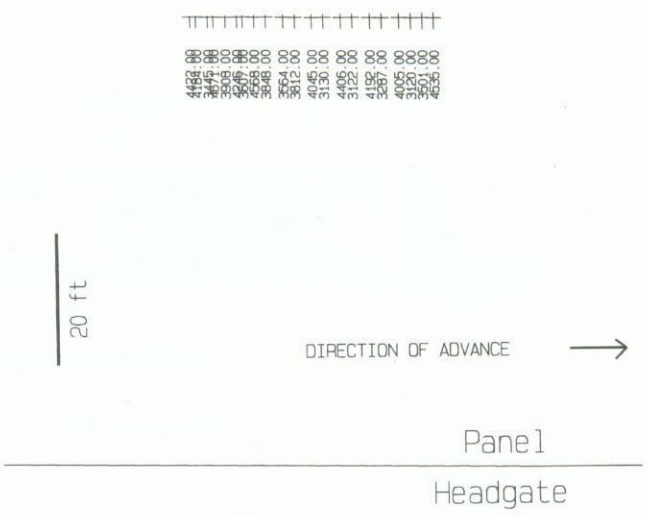

Figure 5. Example of shield pressure reading locations filtered for only those within 110 ft of BPC number B6 at Site 4 (Figure 4). Numbers next to the shield locations are the time-weighted average pressure readings (in psi) at those locations. The pressure value listed for the BPC is the reading at the time that the longwall was closest to the BPC location.

analysis so that the pressure changes in the pillar cells can be viewed in concert with the retreat of the shields along the panel.

Numerical And Textual Information

As noted above, numerical information is entered manually at the keyboard or by transfer of ASCII files from other programs or computer systems such as the mine-monitoring system. Numerical data associated with a coverage can be stored as jointly stored attributes of the coverage or as data base files which are referenced by the coverage but stored separately. Precision (the number of significant figures and decimal places) of the numerical data also can be defined based on the degree of precision needed or warranted for a coverage or data set.

Coverages have certain numerical data included automatically as attributes when topology is created for a coverage. Items such as area, perimeter, and XY coordinates are a part of every coverage. More specialized data can be included as attributes of a coverage or as separate related files. Pressure data from the in-mine instruments could be handled either way. More map-specific ground control data, such as roof fall or water inflow locations, would be

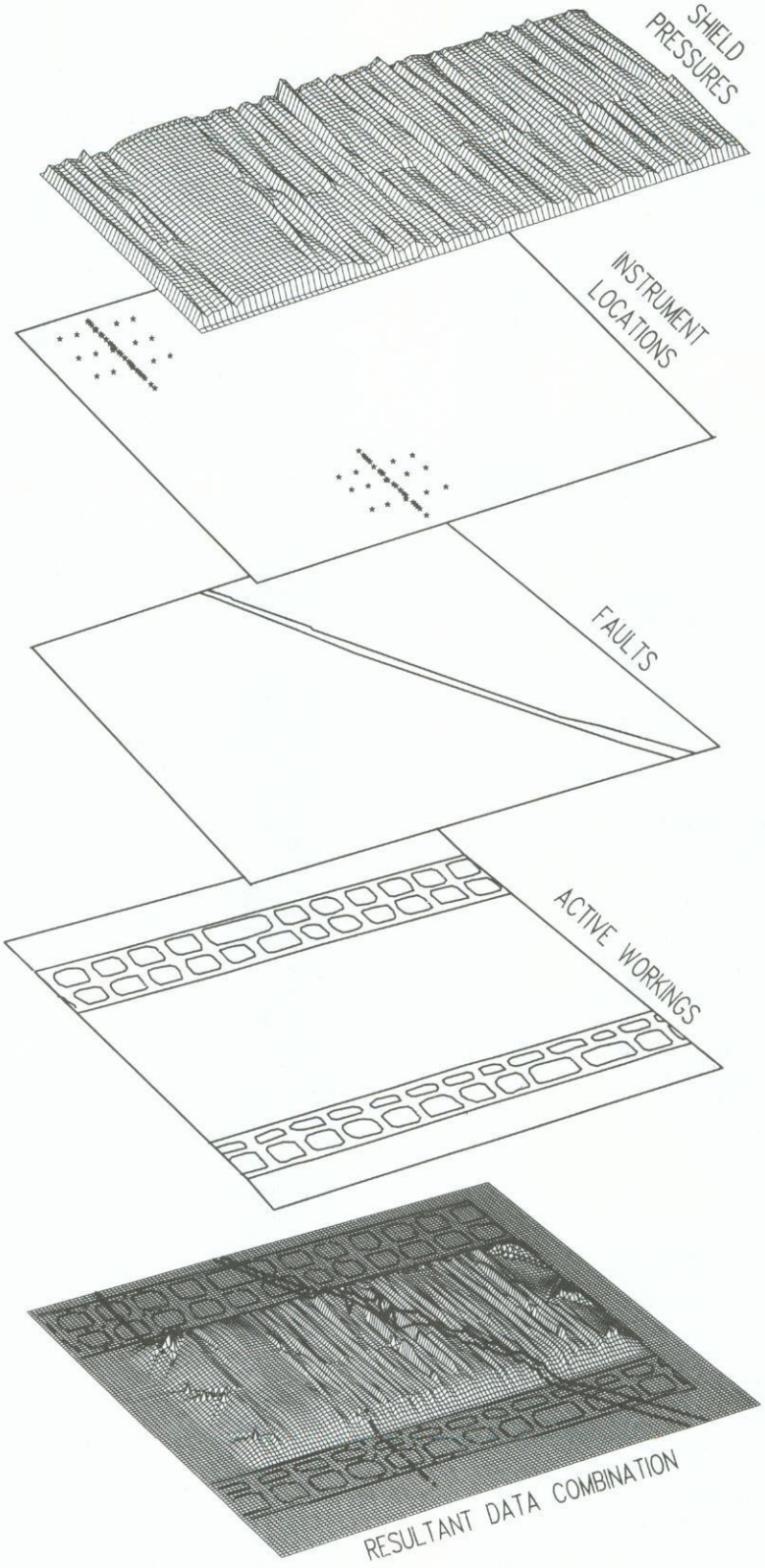

Figure 6. Three-dimensional stack showing individual input coverages and the resultant combined map at bottom.

stored in the form of a coverage. Numerical data concerning the size/volume of each occurrence are attributes tied to the location of the problem.

Most of the textual information being used in the Bureau's application of the GIS to ground control comes from a centralized data base, or "engineering information system," developed by the Bureau on active and inactive underground coal mines located throughout the United States. This system contains ground control research results, roof control plans, mine maps, geological data, and abstracts from coal publications which can be related directly to a mining property. Table 1 shows an outline of descriptive factors and details which have been included for each underground coal mine in the information system.

Table 1. General listing of the mine data available in the engineering information system and which have been transferred to the INFO data base in the GIS.

GENERAL DATA	
Reference Number	Mine Name
MSHA Mine ID #	Mine Operator
Coal Province	Coal Region
Coal Field	Producing District
State	County
Coal Seam(s)	Mining System
Annual Tonnage Class	Year
Mine Status	Date of Entry

****Other Information Available*****

Physical Properties:	Immediate Roof
	Coal Seam
	Immediate Floor
Geologic Information	
Panel Design:	Room-and-Pillar
	Longwall
Artificial Supports:	Room-and-Pillar
	Longwall
In Situ Stress:	Immediate Roof
	Immediate Floor
Site-Specific Practices/Problems	
(Will include any scanned images available for specific mine)	

After the initial data input for the engineering information system was completed using a data base management program on a microcomputer, the information then was loaded onto the minicomputer where the GIS resides. The INFO data base system within the ARC/INFO GIS was used to integrate and relate tables, text, instrument locations, and map data to form a more comprehensive data analysis system.

One type of data in the information system which would not transfer readily to the GIS was the scanned images for the site-specific data, such as drill hole logs. It may in fact be possible to transfer such graphics into a GIS, but the size of the graphics files (generally about 1 Mbyte) prohibits storage of a large number of such files in the GIS. Their practical use in the GIS probably would be limited to the form of "supporting graphics" for interactive recall or map production, rather than as quantifiable coverages such as vector-format maps, because of their diverse nature (vertical cross sections, horizontal maps, drill-hole logs, pictures of mine equipment, etc.).

The numerical and textual information transferred to the GIS is stored in the INFO data base in character, integer, date, and decimal-numeric formats, depending on the type of data. An example of the kind of data from the engineering information system stored in the data base for a given mine is shown by Table 2, which is a portion of the data transferred to INFO for the example mine in Colorado. This information can be processed by a variety of character, arithmetic, search, and logical operations. In addition, lookup tables can be used to reduce memory requirements and simplify items of multiple records which have a number of the same

Table 2. Partial listing of the textual and numerical data for a mine in Colorado as transferred to the INFO GIS data base from the engineering information system.

```
FILE_NO    =  16
PROVINCE   =ROCKY MOUNTAIN
LATITUDE   =0402110
LONGITUDE  =1070420
REGION     =GREEN RIVER
CFIELD     =YAMPA
PROD_DIST  =17
STATE      =CO
COUNTY     =ROUTT
COAL_SEAM  =WADGE
MINING_SYS =LONGWALL (1)
ANNUAL_TON =975
YEAR       =000
STATUS     =1990
MSHA_NO    =05-03836
IDATE      = 4/16/86
UPDATE     = 4/20/90
TYPE_STRAT =MUDSTONE
SMPL_LOCA  = SANDSTONE
UNIAX_COPM =    6580
UN_STN_DEV = 13108
YOUNG_MOD  =     222
YM_STN_DEV =   368
POISSON_SC =      26
PS_STN_DEV =   126
TEST_DATE  = 2/ 5/85
```

references to particular characteristics.

As with any tabular data, textual data can be related to the location of the mine or locations within the mine. Calculations or logical operations performed with a particular data item then can be used in the derivation of new information for a mine or coal field. Maps can be prepared based on or incorporating specific textual data characteristics.

For example, material properties, such as compressive strength for the immediate mine floor

or one of the rock units in the floor, can be compared to the overburden stress calculated from digital topography and coal seam elevation files and the strength of the coal to see if pillar punching or floor heave are possible within the mine property or throughout the field. Derivation of new information also could involve the character data by looking at the type (style and/or manufacturer name) of the artificial support used in a mine to alleviate or prevent ground failure and comparing this information with specified values for rock mechanics and/or production data to estimate effectiveness of support systems for new development sections. Likewise, such analyses can help in designing ground control plans for a new mine based on conditions and experience at a nearby mine. A map depicting such information could show the locations and values of rock mechanics measurements, the existing and proposed mine workings, areas with significant potential for instability, and based on past use and experience as defined by the data base, the type of support recommended for areas of particular conditions in a mine.

Tabular Analysis

Tabular analysis is distinguished from the graphical analysis performed with maps because the data in the table (data base) or coverage can be manipulated without direct reference to the geographic relationships. Tabular analysis usually is performed to accomplish tasks similar to what would be done in a spreadsheet where the user calculates a new field based on existing fields in the data base or searches the data base for particular values based on arithmetic and logic operations. Although fields cannot be set up containing equations as can be done in a spreadsheet, the calculation process can be automated within the GIS. Tabular analysis also can be performed as part of a process within the GIS to generate a standardized report of results. A similarity of tabular analysis to graphical analysis is that the process can be based on geographical overlap or proximity if such a parameter is desired. In other words, the geographic locations of features of interest can be referenced as both implicit locations in graphical analysis and explicit coordinates in tabular analysis, allowing quantitative analysis of numerical coordinates or map locations.

Relating Data Sets

Data bases not explicitly incorporated into a coverage as part of its attributes can be "related" to the coverage or to specified data records in the coverage. This capability allows the user to have an "expanded" attribute data base for a coverage without extra memory being tied up to permanently store the extra data as part of the coverage. Likewise, non-coverage data bases can be related to one another for expanded tabular analysis capabilities.

As noted above, a relate where one item in the main data base or coverage has many data records that could be connected to it (a "one-to-many" relate) does not work in INFO. The only way to handle such a collection of data is to perform graphical and/or tabular analyses on the coverage and separately perform tabular analyses on the associated data file to arrive at a common goal.

This situation arises with the stationary instruments and the pressure readings obtained from them. Unlike the shield leg pressure measurements, which have unique locations for each reading, the measurements from the stationary instruments always reference the same locations. These rock mechanics data must be analyzed by tabular analysis and the results reported separately or combined such that they can be used in a "one-to-one" (one record in the coverage relates to one in the related file) or a "many-to-one" (many records in the coverage relate to one in the related file; similar to the way a lookup table is used) relate format.

AUTOMATING GIS ANALYSES

The complexity of comparative analysis that can be performed with a GIS largely is limited only by the memory and time available for the computer to grind through the necessary steps. Analyses can be done step-by-step by an individual running the GIS, or they can be performed automatically, for the most part, if the sequence of steps and the format of the outcome is known in advance. If the user is to have minimal or no input to the automatic process, other than commanding the GIS to run the process, then the sequence of steps must not vary. Separate automatic processes, known as "macros" (or "AML's" in the ARC/INFO package), have to be written for each variation of the process, or the macro will have to allow user input to direct the GIS at points where variations are possible.

Figure 7 is a "simple" macro in ARC/INFO language, called "SPMCTRANS.AML", to automatically transform coverages from the State Plane coordinate system to the local coordinate system used by a specific mine. Error trapping has not been included in the AML, but easily could be included if desired. What is not visible as part of this macro is that standard coverages of mine coordinate control points and of a matching number of State Plane control points must be available in the working directory under the names MINECOORD and STPLCOORD, respectively, for use in setting up the transformation. The user enters the input and output coverage names explicitly because there is no way for the macro to anticipate what these names should be. The macro also can be set up to read the input and output coverage names when entered as part of the &RUN command line so that there would be no interactive portion of the process after the initial command.

Similarly, any automatic or semi-automatic process can be programmed as a macro. Menus also can be created to help non-expert users of the system or to present multiple choices of automatic processes without the user having to know the names of the macros involved.

SPMCTRANS.AML

```
&type Starting the State Plane to Mine Coordinates transformation process.
&terminal 4205      /* assumes you are using a Tektronix 4205 terminal
&setvar .coverin [response 'Please enter the input coverage name']
&setvar .coverout [response 'Please enter the output coverage name']
&messages &off &all/* turns off on-screen dialog for macro commands
PULLITEMS %.coverin%.TIC %.coverin%.BAK.TIC  /* backup input coverage tics
IDTIC               /* copy across input coverage tic ID numbers
XTIC                /* copy across input coverage tic X values
YTIC                /* copy across input coverage tic Y values
END                 /* end copying process
&setvar status := [delete %.coverin%.TIC -info] /* deletes tic file for input
PULLITEMS STPLCOORD.TIC %.coverin%.TIC  /* start process to replace input tics
IDTIC               /* copy across State Plane tic ID numbers
XTIC                /* copy across State Plane tic X values
YTIC                /* copy across State Plane tic Y values
END
COPY MINECOORD %.coverout%   /* sets up output control coordinates
&messages &on &all /* turns on on-screen dialog for macro commands
TRANSFORM %.coverin% %.coverout%    /* runs the transformation program in ARC
&type Not quite done yet!  The input coverage's tics now will be reset to the~
 original values, and the temporary work files will be deleted.
&messages &off &all
&setvar status := [delete %.coverin%.TIC -info] /* deletes new input tic file
PULLITEMS %.coverin%.BAK.TIC %.coverin%.TIC /* replace old input coverage tics
IDTIC               /* copy across old input coverage tic ID numbers
XTIC                /* copy across old input coverage tic X values
YTIC                /* copy across old input coverage tic Y values
END
&setvar status := [delete %coverin%.BAK.TIC -info] /* deletes backup tics
&messages &on &all
&stop The transformation from State Plane to mine coordinates is complete!
```

Figure 7. An example macro (AML) program to automatically transform coverages from the State Plane coordinate system to a mine coordinate system. Documentation comments are denoted by the "/*" string. The macro is run, assuming that the user already is at the ARC level in ARC/INFO, by the command "&RUN SPMCTRANS.AML."

PROBLEMS WITH USE OF A GIS

Because of the great variety of commands and analysis processes available in most GIS's, their use for ground control data integration and analysis, or for any other data, is limited more by user knowledge and experience and hardware availability than by the software. All GIS work has a high front-end cost in time and money involved with data entry, which probably accounts for at least 75% of the time spent using a GIS. Once the maps and other data sets are entered though, data updating and manipulation is far faster and more reproducible than manual methods. Also, if the mine and ground control data are entered incorrectly or inaccurately, all resultant analyses will suffer the same inaccuracies. Therefore, the person doing the data entry must be careful not to compound any error from drafting or instrument accuracy that may already exist in the data.

One area that GIS's have not been applied to yet is the analysis of truly three-dimensionally continuous data. GIS's reference and manipulate data in multiple two-dimensional layers. These layers all can reference the same plane or surface, or they can represent three-dimensionally arranged planes. For a limited volume or region, such as a flat-lying coal seam, the distinction between two-dimensional layers and continuous three-dimensional data may not be important, and a GIS can "simulate" the three-dimensional referencing of data. However, the number of layers that can be active is limited by both the software and by the memory available on the host computer, thereby limiting the extent to which three-dimensional data can be simulated. True three-dimensional data handling and referencing in a GIS awaits the advance of both software and hardware technologies.

ADVANTAGES OF GIS FOR MINE PLANNING

As noted before, GIS's allow the scale-independent, quantitative comparison of geographically related data sets. This type of comparison cannot be done through CAD systems. Data bases alone do not allow the implicit geographic referencing of data; geographic references must be explicit in data bases, and maps cannot be stored in a database. Paper or mylar maps certainly cannot be related in a quantitative manner without considerable time spent by the personnel using them to extract quantitative information, and then the maps all must be at the same scale if they are to be overlayed.

How do these considerations impact ground control planning? Obviously, the evaluation of mine data and maps still can be done manually if time and strict accuracy are not of concern. The advantage of using computer-aided data analysis techniques, and of GIS's in particular, is that there is no loss in accuracy or precision due to human error, as long as the data are correctly entered in the first place. Analyses or comparisons which would be too time consuming or complex to be done manually can be done relatively easily with a GIS. Moreover, analysis and map generation processes can be automated so that time spent in the data analysis could be reduced even further. Although creation of the analysis processes may require an expert, non-expert personnel could run the GIS and provide mine planners with output data and maps, making their jobs more efficient and accurate. If GIS technology is combined with expert system/artificial intelligence technology, even ground control planning in operations without access to expert planners could benefit.

CONCLUSIONS

GIS's offer a means of making analysis of mine site and ground control data more efficient and more reproducible. GIS's also offer the ability to objectively compare formerly semi-quantitative map data, such as mine and geologic maps, with truly quantitative data from sources such as in-mine instruments, a process that can be fraught with inaccuracies and human error if done manually.

Numerous data types can be incorporated into a GIS through manual or automatic entry. Analysis processes can be done step-by-step by a knowledgeable user or can be automated to limit the need for user input or experience. Analysis processes can be simple or quite complex, and the GIS potentially allows the production of analyses that would be prohibitively time-consuming, if they even are possible, when done manually.

Output of analysis results or original data is available in map or tabular-report form. Production of the maps through a GIS is free of most of the inaccuracies of human error possible in manual drafting, such as misplacement of instrument sites or misposting of data values. Of course, the GIS analyses and outputs only are as good as the original data input to the GIS and the logic involved in analyzing the data.

ACKNOWLEDGMENTS

The authors thank the cooperating mining company and its employees for their cooperation in the ongoing U.S. Bureau of Mines research at the mine in Colorado and for the mine and geological data they have provided. Thanks also are given to D. Conover, A. Fejes, K. Hanna, K. Haramy, R. Kneisley, and J. McDonnell of the Bureau of Mines for the in-mine and subsidence data they have provided as part of the cooperative effort to make the ground control data analysis process more reproducible and more efficient.

REFERENCES

Aronoff, S., 1989, Geographic information systems: A management perspective: Ottawa, WDL Publications, 294 pp.

Bylinsky, G., 1989, Managing with electronic maps: Fortune, April 24, 7 pp. (reprint).

Conover, D., K. Hanna, and T. Muldoon, 1990, Mine-wide monitoring applications in ground control research, in S.S. Peng, ed., Proceedings of the 9th International Conference on Ground Control in Mining, Morgantown, West Virginia, June 4-6, 1990: Morgantown, West Virginia University, pp. 135-141.

Environmental Systems Research Institute, 1990, Understanding GIS--The ARC/INFO method: Redlands, California, 485 pp.

Hanna, K., K. Haramy, and T.R. Ritzel, 1991, Automated longwall mining for improved health, safety, and productivity at the Foidel Creek Mine: Littleton, Colorado, Society for Mining, Metallurgy, and Exploration, Preprint 91-165, 8 pp.

Star, J., and J. Estes, 1990, Geographic information systems--An introduction: Englewood Cliffs, New Jersey, Prentice-Hall, 303 pp.

Warnecke, L., 1990, Geographic information systems: Government Computer News, November 26, pp. 45-47.

DETERMINATION OF THE ROCK STRENGTH FROM PORTABLE ROCK TESTER

K. F. Unrug, *Professor*
Y. J. Zhang, *Graduate Student*

Department of Mining Engineering
University of Kentucky
Lexington, Kentucky

ABSTRACT

A new testing technique for the determination of the rock strength from portable rock tester is proposed. It is a quick and economical method that can determine the rock strength with reasonable accuracy in different conditions. This method is based on the application of portable rock tester working at the principle of forcing steel ball into the rock surface. The correlation between laboratory measured compressive and/or tensile strength and rock tester reading has been determined in terms of the three controlling parameters: (1). diameter of indentation on the testing sample, (2). diameter of indentation on the reference bar, (3). Brinell hardness number of reference bar.

INTRODUCTION

Compressive and tensile strength are the important parameters required in engineering characterization of rocks. They are being determined in uniaxial conditions using laboratory tests or through index tests performed in different conditions, i.e. field and in-situ. The uniaxial compressive and indirect tensile strength tests have been used widely for rock strength classification and other engineering calculations. Large scale in-situ tests on pillar or rock blocks in the field were employed to identify the behavior of rock masses under the loading conditions. These researches allowed the determination of the relationship between small and large sample strength. Since the laboratory tests require machined specimens and sophisticated equipment, and large scale in-situ tests are very costly and time consuming, the applications of these kinds of tests are limited. Therefore, development of a quick and economical method that can estimate the rock strength with reasonable accuracy under any kind of test conditions is of real need.

The Schmidt Rebound Test (1) is such a quick method and it can be used in the field. It was originally developed to compare the surface rebound hardness of concretes. Subsequently, the Schmidt hammer has been used in a similar manner to estimate the uniaxial compressive strength of rocks. Unfortunately the results are insensitive to strength changes and are strongly influenced by variations in test technique (2).

In the 1970's, the point-load strength test gained considerable international approval (3). However, the influence of specimen size and shape effects in point-load strength test is very significant. The complex correction of size and shape effects in point-load testing must be taken into account in compressive strength prediction. That makes this testing method inconvenient for quick rock strength estimation.

An impact tester was recently developed by Z. J. Hladysz at South Dakota School of Mines and Technology. It can be used with both drill cores and rock blocks. Because the tester is portable being small and light, it is suitable for field applications. It can serve for estimate of rock compressive and tensile strength around the opening at a given location, especially in the pre-design stage of investigations in various geotechnical fields. In this paper, the correlation between tester reading and laboratory measured compressive and tensile strength will be presented.

Some tests were conducted previously by Dr. Hladysz inventor of rock tester. The general correlation plot (Fig. 1) which accompanies the South Dakota Rock Tester was given experimentally. Since the

general correlation plot was originally developed for the igneous and metamorphic rocks such as granite and gneiss, it is necessary to develop a new correlation between tester readings and uniaxial compressive strength and/or indirect tensile strength of sedimentary rocks, typically for carboniferous depositional environment.

PRINCIPLE OF THE TESTING METHOD

The basic idea about rock tester comes from the Brinell material hardness testing method. The Brinell test is performed by pressing a steel ball into the flat surface of a test piece under a definite load. In metals the material strength is usually defined through the hardness tests. The hardness number is determined by the ratio of this load to the spherical area of indentation, i.e.,

$$H_B = \frac{P}{\pi \frac{D}{2}(D-\sqrt{D-d^2})} \qquad (1)$$

where: H_B= Brinell Hardness Number of the material
P = the applied load in kilograms
D = the diameter of the steel ball indenter in millimeters
d = the diameter of the impression in millimeters at the surface of the specimen.

After removal of the load this diameter d is measured by means of a special microscope.

Similarly, the Hladysz rock strength tester, shown in Fig. 2, is composed of the following components: barrel housing, detachable end piece which contains a rigid ball of 0.4 in. in diameter, spring, cylindrical plunger, and a number of square cross-section reference bars. It works on the principle that the force of the blow applied to the plunger is equal to the force transmitted through the rigid bearing ball to both the reference bar and rock sample. After hitting the plunger with the hammer, two indentations are obtained, one on the reference bar and another on the testing sample. By comparing these two indentations, the strength of the rock can be correlated with the known strength of the reference bar. In this paper a correlation between the rock tester reading and uniaxial compressive strength and/or indirect tensile strength of rock have been established experimentally.

DESCRIPTION OF TESTING APPARATUS AND ROCK MATERIAL TESTED

Portable Rock Tester

The impact rock tester designed by Z. J. Hladysz is a hand-held portable device for determining the approximate strength of intact rocks in the field or in the laboratory. The tester has a bulk size of only 1 pound in weight with dimensions 7.5 in. in length, and 1.2 in. in diameter. Its compact design enables the engineer or foreman to carry it with him conveniently and have an estimate of opening rock compressive and tensile strength at any place.

To perform the test, a reference bar is inserted between the ball and the flat end of the plunger. The tester is held against a planar sample surface and impacted on the other end. The ball will penetrate into the sample surface as well as into the surface of the reference bar simultaneously. Consequently, a circular indentation appears both on the sample and on the reference bar. The calibrated magnifier is then used to measure the diameters of indentation. Next, the reference bar is advanced to a new spot in the sample being selected for testing, this procedure is repeated five times for each sample. It is assumed that the dimensions of the diameters are related to the hardness of both materials and that the ratio of the diameters of indentation does not depend upon the magnitude of impact applied to the tester (4). The average hardness ratio can then be calculated by the following formula:

$$A = H_B \frac{d^2}{D^2} \qquad (2)$$

where: A = average hardness ratio
H_B= Brinell Hardness number of given reference bar
D = diameter of indentation on the sample
d = diameter of indentation on the reference bar.

Finally, a correlation between the average hardness ratio (A) and the uniaxial compressive and tensile strength of the rock sample may be developed.

Stiffness Compressive Testing Machine System

The hydraulic power testing machine system (CATS/C600MB), used to test a rock specimen's compressive strength in the laboratory, includes three major components: a hydraulic pumping unit, machine frame, and digital controller.

Each plays a unique part in conducting material tests. CATS, the Computer Aided Testing System, refers to the central intelligence component of the testing system. The CATS console originates and directs all movement of the loading frame and collects all data from the test. This data is used to control the test and can be displayed in real time on the CATS Video Display Module and/or transmitted down line to a computer where it can be stored, categorized, and analyzed. A sketch of the control console and its major hardware components is shown in Fig. 3.

The SATEC Model C600MB stiff loading frame is a single test space compression load frame capable of applying 600,000 pounds of compression force to specimens. This high-capacity loading frame responds to any command or series of command sets programmed into the CATS system under load, strain, stress, or position control, in any imaginable combination or set of combinations and over any time period.

The test was performed with a constant rate of loading throughout all portions of tests by itself. The specimens were loaded at a rate of 15 to 50 pounds per second to minimize the effect of loading rate on the strength of samples.

Sample Description and Preparation

Samples tested were obtained from an Eastern Kentucky coal mine. Geological hole cores with the diameters of 2 in. were taken from the depth interval 48 ft. to 640 ft. over the Harlan coal seam. Its lithology was widely varied with coal, shale (light, gray, black and sandy shales), siltstone, and sandstone. The test samples used for the uniaxial compressive and tensile strength test were prepared based on ASTM standards; that is, the ratio of the length to the diameter is larger or equal to 2. Since the uniaxial compressive strength tests by the hydraulic power machine were destructive, the samples which were used for the indirect tensile strength and rock tester test were taken in the location that was as close as possible to the previous machine-tested core. It should be noted that grinding and polishing were not necessary for rock tester testing samples.

More than 100 specimens were prepared and tested using the CATS/C600MB Testing Machine System for obtaining compressive and tensile strength of rock and 76 shale, sandyshale and siltstone samples were tested by the Hladysz rock tester. The reason that 76 samples instead of 100 were tested by the rock tester will be discussed later.

DISCUSSIONS OF TESTING PARAMETERS AND PROCEDURE

Testing Load

The load applied to the rock tester was created by the impact of a regular hammer. The magnitude of an impact is not a factor, because the same amount of force is transmitted to both reference bar and rock sample. The impact should be strong enough to develop the measurable indentations. However, it should be noted that an impact which is too strong may damage the rock specimen being tested.

Reference Bar Strength

The hardness of the reference bar is an important parameter in rock tester tests. The strength of the reference bar is a constant (Brinell Hardness Ratio (H_B)) for a given material in the rock strength calculation. It has to be selected to ensure that indentations on the rock and reference bar will be easily measurable. If the difference of hardness between rock sample and reference bar is too big--for instance, if the hardness of the metal bar is much larger than the specimen--it is difficult to make an indentation on the bar even though a big indentation is created on the rock sample. On the other hand, the indentation can not be read on the specimen either if the rock sample is too strong. These problems were experienced during the tests. It can be concluded that the strength of the reference bar should be compatible with sample tested; that is, the hardness of the bar should be roughly equal to the hardness of the rock surface. In our test, the aluminum bars were used in order to match the hardness of soft rock samples. The hardness number (H_B) of the bar can be obtained from either the bar manufacturer's specification or the Brinell Hardness Number test (H_B was equal to 127 in this particular case). The dimension of the bar is 3/8 x 3/8 sq.in. in cross-section, 6 in. in length.

Rock Strength

In the foregoing discussion it was mentioned that only 76 out of 100 samples had been successfully tested by rock strength tester. Tests on more than 30 samples did not produce indentations on the rock surface. All of them were silica matrix sandstones with high hardness. When these rocks were hit, the indentation was not visible enough to measure by the calibrated magnifier. This means about 30 hard sandstone specimens were not available for the rock tester test. Since most of the critical strata around underground opening from the stability stand point of view are shales or other

weak rocks, the high elastic response problems with strong sandstones do not have major practical meaning for application of the rock strength tests.

Testing Procedure

In order to establish the correlation between the rock tester readings and the uniaxial compressive strength and/or tensile strength of rocks, three specimens with the same core location were tested for finding compressive/tensile strength and indentation readings using the testing machine system and the portable rock tester, respectively.

For the average hardness ratio (A) test, five indentations on each end of a specimen were made using the rock tester. The calibrated optical magnifier was then used to read the diameter of the indentations on both rock sample surface and reference bar. The average hardness ratio can be determined by Eq. 2.

The uniaxial compressive strength tests were done following the ASTM Standards Designation: D2938 Test Method for Unconfined Compressive Strength of Intact Rock Core Specimens. Load on the specimen shall be applied continuously at a constant stress rate such that failure will occur within 5-10 min. of loading with the stress rate 1000 to 3000 lbs/min.

The tensile strength of a material was determined using the indirect Brazilian test, where a disc of rock is loaded across a diameter based on the ASTM testing rules.

ANALYSIS OF TEST RESULTS

The results of rock tester tests on each specimen are presented in Table 1.

Five indentation tests were made on each specimen. The ratio of the diameter of indentation on the reference bar (d) to the diameter of indentation on the rock surface (D) was calculated for each test. The mean value of five ratios was used to develop a certain correlation between the hardness ratio and the rock strength for each specimen.

Linear Regression Analysis:

Fig. 4 shows the linear correlation between the uniaxial compressive strength of the rocks and rock tester tests results. The correlation coefficient of 0.93 is sufficiently high to warrant use of the rock tester test for predicting the uniaxial compressive strength when this is required. The following formula of linear regression can be used to determine the uniaxial compressive strength:

$$C_0 = k_c A + C \qquad (3)$$

where, C_0= uniaxial compressive strength
k_c= 112.38, C = -1007.04
A = average hardness ratio obtained from rock tester tests.

The correlation between the indirect tensile strength of the rocks and the rock tester tests is shown in Fig. 5. The empirical formula for tensile strength can be expressed by a linear regression equation:

$$T_0 = k_T A + C \qquad (4)$$

where, k_T= 7.54, C = 355.66
T_0= indirect tensile strength.

Since the correlation coefficient of this linear regression was only 0.57, the tensile strength of the rock sample can only be predicted roughly by rock tester tests. In other words, an approximate range can only be used to estimate the tensile strength of rock based on the rock tester readings (Fig. 5).

Best-Fit Line Analysis:

In order to create a high-accuracy relationship between the uniaxial compressive strength and rock tester readings, the best-fit line analysis was employed by using a computer program. This program provides the user with six best-fit options: 1) Linear, 2) Logarithmic, 3) Exponential, 4) Power, 5) Cubic Spline, and 6) Polynomial. In this case, three options--Linear, Power, and Polynomial--were used to develop the best-fit line (Fig. 6). Finally, power curve fit was chosen as the best-fit result (Fig. 7). It can be presented by the following equation:

$$C_0 = kA^{\alpha} \qquad (5)$$

where, k = 59.56, α = 1.1145.

CONCLUSIONS

1.) The portable rock tester test is a quick and economical method to determine the uniaxial compressive strength of soft rock. The testing samples in the form of core or irregular lumps can be used and require no machining. Only reasonably flat

surface is required for the test. More tests may be made at the very low cost for most of underground opening rock conditions. With the reliability of the results, this test should become useful in both mining, tunnelling, and geological applications.

2.) Rock tester strength is closely correlated with the results of uniaxial compressive strength. An approximate conversion Uniaxial Compressive Strength $C_o = kA^{\alpha}$ can be used.

3.) The hardness of the reference bar is an important parameter and should be compatible with the sample tested in order to obtain the well-defined indentations on both reference bar and rock specimens.

4.) Since the low correlation coefficient was obtained in tensile strength regression analysis, the indirect tensile strength range (as shown in Fig. 5) is applicable for common rocks, but these should be used with caution. This is particularly true in zones of existing discontinuities, where rock have tensile strength in very small values.

5.) In the present state of research, the portable rock tester is fully applicable for quick field and laboratory determination of uniaxial compressive strength and approximate tensile strength of rocks with strength up to 18,000 psi. One has to keep in mind that, from the stability point stand, weaker rocks are of special interest, e.g. in coal mining. Conversely, when dealing with fragmentation and blasting, hard rocks create problems. Poor or unverifiable indentation on the specimen caused by very high hardness of rock is a problem of this test. How to deal with the elastic response of hard rock will be the goal of further research.

REFERENCES

1. Poole, R. W. and Farmer, I. W. (1980). Consistency and Repeatability of Schmidt Hammer Rebound Data During Field Testing, Int. J. Rock Mech. Min. Sci., Vol. 17, 167 pp.

2. Broch, E. and Franklin, J. A. (1972). The Point-Load Strength Test, Int. J. Rock Mech. Min. Sci., Vol. 9, pp. 669-692.

3. Greminger, M. (1982). Experimental Studies of the Influence of Rock Anisotropy on Size and Shape Effects in Point-Load Testing, Int. J. Rock Mech. Min. Sci., Vol. 19, 241 pp.

4. Hladysz, Z. J. and Erickson, J. D. (1983). Portable Rock Strength Tester and Economic Benefits of Rapid Testing, SME preprint 84-86.

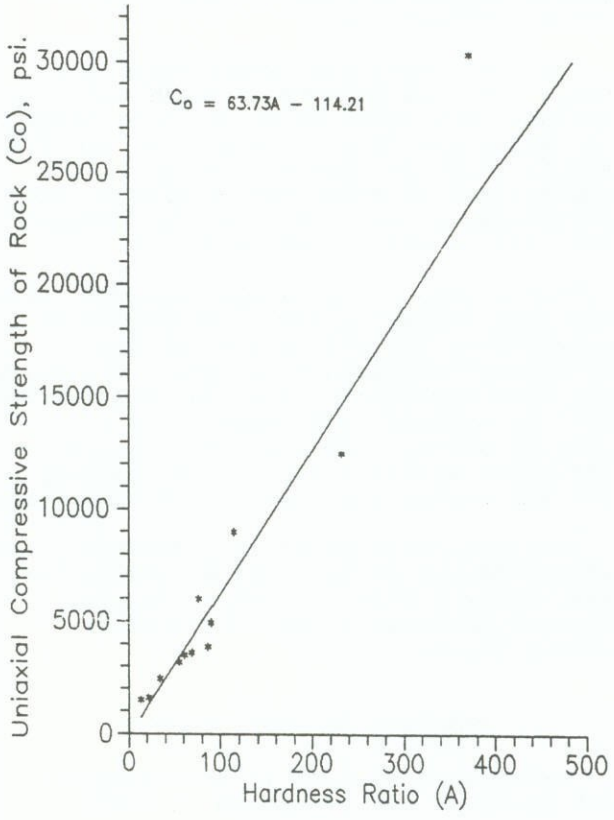

Figure 1. General correlation plot (after Hladysz, 1985).

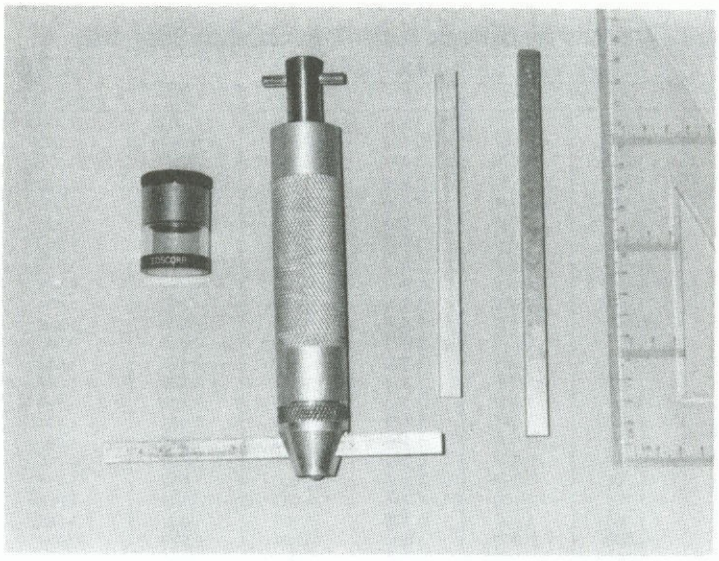

Figure 2. The portable rock strength tester.

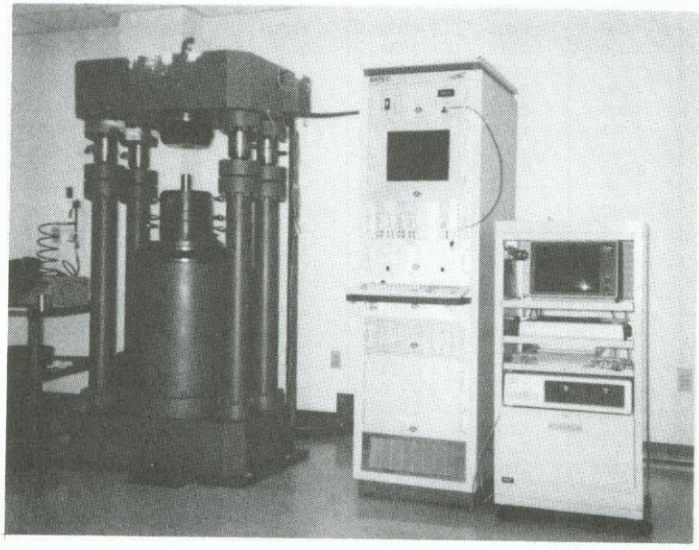

Figure 3. Servo-controlled stiff testing machine system.

Table 1. The Results of Rock Tester Test on Each Specimen

Sample No.	Sample Location	Indentation Ratio of Each Impact(d^2/D^2)					Average d^2/D^2	Average Ratio A *
		#1	#2	#3	#4	#5		
3	62B	1.249	1.410	1.121	2.041	1.361	1.436	182.431
4	69T	0.903	0.907	0.907	0.907	0.907	0.906	115.078
6	88T	1.235	1.210	1.341	1.222	1.384	1.278	162.331
7	98T	1.121	1.108	1.249	1.121	1.000	1.120	142.224
8	109T	1.000	1.121	1.000	1.103	1.000	1.045	132.680
9	117B	1.384	1.249	1.361	1.341	1.494	1.366	173.453
10	125B	1.098	1.098	1.103	1.000	1.103	1.080	137.160
11	138B	1.103	1.235	1.103	1.103	1.103	1.129	143.372
12	148B	1.000	1.000	0.907	0.903	0.903	0.942	119.686
13	157B	1.000	1.000	1.103	1.108	1.108	1.064	135.092
14	167B	0.907	0.907	1.000	1.108	1.108	1.006	127.765
15	175B	0.810	0.810	0.898	0.819	0.826	0.833	105.729
16	185B	1.000	1.000	1.103	1.108	1.103	1.063	134.951
17	194T	1.000	1.000	1.108	1.108	1.222	1.088	138.117
18	199T	1.235	1.108	1.138	1.384	1.108	1.194	151.701
19	207T	1.384	1.341	1.494	1.361	1.675	1.451	184.264
20	213T	1.103	1.000	1.103	1.103	1.098	1.081	137.287
21	228B	0.597	0.826	0.682	0.627	0.826	0.712	90.403
23	245B	1.222	1.098	1.235	1.000	1.000	1.111	141.063
25	265.5B	1.108	1.108	1.114	1.000	1.108	1.088	138.133
26	274.5B	1.108	1.108	1.108	1.108	1.000	1.086	137.976
27	285B	1.000	0.903	1.000	0.898	0.907	0.941	119.559
28	296B	1.000	1.108	1.000	1.000	1.000	1.022	129.744
29	303T	0.907	0.898	0.898	0.723	0.903	0.865	109.907
30	308B	1.103	1.000	1.103	0.903	1.103	1.042	132.334
31	315B	1.235	1.108	1.562	1.361	0.309	1.115	141.601
32	327B	0.898	1.000	1.000	1.000	0.903	0.960	121.920
33	330.5T	0.578	0.706	0.640	0.627	0.627	0.635	80.687
34	333.5B	0.563	0.578	0.592	0.652	0.694	0.616	78.197
35	335T	0.819	0.907	0.826	0.911	0.826	0.858	108.958
41	359B	0.578	0.479	0.518	0.510	0.694	0.556	70.610
42	360.5B	1.000	0.834	1.000	1.000	0.756	0.918	116.581
44	366T	1.000	1.000	1.114	1.108	1.108	1.066	135.389
46	371B	0.826	0.826	1.000	0.907	0.834	0.879	111.597
52	391B	1.000	0.911	0.911	1.000	0.834	0.931	118.261
53	392.5T	1.108	0.810	1.235	1.361	0.826	1.068	135.640
56	401.5B	0.911	0.911	0.911	0.915	1.000	0.930	118.069
57	409B	0.911	0.915	0.911	0.840	0.840	0.884	112.212
58	414.5T	0.810	0.756	0.834	0.756	0.652	0.762	96.731
59	421T	1.103	0.907	0.826	1.103	0.911	0.970	123.181
60	429B	1.114	1.222	1.222	1.103	1.222	1.176	149.391
61	431T	1.384	1.341	1.384	1.410	1.361	1.376	174.756
62	435B	1.000	1.000	1.098	1.093	0.907	1.020	129.477
65	447B	1.000	1.103	1.000	1.103	1.098	1.061	134.684
68	459T	1.108	1.000	1.000	1.000	0.911	1.004	127.487
70	469.5B	1.000	1.000	1.000	1.000	1.000	1.000	127.000
71	472.5B	1.000	0.819	0.834	0.826	0.694	0.835	105.998
72	479B	1.000	1.000	0.911	0.907	0.907	0.945	120.020
74	487B	1.200	1.108	1.235	1.235	1.361	1.228	155.901
75	496T	1.000	0.907	0.907	0.826	0.907	0.910	115.507
76	501B	1.103	1.222	1.384	1.361	1.410	1.296	164.578
77	508T	0.903	0.903	1.108	1.000	1.000	0.983	124.791
78	511	1.000	0.898	0.907	1.000	0.810	0.923	117.209
79	519	1.000	1.384	1.000	1.108	1.108	1.120	142.244
80	521	1.000	1.108	1.114	1.103	1.235	1.112	141.206
81	528	0.898	0.898	1.114	1.114	1.108	1.026	130.339
82	531	1.000	1.108	0.903	1.000	1.129	1.028	130.542
83	538B	1.000	0.810	1.108	1.000	1.000	0.984	124.918
84	541B	1.000	1.000	1.000	1.108	1.108	1.043	132.488
85	549	0.898	0.898	0.801	0.810	0.810	0.843	107.075
86	552T	0.810	0.819	0.751	0.801	0.669	0.770	97.782
87	555B	0.709	0.709	0.597	0.612	0.578	0.641	81.419
88	559B	0.102	0.171	0.154	0.154	0.218	0.160	20.322
89	561B	0.640	0.709	0.790	0.801	0.810	0.750	95.245
90	568B	0.898	1.121	0.903	0.898	1.000	0.964	122.393
91	571B	0.810	1.000	0.810	0.819	0.907	0.869	110.379
92	578T	0.627	0.669	0.682	0.597	0.669	0.649	82.426
94	582B	1.235	0.898	1.114	1.235	1.222	1.140	144.842
95	587B	1.000	1.000	0.907	0.907	1.103	0.983	124.881
96	591B	1.000	1.108	1.000	1.000	0.826	0.987	125.336
98	604T	0.640	0.819	0.597	0.735	0.597	0.678	86.043
99	607T	1.108	0.907	0.826	1.000	0.819	0.932	118.367
100	615T	1.121	1.410	1.384	1.384	1.222	1.304	165.634
101	619T	0.898	0.756	0.819	0.907	0.756	0.827	105.040
102	624.5B	0.756	0.903	0.826	0.756	0.907	0.830	105.366
103	630B	1.103	1.103	1.103	1.108	1.222	1.127	143.183

* "A" value can be calculated by Eq. 2.

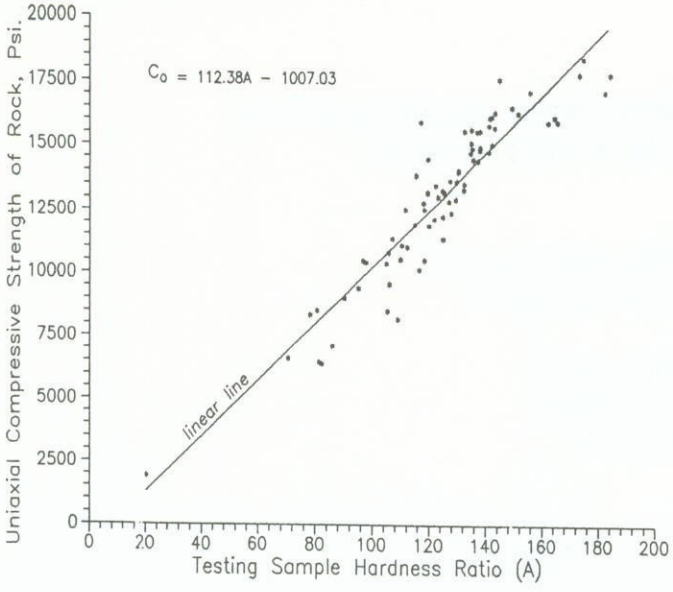

Figure 4. The linear correlation between results from uniaxial compressive strength (C_o) and rock tester tests (A).

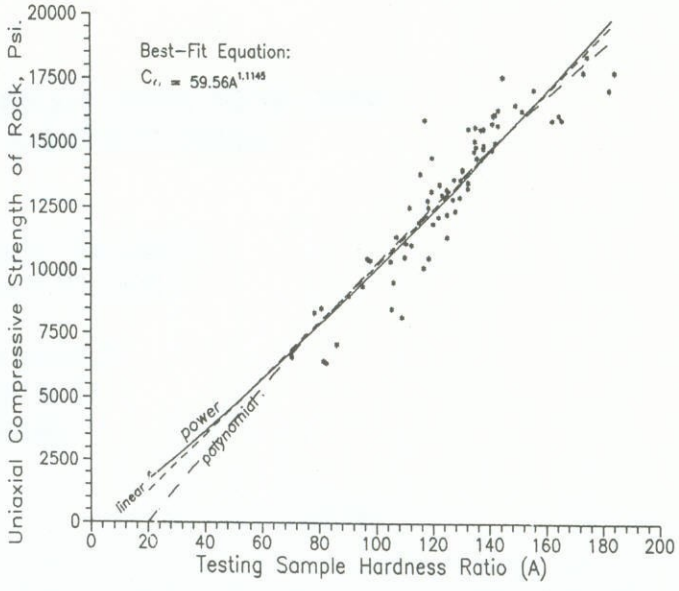

Figure 6. Correlations between uniaxial compressive strength and rock tester readings were developed using best-fit analysis.

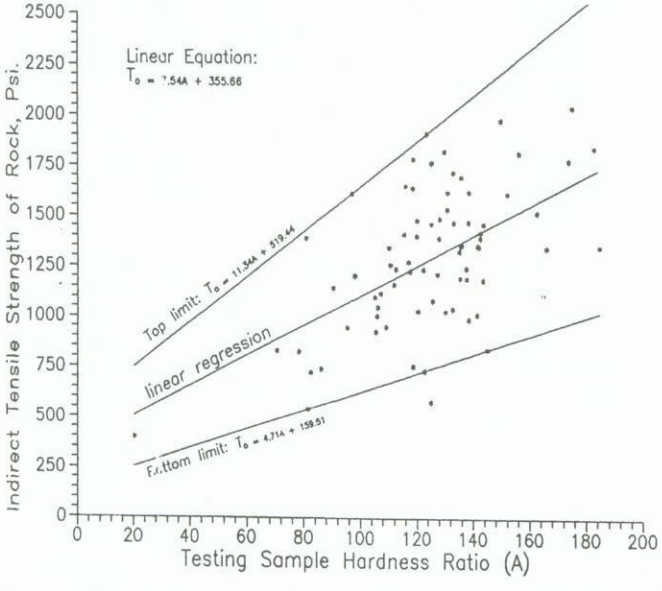

Figure 5. The linear correlation between results from indirect tensile strength (T_o) and rock tester tests (A).

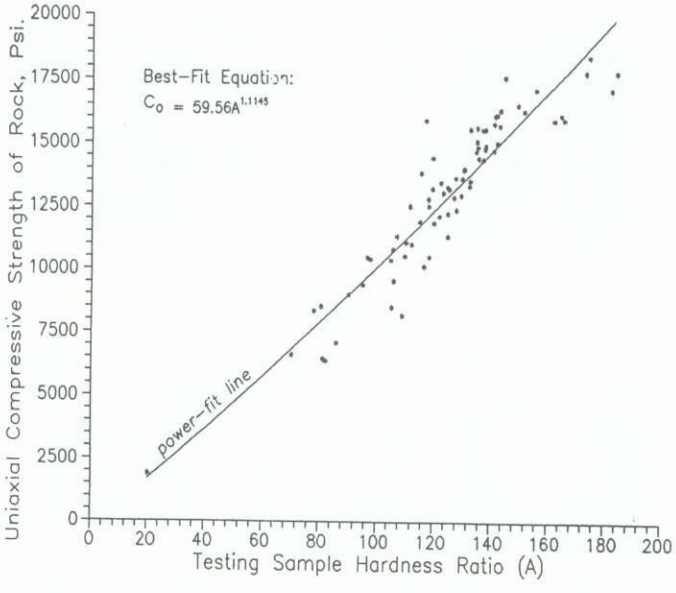

Figure 7. Best-fit correlation between uniaxial compressive strength and rock tester readings.

10th INTERNATIONAL CONFERENCE ON GROUND CONTROL IN MINING

MINE–WIDE PHYSICAL PROPERTY TREND IDENTIFICATION USING PORTABLE ON–SITE TEST DEVICES

Thomas L. Vandergrift, *Mining Engineer*
David P. Conover, *Mining Engineer*

Denver Research Center
U. S. Bureau of Mines
Denver, Colorado

ABSTRACT

The type and severity of coal mine entry failures are affected by the strength and stiffness properties of the roof, floor, and coal. Knowledge of the mine-wide trends of these properties is valuable in developing effective ground control plans. Within the context of a larger effort to improve entry stability in high horizontal stress fields, the U.S. Department of the Interior, Bureau of Mines, has evaluated three portable, on-site test devices to determine their suitability for identifying mine-wide physical property trends. The devices evaluated were the borehole shear tester, the Schmidt hammer, and the point load tester.

Despite the lack of standardized data interpretation procedures, each device provided useful on-site physical property data. The Schmidt hammer was preferred for trend identification because of its speed and simplicity. Schmidt hammer data were collected over a large area of an underground coal mine to compare calculated roof strength trends with a known geologic feature.

INTRODUCTION

Strength and stiffness properties of coal mine roof, floor, and coal affect the type and severity of entry failure. During a recent U. S. Bureau of Mines field study of entry stability in high horizontal stress fields and varying geologic conditions, an attempt was made to identify trends in roof and floor strength using portable, on-site testing devices.

Physical properties of mine roof, floor, and coal are traditionally determined in the laboratory by uniaxial and triaxial testing of core samples. However, these methods are not well-suited for trend identification for the following reasons:

1) The time and expense involved in obtaining, preparing, and testing the number of samples necessary to identify mine-wide trends is prohibitive.
2) Laboratory test results are not representative of rock mass properties since laboratory tests do not duplicate in situ conditions.
3) Laboratory test results are biased toward high strength values since only samples strong enough to survive the preparation process are tested.

To overcome the problems associated with laboratory testing, a number of portable, on-site testing devices have been developed. For this effort, three devices were chosen for evaluation: the borehole shear tester, the Schmidt hammer, and the point load tester. These devices differ in their operation. The Schmidt hammer test is non-destructive and can be performed rapidly with minimal specimen preparation. The point load test also requires little time or preparation, but is destructive. The borehole shear test requires a borehole and is more time and labor intensive than either the Schmidt hammer or point load tests.

Previous investigations utilizing these on-site testing devices have reported conflicting recommendations for interpreting test results. For example, many different equations have been presented to convert Schmidt hammer and point load test indices to compressive strength and elastic modulus estimates. Because of the confusion regarding interpretation procedures, the effort to identify mine-wide physical property trends was divided into two phases. In phase one, on-site data from the portable devices were compared with available laboratory core test data to determine which interpretive equations were applicable. While this evaluation was not intended as a definitive study of these devices, the results illustrate their relative potential for practical geotechnical applications. In phase two, trends of compressive strength in the roof of a mine section were identified using the Schmidt hammer and compared with a known geologic feature in the immediate roof.

DEVICE DESCRIPTIONS AND PROCEDURES

Borehole Shear Tester

The borehole shear tester (BST) is used to determine the shear strength of rock in situ using the Mohr-Coulomb failure criteria (1). Since the test requires an NX (3 in) borehole, it is convenient to use the BST after obtaining core for laboratory compression tests.

In practice, the BST is inserted in an NX borehole (Fig. 1). Shear plates on opposite sides of the BST body are forced radially against the walls of the borehole by hydraulic pressure. Each plate exerts a normal force on a small envelope of rock adjacent to the plate. While the normal hydraulic pressure on the plates is maintained, a shear force is applied along the axis of the borehole by means of a hollow hydraulic jack at the hole collar. The shear force is gradually increased until an envelope of rock is sheared by the shear plates. Shear and normal pressures at failure are recorded from gauges on a hydraulic control console. The normal pressure is then released and the BST body is rotated 45° in the hole to obtain the shear pressure at failure for a different normal pressure. This process is repeated until four shear pressure readings corresponding to four different values of normal pressure are obtained at each horizon.

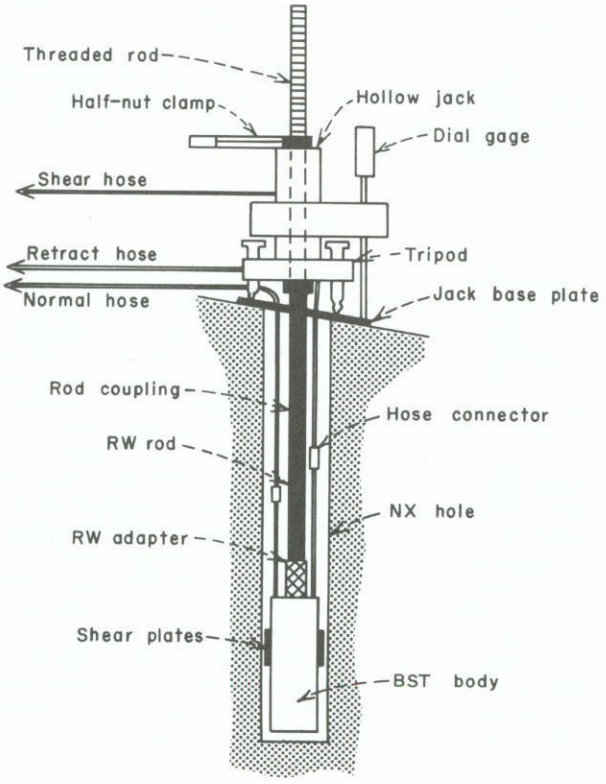

Figure 1 - Borehole shear tester assembly (1).

Shear and normal gauge pressures are converted to shear and normal stresses by means of calibration equations supplied with each BST. Shear stress is then plotted against normal stress, and a straight line is fitted to the data. This straight line (Fig. 2) represents the Mohr-Coulomb equation:

$$\tau_s = c + \sigma_n \tan \phi \qquad (1)$$

where τ_s = shear stress, psi,
σ_n = normal stress, psi,
c = y-intercept
= cohesion, psi, and
ϕ = angle of internal friction
= arc tan of the slope, deg.

In situ uniaxial compressive strength (σ_c) can be determined from the relationship (2):

$$\sigma_c = \frac{2c \cos \phi}{1 - \sin \phi} \qquad (2)$$

After comparing borehole shear test and laboratory triaxial test data, Panek (3) concluded that the results from the two tests are roughly equivalent. He noted that the BST generally produced cohesion values that were lower than those obtained from laboratory tests since laboratory tests are biased toward stronger values.

Schmidt Hammer

The Schmidt hammer was developed to estimate the strength of concrete in-place. The hammer imparts a constant amount of stored spring energy to the test material by means of a sliding hammer mass within the instrument (Fig. 3). The rebound distance of the hammer mass gives an indication of the properties of the test material.

Research into the application of the Schmidt hammer to mining problems began in the early 1960's (5). The first hammers (type N) had an

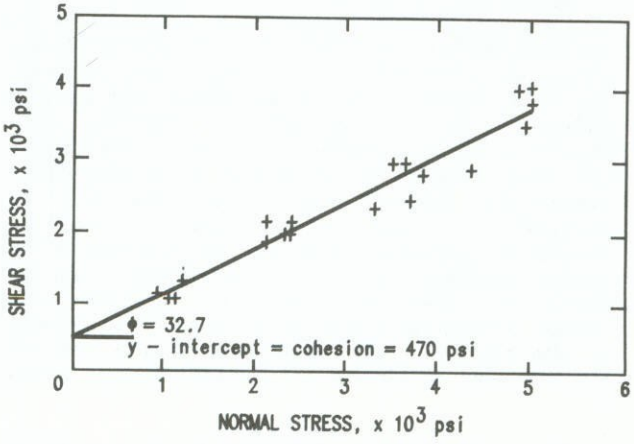

Figure 2 - Example of a borehole shear test data plot.

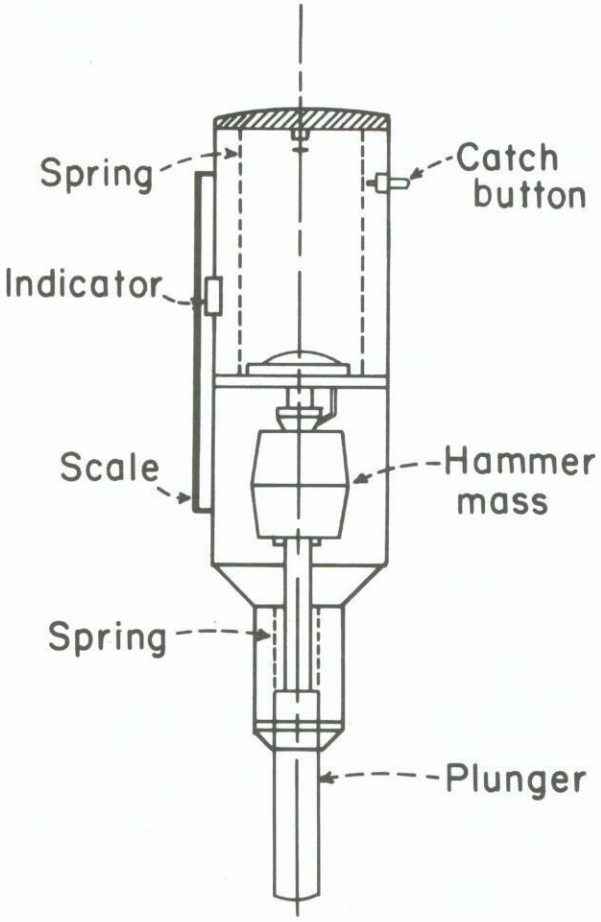

Figure 3 - Schematic of the Schmidt hammer (4).

impact energy of 1.63 ft·lb, which was excessive for weak rocks and coal. Mining applications became more practical with the development of the type L hammer, having an impact energy of 0.54 ft·lb. The type L hammer is now the standard for rock testing. The Schmidt hammer test can be performed in situ or on core or lump samples.

According to guidelines for Schmidt hammer testing established by the International Society for Rock Mechanics (ISRM) (6), the Schmidt hammer should be calibrated prior to each test sequence. The test surface should be clean and free of defects. In the case of core testing, cores should be of NX diameter or larger. Preferably, the test should be conducted with the hammer vertically upward, vertically downward, or horizontal. Readings at other orientations should be corrected using curves supplied by the hammer manufacturer. At least twenty readings should be taken per sample or location, with impact points separated by at least the diameter of the plunger. The upper 50% of the readings are averaged to obtain the Schmidt hammer index, R.

The relationship between R and uniaxial compressive strength, σ_c, and Young's modulus, E, has been studied by many investigators. A summary of some of their findings is presented in Table 1.

Point Load Tester

The point load test (PLT) is an indirect tensile test in which a concentrated load is applied to a rock sample by two opposing pointed platens. The platens induce a tensile stress in the sample perpendicular to the direction of the applied load. Failure occurs along a surface in the direction of the applied load.

Use of the point load test in mines became practical with the development of a portable point load tester (Fig. 4). The test can be performed either on-site or in the laboratory on both core samples (axial and diametral tests) and unprepared specimens (irregular lump tests).

The ISRM (10) has defined the point load strength index, I_s, as:

$$I_s = P/D^2 \qquad (11)$$

where P = load at failure, lb,
D = original distance between the loading points, in.

Several researchers have found good correlation between uniaxial compressive strength and I_s, although Haramy (11) found better correlation when I_s was defined as P/D.

Table 2 summarizes the predictive equations resulting from several studies correlating the point load index to compressive strength and Young's modulus.

TEST SITE

The field investigation was conducted as part of a larger effort to study entry stability in high horizontal stress and varying geologic conditions at an underground coal mine in central Utah. For the entry stability study, a four-way intersection was instrumented with borehole pressure cells, borehole extensometers, and closure meters. As part of the site characterization, cores were drilled from the roof, floor, and pillars and were tested in the laboratory in uniaxial and triaxial compression. Borehole shear tests, Schmidt hammer tests, and point load tests were conducted at the test site. Figure 5 shows the configuration of the test site and the locations of the various tests. The field results were compared with the laboratory compression data to determine which on-site test device was most suitable for identifying mine-wide trends in roof and floor properties.

The test site was located in the submain system of a producing section. Production in the section was by room-and-pillar, leaving 3 to 4 ft of coal in the floor for recovery during pillar extraction on retreat. The roof was generally a

Table 1 - Summary of the relationships between the Schmidt hammer index and σ_c and E.

Equation Number	Predictive Equation		Coeff. of Determination r^2	Scope of the Study
	Compressive Strength, psi	Young's Modulus, psi x 10^6		
3(7)	$\sigma_c = 1445 \times 10^{0.0087\ RxSG}$	---	0.89	Tested 13 rock types from 27 locations
4(7)	---	$E_t = 0.087\ RxSG - 2.94$	0.72	
5(5)	$\sigma_c = 47.3 \times 10^{1.348\ \log_{10} RxSG}$	---	0.64	Tested 25 rock types from over 168 geologic formations
6(5)	---	$E_t = 0.073 \times 10^{1.061\ \log_{10} RxSG}$	0.56	
7(8)	$\sigma_c = 1849e^{0.0185\ RxSG}$	---	0.75	Added to the data of (7), 49 formations total
8(8)	---	$E_t = 0.028\ RxSG^2 - 1.844$(8)	0.71	
9(9)	$\sigma_c = 64.9e^{0.045\ R\ +\ SG}$	---	---	Tested Polish coal-measure rocks
10(4)	$\sigma_c = 137\ R - 55.6$	---	0.71	Tested coal blocks from 10 different U.S. locations

R = Schmidt hammer index
SG = Specific gravity of rock tested

sandy shale occasionally cut by sandstone channels. Coal in the vicinity of the test site could be qualitatively divided into two groups based on resin content: a "low resin" coal which occurred primarily in the floor, and a "high resin" coal which occurred primarily in the upper two-thirds of the pillars.

TEST RESULTS

Borehole Shear Tests

Borehole shear tests were performed in NX boreholes in the roof and floor, as shown in Figure 5. Tests were conducted at 1-ft intervals from the hole collar to depths of 19.5 ft in the roof and 16 ft in the floor. No readings were taken in the interval between 13.5 and 16.5 ft in the roof because the core revealed a fracture zone in this interval.

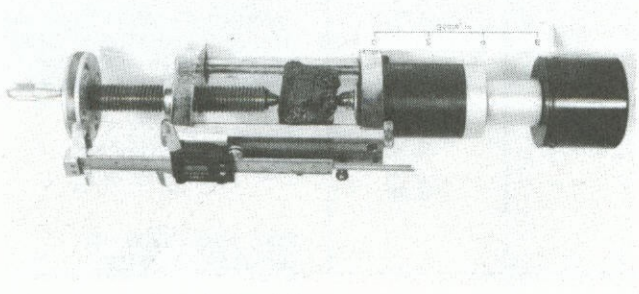

Figure 4 - Point load tester.

The pressure data were converted to stresses using calibration equations supplied with the BST. The calculated stresses were grouped according to roof and floor lithology and plots of shear stress versus normal stress were made for each rock type. Table 3 summarizes the in situ physical properties determined from these plots compared with uniaxial compressive strength determined from laboratory testing.

In general, the BST results of this study are consistent with those of Panek (3). The uniaxial strengths determined in the laboratory are 3 to 20 times the compressive strength values from the BST. The cohesion values show a similar variation, although the triaxial data were insufficient to make a direct comparison for each horizon. The angle of internal friction (ϕ) values appear reasonable, but again no direct comparison with laboratory values could be made.

The low compressive strength and cohesion values resulting from borehole shear tests may be more indicative of in situ rock strengths than laboratory values. This is because laboratory results are biased toward high values. In addition, the Mohr-Coulomb theory may not be an adequate model for interpreting the test data. As noted by Panek, the stress state induced by the borehole shear test is much different than that induced in triaxial tests. He suggests interpreting BST data based on a three-dimensional yield criterion. However, because a direct comparison between the parameters of this yield criterion and cohesion and ϕ cannot be made, it appears that further research is needed to determine how BST results should be interpreted.

The BST is not intended as an index test and the testing process is time-consuming and labor intensive. A two-man crew can only complete about one test location per shift (depending on the hole depth and number of testing intervals). Both the time requirement and the requirement for NX boreholes make testing over the grid required for mine-wide mapping purposes impractical.

Schmidt Hammer Tests

Tests of the floor coal were conducted with the Schmidt hammer at 11 stations indicated in Figure 5. The Schmidt hammer indices were converted to compressive strengths using equation 10 in Table 1, which was assumed to be the most applicable since it was derived from western coal data. The calculated average strength from the floor test sites was 4,100 psi, compared to an average of 4,700 psi determined from uniaxial testing of 10 "low resin" coal samples. It appears that the use of equation 10 is justified for estimating the compressive strength of the coal in this section. No attempt was made to correlate Schmidt hammer indices with the Young's modulus of the coal.

To provide a basis for choosing the most suitable interpretive equation for roof and floor rock from the remaining equations in Table 1, core samples were tested with the Schmidt hammer and subsequently tested in the laboratory under uniaxial compression. Table 4 presents the Schmidt hammer indices and compression test data for the various roof and floor horizons.

Laboratory-determined physical properties of the roof and floor samples did not correspond with values produced using the equations in Table 1, therefore, best-fit equations were generated by linear regression from the data in Table 4. These equations (22 and 23, respectively) and their associated 95% confidence intervals are shown in Figures 6 and 7. The coefficients of determination (r^2), although not particularly high, are within the range of values reported by previous investigators. The best correlation was achieved when the Schmidt hammer index was multiplied by the test material's specific gravity. Equations 22 and 23 were derived from a limited amount of data and are not intended to be applied to other mines or lithologies. Rather, they are intended as calibration equations for this particular field site.

Data collection with the Schmidt hammer can be quickly and easily achieved by one person. Periodic calibration checks and maintenance should be performed to ensure the best results.

Point Load Tests

Point load tests of both "high resin" and "low resin" coal were conducted on lump and core

Table 2 - Summary of the relationships between the point load index and σ_c and E.

Equation Number	Predictive Equation: Compressive Strength, psi	Predictive Equation: Young's Modulus, psi x 10^6	Coeff. of Determination r^2	Scope of the Study
12(12)	$\sigma_c = 14.7\ P/D^2 + 2370$	---	0.90	19 rock types; AX, BX, and NX core tested diametrically
13	---	E_t*= $3.259 \log_{10} P/D^2 - 1.23$	0.67	
14(7)	$\sigma_c = 20.35\ P/D^2 + 3160$	---	0.90	13 rock types from 27 locations; NX core tested diametrically
15(7)	---	$E_t = 4.36 \times 10^{-3}\ P/D^2 + 3.52$	0.63	
16(13)	$\sigma_c = 24\ P/D^2$	---	0.77	15 rock types; 38mm core corrected to a reference diameter of 50 mm, tested diametrically
17(14)	$\sigma_c = 24\ P/D^2$	---	---	4 rock types in addition to the data from (12) and (13), NX core tested diametrically
18(15)	$\sigma_c = 29\ P/D^2$	---	0.88	Sedimentary rocks from the U.K., in addition to other authors' data. Data corrected to NX core, tested diametrically.
19(16)	$\sigma_c = 10.7\ P/D^2 + 50$ (Axial)	---	0.98	Tested 7 sedimentary rock types; NX core
20(16)	$\sigma_c = 16.1\ P/D^2 + 270$ (Diam.)	---	0.99	
21(11)	σ_c=1.72x10^4 $\log_{10}$ $\bar{P}/\bar{D}$-3.39x10^4	---	---	Coal lumps from six western U.S. mines

*Best fit from data presented by D'Andrea (12) et al.

samples taken from the locations indicated in Figure 5. In addition, uniaxial compression tests were performed on samples taken from the same locations. The coal PLT data were reduced using equation 21, derived from tests of coal from six western mines. The results of the PLT and uniaxial tests are shown in Table 5.

The values obtained using equation 21 did not agree with the strength values from uniaxial compression tests. The compressive strengths calculated from the PLT data are significantly higher than the strengths from uniaxial testing.

Sufficient roof and floor cores were not available for point load testing; therefore, point load tests were performed on irregular lump samples. These samples were left from NX coring of the 6-in roof and floor cores taken from the location indicated in Figure 5. Uniaxial compression tests were performed on the NX cores to provide a basis for comparison of PLT and uniaxial data. Table 6 lists the average point load indices for this material expressed both as P/D and P/D^2, and repeats the laboratory compressive strength and Young's modulus data from Table 4. The point load test data were

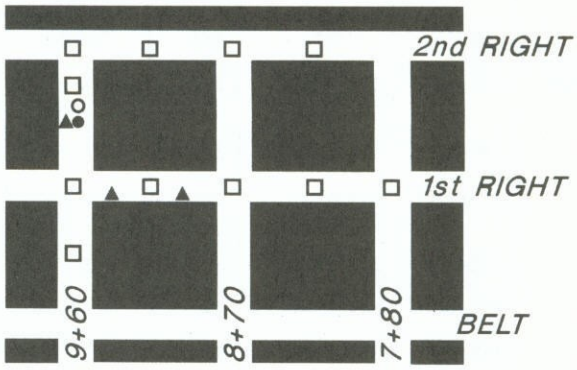

KEY

- ○ NX CORE, BOREHOLE SHEAR TESTS, ROOF AND FLOOR
- □ SCHMIDT HAMMER TESTS, FLOOR COAL
- ▲ POINT LOAD TESTS, RIB COAL
- ● 6" CORE, ROOF AND FLOOR

Figure 5 - Intersection test site.

Table 3 - Uniaxial and borehole shear test data comparison.

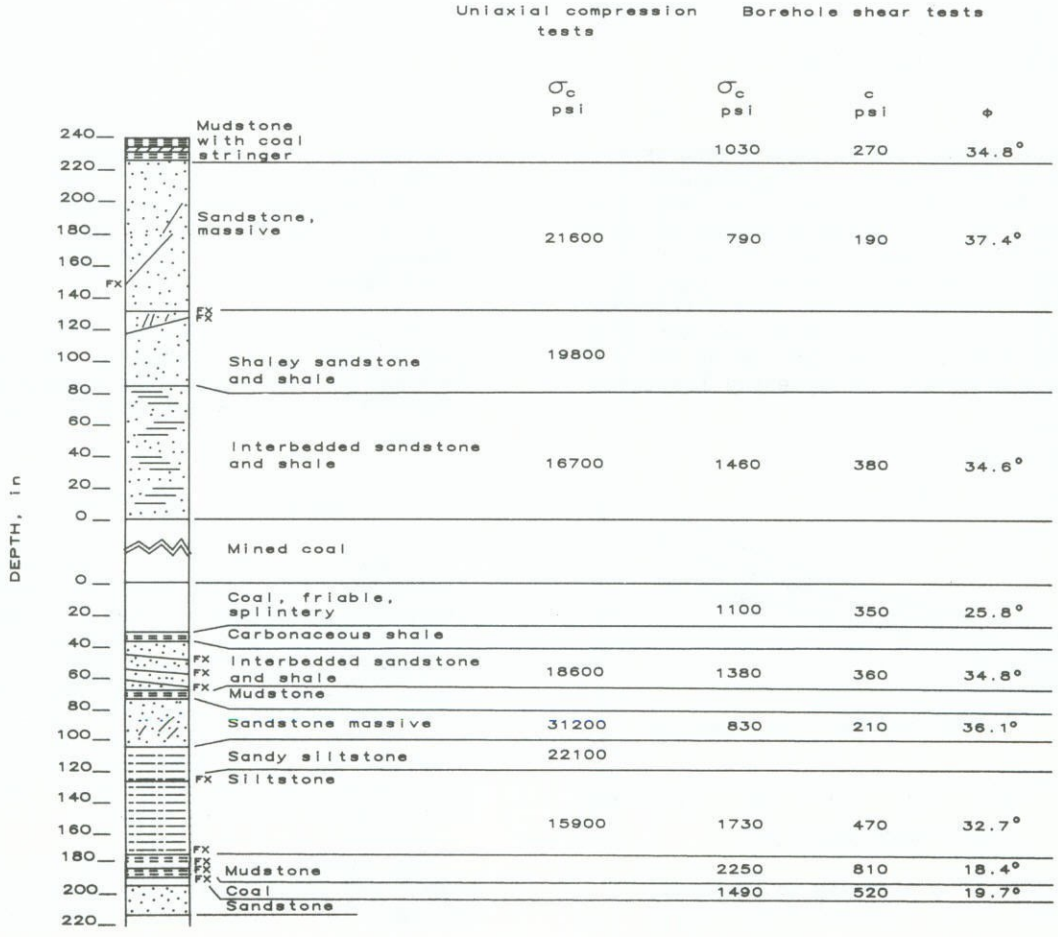

Table 4 - Schmidt hammer indices and compression test data for floor and roof rock.

	Depth	Rock Type	Schmidt Index (R)	Number of Core Samples	Average Specific Gravity (SG)	Average Uniaxial Compressive Strength σ_c, psi	Average Young's Modulus E_t, psi x 10^6
Floor	51-59"	Sandstone & Shale	34.4	4	2.51	18,600	5.290
	97-105"	Sandstone	37.2	4	2.70	33,000	7.245
	99-117"	Silty Sandstone	37.9	5	2.68	24,300	6.101
	122-126"	Siltstone	35.9	5	2.66	18,700	3.992
	134-143"	Siltstone	29.9	4	2.64	14,500	3.439
	146-154"	Siltstone	33.0	2	2.58	11,700	2.535
Roof	43-51"	Sandstone & Shale	36.8	5	2.55	16,700	3.492
	99-107"	Shaley sandstone & shale	40.0	5	2.60	19,400	4.766
	110-118"	Shaley sandstone & shale	42.3	6	2.59	16,400	4.200
	120-132"	Shaley sandstone & shale	42.5	8	2.61	21,400	5.880
	135-148"	Sandstone	44.3	3	2.63	22,700	5.416
	152-160"	Sandstone	36.3	4	2.66	16,700	3.861
	162-175"	Sandstone	48.8	6	2.72	28,100	7.119

converted to values of uniaxial compressive strength and Young's modulus using equations 12 through 20. These equations were derived from point load tests of core, which could explain why the values they produced did not match the uniaxial data. Therefore, best-fit equations were generated from the data in Table 5 (Figures 8 and 9). The highest correlation was achieved when the point load index was defined as P/D. A straight line was chosen to represent the data,

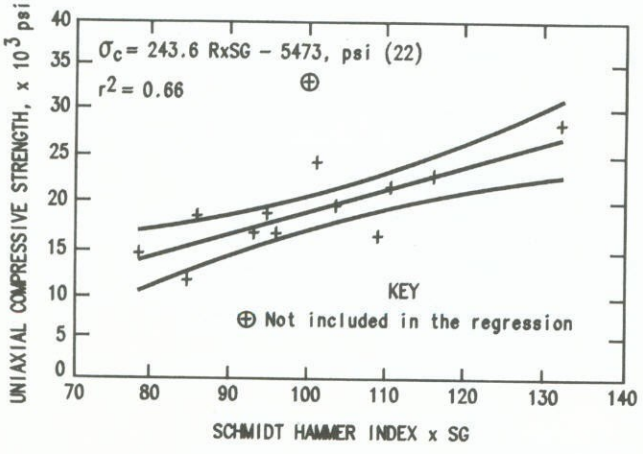

Figure 6 - Compressive strength vs. Schmidt hammer index, R·SG, roof and floor rock.

although an inverse function gave a slightly higher correlation. This difference was judged not to be great enough to warrant a departure from a linear model. The coefficients of determination, r^2, are comparable with those of other researchers.

The point load test is relatively easy to perform, although it cannot be performed in situ. This can be a drawback since obtaining sufficient roof or floor samples may not be possible without coring.

SUMMARY OF ON-SITE TEST DEVICES

Borehole shear test data may be more indicative of in situ physical properties than laboratory compression tests; however, data interpretation using Mohr-Coulomb theory may be inadequate. The BST is different from both the Schmidt hammer and the point load tester in that it is not intended as an index test. A possible application of the BST may be in gathering baseline data. These data could then be correlated with index test data to identify mine-wide physical property trends.

The speed and ease-of-use of the Schmidt hammer and point load tester make both promising devices for identifying mine-wide physical

property trends. In comparing Schmidt hammer and point load test indices with the laboratory physical property data, the coefficients of determination of the two devices were similar. Figure 10 shows the relationship between the Schmidt hammer and point load indices for the roof and floor rock. The correlation for this plot is better than for any of the plots of Schmidt hammer and PLT indices versus compressive strength and Young's modulus. This suggests that much of the variation encountered during this study was due to the variability of compression test results.

IDENTIFICATION OF COMPRESSIVE STRENGTH TRENDS IN THE ROOF

Schmidt hammer tests were conducted over a large area of the mine to construct contour maps of roof strength. The Schmidt hammer was chosen for this task for the reasons previously discussed -- its accuracy and speed, and its capability to test rock in situ.

A second type L Schmidt hammer of different manufacture was purchased for this phase of the study. However, a calibration check showed that the readings produced by the two factory-calibrated Schmidt hammers were approximately 12% apart. This raises the possibility that the findings of previous researchers are inconsistent in part due to inconsistencies between Schmidt hammer brands. Because of this inconsistency, all mine readings were taken with the first Schmidt hammer, which was used to derive site-specific equations 22 and 23.

Table 5 - Point load - uniaxial test comparison, coal.

Test Type	Number of Samples	Compressive Strength σ_c, psi
Low-Resin Content		
Lump	119	7600
Axial	15	4800
Diametral	15	7300
All	149	7400
Uniaxial	10	4700
High-Resin Content		
Lump	45	5200
Axial	29	5700
Diametral	34	6500
All	108	5700
Uniaxial	4	1700

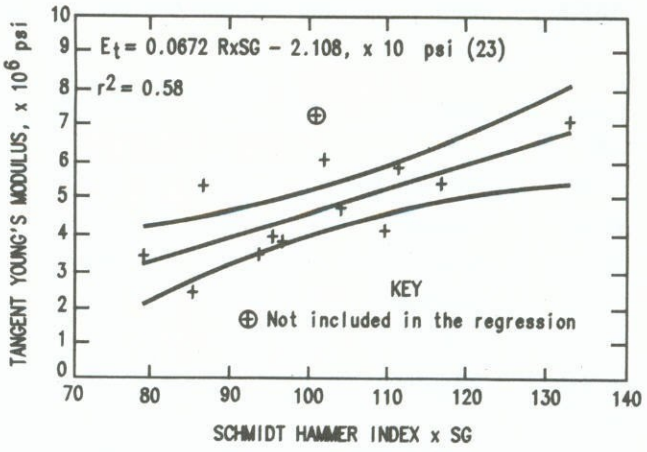

Figure 7 - Tangent Young's modulus vs. Schmidt hammer index, R·SG, roof and floor rock.

The Schmidt hammer indices were converted to compressive strength estimates using equation 22. Determination of the specific gravity at each site was impractical; therefore, the average specific gravity of the immediate roof near the main test site (2.62) was used. Since the measured range of roof specific gravities was narrow, the use of a constant specific gravity does not significantly affect the calculated values of compressive strength.

Calculated roof strengths were contoured and overlain on a map of a sandstone channel in the roof (Figure 11). Because the specific gravity was taken to be constant, the contours correspond to trends in the Schmidt hammer index, R. The average laboratory-determined uniaxial compressive strength of samples within the sandstone channel was 16,200 psi; the strength of sandy shale samples outside the channel averaged 9,800 psi. It is assumed that both roof materials are uniform and that these strengths are representative of the entire section. However, the strength contours indicate

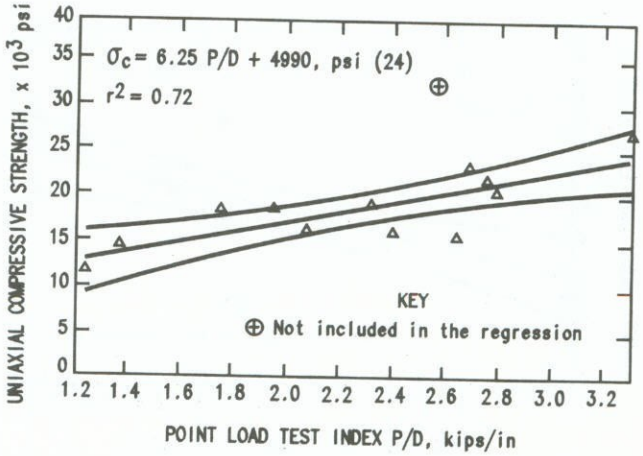

Figure 8 - Compressive strength vs. point load index.

Table 6 - Point load test indices and physical properties of floor and roof rock.

Depth	Rock Type	No. Point Load Tests	Average P/D, lb/in	Average P/D^2, psi	No. of Core Samples	Average Uniaxial Compressive Strength σ_c, psi	Average Young's Modulus E_t, psi x 10^6
FLOOR							
51-59"	Sandstone & Shale	18	1744	1106	4	18,600	5.290
97-105"	Sandstone	10	2553	1346	4	33,000	7.245
99-117"	Silty Sandstone	14	2669	1740	5	24,300	6.101
122-126"	Siltstone	11	1941	1395	5	18,700	3.992
134-143"	Siltstone	14	1372	796	4	14,500	3.439
146-154"	Siltstone	4	1248	905	2	11,700	2.535
ROOF							
43-51"	Sandstone & Shale	6	2394	1769	5	16,700	3.492
99-107"	Shaley Sandstone & Shale	10	2307	1388	5	19,400	4.766
110-118"	Shaley Sandstone & Shale	6	2627	1895	6	16,400	4.200
120-132"	Shaley Sandstone & Shale	17	2771	1827	8	21,400	5.880
135-148"	Sandstone	13	2734	1710	3	22,700	5.416
152-160"	Sandstone	6	2067	1387	4	16,700	3.861
162-175"	Sandstone	16	3273	2636	6	28,100	7.119

significant variation within each material and show no apparent differentiation between the sandy shale and the sandstone. Tests of core samples throughout the section would have to be conducted to determine whether this apparent lack of correlation is due to false assumptions about the roof material or to shortcomings of the Schmidt hammer tests.

SUMMARY AND CONCLUSIONS

In attempting to apply portable on-site test devices to the task of identifying mine-wide physical property trends, a lack of standardization regarding data interpretation procedures was encountered.

The borehole shear test is intended to determine the in situ shear strength of rock. The BST requires coreholes for testing and is impractical for extensive mine-wide testing. Its application in determining mine-wide physical property trends may be as a source of baseline data to which index tests could be related. Strength values from the BST are generally lower than laboratory-determined values, indicating that BST results may be more indicative of in-

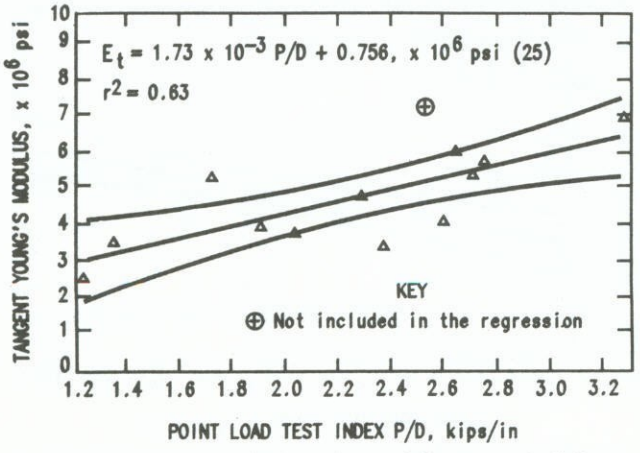

Figure 9 - Tangent Young's modulus vs. point load index.

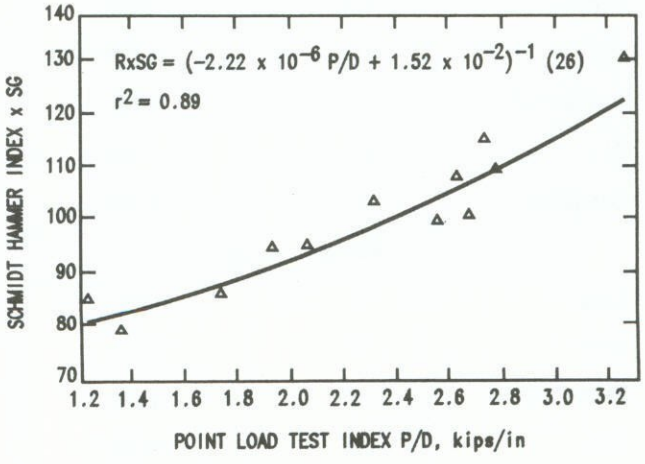

Figure 10 - Schmidt hammer index vs. point load index.

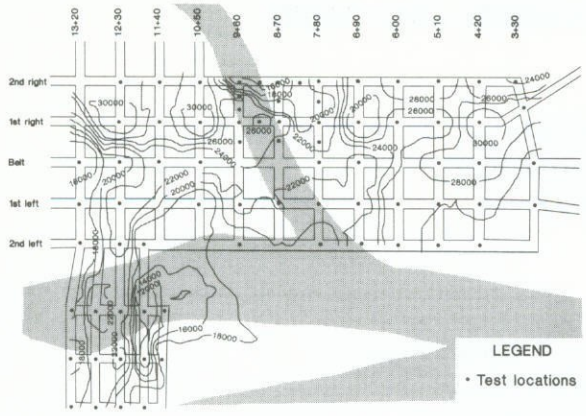

Figure 11 - Roof strength contours identified using the Schmidt hammer.

situ conditions. However, further research is needed to determine which data interpretation procedures are most suitable.

The Schmidt hammer and point load tests are index tests that can be quickly and easily accomplished. Much research has been conducted using these devices, resulting in a proliferation of interpretive equations. The performance of both devices in predicting the compressive strength and Young's modulus of laboratory samples was comparable with previous research. In the field, however, attempts to locate a strong sandstone channel in the roof using the Schmidt hammer were unsuccessful. Further research is warranted to determine whether or not the Schmidt hammer is effective in identifying mine-wide physical property trends.

REFERENCES

1. Haramy, K. Y. Borehole Shear Tester: Equipment and Technique. BuMines IC 8867, 1981, 19 pp.

2. Obert, L. A., and W. I. Duvall. Rock Mechanics and the Design of Structures in Rock. Wiley, 1967, 650 pp.

3. Panek, L. A. Criterion of Failure for Design of Rock Mass Structures as Determined by Borehole Shear Tests. Proc. 4th Cong., ISRM, Montreux, Switzerland, Sept. 2-8, 1979, v. 2, pp. 509-515.

4. Haramy, K. Y., and M. J. DeMarco. Use of the Schmidt Hammer for Rock and Coal Testing. Paper in 26th Symp. on Rock Mech. Rapid City, SD, June 26-28, 1985, pp. 549-555.

5. Aufmuth, R. E. A Systematic Determination of Engineering Criteria for Rock. Bull. Assoc. Eng. Geologists, v. XI, No. 3, 1974, pp. 235-245.

6. Int. Soc. Rock Mechanics. Suggested Methods for Determining Hardness and Abrasiveness of Rocks. Int. J. Rock Mech. Min. Sci., v. 15, 1978, pp. 95-96.

7. Deere, D. U., and R. P. Miller. Engineering Classification and Index Properties for Intact Rock. Air Force Weapons Laboratory Technical Report No. AFWL-TR-65-116. Dec. 1966, 300 pp.

8. Beverly, B. E., D. A. Schoenwolf, and G. S. Brierley. Correlations of Rock Index Values with Engineering Properties and the Classification of Intact Rock. Jan. 1979.

9. Kidybinski, A. Method of Investigations, Estimation and Classification of Roofs in Mines in the United States of America for the Selection of Suitable Mechanized Support for Longwalls. USDI/CMI Joint Research Project, Report No. 3. Katowice, Poland, 1980.

10. Int. Soc. Rock Mech. Suggested Methods for Determining the Point Load Strength Index of Rock Materials. ISRM Committee on Standardization of Laboratory Tests, Doc. No. 1, Oct. 1972, pp. 8-13.

11. Haramy, K. Y., T. A. Morgan, and R. E. DeWaele. A Method for Estimating Western Coal Strengths from Point Load Tests on Irregular Lumps. Proc. 2nd Conf. on Ground Control in Mining, Morgantown, WV, 1982, pp. 123-136.

12. D'Andrea, D. V., R. L. Fischer, and D. E. Fogelson. Prediction of Compressive Strength from Other Rock Properties. BuMines RI 6702, 1965, 23 pp.

13. Broch, E., and J. A. Franklin. The Point-Load Strength Test. Int. J. Rock Mech. Min. Sci., v. 9, 1972, pp. 669-697.

14. Bieniawski, Z. T. Estimating the Strength of Rock Materials. J. S. African Inst. Min. and Metallurgy, Mar. 1974, pp. 312-320.

15. Hassani, F. D., M. J. Scoble, and B. N. Whittaker. Application of the Point Load Index Test to Strength Determination of Rock and Proposals for a New Size Correction Chart. Paper in Proc., 21st U.S. Symposium on Rock Mechanics, Rolla, MO, 1980.

16. Missouri Highway and Transportation Department. Evaluation of the Point Load Test for Rock. Study 79-2, Mar. 1981, 21 pp.

10th INTERNATIONAL CONFERENCE ON GROUND CONTROL IN MINING

SUBSIDENCE PREDICTION IN ILLINOIS COAL BASIN

Ed D. Doney, *Manager*
Kerr-McGee Coal Corporation
Oklahoma City, Oklahoma

and

S. S. Peng, *Chairman and Charles T. Holland Professor*
Y. Luo, *Research Assistant Professor*
Department of Mining Engineering
West Virginia University
Morgantown, West Virginia

ABSTRACT

Based on the subsidence data collected through a comprehensive subsidence monitoring program conducted over two longwall panels in an Illinois coal mine, mathematical models have been proposed for predicting final and dynamic subsidence in the Illinois coal basin.

INTRODUCTION

Until recently, the mathematical and computer models for surface subsidence prediction available in the U.S. have been primarily developed based on the subsidence data collected from and applicable only for longwall mining in the Appalachian coal fields. In order to understand the surface subsidence process in the Illinois coal basin, a comprehensive subsidence monitoring program was conducted over two operating longwall panels in the Galatia mine. The monitoring program resulted in a large amount of subsidence data concerning both the dynamic subsidence process and the final subsidence basin.

Based on the collected data through the subsidence monitoring program and experience with subsidence research in the Appalachian coal field, a number of mathematical models have been proposed and presented in this paper. The capabilities of the proposed mathematical models are:

1. Predicting final subsidence over a mined single longwall panel;
2. Predicting final subsidence over and in the vicinity of the chain pillars between mined longwall panels;
3. Predicting normal dynamic subsidence over an operating longwall panel;
4. Predicting the dynamic subsidence process after stoppage of a longwall face; and
5. Predicting the subsidence initiation and development process in the initial stage of mining a longwall panel.

A number of case demonstrations of the models are also presented in this paper. Comparison between the measured and the predicted subsidences indicates a fairly good agreement.

SUBSIDENCE MONITORING

Surface subsidence process over two longwall panels in Galatia mine of Kerr-McGee Coal Corporation in southern Illinois have been closely monitored during the time period from April 1989 to January 1991. The two panels (Fig. 1) were 7,900 and 7,100 ft long and 670 and 620 ft wide for panel #1 and #2, respectively. Total width of the chain pillars between the two panels was 130 ft. The Herrin #6 coal seam was mined with mining height ranging from 5.6 to 8.1 ft. Both the surface and the coal seam at the monitored site were relatively flat with overburden depth ranging from 350 to 400 ft.

A number of subsidence monument lines were laid over the panels as shown in Fig. 1. The spacing between two adjacent monuments was normally 20 ft. Overburden depth and mining height under each of the monument lines are listed in Table 1. The monuments were surveyed periodically for surface vertical movements as mining progressed. In the most active subsidence period, the monitoring activities were intensified to once per day for those lines of greater interest. The locations of the advancing longwall face and mining heights were also recorded for reference. The subsidence monitoring program has generated a large amount of quality subsidence data which would be very beneficial for better understanding and prediction of the surface subsidence process in the Illinois coal basin.

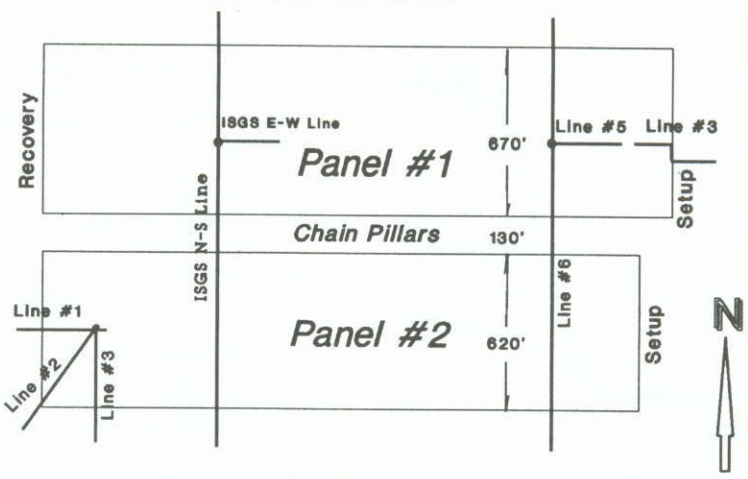

Fig. 1 Panel Layout and Location of Monument Lines

FINAL SUBSIDENCE PREDICTION

Knothe's Method

Experience with subsidence research in the Appalachian coal fields has shown that the Knothe's method (1), one of the influence function methods, can be successfully employed to predict surface final subsidence for U.S. longwall operations. According to the comparison study, by Ingram et al. (2), on a number of subsidence prediction computer models available in the U.S., those models based on the influence function methods appear to generate better prediction. The underlying principle of influence function methods is that the extraction of a tiny elemental area of coal seam will cause surface to subside and final subsidence at a surface point is the summation of the subsidences caused by extractions of the entire mined area element by element. Knothe's method selects the normal probability distribution function for the subsidence distribution function due to the extraction of an elemental area in the coal seam. Final subsidence at a surface point (x,y) can be expressed as:

$$S_f = \frac{S_{max}}{R^2} \iint_A e^{-\pi\left[\frac{u^2+v^2}{R^2}\right]} dA \qquad (1)$$

where: S_{max} - maximum possible subsidence
R - radius of major influence
A - computing area of extraction
dA - elemental area of extraction
u,v - local coordinates with its origin at (x,y).

In Eq. 1, the maximum possible subsidence, S_{max}, is a product of mining height, m, and subsidence factor, a. The computing area of an extraction, A, is determined by indenting, from the edge of the actual extracted area inward, a distance equivalent to the offset of inflection point, d.

Determination of Subsidence Parameters

The accuracy of subsidence prediction is heavily dependent on three parameters to be used in prediction, that is, subsidence factor, a, radius of major influence, R, and offset of inflection point, d. Therefore, the three parameters are called the subsidence parameters. Because of their importance, whenever it is possible, it is recommended that in order to obtain better prediction accuracy the subsidence parameters should be determined from the collected subsidence data for those operating mines where some subsidence monitoring has been conducted. In the process of determining the subsidence parameters for Galatia mine, program SUBDED in CISPM program package, a subsidence prediction model developed by the junior authors (3 and 4) was used. This program performs a nonlinear regression of Eq. 1 on a measured final subsidence profile. It outputs a set of subsidence parameters which define a theoretical subsidence profile having the best fit to the measured profile.

An example of the application of program SUBDED on the final subsidence profile along ISGS N-S line over panel #1 is shown in Fig. 2. The subsidence parameters determined for this line are 0.631, 124 ft and 94 ft for a, R and d, respectively. The regression results in a correlation coefficient r=0.999. Fig. 2 shows that the calculated final subsidence profile agrees very well with the measured one. The subsidence parameters for the other subsidence monument lines are listed in Table 1. It should be noted that for those full profile lines, line #6 and ISGS N-S line over panels #1 and

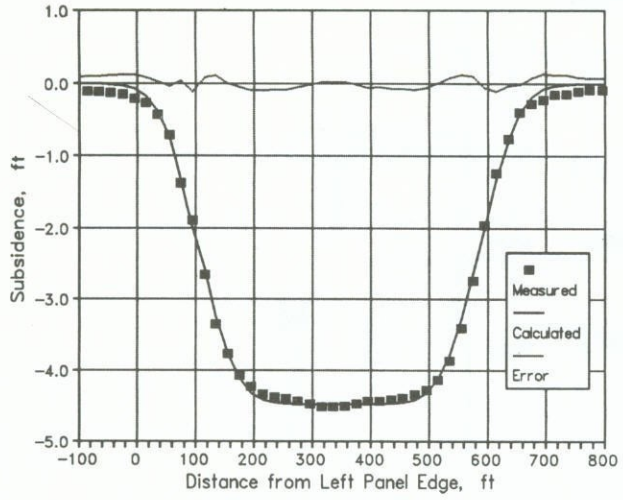

Fig. 2 Comparison of Measured Subsidence Profile vs. Theoretical Subsidence Profile Defined by the Optimum Subsidence Parameters for ISGS N-S Line over Panel #1

Final Subsidence over Chain Pillars

As two or more panels are mined, the chain pillars between the mined panels will be subject to more load and be compressed, and consequently induce additional subsidence on surface which can not be predicted by the existing methods developed for single panel mining. A method has been developed by the junior authors (5) and updated (6) for predicting subsidence over chain pillars between mined longwall panels. In developing that method, it was assumed that the total surface subsidence is a combination of the subsidence induced by mining a single longwall panel and that by roof-to-floor convergence of the chain pillars. Subsidence due to mining of a single panel can be predicted, in fairly good accuracy, by the existing methods. With some modifications on the existing methods, subsidence induced by the convergence of chain pillars can also be predicted. The prediction accuracy depends on the determination of the maximum possible subsidence induced by chain pillar convergence, ΔS_{max}, and the selection of subsidence distribution function, f(x).

Table 1 Subsidence Parameters for Galatia Mine

Panel	Line	h (ft)	W (ft)	m (ft)	a	R (ft)	R h/R	d_1 (ft)	d_1/h	d_2 (ft)	d_2/h	d (ft)	d/h
2nd	#6	356	620	6.95	0.618	140	2.543	97	0.272	43	0.121	70	0.197
2nd	#3	362	620	6.17	0.708	119	3.042					95	0.262
2nd	#1	365		6.17	0.677	132	2.765					84	0.230
1st	#6	376	670	6.17	0.710	118	3.186	87	0.231	87	0.231	87	0.231
2nd	ISGS	384	620	6.67	0.628	115	3.339	102	0.266	70	0.182	86	0.224
1st	#3	384		6.29	0.697	139	2.763					70	0.182
1st	ISGS	396	670	7.10	0.631	124	3.194	105	0.265	82	0.207	94	0.236
Average		375		6.50	0.667	127	2.976	98	0.259	71	0.185	84	0.223
Std Deviation		13		0.37	0.037	10	0.269	7	0.016	17	0.041	9	0.024

Footnote: h - overburden depth; W - panel width; m - mining height;
a - subsidence factor; R - radius of major influence;
d_1 - offset of inflection point on tailentry side;
d_2 - offset of inflection point on headentry side;
d - average offset of inflection point, $d = (d_1+d_2)/2$

#2, the offset of inflection point on the panel tailentry side, d_1, is generally different from that on the headentry side, d_2. The average values for the subsidence parameters are 0.667, 0.336h and 0.223h (h represents overburden depth in ft) for subsidence factor, radius of major influence, and offset of inflection point, respectively.

The major factors which affect the magnitude of the subsidence over chain pillars have been identified to be the overburden depth, h, panel width, W_m, total width of the chain pillars, W_p, and mining height, m. The relationship among ΔS_{max} and those identified factors has been determined based on the collected subsidence data to be:

$$\frac{\Delta S_{max}}{m} = -0.04905+4.4254\times10^{-5}\frac{h}{1-\rho} \qquad (2)$$

In Eq. 2, ρ is the recovery ratio of the longwall operation, which is defined by:

$$\rho = \frac{W_m}{W_m + W_p} \qquad (3)$$

Subsidence induced by the convergence of chain pillars at any surface point can be calculated by Eq. 4. The subsidence distribution function, f(x), is assumed to take the form proposed by Knothe (1). The setup of the coordinate system for calculating S'(x) and the computation method have been introduced elsewhere (5).

$$S'(x) = \Delta S_{max}\, f(x) \qquad (4)$$

The application of this method to predict final subsidence over the chain pillar area along monument line #6 is shown in Fig. 3. Using Eq. 2, ΔS_{max} was determined to be 0.31 ft. The average subsidence parameters in Table 1 were used in the prediction. It is apparent that the prediction without considering the subsidence induced by chain pillar convergence (SCP shown in Fig. 3) underestimates the final subsidence in the area above the chain pillars about 0.35 ft. The predicted subsidence profile with SCP agrees fairly well with the measured one. As overburden depth and panel width become larger, and as the total width of chain pillars becomes smaller, the prediction error without SCP will reach a very significant level as compared to the subsidence measured at the panel center.

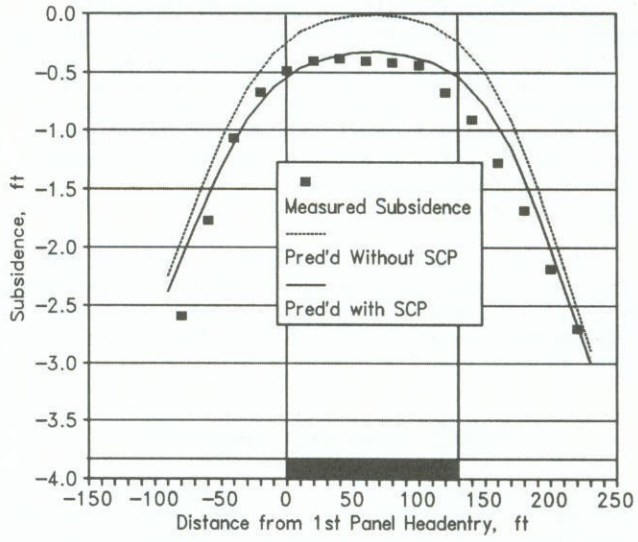

Fig. 3 Measured and Predicted Subsidence over Chain Pillars Between the Two Panels Along Line #6
SCP - Subsidence Induced by Chain Pillar Convergence

Case Demonstration

Figure 4 shows the measured and predicted subsidence along ISGS N-S line over the two longwall panels in two stages, that is, after panel #1 was mined and after panel #2 was mined, respectively. Again, those average subsidence parameters in Table 1 were used in the predictions, and subsidence induced by chain pillars convergence had been taken into consideration.

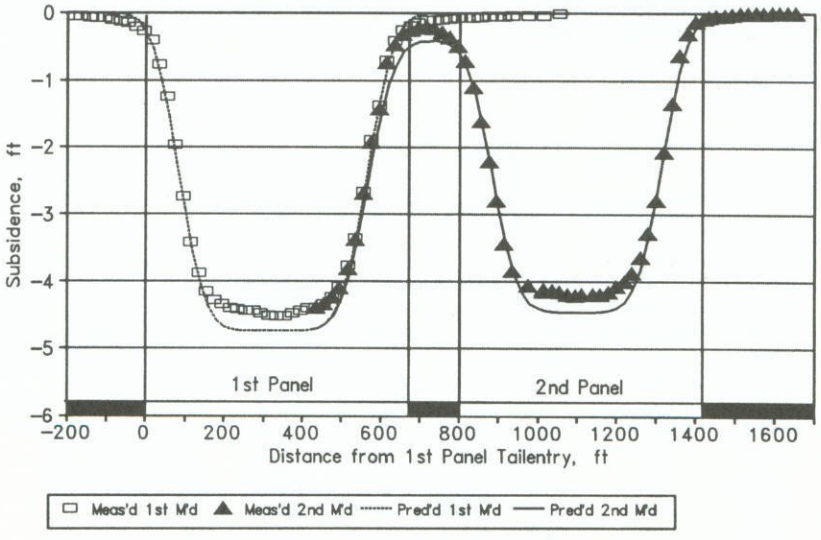

Fig. 4 Measured vs. Predicted Final Subsidence Along ISGS N-S Line over Multiple Panels

For the extraction of panel #1 only, the predicted subsidences agree with the measured ones along most portion of the cross-section but in the center portion where the prediction results in an overestimation of about 0.25 ft. The reason for this discrepancy is that the average subsidence factor used in the prediction, 0.667, is higher than the actual subsidence factor determined for this line, 0.631 (Table 1).

For the case after panel #2 was mined, the final subsidence profile again shows a close agreement with the measured profile except for those portion over chain pillars and in the center of panel #2.

DYNAMIC SUBSIDENCE PREDICTION

The ultimate goal of surface subsidence studies is to use the acquired knowledge of surface subsidence in structural and environmental protection against subsidence damage and disturbance. For this purpose, accurate prediction of dynamic subsidence plays a much more important role than that of final subsidence. Based on the collected data in this subsidence monitoring program and the subsidence research results in Appalachian coal fields, the following prediction methods have been established for Galatia mine for predicting: (1) normal dynamic subsidence, (2) subsidence process after face stop, and (3) subsidence initiation and development process over panel setup area.

Normal Dynamic Subsidence

Normal dynamic subsidence refers to the dynamic subsidence process in the surface area affected by an operating longwall face with relatively constant advancing rate but excluding an area near the panel setup entry. The main feature of a normal dynamic subsidence process is that the distribution of its subsidence velocity assumes a shape of normal probability distribution function (4 and 7). The peak subsidence velocity is ℓ distance behind the advancing face, and the detectable amount of subsidence occurs an ℓ_1 distance in front of the face. Subsidence at a surface point at time t is the integration of the subsidence velocity distribution function over the time period starting from movement initiation to the time of interest.

When a constant face advance rate is maintained, normal dynamic subsidence at a surface point (x',y') in a dynamic coordinate system (4 and 7), in which x'-axis is parallel to mining direction and its origin is placed over the advancing longwall face, can be expressed as:

$$S_d = \sqrt{\frac{\pi}{2}} \frac{S_f}{\ell+\ell_1} \int_x^{\ell} e^{-2\left[\frac{x+\ell}{\ell+\ell_1}\right]^2} dx' + \frac{1}{2} S_f \quad (5)$$

In Eq. 5, S_f is the final subsidence at that surface point which can be calculated by Eq. 1.

Determination of Parameters ℓ and ℓ_1

As indicated in Eq. 5, ℓ and ℓ_1 are two important parameters for successful prediction of dynamic subsidence for an operating longwall panel. They are dependent on overburden depth, face advance rate, and the overall mechanical property of the overburden strata. The ℓ and ℓ_1 determined from the subsidence data are listed in Table 2. By comparison, it is found that in average the values for ℓ and ℓ_1 listed in Table 2 are 0.753 and 1.063 times of those found in the Appalachian coal field (4), respectively. Based on the limited dynamic subsidence data in Illinois coal basin (Note: lack of data with largely varying overburden depth and

Table 2 Dynamic Subsidence Parameters for Galatia Mine

Panel	Line	h	v	ℓ_1		ℓ	
		(ft)	(ft/d)	ILL*	APP**	ILL*	APP**
1st	ISGS N-S	396	22.8	25.0	23.7	115.0	139.5
2nd	ISGS N-S	384	36.0	20.0	18.1	117.0	170.0
1st	#6	376	35.8	20.0	17.6	128.0	166.0
2nd	#6	356	27.0	20.0	18.7	109.0	136.5
1st	ISGS E-W	396	12.7	30.0	31.8	88.0	104.1
1st	#3	384	14.6	16.0	28.4	96.0	108.3
2nd	#1	365	27.0	21.0	19.4	91.0	139.9
2nd	#1	365	29.0	23.0	18.7	104.0	145.0
2nd	#1	365	40.0	17.5	16.0	108.5	170.3
2nd	#3	362	30.0	22.0	18.2	104.1	146.3

* ILL - Measured from Galatia Mine
** APP - Calculated for Appalachian Coal Field

face advance rate), the formulas for calculating ℓ and ℓ_1 for the Illinois coal basin are tentatively established for the time being as:

$$\begin{cases} \ell = (0.223+0.01103\sqrt{v}\,)h \\ \ell_1 = \dfrac{0.113h}{1+0.1825\sqrt{v}} \end{cases} \qquad (6)$$

where v is the average face advance rate in ft/day while the unit for h, ℓ and ℓ_1 is ft.

Subsidence Process After Face Stop

One of the shortcomings of the method proposed above for predicting normal dynamic subsidence (Eq. 5) is its inability to predict the dynamic subsidence after face stop. After face stop due to either a vacation or panel completion, a surface point experiences a process from normal dynamic subsidence progressing to final subsidence. One example of this process along line #1 over panel #2 is shown in Fig. 5. When the face stopped on Nov. 27, the shape of the measured subsidence profile on that day was still very similar to the shape of the normal dynamic subsidence profile on Nov. 26. Thereafter, the profile became steeper and steeper as time went by and the amount of total incremental subsidence is different along the profile. The difference between dynamic subsidence profile when the face stopped on Nov. 27 and the final subsidence is as much as 0.85 ft.

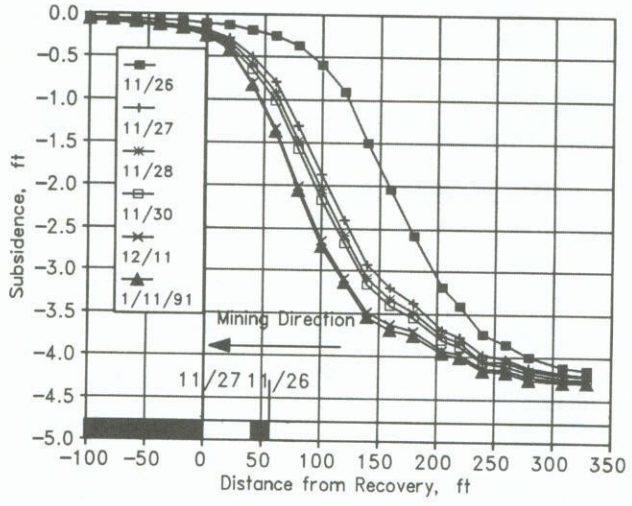

Fig. 5 Measured Dynamic Subsidence Profiles Along Line #1 over Panel #2 After Face Stop

A method has been introduced by the junior authors (6) for predicting dynamic subsidence after face stop. In the development of the method, it was assumed that subsidence velocity at a surface point at any given time t after face stop is proportional to the amount to be subsided thereafter, or expressed in a differential equation as:

$$V(t) = \frac{dS}{dt} = c(S_f - S) \qquad (7)$$

where: S_f - final subsidence at the surface point
t - elapsed time after face stops, in day
S - subsidence at time t
c - coefficient

The equation for subsidence at time t after face stop can be derived by solving Eq. 7 with initial condition $S_{t=0} = S_d$ as:

$$S = S_f - (S_f - S_d)e^{-ct} \qquad (8)$$

In Eq. 8, S_f and S_d can be determined by Eqs. 1 and 5, respectively. Coefficient c is believed to be mainly affected by overburden depth, h, and assumes the following relationship:

$$c = \frac{D}{h^E} \qquad (9)$$

Where D and E are constants. Based on the limited subsidence data collected after face stop so far, D and E in Eq. 9 are determined to be $2\text{x}10^5$ and 2.3, respectively.

Subsidence Initiation and Development Process

The subsidence initiation and development process refers to the surface movement process in the area over and near the panel setup entry in the initial stage of mining a longwall panel. Due to bridging effect of the overburden strata, surface movement during the subsidence initiation process is very small until the longwall face has reached a critical distance (initiation distance) away from the panel setup entry. At that time, a sudden movement will follow. Fig. 6 shows the subsidence initiation and development process along line #3 over panel #1. On May 18 (the face was 186 ft away from the setup entry), surface subsidence was still very small compared with the maximum measured subsidence of about 4.5 ft. Subsequent survey on May 23 (the face was 304 ft away) indicated a large amount of subsidence had been accumulated. A better example of subsidence initiation and development process can be found in reference 6 where subsidence monitoring was performed in daily basis during the initiation process.

Based on the data collected in the Appalachian coal field and Illinois coal basin, the initiation distance, L_1, is empirically determined as:

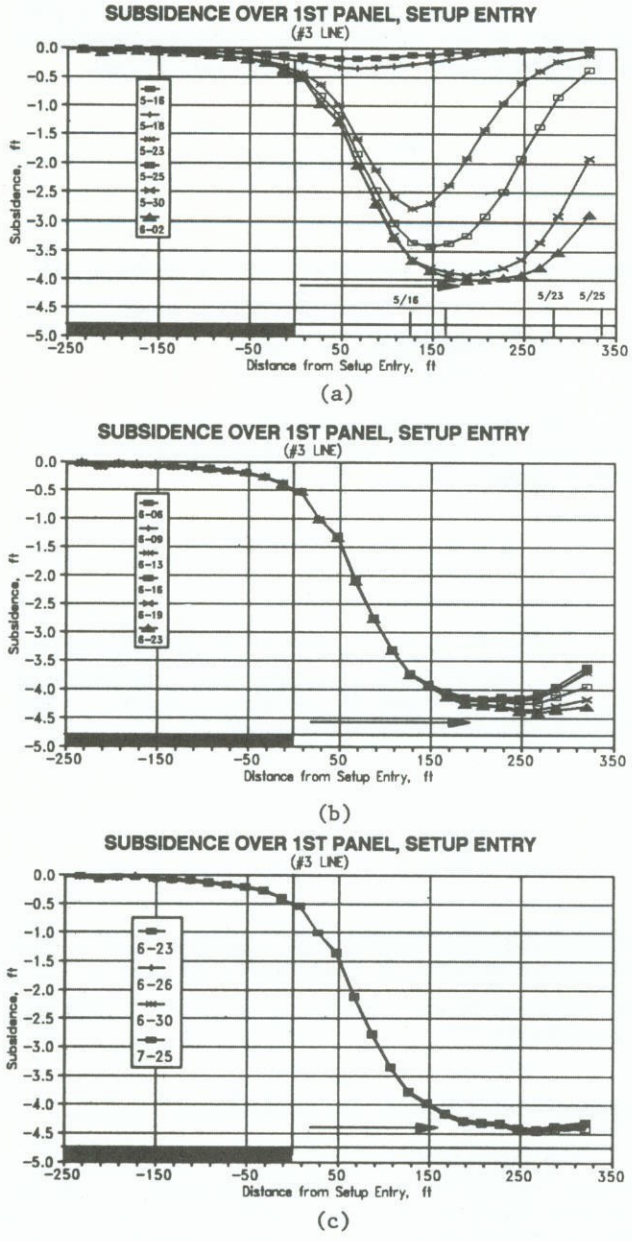

Fig. 6 Measured Dynamic Subsidence Profiles Along Line #3 over Panel #1 in Subsidence Initiation and Development Process

$$L_i = 32.98 + 12.43\sqrt{h} \qquad (10)$$

A mathematical model (6) has been developed for predicting dynamic subsidence after an advancing longwall face has reached and exceeded the initiation distance away from the setup entry. It is assumed that subsidence velocity at a surface point at time t is proportional to the difference between potential subsidence, S_p, and actual subsidence, S, at that point at time t. The mathematical expression for subsidence at time t after the face has reached the initiation distance is:

$$S = S_p - (S_p - S_o)e^{-ct} \qquad (11)$$

The potential subsidence, S_p, is the amount of subsidence at time t assuming that the subsidence process is not affected by the bridging effect of the overburden strata, or simply, it can be calculated in the same way as normal dynamic subsidence by Eq. 5. Time t is the elapsed time after the face has reached the initiation distance in days. S_o is the amount of subsidence at the point of interest when the face is at the initiation distance (t=0). However, since S_o is very small compared with maximum subsidence in the panel center, it can be neglected in the computation for simplicity.

Case Demonstrations

Three cases are presented here to demonstrate the models developed for predicting normal dynamic subsidence, subsidence after face stop, and subsidence initiation and development process, respectively.

Case 1: Figure 7 shows the predicted normal dynamic subsidence along line #1 over panel #2 on three days that is, Nov. 21, 25 and 27. The face locations on those three days are shown in the figure and the face stopped on Nov. 27 due to panel completion. Since the longwall face advanced continuously between the three days, the surface subsidence process can be considered as a normal dynamic subsidence process. The measured dynamic subsidences are plotted in symbols. Using Eq. 5 and the parameters determined by Eq. 6, the dynamic subsidence on those three days are predicted and plotted in curves in the figure. The prediction accuracy is satisfactory.

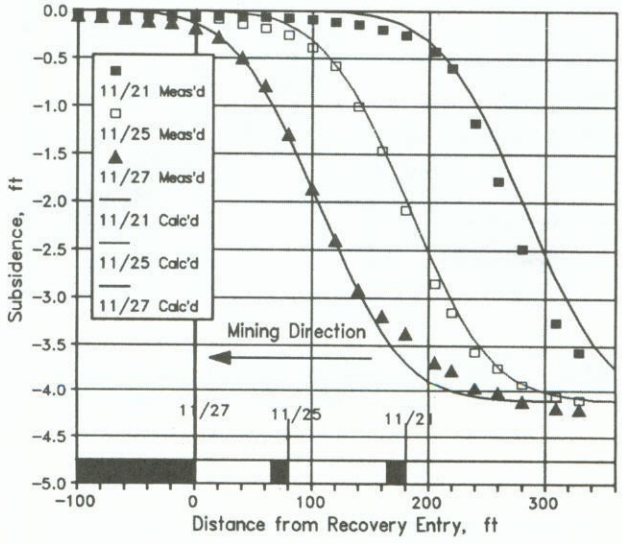

Fig. 7 Measured vs. Predicted Normal Dynamic Subsidence Along Line #1 over Panel #2

Case 2: Figure 8 depicts the predicted dynamic subsidences after face stop verse the measured ones along line #1 over panel #2, which was located over and near the panel recovery entry. Equations 8 and 9 are used to predict the dynamic subsidence process after face stop. As shown in Fig. 5, the longwall face stopped on Nov. 27 due to panel completion. The measured subsidence on that day can be considered as S_d in Eq. 8. The last survey along this line was performed on Jan. 11, 1991 (45 days after face stop), and the measured subsidence was used as the final subsidence, S_f in the calculation. Three measurements are compared with the predictions. Again, the agreement is very satisfactory.

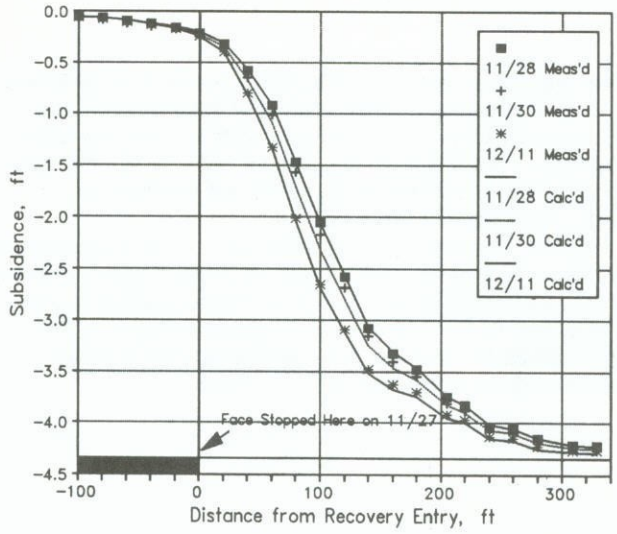

Fig. 8 Measured vs. Calculated Dynamic Subsidence Along Line #1 over Panel #2 After Face Stop

Case 3: The measured and predicted dynamic subsidences along line #3 over panel #1, which was located over and near the panel setup entry area (Fig. 1), in the initial stage of mining that panel are presented in Fig. 9. Predictions are made for three days, May 23, 25 and 30, with the corresponding face locations at 304, 355 and 415 ft away from the panel setup entry, respectively. Eqs. 10 and 11 are used and S_o was neglected in the computations. The predictions show a fairly good agreement with the measured data.

CONCLUSIONS

A large amount of quality subsidence data collected over two longwall panels in Galatia mine has provided us an excellent opportunity to acquire a better understanding of the nature of surface subsidence process in the Illinois coal basin. Based on the collected data in this mine and the experience with subsidence research in the Appalachian coal field, mathematical models have been developed for predicting final and dynamic subsidence for the Illinois coal basin. The models have demonstrated a very promising prediction accuracy.

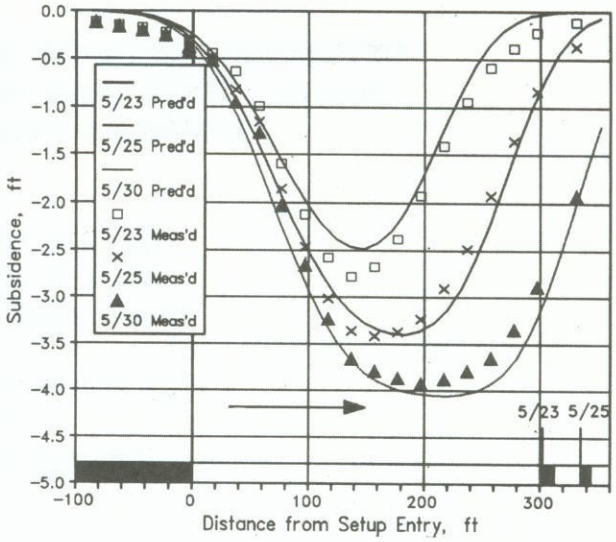

Fig. 9 Measured vs. Predicted Subsidence Along Line #3 over Panel #1 in the Subsidence Initiation Process

REFERENCES

1. Knothe, S., 1957, "Observations of Surface Movements Under Influence of Mining and Their Theoretical Interpretation," *Proc. European Cong. Ground Movement*, Leeds, pp. 210-218.

2. Ingram, D.K., M.A. Trevits and J.S. Walker, 1989, "A Comparison of Subsidence Prediction Models for Longwall and Room-and-Pillar Conditions," *Proc. American Mining Cong. Coal Convention*, Pittsburgh, PA, pp. 545-561.

3. Peng, S.S.and Y. Luo, 1989, *CISPM Owner's Manual*, Dept. Mining Engineering, West Virginia University, Morgantown, WV, 63 pp.

4. Luo, Y., 1989, *An Integrated Computer Model for Predicting Surface Subsidence Due to Underground Coal Mining - CISPM*, Ph.D. Dissertation, West Virginia University, Morgantown, WV, 168 pp.

5. Luo, Y. and S.S. Peng, 1990, "A Mathematical Model for Predicting Surface Subsidence over Chain Pillars Between Mined-out Longwall Panels," *Proc. Mine Subsidence - Prediction and Control*, Edited by C.D. Elifrits, Pittsburgh, PA, pp. 247-257.

6. Luo, Y. and S.S. Peng, 1991, *Some New Findings from Surface Subsidence Monitoring over Longwall Panels*, Paper Presented at SME-AIME Annual Meeting, Denver, CO, Pre-print No. 91-150, 5 pp.

7. Peng, S.S. and Y. Luo, 1988, "Monitoring and Prediction of Surface Dynamic Subsidence Due to Longwall Coal Mining," *Proc. 5th International (FIG) Symposium on Deformation Measurements*, Fredericton, N.B., Canada, pp. 420-429.

10th INTERNATIONAL CONFERENCE ON GROUND CONTROL IN MINING

DETERMINATION OF THE STOPLINE SUBSIDENCE PROFILE OF PHALEN 2 WEST PANEL FROM WITHIN A NEAR HORIZONTAL BOREHOLE OVER THE PANEL STOPLINE

William D. Gallant, *Senior Technologist*
David J. Forrester, *Group Leader*
Dan A. Payne, *Strata Mechanics Engineer*

Cape Breton Coal Research Laboratory
CANMET
Sydney, Nova Scotia, CANADA

ABSTRACT

This paper presents the results of a joint cooperative research project between the CANMET Cape Breton Coal Research Laboratory and the Cape Breton Development Corporation to observe the subsidence profile over the stopline of 2 West panel, Phalen Mine. A novel technique was designed and implemented to determine vertical displacements of the overlying strata from within a near horizontal borehole drilled over the 2 West panel.

Restrictions on data collection techniques due to the submarine nature of the coalfield are discussed. Development and implementation of the borehole technique using a piezometer and inclinometer is described. Performance of the instruments and profiles obtained by them are presented and compared. Recommendations for design improvements are made to improve the efficiency of the technique.

INTRODUCTION

The Cape Breton Coal Research Laboratory (CBCRL) of CANMET was established in 1982 to carry out safety related research in underground coal mining in Canada. A joint collaborative research program was established between CBCRL and the Cape Breton Development Corporation (CBDC) and is now entering its tenth year. Strata mechanics or ground control continues to be a prime component in this program.

CBDC operates three underground coal mines in the Sydney Coalfield. All are submarine, with slope entries on the cliffs, the workings following the seams under the ocean. Phalen Colliery produces approximately 1.5 million tpa from two single entry retreat walls in the Phalen Seam. It lies approximately 140 m (500 ft) below the Lingan Colliery workings in the Harbour Seam. Thus, the resultant ground movement above the Phalen longwalls will not only affect the seabed but also the intermediate Lingan workings.

Although the basic principles of longwall interaction are understood for other coalfields (e.g. in Europe) and are thought to be applicable to Cape Breton, little local quantitative information is available. Using data extrapolated from elsewhere, the Phalen walls were designed so that no interaction effects would occur on the active Lingan roadways.

One area of current strata mechanics research is concentrating on two aspects: 1) measurement of deformation in the Lingan slopes closest to the Phalen walls to verify the latter assumption - this has been the case for both 1 West and 1 East panels and 2) direct monitoring of the full development of effects over Phalen 2 West wall.

This paper describes a novel application of two measurement techniques from other related fields which have been pioneered to measure vertical deformation over Phalen 2 West wall as it retreats over its final 90 m to the stopline adjacent to the Lingan slopes 140 m above. The general concept is shown schematically in three dimensions in Figure 1.

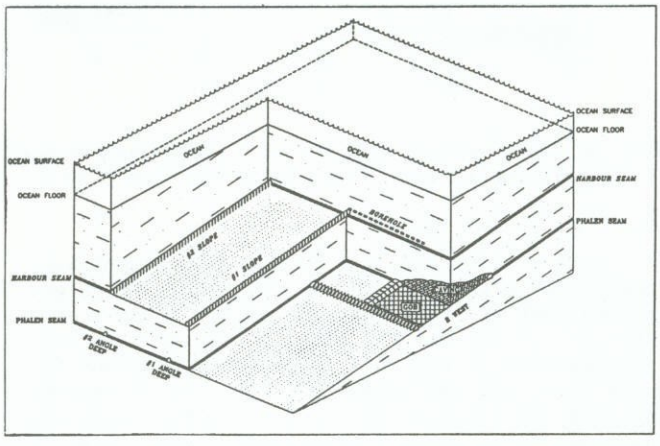

Figure 1 - Schematic 3-D representation of 2 West stopline borehole.

A 4.5" (114 mm) horizontal borehole was drilled over the roof of the Harbour Seam from #1 Slope into the roof above an adjacent coal pillar. The 198 m long borehole had a special casing cemented in place and is water filled. A precise vibrating wire piezometer has been used to vertically profile the hole from pressure head/distance data. This has been repeated successively as the wall retreats below the hole, hence enabling vertical deformation or subsidence profiles to be derived. Further, a horizontal borehole inclinometer is

being used 'in parallel' to observe the same vertical deformation. The study has not only produced quantitative data to define the interaction effects through time, but has also enabled the two measurement techniques to be evaluated. The results will be assessed and mine planning procedures modified as appropriate. Suitable sites for this work are limited, but it is hoped to proceed with further studies over the next few years.

Objectives

The prime objectives were to obtain a reliable set of quantitative data defining the strata movement at the Harbour horizon caused by the underlying Phalen 2 West wall. The location and concept are shown schematically in Figure 2. This data would ideally include: vertical displacement, horizontal displacement, tilt, and stresses/loadings.

It would enable the following to be derived:

- subsidence profile (development through time and residual)
- strains, in magnitude and direction
- angle of draw
- understanding/mechanisms of strata response
- stress redistribution

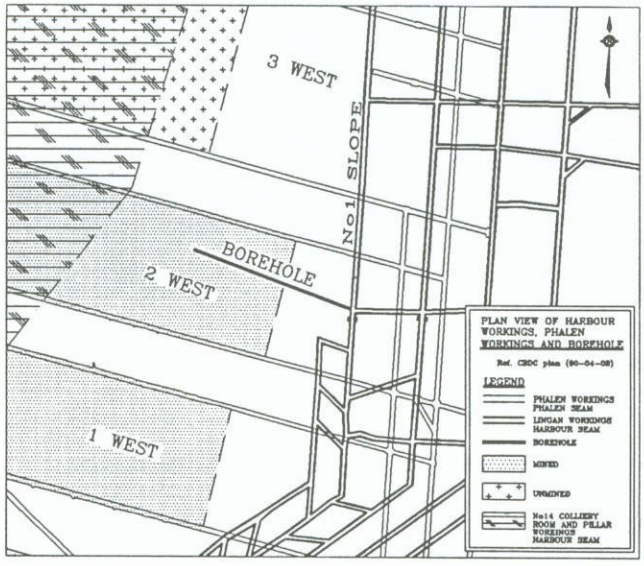

Figure 2 - Location plan of 2 West stopline borehole.

Site

The detailed location in plan is shown in Figure 2 which shows the superimposed workings in both seams at the site. Unfortunately, this is complicated due to the two sets of main slopes or deeps and connecting roadways. The following points are of particular interest:

- Lingan slopes
- edge of old #14 Colliery workings in the Harbour Seam
- intersection of Lingan #1 Slope and 1 East top level (drill site)
- Phalen 2 West panel
- projected stopline of 2 West wall
- proposed alignment of the instrumentation borehole

A cross-section along the borehole alignment is shown in Figure 3 indicating interburden geology comprising typical coal measures: coal, sandstones, siltstones, mudstones, etc.

The drill site is at the intersection of #1 Slope - the main return airway and former 1 East top level in Lingan. This is an older part of the mine and is rarely used. However, the area was cleared and rehabilitated for this project. The need for electrical power for drilling in the main return, where CH_4 content can be up to 1%, dictated a narrow time window for drilling - the three-week annual summer vacation, July 22 to August 11, 1990.

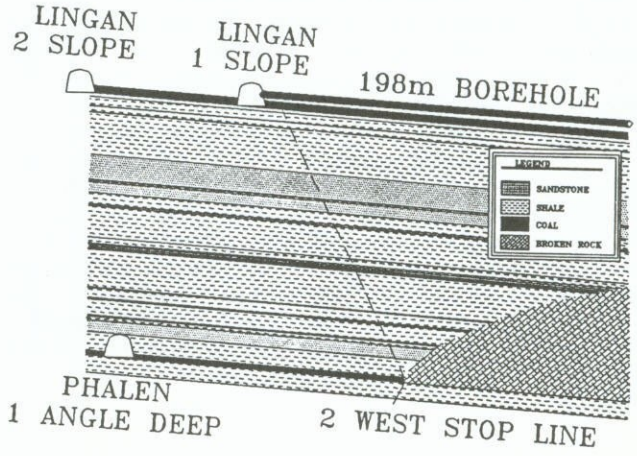

Figure 3 - Cross-section through 2 West stopline borehole.

Borehole

The borehole dimensions are:

- diameter approximately 4.5" (114 mm)
- length up to 650 ft (198 m)
- distance from end of borehole to #14 Colliery workings approximately 300 ft (100 m)
- 1% to 2% descending grade
- starting in immediate roof strata of Harbour Seam at #1 Slope/1 East top level intersection

The casing is steel (ABS plastic was discounted as it may not have been robust enough during installation). This is 3" (0.075 m) square cross-section, 1/4" (0.006 m) wall thickness in 10 ft (3.3 m) lengths and with flush connections. It was grouted into the hole, see Figure 4 for the general arrangement, in cross-section.

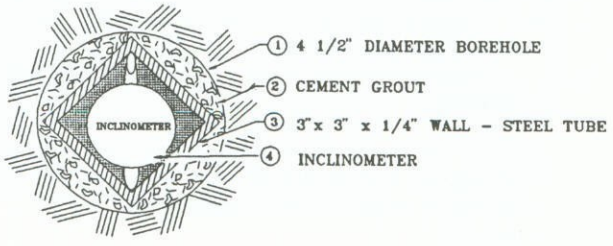

Figure 4 - Cross-section general arrangement of borehole.

Drilling

The drill site is in the main return with normal general body methane readings of 0.5-0.6%. To avoid any dangerous conditions, two precautions were adopted:

- automatic electricity cut-off (interlock BM1 methane monitor and electrical supply)
- schedule operations for summer vacation period, when methane will be much reduced

The interpretation of inclinometer data requires initial readings from as smooth and as straight a hole as possible. That is, this allows easier installation of the casing and a more stable base for initial readings. Therefore, an approximately 4.5" (114 mm) diameter hole was used, positioned in the rock strata immediately above the Harbour Seam. This was cored at 2 3/8" (60 mm) diameter and then reamed to 4.5" (114 mm). As the hole is directed into a barrier pillar against old and possibly flooded workings, the precaution of drilling through a 'stuffing box' was taken. This allowed for initial diversion of any possible sudden water/gas flows; however, none were encountered. That is, the equipment and method was the same as that currently being used further inbye at Lingan for sandstone/gas tests. The use of coring not only provided a more stable hole, but also made available a detailed log and the core itself, for further analysis as required.

INSTRUMENTATION

Inclinometer

The first instrumentation system is the Sinco "horizontal digitilt" inclinometer sensor. The general arrangement is shown schematically in Figure 5. A photograph of the site is shown in Figure 6. The procedure for use of the instrument is as follows:

- a series of measurements of inclination of the borehole are made every metre along the hole. From these, a borehole profile is derived. Following initial calibration runs, a series of sets of readings were made throughout the period of mining induced movement.
- the data obtained enabled calculations to be made of the profile of the borehole on each occasion. In this way, by comparing successive profiles the relative vertical displacements along the hole can be determined.
- further calculation will be done to derive the magnitudes of tensile and compressive strains.
- the readings are taken as follows:
  - . the inclinometer is positioned and moved through the casing using a stainless steel wire around a pulley wheel at the end of the hole.
  - . the inclinometer control cable is graduated for precise positioning.
  - . instrument tilt is observed every metre.
  - . after one full set of measurements, the instrument is withdrawn and turned through 180 degrees and the whole set of measurements repeated (for error reduction).

It is considered that this procedure has yielded the reliable borehole profiles and mining induced displacement profiles.

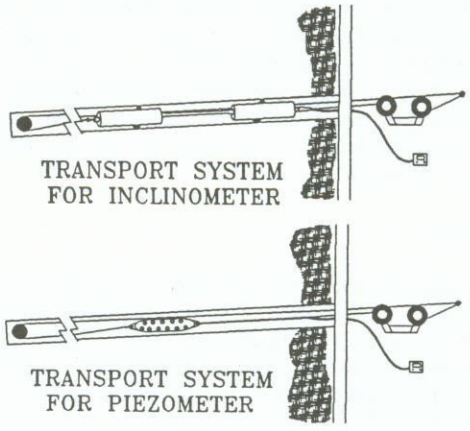

Figure 5 - General arrangement for borehole measurements.

Figure 6 - Photograph of borehole site.

Vibrating Wire Piezometer

The second instrument chosen is capable of measuring relative vertical displacement in the borehole. This is a vibrating wire piezometer (VWP) which measures water pressure to the accuracy of +/-1" (25 mm) vertical position. The instrument used is the Sinco Vibrating Wire Piezometer. Thus, in a water-filled borehole the relative vertical position of any part of the borehole relative to the collar can be determined. When measured on successive dates during the undermining of the borehole, the magnitude and extent of the mining induced subsidence was calculated.

This technique has the advantage over the inclinometer method of giving direct/absolute measurement rather than the indirect adding of successive readings. That is, the VWP reading furthest from the collar would incur an error from a single reading [+/-1" (25 mm)] rather than the cumulative error of maybe 200 readings from the inclinometer [+/-5" (0.130 m)]. However, to the best of our knowledge, neither has been used previously in a near horizontal borehole in an underground coal mine. Also, despite the precautionary use of silicon-sealed joints in the steel casing and a declining gradient, it has at times proved difficult to maintain water in the hole during mining induced movement.

The decision to proceed with both instruments ensured an ongoing cross-check of data and also comparison of the practicality, accuracy and suitability of the two techniques.

Two precautions, in particular, have been taken during measurement: firstly, the use of hand held methanometers at the borehole collar to ensure the detection of any emissions, and secondly, keeping the piezometer head submerged in water, when not in use, to prevent air-induced anomalies.

The procedure for use of the VWP instrument is as follows:

- a series of measurements of water pressure in the borehole are made every metre in from the collar. From these the head of water and hence relative vertical displacement of each point is derived. Following initial calibration runs, a series of sets of readings were made throughout the period of mining induced movement.
- the data obtained enabled calculations to be made of the profile of the borehole on each occasion. These will be compared to the equivalent results of the inclinometer readings.
- the readings are taken as follows:

  . the VWP is positioned and moved through the casing using stainless steel wire around a pulley wheel at the blind-end of the hole.
  . the VWP control cable is graduated for precise positioning.
  . water pressure readings, plus distance from the collar, are recorded at many points.

Casing Alignment

The somewhat novel use of square steel casing instead of round plastic has permitted operation of both the inclinometer and piezometer using a stainless steel haulage cable and return pulley in the blind-end of the hole. However, for either casing some kind of check on the actual alignment as installed is required to enable the appropriate arithmetic calculations of relative vertical displacement to be made.

A spiralmeter was used for this purpose. This was rented for use after installation. The instrument used was the Sinco Spiral Sensor. This will simply measure the casing twist along its length. The instrument is interchangeable with the inclinometer in the context of the readout instrumentation and haulage arrangements.

RESULTS

At the time of writing, readings are still being taken. Thus, the results presented below are preliminary, full analysis and appropriate corrections, checks and balances still have to be applied.

Profiles from Both Instruments

Figure 7 presents typical profiles, obtained at the time 2 West wall production ceased on March 19, 1991, using both instruments. This indicates the close similarity of both profiles. Indivdual profile characteristics are discussed below.

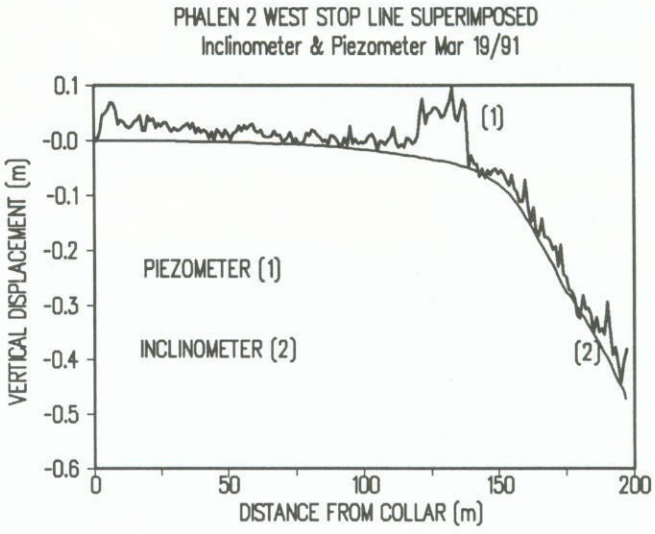

Figure 7 - Comparison of subsidence profiles for both inclinometer and piezometer, March 19, 1991.

General Profiles

Figure 8 shows the development of mining subsidence in the borehole using the inclinometer. The general characteristics, also shown by the VWP results, are:

- onset of movement clearly indicated between January 24 and February 7 (when face was approximately 30 m from end of hole).
- an incomplete subsidence profile has developed over time similar to the expected, classic form of an 'S' curve.
- purely time related movement is shown developing after the end of production on March 19, 1991. The final residual profile should become clear over time.
- angles of draw for both the 'travelling profile' and the final residual profile will be clearly shown.
- the point of development of maximum subsidence may not be detected because the planning restriction on borehole length prevented its detection (the 198 m was dictated by a 100 m solid barrier to the old workings).

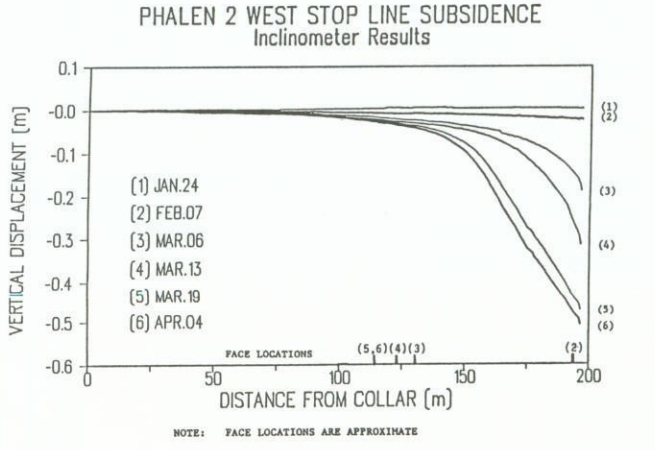

Figure 8 - Development of subsidence profile over 2 West - inclinometer results.

Inclinometer Profile

Derived profiles are smooth and consistent, see Figure 8. This is a function of the cumulative nature of the 197 consecutive dependent readings. The estimated error thus increases from ±65 mm at 100 m to ±130 mm at 198 m.

Piezometer Profiles

Derived profiles are 'jagged', see Figure 7, again a function of the independent value of each of the 197 measurements. There is no cumulative error, presumably the 'jagged' nature approximately indicates the width of the error band.

The steps at lengths 120 m (up) and 140 m (down) were a puzzle. However, they correspond to suspected breaks in the casing and associated outflows totalling approximately 2 gal/min. The water outflow is thought to create dynamic events with associated localised pressure changes. Further study is being carried out.

DISCUSSION

The principal experiences or 'lessons learned' to date are summarized as follows:

Drilling/Installation: the hole was cored at 'N' size 2 3/8" (60 mm) diameter and successfully reamed to 'H' size 4.5" (114 mm) diameter. Rod stabilisers were tried but rejected as ineffective. Casing was installed surprisingly well. Grouting took longer than expected. Novel 'fishing' techniques were developed to recover lost guide tubes.

Piezometer: subject to the final detailed analysis, the piezometer is preferred due to: its simplicity; less labour intensive in installation and observation; and a smaller hole with ungrooved circular casing would suffice. This implies it is the more cost effective (lower capital, installation and operating and analytical effort). However, the implied risk of ineffectiveness is high, e.g. casing breaks leading to pressure anomalies and even of total water loss. Accuracy is approximately ±50 mm.

Inclinometer: it worked very successfully but requires a larger hole with special casing (for wheel locators). However, a four-man team was needed for measurement and there is a significant risk of loss of instrument due to wedging in a deformed section of the hole due to mining induced movement. Accuracy is length dependent: ±65 mm at 100 m, ±130 m at 198 m.

Haulage: the pulley wheel and stainless steel "aircraft" cable gave no problems. The winch gearing proved inadequate and haulage was time consuming. The winch often being rejected in favour of hand power.

CONCLUSIONS

1. A long 'blind' near horizontal borehole system has been demonstrated to be capable of accurately monitoring the development of mid-horizon interaction effects over longwall retreat walls.
2. The resulting subsidence profiles seem to be of classic 'S' shape and finally dispell any doubts that strata movements in the Sydney Coalfield are grossly anomalous to those recorded in similar geology elsewhere (e.g. U.K., Appalachian, U.S.A.).
3. Much useful data is being obtained on the angle of draw, magnitudes and extent, time-related characteristics of interaction. For example, Phalen 2 West effects have, so far, fallen at least 25-30 m short of the Lingan slopes.
4. The preferred choice of instruments depends on the geology, geometry and requirements from the site. For relatively small, mild magnitudes, the VWP appears to be most cost-effective but the risk of possible total water loss is significant and has to be carefully considered.
5. The results are so encouraging that we are planning a second borehole over the adjacent 3 West panel later in 1991.

RECOMMENDATIONS

The above instrumentation procedure should be fine tuned and developed to reduce the observational labour requirements and increase efficiency.

Alternative instrumentation techniques merit further serious consideration to widen and improve the available options:

- time domain reflectometry (TDR) in long horizontal boreholes.
- direct measurement of strain (e.g. long sonic probe permanently installed and 'floating' within rigid anchors).
- strain gauged cable(s).
- clusters of multiple tiltmeters permanently fixed in the borehole.

ACKNOWLEDGEMENTS

The authors wish to express their appreciation to CBDC senior management and colliery staff throughout the implementation of the project. Also, to Logan Drilling and recent CO-OP students from the University College of Cape Breton for their invaluable assistance. The views expressed are those of the authors.

10th INTERNATIONAL CONFERENCE ON GROUND CONTROL IN MINING

EVALUATION OF SUBSIDENCE PARAMETERS FOR INCLINED SEAMS IN UK COALFIELDS

X. L. Yao, *Postgraduate Research Student*
D. J. Reddish, *Lecturer*
B. N. Whittaker, *Professor of Rock Mechanics*

Department of Mining Engineering
University of Nottingham
Nottingham, NG7 2RD
UNITED KINGDOM

ABSTRACT

This paper analyses the effects of mining extraction geometry (width/depth ratio) and dip of seam on subsidence parameters based on a large Database, containing 120 longwall mining cases all within the UK coalfields. The subsidence parameters evaluated in this paper include the following: the maximum subsidence value with different goaf-treatments, the position of maximum subsidence, the position of half-subsidence, subsidence value over the rib-side, positions of maximum tensile strains, positions of inflection points and the magnitude of maximum tensile strains on both rise and dip sides. Additionally, the maximum compressive strain and two limit angles are also studied in this paper.

Based on a comprehensive Database analysis, several equations are derived relating these parameters to the width/depth ratio and the dip of seam. The results should assist engineers to design new structures, or take measures to protect existing structures from strain effects. The findings of the research assist in extension of the SEH to inclined seams with greater certainty.

INTRODUCTION

If geological factors are ignored, the main factors controlling subsidence characteristics are mining geometry, usually the width/depth ratio, and the dip of seam. Although SEH is thought to be a reliable method of prediction for level seams, for slightly inclined seams it assumes the surface zones produced are perpendicular to the relevant point in the workings in the case where the dip of seam ranges from flat to a dip of 18^0 [2].Therefore, the effects of more steeply inclined seams should be researched in order to gain some knowledge of subsidence characteristics due to mining steeply inclined seams. The authors thus have collected case data recorded since the SEH Second Edition in the UK coalfields, in which the dip of seam ranges from flat to 35^0. All the data, which include 120 longwall mining cases, have been placed into a Database package on an IBM personal computer for processing purposes. Serial equations have been derived to show the relationships between some subsidence parameters, and the width/depth ratio and dip of seam.

This work is of importance since it provides a convenient and flexible way to evaluate subsidence parameters with reference to mining inclined seams. Furthermore, this paper demonstrates the general subsidence characteristics due to mining an inclined seam, which is not extensively covered in the published literature.

EVALUATION OF SUBSIDENCE PARAMETERS

Each parameter has been evaluated in a separate section describing the results.

Maximum Subsidence Value

The determination of the magnitude of maximum subsidence for inclined seams requires consideration of the width/depth ratio.

Critical or Supercritical Situation In the case of mining a inclined seam, the roof is believed to converge perpendicular to the seam [3], as shown in Fig.1. Clearly, the maximum subsidence is the vertical component of the perpendicular movement, which can be expressed by the equation below:

$$Smax = m\ a \cos\alpha$$

Where m is the seam thickness, a is the subsidence factor and α is the seam inclination.

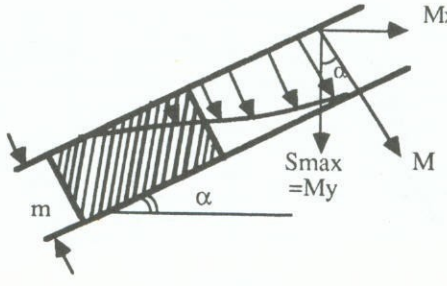

Fig.1 Calculation of maximum subsidence

Subcritical Situation Ls and Ld are assumed to be the minimum panel length and width respectively for reaching critical condition when the mining depth is fixed. Obviously, Ls and Ld are dependant on the mining depth, usually having a

proportional relationship. Therefore, whether a case reaches a critical situation is determined by Ls/h and Ld/h ratios. Accordingly, maximum subsidence under subcritical conditions can be determined by:

$$Smax = m \cos\alpha \, f(Ls/h, Ld/h)$$

Where m is the seam thickness, α is the seam inclination, h is the mining depth and Ls, Ld are the minimum panel length and width respectively for reaching a critical situation.

Assuming the panel length is long enough for subsidence to be fully developed along strike, which all the cases collected in this paper are based on, the influence of Ld/h on the maximum subsidence along dip can be analyzed by using the following relationship:

$$Smax = m \cos\alpha \, f(Ld/h)$$

Apparently, Smax/m cosα has a functional relationship with Ld/h, i.e.width/depth. In order to gain this relationship, all the data are plotted in Fig.2. The trend indicates that when the width/depth ratio exceeds 1.2, Smax/m cosα is a constant, approximately 0.8. i.e. the maximum subsidence factor.

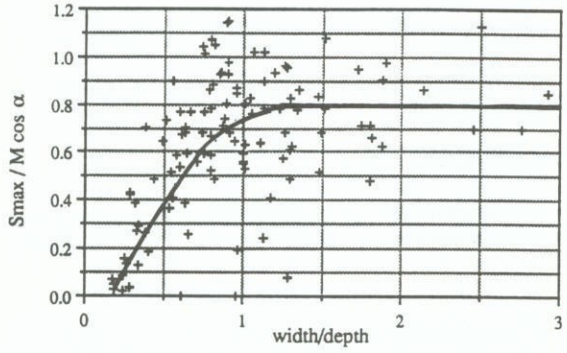

Fig.2 Relationship between Smax/Mcosα and width/depth ratio

In order to find the effects of different goaf-treatments and previous mining on the magnitude of maximum subsidence, three situations, i.e. partial packing & previous working, caving & non-previous working and caving & previous working, have been evaluated, as shown in Fig.3. It demonstrates that a greater value of maximum subsidence occurs for caving than partial packing, and previous workings

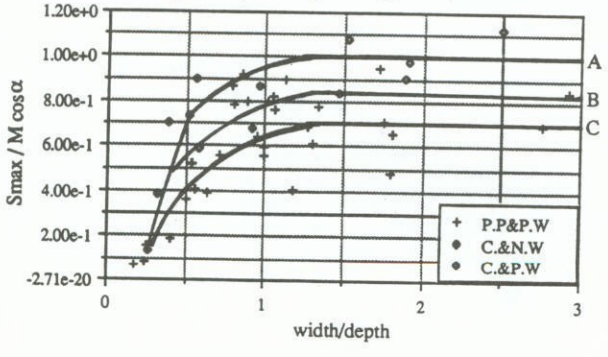

A = Caving and previous working; B = Caving and non - previous working; C = Packing and previous working

Fig.3 Relationship between Smax/Mcosα and width/depth ratio with different goaf-treatments and mining situations.

result in a greater value of maximum subsidence than non-previous workings, which is consistent with the results from Whittaker and Reddish [4].

Subsidence over Rise-Side and Dip-Side Rib Edges

In order to develop a suitable relationship between ribside subsidence and width/depth ratio and dip of seam, a statistical analysis has been undertaken. Two categories have been considered.

Dip of Seam less than 10^0 A statistical analysis indicates that when the dip of seam ranges from flat to 10^0, the width/depth ratio is the main factor controlling the ribside subsidence. Ribside subsidence on the rise and dip side as percentage of maximum subsidence is plotted against the width/depth ratio of the cases concerned, which are shown in Fig.4.a and Fig.4.b respectively. The two regression equations obtained are given as follows:

$$Sr/Smax = 20.5524 \times (\text{width/depth})^{-0.6993}$$
$$Sd/Smax = 28.7455 \times (\text{width/depth})^{-0.6150}$$

The correlation coefficients for the above two equations are 0.56, 0.51 respectively.

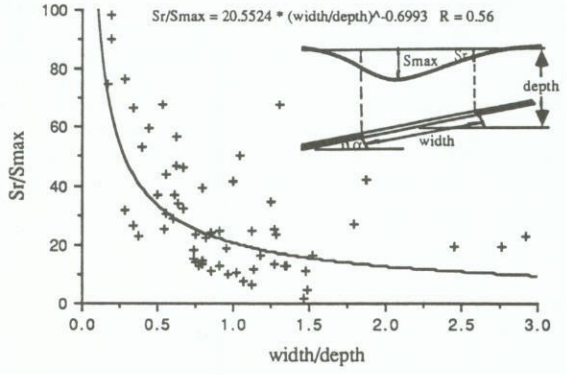

Fig.4.a Relationship between subsidence over ribside in terms of depth on riseside and width/depth ratio. (Dip of seam < 10^0)

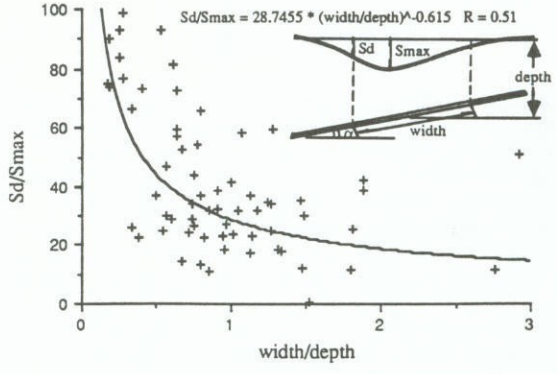

Fig.4.b Relationship between subsidence over ribside in terms of Smax on dip-side and width/depth ratio. (Dip of seam < 10^0)

From Fig.4.a, it can be seen that the ribside subsidence on the rise-side varies from virtually 100% at w = 0.15h to less than 10% at w = 2.5h or wider; while from Fig.4.b, it is clear that the ribside subsidence on the dip-side varies from 100% at w = 0.15h to less than 17% at w = 2.5h or wider.

Dip of Seam greater than 10^0 When the dip of seam exceeds 10^0, both Sr/Smax and Sd/Smax seem to approach a constant, which are shown in Fig.5.a and Fig.5.b respectively. For the rise-side, out of 12 cases examined, the ribside subsidence of 10 cases is approximately 10% of Smax; while for the dip-side, out of 14 cases investigated, the ribside subsidence of 11 cases is about 90% of Smax.

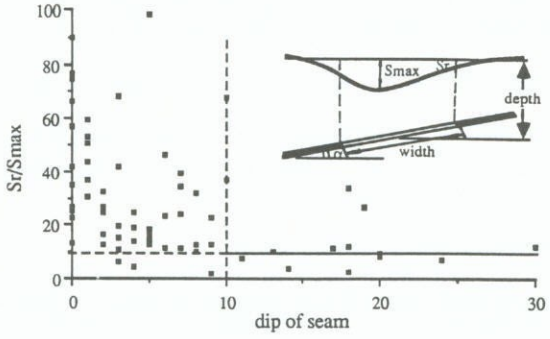

Fig.5.a Relationship between subsidence over ribside in terms of depth on rise-side and the dip of seam

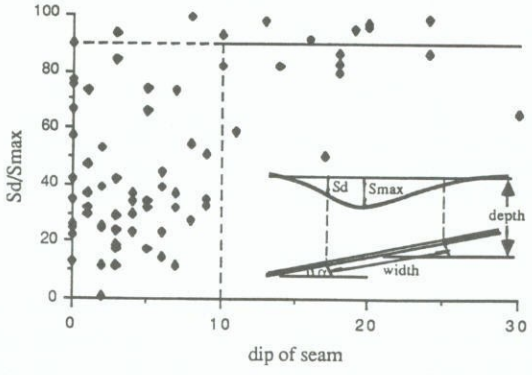

Fig.5.b Relationship between subsidence over ribside in terms of depth on dip-side and the dip of seam

Maximum Tensile and Compressive Strains

Strains are directly proportional to the maximum subsidence (Smax) and inversely proportional to the cover depth (h) resulting in the following expressions:

Er = 1000 x Kr x Smax/h
Ed = 1000 x Kd x Smax/h
Ec = 1000 x Kc x Smax/h

Where Er, Ed and Ec are the maximum tensile strains on rise and dip-side, and the maximum compressive strain respectively. Kr, Kd and Kc are coefficients of proportionality. They are plotted against width/depth ratios for tensile strains on rise and dip-side and compressive strain in Figures 6, 7 and 8 respectively. From the mean trends presented in these figures, it can be seen that for critical extraction situations, magnitudes of the maximum strains can be calculated by the following equations:

Er = 1000 x 0.4 x Smax/h
Ed = 1000 x 0.5 x Smax/h
Ec = 1000 x 0.7 x Smax/h

Although there is a lack of data in Figures 6 and 7 when the width/depth ratio ranges from 1.5 to 2.5, researchers in the UK and the Australia have also experienced similar trends in their studies. The scatter indicates that it is very difficult to obtain consistent strain values because of many factors which influence the magnitude of strain, such as, the existence of joints within the overburden; measured error; and variations in non-mining strains. etc. It should be mentioned that these three models can only be valid in the case where the width/depth ratio is bigger than 0.18, for the case, in which the width/depth ratio is less than 0.18, it is unpredictable because of the lack of data. More data should be collected in order to obtain perfect models.

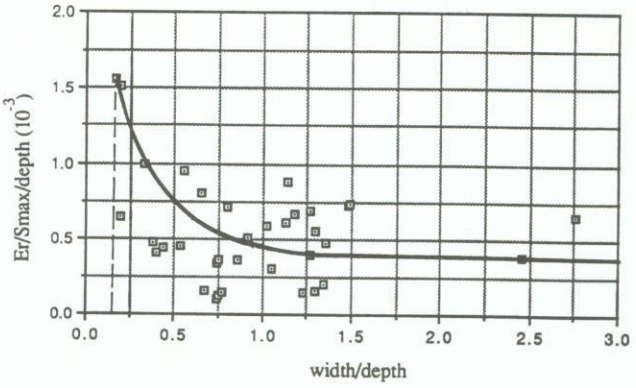

Fig.6 Relationship of width/depth ratio to Er/Smax/depth. Note: Er is the maximum tensile strain on rise-side

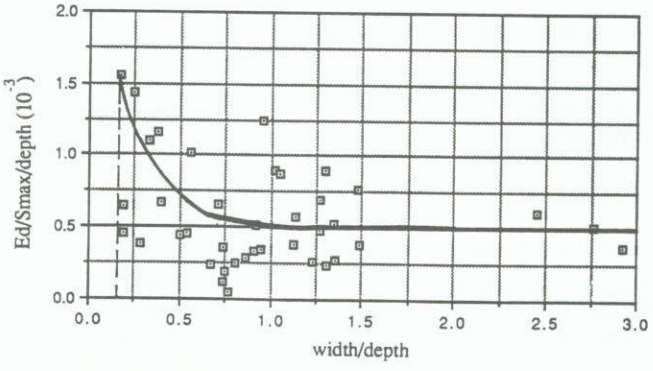

Fig.7 Relationship between width/depth ratio to Ed/Smax/depth. Note: Ed is the maximum tensile strain on dip-side

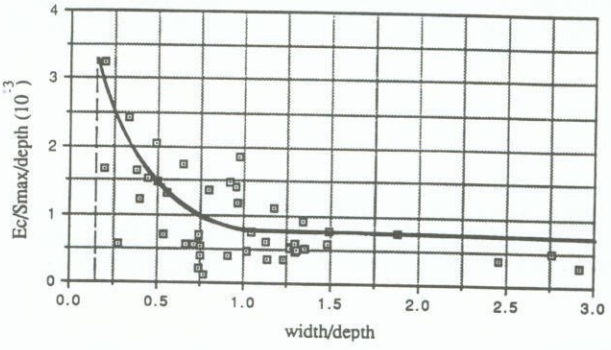

Fig.8 Relationship od width/depth ratio to Ec/Smax/depth. Note: Ec is the maximum compressive strain

The tensile strains on rise and dip-side for the cases studied vary from less than 1 mm/m to 8 mm/m, and from less than 1 mm/m to 9 mm/m respectively, while compressive strain varies from less than 1 mm/m to 8 mm/m.

Position of Maximum Subsidence

Figure 9.a shows the relationship between the distance from mining extraction centre to the point of maximum subsidence in terms of depth and the dip of seam. The linear relationship is found to fit the data best with a correlation coefficient of 0.71, the empirical equation is as following:

$$Dc/depth = - 0.0292 + 0.0185\ \alpha$$

It is apparent that the maximum subsidence point becomes displaced towards the dip with increasing dip in the seam.

An effort is made to find the relationship between Dc/depth (see below) and width/depth ratio, as shown in Fig.9.b. The linear relationship found can be expressed as following:

$$Dc/depth = 0.2604 - 0.2154\ (\ width/depth\ )$$

The correlation coefficient is only 0.47, which maybe means the "Dc/depth" parameter is less related to width/depth ratio than to the dip of seam.

If one considers the effects of both two factors, width/depth ratio and dip of seam, on Dc/depth, a combined relationship can be assumed as following:

$$Dc/depth = - 0.2154 \times (\ width/depth\ ) + 0.0185\ \alpha + a \qquad (1)$$

Substituting all the measured data into Eq. (1), we obtain a = 0.1379. Therefore, the general equation for determining Dc/depth can be described as below:

$$Dc/depth = -0.2154 \times (\ width/depth\ ) + 0.0185\ \alpha + 0.138 \qquad (2)$$

Where Dc is the distance from the mining extraction centre to the point of maximum subsidence, and α is the dip of seam. By the use of a short computer program, it has been demonstrated that the mean error in using Eq. (2) is within $\pm$ 0.099.

Position of 1/2 Smax

Position of 1/2 Smax on the Rise-side Figure 10.a and Figure 10.b illustrate the relationships between Dr/depth (see below) and the dip of seam and width/depth ratio respectively. The two linear relationships can be written as below:

$$Dr/depth = 0.0912 + 0.013\ \alpha$$
$$Dr/depth = 0.034 + 0.1712 \times (\ width/depth\ )$$

The correlation coefficients for above two equations are 0.63, 0.41 respectively, which indicates Dr/depth is more related to the dip of seam than width/depth ratio. However, if the two equations are combined together, the following equation can be derived,

$$Dr/depth = 0.013\ \alpha + 0.1712 \times (\ width/depth\ ) - 0.0943 \qquad (3)$$

Where Dr/depth is the distance from ribside on the up-side to the point of half-maximum subsidence, α is the dip of seam. Equation (3) has a mean error of $\pm$ 0.08989.

Position of 1/2 Smax on the Dip-side The effects of dip of seam and width/depth ratio on Dd/depth (see below) are shown in Fig.11.a and Fig.11.b respectively. The two empirical relationships are as below:

$$Dd/depth = 0.1762 - 0.0224\ \alpha$$
$$Dd/depth = - 0.1398 + 0.1614 \times (\ width/depth\ )$$

The correlation coefficients for these two equations are 0.74, 0.38 respectively, which illustrates that the "Dd/depth" parameter is much more closely related to the dip of seam than width/depth ratio. However, the general equation with consideration of both factors can be obtained as below:

$$Dd/depth = -0.0224\ \alpha + 0.1614 \times (\ width/depth\ ) + 0.016 \qquad (4)$$

Where Dd/depth is the distance from ribside on the dip-side to the point of half-maximum subsidence, α is the dip of seam. Equation (4) has a mean error of $\pm$ 0.09005.

Position of Maximum Tensile Strain

Position of Maximum Tensile Strain on the Rise-side Figure 12.a and Figure 12.b show the relationships between Sr/depth (see below) and width/depth, the dip of seam respectively. The two linear relationships can be expressed as follows:

$$Sr/depth = - 0.307 + 0.3326 \times (\ width/depth\ )$$
$$Sr/depth = - 0.0471 + 0.0105\ \alpha$$

The correlation coefficients are 0.68, 0.25 for above two equations respectively, which indicates that the width/depth ratio is a more important factor than the dip of seam when calculating Sr/depth. However, if both two factors are taken into account, the general equation can be gained as following:

$$Sr/depth = 0.3326 \times (\ width/depth\ ) + 0.0105\alpha - 0.3969 \qquad (5)$$

Where Sr/depth is the distance from ribside on the up-side to the position of maximum tensile strain in terms of depth, and α is the dip of seam. A mean error of $\pm$ 0.1667 can be adopted in using Eq.(5).

Position of Maximum Tensile Strain on the Dip-side Similarly, following the same procedure and methods as described above, we can obtain two empirical equations, from in Fig.13.a and Fig.13.b, which indicate the relationships between Sd/depth (see below) and the inverse of width/depth and dip of seam,

$$Sd/depth = - 0.0539 - 0.054 \times (\ width/depth\ )^{-1}$$
$$Sd/depth = - 0.0515 - 0.0134\ \alpha$$

Both equations have a poor correlation coefficient, i.e. 0.36, 0.43 respectively. In order to verify the results, more data should be collected. A general equation can be used for calculation of Sd/depth with consideration of both width/depth and the dip of seam,

$$Sd/depth = - 0.054 \times (\ width/depth\ )^{-1} - 0.0134\ \alpha + 0.031 \qquad (6)$$

Where Sd/depth is the distance from ribside on the dip-side to the position of maximum tensile strain in terms of depth. It has been demonstrated that the mean error in using Eq. (6) is within $\pm$ 0.1088.

Position of Transition Point

Transition Point on the Rise-side The transition point is the point of transition from compressive to tensile strain or vice versa. The location of the transition point is important as it

determines the regions of tensile and compressive strains.

With regard to the influence of width/depth ratio on the position of transition point, it has been found that the "Tr/depth" (see below) parameter has a best linear relationship with the inverse of width/depth, i.e. $(\text{width/depth})^{-1}$. Figure 14.a and Figure 14.b show the relationship between Tu/depth and $(\text{width/depth})^{-1}$, the dip of seam. The two empirical equations are as follows:

$$\text{Tr/depth} = 0.342 - 0.1227 \times (\text{width/depth})^{-1}$$
$$\text{Tr/depth} = 0.05 + 0.0205\ \alpha$$

The correlation coefficients for above two equations are 0.81,0.46 respectively, which indicates the "Tr/depth" parameter is much more related to the inverse of width/depth ratio than the dip of seam. If both two factors are taken into considerations together, a general relationship for determining Tr/depth is as following:

$$\text{Tr/depth} = -0.1227 \times (\text{width/depth})^{-1} + 0.0205\ \alpha + 0.245 \quad (7)$$

Where Tr/depth is the distance from the ribside on the up-side to the transition point in terms of depth , and α is the dip of seam. A mean error of $\pm$ 0.07422 can be adopted when using Eq.(7).

Transition Point on the Dip-side Figure 15.a and Figure 15.b show the relationships between Td/depth (see below) and the inverse of width/depth, the dip of seam. Two equations can be expressed as below:

$$\text{Td/depth} = 0.1968 - 0.092 \times (\text{width/depth})^{-1}$$
$$\text{Td/depth} = 0.1095 - 0.01042\ \alpha$$

The correlation coefficient for above two equations are 0.68, 0.36 respectively, which means the "Td/depth" parameter is more related to $(\text{width/depth})^{-1}$ than the dip of seam. If the two factors are considered together, a general equation can be obtained as following:

$$\text{Td/depth} = -0.092 \times (\text{width/depth})^{-1} - 0.0104\ \alpha + 0.254 \quad (8)$$

Where Td/depth is the distance from the ribside on the dip-side to the transition point in terms of depth, and α is the dip of seam. It has been calculated that the mean error in using Eq.(8) is within $\pm$ 0.07197.

Trends in Limit Angles

For the inclined seam, the two angles, rise angle $\alpha 1$ and the dip angle $\alpha 3$, are required to determine the subsidence trough area on the surface. These authors have found that these two limit angles mainly vary with the dip of seam, detail of this work can be seen in another paper [5]. Figure 16.a and Figure 16.b show the relationship between the rise angle $\alpha 1$, the dip angle $\alpha 3$ and the angle of inclined seam. These two curves have a good agreement with the results presented in S.E.H. Additionally, this model can be adapted up to 30^0 dip seam.

CONCLUSIONS

Based on the results presented in this paper, some subsidence

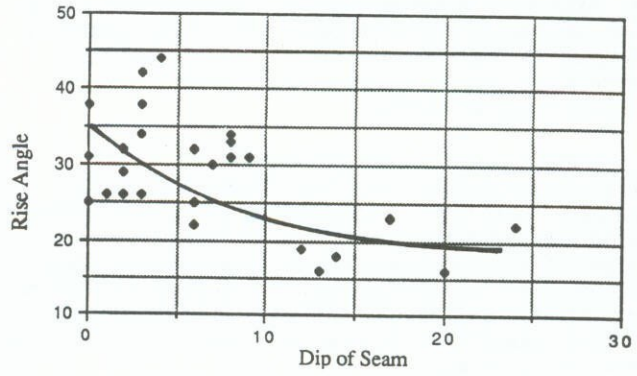

Fig.16.a Relationship between rise angle and dip of seam

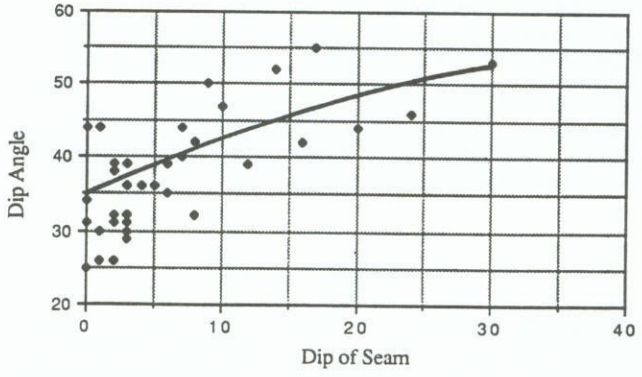

Fig.16.b Relationship between dip angle and dip of seam

parameters due to mining inclined seam, with the measures ranging from flat to 35^0, can be evaluated with a certain degree of accuracy since a mean error for each equation in the paper is provided. The following subsidence parameters or characterises can be predicted by making use of the empirical equations obtained in this paper:

1. For all practical purposes, an approximate idealised shape of subsidence profile for any width/depth ratio and dip of seam can be derived by using the following pertinent characteristics given in this paper:

. The subsidence limit positions for both rise-side and dip-side can be determined from Figures 16.a and 16.b respectively.

. Magnitude of maximum subsidence can be evaluated from Fig.2 or Fig.3, and the position of maximum subsidence can be determined from Eq.(2).

. When the dip of seam is less than 10^0, subsidence values over ribside on both rise-side and dip-side can be predicted from Figures 4.a and 4.b respectively; while if the dip of seam exceeds 10^0, they can be evaluated from Figures 5.a and 5.b respectively.

. Positions of half-maximum subsidence on both rise-side and dip-side can be calculated from Equations (3) and (4) respectively.

2. A knowledge of the maximum strains will enable the risk of damage to be assessed. The maximum tensile strains on rise-side and dip-side can be determined from Figures 6 and 7 respectively if width/depth ratio, maximum subsidence and mining depth are known; while the maximum compressive strain can be evaluated from Fig.8.

3. Positions of maximum tensile strains on rise-side and dip-side can be predicted from Equations (5) and (6) respectively. Provision of these two parameters will allow the mining engineers to optimism mining layouts to minimise potential damage to surface structures.

4. Transition points on rise-side and dip-side can be determined from Equations (7) and (8) respectively with consideration of both width/depth ratio and dip of seam factors. It has been found that the inverse of width/depth ratio is an important factor for determining the transition points. These two parameters are very important for civil engineers to define extension zones and compression zone on the surface, thus suitable measurements can be taken to protect surface structures from mining damage.

The methods adopting in this paper for subsidence parameters prediction can be used world-wildly. However, since the geological condition varies from one coalfield to another, all the empirical models for subsidence prediction should be validated in their own area. The models in this paper can be applied in the UK coalfields, or to one with similar geological conditions to the UK coalfields. The results presented in this paper are believed to contain important subsidence characteristics with reference to the mining of inclined seams, of interest to both mining engineers and civil engineers.

ACKNOWLEDGEMENT

The research described in this paper has been supported by the Headquarters Technical Department, Subsidence Division of the British Coal. Any views expressed in the paper are those of the authors and not necessarily those of the British Coal.

REFERENCES

1. Subsidence Engineers' Handbook, Mining Department, 1975, NCB.

2. R.J.Orchard, " Recent Development in Predicting the Amplitude of Mining Subsidence ", R.I.C.S. Journal, May, 1954.

3. " Mining Rock Behaviour and Ground Movement ", China University of Mining Technology, China Coal Industry Publ., Peking, 1981.

4. B.N.Whittaker and D.J.Reddish, " Subsidence Occurrence, Prediction and Control ", Elsevier. 1989, p. 128

5. X.L.Yao, B.N.Whittaker and D.J.Reddish " Influence of Overburden Mass Behavioural Properties on the Subsidence Limit Characteristics ", Mining Science and Technology. (to be published).

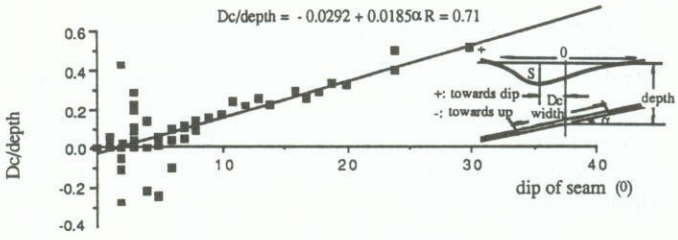

Fig.9.a Relationship between the distance from the extraction centre to the point of maximum subsidence in terms of depth and the dip of seam

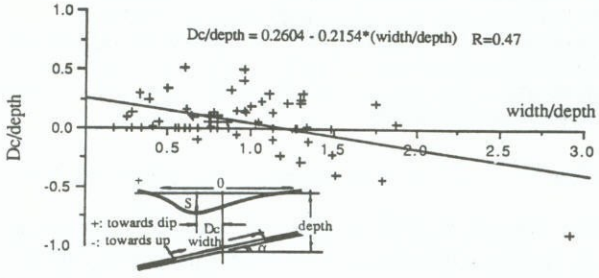

Fig.9.b Relationship between the distance from the extraction centre to the point of maximum subsidence in terms of depth and width/depth ratio

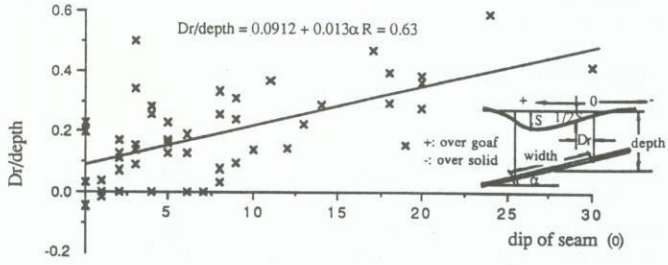

Fig.10.a Relationship between the distance from ribside on the rise-side to the point of 1/2 Smax in terms of depth and the dip of seam

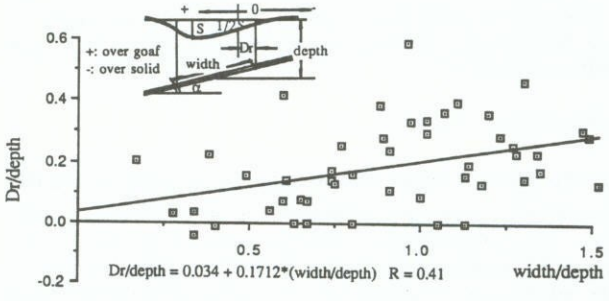

Fig.10.b Relationship between the distance from ribside on the rise-side to the point of 1/2 Smax in terms of depth and width/depth ratio

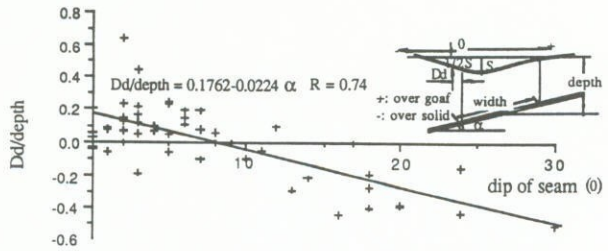

Fig.11.a Relationship between the distance from ribside on the dip-side to the point of 1/2 Smax and the dip of seam

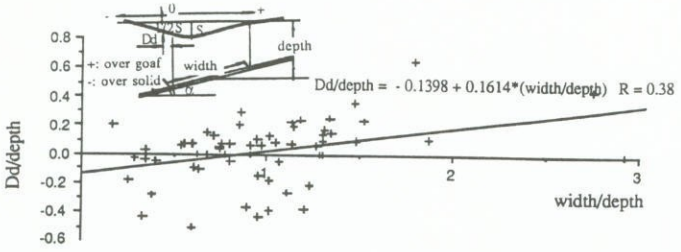

Fig.11.b Relationship between the distance from ribside on the dip-side to the point of 1/2 Smax and width/depth ratio

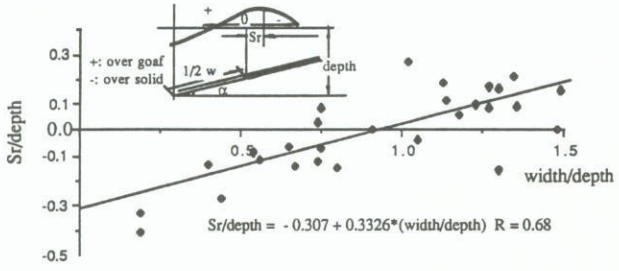

Fig.12.a Relationship between the distance from ribside on the rise-side to the point of maximum tensile strain in terms of depth and width/depth ratio

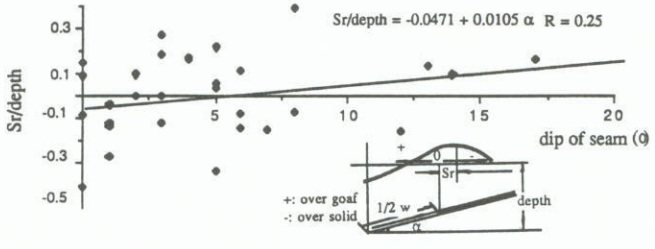

Fig.12.b Relationship between the distance from ribside on the rise-side to the point of maximum tensile strain in terms of depth and dip of seam

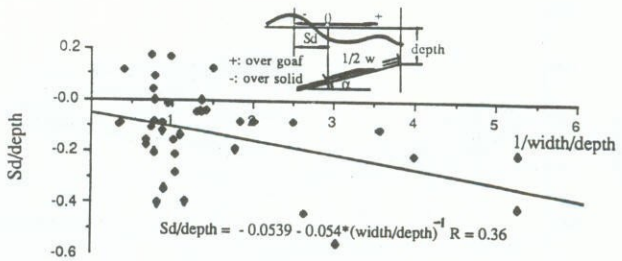

Fig.13.a Relationship between the distance from ribside on the dip-side to the point of maximum tensile strain in terms of depth and (width/depth)$^{-1}$

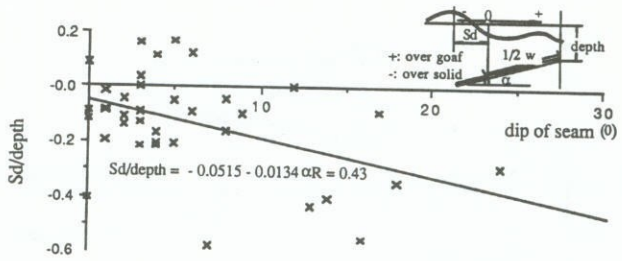

Fig.13.b Relationship between the distance from ribside on the dip-side to the point of maximum tensile strain in terms of depth and dip of seam

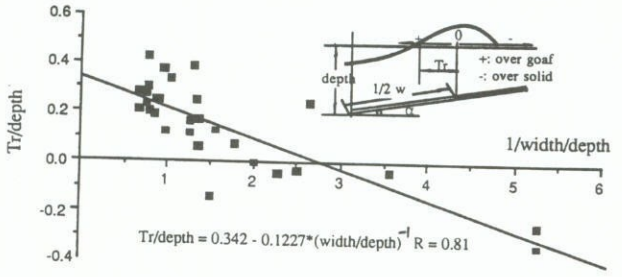

Fig.14.a Relationship between the distance from ribside on the rise-side to the point of transition in terms of depth and (width/depth)$^{-1}$

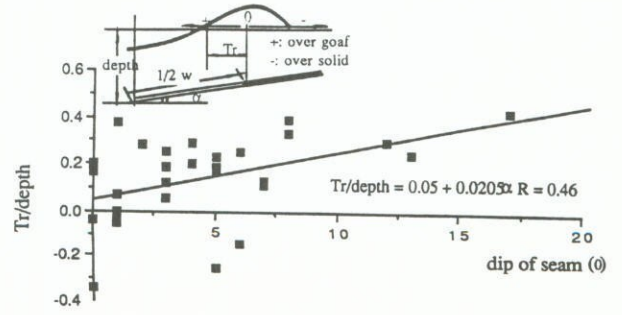

Fig.14.b Relationship between the distance from ribside on the rise-side to the point of transition in terms of depth and dip of seam

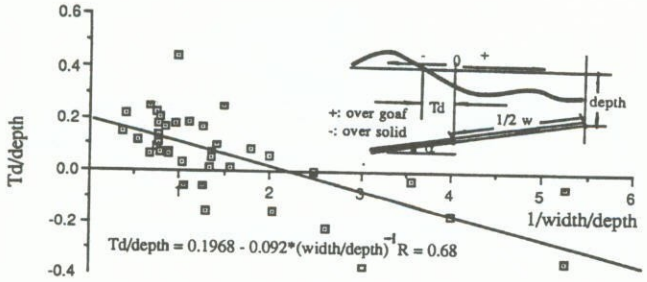

Fig.15.a Relationship between the distance from the ribside on the dip-side to the transition point in terms of depth and $(width/depth)^{-1}$

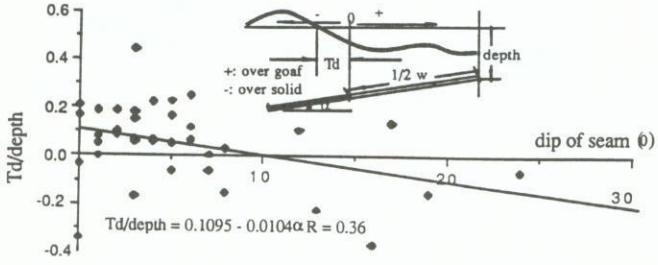

Fig.15.b Relationship between the distance from the ribside on the dip-side to the transition point in terms of depth and dip of seam

10th INTERNATIONAL CONFERENCE ON GROUND CONTROL IN MINING

MEASUREMENT OF STRUCTURAL DEFORMATION AND TILT DURING SUBSIDENCE

Revendra Awasthi, *Research Engineer*
Institute for Geotechnology, Dept. of Civil Engineering
The University of Tennessee, Knoxville, Tennessee

Larry R. Powell, *Supervisory Geologist*
U. S. Bureau of Mines, Twin Cities Research Center
Minneapolis, Minnesota

Eric C. Drumm, *Associate Professor*
Institute for Geotechnology, Dept. of Civil Engineering
The University of Tennessee, Knoxville, Tennessee

ABSTRACT

The application of a horizontal inclinometer and a tiltmeter to measure tilt, curvature, and deformations of shallow footings during mine subsidence is described. The measurements were taken during mining of a longwall panel in Southern Illinois and were supplemented with precision level survey data. Monitoring was conducted under a cooperative agreement between the Institute for Geotechnology at The University of Tennessee, Knoxville, the U.S. Bureau of Mines, the National Science Foundation, the Illinois Mine Subsidence Insurance Fund, and Old Ben Coal Company. Six different footings were constructed and instrumented at two sites; one above the panel centerline, and the second inside the edge of the panel in the anticipated zone of maximum tension.

A brief description of the inclinometer casing and tiltplate installation is described, and the results obtained from the two instruments on a plain concrete footing compared. Observations of footing deformations and curvatures calculated from the inclinometer and tiltmeter data are also presented, and the results compared with observed structural damage.

INTRODUCTION

Structural damage due to mining-induced subsidence is a major concern to the mining industry (1). Regulations require prevention, mitigation, or compensation for any damage incurred as a result of active mining. Structural damage over abandoned mines is a concern because of the uncertainty of occurrence and the repair costs incurred. Data on the mechanics of ground subsidence has been compiled (2-3), but more importantly, studies are beginning to address how subsidence-induced ground movements affect structures over both active and abandoned mines (4-12).

Damage to residential structures from mine subsidence is a complex phenomenon. Structural damage is mainly the result of stress caused by bending of the ground surface. Little information exists on the limits of structural deformation and the mechanism of subsidence induced damage. The infinite variation in structural type, footings, orientation to mining, and subsidence characteristics makes observations on actual structures economically prohibitive for developing damage mitigation procedures. Therefore, the Bureau of Mines, the Institute for Geotechnology, and the Illinois Mine Subsidence Insurance Fund initiated a program to build, instrument, and monitor full-scale foundations to determine the deformations produced by mine subsidence. This cooperative research program (13) was initiated to investigate several different construction practices and to develop computer-aided numerical techniques to analyze structures undergoing subsidence (14-15). If the ground movements caused by subsidence can be predicted, then this data can be used in a computer model to predict the amount of damage a structure may be expected to experience. Such a model could also be used to test various damage prevention and mitigation strategies while avoiding the time and expense of actual in-situ studies.

To evaluate the behavior of the ground and structures during subsidence, 12 test footings were constructed near West Frankfort, IL (Fig. 1). Six footings were constructed above the centerline of the longwall panel and six were located in the predicted zone of maximum tension, approximately 23 m inside the edge of the panel. All the footings were constructed with identical dimensions; 12.2 m long, 0.45 m wide, and 0.25 m thick. Six different methods of construction were investigated, however, only the response of a conventional, plain concrete footing is described here. Four courses of hollow core concrete block were laid on the footing. Soil-filled load bins were placed on the top of the block wall to simulate a contact pressure of 35 kPa. The footings were designed to simulate typical crawl space foundation construction practices in southern Illinois. The longwall panel is approximately 260 m wide and the mine is removing about 2.1 m of coal at a depth of about 200 m. Mining is from east to west.

A variety of instruments were used to obtain the free-field (the ground response unaffected by the presence of any structure) and footing response.

Surveying of free-field monuments, horizontal inclinometers, and soil strain gages were used to obtain the free-field response. In addition to these instruments, tiltmeters, extensometers, and strain gages were used to monitor the response of the footings. Figure 1 shows the locations of inclinometer casings and survey monuments in the free-field.

In recent years, efforts have been made to collect case histories and describe mechanisms of mining-induced subsidence and damage (16). One of the most debated questions has been the nature of deformations induced in structures during subsidence. Several mechanisms may contribute to damage. Rigid body tilt of the structures, extension of the footing from tensile ground strain transmitted to the structure through soil-structure friction, and curvature resulting from the bending of the footing due to differential settlement (5-6) can all cause damage. The results from instrumented footings can be used to investigate the relative contribution of these mechanisms.

INSTRUMENTATION AND INSTALLATION

To investigate damage causing mechanisms due to subsidence, a combination of optical surveying, a horizontal inclinometer system, and a tiltmeter system was used to measure the response of the footings. Tiltmeters have been used in the past to measure structural tilt (17). The tiltmeter system consists of a portable sensor, digital indicator and tiltplates. The smallest change in tilt that can be detected is 0.1 mm/m. To minimize errors, readings are obtained by aligning the sensor on the tiltplate in four directions. The tilt is obtained as a function of the sine of the angle that the tiltplate makes with the horizontal in two perpendicular directions (18-19). Nine brass tiltplates were fastened to the surface of the concrete footings at about 1.2 m intervals using drive pin masonry anchors. Figure 2 shows the installation of the tilt plates on the structural footings.

The inclinometer system consists of a sensor, portable digital indicator, interconnecting electrical cable, and guide casing as shown in Figure 3. The sensor is accurate to ± 2.5 mm per 30 m of casing. The sensor is operated inside the casing on guide wheels that run in two longitudinal grooves at the top and bottom of the casing. To minimize instrument error, readings are taken twice by turning the sensor end for end. Slopes are obtained as a sine of the angle that the sensor makes between its two guide wheels. Telescoping couplings were used to accommodate compression and extension of the casing during subsidence. The casings were clamped to the footings using masonry anchors at approximately 0.7 m intervals. The advantage of the inclinometer system is the ability to obtain data rapidly at 0.5 m intervals. Figures 2 and 3 show details of the inclinometer casing attached to the footing. The sign convention adopted for both inclinometer and tiltmeter is such that if the east (right) end of a segment is below the west (left), the slope is positive.

Table 1 Longwall Face Position Relative to East End of the Footings

DATE	DAY	POSITION (meters)
May 10, 1990	0	84.4
May 14, 1990	4	42.97
May 18, 1990	8	0.61
May 22, 1990	12	-29.57
May 23, 1990	13	-42.06
May 24, 1990	14	-66.14
May 30, 1990	20	-124.05
June 1, 1990	22	-151.49
June 13, 1990 (Panel Completed)	34	-277.67

INCLINOMETER AND TILTMETER RESULTS

The free-field and footing measurements were taken before, during, and after the longwall face passed under the structures. Results from the plain concrete footing over the centerline panel are presented in terms of elapsed time since "Day 0", the first day when measurable vertical ground movement occurred at a monument in the centerline zone about 10 meters east of the footings. On Day 0 the longwall face was at a distance of 84.4 meter from the east end of the footing. Longwall face positions relative to the east end of the footing are given in Table 1. Negative positions indicate that the mining has passed under the east end of the footings.

Vertical displacements were taken on the footings using the tiltplates as survey points. In Figure 4, subsidence profiles developed from inclinometer data are compared with those measured using survey methods. The subsidence profiles are compared with respect to Day 4, before any movements occurred. The subsidence profiles measured using the two techniques compare very well.

Measured values of subsidence from the inclinometer in the free field are compared with those on the footing in Figure 5. The free-field inclinometer is parallel to the one on the footing. The subsidence is presented with respect to Day 8 because no measurements were taken in the free-field casing before then. The subsidence profiles from the footing compare well with the free-field response for each day, although there are some localized differences in the free-field and structural response.

The slope obtained from the inclinometer and tiltmeter are compared in Figure 6 with respect to Day 8. The slopes from the two instruments are comparable, although there is a localized change of slope at about 4.5 to 6.0 meter in the inclinometer data. Figure 7 shows the curvatures calculated from the inclinometer slope data relative to Day 8. The curvature was calculated
as the rate of change of the slope over a finite distance given by:

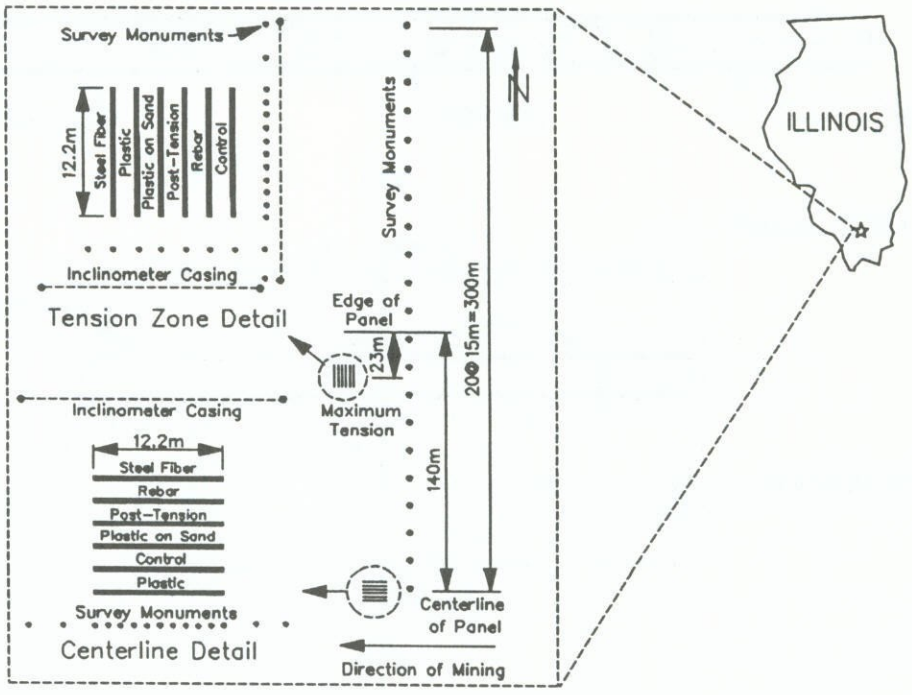

Figure 1 Test Foundations and Field Instrumentation

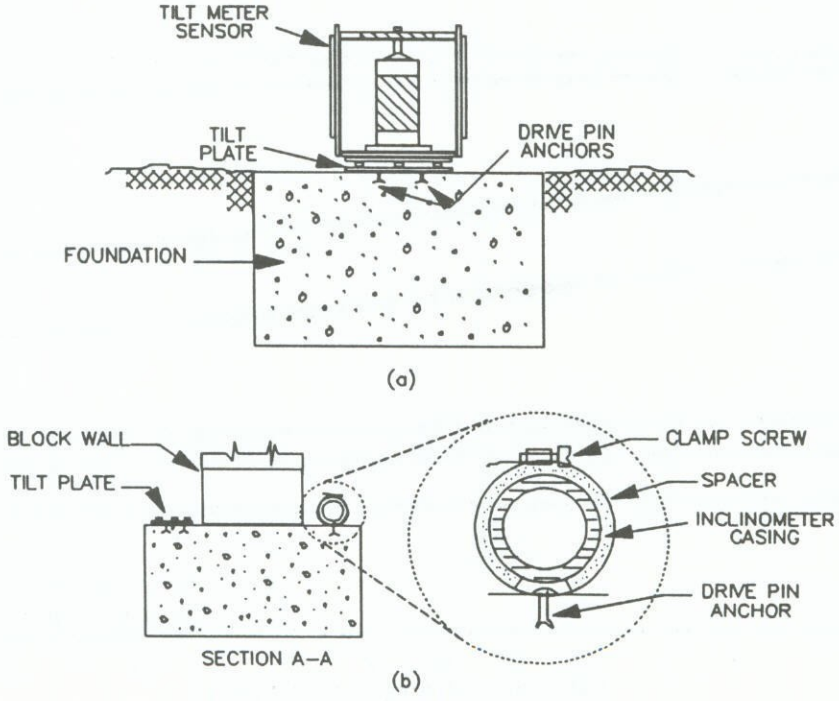

Figure 2 Details of (a) Tiltmeter Installation and (b) Inclinometer Casing Installation

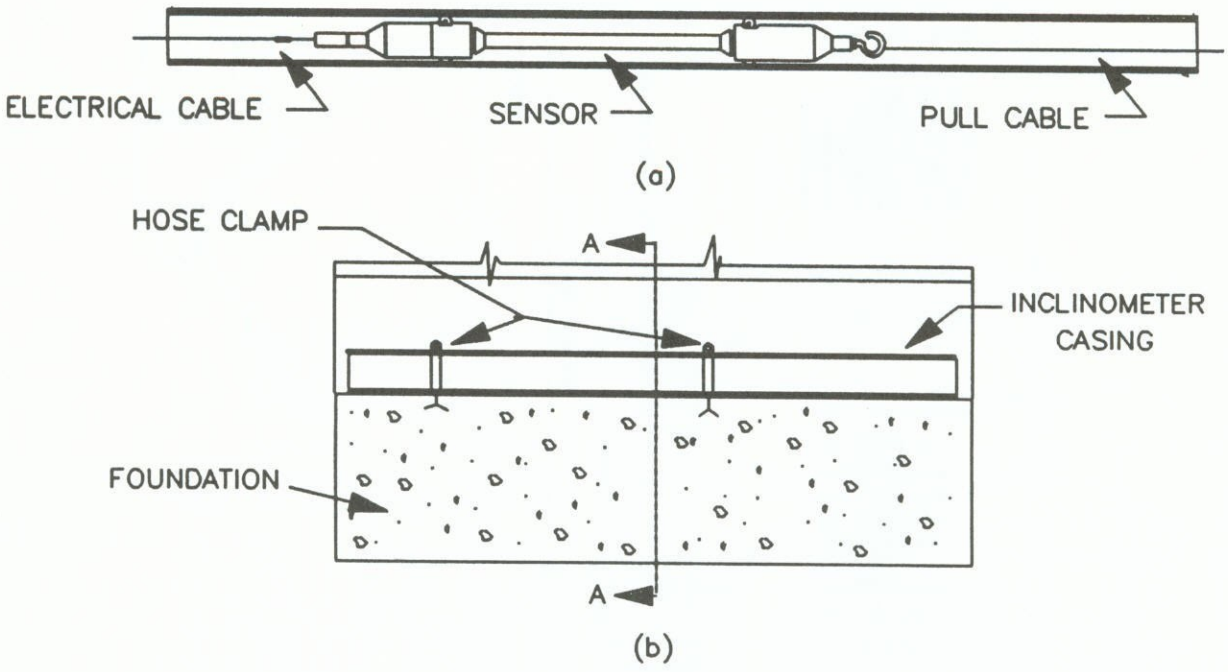

Figure 3 (a) Inclinometer Sensor
(b) Installed Casing

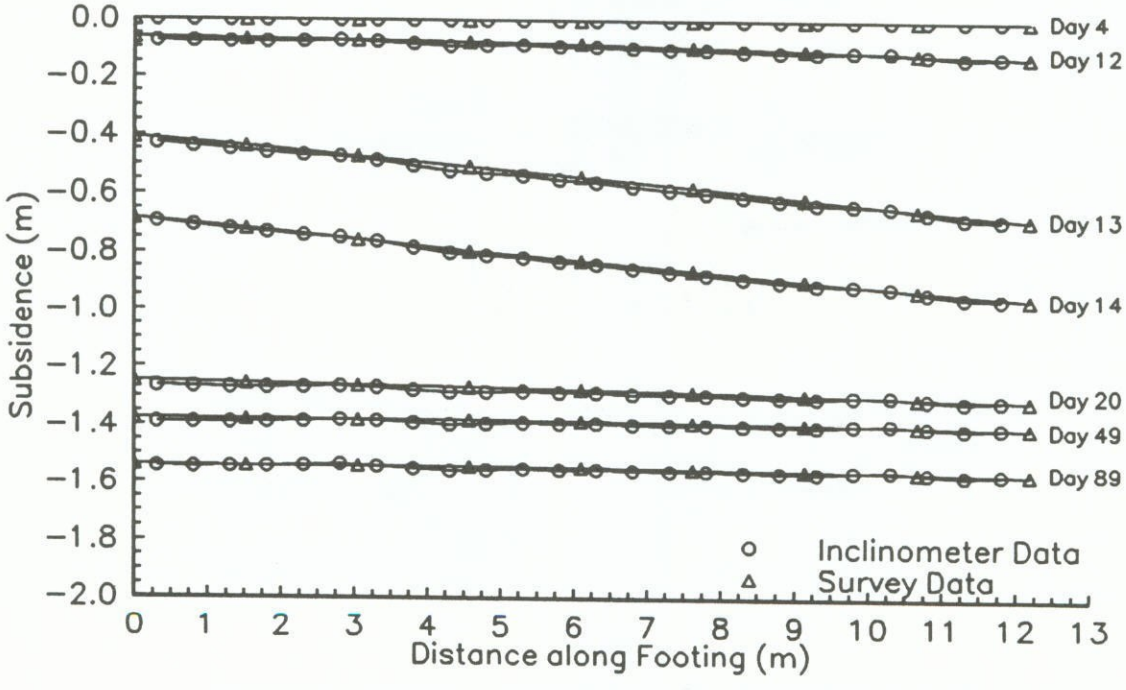

Figure 4 Comparison of Structural Subsidence Using Inclinometer and Optical Survey (Looking North)

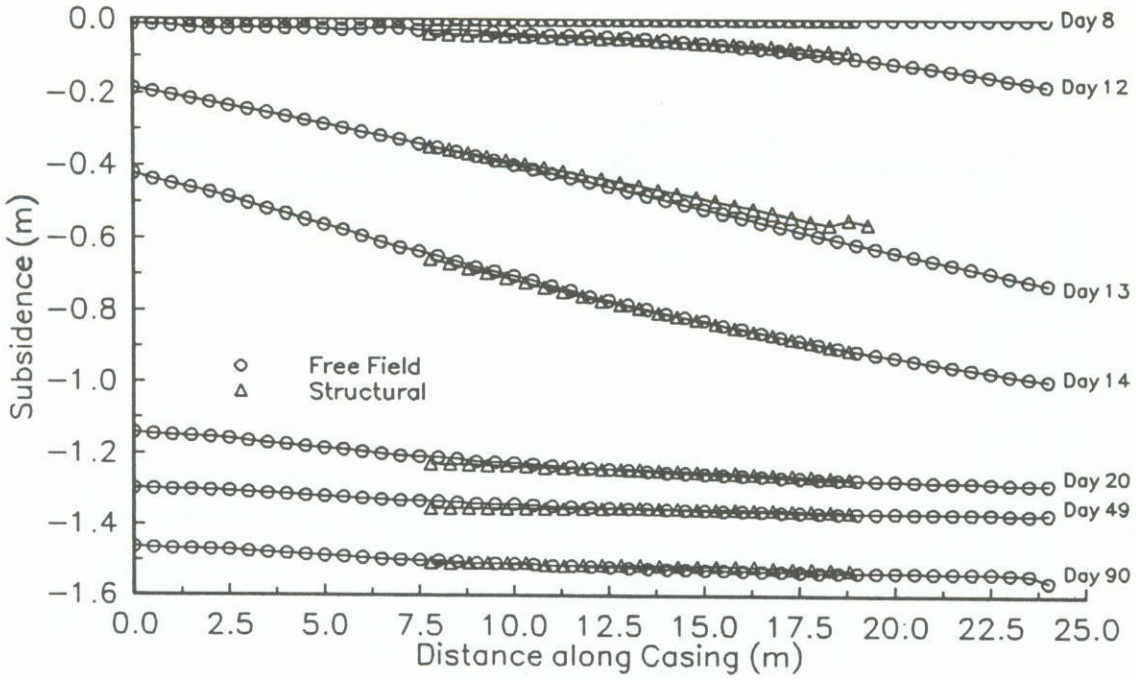

Figure 5 Comparison of Structural and Free-Field Subsidence Profiles (Looking North)

$$Curvature = \frac{d\theta}{dx} = \frac{\theta_1 - \theta_2}{x} \qquad (1)$$

where θ_1 = slope at point 1
θ_2 = slope at point 2
x = horizontal distance between points 1 and 2

The calculated curvatures over a given interval are plotted at point 2.

Curvatures calculated from the tiltmeter data are plotted in Figure 8 with respect to Day 4. The results are similar, although the inclinometer indicates a greater magnitude of curvature. Also superimposed on Figure 7 and 8 is the limit of curvature required to cause cracking of plain concrete. The cracking limit of curvature was obtained from concrete tests and beam theory (20).

DISCUSSION OF RESULTS

The subsidence profiles obtained from the inclinometer data agree very well with those obtained from survey data as shown in Figure 4. The rate of subsidence is highest between Day 12 and Day 14. During this time, bending of the footing caused the top of the footing to be placed in tension, followed by compression. By Day 20 the top of the footing was back in tension. On Day 12 and 13, a slight difference between the free-field and footing response is observed (Fig. 5). The footing does not appear to follow the deformed shape of the ground immediately after the initiation of subsidence but tends to behave rigidly as a cantilever. One major crack occurred in the footing on Day 12 at a distance of about 4.67 meter from the west end of the footing. No other cracks formed in the footing. After the footing cracked, the two segments may have acted independently resulting in more flexible footing behavior. The comparison of the free field and footing subsidence profiles (Fig. 5) on Day 14 (after the footing had cracked) indicates that the footing more closely assumed the shape of the deformed ground. Cantilevering of the footing before cracking was due to the differential movement of the ground beneath the footing from the dynamic subsidence wave.

By Day 13, the subsidence wave had moved further westward, and the crack in the top of the footing closed because bending placed the top in compression. This corresponds to the compression zone of the travelling subsidence wave. By Day 20, the subsidence wave was well beyond the footing, and the remaining movement was primarily rigid body tilt and vertical displacement of the two segments of the footing. The crack reopened from the relaxation of the footing as it moved back to a near horizontal position. By Day 49, the footing was nearly horizontal and continued to subside uniformly until the last measurements were taken. By Day 89, the footing had subsided a total of about 1.5 meters.

Investigation of slopes from both the devices, Figure 6, indicates an increase of slope from Day 8 to Day 12. The increase in slope is greater in the east portion of the footing than in the west. This difference is observed because the east portion of the footing has undergone more subsidence than the west. From Day 12 to Day 13, a large increase in slope everywhere along the footing indicates a

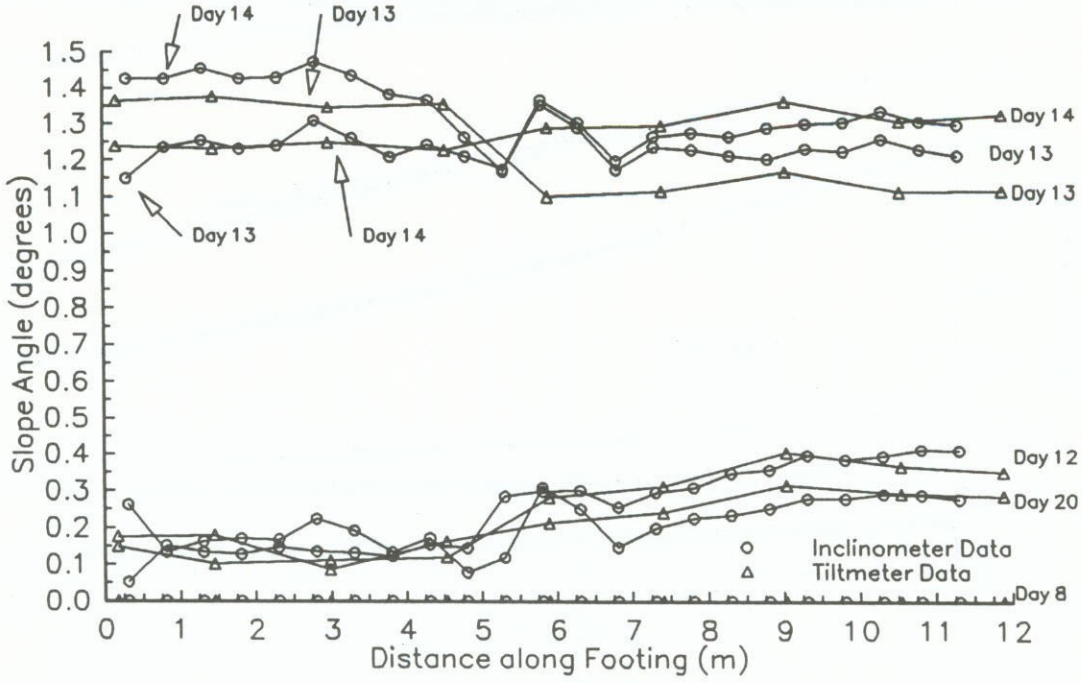

Figure 6 Structural Slope Angles using Inclinometer and Tiltmeter from Day 8 to Day 20 (Looking North)

substantial rigid body tilt. On Day 13, as indicated by tiltmeter data, and on Day 14, as indicated by inclinometer data, the increase in slope in the west segment of the footing is more than in the east segment. This resulted in the closure of the crack from compression. On Day 20, the slope along the footing reduced uniformly, and the footing generally acted in a rigid body fashion. However, the slopes are greater in the east segment than in the west segment, resulting in opening of the crack. This indicates that the footing experienced relaxation after going through compression. On Day 49 (not shown), the slopes are greater in the east segment, but have reduced uniformly since Day 20 along the footing. Minor changes are observed in slopes from Day 49 to Day 89 (not shown), confirming rigid body movement of the footing in the last phase.

The discontinuity shown by inclinometer and tiltmeter data in Figure 6 indicates the possible location of a crack between 4 and 6 m from the west end of the footing, where the slope angles are changing rapidly. Figure 7 shows curvatures relative to Day 8 obtained using the inclinometer. On Day 12, at about 5 meters from the west end of the footing, the results indicate large negative curvature which corresponds to tension at the top of the footing. These results are consistent with the observed crack on Day 12 at 4.67 meters from west end of the footing. Following the changes in curvature with time at about 4.8 meters from west end of the footing, on Day 13 and Day 14, the crack closed due to compression (positive curvature) at the top of the footing. By Day 20, after the subsidence wave had passed, the crack reopened under tension (negative curvature).

A similar response was shown by the tiltmeter data (Fig. 8). Although the magnitude of the curvature from the inclinometer is about twice that computed from the tiltmeter, the overall trend in the change of curvature is the same over the length of the footing. Maximum negative curvature from the tiltmeter data is located at about 4.5 m on Day 12. On Day 14 the curvature is positive, and the crack closed, while on Day 20, it is back to negative, confirmed by reopening of the crack. The crack remained open until the last day measurements were taken. For comparison, the curvature corresponding to cracking of a plain concrete footing as determined from measured concrete properties and beam theory is 0.056 degrees/meter. This value has been superimposed on Figures 7 and 8. The calculated curvature from the tiltmeter exceeds the theoretical cracking curvature on Days 12 and 13 at about 4.8 meter from the west end. This corresponds to the location and time that cracking was first observed. Several other locations along the footing display curvatures close to the cracking limit. The calculated inclinometer curvatures are qualitatively similar to those from the tiltmeter. However, the magnitudes are greater and exceed the cracking limit at several locations.

The difference in the results obtained from the tiltmeter and inclinometer systems are therefore related to the nature of the deformation. The tiltmeter system records tilt at a point and is independent of adjacent data points. The inclinometer system also records slope at discrete points. However, after cracking, the calculated curvatures are affected by the continuous nature of the casing. The inclinometer system is therefore

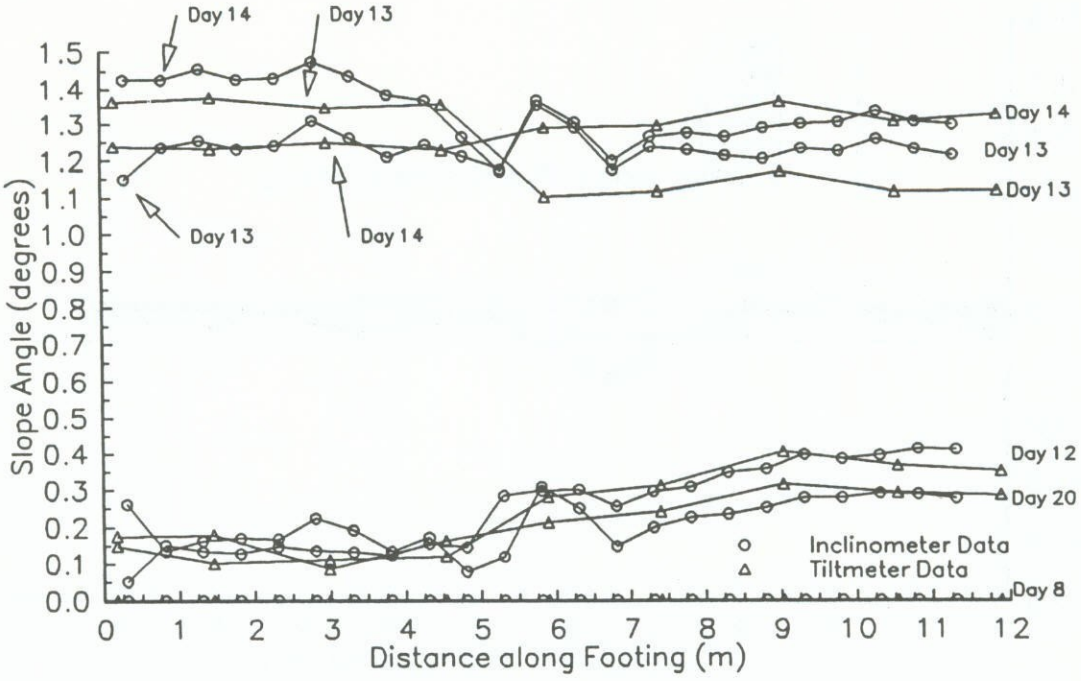

Figure 6 Structural Slope Angles using Inclinometer and Tiltmeter from Day 8 to Day 20 (Looking North)

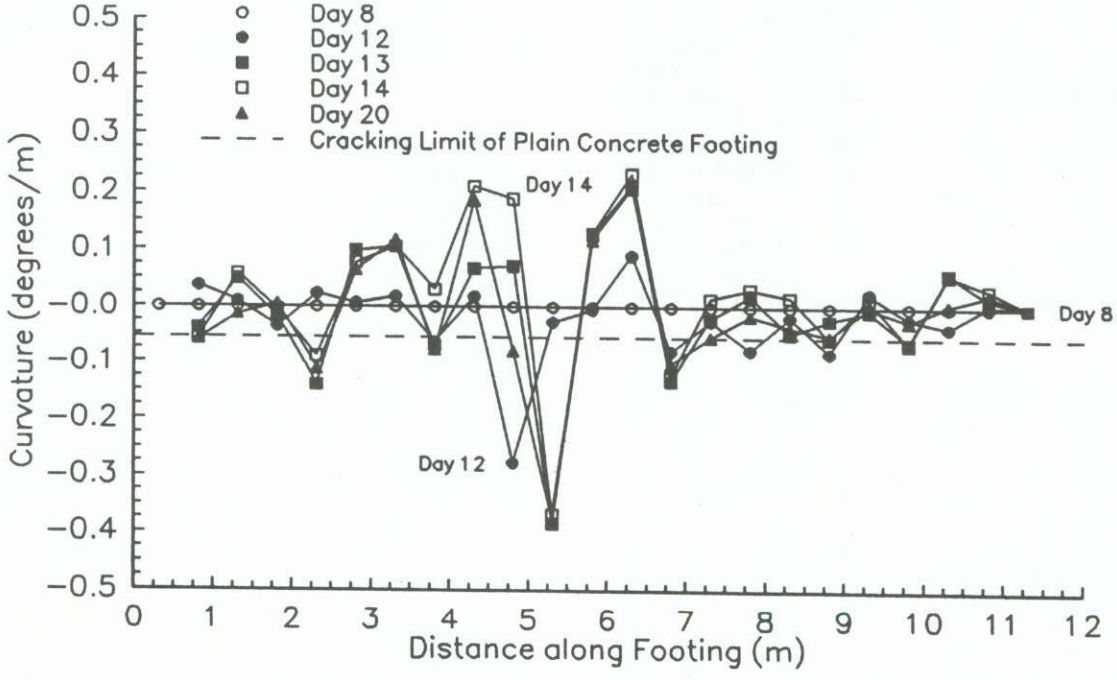

Figure 7 Structural Curvatures using Inclinometer from Day 8 to Day 20 (Looking North)

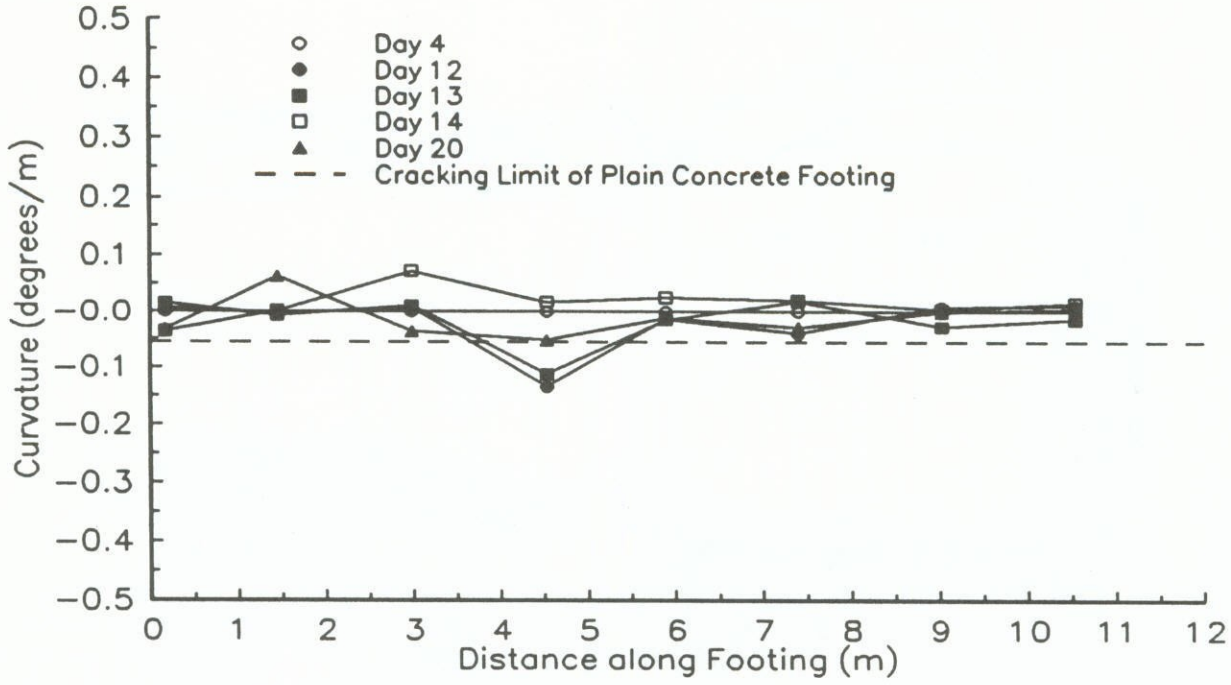

Figure 8 Structural Curvature using Tiltmeter from Day 4 to Day 20 (Looking North)

more suitable for use in a soil mass, such as the free-field installation, where the deformations of the ground are continuous like the casing. Although, the casing is much more flexible than the footing, the local differences between casing and structural deformations will exist after cracking, affecting casing deformation at locations away from the crack. Thus, after cracking, since the footing is not continuous, the curvature as defined by equation 1 is only valid in the two segments and not across the crack. Computed curvatures across a crack have no meaning. Unlike the continuous inclinometer casing, the discrete tiltmeter points are able to accurately record the different slopes on each side of the crack without getting affected by other points.

The overall behavior of the footing during subsidence can be explained in a sequence of three major phases (Fig. 9): Phase 1) initial deformation (tension at the top and formation of crack) in cantilever mode as a result of bending at the initiation of subsidence due to differential settlement, followed by; Phase 2) rigid body tilt and compression at the top of the footing as the subsidence wave passes beyond the footing; and Phase 3) relaxation phase resulting in tension at the top of the footing. This behavior corresponds to that described in the literature (13, 16, 18, 20). The initial phase is analogous to the tension zone (Day 12), the second phase to the tilt and maximum compression zones (Day 13), which is followed by tension due to relaxation of the footing (Day 14). In longwall mining, subsidence passes along the footing such that each zone is experienced consecutively at all points on the footing. Because of crack formation, the tension and compression states are localized and are displayed by the opening and closing of cracks.

CONCLUSIONS

The application of a tiltmeter and horizontal inclinometer for the determination of footing tilt and curvature has been described. An advantage of using the inclinometer is that a continuous profile of the footing can be obtained easily. A large number of tiltmeter data points is required for a similar profile. The close spacing of data points is important when evaluating the magnitude of curvature resulting in structural damage. However, since structural cracking results in a discontinuity of the slope, measurement of the slope by the tiltmeter may be more accurate. The continuous inclinometer casing cannot follow the discontinuous footing and, therefore, cannot be expected to yield good results after cracking. The inclinometer can be expected to provide good results provided the casing is installed such that the deformations of the casing and the footing are the same.

Subsidence profiles derived from inclinometer data compare very well with those obtained from optical surveying. Also, the slopes calculated from inclinometer data compare closely with the slopes obtained from the tiltmeter. Though the magnitude of the curvature from the two techniques differ, the qualitative response during different phases of the

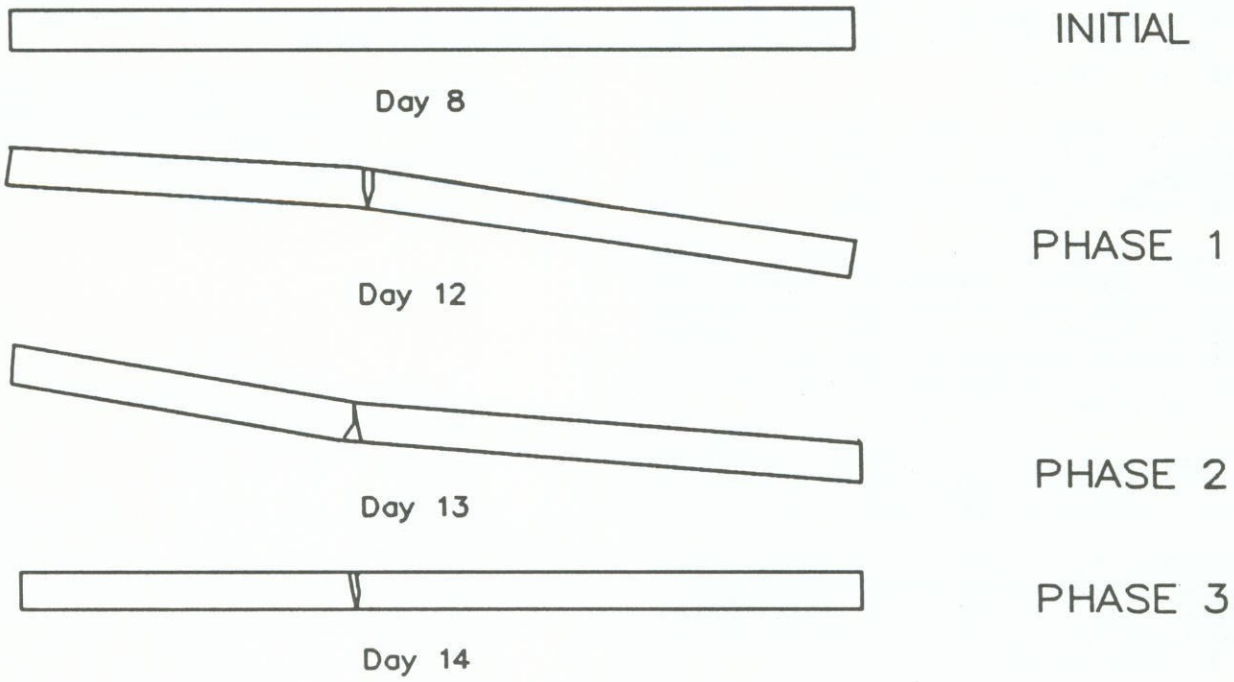

Figure 9 Different Phases of Structural Deformation during Subsidence

subsidence is the same. Cracking occurred near the point of calculated maximum curvature obtained from both methods, suggesting that curvature is the primary cause of damage.

The results presented in this paper indicate that the response of the test footings to mining-induced subsidence consists of three major phases: 1) initial bending by cantilevering due to differential movement of the ground along the footing; 2) rigid body tilt and compression of the top of the footing; and 3) a relaxation phase. The analysis of the remaining footings, which exhibit different construction techniques, will provide additional information related to the mechanisms of structural damage during subsidence.

ACKNOWLEDGMENTS

The authors would like to thank Dr. W.F. Kane, Dr. R.M. Bennett, Jomaa Ben-Hassine, David Johnson, Jamie Hudson, and Allen Hughes of the Institute for Geotechnology, Department of Civil Engineering, University of Tennessee, for their critical review and valuable comments on the investigations presented in this paper. The thoughtful reviews by Richard A. Allwes, Pittsburgh Research Center, the U.S. Bureau of Mines, and Robert A. Bauer, Illinois Geological Survey, clarified several points and are appreciated. In addition, the support for this project from the National Science Foundation, Grant No. BCS-8915243, the Illinois Mine Subsidence Insurance Fund, U.S. Bureau of Mines, and Old Ben Coal Company is gratefully acknowledged.

REFERENCES

1. Lewis, B. C. Longwall Mining: Future Concerns that Must Be Addressed. Mining Engineering, v. 42, n. 10, 1990, pp. 1170-1171.

2. Peng, S. S. Coal Mine Ground Control, 2nd Edition. John Wiley and Sons, NY, 1986, 491 pp.

3. Kratzsch, H. Mining Subsidence Engineering. Springer-Verlag, Berlin, 1983, 543 pp.

4. Drumm, E. C., R. M. Bennett, and W. F. Kane. Mechanisms of Subsidence Induced Damage and Techniques for Analysis. Paper in Mine Induced Subsidence: Effects on Engineered Structures, ed. by H.J. Siriwardane, ASCE Geotech. Spec. Publ. 19, 1988, pp. 168-188.

5. Powell, L. R., T. L. Triplett and R. E. Yarbrough. Foundation Response to High Extraction Mining in Southern Illinois. BuMines RI 9187, 1988, 45 pp.

6. Triplett, T. L., R. E. Yarbrough, and L. R. Powell. Foundation Response Induced by High Extraction Mining in Southern Illinois. Proc. 27th U.S. Symposium on Rock Mechanics, Tuscaloosa, AL, June 23-25, 1986, Soc. Mining Engrs., Littleton, CO, pp. 283-290.

7. Marino, G. G., J. W. Mahar, L. R. Powell, and R. E. Thill. Ground Subsidence and Structural Damage Over an Abandoned Room-and-Pillar Coal Mine at Hegeler, IL. BuMines RI 9072, 1986, 24 pp.

8. Marino, G. G. and J. W. Mahar. House Damage Criteria for Sag-Subsidence Over Illinois Room-and-Pillar Coal Mines. Soc. Min. Engrs., Trans., v. 278, 1984, pp. 1818-1825.

9. Peng, S. S. and S. L. Cheng. House Damages Due to Room-and-Pillar Mining. Proc. 22nd U.S. Symp. on Rock Mechanics, Cambridge, MA, Jun 29 - Jul. 2, 1981, MIT, Cambridge, MA, pp. 335-340.

10. Peng, S. S. and C. T. Chyan. Surface Subsidence, Surface Structural Damages and Subsidence Predictions and Modeling in the Northern Appalachian Coalfield. Workshop on Surface Subsidence Due to Underground Mining, ed. by S. S. Peng and M. Harthill, Morgantown, WV, Nov. 30 - Dec. 2, 1981, pp. 73-84.

11. Walker, J. S. and J. C. LaScola. Foundation Response to Subsidence-Induced Ground Movements: A Case Study. BuMines RI 9244, 1989, 12 pp.

12. O'Connor, K. M. Comparison of Mining-Induced Displacements of the Ground Surface and Residential Structures. Proc. 3rd Conf. on Ground Control Problems in the Illinois Coal Basin, Mt. Vernon, IL, Aug. 8-10, 1990, pp. 285-299.

13. Kane, W. F., R. M. Bennett, and E. C. Drumm. Construction and Instrumentation of Test Foundations for Subsidence Damage Assessment. Proc. of 3rd Conf. on Ground Control Problems in the Illinois Coal Basin, Mt. Vernon, IL, Aug. 8-10, 1990, Southern IL Univ., Carbondale, IL, pp. 311-321.

14. Hudgings, R. A., R. M. Brnnett, and L. A. Sneed. Experimental Testing of Damage Mitigation Techniques, Paper in Symp. on Mine Subsidence - Prediction and Control, ed. By C. D. Elifrits, 33rd Ann Mtg., Assoc. of Eng. Geol., Pittsburgh, PA, Oct. 2-3, 1990, pp. 173-176.

15. Ben-Hassine, J., E. C. Drumm, and W. F. Kane. Finite Element Modelling of Subsidence Effects on Structures, 10th International Conference on Ground Control in Mining, Morgantown, West Virginia, June 10-12, 1991.

16. Siriwardane, H. J. Mine Induced Subsidence: Effects on Engineered Structures, Geotech. Spec. Publ. 19, Am. Soc. Civil Engrs., NY, 1988, 209 pp.

17. Powell, L. R., T. L. Triplett and R. E. Yarbrough. Measurement and Analysis of Foundation Tilt Resulting from Mine Subsidence in Southern Illinois. Proc. Second Workshop on Surface Subsidence due to Underground Mining, Morgantown, WV, Jun. 9-11, 1986, pp. 142-152.

18. Dunnicliff, J. Geotechnical Instrumentation for Monitoring Field Performance. John Wiley and Sons, NY, 1988, 507 pp.

19. Hanna, T. H. Field Instrumentation in Geotechnical Engineering. Trans Tech Publications, Germany, 1985, 843 pp.

20. Johnson, D. C. Structural Behavior and Damage Assessment of Residential Foundation Subjected to Subsidence. M.S. Thesis, Univ. of Tennessee, Knoxville, TN, 1991, in preparation.

10th INTERNATIONAL CONFERENCE ON GROUND CONTROL IN MINING

DRAG PICKS – INFLUENCE OF TOOL GEOMETRY AND ANGLE OF ATTACK ON THE STRESS EVOLUTION AND CUTTING EFFICIENCY

Naj I. Aziz
University of Wollongong
Wollongong, NSW, AUSTRALIA

H. Guo
Pasminco Mining
Broken Hill, NSW, AUSTRALIA

G. Rossi, R. Rossi, and P. Trois
University of Cagliari
Sardinia, ITALY

ABSTRACT

During the last decade mechanical rock excavation has become increasingly widespread in the mining industry and, more in general, in excavation engineering. This technology, especially the tools and their operating mode, has developed according to empirical procedures and for this reason their validity should be ascertained by systematically re-examining the rock breakage processes.

This topic has been approached in the framework of a joint research project involving the Universities of Cagliari (Italy) and Wollongong (Australia). The investigation has been carried out experimentally as well as with the methods of numerical modelling which is based on fracture mechanics principles.

The first results of this integrated research led to the proposal of an interpretation of rock breakage by means of drag tools and to the identification of a basic correlation between the rake angle of the tool and the grain size of the rock fragments produced and, therefore, the energy efficiency of the operation.

INTRODUCTION

In recent years, rock excavation engineering has been increasingly relying on mechanical excavation techniques and this trend has resulted in the development of a large number of machine types covering a wide range of rock excavation operations. Among these, worthy of note, are percussive drilling of relatively small diameter holes, rotary drilling, coal and potash mining, rapid excavation of tunnels, raises and shaft sinking. All these excavation methods, though carried out with structurally diverse machines, only rely on two basic rock breakage processes: abrasion, produced by shear actions, and compression, produced by static or quasi-static compression. These are described by Aziz, et al (1990).

The coal mining industry was the first to resort to mechanical rock breakage using drag picks both in development stage and secondary operations. Drag picks are considered to be efficient tools in rock cutting, particularly with regard to fragmentation process.

The early description of the fragmentation process due to drag pick cutting has been given by Goodrich (1956), and Fish and Baker (1956). Three distinct stages of cutting have been defined. Crushing, crushing and chipping, and major chip formation. Efficient implementation of the tool can be achieved by clear understanding of the interaction between the rock and the tool particularly with regard to various design parameters, such as rake angle, clearance angle, angle of attack, pick spacing etc. as described by Evans (1958) and Roxborough (1981).

In this paper, emphasis has been placed on the understanding of the rock and tool interaction through the evaluation of the stress distribution in the rock and the tool. Also, discussed are the effect of attack angle and tool bluntness on the efficiency of cutting. The work reported in this paper is the result of a collaborative research work jointly undertaken between the University of Wollongong, NSW, Australia, and The University of Cagliari, Sardinia, Italy.

THEORIES OF ROCK BREAKAGE MECHANISMS

Modes of Fragmentation

The mechanical fragmentation of rocks is accomplished with current excavation techniques according to two basic modes that differ in the types of forces acting on the tools and the duration of the action.

Regarding the rate of load application, the tools used in modern excavation machinery all operate in static or quasi- static conditions. As for the forces that the tool transfers to the rock, a distinction should be made between the case where the resultant force acts perpendicular to the rock and that where the force component parallel to the rock surface also plays a role. In the first case, the tool moves normal (parallel to rock surface) to the rock . The breakage action is discontinuous and in the intervals between one breakage action and next the tool may be moved parallel to the rock surface, not to produce further fragmentation, but as it happens with chisel, disc and button bits, to locate it in front of an area of intact rock. Any further fragmentation that may occur in the region located between two adjacent impact zones should not be directly attributed to the tool , but to indexing, for instance the effect of the proximity of the impact zones. In the second case the force component acting parallel to the rock surface plays a predominant role and a typical example of this mode is represented by the action of drag picks.

Tools Acting with Predominantly Normal Forces The tools acting perpendicular to the rock surface with static or quasi-static forces can be classified into three main categories: sharp wedge tools (drill bits and discs), blunt wedge tools and button bits. The stress field produced within an homogeneous, isotropic and continuous rock mass by these types of tools may be analysed by means of the physio - mathematical theories developed more than a century ago by Flamant (1892), Boussinesq (1892) and Hertz (1881). The approach by Flament was supported by experimental evidence. The stress field produced within the rock mass by a sharp wedge tool is radial, with components, in polar coordinates, given as follows:

$$\sigma_r = \frac{2P}{\pi.t} \quad \frac{\cos\theta}{r}$$

$$\sigma_\theta = 0$$

$$\tau_{r\theta} = 0 \qquad (1)$$

where :

P = intensity of force acting perpendicular to the rock surface;

t = thickness of the rock mass two dimensional slice;

r = radius vector, and

θ = angle.

Also the isochromatics are two families of logarithmic spirals with origin in the point P of force application. The experimental analysis (Hartman, 1959; Maurer and Rinehart, 1960) showed that rock failure occurs in two simultaneous modes under the tool action; crushing and shear failure. Crater formation is the result of shear failure as shown in Fig. 1.

One of the interesting features of the theory of Paul and Sikarskie (1965) is the semi- quantitative prediction of chip formation and the resulting crater, and it provides the condition

$$\psi = 45^0 - \frac{\theta + \phi}{2} \qquad (2)$$

where

ψ = failure angle of chip

θ = one - half the wedge angle

ϕ = angle of internal friction of rock

which must be satisfied for chipping to occur at all.

Equation 2 is considered to be an important one as it represents the first successful attempt to analytically predict the type of relationship that must exist between the rock properties and tool geometry for an optimum tool performance in the chip formation process.

Tools Acting Normal and Parallel to the Rock surface Rock fragmentation by the combined action of forces perpendicular and parallel to the rock surface is achieved by tools employed in rotary drilling, a typical example being the blade bit. In fact these tools were chronologically the first to exploit this mode of rock disintegration.

The machines that operate according to this principle include coal shearers, ploughs, continuous miners and minifullfacers, as well as various rotary drilling machines including roof bolters used for ground support purposes. The cutting action of a drag bit is a discontinuous process and the various stages involved are described by Goodrich (1956), Fish and Baker (1956) and de Vergeron (1962). These authors identified three stages for rock fragmentation as shown in Fig. 2: initial crushing, crushing associated with chipping and finally major chip formation. Fairhurst (1964) and Gray, Armstrong and Galtin (1962) produced evidence that the thrust force and torsional couples acting on a drag bit undergo rapid oscillations due to the discontinuous nature of chip formation. Fig. 3 is a graphical representation of this phenomenon for a typical drilling cycle. The stresses involved in chip formation have not been fully studied because of the complexity of the process.

Although a considerable number of experiments has been carried out to provide guidelines for the design of cutting heads with drag bits for various cutting machines, the mechanism of rock fracture processes involved are not fully understood satisfactorily. A few empirical rock cutting models have been proposed to explain the observed behaviour in experiments, among them are the tensile failure model of Evans (1958), the shear models of Potts and Shuttleworth (1959) and Nishimatsu (1972) as shown in Table 1. These models assume that tensile or shear failure occurs along a line in a two - dimensional plane with the force components acting on the major chip in a state of equilibrium. The predictions of the cutting force from these models are in general agreement with the experimental results reported by Evans and Pomeroy (1966), and Roxborough (1986) over some basic cutting tool parameters, such as rake angle , depth of cut and pick width. For example, all three models predict that cutting force requirements decrease as the rake angle of the cutting drag bit increases and conclusions drawn from these models are similar or close.

In the above three models the cutting forces are predicted on the basis of the geometry of rock failure (tensile and shear) plane and of the assumed state of stress along this plane. Ranman (1985) argued that the assumption of the chip geometries may not be valid in continuous cutting.

EXPERIMENTAL RESEARCH- STATE OF THE ART

Background to Joint Research Programme

Most of the published experimental research has been carried out in the laboratory whereas the number of investigations performed on site is very limited. One of the early exhaustive experimental investigations on rock fragmentation using wedge tools acting quasi-elastically normal to the rock surface is due to Hartmann (1959). He identified the sequence

of the various rock breakage phases which culminates in the formation of a crater produced by the detachment of chips when the wedge is sharp. A wealth of information was also collected by de Vergeron (1962) who succeeded in analysing drag bit operation using a purpose built test rig. Similar investigations were reported by Pechalat (1977) and Valantin (1975).

Because of the way in which the test procedure was designed and developed, all these investigators worked with specific rocks (marble, limestone, sandstone, etc.) and analysed the process once the rock had been broken. Consequently, they were unable to follow its evolution from the initial attack of the tool on the rock. This is very likely to be one of the reasons why there are discrepancies in the models of rock fragmentation by drag picks proposed by the above mentioned authors, particularly with regard to the stress state produced in the rock by the tool. It was therefore felt necessary to further research in rock cutting by drag pick to include non-destructive analysis of the stress evolution in the rock and tool at the stage immediately preceeding disintegration. This joint research led to the definition of an integrated research programme. Topics examined include:

a) the stress distribution patterns in both rock and tool (pick),
b) the effect of tool geometry (tool bluntness) on rock cutting efficiency,
c) the relationship between angle of attack and stress distribution within the rock with reference to the characteristics of the chips produced.

Stress Distribution Patterns in Both Rock and Tool A photoelastic apparatus was designed to analyse the stress distribution patterns produced in rock and tool models during the simulation of rock breaking. The apparatus consisted of a diffuse-light polariscope (type Optotechnick by Kreuznach), and a light source of either tungsten filament lamp or sodium lamp for observation in white or monochrome light respectively. Quarterwave filters fixed to the support rings of the polariser and analyser were necessary to produce stress fringe patterns. Fig. 4 gives an isometric view of the loading set-up. The loading set-up consisted of two thick stainless steel rectangular plates P connected at the corners by four stainless steel threaded columns C. This arrangement permits the distance between the two plates to be varied in order to accommodate the geometry of the investigated tools. The tool holder is fixed to the upper plate and consists of two stainless-steel semi-circular plates perforated with a certain number of holes for the screws that hold the tool model. The longitudinal axis of the tool can be oriented consistently with the desired value of the rake angle by appropriately choosing the holes. The rock model is mounted on a stainless steel trolley system fitted with four roller bearings. The trolley moves along the specially designed tracks bolted on the lower plate of the loading frame. Thrust is applied to the plate K through a steel wire by the weight of a small bucket B filled with the required amount of lead shot. The materials used for the models include plexiglass (Rohm Italia, Milan, Italy), polycarbonate (Bayer A.G., Leverkusen, Germany) and CR39 plates of suitable thickness. The shape of the model picks used in the test was similar to commercially available shearer picks. Tests were made with the pick rake angles of 0^0 and 7^0 respectively.

The Effect of Cutting Tool Bluntness in Drilling Efficiency
Fig. 5 shows the general layout of the laboratory set-up used to compare the actual cutting performance of a blunted tool with that of a sharp tool in terms of the specific energy. The equipment uses a fully automated computer controlled and monitored, pneumatically operated roof bolting machine. The tests were carried out using bits commonly used for rock bolting operations. The reason for choosing to study drag-bit drilling was that the rock breakage action of the rotary drill drag bit is similar to the drag pick in cutting. Also, the pneumatic rotary drill is relatively easy to monitor in the laboratory. The data acquisition system used to monitor the drilling performance consisted of a keithly / soft 500 data logger. Two load cells, a potentiometer and a frequency analyser were installed on the drilling cradle to give returns on the torque, thrust, displacement and RPM respectively of the drill during test. A Wombat pneumatic drill bolter and various 27 mm diameter wing bits were used in the test.

The sharpness or bluntness of a bit is determined by the 'print' width of the bit tip. The sharp bit leaves an impression of less than 1mm width, and the blunted bit furnishes an impression of about 3mm. A series of thirty holes was drilled in a sand-cement concrete block of 40 MPa uniaxial compressive strength. Fig. 6 shows typical drill parameter signals for sharp bits and for blunt bits.

Table 2 presents the specific energy results and the average mean sizes of the drill flushing from the boreholes. Specific energy (SE) is calculated from the measurements to assess the drilling performance, using the following formula by Teal (1965):

$$SE = (F / A) + 2p\,NT / (Au)$$

where,

F is the thrust applied,
A is the cross- sectional area of the hole,
N is RPM,
T is torque, and
u is the penetration rate.
P is the thrust

The mean size was calculated on the basis of the weight retained for each successive screen as,

$$S = \sum_{i=1}^{n} Wi \quad Si$$

where:

S is the mean particle size,

Wi is the weight retained on the i th screen,

Si is the size of the i th screen and,

n is the number of screens.

The Effect of Changing Angle of Attack on Chip Formation

The operation of rock excavation machinery employed in mining led to the empirical deduction that a correlation must exist between the rake angle and the characteristics of the debris produced. As the formation of the surface chips is closely related to the stress distribution inside the rock, as indicated by non-destructive photoelastic analysis, a device by means of which the chips can be studied at the very moment they are formed, was therefore required for integrating and complementing the information provided by such analysis.

Fig. (7) shows a general layout of Rock Cutting Simulation Rig (RCSR) used for evaluating the effect of changing attack angle on chip formation. It can also be used for fundamental study of the crack behaviour due to tool configurations and of the nature of chip formation, under controlled laboratory conditions. Tests are normally carried out on 150 mm cubes of rock or cement mortar.The specimen (1) is placed on a 25 mm thick base plate and is held firmly in place by a lateral force exerted by a 50 tonne capacity jack (5) via side plates. The magnitude of applied lateral confining force is monitored by two 300 kN load cells (6) at both sides of the specimen. The cutting tool is forced against the top surface of the block by a 100 tonne capacity hydraulic jack (4). A specially designed load cell (3) mounted on the end of the jack piston and carrying the cutting tool at its other end permits monitoring of axial load applied and bending forces generated due to the applied load. The 60^0 wedge shaped cutting tool (2) is machined from a 40 mm diameter hard steel bar. The base of the 100 tonne jack is fitted with a pair of sliding shoes. These shoes slide in a pair of slots cut in the arc plate. With this arrangement it is, thus, possible to vary the angle of pick attack. A winch (7) assists in sliding the pick attached to jack along the arc (8). Once the jack is positioned at the desired angle it is then clamped to the arc plate by tightening a pair of bolts on the sliding shoes of the jack. All the load cells are connected to an HP computer data acquisition system controlled by a HP9826 microcomputer. In this way, the loading signals are recorded every second and the time for each test is usually less than 3 minutes. The force system and parameters involved in the cutting are shown in Fig. 8. The measured forces acting on the cutting wedge are the axial force F_a acting in the direction of the axis of the wedge tool, and Force F_b acting normal to the axis. These forces can be converted into the cutting force F_c in the horizontal direction and the thrust force F_t in the vertical direction by the following formulae,

$$F_c = F_a \cos\alpha + F_b \sin\alpha$$
$$F_t = F_a \sin\alpha + F_b \cos\alpha$$

where

α is the attack angle which is defined as the angle between the cutting tool axis and the cutting direction, which is, in the case shown in Fig. 8, the horizontal direction.

The resultant force F_r can be calculated from F_a and F_b, or F_c and F_t.

Preliminary experiments were carried out to investigate the occurrence of a major chip in a relatively more realistic situation and this process has been the cornerstone for various semi-empirical rock cutting models. The observations were aimed to provide some useful information for numerical modelling based on fracture mechanics principles (Guo, et al, 1988). The experimental procedure involved the application of the wedge tool at an attack angle of 60^0 which gives a neutral rake angle and a clearance angle of 30^0.

Four tests were conducted on each of sandstone (UCS 50 MPa) and concrete blocks (UCS 30 MPa). The wedge tool penetration displacement rate was maintained constant at 2mm per minute. Fig. 9 shows a typical failure sequence in sandstone rock.

Table 3 shows the results of tests carried out to examine the effect of the rake angle on the efficiency of the cutting tool. The attack angles were 67.5^0, 60^0, 52.5^0 and 45^0. These values correspond to cutting rake angles of -7.5^0, 0^0, 7.5^0 and 15^0, and clearance angles of 37.5^0, 30^0, 22.5^0 and 15^0 respectively. The measured axial force F_a the bending force F_b, the calculated cutting force F_c thrust force F_t and the resultant force values are shown in Table 3. Table 4 shows the average values of these parameters. The effects of attack angle and rake angle on cutting, thrust and resultant forces are shown in Fig 10.

RESULTS AND DISCUSSION

Photoelastic Investigations

At constant cutting rake angle of 7^0 the isochromatics lines (Figs. 11 and 12) within the rock display the same pattern for different tools. For both picks the isochromatics that depart from the point of contact of the pick tip with the rock initially form a negative angle with the horizontal and then turn upwards. The same isochromatic patterns are observed when the pick acts with the same cutting rake angle on any other point of the rock (Fig.13). Since it is reasonable to assume that the cracks propagate along the isochromatics that are the loci of maximum shear stresses, it may be said that at a positive cutting rake angle the cracks which lead to the formation of chips initiate along a line directed upward at an angle of approximately 45^0 with the horizontal.

When the cutting rake angle is neutral or negative then the isochromatics pattern is quite different (Figs. 14 and 15). The contact between tool and rock is discontinuous and each point of contact becomes the source of circular isochromatics. The isochromatics originating at the base of the rockstep are always parallel to the horizontal. If the shear strength of the rock is less than the shear stress induced on the rock by the tool, the crack path penetrates beneath the horizontal line and the lower boundary of the chip penetrates below the tangent to the bottom of the groove . This is in agreement with the empirical tests of de Vergeron (1962) and with the numerical predictions by Guo et al (1988) (Fig. 16). In this case, the tool produces at the groove bottom a sequence of small depressions that de Vergeron (1962) observed in the rock both in the laboratory and in the field. These observations help to elucidate the sudden and periodic variations detected in the magnitude of the forces to which the tool is subjected during its action. (Figs. 3, 6) If the

shear strength of the rock is too great, the tool does not produce any chipping and a neutral cutting rake angle is preferable. At the points of contact between tool and rock some initial crushing occurs, from which chipping may result . If there is no chipping then penetration could be diminished and rock breakage only occurs by crushing.

When the mechanical properties of the rock are such that positive cutting rake angles can be adopted, the column of crushed rock to chips is a minimum and consequently the energy efficiency of the machine in the cutting operation is maximized. Obviously, if the strength of the rock is such that not even neutral cutting rake angles represent an acceptable practical solution, then an alternative excavation process should be opted for.

Cutting tool bluntness As shown by Figs. 6a and 6b, thrust, torque and rpm underwent rapid oscillations during drilling with both sharp and blunt bits. This suggests that the cutting action is a discontinuous process, as previously reported by de Vergeron (1962), Valantin (1975) and Fairhurst (1964). The highest peaks in Fig. 6 perhaps correspond to the moment just before the formation of a major chip as observed in the RCSR. Immediately afterwards, the magnitudes of thrust, torque and, in the case of drilling tools, rpm, fall to relatively low values, and then start to build up again before becoming high enough to form another major chip, after minor chips are formed.

From Table 2 it can be seen that there is an obvious increase in the values of specific energy required for drilling with blunt bits. Also cutting with blunt bit reduces the proportion of large chip formation leading to increased dust formation. All this leads to inefficient utilization of cutting energy in the case of cutting with a blunt bit tool.

Major chip formation Generally, three stages of failure process can be identified as shown in Fig. 9. The first stage is defined as initial surface crushing. In this stage, very fine rock fragments or particles are formed on the specimen surface due to the crushing by the wedge tip, applying a very concentrated force to the rock. The second stage starts when small chips form ahead of the wedge tool. At the same time, more fine fragments, like those in the first stage, are formed and relatively deeper penetrations into the specimens are achieved. The third stage is marked by a significantly larger chip ahead of the wedge tool. This major chip is chiefly formed by a curvilinear crack and can be called a major crack that propagates from the near vicinity of the wedge tool tip to the free surface of the specimen. Fig. 17 shows a simplified model of the major chip formation based on the above observations.

Rake Angle Tests conducted have shown that the size of the major chips is inversely proportional to the rake angle. This is in agreement with the numerical modelling predictions (Guo, 1990) as shown in Fig. 18. However, when the rake angle becomes negative, say 7.5^0, no trend of further increase on the major chip size can be observed. This effect is believed to be due to the increase of the contact area between the rock and the tool from surface and the direction of this contact stress becoming inclined downward. Consequently, the major chip formation process is suppressed to some extent.

This study also showed that as the angle of tool attack decreases and the cutting rake angle increases, the areas of finely crushed surfaces tend to increase, resulting in an increase in the energy loss due to friction.

In general, the results of the tests on sandstone specimens are similar to those for concrete specimens. In the numerical modelling, and in many rock-cutting models, only the cutting force F_c was considered. However, significant thrust force F_t is consistently observed in the tests undertaken.

CONCLUSIONS

Integration of the information acquired by applying various different investigative and a numerical modelling techniques led to a better understanding of mechanical rock disintegration under the action of drag picks. Understanding of the correlation of tool geometry and the process of rock fragmentation was characterized by the specific energy involved and the grain size distribution of the debris.

The photoelastic analysis indicated the distinguishing features of the stress fields and, especially, the maximum shear trajectories produced within the rock under the action of a sharp - or blunt wedge drag bit.

When the shear strength of the rock is inferior to the maximum shear stress generated in the rock by the sharp tool operating at a positive rake angle, this cutting mode appears the most energy effective. In effect, both the photoelastic investigation and the numerical model show, or predict, the maximum shear trajectories which penetrate underneath the line of the groove bottom. A crack forms along this trajectory which mainly defines the volume of rock to be removed. The RSCR not only confirmed this prediction but provided evidence that in this case the rock disintegration process occurs in three stages: an initial stage during which the area of the rock surface, in contact with the tool, is so small that the normal stresses generated therein are greater than the compressive strength of the rock and localised failure occurs. The second stage is characterized by detachment of small chips as well as crushing; the third and final stage is the detachment of the major chip (Fig. 2).

Under the test conditions applying herein, the prediction of the numerical model that with decreasing positive cutting rake angle the size of the major chip increases, appears to be confirmed by the results of the tests conducted with the RCSR on sandstone and concrete specimens. When the shear strength of the rock is greater than the maximum shear stresses induced in it by the sharp wedge tool, the resistance of the rock may actually damage the tool. In this case the sharp wedge tool may still be used for rock breakage provided that due care is taken to adequately decrease penetration and set at neutral the cutting rake angle.

ACKNOWLEDGEMENTS

The authors wish to express their thanks to Prof. Marino Dalu for providing the isometric view of the photoelastic set-up. Thanks are also due to Mr Franco Chessa, Technician of the Mining and Mineral Dressing Department of the University of Cagliari and to Mr Ian Laird of the Civil and Mining Engineering Department of the University of Wollongong who fabricated the experimental equipment. Financial support for the work carried out at Cagliari was provided by the Italian

Ministry of University and Scientific Research Project (60%) and that at Wollongong by the NSW Joint Coal Board, Australia.

REFERENCES

AZIZ, N. I., GUO, H., ROSSI, G., ROSSI, R. AND TROIS, P., 1990. Mechanical Rock excavation - Interaction of tools and rock, Proc. 1st Italian-Brazilian Conf. held at the Uni. of Cagliari, Italy, 27-28 Nov. 1990, 99-130. (in Italian)

BOND, F.C., 1952. The third theory of comminution, Mining Engineering, 4, 484-494.

BOUSSINESQ, M.J., 1892. Des perturbations locales que produit au-dessous d'elle une forte charge, repartie uniformement le long d'une droite normale aux deux bords, a la surface superieure d'une poutre rectangulaire et de longueur indefinie posee de champ soit sur un sol horizontal, soit sur deux appuis transversaux equidistants de la charge, Comptes Rendus des Seances Hebdomadaires de l'Academie des Sciences, Paris, 114, 1982, 1510-1516.

EVANS, I., 1958. Theoretical Aspects of Coal Ploughing, Mechanical Properties of Non -metallic Brittle Materials, Interscience Publishers Inc., New York, 451.

EVANS, I. and POMEROY, C.D., 1966. The Strength, Fracture and Workability of Coal (Pergamon Press, Oxford).

FISH, B.R., and BAKER, J.S, 1956. Studies in Rotary Drilling, National Coal Board, MRDE Report No. 209.

FAIRHURST, C., 1964. Discussion of J. Furby " Strain Wave Behaviour in the Percussive drilling process", Trans. Inst. Min. Met.73, 671- 411.

FLAMANT, M., 1892. Comptes. Rendus., 114, 1510. Sur la repartition des pressions dans un solide rectangulaire charge transversalement, Comptes Rendus, etc., 114, 1892, 1465-1468.

GOODRICH, R.H., 1956. High Pressure Rotary Drilling Machines, Proc. 2nd Annual Symp. on Mineral Resources, Missouri University, 25.

GRAY, K.E., ARMSTRONG , F., AND GALTIN C., 1962. Two - Dimensional Study of Rock Breakage in Drag -Bit Drilling at Atmospheric Pressure , A.I.M.E. Trans. 225, 1-96, 1-98.

GUO, H., 1990, Rock cutting studies using fracture mechanics principles, Ph. D. Thesis, Chapter 4, The University of Wollongong, N.S.W., Australia.

GUO, H., STANDISH, P., SCHMIDT. L.C., and AZIZ, N.I., 1988, A Method of Mechanical Efficiency Analysis for Rotary Drag Bits, Second International Conference on Mining Machinery, Brisbane, Australia, pp 322 - 326.

HARTMAN, H.L., 1959. Basic studies of percussion drilling, A.I.M.E. Trans, 214, 68-75.

HERTZ, H., 1881. Hertz's Miscellaneous papers, Ch. 5, London, McMillan.

MAURER, W.C., and RINEHART, J.S., 1960. Impact crater formation in rock, J. Appl. Physics, 31, No. 7, 1247-1252.

NISHIMATSU, Y., 1972. The mechanics of rock cutting, Int J. Roc. Mech. and Min. sci., 9: 261-270.

PAUL, B., and SIKARSKIE, D.L., 1965. A preliminary theory of static penetration by a rigid wedge into a brittle material, A.I.M.E. Trans., 232, 372-383.

PECHALAT, F., 1977. Destruction des roches par les molettes. Industrie minerale-mine, 138-144.

POTTS, E.L.J., and SHUTTLEWORTH, P., 1959. A study of the ploughability of coal, with special reference to the effect of blade shapes, direction of ploughing to the cleat, ploughing speed and the influence of water infusion, Trans. Inst. Min. Engr., London, 117, 520-548.

RANMAN, K.E., 1985, A model describing rock cutting with conical picks, Rock Mechanics and Rock Engineering, 18, 131-140.

RITTINGER, P., RITTER V., 1867. Lehrbuch der Aufbereitungslunde, Berlin, Verlag Ernst und Korn. (in German)

ROXBOROUGH, F.F., 1981, Applied rock and coal cutting mechanics, Workshop Course, Australian Mineral Foundation Inc.

ROXBOROUGH, F.F., 1986. A review of research progress in coal and rock cutting, The Coal Journal, No. 13 pp 37-48.

TEAL, R., 1965. The concept of specific energy in rock drilling, Int. J. Rock. Mech. Min. Sci. 2, 57-73.

VALANTIN, A., 1975. Machine a attaque ponctuelle. Etude de la destruction de la roche. Travail des pics. Industrie minerale-mine, 2-75, 253-265.

de VERGERON, M., 1962. Le probleme des pics des engins d'abattage. Etude des pics de la Marietta Revue de l'Industrie Minerale, 44, No 1, 1-36.

TABLE 2

Specific energy and average mean sizes of fragments

Hole No.	Bit sharp (S) or blunt (B)	Specific Energy (J x 10^7)	Mean Cutting Size (mm)
BH2	S	1.95	
BH3	S	1.31	
BH4	S	1.83	
BH5	S	1.76	0.81
BH6	S	1.85	
BH7	S	1.34	
BH8	S	1.98	
BH9	S	1.70	
BH10	S	1.76	
BH11	S	1.79	
BH12	S	1.93	
BH13	S	1.44	
BH14	S	1.51	
BH15	S	1.31	0.91
BH17	S	1.37	
BH18	S	1.51	
BH19	S	1.72	
BH20	S	1.27	
BBH1	S	1.53	
BBH2	S	3.37	
BBH3	S	2.79	
BBH4	S	3.26	
BBH5	S	2.54	0.56
BBH6	S	2.34	
BBH7	S	3.97	
BBH8	S	4.03	
BBH9	S	2.79	
BBH10	S	3.38	0.51

TABLE 1

Empirical approaches to drag bit cutting.

MODEL	DETAILS	COMMENT
EVANS	$\frac{2\ St\ d\ w\ \sin^{1/2}(\frac{\pi}{2} - \alpha)}{\{1 - \sin^{1/2}(\frac{\pi}{2} - \alpha)\}}$ 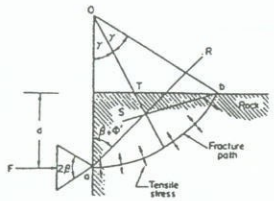	**Failure by tension** S_t = tensile strength of coal W = drag bit width d = cutting depth α = rake angle Ref: EVANS (1958)
POTTS AND SHUTTLEWORTH	$F_c = \frac{2\ S\ d\ w\ \cos(\tau - \alpha)}{\sin(\gamma+\tau+\alpha)}$ 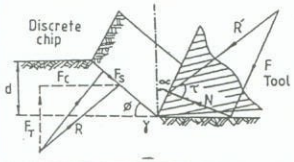	**Failure by shear** S = shear strength γ = angle of shear τ = friction angle Ref: Potts and Shuttleworth (1959)
NISHITMATSU	$F_c = \frac{2\ S\ d\ w\ \cos(\tau - \alpha)\ \cos\phi}{(n+1)\ \{1 - \sin(\phi - \tau + \alpha)\}}$ 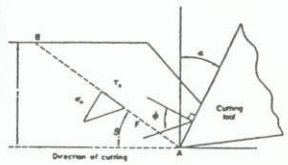	**Failure by shear** ϕ = angle of internal friction of the rock n = stress distribution factor Ref: Nishimatsu (1972)

TABLE 3 Cutting Related Forces for Various Tests

Attack angle (degrees)	Rake angle (degrees)	Test No.	sandstone specimens					concrete specimens				
			Axial force (kN)	Bending force (kN)	Cutting force (kN)	Thrust force (kN)	Resultant force (kN))	Axial force (kN)	Bending force (kN)	Cutting force (kN)	Thrust force (kN)	Resultant force (kN)
67.5	-7.5	1	37.56	7.59	7.48	37.63	38.32	38.54	7.56	7.88	38.53	39.28
		2	39.87	6.16	10.04	39.92	40.34	40.65	9.87	6.56	41.36	41.83
		3	33.45	6.21	7.16	33.92	34.02	40.78	8.65	12.39	41.01	41.9
60	0.0	1	43.56	8.65	9.52	42.05	44.41	43.84	11.24	12.19	43.59	45.26
		2	41.24	9.87	12.07	40.65	42.41	36.18	10.98	8.58	36.82	37.81
		3	46.85	10.42	14.10	45.78	48.00	40.20	10.28	11.20	39.95	41.49
52.5	7.5	1	35.00	12.12	11.69	39.28	37.04	36.32	10.56	13.74	35.25	37.82
		2	32.49	11.30	10.82	32.66	34.40	35.22	11.76	12.11	35.10	37.13
		3	35.77	7.59	15.76	33.00	36.57	24.28	12.25	5.06	26.72	27.20
45	15.0	1	35.77	10.65	17.76	32.82	37.32	35.77	12.12	16.72	33.86	37.77
		2	32.76	13.83	13.39	32.94	35.56	32.49	12.02	14.47	31.47	34.64
		3	37.82	12.50	17.70	35.58	39.83	35.00	11.20	16.83	32.67	36.75
67.5 Blunt tool	-7.5	1	31.80	6.07	6.66	31.72	32.37	32.25	6.07	6.83	32.69	32.82
		2	30.98	7.50	5.02	31.52	31.88	28.45	7.50	5.60	29.85	29.42
		3	26.14	6.33	4.23	26.59	26.90	29.67	6.33	4.04	29.17	30.34

Note: Confining pressure on specimen sides is about 1.0 Mpa - ends unconfined.

TABLE 4 Average cutting related forces

Attack angle (degrees)	Rake angle (degrees)	sandstone specimens					concrete specimens				
		Axial force (kN)	Bending force (kN)	Cutting force (kN)	Thrust force (kN)	Resultant force (kN))	Axial force (kN)	Bending force (kN)	Cutting force (kN)	Thrust force (kN)	Resultant force (kN)
67.5	-7.5	36.96	6.65	8.23	37.16	37.56	39.99	8.69	8.94	40.30	41.00
60	0.0	43.88	9.65	11.90	42.83	44.94	40.07	10.83	10.66	39.95	41.52
52.5	7.5	34.42	10.34	12.76	34.98	36.00	31.94	11.52	10.30	32.36	34.05
45	15.0	35.45	12.33	16.28	33.78	37.57	34.42	11.78	16.01	32.67	36.39
67.5 Blunt tool	-7.5	29.64	6.63	5.30	29.94	30.38	30.12	6.63	5.49	30.57	30.86

Note: Confining pressure on specimen sides is about 1.0 Mpa - ends unconfined.

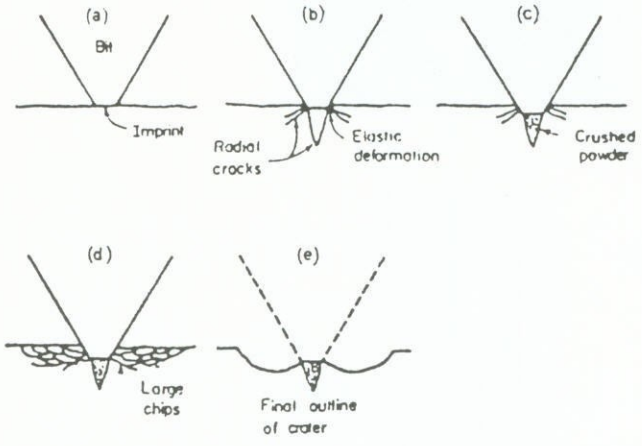

Fig. 1. Sequence of rock failure and crater formation in percussive drilling (Hartman, 1959)

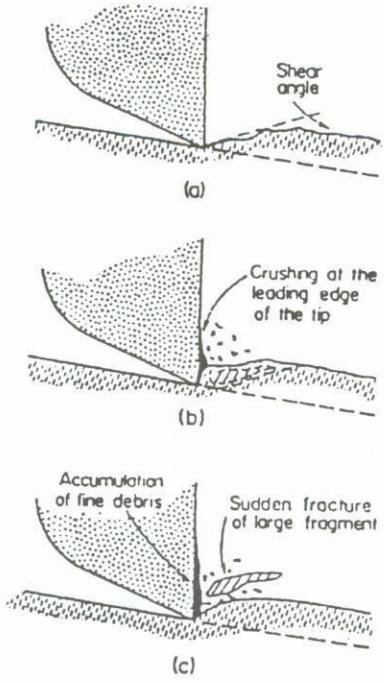

Fig. 2. Drag bit cutting sequence (Fish and Barker, 1956)

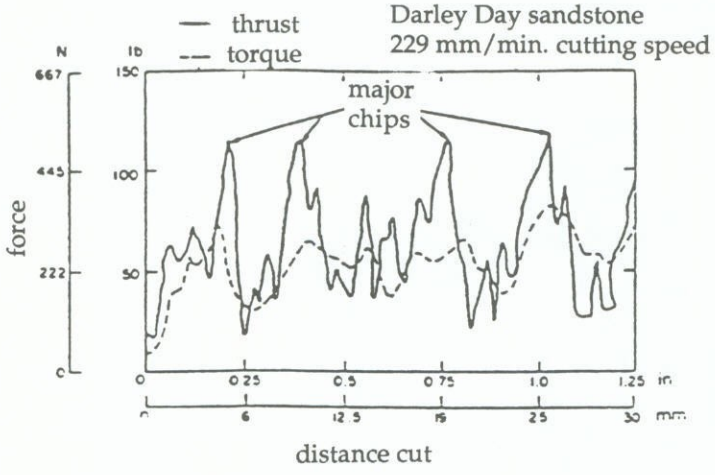

Fig. 3. Drag pick force - displacement curves (after Fairhurst, 1964)

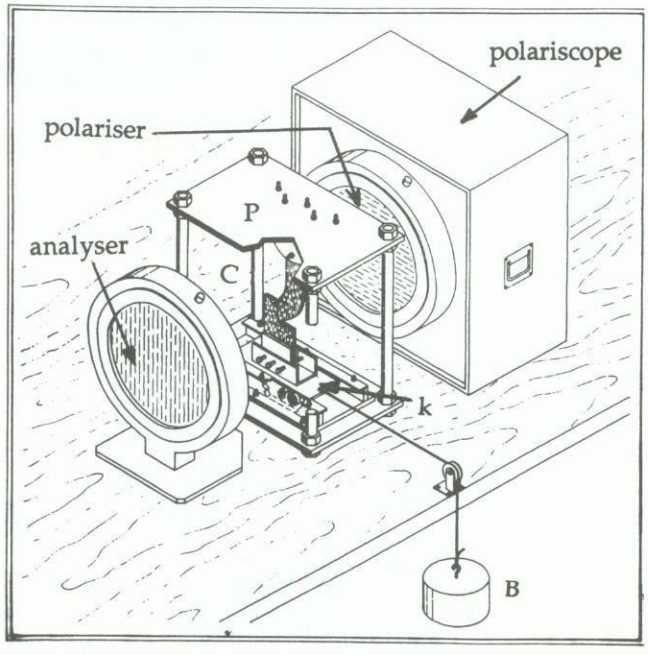

Fig. 4. General set-up of photoelasticity apparatus

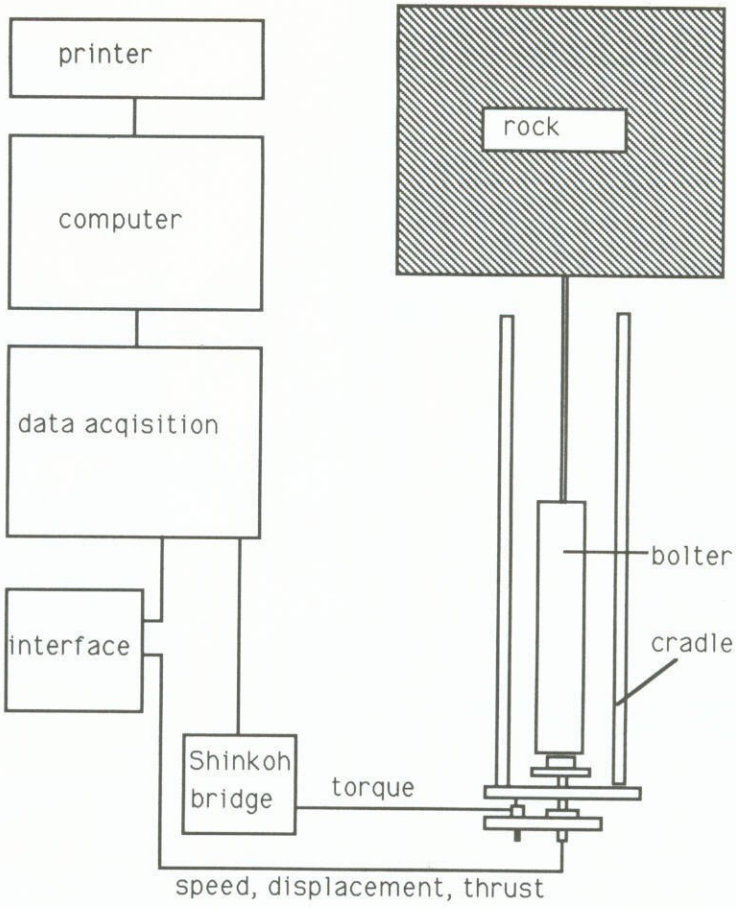

Fig. 5. System diagram of computer controlled data acquisition system of roof bolting set-up

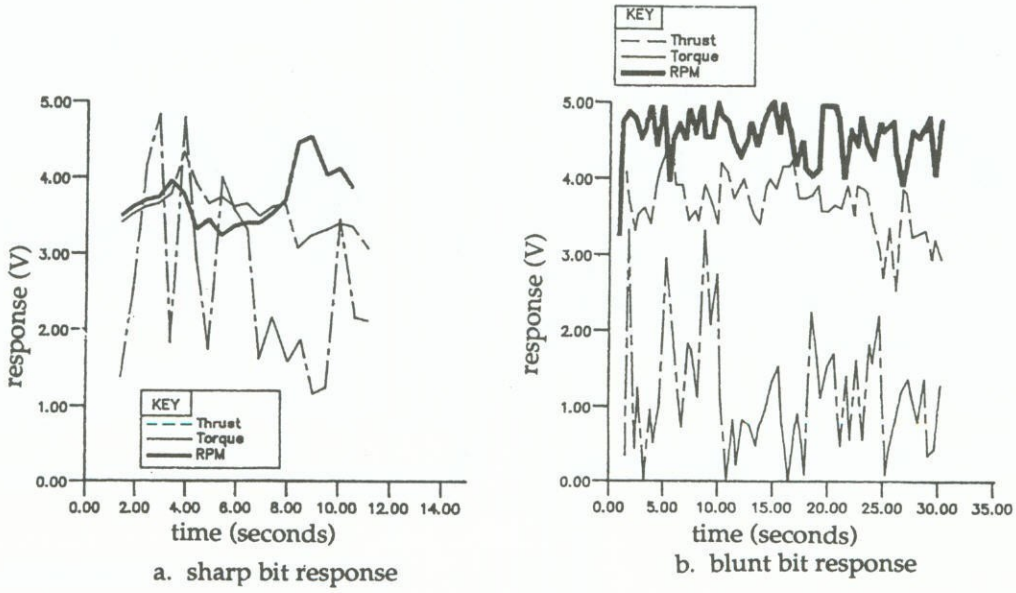

Fig. 6. Drilling parameter output signals.

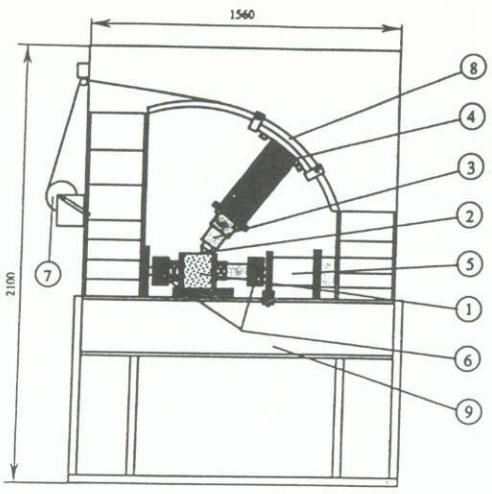

Fig. 7. Rock cutting simulation rig.

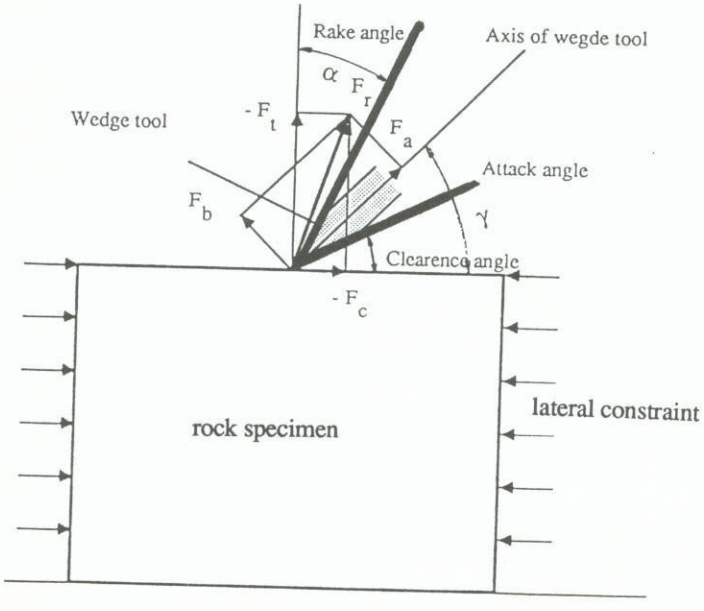

Fig. 8. Force system and parameters involved in cutting.

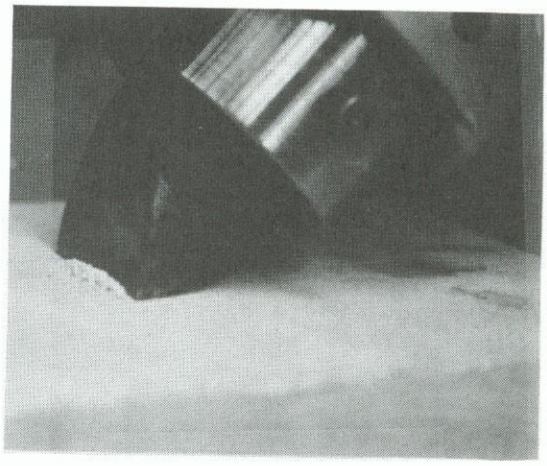

(a) initial surface crushing

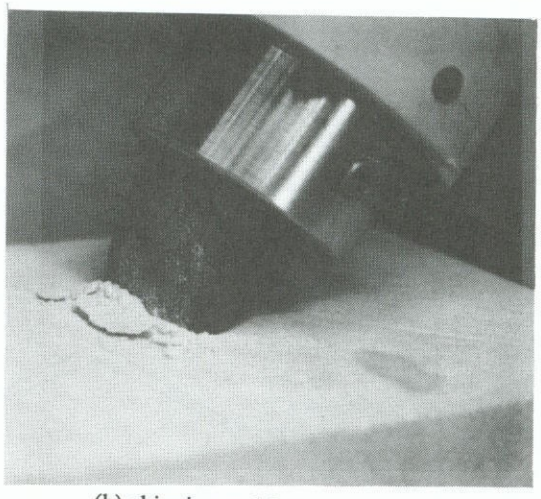

(b) chipping and further crushing

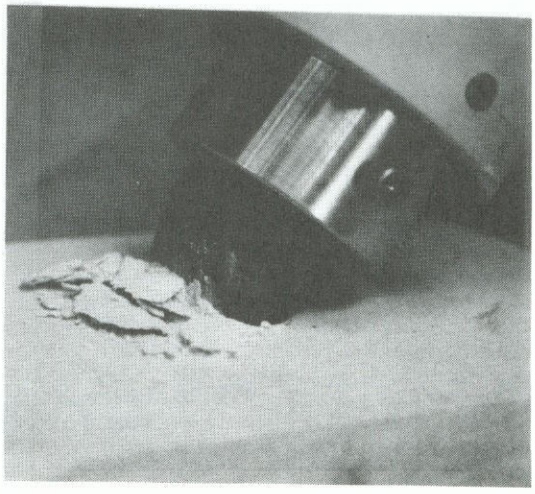

(c) major chip formation

Fig. 9. Progressive failure stages in sandstone.

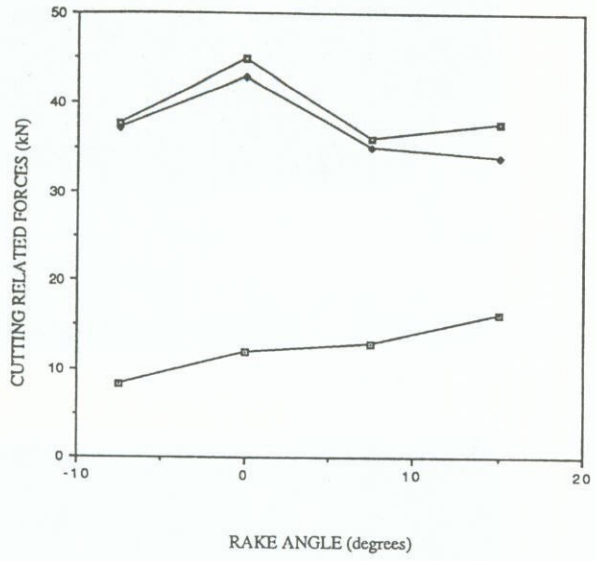

(a) Rake angle effect on cutting for sandstone specimens

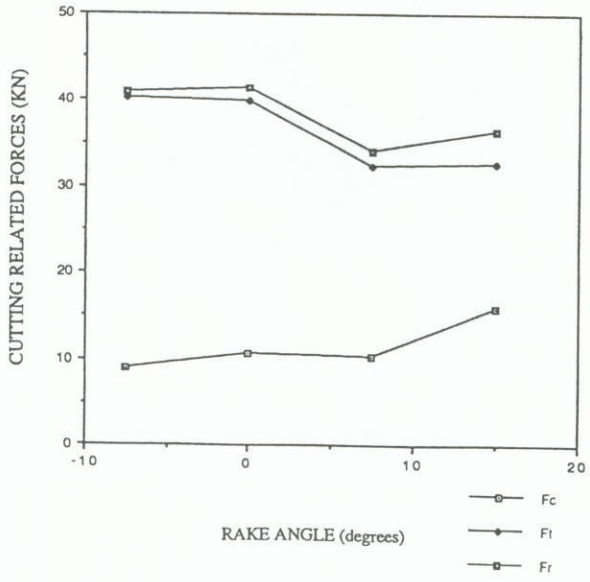

(b) Rake angle effect on cutting for concrete specimens

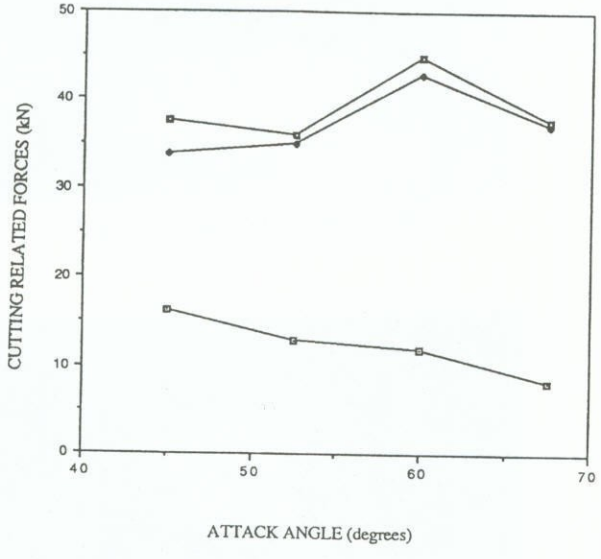

(c) Attack angle effect on cutting for sandstone specimen

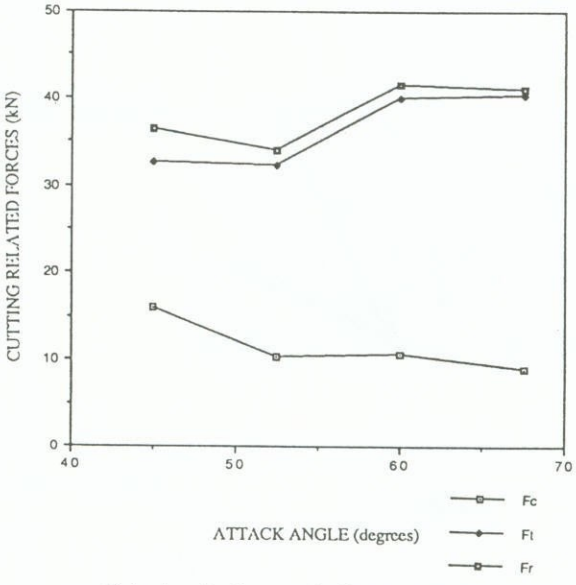

(d) Attack angle effect on cutting for concrete specimens

Fig. 10. Effects of attack angle and rake angle on cutting related forces in sandstone and concrete.

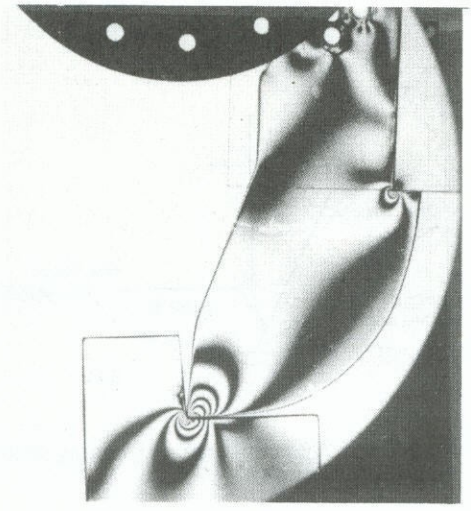

Fig. 11. Isochromatics produced in the rock model by the action of a drag pick (model A) with a positive rake angle

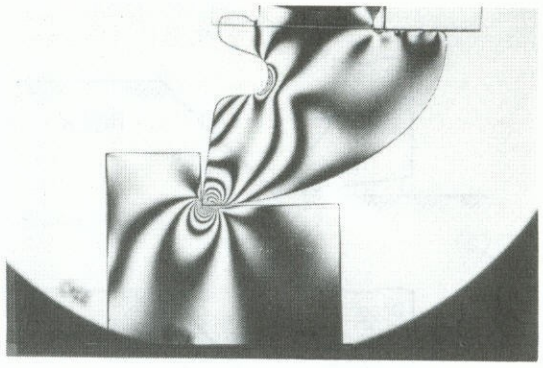

Fig. 12. Isochromatics produced in the rock model by the action of a drag pick (model B)with a positive rake angle

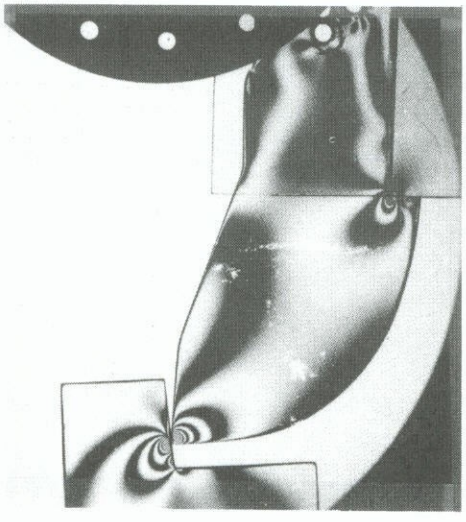

Fig. 13. Isochromatics produced in the rock by the action of a drag pick acting on a point of the rock higher than the bottom of the groove. Positive rake angle.

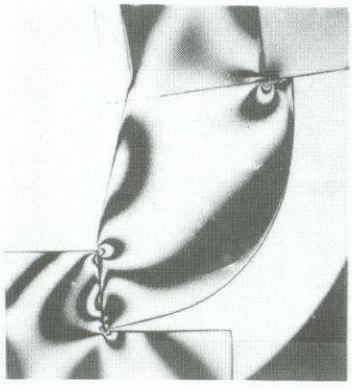

Fig. 14. Isochromatics produced in the rock model by the action of a drag pick acting with zero rake angle.

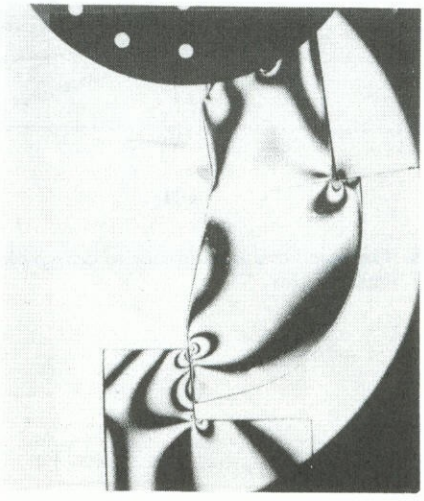

Fig. 15. Isochromatics produced in the rock model by the action of a drag pick with zero rake angle acting at a point of the rock higher than the groove bottom.

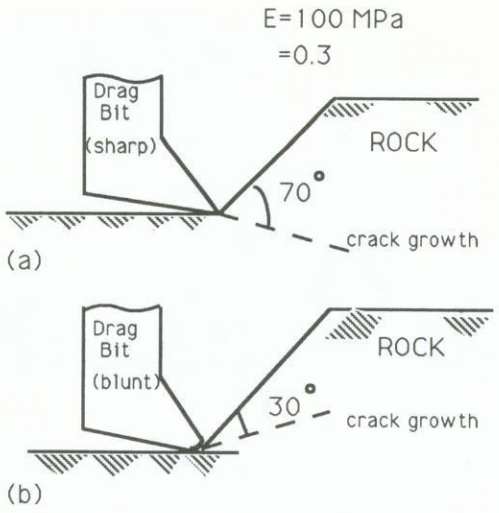

Fig. 16. Predicted crack path for (a) sharp bit and (b) blunt bit (after Guo et al., 1988)

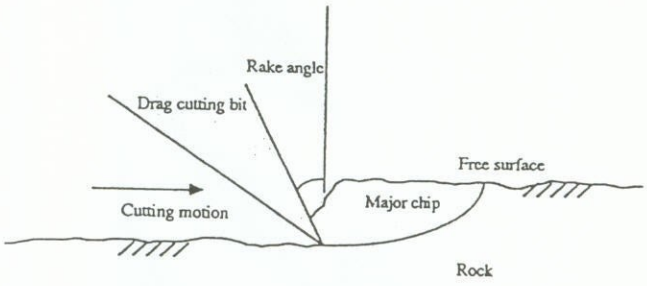

Fig. 17. Simplified diagram of drag pick cutting action for major chip formation

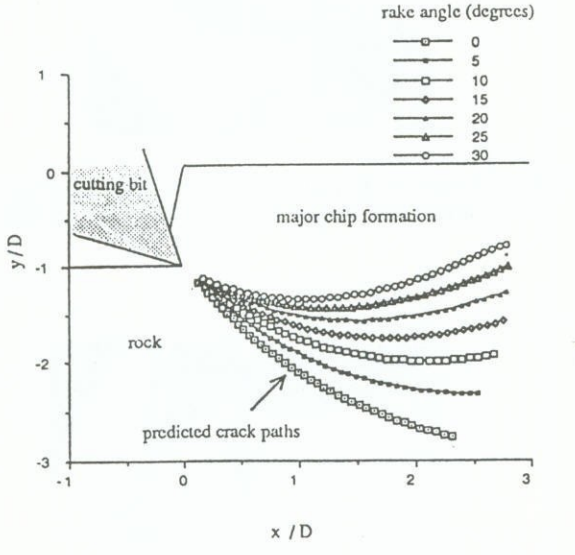

Fig. 18. Predicted crack paths due to drag picks at various rake angles.

10th INTERNATIONAL CONFERENCE ON GROUND CONTROL IN MINING

ROOF SOUNDING DEVICE -- A LOOSE ROCK DETECTOR

Richard C. Repsher, *Geophysicist*

Denver Research Center
U. S. Bureau of Mines
Denver, Colorado

ABSTRACT

The U.S. Bureau of Mines has developed a method and device designed to detect loose rock material in underground mines. The technology is designed to be an aid to mine workers in detecting hazardous roof conditions in underground mines which can complement or replace the traditional roof sounding techniques where the miner relies on experience to determine whether rock conditions are sound. The leading cause of accidents and fatalities in underground mines is falls of loose rock pieces or rock slabs from the mine roof. The device is an electronic roof sounding device that acoustically determines the integrity of mine rock.

In previous research the Bureau of Mines found that loose rock, when impacted, vibrates at a much lower frequency than intact rock material. A major problem in determining rock stability using this technique has been the repeatability of the impact signal. This difficulty has been greatly reduced in the current design by measuring the power spectra contained in two separate frequency bands of the signal produced by striking the rock in question. The ratio of the energy contained in each band is computed. This process minimizes any striking force differences, producing accurate, repeatable results for solid rock as well as loose, drummy material. The prototype has been successfully tested in a variety of underground environments including coal, uranium, molybdenum, silver, and salt. The technology has been investigated by the U.S. Mine Health and Safety Administration and the Department of Energy for use in detecting detached tunnel lining areas in nuclear repositories. The paper will discuss the technique, applicable results, and future applications.

INTRODUCTION

Roof falls remain the most significant factor in accidents and fatalities in underground coal mines. Under U.S. mining law, the roof must be tested for stability before any mining may commence in a new work day. The normal method to test stability is to "sound" the roof by tapping the roof rock in question to listen and feel for pieces of loose rock material. As the average age of underground miners becomes younger, less experience is available to adequately determine roof conditions. The electronic "roof sounding device" has been designed to minimize the need for human interpretation of standard techniques. He/she may use the equipment reliably, without concern for mining conditions, to accurately locate and determine hazardous material in the roof of underground mines.

TECHNICAL CONCEPT

Many scientists have attempted to determine loose mine roof material using acoustic means. (2,3,4) A significant problem encountered in consistently identifying loose material is to have a constant input energy into the rock. When the input signal is inconsistent, the resulting data cannot be evaluated consistently. The goal of achieving a uniform acoustic signal input to locate areas of instability has remained elusive. The U.S. Bureau of Mines has developed a new method to measure rock stability using innovative acoustic technology. The principle is to measure the energy content (power spectra) of the return signal from the sounding process in separate frequency bands. A ratio of these numbers is made by the instrument, providing a measure of detachment, which is related to the stability of roof rock (1). Loose, or drummy material in the roof is more likely to be detached from the mine structure and prone to fail. For example, in roof material that is solid, and contiguous, the input energy from the tapping of the roof dissipates into the rock mass, resulting in similar energy in each frequency band. Conversely, when a loose, or detached, rock block is sounded, the imparted sounding signal is confined to the loose rock, reflected off the parting creating the loose piece. This reflected

energy remains in the rock block, resulting in enhanced frequency data value in the lower frequency band (2). A ratio of the power spectra value (energy) contained in each band is calculated within the instrument and displayed on the front panel. The unitless value displayed characterizes solid and loose material, providing a measure of rock detachment and, therefore, the stability of roof material.

PRINCIPLES OF OPERATION

Field surveys can be carried out by nontechnical individuals. The instrumentation consists of a sensor, instrument, pole for sensor placement, and connecting cables.

The sensor is mounted on a spring-loaded, telescoping pole, which, in turn, is mounted on the rock piece to be examined. (Figure 1)

Figure 1 - In-mine test for rock stability, showing sensor placement, tapping of rock in question are instrument.

The rock is tapped with a sounding bar or walking stick. The device automatically measures the energy contained in two frequency bands (500 to 1,000 Hz and 3,000 to 3,500 Hz) resulting from the impact of the rock in question. A computation of the ratio of energy content between the two bands is made, the result is a measure of the degree of detachment for the rock in question. Several generations of the device have been developed by the Bureau of Mines and each has slightly different features for ease of use. The prototype device described by Hanson (1), contains a sample-and-hold feature, allowing the electronics to turn off at the correct time. The Bureau of Mines also developed a second generation piece of equipment that contained a feature allowing the device to clear itself of the original reading upon another tapping for a different test.

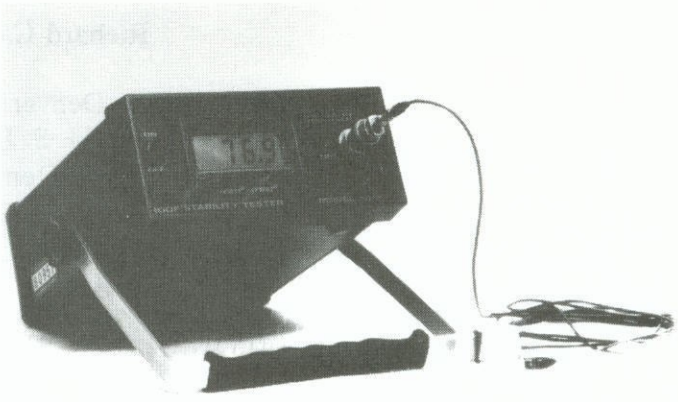

Figure 2 - Second generation roof sounding device developed for the Bureau of Mines.

The prototype roof sounding device is portable, battery powered, and weighs less than 3 lb. The dimensions are approximately 6 by 9 by 3 in. The second generation device was packaged to more easily facilitate field studies. The device has a carrying handle, has been reduced in size to approximately 3 by 6 by 2 in and weighs less than a pound. The reduction in weight is achieved through use of smaller batteries, use of printed circuits, and reduced size of the enclosure. (Figure 2)

PRELIMINARY FIELD

Operation

Laboratory and field research done during the research phase indicated the optimum frequency bands for data analysis were:

High band-pass filter (3,000 to 3,500 Hz)
Low band-pass filter (500 to 1,000 Hz)

In testing the roof for stability, the energy source for the input signal can be any "sounding" bar material. A typical mine company employee uses a sounding bar with a blade, and, Mine Health and Safety Administration (MSHA) mine inspectors often use a walking stick with a rounded, metal head. Either means is adequate, but the rounded head of a walking stick provided the most consistent results.

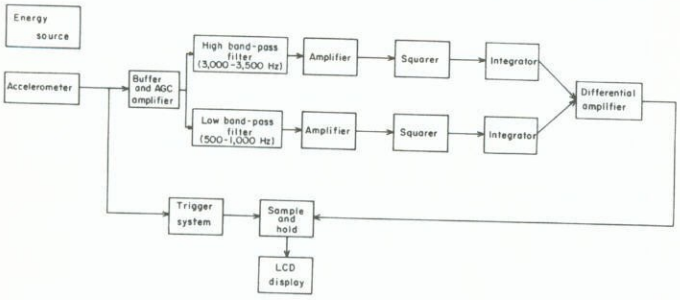

Figure 3 - Block diagram of system operation. (After Hanson, 1985)

The block diagram (Figure 3) indicates the electronic package used to gather and display the data on the prototype device. The device generally operates in the following manner:

1. The signal is detected by an accelerometer.
2. Signal is input to a buffer and Automatic Gain Control Amplifier (AGC).
3. The amplified signal is split into the two frequency band filters.
4. The filter outputs are amplified, squared, and integrated.
5. The integrated signals are input to a differential amplifier, creating a voltage proportional to the difference in power contained in the frequency bands.
6. This voltage is input to a sample-and-hold circuit and displayed on a low-power liquid crystal display.

The difference in energy (power) between the low- and high-frequency bands gives a number which is reflective of the stability of the block. During the actual in-mine testing, solid rock typically had a response between zero and +10. Loose rock blocks typically had values between 20 and 40, although the numbers varied depending on the rock type being tested. The input signal can be a slight tap of the block in question, which provided consistent results with different input energies. The use of this method minimizes the effect of various impact levels on the rock material, which had been a significant problem in the past.

FIELD TESTING

A number of field experiments were conducted with the prototype device, which indicated a predominance of low-frequency energy in loose or drummy rock. (1) Tapping the rock produces an input signal with both low and high frequencies. Through laboratory and field studies of known conditions, a loose block is more decoupled than normal. Low frequencies which normally travel into the rock mass are reflected, producing enhanced low-frequency energy. In the field, a loose block of material is potentially dangerous and prone to falling. Conversely, a solid block will dissipate all frequency bands and will have a more equal value. (2) Field tests using the prototype device were made in various mine geological environments, including coal measure rocks, uranium- bearing sediments, salt, and hard rock mines, including silver and molybdenum. Figure 4 displays spectral data gathered from

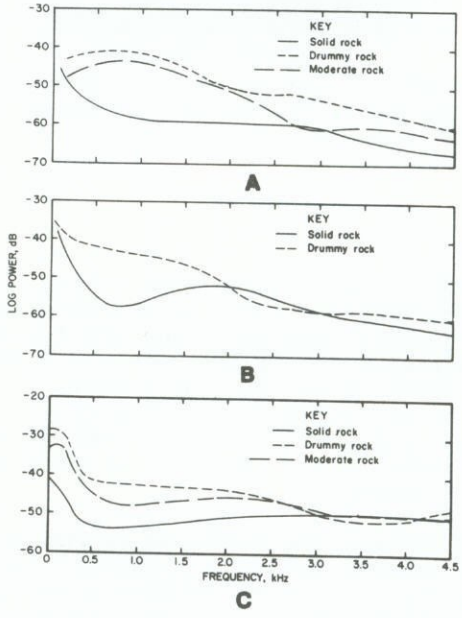

Figure 4 - Power spectra for various rock types connected in underground mine testing. (After Hanson, 1985)
(a) Henderson Mine, AMAX, (b) CSM Experimental Mine, (c) L.S. Wood Mid Continent Resources

experiments at the Colorado School of Mines Experimental mine (silver) near Idaho Springs, Colorado, the AMEX Mine (molybdenum) near Henderson, Colorado, and the Mid-Continent Resources, Inc., L.S. Wood #3 Mine (coal) near Redstone, Colorado. Despite different lithologies at these sites, the data indicated significant changes in the low-frequency bands between drummy and solid rock. Although the data have not been published, the same trends were noted in Louisiana salt domes, tested for fracturing of roof rock due to overblasting.

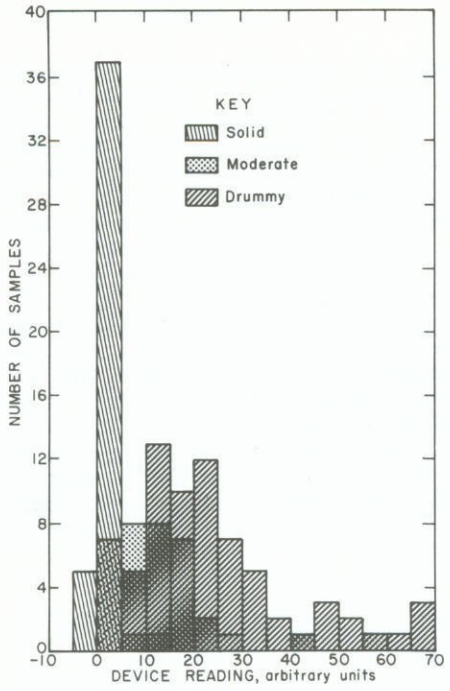

Figure 5 - Device readings obtained during in-mine testing during the research phase of the project (After Hanson, 1985).

This trend is more evident when the device readings obtained in all mine environments are plotted together (Figure 5). From this figure, a low device reading is indicative of more uniform values of energy (power spectra) in both frequency bands, representative of solid material. A high reading means a predominance of lower frequency energy, indicative of loose or drummy rock material.

Several tests of the instrument by various government agencies have been conducted. The results of the testing are confidential to the parties involved, and the test results will be reported in general terms. Reports have been written to the Bureau of Mines, but the results have not been published.

MSHA investigated the device in the lead-zinc mining district of the central United States. Their testing of the device and technology provided readings which indicated a difference between known solid and drummy material. Their conclusion was, the device, when used by trained individuals, was capable of delineating areas of drummy roof rock in the mines investigated.

CANMET, the Canadian mining research organization, evaluated the technology in deep uranium mines in Canada. The device worked well in this environment. Drummy rock was easily detected, and solid rock provided consistent readings. Concern was expressed for the durability and reliability of the device. Suggested improvements in the electronics were provided. These concerns will be addressed later in the paper.

The Department of Energy (DOE) evaluated the device for use in underground waste repositories. Again, the device provided readings indicative of rock conditions, with some difficulties with reliability. Loose rock material was detected. Also investigated was the possibility of evaluating tunnel lining material at repository sites with the device. Shotcrete was used to line several tunnel openings at the BWIPP (Basalt Waste Isolation Pilot Plant) site at Hanford, Washington. The investigation was to detect where the lining material had detached from the wall rock, producing a potentially hazardous ground control condition. The results from testing known conditions were not consistent. In certain areas the device provided data defining suspect areas of shotcrete separation for the intended purpose, and in other cases, the device did not appear to be successful. Another application investigated was to detect areas of the tunnel lining with very thin application of the shotcrete. The results of this study were inconclusive. Differing rock types have optimum frequencies for determining rock conditions. Softer, less dense rocks, have enhanced information in lower frequency bands (i.e. 200-700 Hz rather than 500- 1,000 Hz). One feature of the Bureau of Mines prototype device is the capability to change the values of the frequency bands the energy (power spectra) is monitoring. By changing the ranges of the low- and high-frequency band pass filters, the results better defined the conditions present, for both location of detached tunnel lining material and detecting thin areas of shotcrete application. The Department of Energy determined through their studies, a device could be constructed with the different frequency bands, better capable gathering data for their needs. The Department of Energy was notified that a device could be built by themselves, for their use, as long as no production of units for sale was involved. The Bureau of Mines has received no further information as to any units being built.

In addition, the technology was demonstrated to the Department of Energy in a bedded salt environment. Data from known unstable roof conditions were conclusive. The device readings were consistent over several tests at different times at the same site, clearly indicating reliability in detecting loose material. Information from roof testing of unknown conditions provided data indicating loose material in areas where none were expected. The roof had deteriorated with time, and the technology was capable of detecting the conditions. The device used had in fact been developed for laboratory use and was not in a field-ready condition. As a result of this testing, the technology is being refined by Sandia National Laboratory. State-of-the-art electronic components will be used, and packaging will be developed for in-mine use, with the thought of deploying the technology at

underground sites for the Department of Energy.

The Bureau of Mines also responded to a request to evaluate the device in underground salt domes to detect overbreak from blasting during the mining cycle. If overbreak from blasting occurs in the roof, a dangerous condition develops. In future bench development, the roof height exceeds 90 feet. If loose rock material were to fall, equipment could be extensively damaged, and even a small piece of rock from that height would be fatal to an individual. In-mine testing indicated the technique could detect overbreak, or areas of detached rock material several inches thick. In addition, pillar ribs were tested for possible spalling. In known cases of pillar material separation, the device proved capable of detecting slabs up to 6-ft thick.

LIMITATIONS OF THE TECHNOLOGY

The device and technology can only detect the presence of the first parting of material. The imparted energy will not pass through an open fracture. Any loose material past the first break, or parting, cannot be detected. In the majority of cases this is not a concern, but in the case of overbreak, or multiple partings, a false sense of security could result from a misunderstanding of the capabilities of the equipment. The equipment will not locate the parting, the thickness of the loose, detached material, or the extent of the detached material. The technology will only indicate whether a piece of material is "drummy" and detached from the structure. This understanding should be made clear to anyone using the technology. The technique has been successfully used in several underground mining environments, and its limitations must be understood before incorrect conclusions are drawn.

ELECTRONIC DESIGN

The prototype design contains analog signal circuitry. At the time the technique was being developed, digital electronics was an emerging field and not implemented for this application. Digital circuitry would be an improvement in the design of this instrument. Currently, the Bureau of Mines is not developing future designs. The technique has been shown to be technically correct and feasible for use in the mining industry. Future development of the technology would conceivably be done by private industry.

A concern expressed during evaluation of the device by the various parties is packaging of the original prototype equipment. This device was a research-grade instrument, and the electronics were "breadboarded" for a laboratory environment. This piece of equipment had extensive shipping and handling between evaluation sites. Some inconsistencies in operation could be expected with a prototype device with this generation of electronics and packaging. Although the interest in the developed technology was sincerely appreciated, the Bureau of Mines had concluded the research efforts and did not assemble a revised unit for extensive field trials. An effort to design and assemble a field unit would be the next logical step in the development of a commercially available unit for use in the mining industry.

The Department of Energy is addressing changes in circuit design, electronic components and packaging for in-mine use, and is scheduled to assemble upgraded units and provide the Bureau of Mines with prototypes during the summer of 1991. In addition to improved electronics, the frequency bands to be monitored will be adjustable to allow optimum use of the technique in a variety of underground environments. The higher the elastic constants of the material, the higher the frequency range of the lower two bands should be. The testing in underground salt proved that the frequency detection of the lower band should be approximately 250 to 750 Hertz. For harder, brittle, more dense material (hard rock mines), the lower frequency band should be 500 to 1,000 Hertz. The frequency range for the upper band can remain 3,000 to 3,500 Hertz, independent of the medium to be tested. The best range for frequency bands can be determined with in-mine testing.

CONCLUSIONS

A significant amount of evidence, compiled through laboratory and field studies, indicates the new technology of measuring power spectra in separate frequency bands can be used to detect loose roof and rib rock material in underground mines. The use of energy content in frequency bands is a new method to determine hazardous roof conditions. The product is not in a final or marketable state as yet, but this should have no bearing on the applicability of the technique. Additional work should be conducted by the mining industry to assess all uses of the technology.

ACKNOWLEDGMENT

The key effort in this research was accomplished by David R. Hanson, who researched acoustic methods to determine rock stability, developed the new acoustic method, and performed the majority of the field testing. Mr. Hanson is currently enrolled in a Doctoral Program with the University of Colorado, Boulder, Colorado. During his educational pursuits Bernard Steblay continued to improve system performance, field testing, calibration, and technology transfer.

BIBLIOGRAPHY

1. Hanson, D.R. Rock Stability Analysis Using Acoustic Spectroscopy. BuMines RI 8950, 1985, 21 pp.

2. Summerfield, P.N. A Study of the Air and Rock Vibrations Produced by Impact Testing of Mine Roof. BuMines RI 5251, 1956, 37 pp.

3. Palmer, E.P., and J.B. Czirr. Spectral Analysis of Coal Mine Roof Vibrations. Min. Eng. v. 34, no.10, Oct. 1982, pp. 1477-1479

4. Allison, H., and R.D. Lama. Low Frequency Sounding Technique for Predicting Progressive Failure in Rock. Rock Mech., v. 12, 1979, pp. 79-97.

ADVANCED SURVEYING METHOD FOR MEASURING ROOF CONVERGENCE

M. Zaki Rashad, *Associate Professor*
H. Ali El-Sageer, *Lecturer*

Mining & Metallurgical Department
Assiut University
Assiut, EGYPT

ABSTRACT

In this paper, if three slant distances are measured from three given points of known coordinates to an unknown point, the position of this point (X, Y, and Z coordinates) can be determined. A computer program was designed for observing the movement of a point in the roof in Abu–Tartour mine (western desert, Egypt) to measure the convergence. This method, for general using, is very fast and can be applied without any restrictions.

INTRODUCTION

The underground cavity artificially created by extraction of mineral, removes the natural support from the overlying strata. So, successive layers of rocks over the mine working bend under the influence of gravity forming roof convergence. It can reach the earth surface leading to the so called mining subsidence. Strata movement originates and begins at the mining horizon. The roof settlement which takes place at that horizon is the starting point for calculating convergence and consequently subsidence in successively higher strata. Many calculation procedures rest on model assumptions such as elastic bending of a slab, or elastic movement in a loose rock medium, or rheological flow in a Kelvin body. Empirical approximation procedures are resting on survey observations and dispensing with any similarity to a mechanical model.

Convergence should be used as a starting point for subsidence calculations only where the floor heave is relatively slight. The question here is, what is the accuracy of the various methods and which is the best of them to be employed and adapted to the particular strata and extraction conditions. More information about the strata movement, ground subsidence, and the different methods of calculations can be found by Aynsley (1961), Berry (1963), Hardy (1978), and Kratzsch (1983).

With electronic distance–meters, air photos, and computers, there is no doubt that changes in the positions of points in the ground can be measured and worked out very rapidly. In this research, we tried to determine the three components of the movement of a point p (X, Y, and Z) by using the cartesian coordinates of three fixed stations and the slant distances from these stations to the moving p as shown in Fig. 1. A computer program was designed for this purpose. This method, for a general use, is very fast and can be applied without any restrictions.

MATHEMATICAL PRESENTATION OF THE PROBLEM

Let three points p_i (X_i, Y_i, Z_i) with $i = 1, 2, 3$ be given, and let p (X, Y, Z) be an unknown point, from which D_i the straight lines to these points are given too, see Fig. 1. It is required to find out the coordinates of the point p (X, Y, Z). In Figure 1, the sides S_i and the angles A_i of the triangle $p_1p_2p_3$ can be expressed in terms of the given coordinates. With p_1 as the origin let us establish a rectangular local system of coordinates u, v, w such that (Lourila, 1985):

1. The u-axis unit vector is:

$$i = s_3 / s_3 \qquad (1)$$

2. An auxiliary unit vector $\bar{j}$ is:

$$\bar{j} = s_2 / s_2 \qquad (2)$$

3. The W-axis unit vector is:

$$k = (i * j) / \sin A \qquad (3)$$

4. The v-axis unit vector is:

$$j = k * i \qquad (4)$$

The auxiliary vector $\bar{j}$ is defined by its direction cosines as (Rees, 1969):

$$\bar{l}_2 = (X_3 - X_1) / s_2 \quad (5)$$
$$\bar{m}_2 = (Y_3 - Y_1) / s_2 \quad (6)$$
$$\bar{n}_2 = (Z_3 - Z_1) / s_2 \quad (7)$$

So, the direction cosines of the local system unit vectors are given as (Rees, 1969):

for_i
$$l_1 = (X_2 - X_1) / s_3 \quad (8)$$
$$m_1 = (Y_2 - Y_1) / s_3 \quad (9)$$
$$n_1 = (Z_2 - Z_1) / s_3 \quad (10)$$

for_k
$$l_3 = (m_1.\bar{n}_2 - n_1.\bar{m}_2) / \sin A_1 \quad (11)$$
$$m_3 = (n_1.\bar{l}_2 - l_1.\bar{n}_2) / \sin A_1 \quad (12)$$
$$n_3 = (l_1.\bar{m}_2 - m_1.\bar{l}_2) / \sin A_1 \quad (13)$$

for_j
$$l_2 = (m_3.n_1 - n_3.m_1) \quad (14)$$
$$m_2 = (n_3 l_1 - l_3.n_1) \quad (15)$$
$$n_2 = (l_3.m_1 - m_3.l_1) \quad (16)$$

In the proposed local system of Fig. 1, coordinates of the given points are:

	u	v	w	
p_1	0	0	0	(17)
p_2	s_3	0	0	(18)
p_3	$s_2\cos A_1$	$s_2\sin A_1$	0	(19)

and the unknown point p satisfies the following equations:

$$u^2 + v^2 + w^2 = D_1^2 \quad (20)$$
$$(u-u_2)^2 + v^2 + w^2 = D_2^2 \quad (21)$$
$$(u-u_3)^2 + (v-v_3)^2 + w^2 = D_3^2 \quad (22)$$

The roots of these three equations are:

$$u = (u_2^2 + D_1^2 - D_2^2) / 2u_2 \quad (23)$$
$$v = (s_2^2 + D_1^2 - D_3^2 - 2u_3.u) / 2v_3 \quad (24)$$
$$w = (D_1^2 - u^2 - v^2)^{1/2} \quad (25)$$

The coordinates of p in the global system are the projection of:

$$op = op_1 + u.i + v.j + w.k \quad (26)$$

Finally :

$$X_p = X_1 + ul_1 + vl_2 + wl_3 \quad (27)$$
$$Y_p = Y_1 + um_1 + vm_2 + wm_3 \quad (28)$$
$$Z_p = Z_1 + un_1 + vn_2 + wn_3 \quad (29)$$

This procedure is very general and applicable without any restrictions. Also, the solution is circular, i.e., it is possible to recompute the coordinates in three different ways with the origin of the local system at p_1, p_2, or p_3 as a check if necessary.

PRACTICAL APPLICATION

We tried to apply that method to measure the roof convergence in Abu–Tartour mine. At first, the cartesian coordinates of three selected underground stations (p_1, p_2, and p_3) were calculated and the slant distances (D_1, D_2, and D_3) from these points to an unknown point p in the roof are measured. Then, the point p is moved to five different positions p_1^*, p_2^*, p_3^*, p_4^*, and p_5^* and the corresponding slant distances were measured for each position.

The three dimensional positioning of p^*, p_1^*, p_2^*, p_3^*, p_4^*, and p_5^* is the aim of this work, so a computer program was designed. The input of the program is the coordinates (X, Y, and Z) of the three fixed underground stations on the floor of the mine and the slant distances from these points to the unknown point at the different stages of convergence. At first, the computer calculates the three sides of the bottom triangle $p_1p_2p_3$ and its angles as follows:

$$s_i = \sqrt{((X_i - X_{i-1})^2 + (Y_i - Y_{i-1})^2 + (Z_i - Z_{i-1})^2)} \quad (30)$$

$$A_i = \cos^{-1} ((s_{i-1}^2 + s_{i+1}^2 - s_i^2) / (2 s_{i-1})(s_{i+1})) \quad (31)$$

Then, the equations from 1 to 29 are applied to give the required coordinates.

The different steps of calculations are the results of the computer program for six input cases are listed as follows, taking into consideration the coordinates of the point P are X_4, Y_4, and Z_4:

THE GIVEN DATA
The first position

1) THE COORDINATES OF THE THREE DATA POINTS

X	Y	Z
303454.679	522893.351	409.981
303445.594	522900.745	409.586
303451.422	522881.588	409.425
303454.679	522893.351	409.981

2) THE THREE SLANT DISTANCES

D(1)	D(2)	D(3)
6.960	15.600	5.780

THE COMPUTATION STEPS

1) LENGTH OF SIDES

S(1)	S(2)	S(3)
20.025	12.218	11.720

2) THE ANGLES OF THE TRIANGLE

A(1)	A(2)	A(3)
1.981	0.594	0.566

3) THE AUXILIARY VECTOR

l	m	n
-0.267	-0.963	-0.046

4) THE DIRECTION COSINES

L	M	N
-0.775	0.631	-0.034
-0.628	-0.775	-0.064
-0.067	-0.029	0.997

5) THE LOCAL COORDINATES

U(2)	U(3)	U(4)
11.720	-4.878	-2.455

V(3)	V(4)
11.202449	6.265000

W(4)
1.778

THE RESULTS

X(4)	Y(4)	Z(4)
303452.528	522886.893	411.435

THE GIVEN DATA
The second position

1) THE COORDINATES OF THE THREE DATA POINTS

X	Y	Z
303454.679	522893.351	409.981
303445.594	522900.745	409.586
303451.422	522881.588	409.425
303454.679	522893.351	409.981

2) THE THREE SLANT DISTANCES

D(1)	D(2)	D(3)
6.920	15.580	5.550

THE COMPUTATION STEPS

1) LENGTH OF SIDES

S(1)	S(2)	S(3)
20.025	12.218	11.720

2) THE ANGLES OF THE TRIANGLE

A(1)	A(2)	A(3)
1.981	0.594	0.566

3) THE AUXILIARY VECTOR

l	m	n
-0.267	-0.963	-0.046

4) THE DIRECTION COSINES

L	M	N
-0.775	0.631	-0.034
-0.628	-0.775	-0.064
-0.067	-0.029	0.997

5) THE LOCAL COORDINATES

U(2)	U(3)	U(4)
11.720	-4.878	-2.452

V(3)	V(4)
11.202449	6.357800

W(4)
1.204

THE RESULTS

X(4)	Y(4)	Z(4)
303452.505	522886.840	410.856

THE GIVEN DATA
The third position

1) THE COORDINATES OF THE THREE DATA POINTS

X	Y	Z
303454.679	522893.351	409.981
303445.594	522900.745	409.586
303451.422	522881.588	409.425
303454.679	522893.351	409.981

2) THE THREE SLANT DISTANCES

D(1)	D(2)	D(3)
6.850	15.520	5.450

THE COMPUTATION STEPS

1) LENGTH OF SIDES

S(1)	S(2)	S(3)
20.025	12.218	11.720

2) THE ANGLES OF THE TRIANGLE

A(1)	A(2)	A(3)
1.981	0.594	0.566

3) THE AUXILIARY VECTOR

l	m	n
-0.267	-0.963	-0.046

4) THE DIRECTION COSINES

L	M	N
-0.775	0.631	-0.034
-0.628	-0.775	-0.064
-0.067	-0.029	0.997

5) THE LOCAL COORDINATES

U(2)	U(3)	U(4)
11.720	-4.878	-2.414

V(3)	V(4)
11.202449	6.380630

W(4)
0.619

THE RESULTS

X(4)	Y(4)	Z(4)
303452.500	522886.863	410.269

THE GIVEN DATA
The fourth position

1) THE COORDINATES OF THE THREE DATA POINTS

X	Y	Z
303454.679	522893.351	409.981
303445.594	522900.745	409.586
303451.422	522881.588	409.425
303454.679	522893.351	409.981

2) THE THREE SLANT DISTANCES

D(1)	D(2)	D(3)
6.820	15.500	5.430

THE COMPUTATION STEPS

1) LENGTH OF SIDES

S(1)	S(2)	S(3)
20.025	12.218	11.720

2) THE ANGLES OF THE TRIANGLE

A(1)	A(2)	A(3)
1.981	0.594	0.566

3) THE AUXILIARY VECTOR

l	m	n
-0.267	-0.963	-0.046

4) THE DIRECTION COSINES

L	M	N
-0.775	0.631	-0.034
-0.628	-0.775	-0.064
-0.067	-0.029	0.997

5) THE LOCAL COORDINATES

U(2)	U(3)	U(4)
11.720	-4.878	-2.405

V(3)	V(4)
11.202449	6.375945

W(4)
0.276

THE RESULTS

X(4)	Y(4)	Z(4)
303452.519	522886.882	409.927

THE GIVEN DATA
The fifth position

1) THE COORDINATES OF THE THREE DATA POINTS

X	Y	Z
303454.679	522893.351	409.981
303445.594	522900.745	409.586
303451.422	522881.588	409.425
303454.679	522893.351	409.981

2) THE THREE SLANT DISTANCES

D(1)	D(2)	D(3)
6.820	15.460	5.370

THE COMPUTATION STEPS

1) LENGTH OF SIDES

S(1)	S(2)	S(3)
20.025	12.218	11.720

2) THE ANGLES OF THE TRIANGLE

A(1)	A(2)	A(3)
1.981	0.594	0.566

3) THE AUXILIARY VECTOR

l	m	n
-0.267	-0.963	-0.046

4) THE DIRECTION COSINES

L	M	N
-0.775	0.631	-0.034
-0.628	-0.775	-0.064
-0.067	-0.029	0.997

5) THE LOCAL COORDINATES

U(2)	U(3)	U(4)
11.720	-4.878	-2.352

V(3)	V(4)
11.202449	6.427870

W(4)
0.000

THE RESULTS

X(4)	Y(4)	Z(4)
303452.464	522886.883	409.647

THE GIVEN DATA
The sixth position

1) THE COORDINATES OF THE THREE DATA POINTS

X	Y	Z
303454.679	522893.351	409.981
303445.594	522900.745	409.586
303451.422	522881.588	409.425
303454.679	522893.351	409.981

2) THE THREE SLANT DISTANCES

D(1)	D(2)	D(3)
6.860	15.480	5.350

THE COMPUTATION STEPS

1) LENGTH OF SIDES

S(1)	S(2)	S(3)
20.025	12.218	11.720

2) THE ANGLES OF THE TRIANGLE

A(1)	A(2)	A(3)
1.981	0.594	0.566

3) THE AUXILIARY VECTOR

l	m	n
-0.267	-0.963	-0.046

4) THE DIRECTION COSINES

L	M	N
-0.775	0.631	-0.034
-0.628	-0.775	-0.064
-0.067	-0.029	0.997

5) THE LOCAL COORDINATES

U(2)	U(3)	U(4)
11.720	-4.878	-2.355

V(3)	V(4)
11.202449	6.460533

W(4)
0.000

THE RESULTS

X(4)	Y(4)	Z(4)
303452.446	522886.856	409.645

DISCUSSION

To know the accuracy of the method under considerations, the coordinates of the six positions are recalculated by the conventional surveying method and the results are compared and given in Table 1.

The results in Table 1 indicate identical values of the two methods with minor differences. so far the vertical movement of a datum point at the mining horizon has been considered. However, individual points in the roof stratum do not go down absolutely vertically, but the vertical component of this movement is several times greater than the horizontal one as shown in Table 1.

CONCLUSIONS

Roof convergence can be easily measured by using this method. The required data are the coordinates of the three fixed stations and the slant distances from these points to the unknown station. Through a computer program, the coordinates of the unknown station can be calculated. The solution is very fast and can be obtained in one series of operations.

Table (1): The final results of the two methods.

	The conventional method			The new method		
	X	Y	Z	X	Y	Z
p	303452.57	52286.872	411.414	303452.528	522886.893	411.435
p_1^*	"	"	411.014	303452.505	522886.840	410.856
p_2^*	"	"	410.614	303452.500	522886.863	410.269
p_3^*	"	"	410.214	303452.519	522886.882	409.927
p_4^*	"	"	409.814	303452.464	522886.883	409.647
p_5^*	"	"	409.414	303452.446	522886.856	409.645

REFERENCES

1. Aynsley, W. J. and G. Hewitt, 1961, Subsidence Observations Over Shall Workings, Mining Engineering 120, pp. 552–569.

2. Berry, D. S., 1963, Ground Movement Considered as an Elastic Phenomenon, Mining Engineering 37, pp. 28–39.

3. Hardy, R. L., 1978, The Application of Multiquadric Equations and Point Mass Anomaly Models to Crystal Movement Studies, NOAA Technical Report NOS 76, NGS 11.

4. Kratzsch, K., 1983, Mining Subsidence Engineering, Springer–Verlag, Berlin Heidelberg, New York.

5. Lourila, S. H., 1985, First Order Positioning by 3D EDM, Surveying and Mapping, Vol. 45, No. 2, pp. 45–150.

6. Rees, P. K. and F. W. Sparks, 1969, Calculations with Analytic Geometry, McGraw–Hill, Inc., Tokyo.

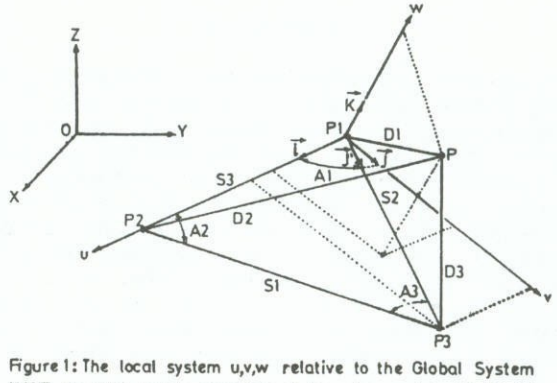

Figure 1: The local system u,v,w relative to the Global System X,Y,Z, the plan u,v is the plane of the given points P1, P2, P3. S1, S2 and S3 are the computed sides of the Triangle P1, P2, P3. A1, A2 and A3 are the computed angles of the Triangle P1, P2, P3.

GEOMECHANICAL SUBSTANTIATION OF EXTRACTION OF UNDERMINED ORE DEPOSIT

M. V. Kurlenya
S. N. Popov
I. L. Boltenhagen

Institute of Mining
Siberian Division, Academy of Sciences
Novosibirsk, USSR

ABSTRACT

The experience of application of geomechanical investigations for substantiation of extraction of undermined ore deposit in the north of Siberia is discussed. The finite element method was used for forecasting the state of massif during the development of mining works. The results of calculations were compared with the experimental data of observations *in situ* for evaluation of authenticity of numerical modelling.

INTRODUCTION

The problem of geomechanical substantiation of mining disseminated ores is a topical one for the Talnakhsky copper-nickel deposit in the north of Siberia. The peculiarity of the problem consists in the unique mining technical situation. For instance, a flat deposit of rich ores with a thickness of 30 m was mined at the depth of 600 m in one of the mines. The mined-out space with dimensions of 0.4x1.0 km was filled in with the solidifying mine-fill (fig. 1a). As a result a 50-meter thickness of disseminated ores directly over the filling massif has been undermined. It is planned to begin a disseminated ore extraction in the center of undermined region in the nearest time (dash line in fig. 1b). Under these conditions two main variants of mining disseminated ores are being discussed. The first one is a widely applicable mining with filling of the mined-out space under the extraction of rich ore deposits of Talnakh. The combined method of mining is an alternative one with a high enough cost of solidifying filling and a relatively low cost of disseminated ores. This method consists in the following. At first the primary strips with the use of solidifying filling are mined. As a result ore pillars are formed between them, which are mined by ore and enclosing rocks caving with some lagging (fig. 2). This variant is economically more profitable, but when it is used a number of geomechanical problems arises. The question about stresses in ore pillars is the main one. The experience of application of geomechanical investigations for the solution of this problem is discussed in the paper. The method of finite elements was used for forecasting the state of massif during the development of mining works. The results of calculations were compared with the experimental data of observations *in situ* for evaluation of authenticity of numerical modelling.

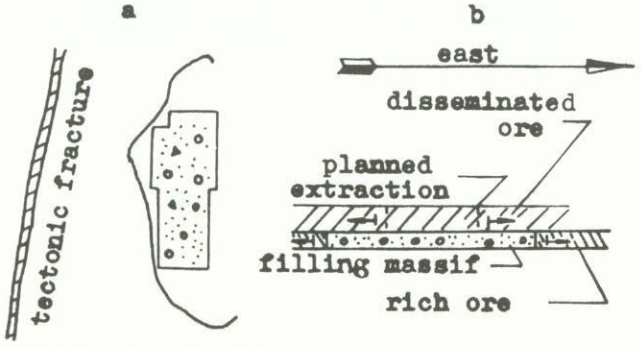

Fig. 1. Plan (a) and cross section (b) of the mine.

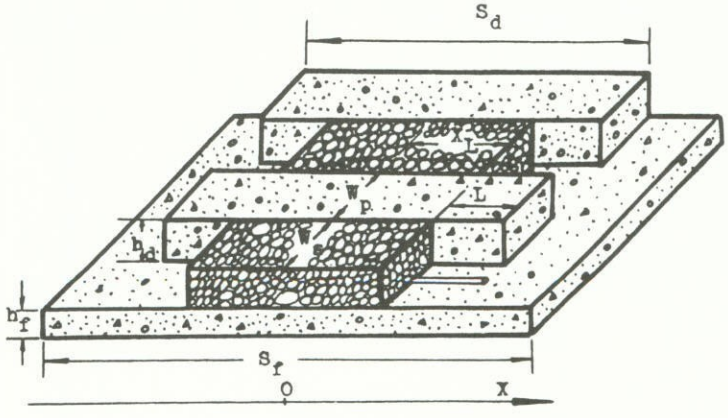

Fig. 2. Lay-out of disseminated ore extraction by the combined method.

SUBSTANTIATION OF FINITE ELEMENT MODEL

The necessary stage of solving the problem is a construction of a geomechanical model, the analysis of which allows to forecast the behaviour of rock massif in the process of mining the deposit. The solutions of problems of deforming the elastic half-space with prismatic cavity in two- and three-dimensional statement were compared (fig. 3)

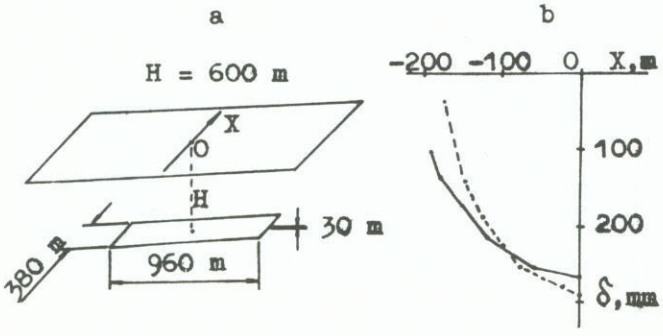

Fig. 3. Comparison of numerical results obtained from the solutions of three-dimensional (full line) and two-dimensional (dash line) problems. Scheme for the three-dimensional problem (a) and convergence of roof and floor in the central part of prismatic cavity (b).

and the solutions of problems in two- dimensional statement may be used for forecasting the state of massif near the central part of the mine. In two-dimensional statement the computations are performed in two meshes, one of which reproduces the real geometry and the structure of massif in more details (fig. 4). To get qualitative evaluations, it is enough to use the deformation properties average for the massif. To save computer time , all subsequent computations were performed in a simple mesh. The scheme of calculating domain

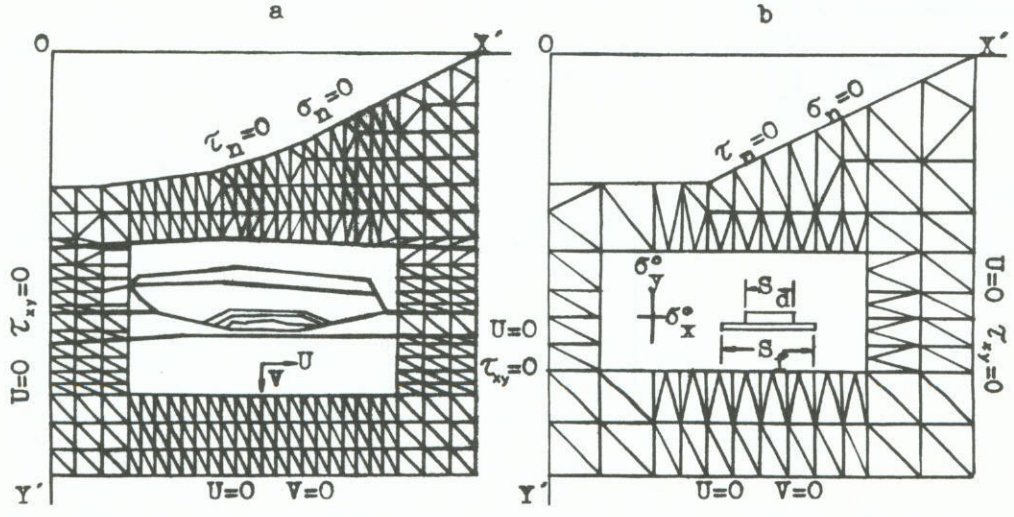

Fig. 4. Detailed (a) and simple (b) mesh for the solution of two-dimensional problems.

is given in fig. 4b. The massif of disseminated ores with a thickness h_d = 45 m and a span S_d is extracted after the rich ore body with a span S_f and a thickness h_f = 30 m has been mined and filled.

RICH ORE EXTRACTION

The situation which should be expected at the moment of starting mining disseminated ores (S_d = 0) was modelled in the first stage. The nonlinear dependence of pressure in the filling massif on the convergence of roof and floor connected with a not full filling Δ of the mined-out space (fig. 5) was taken into account. For this purpose the sequence of linear-elastic problems was considered. In the first step the convergence of roof and floor of the unfilled mined-out space was calculated, compared with Δ and the positive difference was taken as the first approximation for the vertical strains of filling massif. Reaction of filling massif was evaluated by

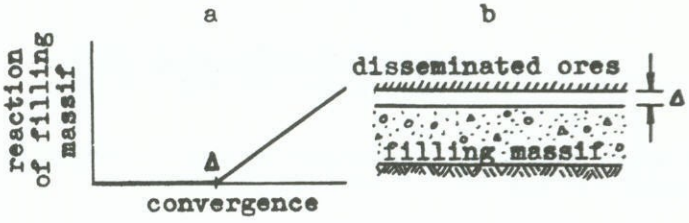

Fig. 5. The nonlinear dependence of fill pressure on the convergence of roof and floor (a).The parameter Δ characterizes the ultimate convergence of the mined-out space without reaction of filling massif. Its value is determined by compressive properties of the filling massif and the volume of unfilled cavities in the "filling-rock" contact (b)

elastic relations under the condition of the absence of its horizontal strains. In the second and the following steps the problem for weightless area when the surface forces statically equivalent to the reaction of filling massif are applied on the contour of the mined-out space was being solved, and then primarily found strains of the filling massif and its reaction were being corrected. Three - five iterations were enough to evaluate with acceptable error the stress distribution in the rock, ore and filling massif. The main parameters of the model, such as the effective elasticity modulus of massif (E_d = 33 GPa) and the value of not full filling (Δ = 210 mm) were chosen in that way, so the results of calculations corresponded to the experimental data on the displacements of the undermined massif and the pressures on the filling massif. The deformation properties of the

filling massif (E_f = 2.5 GPa , ν_f = 0.3) were determined *in situ*. Fig. 6a gives the comparison of experimental and calculated data on the vertical displacements of the undermined massif. Fig. 6b presents the pressures in the filling massif under the different spans of the mined-out space. An experimental evaluation of the pressure in the

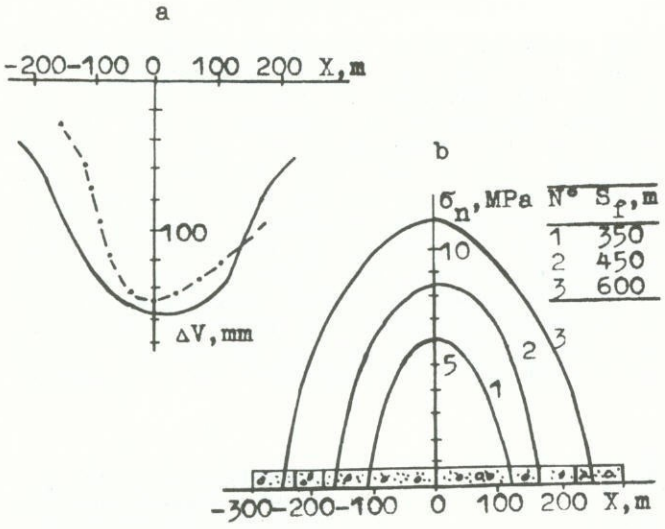

Fig. 6. Vertical displacements of the undermined massif (a) and fill pressure (b).

central part of the filling massif with the span of approximately 300 m was 5-6 MPa. The additional experimental data obtained with the help of the method of hydraulic fracturing of holes confirmed the correctness of the applicable model for a forecast of the state of massif under the development of mining works.

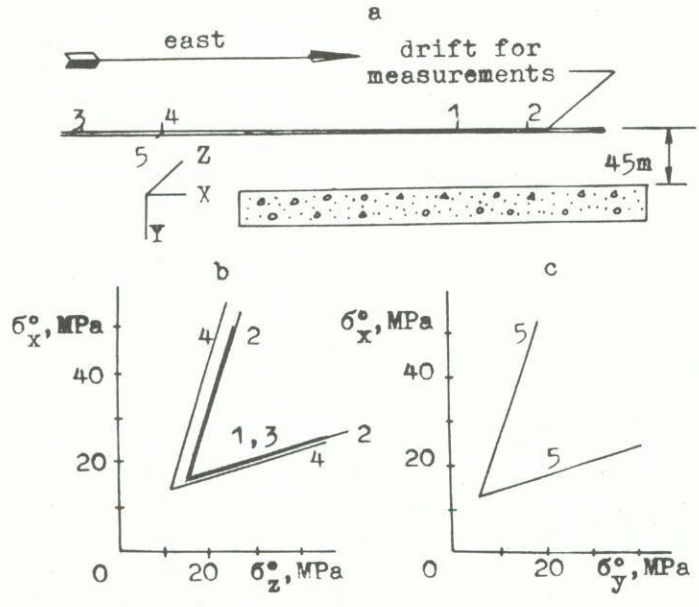

Fig. 7. Vertical section of the central part of ore body and the experimental opening for measurements of displacements and stresses (a) and possible values of the initial stresses (b and c).

EXPERIMENTAL EVALUATION OF STRESS FIELD

A change of relation of horizontal stresses to vertical ones in the initial stressed state over a wide range of values (from 0.2 to 3.0) essentially influenced neither the value of additional displacements induced by mining of the lengthy horizontal deposit nor the level of pressure in the filling massif. So the corresponding results may be generalized for other values of horizontal tectonic stresses in the indicated interval as well. This peculiarity was used under the experimental evaluation of stress field in the mine. Fig. 7a shows the schematic section of the central part of ore body being mined and the drift for measurements. There were carried out experiments by hydraulic fracturing method in the horizontal (5) and vertical (1,2,3,4) holes. Let us suppose that the initial horizontal principal stresses are oriented in the south - north and west - east directions. Let σ_x^o, σ_y^o, σ_z^o be the initial stresses. After mining the deposit the stresses are equal to

$$\sigma_x = \sigma_x + \Delta\sigma_x \qquad \sigma_y = \sigma_y + \Delta\sigma_y$$
$$\sigma_z = \sigma_z^o + \Delta\sigma_z \qquad \tau_{xy} = \Delta\tau_{xy} \quad .$$

Additional stresses $\Delta\sigma_x$, $\Delta\sigma_y$, $\Delta\sigma_z$, $\Delta\tau_{xy}$ were obtained with the help of numerical modelling. The stresses in the region of holes and the average values of the fracture reopening pressures P_r outside the zone of influence of the drift are presented in the table 1.

Table 1

Hole NR	σ_x MPa	σ_y MPa	σ_z MPa	τ_{xy} MPa	$\bar{P}_r$ MPa
1	σ_x^o -6.0	σ_y^o -12.0	σ_z^o -5.5	1.0	20.0
2	σ_x^o -5.5	σ_y^o -13.5	σ_z^o -5.5	1.5	22.0
3	σ_x^o +1.5	σ_y^o +4.0	σ_z^o +2.0	0.0	35.0
4&5	σ_x^o +1.0	σ_y^o +8.0	σ_z^o +3.0	0.0	28.5

In the vertical holes the fracture reopening pressure is determined in the following way:

$$P_i = 3\,\sigma_x - \sigma_z \quad \text{under} \quad \sigma_x \geq \sigma_z$$
$$P_i = 3\,\sigma_z - \sigma_x \quad \text{under} \quad \sigma_z \geq \sigma_x$$

Under the fixed value of the fracture reopening pressure the admissible values of stresses in the plot (σ_x, σ_z) correspond to the set of points in two half-lines. The combined plot for the vertical holes (fig. 7b) allows to evaluate the possible values σ_x^o and σ_z^o of the initial stress field. Good co-ordination of experiments in different holes (hole 4 was deviated by 27° from the vertical) should be noted that is an evidence of reliability of results of numerical modelling. Fig. 7c shows the area of the admissible values of stresses σ_x^o and σ_y^o which was obtained from the experiments in the horizontal hole 5. Supposing that $\sigma_y^o = \rho gH$ = 16 MPa and using fig. 7b and c we shall obtain three possible variants of the relation of stresses (Table 2). Additional conceptions of qualitative

Table 2

NR	σ_x^o,MPa	σ_y^o,MPa	σ_z^o,MPa	σ_x^o/σ_y^o	σ_z^o/σ_y^o
1	16.	16.	16.	1.0	1.0
2	42.	16.	24.	2.6	1.5
3	42.	16.	93.	2.6	5.8

character of distributing the fracture reopening pressure in the vicinity of the drift for measurements were used for the choice of the most verisimilar variant. For every variant of the initial stress field the components of the stressed state of three parts of massif where the experiments were carried out in the holes 1,2,3 have been calculated. The characteristic dependences of P_{reop}^{theor} on the distance to the roof of drift under different initial stresses were obtained from the solution of the problem about stress distribution near the cylindrical opening. Having compared theoretical and experimental results, one can draw a conclusion that the initial stress field is close to the hydrostatic one.

DISSEMINATED ORE EXTRACTION

The change of the state of massif in the process of disseminated ore extraction by the combined method was calculated in the second stage. Fig. 2 explains the technological scheme. The front of winning works moves from the central part of the mined-out space, where W_p is the width of the primary strips mined with filling, W_s is the width of the secondary strips mined with caving and lagging L. The evaluation of stresses in the face of the secondary strips is of the greatest interest. The additional convergence of roof and floor in the process of the full disseminated ore extraction ($S_d=S_f$) was determined with the help of numerical modelling. Fig. 8a shows the values of additional convergences $\delta_{fe}(X)$ for the different spans S_d. The additional convergence of roof and floor under the partial disseminated ore extraction by the combined method was evaluated with the use of the simplest linear approximation

$$\delta_{pe}(X) = \frac{S_d\ W_p + 2\ X_L\ W_s}{S_f\ (W_p + W_s)}\ \delta_{fe}(X)$$

where $2\ X_L = S_d - 2\ L$ is the distance between the faces of the secondary strips (fig. 2). The vertical stresses in the face of the secondary strips were determined in the following way

$$\sigma_L = K\ \delta_{pe}(X_L) + \sigma_n(X_L)$$

where $\sigma_n(X_L)$ - the vertical stresses in the mined-out space before the beginning of disseminated ore extraction (fig. 6b), and $K = (h_f/E_f + h_d/E_d)^{-1}$ is the coefficient determining the stiffness of the "ore pillar - underlying filling massif" system (fig. 8b). The graphs presented in fig. 9 illustrate the dependence of σ_n on S_d under the different spans of undermining S_f, the relations of

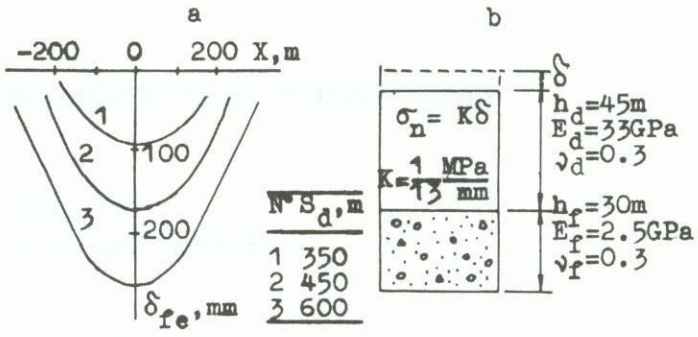

Fig. 8. Additional convergences under the full disseminated ore extraction (a) and "ore pillar - underlying filling massif" system (b).

sizes of the primary and the secondary strips W_p/W_s and the values of lagging L. One can see, that basically, the pressure is determined by the span of undermining S_f.

N°	1	2	3	4	5	6
W_s/W_p	2	1/2	2	1/2	2	1/2
S_f,m	350		450		600	

N°	1	2	3	4	5	6	7	8	9
L,m	0	50	100	0	50	100	0	50	100
S_f,m	350			450			600		

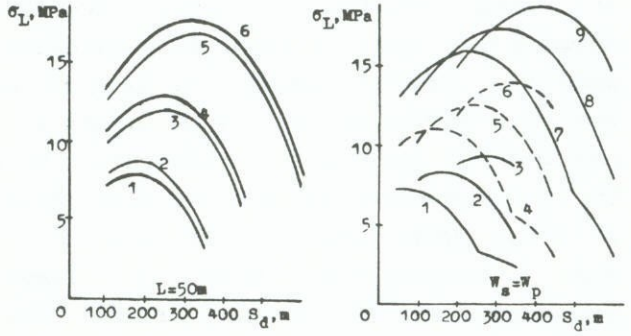

Fig. 9. Vertical stresses in the face of the secondary strips under various values of parameters

CONCLUSIONS

The carried out approximate analysis allowed to draw the following conclusion concerning the order of mining the secondary strips from a position of stability of workings before the breakage face. The early mining is the most expedient. Distance between the faces of the primary and the secondary strips must be minimally possible. The worst conditions of mining should be expected under the divergence of faces ($2X_L$) by 0.3-0.6 S_f.

10th INTERNATIONAL CONFERENCE ON GROUND CONTROL IN MINING

RELATIONSHIP BETWEEN FLOOR ROCK STRESS AND FLOOR FAILURE

X. S. Tan, *Research Fellow*
S. S. Peng, *Chairman and Charles T. Holland Professor*

Department of Mining Engineering
West Virginia University
Morgantown, West Virginia

Abstract

This paper deals with the analysis of stress condition on the interface between two types of floor rock materials when the vertical stress is larger, or when the horizontal stress is larger in a rectangular opening. It indicates that the floor Failure and the failure stress of floor rocks are closely related. It also demonstrates that a larger horizontal stress is one of the most important factors in increasing the potential for floor rock failure and floor heave.

Introduction

The causes of floor heave in underground opening have been attributed to many factors including a high horizontal tectonic stress acting on the floor layers and a high vertical stress acting on the pillars, geological discontinuities, mechanical and physical properties of coal and roof and floor rocks, mine layout, mining sequence, entry orientation, stress and energy conditions on the interface between the coal and floor rock(or roof rock), and the gob condition[1,2]. But the most important factor is a large tectonic stress, especially a high horizontal tectonic stress acting on the floor rocks. Traditionally researchers believe that the horizontal stresses in underground rock masses were due solely to Poisson's effect[2]. However, numerous in-situ stress measurements all over the world indicate that a high horizontal stress exceeding that induced by Poisson's effect exists widely in the underground rock masses and the horizontal tectonic stress is generally 0.5 - 5.5 times larger than the vertical stress, even over 30 times larger than the vertical stress in some complicated geological areas[2].

In this paper, the basic mechanics principles, such as the deformation continuity condition, static force equilibrium condition and superposition principle are used to analyze the stress condition in the floor rocks and the relationship between floor heave and floor rock strength when the vertical stress is larger, or when the horizontal stress is larger.

Stress Analysis of Floor Rock When Vertical Stress is Larger Than Horizontal Stress

Figure 1 shows an opening in underground rock masses. For stress analysis, a small rock mass containing the intersection between floor rock A and rock B(Figure 2a) is taken from the floor rocks in Figure 1. In Figure 2a, the small rock mass is subjected to three-dimensional compressive stress, i.e. σ_1, σ_2, σ_3 and is composed of two types of floor rock materials, i.e. rock A(2nd immediate floor rock) and rock B(immediate floor rock). Notice in this paper $\sigma_1 > \sigma_2 > \sigma_3$ and when vertical stress is larger than horizontal stress, σ_1 is vertical and σ_2 and σ_3 is horizontal.

Assuming that rock A and rock B are tightly bonded and rock B deforms more than rock A when the vertical stress is larger than the horizontal stress.

The small rock mass acted simultaneously by stresses σ_1, σ_2 and σ_3(Figure 2a) can be transformed into another set of three small rock masses acted, respectively, by horizontal stresses σ_3 and σ_2 and vertical stress σ_1 in Figure 2b, 2c and 2d, respectively, according to the superposition principle in basic mechanics[2].

First, consider the small rock mass acted by the horizontal stress σ_3 in Figure 2b. Obviously, both rock A and rock B will produce a horizontal deformation but the horizontal deformation for rock B will be larger than that of rock A. As a result, rock A and rock B will respectively produce additional compressive and tensile stresses along the direction 3 and will respectively produce additional tensile and compressive stresses along the direction 2 because of the nonuniformity of horizontal deformation. In order to analyze the stress and strain conditions on the interface between rock A and rock B, a three-dimensional tiny rock element with different elastic modulus shown in Figure 3 is taken from the interface between rock A and rock B in the small rock mass in Figure 2b. Based on the analysis of the deformation continuity and static force equilibrium conditions on the element in Figure 3, the following relationships between stress and strain can be obtained:

$$\begin{aligned} \varepsilon'_{3A} &= \varepsilon'_{3B} = \varepsilon'_3 \\ \varepsilon'_{2A} &= \varepsilon'_{2B} = \varepsilon'_2 \end{aligned} \qquad (1)$$

$$\begin{aligned} \sigma_{3A} &= \sigma_3 + \sigma'_{3A} \\ \sigma_{3B} &= \sigma_3 + \sigma'_{3B} \\ -\sigma'_{3A} &= \sigma'_{3B} \\ \sigma_{2A} &= -\sigma_{2B} = \sigma'_{2A} = -\sigma'_{2B} \\ \sigma_{1A} &= \sigma_{1B} = 0 \end{aligned} \qquad (2)$$

Where, ε'_{3A} and ε'_{3B} are, respectively, the strain of rock A and rock B along the direction 3; ε'_{2A} and ε'_{2B} are, respectively, the strain of rock A and rock B along the direction 2; σ'_{3A} and σ'_{3B} are, respectively, the additional stresses in rock A and rock B induced by the nonuniformity of the horizontal strain along the direction 3; σ'_{2A} and σ'_{2B} are, respectively, the additional stresses in rock A and rock B induced by the nonuniformity of the horizontal strain along the direction 2; σ_{3A}, σ_{3B}, σ_{2A}, σ_{2B}, σ_{1A}, σ_{1B} are the stresses in rock A and rock B along the direction 3, 2 and 1, respectively.

Substituting Equations 1 and 2 into the Equation 3, a constitutive equation in basic mechanics[2], and rearranging and solving for the solutions,

$$\{\varepsilon\} = \begin{bmatrix} \frac{\partial U}{\partial 1} \\ \frac{\partial U}{\partial 2} \\ \frac{\partial U}{\partial 3} \end{bmatrix} \qquad (3)$$

the stresses in rock A and rock B on the interface in Figure 2b can be obtained as follows:

$$\begin{aligned}
\sigma_{3A} &= \sigma_3 + K_1\sigma_3 \\
\sigma_{3B} &= \sigma_3 - K_1\sigma_3 \\
\sigma'_{3A} &= K_1\sigma_3 \\
\sigma'_{3B} &= -K_1\sigma_3 \\
\sigma_{2A} &= -K_2\sigma_3 \\
\sigma_{2B} &= K_2\sigma_3 \\
\sigma_{1A} &= \sigma_{1B} = 0
\end{aligned} \tag{4}$$

Where,

$$K_1 = \frac{E_A^2(1-\upsilon_B^2) - E_B^2(1-\upsilon_A^2)}{(E_A+E_B)^2-(E_A\upsilon_B+E_B\upsilon_A)^2}$$

$$K_2 = \frac{2E_AE_B(\upsilon_B-\upsilon_A)}{(E_A+E_B)^2-(E_A\upsilon_B+E_B\upsilon_A)^2} \tag{5}$$

Where, E_A and E_B are Young's modulus of rock A and rock B, respectively; υ_A and υ_B are Poisson's ratio of rock A and rock B, respectively.

From Equations 4 and 5, it can be seen that the uniaxial compressive stress condition in the small rock mass shown in Figure 2b subject to a uniaxial horizontal stress σ_3 has been created into a two-dimensional stress condition on the interface between rock A and rock B.

Similarly, consider the small rock mass subject to horizontal stress σ_2(Figure 2c). On the interface between rock A and rock B, a horizontal constraint occurs on the interface because of the nonuniformity of horizontal strains. As a result, additional tensile and compressive stresses will produce on the interface. By applying the deformation continuity condition and static force equilibrium condition to a unit with different elastic modulus (Figure 4), taken from the interface between rock A and rock B in Figure 2c, the relationships between the stress and strain can be written as follows:

$$\begin{aligned}
\varepsilon''_{3A} &= \varepsilon''_{3B} = \varepsilon''_3 \\
\varepsilon''_{2A} &= \varepsilon''_{2B} = \varepsilon''_2
\end{aligned} \tag{6}$$

$$\begin{aligned}
\sigma_{3A} &= -\sigma_{3B} = \sigma''_{3A} = -\sigma''_{3B} \\
\sigma_{2A} &= \sigma_2 + \sigma''_{2A} \\
\sigma_{2B} &= \sigma_2 + \sigma''_{2B} \\
-\sigma''_{2A} &= \sigma''_{2B} \\
\sigma_{1A} &= \sigma_{1B} = 0
\end{aligned} \tag{7}$$

Similarly, substituting Equation 6 and 7 into the constitutive equation in basic mechanics, the stresses in rock A and rock B on the interface (Figure 2c) are as follows:

$$\begin{aligned}
\sigma_{3A} &= -K_2\sigma_2 \\
\sigma_{3B} &= K_2\sigma_2 \\
\sigma_{2A} &= \sigma_2 + k_1\sigma_2 \\
\sigma_{2B} &= \sigma_2 - K_1\sigma_2 \\
\sigma''_{2A} &= K_1\sigma_2 \\
\sigma''_{2B} &= -K_1\sigma_2 \\
\sigma_{1A} &= \sigma_{1B} = 0
\end{aligned} \tag{8}$$

Finally, consider the small rock mass subject to vertical stress σ_1(Figure 2d). By applying the same technique to a unit with different elastic modulus shown in Figure 5, the relationships between the stress and strain, and the stresses in rock A and rock B on the interface in Figure 2d are, respectively,

$$\begin{aligned}
\varepsilon'''_{3A} &= \varepsilon'''_{3B} = \varepsilon'''_3 \\
\varepsilon'''_{2A} &= \varepsilon'''_{2B} = \varepsilon'''_2 \\
\varepsilon'''_3 &= \varepsilon'''_2
\end{aligned} \tag{9}$$

$$\sigma_{3A} = -\sigma_{3B} = \sigma'''_{3A} = -\sigma'''_{3B}$$
$$\sigma_{2A} = -\sigma_{2B} = \sigma'''_{2A} = -\sigma'''_{2B}$$
$$\sigma_{2A} = \sigma_{3A} \quad (10)$$
$$\sigma_{2B} = \sigma_{3B}$$
$$\sigma_{1A} = \sigma_{1B} = \sigma_1$$

$$\sigma_{3A} = -K_3\sigma_1$$
$$\sigma_{3B} = K_3\sigma_1$$
$$\sigma_{2A} = -K_3\sigma_1 \quad (11)$$
$$\sigma_{2B} = K_3\sigma_1$$
$$\sigma_{1A} = \sigma_{1B} = \sigma_1$$

Where,

$$K_3 = \frac{(E_A\upsilon_B - E_B\upsilon_A)(E_A\upsilon_B + E_B\upsilon_A + E_A + E_B)}{(E_A+E_B)^2 - (E_A\upsilon_B + E_B\upsilon_A)^2} \quad (12)$$

From Equation 11 it can be seen that the uniaxial compressive stress condition in the small rock mass in Figure 2d subject to the vertical stress σ_1 has been created into a three dimensional stress condition on the interface between rock A and rock B because of the nonuniformity of the horizontal strains.

As mentioned above, the principle of superposition in basic mechanics was used to study the relationship between the stress and strain. So from Equations 4, 8 and 11, the total stress on the interface of the small rock mass subject to σ_1, σ_2, and σ_3 simultaneously(Figure 2a) can be obtained by:

$$\sigma'_{3A} = \sigma_3 + K_1\sigma_3 - K_2\sigma_2 - K_3\sigma_1$$
$$\sigma'_{2A} = -K_2\sigma_3 + \sigma_2 + K_1\sigma_2 - K_3\sigma_1 \quad (13)$$
$$\sigma'_{1A} = \sigma_1$$

$$\sigma'_{3B} = \sigma_3 - K_1\sigma_3 + K_2\sigma_2 + K_3\sigma_1$$
$$\sigma'_{2B} = K_2\sigma_3 + \sigma_2 - K_1\sigma_2 + K_3\sigma_1 \quad (14)$$
$$\sigma'_{1B} = \sigma_1$$

Where, σ'_{3A}, σ'_{2A}, σ'_{1A}, σ'_{3B}, σ'_{2B} and σ'_{1B} are the total stresses of rock A and rock B on the interface along the direction 3, 2 and 1, respectively.

Stress Analysis of Floor Rock When Horizontal Stress is Larger Than Vertical Stress

Now by applying the same techniques mentioned above, the total stresses on the interface of the floor rocks subject to vertical stress σ_1, horizontal stresses σ_2 and σ_3 simultaneously, can be determined as follows:

$$\sigma''_{3A} = \sigma_3$$
$$\sigma''_{2A} = \sigma_2 - K_1\sigma_2 + K_2\sigma_1 + K_3\sigma_3 \quad (15)$$
$$\sigma''_1 = K_2\sigma_2 + \sigma_1 - K_1\sigma_1 + K_3\sigma_3$$

$$\sigma''_{3B} = \sigma_3$$
$$\sigma''_{2B} = \sigma_2 + K_1\sigma_2 - K_2\sigma_1 - K_3\sigma_3 \quad (16)$$
$$\sigma''_{1B} = -K_2\sigma_2 + \sigma_1 + K_1\sigma_1 - K_3\sigma_3$$

Notice in this case σ_1 and σ_2 are horizontal while σ_3 is vertical stress

Relationship Between Floor Rock Stress And Floor Heave

In this paper, the Mohr's failure criterion is used to analyze the stability of the floor rocks (Figure 1). The Mohr's failure criterion can be written [4] as:

$$\sigma_{1j} = \frac{1+\sin\varphi}{1-\sin\varphi}\sigma_{3j} + \frac{2C\cos\varphi}{1-\sin\varphi} \quad (17)$$

or

$$\sigma_{1j} = \sigma_c + q\,\sigma_{3j} \quad (18)$$

Where, σ_{1j} and σ_{3j} are the ultimate major stress and minor stress acting on the floor rocks, respectively; q and σ_c are the triaxial stress factor and uniaxial compressive strength, respectively; C and φ are the internal cohesion and angle of

internal friction, respectively.

The Mohr's failure criterion postulates that a rock material will fail when either Equation 17 or 18 is satisfied.

Substituting Equations 13 and 14 into Equation 17, the vertical stresses at failure on the interface of rock A and rock B when the vertical stress is larger than the horizontal stress, can be written as follows:

$$\sigma'_{1Aj} = \frac{(1+ K_1- K_2)q_A\sigma_3+ \sigma_{CA}}{1 + q_A K_3} \quad (19)$$

$$\sigma'_{1Bj} = \frac{(1+ K_1- K_2)q_B\sigma_3+ \sigma_{CB}}{1 - q_B K_3} \quad (20)$$

Where,

$$q_A = \frac{1+ \sin\varphi_A}{1- \sin\varphi_A}$$

$$q_B = \frac{1+ \sin\varphi_B}{1- \sin\varphi_B}$$

$$\sigma_{CA} = \frac{2\ C_A\ \cos\varphi_A}{1- \sin\varphi_A}$$

$$\sigma_{CB} = \frac{2\ C_B\ \cos\varphi_B}{1- \sin\varphi_B}$$

Similarly, substituting Equations 15 and 16 into Equation 17, the vertical stresses at failure on the interface of Rock A and rock B when the horizontal stress is larger than the vertical stress, can be written as follows:

$$\sigma''_{1Aj} = \frac{(q_A- K_3)\sigma_3 + \sigma_{CA}}{1- K_1+ K_2} \quad (21)$$

$$\sigma''_{1Bj} = \frac{(q_B+ K_3)\sigma_3 + \sigma_{CB}}{1- K_1+ K_2} \quad (22)$$

The significance of Equations 19-22 can be illustrated by the following example. the floor rock mechanical properties are chosen as follows: Young's modulus of rock B and rock A are 16,600,000 psi and 18,200,000 psi, respectively; Internal cohesion of rock B and rock A are 1180 psi an 1422 psi, respectively; Angles of internal friction of rock B and rock A are 42°and 44°, respectively; Poisson's ratios of rock B and rock A are 0.34 and 0.29, respectively.

Substituting the above data into Equations 19 and 20, the vertical stresses at failure for rock B(immediate floor rock), σ'_{1Bj},and rock A(2nd immediate floor rock), σ'_{1jA}, on the interface, when the vertical stress is larger than the horizontal stress, are shown in Figure 6.

Similarly, from equations 21 and 22, the vertical stresses at failure for rock B(immediate floor rock), σ''_{1jB}, and rock A(2nd immediate floor rock), σ''_{1jA}, on the interface, when the horizontal stress is larger than the vertical stress, are also shown in Figure 6. It can be seen that the stress at failure for rock A decreases while that of rock B increases when the vertical stress is larger than the horizontal stress. So the immediate floor rock becomes more difficult to fail in this case.

However, when the horizontal stress is larger than the vertical stress, the stress at failure for rock B decreases while that of rock A increases. So the immediate floor rock (rock B) becomes easier to fail and the possibility of the floor failure or heave is relatively higher, especially, when the immediate floor rock (rock B) is weaker than the 2nd immediate floor rock, it is much easier to cause failure of the floor rock and induce floor heave.

Based on some research achievements[4], the floor vertical displacement with the larger horizontal

stress is much larger than that with the smaller horizontal stress. Combining the research result with our calculation result, it is very clear that the smaller rock strength and the larger vertical displacement for the floor rock, when the horizontal stress is larger than the vertical stress, are helpful to induce the floor heave, etc.

Conclusions

When the vertical stress is larger than the horizontal stress, the stress at failure for the immediate floor rock increases with the increment of the vertical stress. In this case, the immediate floor rock becomes more difficult to fail.

However when the horizontal stress is larger than the vertical stress, the stress at failure for the immediate floor rock decreases with the increment of the horizontal stress. In this case, it becomes easier to fail and induce the floor heave, especially, if the immediate floor rock is weaker.

The larger horizontal stress is one of the most important factors that cause failure of the floor rock and induce the floor heave.

References

1. S.S. Peng, Coal mine ground control, John Wiley and Sons, Inc., New York, 1986, pp.26 - 28.

2 X.F. Xian and X.S.Tan, Failure mechanism on stratified rock masses, Chongqing publication Inc.(in China), 1989, pp.35 - 55.

3 T.L. Li and X.S. Tan, foundation of rock mechanics, Chonqqing University publication Inc. of China national education committee(in China), 1990, pp.38 - 46, 62 - 68.

4 S.S. Peng and X.S. Tan, The study of floor heave and its prevention, To be published in J. of Chongqing University, 1991.

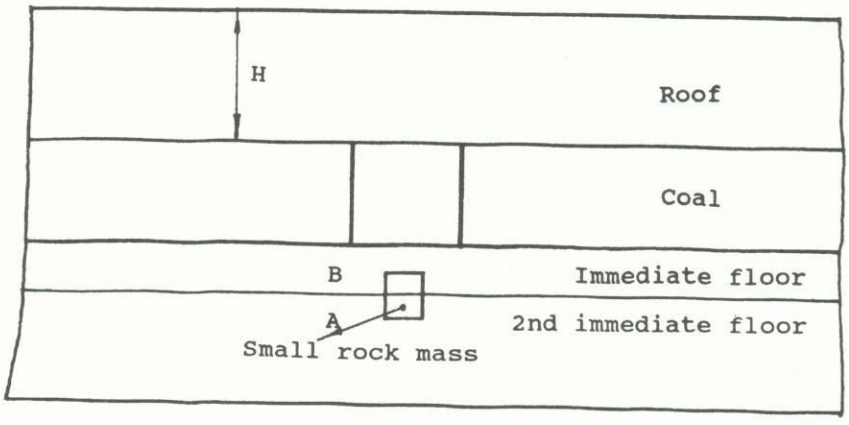

Figure 1 An opening in an underground rock mass

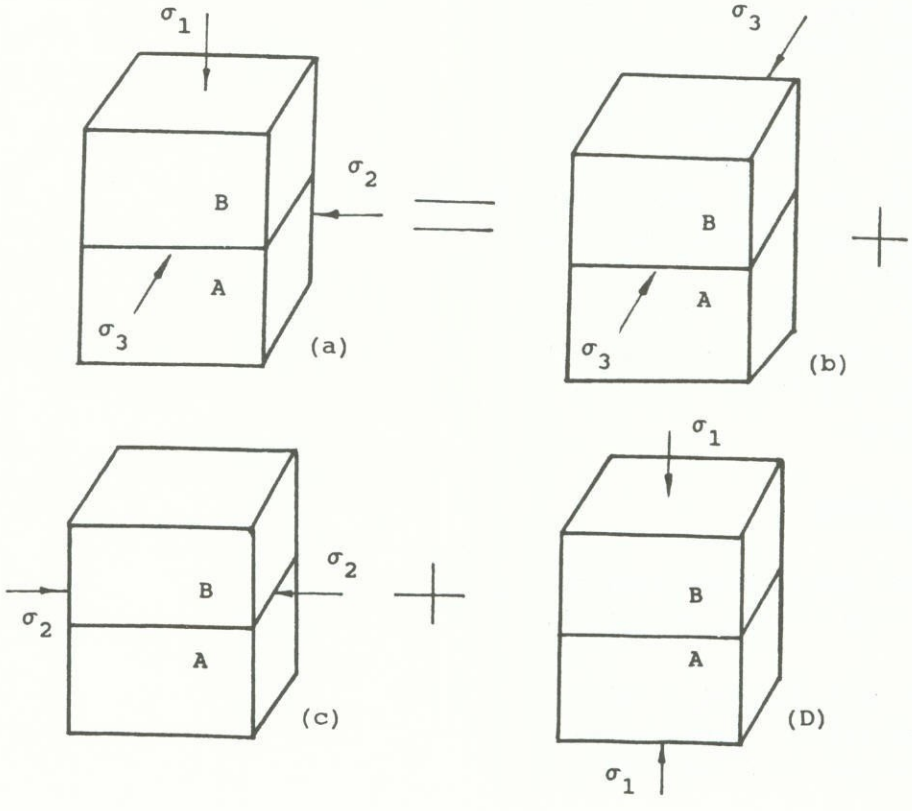

Figure 2 Stress components in a small rock mass

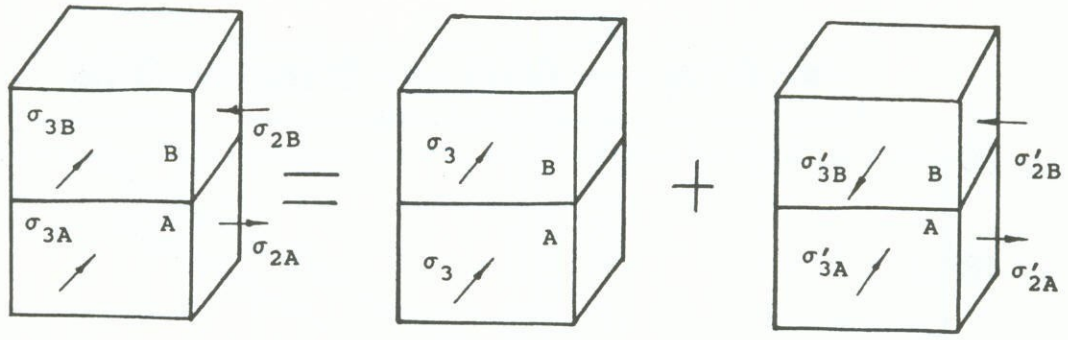

Figure 3 A tiny rock element with different elastic modulus subject to σ_3

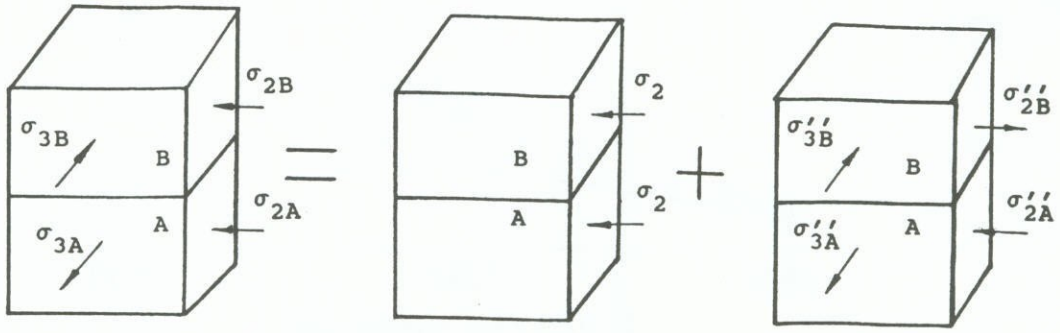

Figure 4 A tiny rock element with different elastic modulus subject to σ_2

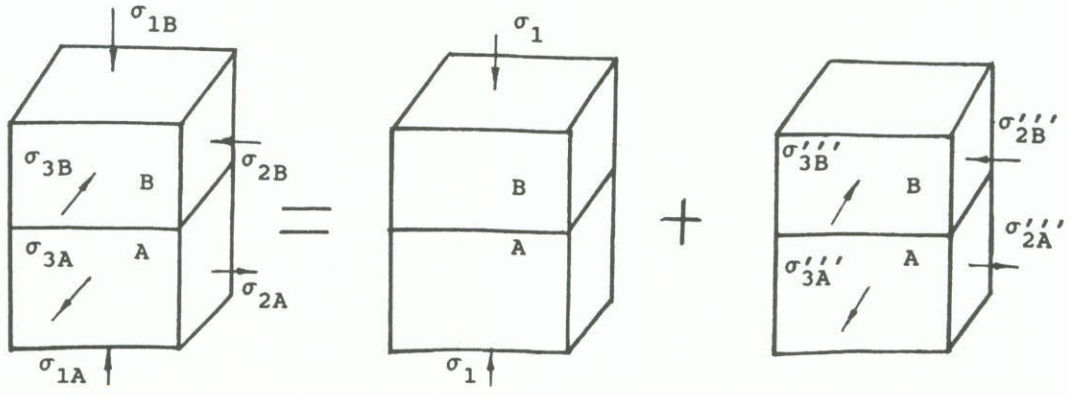

Figure 5 A tiny rock element with different elastic modulus subject to σ_1

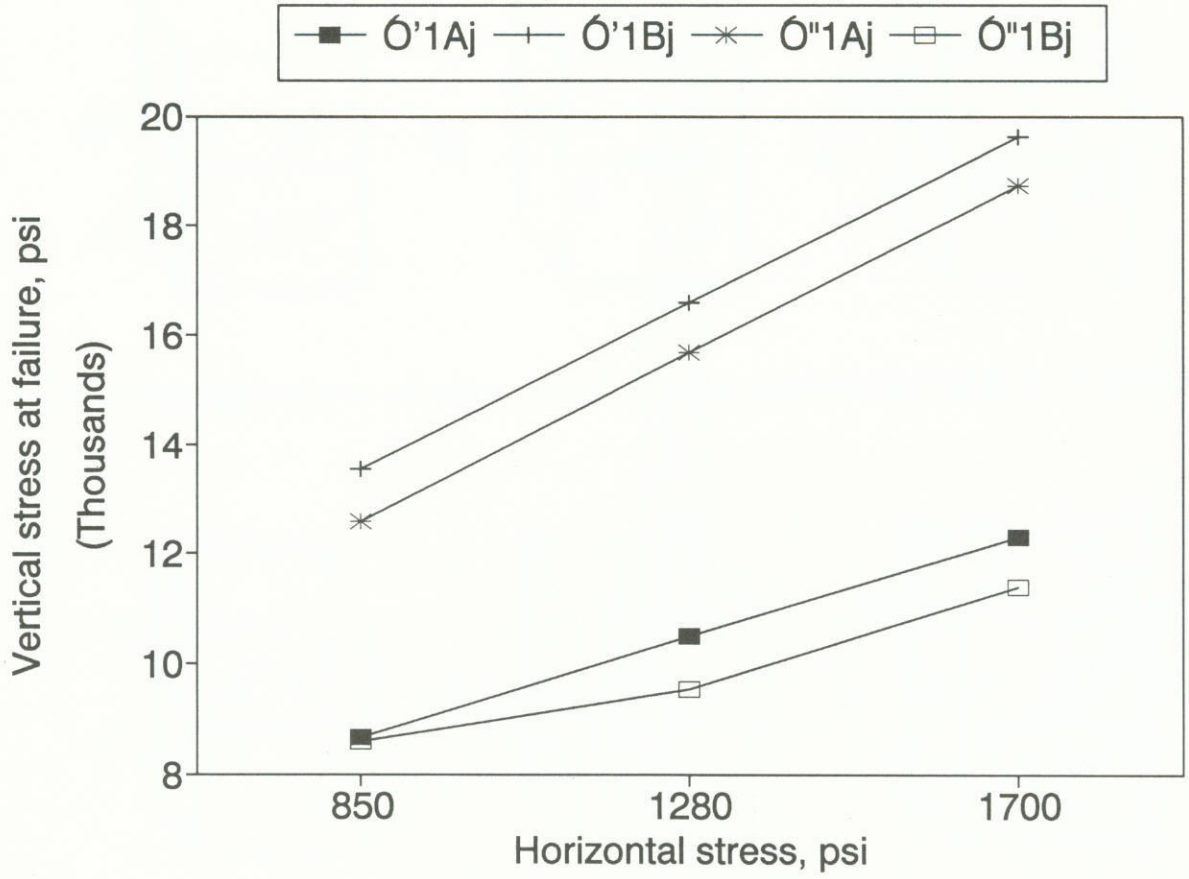

Fig.6 Comparison of floor rock stress

10th INTERNATIONAL CONFERENCE ON GROUND CONTROL IN MINING

THE INFLUENCE OF GEOMINING PARAMETERS OVER STRESS DISTRIBUTION IN AND AROUND DEPILLARING FACES

Rajendra Singh, *Scientist*
D. Prasad, *Scientist*
M. A. Rafiqui, *Scientist*
T. N. Singh, *Dy. Director*

Central Mining Research Station
Barwa Road, Dhandbad 826001
Bihar, INDIA

ABSTRACT

In India, pillar mining is contributing more than 90% of underground production which involves extraction of a part of coal from bords with pillars around as natural support in the development stage. Liquidation of these pillars with splitting and stooking, broken nature of face during mining under complex geomining factors like massive roof, varying treatment of goaf and over or underlying workings result in high stresses and deformation in and around the neighbouring pillars, causing operational problem and hazards to mine safety.

This paper summarises the results of three case studies of depillaring under shallow depth with or without stowing. Assessment of nature and amount of mining induced stresses and deformation was done under these conditions, by insitu instrumentation and observation at three depillaring panels of Girmint, Samla and Lachhipur collieries of ECL at 54, 90 and 110 m depth cover respectively. The value of induced stresses and associated deformations was comparatively low in well caved and stowed goaves, whereas for massive roof the roof fall followed overriding of pillars and stooks, with very high value of induced stresses and deformaton in absence of stowing. The stress in the centre and outer edges of the pillars changed with respect to depillaring face advance or splitting of pillars. The caving panel of Girmint colliery under weak coal measure formation, showed maximum induced stress in the pillar at 4 m distance from the face which was 1.2 times (16.6 kg/sq.cm) the premining stress of the area. The main roof fall over partially stowed goaf of Lachhipur colliery under massive roof strata caused overriding of pillar after crushing 39 stooks of 7.5 x 7.5 sq.m in rythmic sequence with development of 133/sq.cm maximum induced stress. Well stowed goaf of the same panel reduced this value of abutment stress to 2.3 times (65 kg/sq.cm.) body stress after 40 m further advance of the face from the crushed zone. The depillaring at Samla colliery even under massive roof strata induced low stress, equal to 0.8 times field stress only under the same condition with stowed goaf. The studies revealed the effectiveness of stowing in the goaf over loading of pillars and stooks.

INTRODUCTION

The bord and pillar method of mining is still dominating in Indian coal mining scenario and more than 98% of underground coal production is coming through this method. This method of mining involves extraction of a part of coal from the bords with pillars around as natural support in the development stage and hence about 150-300 million tons of coal of the country is being locked in pillars every year. The liquidation of these pillars under a particular condition could be partial or full, depending upon the safety and stability of the overlying strata and extraction of thick seam in sections. The state of stress and its manifestation as deformation of the left over coal section in pillar, stook and rib influenced the stability of working, dimension of pillars, stooks and fenders and level of recovery.

The key to success of depillaring is thus influenced by the stability of natural supports of pillars, stooks, ribs and surrounding rock mass, which is directly related with the value and nature of induced stresses in and around the line of extraction. Due to complex nature of overlying strata behaviour and broken nature of depillaring process, it is extremely difficult to picturise the stress redistribution by any physical or mathematical modelling technique in the laboratory and hence observation of working faces in the field.

To assess the mining induced stresses associated with depillaring, an extensive insitu instrumentation and observation programme was undertaken for a number of depillaring panels under different geomining conditions. This paper presents loading history of pillars, stooks and ribs against stowed, caved and partially stowed goaves of three collieries. The influence of nature of overlying strata, goaf

treatment and depth cover on the quality and quantity of the induced stresses, over the pillars around the face, is also discussed.

GEOLOGICAL DOMAIN AND COAL MEASURE FORMATION OF THE SITES

The study was conducted during liquidation of pillars in three panels each of Sonachora, Samla and Rana coal seams of Lachhipur, Samla and Girmint collieries respectively of Ranigunj coalfield. The generalised lithology of the field and property of upper stratigraphic measures of the panels are shown in Fig.1. The average working depth of the observation panels of Sonachora, Samla and Rana collieries were 110, 90 and 54 m respectively. The detailed geomining parameters of the three sites are depicted in Table 1. The immediate roof of Sonachora seam was massive sandstone whereas that of the Samla seam it was moderate in comparison to weak, laminated roof of Rana seam.

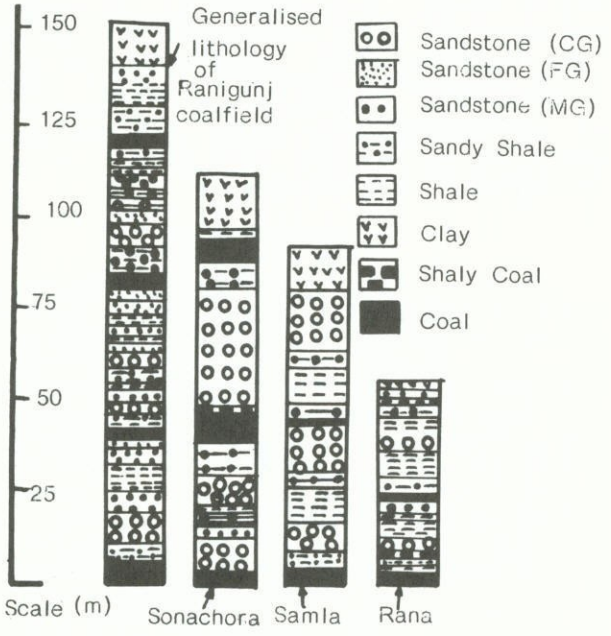

Fig.1 - Generalised upper stratigraphic column of the three coal seams

STATUS OF WORKING AND FACE ADVANCE

Depillarng of the panels in the these collieries was carried out under widely varying conditions like underlying or overlying developed coal seams, protected land and high flood level of rivers. The liquidation of pillars from Samla and Sonachora seams was planned with stowing while that of Rana seam it was proposed with caving. The workings in the stowing panels were erratic due to operational constraints of stowing plants, nonavailability of sand and production thrust. The scarcity of sand caused a mixed operation of goaf treatment, partly stowed and partly caved in Sonachora seam, but in case of Samla seam the goaf was perfectly stowed. The Rana seam depillaring operation was relatively smooth with regular caving of roof behind the goaf.

RANA SEAM OF GIRMINT COLLIERY

The study panel of Rana seam had 39 pillars of 18.3 x 18.3 sq.m in 3 rows consisting 13 pillars in each row. The panel width was 55 m, subcritical for the depth cover. The pillars within the panel were extracted by splitting in two stooks by level splits and the stooks were recovered by driving two slices of 5.9 m width leaving a rib of 1.5 m thick (Fig.2) against the goaf. Against 2.1 m development height, the splitting and extraction were done for total seam thickness of 3.0 m. Complete liquidation of the panel took four months time, maintaining diagonal line of face during depillaring and face advance from dip to rise.

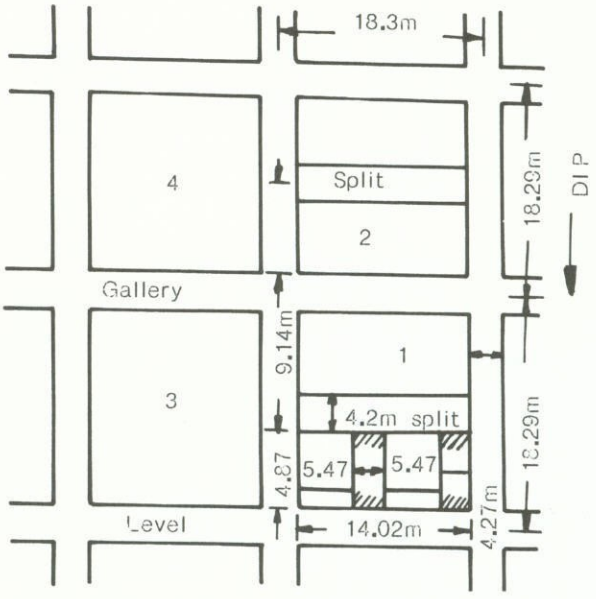

Fig.2 - Stooking sequence of Rana seam at Girmint colliery

SONACHORA SEAM OF LACHHIPUR COLLIERY

The liquidation of 43 pillars of 24 m x 24 m size of Sonachora seam, 34 m below developed Lower Kajora seam, was by splitting and stooking with hydraulic sand stowing in part and caving, when the stowing lagged behind. Depillaring started with splitting of pillars in four stooks by level and dip rise splits, maintaining diagonal face line and advancing from dip to rise. First two and half pillars of 1500 sq.m area (Zone A, Fig.3) were worked with stowing as per plan. Another five and half pillars of 3200 sq.m area (zone B) thereafter were split to stooks and were extracted in half moon fashion leaving fender of 2 m thickness against the goaf. Subsequently nine and half pillars of 6800 sq.m area (zone C) were split in four stooks and the stooks were left intact without stowing (Table 2). At this juncture the overlying strata destabilised and local roof fall occurred inside the goaf. Further stooking of pillars was stopped with the fall but the first row of stooks facing goaf line were crushed. This followed major roof fall up to the goaf line and

Table 1 - Geomining parameters of the observation sites

Parameters	Collieries		
	Lachhipur	Samla	Girmint
Name of seam	Sonachora	Samla	Rana
Depth cover	109 m	90 m	54 m
Thickness	3.4 m	4.7 m	3.04 m
Development height	2.4 m	2.8 m	2.1 m
Depillaring height	3.4 m	4.2 m	3.0 m
Pillar size	24 x 24 m^2	21 x 21 m^2	18.3 x 18.3 m^2
Bord size	4.5 m	4.5 m	4.3 m
% of recovery at development	24%	19%	27%
Proposed ultimate recovery	82%	80%	85%
Goaf treatment	Caving/stowing mixed	Stowing	Caving
No. of pillars in the panel	43	68	39
Overlying or underlying working	Underneath of developed seam	-	-
Composition of overlying strata:			
Sandstone with intercalation	64%	51%	42%
Shale	8%	27%	39%
Coal	12%	9%	5%
Clay	13%	13%	14%

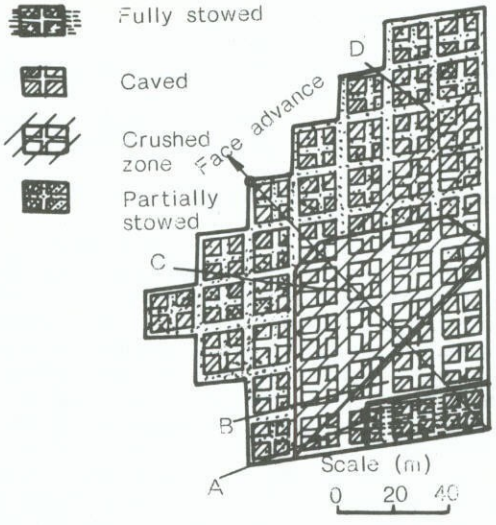

Fig. 3 - Summary of mining propositions of the panel of Lachhipur colliery

crushing of the other stooks in rythmic sequence. The progressive crushing wave was arrested only after it reached up to the last row of stooks formed against the solid pillars. The remaining 26 pillars of the panel covering 14500 sq.m area were extracted with stowing, but due to lag in stowing, only 65% of the extracted area of this zone was stowed.

SAMLA SEAM OF SAMLA COLLIERY

The study panel of Samla seam of 187 x 170 sq.m dimension had 68 pillars of 18 x 18 sq.m size developed upto 2.8 m height along the floor. The liquidation of the pillars was done from dip to rise forming diagonal line of face advance with hydraulic sand stowing of the goaf. A pillar was divided in four stooks and stooks were recovered by conventional half moon fashion, leaving 2 m thick rib against stowed goaf. Leaving 0.5 m coal band along the roof, the height of final extraction was maintained upto 4.2 m. The total area of extraction was stowed, but due to slow process of stowing and multiple simultaneous activities the face advance was slow and erratic and the total extraction of the panel took one and half year time. Due to effective stowing there was no break of overlying strata along the

Table 2 - Extraction summary of the study panel of Lachhipur colliery

Zone	No. of pillar	Area m^2	Method of working	Goaf treatment
A	Two & half	1500	Split, stooked and stooks were extracted with stowing	Fully caved
B	Five and half	3200	Split,stooked and stooks were extracted without stowing	Caved
C	Nine and half	6800	Split, stooked and stooks were left without stowing	Stooks crushed and roof caved
D	Twenty five and half	15500	Split, stooked and stooks were extracted partial stowing	Partially stowed

face during the observation.

OBSERVATION

The induced stresses in pillars and stooks were measured with the help of vibrating wire stress capsules installed 2 to 6 m inside the pillars 50 to 60 m in advance of the extraction line. In all 60 such stress capsules were installed in 13 pillars, including 5, 5 & 3 pillars in Sonachora, Samla & Rana seams respectively. The change in stress was monitored regularly and it was correlated with the mining activities vis a vis face position, goaf line and major falls.

STRESS DISTRIBUTION WITH IRREGULAR GOAF PACKING

The panel containing 43 pillars at Lachhipur colliery was extracted by stooking and stowing, partial stowing and no packing in parts. The stress variation in pillars and stooks was studied for stowed and caved goaf. The stress capsules were installed in the split stooks and solid pillars. The capsules in the stooks showed increase in stress immediately after installation while this increase became sharp when the overlying strata destabilised due to crushing of stooks facing goaf line. After the first major fall followed by crushing of 39 stooks of 7.5 x 7.5 sq.m one after another, the maximum change in stress in the stook was 133 kg/sq.cm (Fig.4) which was 4.8 times that of premining stress (rH). The stress sustained by the stooks before the destruction was coincidently near equal to the laboratory strength of 41 mm core sample (176 kg/sq.cm) and nearly double of the insitu strength (80 kg/sq.cm) of a 30 cm cube. This could be justified by the fact that the core of the pillar acted under confined triaxial state.

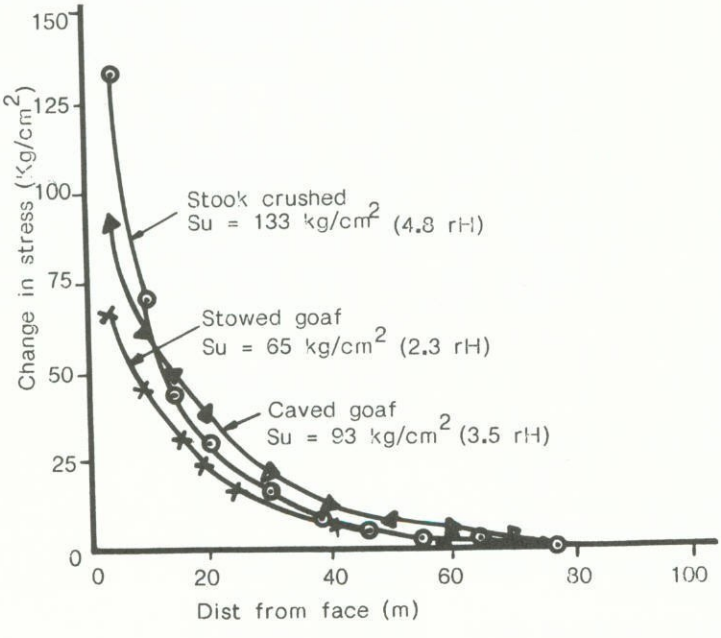

Fig.4 - Influence of pillar overriding and goaf treatment on abutment stress on pillars and stooks at Lachhipur colliery.

Further advance of the face with stowing or caving of the goaf induced stress on pillars or stook. It remained below premining stress (rH), till the extraction line was more than 20 m away though the change in stress was observed 50 m in advance of the face line. The change of stress with the splitting of the pillars against caved and stowed goaves were 14.2 kg/sq.cm and 11.4 kg/sq.m respectively (Table 3). The stress variation within 20 m of extraction line in case of stowed goaves increased slowly while the trend was sharp in case of caved face (Fig.4). The average ultimate stresses on stooks facing goaf line for stowing and caving goaves were observed to be 65 kg/sq.cm (2.3 rH) and 93 Kg/sq.cm (3.5 rH) respectively. The change in stress became very sharp as the observation point came within 5 m against caved goaf. The trend of stress variation vis a vis loading condition of pillars and stooks is depicted by generalised curve of exponential nature given below:

$$S = aD^b \quad \ldots \quad (1)$$

Where, S is change in stress
a and b are dimensionless constants,
D is distance of the observation station from the goaf line.

The value of constants 'a' and 'b' varied extensively (Table 4) due to different geomining conditions.

STRESS DISTRIBUTION WITH CAVING

The liquidation of pillars of size 18.3 x 18.3 sq.m of Rana seam under weak overlying strata was by stooking and slicing, leaving thin rib of 1.5 m against goaf. The stress capsules were installed 60 m in advance of the face and the change became perceptible only when a pillar was split within 30 m of the observation point. The splitting of the instrumented pillar induced 10 kg/sq.cm (0.74 rH) stress even though the goaf line remained at the same distance. There was no appreciable increase in stress in stooks till the face was more than 15 m away. With the face reaching within 15 m zone (Fig.5) the value of induced stress increased rapidly and the maximum observed value on stooks reached up to 16.6 kg/sq.cm (1.2 rH) when the adjacent stooks were extracted in the conventional manner. Under the influence of the adjacent workings, the stress concentration over the stooks incrased in a fashion shown in Fig.6. The stooks were subjected to high stress concentration along the side while the core remained under comparatively low stress. With the extraction of the adjacent stooks within 5 m, the core also came under high stress concentration apparently with the yield of the sides. Frequent roof fall behind the goaf and settlement of goaf reduced the chance of overriding or dynamic loading of stook.

STRESS VARIATION WITH FULL STOWING

Depillaring of Samla seam was with full packing, leaving rib of 2 m thickness inside the goaf, was from dip to rise. Splitting of two pillars in advance of the face line induced perceptible change in stress when the extraction line was 45 m away. The change was very slow till the face line was beyond 15

Table 3 - Details of stress concentration on pillar & stooks

Parameters	Mines			
	Lachhipur	Lachhipur	Samla	Girmint
Goaf treatment	Caving with overriding	Stowing	Stowing	Caving
Premining stress (rH)	27.25 kg/cm^2	27.25 kg/cm^2	22.5 kg/cm^2	13.5 kg/cm^2
Uniaxial compressive strength of coal	176 kg/cm^2	176 kg/cm^2	255 kg/cm^2	280 kg/cm^2
Average change in stress due to splitting	14.2 kg/cm^2 (0.52 rH)	11.4 kg/cm^2 (0.42 rH)	11.2 kg/cm^2 (0.5 rH)	10.0 kg/cm^2 (0.74 rH)
Ultimate average stress in stook	133 kg/cm^2 (4.8 rH)	65 kg/cm^2 (2.3 rH)	18.4 kg/cm^2 (0.8 rH)	16.6 kg/cm^2 (1.2 rH)

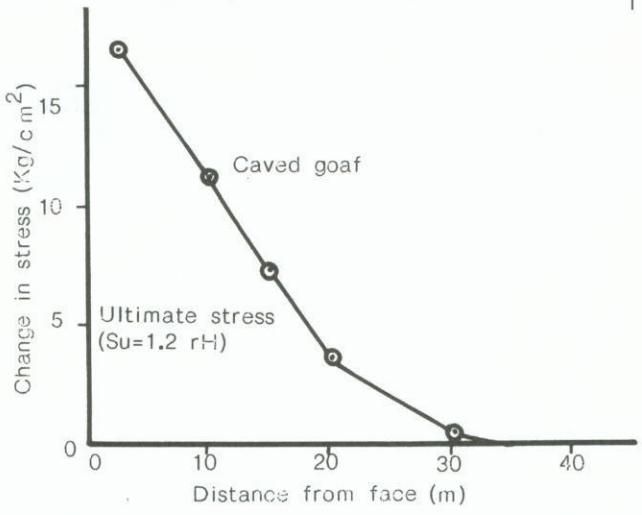

Fig.5 - Development of induced stress during pillar liquidation under weak overlying strata of Girmint colliery.

m. The change in induced stress was sharp when the goaf line came closer within 15 m. After splitting of the instrumented pillars, the stress increased up to 11.2 kg/sq.cm (0.5 rH) and up to 18.4 kg/sq.cm (0.8 rH, Fig.7) when the adjacent stooks were extracted. Due to effective sand stowing and left over rib within the goaf, the immediate roof and overlying strata was practically stabilised, saving the face from overriding or heavy induced stress.

RESULTS AND CONCLUSION

The nature and amount of stress redistribution during the extraction of developed pillars is a function of large number of parameters like goaf treatment, strength of overlying strata, overlying or underlying workings, geology of the area, depth cover and insitu stress condition. Change of stress under shallow depth cover (54 to 110 m) during

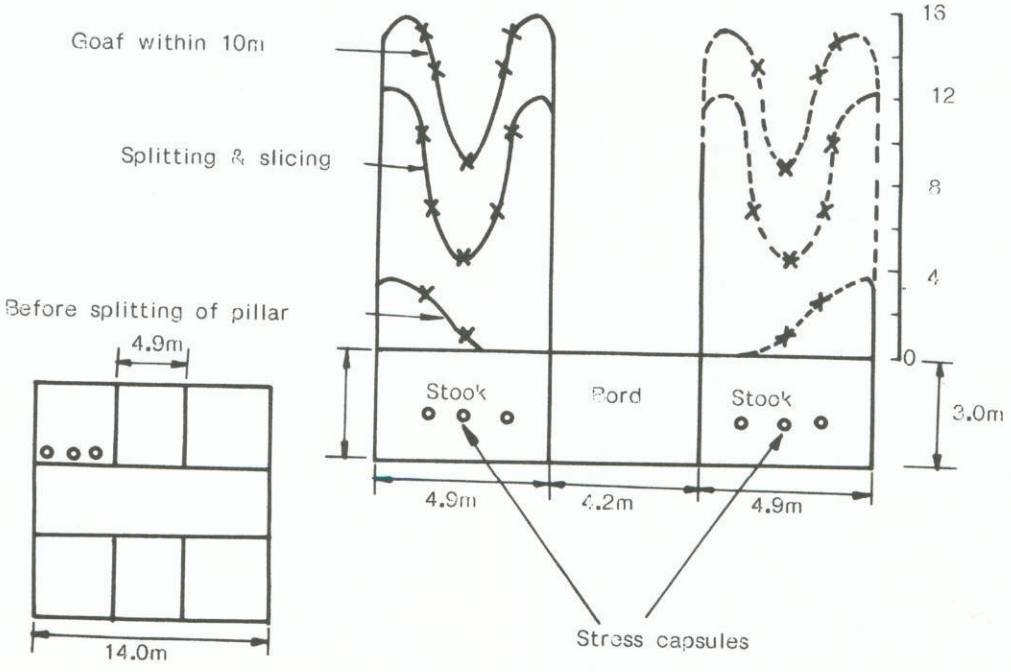

Fig.6 - Stress concentration over stooks during splitting of recovery of neighbouring pillars of Girmint colliery

Table 4 - Stress concentration for different positions in mines

Mine	Goaf treatment	Range of distance (D)	Constant a	Constant b	Expression	Regression coefficient	Index of determination
Lachhipur	Pillar crushing	5-60 m	372.307	-0.89138	$S=aD^b$	0.97	0.96
Lachhipur	Partial stowing	5-70 m	298.328	-0.7727	$S=aD^b$	0.92	0.85
Lachhipur	Stowing	5-70 m	204.88	-0.812201	$S=aD^b$	0.93	0.86
Girmint	Caving	5-35 m	75.1219	-0.83082	$S=aD^b$	0.95	0.91
Samla	Stowing	5-50 m	92.9262	-1.63305	$S=aD^b$	0.94	0.88

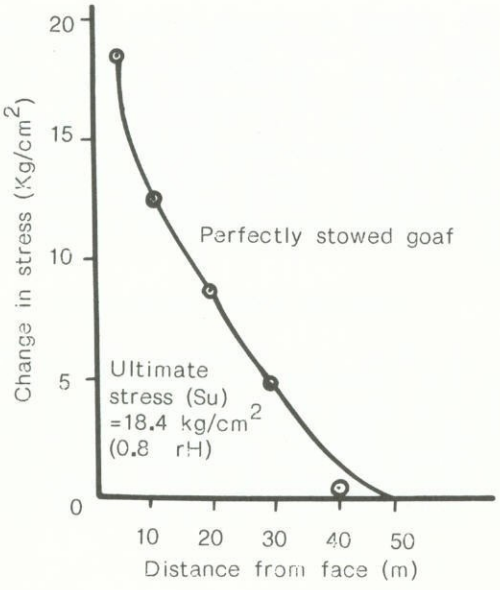

Fig. 7 - Change in stress during depillaring against well stowed goaf of Samla colliery.

splitting, stooking and caving or stowing, was studied with widely varying goaf treatment. Additional information were gathered regarding stress concentration over stooks or ribs formed or left within the goaf.

The mines covered in the present study were practically free from major geotechnical disturbances. Under the condition, body weight could safely be taken as normal stress, defined as rH, where r is bulk density of overlying strata and H is depth cover. The percentage of recovery with the development in different mines was around 20% and so the pillar stress concentration accordingly could be 1.2 rH before instrumentation and observation was resumed. The loading pattern of a pillar due to splitting or stooking at Rana Seam of Girmint colliery is shown in Fig.6. The stress concentration over pillar edge was up to 0.25 rH and dropped assymptotically to near zero about 3 m within. The magnitude of vertical stress, under shallow depth cover up to 100 m, could accordingly be 25 kg/sq.cm and even the edge of the coal pillar remained safe with safety factor of 3-4. No spalling under the condition was envisaged under such a shallow depth cover.

Irrespective of stowing or caving, depillaring in all the mines was by splitting and stooking by slicing or winning in half moon fashion. The value of ultimate stress (Su) sustained by a stook or rib before it was crushed could be expressed as follows:

$$Su = Si + Sd + Ss + Sc \quad \ldots \quad (2)$$

Where, Si is insitu premining stress
Sd is change in stress due to development of pillar
Ss is change in stress due to pillar splitting,
and Sc is stress concentration due to overriding or extraction of neighbouring pillars.

Under the condition of Lachhipur colliery subjected to ultimate crushing the value of ultimate induced stress on stook could be written as follows:

$$Su = rH + 0.2rH + 0.5rH + 4.8rH = 6.5\ rH \quad \ldots (3)$$

The goaf treatment in the presence of massive overlying strata caused remarkable change in the value and nature of induced stress. The stooks experienced 65 kg/sq.cm (2.3 rH) maximum induced stress under the same condition with stowed goaf with cumulative stress upto 4.0 rH. With partial stowing of the goaf, the value of maximum cumulative stress over the stooks was 5.2 rH.

The maximum induced stress over the stooks with weak overlying strata, was 16.6 kg/sq.cm (1.2 rH) at Girmint colliery. The stooks with well stowed goaf under the same condition at Samla colliery experienced only 18.4 kg/sq.cm (0.8 rH) induced stress. This also corroborated the effectiveness of stowing in reducing the stress concentration and arresting abutment loading.

ACKNOWLEDGEMENT

The field investigations were funded by the Ministry of Energy, Dept. of Coal, Govt. of India. The cooperation of the management of Eastern Coalfields Ltd. in undertaking field studies over 3 years period is thankfully acknowledged.

Thanks are due to Director, Central Mining Research Station, Dhanbad for presentation of the paper.

10th INTERNATIONAL CONFERENCE ON GROUND CONTROL IN MINING

FINITE ELEMENT MODELING OF SUBSIDENCE INDUCED BY UNDERGROUND COAL MINING: THE INFLUENCE OF MATERIAL NONLINEARITY AND SHEARING ALONG EXISTING PLANES OF WEAKNESS

Daniel W. H. Su, *Senior Research Engineer*

Consolidation Coal Company
Library, Pennsylvania

ABSTRACT

Surface subsidence induced by multiple-panel coal extraction was calculated with finite element stress analysis. The use of nonlinear material behavior and GAP elements, which provide a realistic representation of shearing along existing planes of weakness, allows the finite element program to accurately reproduce observed subsidence profiles. A reduction factor of 1/6 is applied to the measured rock strength and modulus for use in the finite element model. The models satisfactorily predict a significant change in maximum subsidence and subsidence profile associated with an increase from subcritical to near critical panel width. Modeled shearing along planes of weakness is in good agreement with available time domain reflectometry field observations and is demonstrated to have a very profound effect on the maximum subsidence and the shape of the subsidence profile. When both material nonlinearity and planes of weakness are incorporated, the finite element model appears to possess great potential for accurately predicting surface subsidence and subsurface strata deformation in environments where little subsidence information is available.

INTRODUCTION

In the past few decades, numerous methods for predicting mining subsidence have been proposed. The basic aim of all prediction methods is to produce an acceptably accurate assessment of mining subsidence and in some cases its associated effects on surface features and structures. The various principal methods of predicting mining subsidence can be grouped as follows (Whittaker and Reddish, 1989):

1. Empirically derived relationships
2. Profile functions
3. Influence functions
4. Physical models
5. Analytical models

The empirically derived relationships rely on sufficiently large numbers of observations and case studies in order to establish levels of accuracy for subsidence prediction. The profile functions and the influence functions, on the other hand, use equations and functions with constants derived empirically from local observations. Physical models employing a wide range of model materials have been used with various degrees of success in many countries for the purpose of observing the resulting subsidence. Although the actual mechanisms of deformation and failure can be observed, physical models generally involve much more time than theoretical models in performing similar investigations. The group of analytical models contains those models which are based on treating subsidence as a problem which can involve the laws of elasticity, plasticity, and viscoelasticity. Finite element methods are probably the most advanced form of mathematical modeling within this group, but care needs to be exercised in the choice of rock mass behavioral properties since a purely isotropic elastic solution tends to predict profiles which are much flatter than the real subsidence profiles.

Simulation of rock failure and resulting ground movement using nonlinear analysis provides a more realistic basis for mathematical prediction of surface subsidence. This method of modeling mining subsidence offers the advantages of predicting the extent of fracture zones above excavation and predicting ground movement at intermediate horizons. It also allows scope for incorporating geological variations, such as lithology, ***in situ*** stresses, and joints, in the model. The finite element models play an important role in the prediction of caving and subsidence and are particularly flexible and advantageous to investigating new geological and mining environments. They have proven useful in supplementing the other prediction models discussed earlier.

During the past several years, Consol has engaged in numerous subsidence research studies, particularly in Northern Appalachia. To date, the results have indicated that shearing along planes of weakness plays a very

important role in the overall subsidence process (Su and Hasenfus, 1987, Hasenfus, et al., 1988). Using the finite difference and distinct element methods, Coulthard and Dutton (1988) also pointed out the importance of the ubiquitous horizontal joints and nonlinear material models. Therefore, it is concluded that a realistic finite element model for predicting mining subsidence must simulate the shearing along planes of weakness and the nonlinear rock behavior. This paper presents the results of such modeling recently conducted at Consol. Modeled shearing along planes of weakness and calculated subsidence profiles are compared with those observed in the coalfield, and the potential of the finite element model for predicting subsidence in enviroments where little subsidence information is available is assessed.

OBSERVATIONS OF MINING SUBSIDENCE IN THE APPALACHIAN COALFIELD

Subsidence data from a variety of mining and geological conditions in the Appalachian coalfield have been gathered by a number of researchers in the past decade (Adamek and Jeran, 1981; Bauer and Hut, 1981; Peng and Geng, 1982; Geng and Peng, 1983; Karmis, et al., 1983; Karmis, et al., 1984; Trevits and King, 1986; Karmis, et al., 1987; and Su and Hasenfus, 1987). Their observations concerning subsidence above longwall workings can be summarized as follows:

- As the ratio of panel width (W) to depth of cover (H) increases, the maximum subsidence (S_{max}) increases.
- As the ratio W/H increases, the subsidence above the edge of the panel decreases relative to S_{max}.
- As the ratio W/H increases, the inflection point moves towards the center of the panel, which results in a steeper profile.
- The observed angle of draw ranged from 12 to 34°.
- The maximum subsidence appears to be attained when W/H reaches around 1.2, at which point S_{max} reaches 0.45-0.65 M, where M is the extraction thickness.
- At or beyond the critical width, the inflection point is a maximum distance of $D \geq 0.2$ H inside the edge.
- At or beyond the critical width, the subsidence above the edge of the panel is a relative minimum of less than 10% of S_{max}.

Similar to that described by Coulthard and Dutton (1988), observations of mining subsidence in the Appalachian coalfield also indicated a transition from subcritical to supercritical panel widths. The transition was marked by a significant change in the shape of the subsidence profile.

PREDICTION OF SURFACE SUBSIDENCE BY THE FINITE ELEMENT METHOD

The finite element method (FEM) is a powerful numerical modeling procedure and its applications to engineering problems have been discussed in detail by Zienkiewicz (1977). However, many subsidence predictions using the finite element method have been attempted with limited success, when shearing and separation along existing planes of weakness in the overburden were not incorporated.

The finite element program employed in the current research is MSC/NASTRAN version 66B, which possesses the capability of modeling shearing and separation along existing planes of weakness and nonlinear material behavior. Figure 1 shows a two-dimensional, three-panel model, which includes twenty-eight layers of GAP elements for simulating the important shearing and separation along existing planes of weakness. By thoroughly examining the geological log shown in Figure 2, the planes of weakness were defined by identifying layers of relatively soft and thin material when compared with the layers immediately above and below. The planes of weakness were assumed to have a friction coefficient of 0.3 and possess little cohesion. When positive pressure exists, the GAP elements used to simulate these planes can carry any transverse shear load which is less than the coefficient of friction times the normal load.

Figures 3 and 4 illustrate the important characteristics of the GAP elements used in MSC/NASTRAN. Nonlinear analysis adopting elastoplastic material behavior was used to simulate the plastic deformation in rocks surrounding the longwall excavation. The Drucker-Prager criterion was chosen as the yield criterion. It states that:

$$f(\sigma) = \frac{6 \sin\phi}{3 - \sin\phi}\,\sigma_m + \sqrt{3}\,(J_2')^{\frac{1}{2}} - \frac{6c\cos\phi}{3-\sin\phi} = 0$$

where

$$\sigma_m = (\sigma_1 + \sigma_2 + \sigma_3)/3,$$

$$(J_2')^{\frac{1}{2}} = \left\{\frac{1}{6}\left[(\sigma_1-\sigma_2)^2 + (\sigma_2-\sigma_3)^2 + (\sigma_3-\sigma_1)^2\right]\right\}^{\frac{1}{2}},$$

ϕ = Angle of internal friction, and

c = Cohesion

The rocks were assumed to exhibit isotropic strain hardening. Their laboratory-determined mechanical properties are summarized in Table 1. Depending on the size of the element representing the rocks, the rock

moduli and strengths shown in Table 1 were reduced by a scale factor of approximately 1/6 for input into the model to account for discontinuities and effects of pore pressure. The reduction factor was estimated according to $(V/V_o)^{0.167}$, where V_o is the volume of the rock used in the laboratory testing and V is the volume of the rock used in the finite element model.

The behavior of the rubblized zone or gob which was assumed to be formed under an initial bulking factor of 1.50 (Peng and Chiang, 1984), was simulated by a series of GAP elements. After reviewing published data (Rice, 1929 and Trueman, 1990) regarding the properties of broken rocks, the GAP elements were assumed to possess very low initial stiffness ($E \approx 1050$ psi) and to acquire much higher stiffness ($E \approx 42{,}000$ psi) after a gob compaction of approximately 22%. The gob material, with a relatively high width to height ratio, thus behaves as though it is constrained (Jaeger and Cook, 1977) and follows a nonlinear load-deformation curve.

RESULTS FROM THE FINITE ELEMENT MODELS

Model Verification

Results from the finite element modeling are presented in terms of predicted fracture zones above the longwall, predicted overburden deformation and the associated shearing along planes of weakness, and predicted surface subsidence. These predictions are compared with observations made in the coalfield to verify the versatility and accuracy of the model.

Figure 5 illustrates the predicted fracture zones above a longwall extraction 640 feet wide under 710 feet of cover. The extraction thickness is assumed to be 6 feet. The highest elevation of fracturing is seen near the edges of the panel at a horizon 164 feet above the mining level. For the purpose of comparison, the extent of the fracture zone estimated from post-mining coring of the overburden strata was approximately 165 feet above the mining level (Su and Hasenfus, 1987).

Overburden deformation above the longwall extractions and the associated shearing along planes of weakness are shown in Figure 6. The small gaps along the GAP elements near the edge of the panel do not indicate bedding plane separation. Rather, they indicate a combination of shearing and compressive deformation along the planes of weakness. The predicted final transverse shear deformations along those planes of weakness close to the surface are listed in Table 2. To correlate with field Time Domain Reflectometry (TDR) measurements shown in Figure 7 (Su and Hasenfus, 1987), however, shear deformations or shear forces along the traveling (longitudinal) profile are needed. Since the coaxial cables used for TDR measurements are usually embedded in a grout column, which constitutes a circular inclusion in a multiple-phase material in the horizontal plane, shear forces rather than shear deformations would be the better indicator for correlating with field TDR measurements. Table 3 lists the predicted shear forces acting on a grout column 3.25 inches in diameter along the longitudinal profile. Assuming that a shear force of 15,500 lbs is required to completely sever the grout column and the embedded coaxial cables 0.25 inch in diameter, the predicted TDR response is shown in Figure 7. It is seen that the predicted TDR response is in close agreement with that observed in the field.

The predicted surface subsidence as a result of the longwall extractions is shown in Figure 8. The surface subsidence observed in the field (Su and Hasenfus, 1987) is also included for comparison. It is seen that the predicted subsidence is in close agreement with that observed in the field.

In summary, the finite element model incorporating shearing along planes of weakness and material nonlinearity yields fairly accurate predictions of induced fracture zones, overburden deformation, and the resulting surface subsidence above longwall extractions.

Effect of Shearing Along Planes of Weakness on Surface Subsidence

Several factors were found to influence the development of surface subsidence over a longwall panel; namely, seam thickness, width and depth of the panel, type of support, seam inclination, time, and angle of draw (Peng, 1978). In addition, the number of planes of weakness and the geomechanical properties of the overburden have been found to be among the most important factors affecting development of surface subsidence.

Figure 8 also shows the effect of shearing along planes of weakness on the development of surface subsidence. It is apparent that incorporating the shearing along planes of weakness has a very profound effect on the maximum subsidence and the subsidence profile predicted by the model. The planes of weakness serve to reduce the overburden strata from a thick beam to numerous thin beams, thereby greatly reducing the flexural stiffness of the overburden strata. With nonlinear material properties, the maximum subsidence predicted by the model with planes of weakness is approximately five times that for the model without planes of weakness.

Effect of Material Nonlinearity on Surface Subsidence

Figure 8 also indicates that the effect of material nonlinearity on surface subsidence is relatively small compared to that of planes of weakness. With planes of weakness, a model with elastoplastic material would only increase the predicted maximum subsidence by 2% compared to that of a model with elastic material. The material nonlinearity alone is seen to have little effect on the shape of the subsidence profile.

The effect of panel width on the anticipated maximum subsidence and the subsidence profile is illustrated in Figure 9. With a cover depth of 710 feet and an extraction thickness of 6 feet, the subsidence profile above a 440-foot-wide panel is relatively flat with the inflection point only 75 feet inside the edge of the panel and a maximum subsidence of about 1.1 feet. The ratio of panel edge subsidence to the maximum subsidence is nearly 22%. Increasing the panel width to 640 feet is seen to increase the maximum subsidence by a considerable amount and shift the inflection point to 155 feet inside the edge of the panel. The ratio of panel edge subsidence to the maximum subsidence is also reduced to 9.2%. When the panel width is further increased to 1000 feet, the maximum subsidence is now 4.10 feet with the inflection point 180 feet inside the panel edge. The ratio of panel edge subsidence to the maximum subsidence now reaches a relative minimum of about 6%.

DISCUSSION

Finite element models which include planes of weakness and material nonlinearity are able to predict the significant subsidence profile change and associated increase in maximum subsidence resulting from an increase of the longwall panel width from subcritical to near critical width. This phenomenon has been frequently observed in the coalfields of Eastern United States and New South Wales, Australia. Figure 9 suggests that the change would occur at a width between 440 and 640 feet for a cover depth of 710 feet. Most empirical and analytical subsidence prediction models, including the profile and influence function methods, fail to predict such significant changes in maximum subsidence and profile shape with increasing panel width. It is hypothesized that additional fracture zone development near the critical width and possible buckling of the overburden rock beams at a beam length close to the critical width are responsible for the observed increase in maximum subsidence and subsidence profile curvature.

When planes of weakness are incorporated into the finite element model, a material reduction factor of approximately 1/6 is needed to produce accurate maximum subsidence and subsidence profile predictions. However, a reduction factor of nearly 1/30 would be required if planes of weakness were not incorporated into the model. A reduction factor of approximately 1/6, depending on the volume of the rock in question, appears to be quite reasonable.

The computed shearing along planes of weakness also has the potential for predicting the temporary permeability increase in the overburden after longwall mining. It should be noted that the shearing motions outside the fracture zone are accompanied by high compressive strain and therefore would heal with time.

CONCLUSIONS

Results from the finite element model development to date indicate that the use of nonlinear material behavior and GAP elements, which provides a realistic representation of the shearing along planes of weakness, allows the models to accurately reproduce observed subsidence profiles. The models also satisfactorily predict significant changes in maximum subsidence and the subsidence profile as the longwall panel increases from subcritical to near critical width. Shearing along planes of weakness has been found to have a very profound effect on the maximum subsidence and the shape of the subsidence profile. With the capabilities of incorporating material nonlinearity and planes of weakness, the finite element model appears to possess great potential for predicting surface subsidence and subsurface strata deformation for environments where little subsidence information is available.

REFERENCES

Adamek, V. and Jeran, P. W. (1981). Evaluation of existing predictive methods for mine subsidence in the U.S., Proc. 1st Annual Conf. Ground Control in Mining, Morgantown, WV, p. 209-219.

Bauer, R. A. and Hunt, S. R. (1981). Profile, strain and time characteristics of subsidence from coal mining in Illinois, Proc. Workshop on Surface Subsidence Due to Underground Mining, Morgantown, WV, pp. 207-219.

Coulthard, M. A. and Dutton, A. J. (1988). Numerical modeling of subsidence induced by underground coal mining, Proc. 29th U.S. Symposium on Rock Mechanics, Tucson, AZ, pp. 529-536.

Geng, D. Y. and Peng, S. S. (1983). Longwall mining techniques for minimizing surface structure damage. SME-AIME Annual Meeting, Atlanta, GA, Preprint No. 83-99.

Hasenfus, G. J., Johnson, K. L., and Su, W. H. (1988). A hydrogeomechanical study of overburden aquifer response to longwall mining. Proc. 7th International Conf. Ground Control in Mining, Morgantown, WV, pp. 149-162.

Jaeger, J. C. and Cook, N. G. W. (1977). Fundamentals of Rock Mechanics, John Wiley & Sons, New York, 585 pp.

Karmis, M., Haycocks, C. and Triplett, T. (1984). Ground settlement and deformation characteristics above undermined areas: experiences from the eastern U.S. coalfields, Fourth Australia-New Zealand Conf. on Geomechanics, Perth, May, pp. 647-653.

Karmis, M., Jarosz, A. and Schilizzi, P. (1987). Monitoring and prediction of ground movement above under-

ground mines in the eastern U.S., Proc. 6th International Conf. Ground Control in Mining, Ed. S.S. Peng, West Virginia University, Morgantown, WV, June, pp. 184-194.

Karmis, M., Triplett, T., Haycocks, C. and Goodman, G. (1983). Mining subsidence and its prediction in the Appalachian coalfield, Proc. 24th U.S. Symp. on Rock Mechanics, June, pp. 665-675.

Peng, S. S. and Geng, D. Y. (1982). Surface subsidence, overburden behavior and structural damages due to longwall mining -- two case studies, Proc. 2nd International Conf. Stability in Underground Mining, University of Kentucky, pp. 497-523.

Peng, S. S. and Chiang, H. S. (1984). Longwall Mining. John Wiley & Sons, New York, 708 pp.

Rice, G. S. (1929). Tests of strength of roof supports used in anthracite mines of Pennsylvania. U.S. Bureau of Mines, Bull. 303, 44 pp.

Su, W. H. and Hasenfus, G. J. (1987). Field measurements of overburden and chain pillar response to longwall mining. Proc. 6th International Conf. Ground Control in Mining, Morgantown, WV, pp. 296-311.

Travits, M. A. and King, R. L. (1986). Overview of the Bureau of Mines subsidence research program. 88th Annual General Meeting of C.I.M., Montreal, May, 14 pp.

Trueman, R. (1990). A finite element analysis for the establishment of stress development in a coal mine caved waste, Mining Science and Technology, 10, pp. 247-252.

Whittaker, B. N. and Reddish, D. J. (1989). Subsidence - Occurrence, Prediction and Control, Elsevier, New York 528 pp.

Zienkiewicz, O. C. (1977). The finite element method. McGraw-Hill, New York, 787 pp.

Table 1. MECHANICAL PROPERTIES OF OVERBURDEN ROCKS AS DETERMINED FROM LABORATORY TESTINGS

Rock Type*	Young's Modulus (x 10^6 psi)	Poisson's Ratio	Unconfined Compressive Strength (psi)	Cohesion (psi)	Friction Angle (°)
(1) Sandstone	3.15	0.22	8831	1966	42
(2) SW Sandstone	2.10	0.22	8837	2500	31
(3) RS Limestone	2.52	0.22	9472	2310	38
(4) FP Limestone	4.20	0.18	12610	2940	40
(5) Shale w/Sandstone Lenses	1.68	0.25	5200	1625	26
(6) BW Limestone	3.15	0.22	5480	1336	38
(7) Limey Shale	2.10	0.25	8060	1966	38
(8) Interbedded Shale Sandstone	1.68	0.25	6530	1700	35
(9) Surface Material	0.168	0.35	660	210	25
(10) Coal	0.42	0.35	3450	900	35
(11) Claystone	1.26	0.30	2620	756	30

* Rock type used in Figure 1.

Table 2. SHEAR DISPLACEMENTS ALONG NEAR-SURFACE PLANES OF WEAKNESS AT THE CENTER-PANEL AND THE QUARTER-PANEL POINTS

Depth From Surface (feet)	Shear Displacements (inches) Tailgate Quarter-Panel	Center-Panel	Headgate Quarter-Panel
30	1.13	0.066	1.76
50	3.55	0.26	3.84
75	3.54	0.26	3.96
100	3.52	0.26	3.984
125	3.47	0.28	4.02
150	3.432	0.312	4.06
175	3.408	0.336	4.10
200	3.40	0.356	4.152
225	3.372	0.384	4.212
250	3.358	0.419	4.296
275	3.335	0.46	4.378
300	3.312	0.50	4.482

Table 3. SHEAR FORCES ACTING ON A GROUT COLUMN 3.25 INCHES IN DIAMETER

Depth Below Surface, ft	Shear Forces, x 10^3 lbs 200 ft Prior to Face Passage	Directly Above Face	100 ft After Face Passage	150 ft After Face Passage	500 ft After Face Passage
30	0.63	2.06	4.67	5.35	0.98
50	2.22	6.18	13.37	13.47	2.75
75	1.92	9.80	19.41	20.28	2.89
100	1.22	11.23	24.54	26.24	2.89
125	0.49	12.07	29.32	31.62	2.94
150	0.23	12.66	33.78	36.80	2.97
175	1.00	13.26	38.21	41.82	3.02
200	1.84	13.74	42.82	46.68	3.08
225	2.78	14.20	47.84	51.52	3.11
250	3.89	14.72	49.46	56.43	3.13
275	5.18	15.15	50.17	61.32	3.16
300	6.64	15.66	51.38	66.47	3.19
325	8.26	15.98	52.19	71.85	3.19
350	9.99	16.15	53.00	75.76	3.13
375	11.77	16.04	52.87	78.65	3.00
400	13.53	16.63	50.71	77.60	2.84
420	14.83	16.40	49.49	75.52	2.67
440	15.42	16.44	49.01	76.01	2.57
460	15.50	15.71	48.63	77.22	2.48

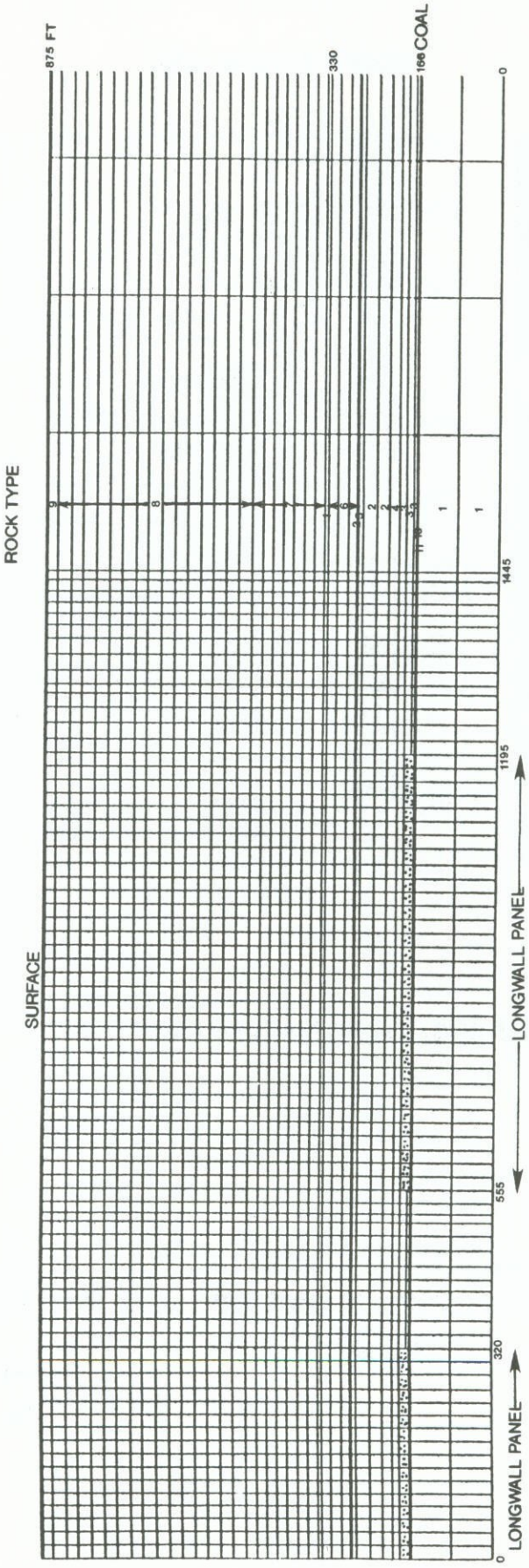

FIGURE 1. A THREE-PANEL FINITE ELEMENT MODEL.

FIGURE 2. CORE LOG.

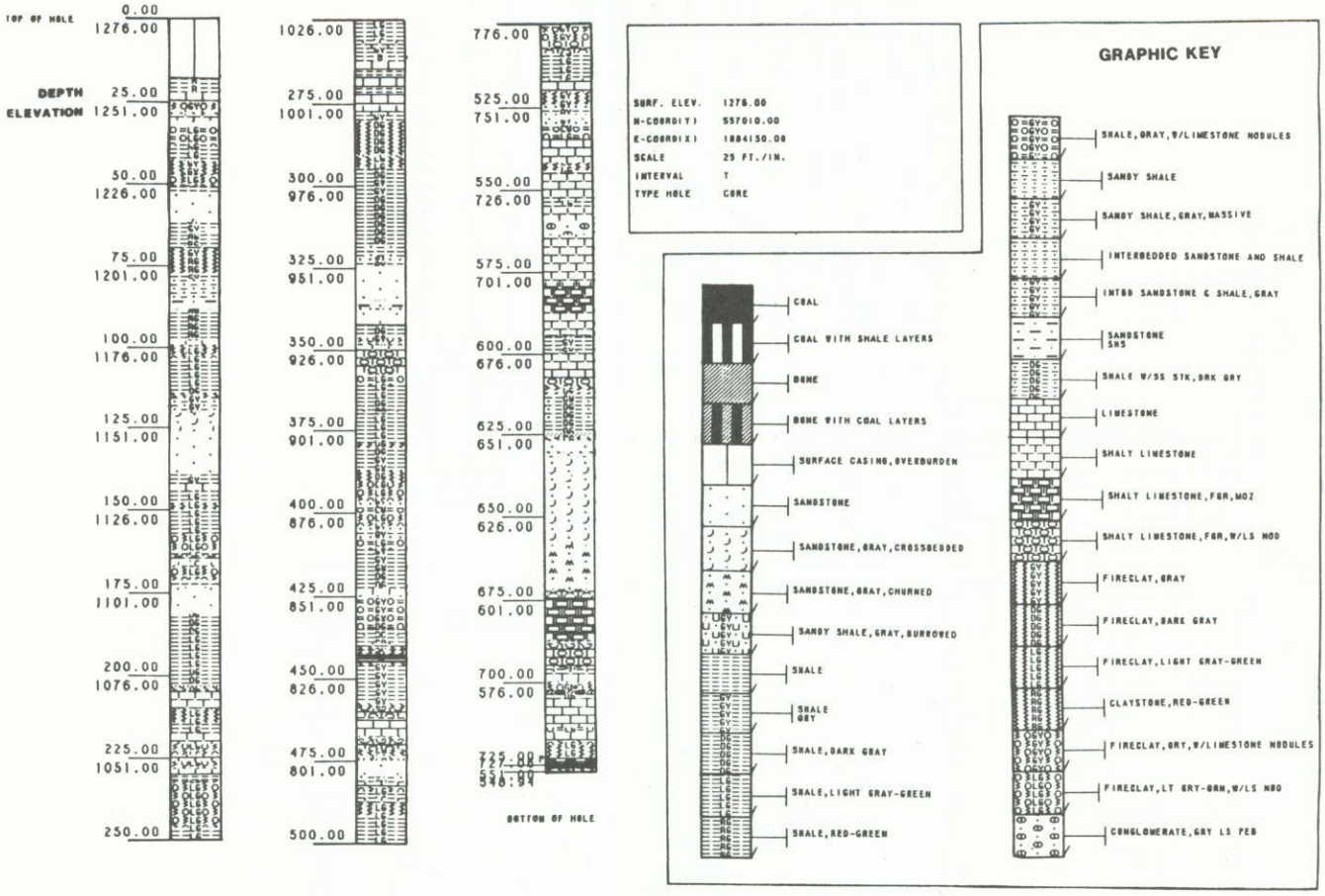

FIGURE 3. THE GAP ELEMENT

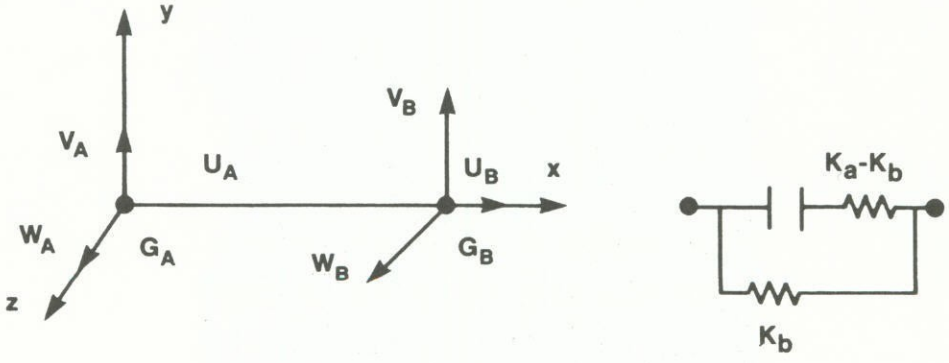

FORCE-DEFLECTION CURVE FOR NONLINEAR ANALYSIS OF GAP ELEMENT

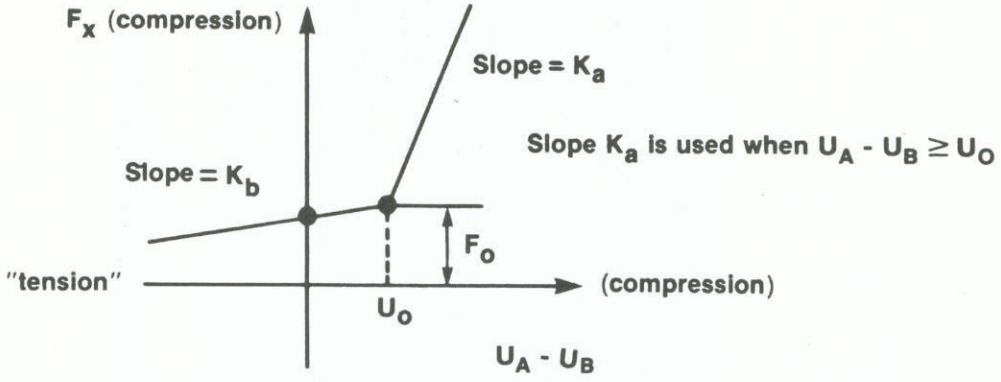

SHEAR FORCE FOR GAP ELEMENT

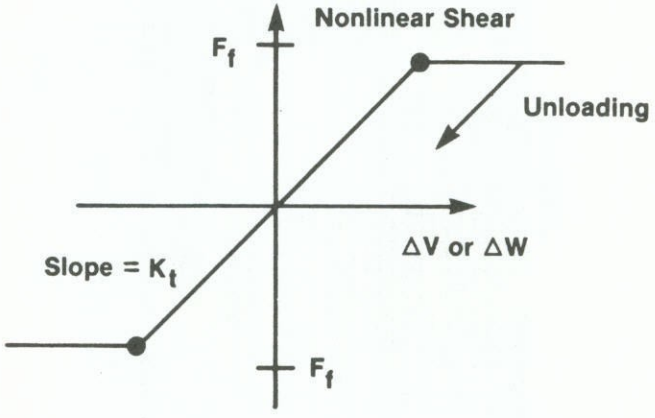

where $F_f = \begin{cases} \mu F_x \text{ if } F_x > 0 \\ 0 \text{ if } F_x \leq 0 \end{cases}$ slope for linear analysis $= \begin{cases} K_t \text{ if } U_o \leq 0 \\ 0 \text{ if } U_o > 0 \end{cases}$

FIGURE 4. FORCE–DEFLECTION CURVE AND SHEAR FORCE FOR NONLINEAR ANALYSIS OF GAP ELEMENT.

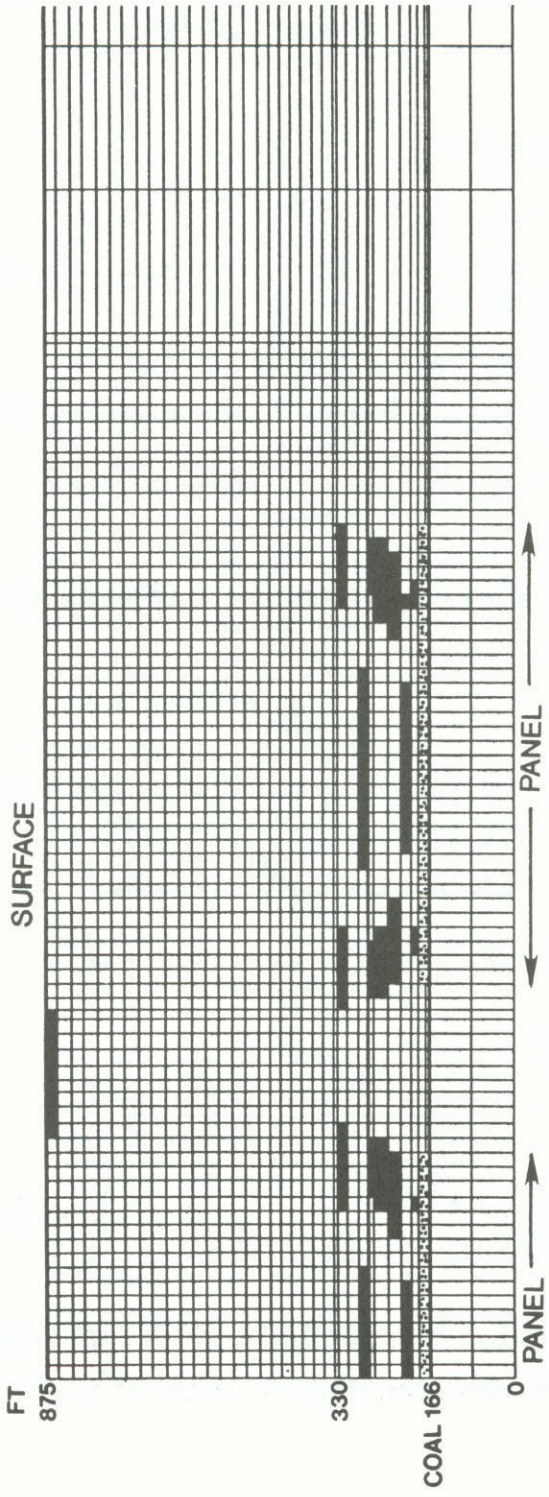

FIGURE 5. INDUCED FRACTURE ZONES ABOVE LONGWALL PANELS.

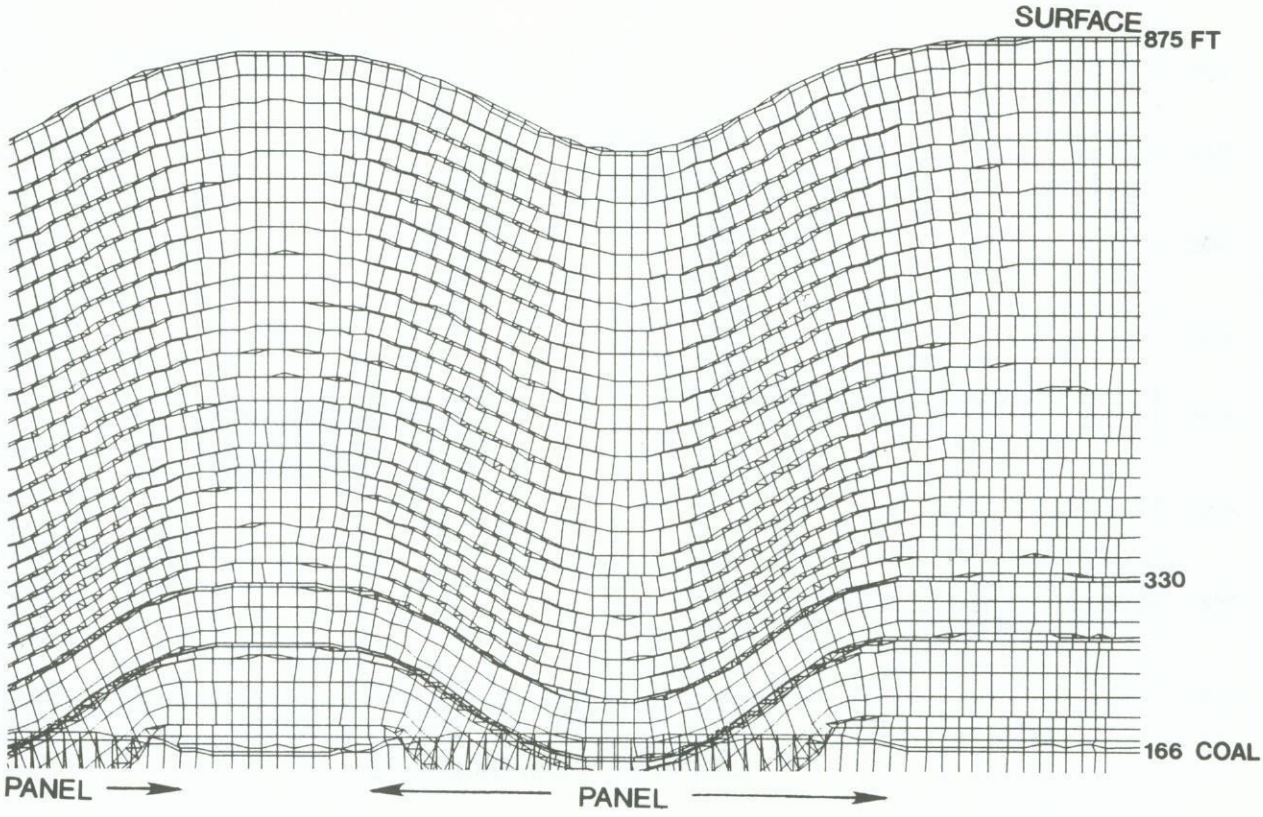

FIGURE 6. OVERBURDEN DEFORMATION OVER LONGWALL PANELS.

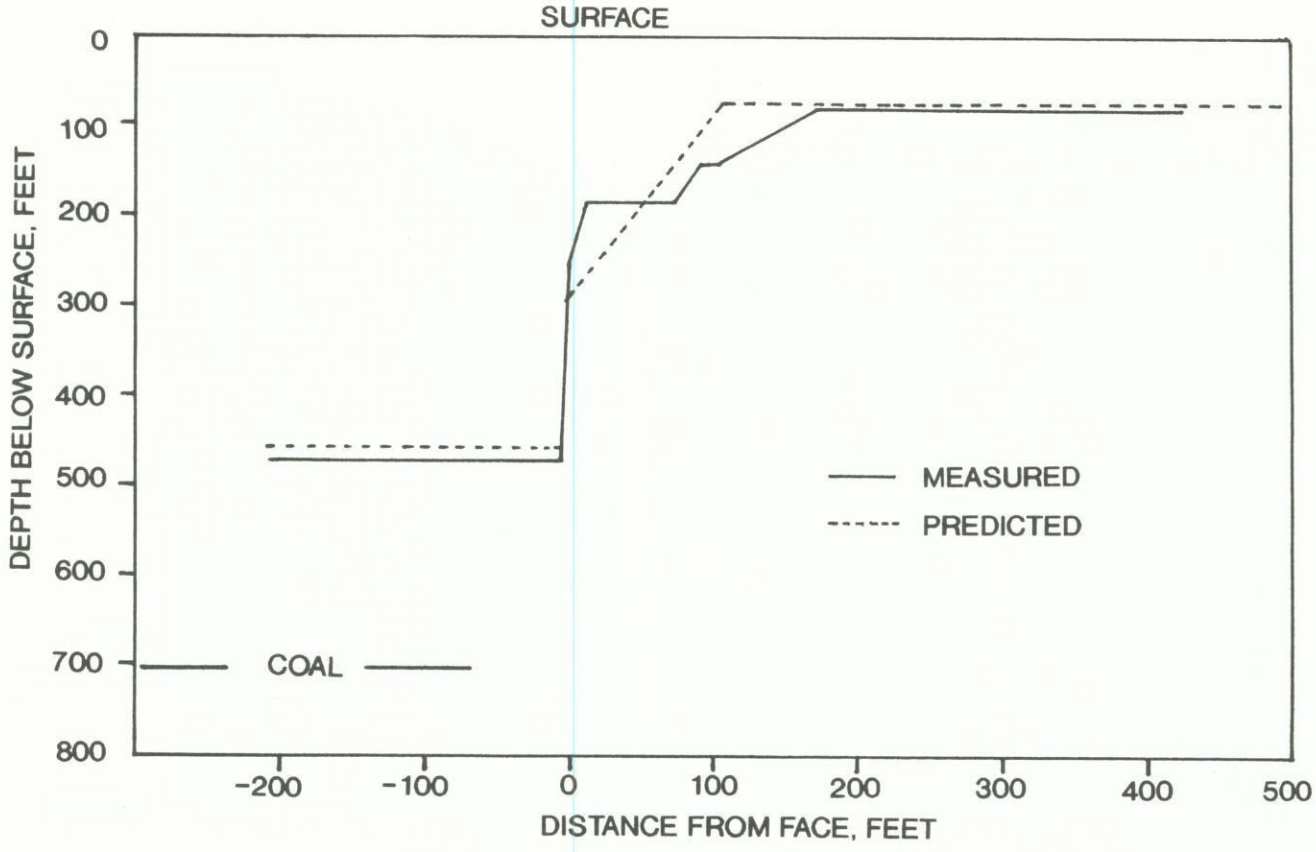

FIGURE 7. TDR RESPONSE ABOVE A LONGWALL PANEL VS FACE POSITION.

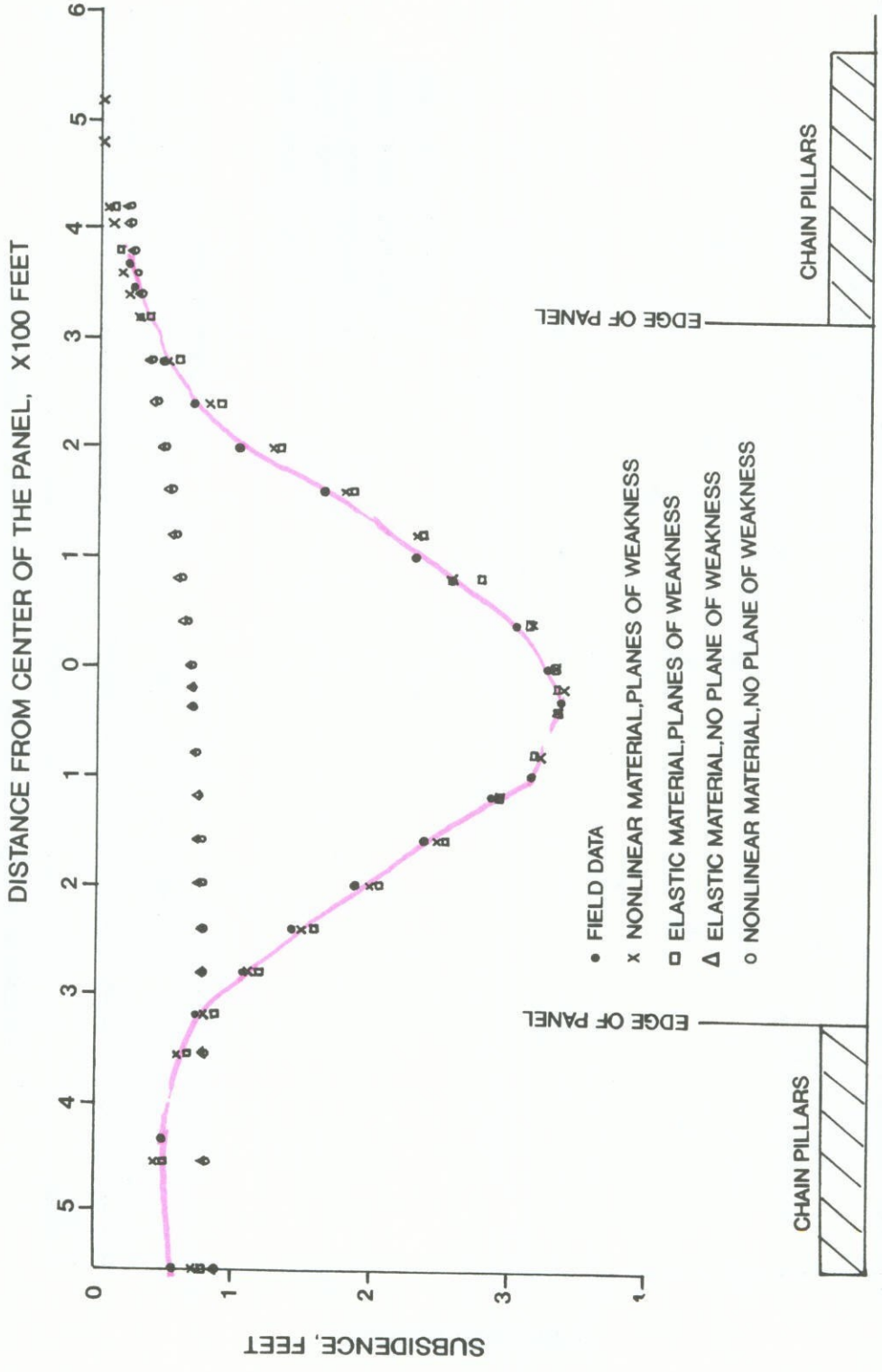

FIGURE 8. SURFACE SUBSIDENCE PROFILES OVER A 640-FOOT-WIDE LONGWALL PANEL.

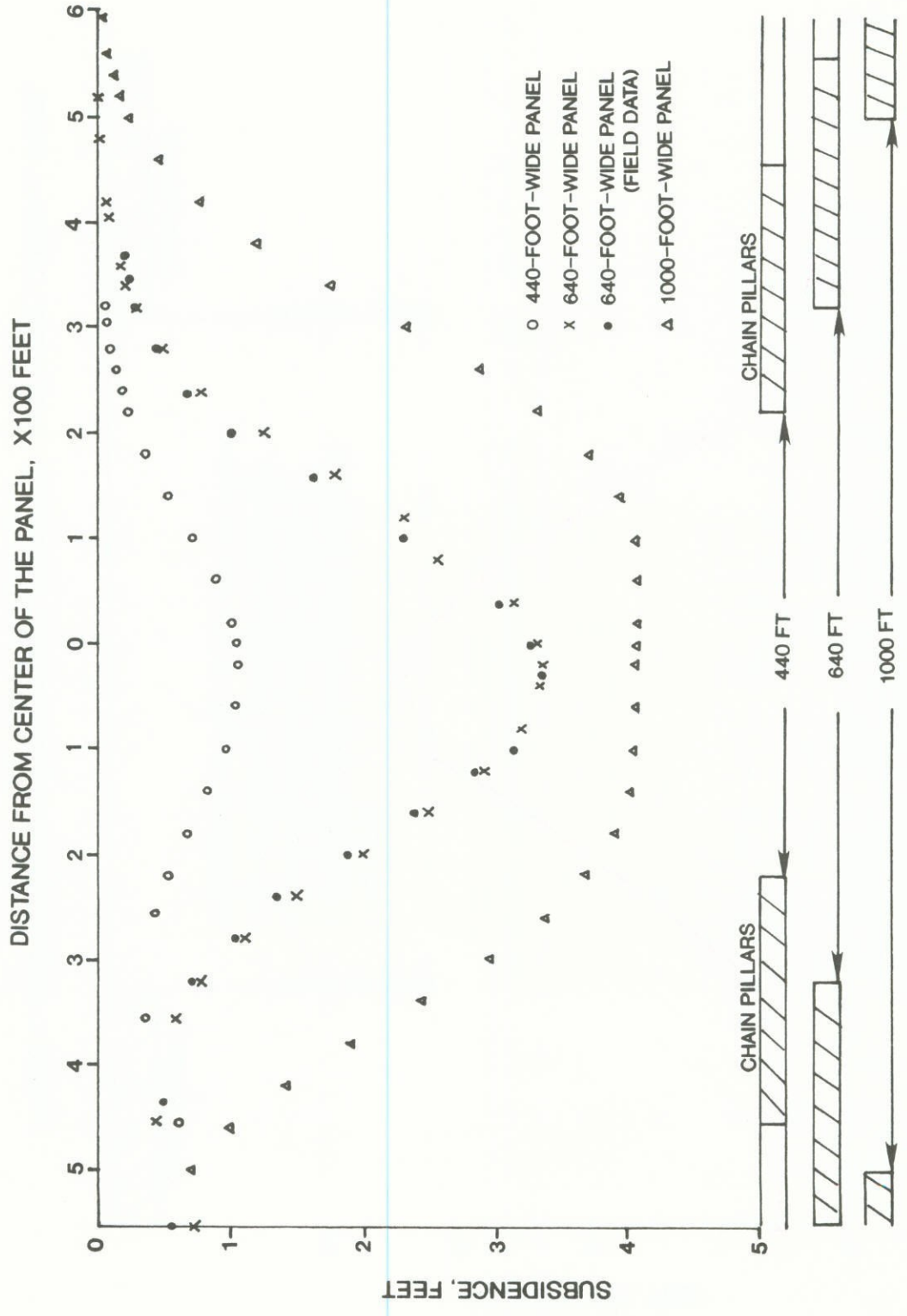

FIGURE 9. EFFECT OF PANEL WIDTH ON SURFACE SUBSIDENCE.

10th INTERNATIONAL CONFERENCE ON GROUND CONTROL IN MINING

THE STRUCTURAL RESPONSE OF A STEEL LATTICE TRANSMISSION TOWER TO MINING–RELATED GROUND MOVEMENTS

Robert W. Bruhn, *Engineering Manager*
GAI Consultants, Inc., Monroeville, PA

George W. Luxbacher, *Director-Technical Services*
Island Creek Coal Company, Lexington, KY

Joseph R. Ferrell, *Manager of Engineering*
Island Creek Coal Company, Mt. Storm, WV

Thomas A. Gray, *Engineering Manager*
GAI Consultants, Inc., Monroeville, PA

ABSTRACT

A 125 foot high steel lattice frame tower supporting a 500 kV EHV transmission line and located over the gateroads of a longwall mining operation was subjected to ground movements from the mining of adjacent longwall panels. Under an agreement with the owner of the powerline, the mine operator was required to minimize mining impacts on the transmission line. In view of this requirement, the mine operator prepared a forecast of the expected subsidence ground movements prior to the onset of mining. These forecasts, in conjunction with finite element analyses of the tower superstructure under the imposed ground movements and wind loadings, suggested that the structural capacity of the tower would probably be diminished little, if at all, by mining. Ground movements determined by survey during mining of the two longwall panels were found to be in close agreement with predictions. Strains measured in selected tower members during mining generally agreed with values calculated by the finite element analyses. The study confirmed a methodology to predict subsidence and to assess its effects on steel lattice transmission towers.

INTRODUCTION

During the period September, 1989 to September 1990, Laurel Run Mining Company (Laurel Run) successfully mined two longwall panels beneath a 500 kV transmission line at its Laurel Run No. 2 Mine located in Grant and Tucker Counties, West Virginia. The transmission line was constructed in the 1960's.

The undermining agreement between Laurel Run and the utility owning the line required that Laurel Run evaluate subsidence impacts to the tower structures along the transmission line prior to the initiation of longwall mining and to take necessary steps to assure the integrity of the line. An initial evaluation was performed by several consultants (Sverdrup Technology, Inc., John T. Boyd Company, and D'Appolonia) under Laurel Run's direction to establish the feasibility of undermining the line tower structures. This evaluation forecasted the subsidence and structural impacts on all the towers within the mine reserve areas, based on a life-of-mine plan. As longwall mining began, Laurel Run retained GAI Consultants, Inc. (GAI) to reforecast the subsidence and structural impacts on Tower A and, subsequently, evaluate these impacts in terms of the subsidence measured at the site. Tower A is one of several transmission towers located on the mine property, but the only tower to lie within the expected zones of influence of the first two longwall panels driven beneath the transmission line.

THE TOWER STRUCTURE

The tower consists of a 125'2" high steel lattice frame structure (Figure 1). The tower is a line tangent structure and consists of a 70'-8" high basic tower body, a 30' body extension, and 24'-6" legs. The main load carrying members in the tower are structural angles constructed of high-strength low-alloy steel. The secondary bracing members are constructed of carbon steel. The tower supports a single 3-phase 500 kV circuit at approximately 95 feet above ground level. The conductors are 1.68" diameter, stranded subconductors with two subconductors per phase. The typical design life of such a tower is approximately 50 years.

Tower A is located on a hillside, with Tower B approximately 55 feet higher and 1365 feet northwest and Tower C approximately 55 feel lower and 1127 feet southeast. Tower A is a tangent suspension structure, but was designed for a line angle of two degrees or less.

The transmission line forms an angle of approximately 70 degrees with the bearing of the underlying longwall panels.

THE MINING OPERATION

Tower A lies above a series of chain pillars in the gateroads located between two longwall panels. The tower is midway down the length of the

panels. Mining is done in the 84 inch thick Upper Freeport Coal seam. Longwall Panel 2-North, referred to in this paper as Panel 1, is located immediately east of Tower A (Figure 2) and was mined first. Longwall Panel 3-North, referred to here as Panel 2 is located immediately west of Tower A, and was mined following the completion of Panel 1.

Longwall Panels 1 and 2 are approximately 640 feet wide. In the vicinity of Tower A, the Laurel Run panels lie approximately 300 feet below ground surface. The width-to-depth ratio (W/H) of the panels is nominally 2.2. About 30 percent of the overburden is composed of hard rock (sandstone and limestone).

CONSIDERATIONS IN THE ANALYSES OF TOWER A

The analysis of Tower A was conducted with the recognition that, over the years, a significant number of transmission towers have been mined under in the United States and abroad, with few reports of adverse effects. Unfortunately, details surrounding these cases are not well documented (either in the literature or in available industry files), negating the usefulness of past experience as a basis for concluding that the effects of undermining Tower A would be negligible or as a means for predicting these effects.

Equally as important, experience in structural mechanics has indicated that even though an undermined structure may exhibit no outward signs of distress, its load capacity may, in fact, be affected by the presence of induced stresses imposed on the structural framework as a result of differential movements in horizontal and vertical planes. This suggests that some of the previously undermined transmission towers may have suffered a reduction in load capacity, although the impact had not been quantified.

These factors provided justification for a detailed study of Tower A. Quantification of the subsidence effects experienced by that tower and a comparison of predicted subsidence and structural impacts will have fostered confidence in the analytical procedures used here. These procedures have potential application to other transmission tower structures located in more adverse positions above future longwall panels at the mine.

The study was conducted in a systematic manner involving the following steps:

A. Development of a finite element model of the tower (done by Sverdrup).

B. Identification of a standard measure -- wind capacity -- for quantifying the effect of undermining on the tower.

C. Computation of the operative wind capacity of the tower after each of the two episodes of longwall mining. For each episode:

1. Estimation prior to mining of the vertical and horizontal ground movements that may arise due to undermining.

2. Computation prior to mining of stresses that may be induced in the tower structure under the estimated ground movements and assumed wind loads using the finite element procedure.

3. Computation of estimated resultant wind capacity of the tower.

4. Recommendation of safety measures during mining, as appropriate, assuming that the pre-mining analysis is valid.

5. Measurement of horizontal and vertical ground movements at the tower and on profiles across the mine panels for comparison with anticipated ground movements.

6. Measurement of strains induced in the structural framework of the tower by strain gages mounted on selected structural members (Second episode of mining only).

7. Recomputation of stresses induced in tower structure, if actual (measured) ground movements depart significantly from anticipated ground movements.

D. Formulation of mitigative measures, if warranted, to relieve induced stresses in the tower framework to restore the tower's initial wind capacity or enhance the towers stability in some other manner.

These items are elaborated upon in the following sections.

PREMINING ESTIMATES OF GROUND MOVEMENTS

Prior to mining, GAI prepared a forecast of possible ground movements that might result from mining each of the two longwall panels. The forecast took into account both horizontal and vertical components of ground movement and was made on the basis on an empirical model involving a negative exponential profile function calibrated using data provided by Laurel Run for longwall panels at the nearby North Branch Mine. The forecast encompassed a series of scenarios to account for uncertainties in critical panel dimensions and for deflection of the chain pillars.

The scenarios ranged from "mild", where ground movements at the tower were negligible, to "extreme", where some crushing of the underlying chain pillars was assumed to occur. Each scenario was assigned a probability based on a consensus of its likelihood of occurrence.

THE FINITE ELEMENT MODEL

Stress analyses of the tower under conditions of subsidence and other loadings were performed by GAI using the Electric Power Research Institute's computer programs TAG (Tower Analysis Generator) and ETAP (EPRI Tower Analysis Program). TAG and ETAP are modules of Version 1 of EPRI's Transmission Line Workstation (TLW) software package.

The finite element model of Tower A developed for ETAP consisted of 442 elements and 232 nodes. The elements consisted of beam, ordinary truss, and tension-only truss elements. Analyses were non-linear to account for the non-linear force displacement relationship associated with tension-only elements. Non-linear effects due to bolt or connection slippage were not considered. Connection slippage would redistribute and reduce stresses induced by ground displacement from those predicted by the model. The model results are considered conservative predictions of the response of the tower to subsidence.

The ground movement estimates were applied to the finite element model to establish the anticipated structural response of Tower A to the subsidence. The assessment of the most probable conditions was that mining of the first longwall panel would have a negligible, virtually imperceptible effect on the integrity of Tower A. Mining of the second longwall panel would result in no more than a minor reduction in wind capacity of the tower.

FIELD VERIFICATION OF GROUND MOVEMENTS

A baseline was established approximating the longitudinal centerline of the first panel along with a series of five survey lines across the first and second longwall panels transverse to the direction of mining.

The profiles were directed east-west, transverse to the direction of mining.

In general, the monuments were spaced at 50 foot intervals. In Panel 1, the monuments were spaced at 25 foot intervals over half the panel width along Profiles A-F. In a few locations, the monuments were spaced at 100 foot intervals.

During mining of the first longwall panel, each profile extended from the east abutment of the first longwall panel westward to the midpoint of the second longwall panel. The eastern extremity of each profile was 250 feet outby the gob of the first panel. During mining of the second longwall panel, each profile extended from the midpoint of the first longwall panel westward to the left abutment of the second longwall panel. The western extremity of each profile during the second episode of mining was 430 feet outby the gob of the second panel.

Thirty one surveys were conducted during mining of the first longwall panel and twenty-one during mining of the second longwall panel. In reference to the longitudinal centerline of the longwall panel, ground movements were first discerned when the longwall face had approached to within about 100 feet of the profile line and were complete except for minor residual movements by the time the face had progressed about 500 feet (1.7 H) beyond the profile line.

First Panel

Surveys conducted during mining of the first panel showed the subsidence factor and angle of draw along the profile through Tower A to be within ten percent of the best estimate, which had been projected at a probability of occurrence of greater than eighty percent (Table 1). This lent credence to the predictive methods employed in this application.

At Tower A, final ground movements due to mining of the first panel were negligible and virtually imperceptible, as expected. The movements in the immediate vicinity of Tower A ranged between +/- 0.01 foot. The horizontal movements were also very small. Tower A leg tilt measurements (north-south and east-west) were less than 0.08 degree and changes in distance between Tower A legs near the groundline were less than 0.01 foot.

Second Panel

Ground movements measured at Tower A ranged from 0.08 to 0.10 feet in the downward direction; 0.171 to 0.221 feet in the longitudinal directional (parallel to the transmission line, in the direction towards the centerline of longwall panel); and 0.174 to 0.183 feet in the transverse direction (perpendicular to the transmission line, opposite to the direction of mining).

Differential movements at Tower A (relative to Leg C) ranged from 0.01 to 0.02 feet in the downward direction, 0.030 to 0.048 feet in the longitudinal direction, and 0.024 to 0.041 feet in the transverse direction. Overall, the correspondence between predicted and actual ground movements in terms of differential displacements was quite good. Actual ground movements being slightly greater than anticipated can be attributed largely to the finding by survey that Tower A was located 15 feet closer to the second panel than had been indicated by information available at the time the predictions were made.

TOWER EVALUATION DURING MINING

To ensure that any structural distress occurring during mining of the first panel (although unexpected) would be promptly recognized and acted upon, an electrical contractor experienced in work on high voltage tower structures was engaged to standby the tower over the critical three week period when the mine face would induce the most significant ground movements at the tower location.

Finite element analyses of the tower under assumed extreme ground movement led to the identification of a number of bracing members in the tower's lower body extension that were most likely

to exhibit distress, if in fact, any excessive distortion were to occur at all. The electrical contractor was directed to watch these members in particular for signs of buckling.

During the mining of Panel 1, no signs of excessive distortion of the tower members were observed. No corrective action was deemed necessary during or after mining to prepare the tower for mining of the second panel.

Based on the positive experience gained during the mining of the first panel, the standby electrical contractor was not employed on site during mining of the second panel.

FIELD VERIFICATION OF STRUCTURAL STRAINS -- THE STRAIN GAGE INSTRUMENTATION OF TOWER A

Prior to mining of the second longwall panel, GAI mounted strain gages on selected structural members of Tower A. The instrumentation included strain gage circuits on each of the four tower legs and on one horizontal strut at the bottom of the body extension directly above the legs. On Leg B two sets of strain gages were installed at different heights.

At each instrumented location, two circuits were used, one circuit to measure strain on each leg of the angle. Each circuit was constructed using two strain gages attached on perpendicular axes near the neutral axis of the member. The two gages were connected into a half bridge circuit for readout of strain. This arrangement of gages on both legs of the angle allowed for the determination of separate axial and bending strain by adding and subtracting readings, respectively. The half bridge circuits were completed in two switch and balance units that were located in fiberglass boxes at ground surface at the base of the tower. Strains were read and recorded manually using portable strain indicators. Shielded twisted-pair cable was used in making the connection. Non-inductive strain gages were used to minimize noise from electromagnetic fields.

Strain gages were bonded to the members using epoxy resin. The surface of the metal was prepared for bonding by sanding until most of the galvanizing was removed. A metal enclosure, protective tar coating, and tape were used to protect gages from weather effects.

Strain gage readings were recorded once or twice per day during the three week period that the tower was within the active zone of influence of the mine face.

Success in use of the strain gages was tempered by difficulties experienced in maintaining the electronic system operational in the harsh, moisture-laden environment at the site. Strain gage readings were sometimes spurious or lost altogether due to drift during periods of high humidity or rain as well as to locally uncompensated temperature variations and/or variations in humidity and moisture on the equipment with respect to the time of day. (The most reliable readings appeared to be those taken in late afternoon.) Some degradation in readings also occurred over time due to the delamination of gages.

In a broad sense, strains measured at particular stages of mining compared favorably with those computed by the finite element model when subjected to differential ground surface movements corresponding to those measured in the field. On this basis, it was concluded that the strain gages produce a possible means to monitor subsidence strains in the tower legs.

The strain gage system was decommissioned at the conclusion of the monitoring program. The strain gages were removed and the gage locations were resealed with paint.

STRUCTURAL ANALYSES

Pre-Mining Analyses

To investigate the effects of subsidence-related ground movements on the structural integrity of Tower A, a series of detailed stress analyses were conducted. In each analysis, the tower superstructure was subjected to a specified set of design loads and ground level displacements at the legs. The displacements included vertical and horizontal components corresponding to a specific subsidence scenario. Design loads included wind, ice, dead loads and stringing loads.

The wind forces imposed on the structure and wires were established using state-of-practice methods that are described in a document to be published by the American Society of Civil Engineers (ASCE), "Guidelines for Electrical Transmission Line Structural Loading" (draft, October 1989). The design wind speed is defined as the "fastest mile" wind speed at 33 feet (10 meters) above ground surface in flat and open terrain associated with a 50-year return period. The "fastest mile" wind speed is the typical value recorded by most Class 1 weather stations in the United States for extreme winds. It is recorded by an anemometer and is the wind speed corresponding to the shortest time for a mile of wind to pass the anemometer.

The wind direction was specified in terms of a "yaw angle" measured in a horizontal plane from a normal to the transmission line.

Under an extreme wind condition, failure of the tower would be initiated by buckling of one of the legs under compression. Initial analyses identified the tower leg that would experience maximum compression due to subsidence. The wind load was then imposed upon the tower superstructure at the yaw angle that produced the maximum additional compression of that critical leg member. Stresses computed for each member were evaluated in terms of the allowable ultimate strength of the member calculated according to ASCE Manual 52, "Guide for the Design of Steel Transmission Towers", Second Edition (1988).

For each load case, the wind velocity that would cause failure was determined based on the stress ratio in the critical leg member.

Tower A was designed to withstand winds of 80 mph. The analyses indicated that under initial (pre-subsidence) conditions, Tower A could actually be expected to withstand winds of 84 mph; this was because the actual spans between successive tower structures (B to A, A to C) were less than assumed in the original design.

The premining analyses indicated the wind capacity of the tower would be undiminished if mining were to produce the "mildest" subsidence condition but would be reduced to 82, 74, and 0 mph for the best estimate, intermediate and extreme case scenarios.

In terms of probabilities, it was estimated that the chance of Tower A's wind capacity being reduced below 80 mph was minor.

Post Mining Analyses

As expected, mining of the first longwall panel resulted in negligible ground movements in the vicinity of Tower A. The wind capacity of the tower was undiminished.

As expected, mining of the second longwall panel resulted in greater ground movements than mining of the first panel. Final ground movements at Tower 300 resulted in a reduction in the computed wind capacity of Tower A from 84 mph to 81 mph based on current design codes and as-built tower dimensions and spans. This is very close to the best estimate wind capacity of 82 mph estimated prior to mining and slightly exceeds the 80 mph design wind capacity of the tower. To further ensure that Tower A's wind capacity is preserved, the entries and cross-cuts bounding the four chain pillars nearest the tower were backfilled with cement grout injected by way of boreholes drilled from ground surface. This work was performed by Morgan Mining and Environmental Consultants, Ltd. (MMEC) and the Judy Company under separate contract to Laurel Run Mining Company.

CONCLUSIONS

- Subsidence of Tower A took place nearly as predicted. This leads us to conclude that regionally-based empirical subsidence prediction methods when calibrated in relation to subsidence data local to the site can be used to develop reasonable predictions of ground movements in three dimensions.

- Verification of predictions of horizontal and vertical ground movements by survey is necessary in order to develop a confident assessment of tower performance.

- Data from strain gages installed on selected tower members were in general agreement with strain, computed by the finite element method for conditions of known ground movements. This lends support to use of the finite element method for predicting strains and stresses in structural members under other ground movement conditions.

- Final ground movements at Tower A were achieved within 6 months following mining and resulted in a slight reduction of the wind capacity of the tower from an estimated 84 mph to 81 mph, based on current design codes and as-built tower dimensions and spans. The original design wind speed for the tower was 80 mph. Thus, the effect of longwall mining alongside the tower was negligible.

- The structural reliability of Tower A under the effects of subsidence has remained acceptable by standards used in current transmission line design. The analysis did not account for the beneficial effect of possible slippage of joints between structural members and the consequent relief of subsidence-induced stresses. This is conservative.

- No post-mining mitigation procedures needed to be performed on the tower superstructure. The act of loosening and retightening bolts to relieve the minor subsidence-induced stresses that may have developed would be complicated by the need to provide structural support while loosening certain joints. The procedure could lead to more risk than if no mitigation were performed.

- The tower leg relative displacements were less than what would be normal framing eccentricities. If for the undermining of other towers the relative movements between tower legs exceed normal framing eccentricities, then additional criteria need to be defined for allowable movements in the tower legs.

Table 1

COMPARISON OF PREDICTED AND ACTUAL GROUND MOVEMENTS APPROXIMATE TO TOWER A

Parameter	Predicted	Actual
Mined Height, m	7.25 feet (assumed)	7.1 to 7.3 feet
Subsidence Factor, a = S/m	0.6 (best) 0.68 (conservative)	0.55
Maximum Subsidence above panel	4.35 feet (best) 5-5.5 feet (conservative)	4 feet
Angle of Draw	18-20 degrees	18-20 degrees

FIGURE 1 - TOWER A

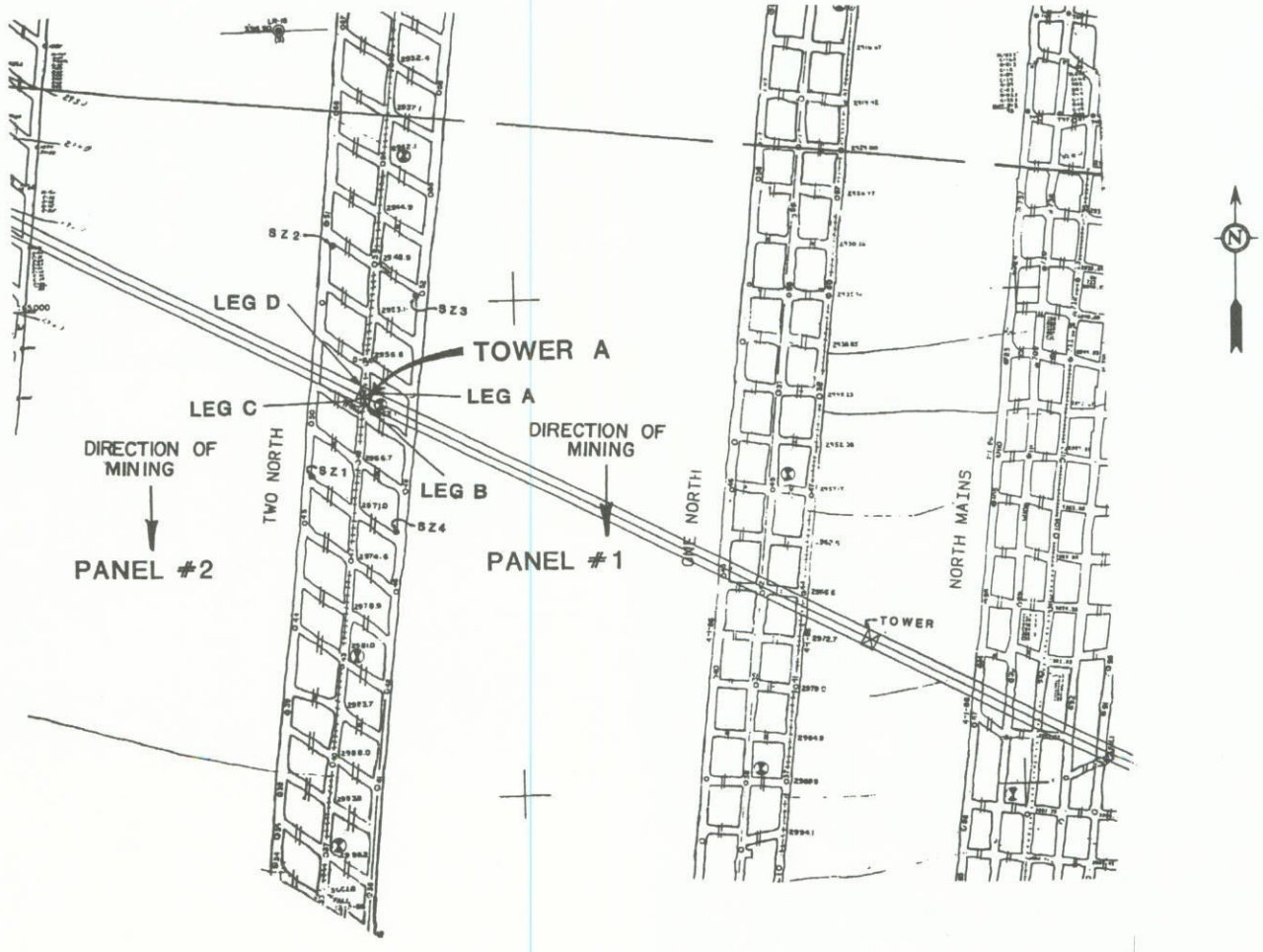

FIGURE 2 - LOCATION OF TOWER A ABOVE MINE WORKINGS

AUTHOR'S INDEX

Anderson, R. P., 52
Awasthi, R., 233
Aziz, N. I., 243

Basar, C., 26
Barczak, T. M., 35
Boltenhagen, I. L., 268
Bruhn, R. W., 301

Choquet, P., 96
Conover, D. P., 202
Cybulski, J. A., 85

Doney, E. D., 212
Dolinar, D. R., 76
Drumm, E. C., 233

El-Sageer, H. A., 263

Farmer, I. W., 177
Ferrell, J. R., 301
Forgeron, S., 96
Forrester, D. J., 220

Gallant, W. D., 96, 220
Geldmacher, I., 130
Gray, T. A., 301
Gray, W. J., 85
Guo, H., 243

Haycocks, C., 161
Haycocks, S. G., 161
Heasley, K. A., 122, 151

Ichinose, M., 43
Irvin, R. A., 177

Jones, J. R., 151

Karmis, M., 161
Khair, A. W., 14
Krupa, E. D., 14
Kurlenya, M. V., 268

Liang, Y. H., 167
Luo, Y., 212
Luxbacher, G. W., 301

MachLachlan, J., 96
Mark, C., 1
Matsui, K., 43
Mitri, H. S., 90
Molinda, G. M., 151

O'Connor, K. M., 115
Oyler, D. C., 35, 151
Ozel, R., 26

Payne, D. A., 220
Peng, S. S., 212, 272
Peters, D. C., 184
Popov, S. N., 268
Powell, L. R., 233
Prasad, D., 281

Qian, M. G., 59

Rafiqui, M. A., 281
Rajaie, H., 90
Rashad, M. Z., 263
Reddish, D. J., 225
Repsher, R. C., 257
Rossi, G., 243
Rossi, R., 243

Schotsch, J. G., 144
Singh, R., 281
Singh, T. N., 281
Slade, J., 130
Smith, M. A., 184
Stankus, J. C., 65
Su, D. W. H.
Sutton, T., 144

Tadolini, S. C., 76
Tan, X. S., 272
Travis, B. E., 52
Trois, P., 243

Uchino, K., 43
Unal, E., 26
Unrug, K. F., 194

Vandergrift, T. L., 202

Wan, M., 59
Whittaker, B. N., 225
Wilson, H. G., 103

Xiao, G. C., 177

Yao, C. S., 167
Yao, X. L., 225

Zhang, Y. J., 194
Zhou, B. W., 161
Zhou, Y., 161
Zhu, D. R., 59
Zimmerly, T., 115

Ground
Control
in
Mining